# FRACTURE AND TOUGHENING OF HIGH VOLUME FRACTION CERAMIC PARTICLE REINFORCED METALS

THÈSE N$^{O}$ 2703 (2002)

PRÉSENTÉE À LA FACULTÉ SCIENCES ET TECHNIQUES DE L'INGÉNIEUR

SECTION DES MATÉRIAUX

ÉCOLE POLYTECHNIQUE FÉDÉRALE DE LAUSANNE

POUR L'OBTENTION DU GRADE DE DOCTEUR ÈS SCIENCES

PAR

Ali Gilles Tchenguise MISEREZ

ingénieur en science des matériaux diplômé EPF
de nationalité suisse et originaire de Lajoux (JU)

acceptée sur proposition du jury:

Prof. A. Mortensen, directeur de thèse
Prof. F. Delannay, rapporteur
Prof. J. Giovanola, rapporteur
Prof. A. Pineau, rapporteur

Lausanne, EPFL
2003

# Remerciements

Un travail de thèse n'est jamais l'oeuvre d'un seul individu. Nombre de personnes doivent ici être remerciées chaleureusement pour les diverses contributions qu'elles auront apportées à ce travail, qui a été financé par le Fonds National pour la Recherche Scientifique, sous projets N° 20-55291.98 et 2000-63575.00. En premier lieu, mon directeur de thèse, Andreas Mortensen, qui m'a acceuilli au sein de son laboratoire et m'a guidé au cours de ces quatre années, tout en me laissant la liberté d'action nécessaire à un travail de recherche. Je le remercie ici pour la rigueur scientifique qu'il m'a enseigné et pour la confiance qu'il m'a accordé. Je lui suis aussi gré d'avoir toujours été disponible lorsque, souvent, je passais la porte de son bureau à l'improviste.

Les membres du jury, Messieurs Francis Delannay, Jacques Giovanola et André Pineau ont pris le temps, en dépit d'agendas chargés, de lire en détail le rapport final, d'y apporter leurs remarques constructives, de le critiquer, de corriger même parfois les multiples imperfections de mon anglais. Je les en suis sincèrement reconnaissant, de même qu'au directeur de l'Institut des Matériaux, Monsieur Jan-Anders Manson qui a eu l'amabilité de présider le jury.

J'ai eu la chance de pouvoir compter sur un encadrement scientifique idéal au sein du laboratoire; je salue donc ici le soutien que m'a apporté le "post-doc team" constitué de Chris "Dude" San Marchi, Andreas "Charpy" Rossoll et Ludger "Gaudi" Weber. Sans Chris, je serais peut-être à l'heure actuelle encore en train de fabriquer mon premier composite; Andreas a effectué toutes les simulations par éléments finis, sans compter nos innombrables discussions animées qui auront eu le mérite de constamment remettre en doute des certitudes parfois trop confortables; enfin je ne compte pas les heures que Ludger m'a accordées afin de me faire bénéficier de ses talents hors-pair dans le domaine des tests mécaniques.

Les moments de découragement d'une thèse sont nettement plus faciles à surmonter lorsque l'environnement de travail est chaleureux, ce qui ne fût jamais démenti au sein du LMM. Tout d'abord avec mes deux collègues de projet, soit successivemement Marianna et Rando, avec qui ce fût toujours un plaisir de collaborer sur les multiples aspects du projet, et en-dehors de celui-ci aussi ! Les autres collègues doctorants du LMM ont également largement contribué à l'ambiance unique qui règne au sein du laboratoire. Merci à Laurent et Jean-François, pour les innombrables activités, fêtes, repas partagés en commun, merci aussi pour leur tolérance face à mon caractère quelque fois contestataire. Dans le même ordre d'idée, merci aussi aux derniers arrivés, Arnaud et Cédric. Pour tout problème technique, pièce manquante, etc... une seule adresse, Goekhan, que je remercie pour tous les divers problèmes techniques qu'il m'a aidé à résoudre, toujours dans la bonne humeur. Enfin, je ne saurais oublier notre secrétaire Mme Zanetta, sa gentillesse et sa patience à résoudre moult problèmes administratifs.

Au sein de l'Institut (ex Département) des Matériaux, je tiens également à remercier:

- tous les membres de l'atelier pour les multitudes de travaux qu'ils ont pu fournir, plus particulièrement Louis Masson à qui je ne compte pas les travaux demandés "dans l'urgence", et Eric

Vassalli qui a fait de véritables miracles pour usiner toutes les éprouvettes par électroérosion, éprouvettes qu'il devait ensuite se résigner à voir lâchement cassées lors des tests mécaniques;

- Philippe Buffat, du Centre Interdépartemental de Microscopie Electronique (CIME), pour l'aide apportée lors des premières reconstructions stéréographiques, et qui sur cette base, a ensuite acquis le logiciel de reconstruction;
- Pedro Möckli, du laboratoire de Céramique (LC), pour les mesures de diffraction par rayon-x;
- Didier Léonard, du laboratoire de Métallurgie Chimique (LMCH), pour le temps qu'il m'a accordées lors des mesures par TOF-SIMs données en annexe;
- Enfin, les étudiants que j'ai encadrés au cours de leurs projets de semestre, Stephan Stücklin, Samuel Rey-Mermet et Florian Jeanrichard, qui, par leurs questions pertinentes et leur intérêt, auront contribué à approfondir mes propres connaissances du sujet; je suis également reconnaissant à Stephan de m'avoir laissé à disposition quelques unes des images obtenues lors de son travail de diplôme.

Je tiens ici aussi à exprimer ma plus profonde reconnaissance envers toute ma famille, mes parents Firouzeh et Jean-Jacques, et ma soeur Leyla, pour les valeurs qu'ils m'ont inculqué, et pour leur appui financier et moral au cours de mes études, puis durant tout le déroulement de cette thèse; de même que mon frère Teymour avec qui j'ai partagé mon appartement à Lausanne. Que ce dernier m'excuse de mes humeurs parfois maussades, au sortir de journées de labo au cours desquelles j'accumulais les échecs.

Enfin pour le soutien moral, pour les bons petits plats mijotés tard dans la soirée après de longues journées durant la phase de rédaction, pour la patience, et pour tout le reste encore, grazie per tutto Lucia.

# ABSTRACT

This work contributes to the fundamental understanding of fracture properties of Particle Reinforced Metal Matrix Composites (PRMMCs), by identifying the key microstructural parameters that control fracture.

To this end, PRMMCs with a high volume fraction of ceramic reinforcement (40 - 60 vol.%) are produced by gas-pressure infiltration. These composites are considered as model ductile/brittle two-phase materials in that (i): the particles are homogeneously distributed in the matrix, (ii): the matrix microstructure is kept simple, and (iii) the composites are free of processing defects. The reinforcements used are alumina ($Al_2O_3$) particles of various shape (angular, polygonal) and size (5 to 60 µm), and boron carbide ($B_4C$) particles (5 to 60 µm). The matrix materials are (i): pure Al, (ii): Al-Cu2% alloy, and (iii): Al-Cu4.5% alloy, all being chosen in order to obtain a single-phase matrix (Cu in solid-solution for the Al-Cu alloys), and to minimize chemical reactivity with the reinforcement.

Pure Al matrix composites exhibit marked *R*-curve behaviour; they are characterized by *J*-integral fracture testing. The fracture toughness increases with the interparticle distance. At a given particle size, polygonal $Al_2O_3$ particle composites are the toughest, followed by $B_4C$ particle composites, and by angular $Al_2O_3$ particle composites. Al-Cu matrix composites feature a flatter *R*-curve, and are tested by a Linear Elastic Fracture Mechanics (LEFM) method: the chevron-notch test. Again, polygonal particles yield tougher composites than angular ones. In the as-cast condition, coarse intermetallics formed at the interface matrix/reinforcement during solidification are strongly detrimental to the toughness. After heat-treatment, on the other hand, toughness of the alloyed matrix composites is improved and increases as the matrix is strengthened by raising the Cu content in the matrix.

Using an arrested-crack technique, it is found that the dominant micromechanisms of fracture of pure Al matrix composites are strongly dependent on the particle type, shape and size: the stronger the reinforcement, the more the crack tends to propagate by a ductile mechanism of nucleation, growth, and coalescence of micro-cavities. With weaker particles, cracking of the composite is promoted by premature particle cracking. A stereoscopic method coupled with Scanning Electron Microscopy (SEM) imaging is used to reconstruct the fracture surfaces in 3D. The final dimple size (diameter, depth) is found to depend on the microstructural length scale of the composites, *i.e.* the interparticle distance. Data obtained from two types of measurement (quantitative metallography, dimple depth) are used to estimate the local energy necessary to create the fracture profile, by using simple micromechanical models.

At the *global* scale, surface strain fields are revealed by photoelasticity. The observed crack-tip strain fields are fully confirmed by 3D Finite Element (FE) computations. Although most of the fracture energy is spent in the plastic zone, it is shown that toughness is controlled by the *local* fracture energy that is dissipated in the crack-tip process zone: the macroscopic fracture toughness is an “amplification” of the local fracture energy. This simple and linear correlation breaks down when, for a given ceramic particle type and size, a transition in the dominant micromechanism of fracture occurs as the matrix is strengthened. The local/global correlation is discussed in more detail, using a simplified approach based on the Cohesive Zone Model (CZM) for ductile fracture: the fundamental parameters allowing to achieve attractive toughness are identified as: (i) the intrinsic particle strength, and (ii) the high local stress triaxiality between the closely spaced particles, made possible by the strong interfacial bonds between matrix and reinforcement.

Overall, the composites feature very high toughness for materials made of up to 60 vol.% of brittle phase. The toughest pure Al matrix composites feature a $K_{\mathrm{Jeq}}$ as high as 40 MPa·m$^{1/2}$. For Al-Cu matrix composites, $K_{\mathrm{Iv}}$ (the plane-strain chevron notch fracture toughness) exceeds 30 MPa·m$^{1/2}$ (a value, to our knowledge, never reported for this class of materials) together with a Young's modulus of 180 GPa, a yield strength of 400 MPa and an ultimate tensile strength approaching 500 MPa. This combination of values gives an interesting potential for these composites as engineering materials.

# VERSION ABRÉGÉE

Ce travail contribue à la compréhension fondamentale des propriétés en rupture des matériaux composites à matrice métallique (CMMs) renforcés par des particules céramiques, en identifiant les principaux paramètres microstructuraux contrôlant la ténacité de ces matériaux.

Dans cette optique, des CMMs à haute fraction volumique de renforts particulaires (40 - 60 % vol.) sont fabriqués par infiltration sous haute pression de gaz. Ces composites sont considérés comme des matériaux bi-phasés fragile/ductile “modèles”, dans le sens que (i): les particules sont distribuées de manière homogène dans la matrice, (ii): cette dernière présente une microstructure simple et (iii): les composites sont exempts de défauts d’élaboration. Les renforts utilisés sont des particules céramiques d’alumine ($Al_2O_3$) de formes diverses (angulaires et polygonales) et de tailles variant de 5 à 60 µm, et des particules de carbure de bore ($B_4C$). Les matériaux de matrice sont choisis dans le but d’obtenir une microstructure monophasée de la matrice, ainsi que de minimiser les éventuelles réactions chimiques avec les renforts durant la fabrication. L’aluminium pur et des alliages d’Al-Cu permettant une solubilité complète du cuivre dans l’aluminium sont utilisés.

Les composites à matrice Al pur présentent un comportement en courbe *R*, et leur ténacité est mesurée au moyen d’essais d’intégrale *J*. La ténacité augmente avec la distance interparticulaire. A taille donnée de particules, les composites à particules polygonales d’$Al_2O_3$ sont les plus tenaces, suivis des composites à particules de $B_4C$, alors que les composites à particules d’$Al_2O_3$ angulaires sont les moins tenaces. Les composites à matrice Al-Cu ont un comportement en courbe *R* moins marqué. Leur ténacité est mesurée au moyen d’une méthode de la mécanique de la rupture en élasticité linéaire, en utilisant des échantillons à entaille “chevron”. Les composites à particules polygonales présentent également de meilleures ténacités que ceux à particules angulaires. A l’état brut de coulée, des intermétalliques se formant à l’interface matrice/renfort au cours de la solidification sont préjudiciables pour les propriétés en rupture. Après traitement thermique en revanche, la ténacité est nettement améliorée et augmente lorsque la concentration de cuivre dans la matrice augmente.

Une méthode d’arrêt de propagation de fissure est utilisée pour déterminer les micromécanismes dominants de fissuration. Dans les composites à matrice d’Al pur, ils dépendent du type, de la forme et de la taille des particules. Plus les renforts sont résistants, plus la fissure tend à se propager par un mécanisme ductile de germination, croissance et coalescence de cavités au sein de la matrice. Lorsque les renforts sont plus fragiles, la fissure se propage par rupture des particules et cavitation entre particules cassées. Une méthode de stéréoscopie est associée avec des images prises au microscope électronique à balayage (MEB) pour reconstruire les faciès de rupture en 3D. La taille finale des cavités (diamètre, profondeur) est directement déterminée par l’échelle de la microstructure, en d’autres termes par la distance interparticulaire. Les valeurs obtenues par les deux types de mesures (métallographie quantitative et profondeur de cavités) sont utilisées pour estimer l’énergie locale de création de surface de rupture, au moyen d’analyses micromécaniques.

A l’échelle *globale*, les champs de déformation de surface en pointe de fissure sont observés par photoélasticité. Les observations sont confirmées au moyen de calculs par éléments finis en trois dimensions. Bien que la majeure partie de l’énergie de rupture soit dépensée dans la zone plastique en pointe de fissure, on montre que la ténacité est contrôlée par l’énergie *locale* de rupture dissipée dans la zone d’endommagement. En d’autres termes, la ténacité macroscopique est une “amplification” de l’énergie

locale de rupture. Cette relation simple n'est pas complètement confirmée, lorsque pour des renforts de type et de taille donnés, une transition du micromécanisme de propagation de fissure a lieu quand la contrainte d'écoulement est augmentée. De ce fait, la corrélation locale/globale est discutée avec plus de détails, en se basant sur les modèles d'une zone cohésive. Les paramètres fondamentaux qui ressortent de cette analyse simplifée en vue d'obtenir des matériaux à relativement haute ténacité sont: (i) la résistance intrinsèque des particules et (ii): la forte triaxialité locale des contraintes entre les particules rigides finement espacées, elle-même résultante des liaisons fortes aux interfaces matrice/renforts.

En termes quantitatifs, les composites présentent des ténacités très élevées pour des matériaux contenant une phase fragile à hauteur de 60% vol. Les composites à matrice d'Al pur les plus tenaces sont caractérisés par une valeur de $K_{\mathrm{Jeq}}$ de 40 MPa·m$^{1/2}$. Pour les composites à matrice d'Al-Cu, des valeurs de $K_{\mathrm{Iv}}$ (ténacité chevron mesurée en conditions de déformation plane) dépassant 30 MPa·m$^{1/2}$ sont mesurées (des valeurs qui à notre connaissance n'ont jamais été obtenues auparavant pour cette classe de matériaux). Couplées avec des valeurs du module d'Young de 180 GPa, des limites élastiques de 400 MPa et des résistances maximales approchant 500 MPa, ces ténacités en font des matériaux prometteurs pour diverses applications structurelles.

# TABLE OF CONTENTS

## CHAPTER 1: INTRODUCTION

**1.1 OVERWIEW** **1**

**1.2 METHODOLOGY** **2**

**1.3 ORGANIZATION OF THE THESIS** **3**

## CHAPTER 2: LITERATURE REVIEW

**2.1 PARTICLE REINFORCED MMCS** **5**

- *2.1.1 Overview* **5**

**2.2 PARTICLE REINFORCED MMCS: PROCESSING** **10**

- *2.2.1 Solid state processing* **10**
- *2.2.2 Liquid state processing* **11**

**2.3 FRACTURE TOUGHNESS OF PRMMCS: REVIEW OF EXPERIMENTAL DATA** **22**

- *2.3.1 Summary of existing reviews* **22**
- *2.3.2 Testing procedures* **24**
- *2.3.3 Effects of particle volume fraction and particle clustering* **25**
- *2.3.4 Effects of the reinforcement* **27**
- *2.3.5 Effects of matrix alloy and microstructure* **29**
- *2.3.6 Extrinsic factors influencing fracture toughness: specimen geometry and stress state* **31**
- *2.3.7 Typical data* **34**
- *2.3.8 Summary and comments* **35**

**2.4 MICROMECHANICAL MODELS OF FRACTURE TOUGHNESS IN PRMMCS** **36**

- *2.4.1 Rice and Johnson based approaches* **36**
- *2.4.2 Hahn-Rosenfield models* **37**
- *2.4.3 Fractography-based models* **39**
- *2.4.4 Energy based models: work spent in the plastic zone* **40**
- *2.4.5 Summary and comments* **40**

**2.5 LOCAL AND GLOBAL FRACTURE ENERGY** **42**

- *2.5.1 Approach of Hirth and Froes* **42**
- *2.5.2 Approach of Gerberich* **44**
- *2.5.3 Approach by Mortensen for the case of PRMMCs* **45**
- *2.5.4 Cohesive zone models (CZMs)* **45**
- *2.5.5 Additional comments and summary* **48**

**2.6 LOCAL MODELS OF FRACTURE FOR MATERIALS SIMILAR TO PRMMCS** **49**

*2.6.1 The work spent to form a ductile fracture surface* **49**
*2.6.2 Toughness of hard refractory alloys (WC-Co composites)* **52**
*2.6.3 Brittle materials toughened by ductile-phase particles* **56**
*2.6.4 Summary and comments* **61**

# CHAPTER 3: EXPERIMENTAL PROCEDURES

**3.1 MATERIALS PROCESSING** **63**

*3.1.1 Selection and characteristics of the constituents* **63**
*3.1.2 Preform preparation* **65**
*3.1.3 Gas-pressure infiltration* **67**

**3.2 MICROSTRUCTURAL CHARACTERIZATION** **70**

*3.2.1 Metallography* **70**
*3.2.2 Volume fraction determination* **70**
*3.2.3 Interparticle distance* ***71***
*3.2.4 Determination of reaction phases* **71**
*3.2.5 Analysis of secondary phases in Al-Cu matrix composites* **72**

**3.3 MECHANICAL TESTING** **74**

*3.3.1 Aging curves and heat-treatments* **74**
*3.3.2 J-Integral fracture toughness testing* **74**
*3.3.3 Observation of crack-tip plastic zones by photoelasticity* **80**
*3.3.4 Chevron-notched fracture testing* **82**
*3.3.5 Tensile testing* **85**

**3.4 OBSERVATION AND QUANTIFICATION OF THE MICROMECHANISMS OF FRACTURE** **87**

*3.4.1 Arrested crack technique* **87**
*3.4.2 Fractography* **88**
*3.4.3 Three-dimensionnal reconstruction of fracture surface topography* **89**

# CHAPTER 4: RESULTS

**4.1 MICROSTRUCTURAL CHARACTERIZATION** **91**

*4.1.1 Powder characteristics* **91**
*4.1.2 Metallography* **92**
*4.1.3 Al-Cu matrix composites* **98**

**4.2 J-INTEGRAL FRACTURE TESTING** **101**

*4.2.1 J-R curves: General characteristics* **101**
*4.2.2 Effect of reinforcement type (chemistry, size, and shape)* **103**
*4.2.3 Influence of specimen geometry* **111**
*4.2.4 Al-Cu matrix composites* **114**
*4.2.5 Summary of data* **116**
*4.2.6 Pure Al matrix composites: fracture micromechanisms* **120**

**4.3 PHOTOELASTIC PATTERNS OF THE CRACK TIP PLASTIC ZONE** **133**

*4.3.1 Sample with notched coating* **134**
*4.3.2 Sample with unnotched coating* **134**
*4.3.3 Deformation fields during fracture testing: comparison of the composites* **137**
*4.3.4 Residual strains after final fracture* **140**

**4.4 AGEING AND TENSILE BEHAVIOUR OF AL-CU MATRIX COMPOSITES** **142**

*4.4.1 Ageing characteristics and macrohardness* **142**
*4.4.2 Tensile flow curves* **143**

**4.5 CHEVRON-NOTCH FRACTURE TESTING** **146**

*4.5.1 Angular-alumina composites* **146**
*4.5.2 Polygonal alumina composites* **147**
*4.5.3 Data summary* **149**
*4.5.4 Al-Cu matrix composites: micromechanisms of fracture* **151**

## CHAPTER 5: DISCUSSION

**5.1 THE GLOBAL FRACTURE ENERGY** **159**

*5.1.1 The crack tip plastic zone* **159**
*5.1.2 Comparison of chevron and J-integral fracture testing in Al-Cu matrix composites* **167**

**5.2 THE LOCAL FRACTURE ENERGY** **170**

*5.2.1 Experimental evidence* **170**
*5.2.2 Matrix flow stress* **170**
*5.2.3 Local fracture energy: approach based on the final fracture process* **173**
*5.2.4 Local energy: Influence of constraint between particles* **185**
*5.2.5 Local energy: particle cracking* **189**

**5.3 TOUGHENING MECHANISMS: INTERPLAY OF LOCAL AND GLOBAL PROCESSES** **194**

*5.3.1 Preliminary remarks* **194**
*5.3.2 Local/global fracture energy relationship* **194**
*5.3.3 Influence of particle fracture* **196**
*5.3.4 Implications* **201**

**5.4 HOW TO PRODUCE TOUGH PRMMCS ?** **203**

*5.4.1 The role of the reinforcement* **203**
*5.4.2 The role of the matrix* **204**
*5.4.3 The role of the interfacial strength* **206**
*5.4.4 The role of processing* **207**
*5.4.5 Comparison of present composites with data from the literature* **207**

# CHAPTER 6: CONCLUSIONS AND PERSPECTIVES

**6.1 CONCLUSIONS** **209**

**6.2 FUTURE WORK** **211**

*6.2.1 Processing* **211**
*6.2.2 Micro and Macro-mechanical characterization* **211**
*6.2.3 Modeling* **212**

**BIBLIOGRAPHY** **213**

# APPENDICES

**A. FRACTURE MECHANICS: BASIC THEORY AND CONCEPTS** **1**

**A.1 Linear-elastic fracture mechanics (LEFM)** **1**

*A.1.1 Energy approach* **1**
*A.1.2 Stress approach* **2**
*A.1.3 Crack tip plasticity* **4**
*A.1.4 Rising crack growth resistance ("R-curve behaviour")* **6**
*A.1.5 Limitations of LEFM* **7**

**A.2 Elastic-plastic fracture mechanics (EPFM)** **8**

*A.2.1 The J-contour integral* **8**
*A.2.2 J as a stress intensity parameter: the HRR field* **9**
*A.2.3 CTOD and equivalence with J* **10**
*A.2.4* $J_{Ic}$ *and the crack growth resistance curves (J-R curve)* **11**
*A.2.5 Limitations of EPFM and recent developments* **12**

**B. PRE-CRACKING CONDITIONS** **17**

**C. SOLUBILITY OF BORON IN ALUMINIUM** **19**

*C.1 Experimental procedure* **19**
*C.2 Results* **19**

**BIBLIOGRAPHY OF APPENDICES** **21**

# CHAPTER 1

# INTRODUCTION

## 1.1. OVERVIEW

The general term “metal matrix composite” (MMC) refers to a specific class of materials that combines a contiguous metallic matrix, and a second phase, often a ceramic, that is added in processing the composite material. Depending on the form of the ceramic phase, MMCs are further subdivided into: (i) long fiber (or continuously reinforced) MMCs; (ii) short fiber and whisker reinforced MMCs; and (iii) particle reinforced (or discontinuously reinforced) MMCs [1].

As in any type of composite materials, the motivation behind the fabrication and the use of MMCs lies in the possibility of combining constituent materials with very different characteristics, thereby obtaining a profile of properties that is otherwise not offered by monolithic materials. For the specific case of MMCs, the ductility and formability of the metallic matrix are important characteristics in the view of toughening the composite; while the utility of strong ceramic reinforcements is to carry a high portion of the stress when the composite is subjected to an external load, and hence to achieve overall superior mechanical properties such as strength and stiffness compared to the matrix alloy. Among other mechanical performance advantages of these composites compared to conventional alloys, one can cite a higher elevated temperature stability as well as a better wear resistance.

For the matrix, aluminium and its alloys have received most attention in both research and industrial applications, because of the following main advantages compared to other matrix systems: relative low cost, low density, limited reactivity compared to other light-weight alloys such as magnesium or titanium, easier machinability and low melting point facilitating liquid state processing. Such composites thus present excellent strength/density or stiffness/density ratios that make them viable candidates in fields such as aerospace, the automotive industry or sport goods [2-6]. Besides structural applications, MMCs also offer unique combination of good electrical and thermal conductivity coupled with low thermal expansion, which gives them a very high application potential in electronic packaging and thermal management [7, 8].

Among the different classes of MMCs, particulate reinforced MMCs (PRMMCs) are certainly those that have been the most widely developped in the past twenty years, due to the relatively low cost of both the reinforcement and the production method compared to long fiber composites, and also because of their generally isotropic properties. Despite promising performance and success in some niche applications, PRMMCs suffer from two main drawbacks that have limited their utilization to a larger scale compared to conventional light-weight alloys: (i) they remain non-competitive from a cost standpoint, and (ii) in terms of mechanical performance they exhibit relatively poor fracture properties, namely low ductility and toughness. This latter point, which is crucial in the view of using these materials in structural applications, is the subject of this thesis.

Intuitively, it is clear that the intrinsic brittle behaviour of the reinforcement should reflect on the overall toughness of the composite, causing an embrittlement as compared to its matrix. Research to date has indeed identified mechanisms at the microstructural level that are responsible for this degradation, at least in a qualitative matter. The effect of main microstructural variables such as the type and size of the reinforcement or the composition and heat-treatment of the matrix have been widely studied and documented in the past two decades. However, clear tendencies on the effect of these variables on the fracture toughness have not yet emerged, mainly because most studies have been conducted on industrially available materials, in which several microstructural features and defects are not controlled. In many cases, it then becomes ambiguous to decide whether data should be explained in terms of a given microstructural variable or by other uncontrolled parameters (for instance oxide inclusions, intermetallic or reaction phase at the matrix/reinforcement interface). Such factors have thus complicated the task of understanding at a fundamental level the mechanisms leading to the relatively poor fracture properties of these composites, such that the prediction of their toughness by micromechanical models is still an open question in the research community. This is emphasized in two of the main reference books devoted to the topic of metal matrix composites, where it is stated that “understanding and predicting fracture toughness of particulate composites has not been achieved yet, specifically for the ceramic-reinforced aluminium alloy materials” and that “neither adequate experimental nor theoretical assessment is available” [9]; or that “fracture toughness models can, for certain cases, produce answers in fair agreement with experimental data; however no current model is really satisfactory” [1].

## 1.2. METHODOLOGY

In this work, the fracture of PRMMCs was studied using the following approach: composites were processed in-house by gas-pressure infiltration method, which permits to obtain materials free of typical defects traditionally observed with other techniques. In a first stage, pure aluminium was used as a matrix material, and reinforcements were ceramic particles of boron carbide ($B_4C$) or of alumina ($Al_2O_3$) of controlled shape and size. These were hence “model materials” in the sense that microstructural variables were kept simple and were systematically controlled: particles were homogeneously distributed within the matrix, with a volume fraction in the range of 40 to 60 %. The room-temperature toughness was systematically measured on each composite by standard techniques of fracture mechanics, while the micromechanisms of fracture were identified and quantified via various microscopic techniques. The primary aim was to study, without ambiguity, the influence of fundamental variables such as particle chemistry, type and size, in a way that clear tendencies could emerge, and then to link fracture toughness results with observed fracture micromechanisms.

In a second step, composites with stronger aluminium-copper alloys matrices were produced and tested with similar techniques, with the aim to understand the role of the matrix flow stress on the toughness of PRMMCs. Here again, the matrix was kept as homogeneous as possible by using binary eutectic alloys in which complete solution of Cu into Al can in principle be attained, such that the presence of second-phases is minimized.

Overall, the goal of the project was to clarify the role played by key microstructural variables on the fracture of particle reinforced metals and to explain what toughness could be expected for a certain combination of initial constituents, using current micromechanical models for the toughness of similar materials. From the engineering point of view, the aim of the work was also to use our fundamental observations to significantly improve the fracture properties of high volume fraction PRMMCs and thereby show their potential for use in structural applications.

## 1.3. ORGANIZATION OF THE THESIS

In the literature review, Chapter 2, first a general description of PRMMCs and of their processing methods is introduced. We then review in more detail the fracture toughness of PRMMCs. Existing models for predicting the toughness of these materials is presented. The literature review is concluded by presenting micro-mechanical modeling approaches for materials exhibiting similar features -in terms of microstructure and fracture behaviour- to the PRMMCs fabricated in this work.

Experimental procedures are described in detail in Chapter 3. These comprise composite fabrication, mechanical testing, and observation methods used to investigate the micromechanisms of fracture.

The results are presented in Chapter 4. General features of the microstructure (particle distribution, volume fraction, second-phases in alloyed matrices) are introduced. Presentation of the results is then divided into three sections. The first comprises *J*-integral fracture testing on pure aluminium matrix composites, as well as detailed investigations of the micromechanisms of fracture in these composites. Next, we present observations of crack-tip deformation zones in the course of *J*-integral fracture testing. The third part is concerned with properties of Al-Cu alloy matrix composites, including general a assessment of their tensile behaviour and more detailed investigations of their fracture behaviour by the means of chevron-notch fracture testing. Determination of fracture micromechanisms in Al-Cu matrix composites is also included in this section.

The discussion, Chapter 5, is divided into four main parts. The first is concerned with the global fracture energy spent by plastic dissipation at the crack tip. Here we compare experimental observations with analytical strain fields and finite element computations in three dimensions. Then, the local fracture energy spent in creating the microfracture surface is estimated, based on the experimental determination of the micromechanisms of fracture, and on simple micromechanical analysis. Such calculations are then systematically compared with the macroscopic toughness. In the third part of the discussion, the link between this local work of fracture and the global fracture energy (or toughness) is discussed. The last part of the discussion is devoted to engineering materials aspects, *i.e.* what features of the microstructure and how processing of these composites have to be tailored in order to produce tough PRMMCs.

A general conclusion and perspectives are given in the last chapter.

# CHAPTER 2

# LITERATURE REVIEW

## 2.1. PARTICLE REINFORCED MMCS

### *2.1.1 Overview*

The development of particle reinforced metal matrix composites (PRMMCs), also called discontinuously-reinforced metal matrix composites (DRC), started about 30 years ago; however, it is in the 1980s that the field gained increasing interest in the research community. This led to the development of commercial products made out of these materials, which have now been available in a significant amount for about fifteen years. The first composites of this type were initially developed as Al-based alloy reinforced with silicon carbide particles (SiC), featuring high modulus and available in large quantities at relatively low prices from the abrasive industry.

**i. Reinforcements**

The distinction between PRMMCs and other type of metal-based composites (namely long fiber and short fiber reinforced composites) is based on the type of reinforcement: the ceramic particles (or particulates) exhibit a roughly equiaxed geometry or at least a low aspect ratio (typically less than 5) and their average size falls in the range of 1 to 100 µm. The most common particle materials employed are silicon carbide (SiC) and alumina ($Al_2O_3$); however many other candidate reinforcements have been studied, including boron carbide ($B_4C$), titanium carbide (TiC), titanium diboride ($TiB_2$), zirconia ($ZrO_2$), or graphite. The shape of the particles may be spherical, angular, platelike, polygonal, or irregular. A schematic distinction of the different types of MMCs and the geometry of the particles is shown in Figure 2-1.

The volume fraction of reinforcements varies over a quite broad range, from 5 to 75 %, and is greatly dependent on the processing method, as will be seen later. Reinforcing particles in composites should ideally present some intrinsic attributes in order to create an MMC with attractive mechanical performance. These are (i) high stiffness, (ii) low density, (iii) high hardness, and (iv) (comparatively) high strength and toughness. In order to reduce the global cost of the composites, availability and cost are also important factors; these are actually the main reason why SiC and $Al_2O_3$ have attracted most of the attention, their other mechanical performance being also quite attractive. Principal mechanical properties of the main ceramic reinforcements used in the fabrication of PRMMCs are summarized in Table 2-1.

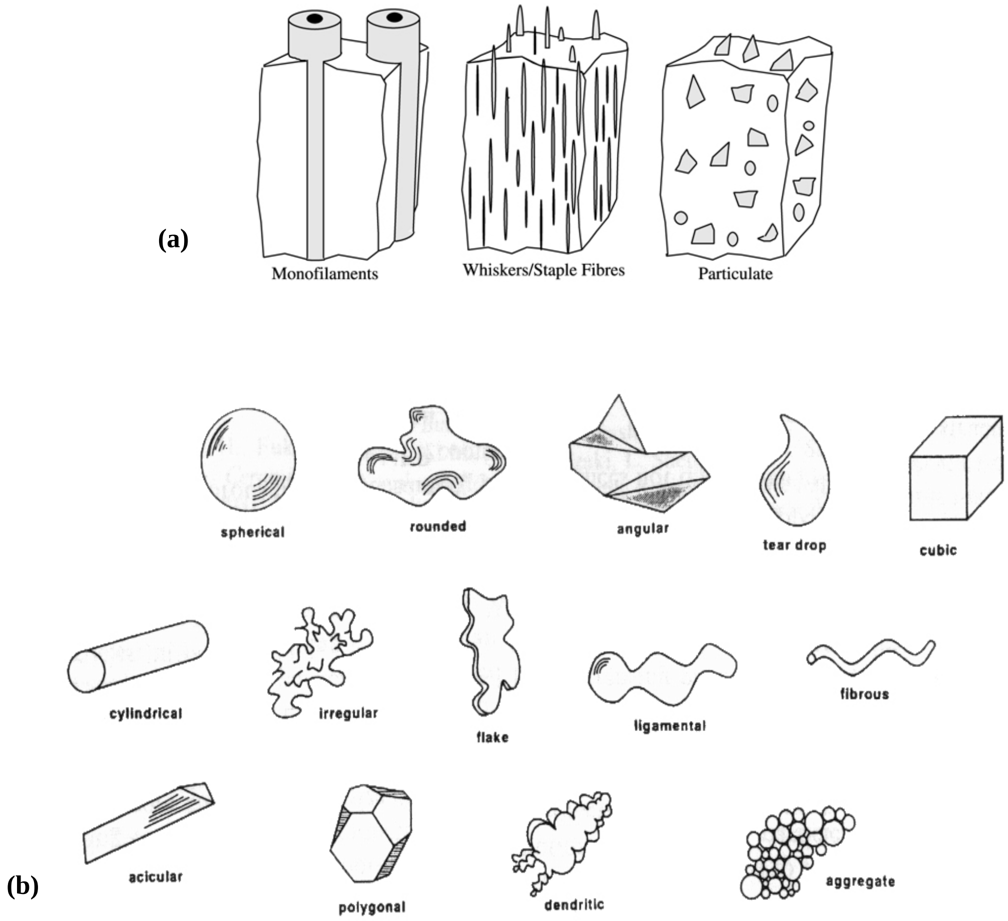

**Figure 2-1.** **(a)**: Schematic view of the different MMC systems, from [1]; **(b)**: definition of particle morphologies from [10].

In addition to these features, which have a rather straightforward effect on the mechanical response of MMCs, other characteristics are known to influence the global performance of the composites, such as particle size and shape, chemical compatibility with the matrix in the processing stage, or the strength of interfacial bond. Their effects are, however, not as evident as those of the characteristics listed previously. The complexity further increases because these variables often depend on each other. The chemical reactivity may be a function of the particle size; the effect of particle size can depend on the particle type or the matrix microstructure, and so on. Due to this complex interaction of microstructural parameters, neither a complete understanding nor agreement in the scientific community concerning the influence of each of these variables on the mechanical properties of MMCs have been achieved, such that many studies are still being conducted in order to clarify these issues. An extensive description of the influence of these microstructural variables on the toughness of MMCs will be given in Section 2.3

An important distinction is also to be drawn between particulate reinforced metals and dispersion or precipitation strengthened alloys that could be considered as composite materials in the sense that they contain fineely dispersed or precipitated particles within a metallic matrix. In the latter, strengthening is brought via the well-known Orowan mechanism: the very small particles are closely spaced (less than 1 µm) and hamper the movement of dislocations. In composites, on the other hand, an accepted definition according to Clyne [11] is that strengthening of these materials is by load transfer from the matrix to the reinforcement. For this mechanism to be effective, it is generally estimated that the volume fraction of reinforcements must be higher that 5%, while dispersion and precipitation alloys typically contain at most a few percent of particles, and typically much less.

**Table 2-1** Mechanical properties of the ceramic typically used as reinforcement in PRMMCs.

| **Particulate materials** | **Density [g/cm$^3$]** | **Elastic modulus, E [GPa]** | **Poisson ratio, $\nu$ [-]** | **Toughness, $K_{Ic}$ [MPa·m$^{1/2}$]** | **Hardness[a] [GPa]** | **References** |
|---|---|---|---|---|---|---|
| $Al_2O_3$[b] | 3.6-3.98 | 345 - 400 | 0.22 - 0.26 | 1.5 - 6 | 18 - 23 | A, B, C |
| $B_4C$ | 2.52 | 430 - 480 | 0.14 - 0.18 | 1.8 - 3.7 | 29 - 31 | D, E, B |
| SiC | 3.21 | 408 - 480 | 0.14 - 0.19 | 2.6 - 6.1[c] | 20 - 30 | B, D |
| $TiB_2$ | 4.5 - 4.54 | 514 - 574 | 0.09 - 0.13 | 6 - 8 | 15 - 45 | B, D |
| TiC | 4.92 | 430 - 490 | 0.19 | 2.0 | 28 - 35 | B, D |
| $ZrO_2$ | 5.5 - 6.1 | 140- 240[d] | 0.23 - 0.32 | 2.8[e]; 6 - 15[f] | 10 - 15 | A, B |

a. Vickers or Knoop hardness.
b. Properties of alumina are highly dependent on purity and porosity.
c. Dependent on the densification method (*i.e.* sintering or hot pressed) .
d. 200-240 GPa for partially stabilized zirconia; 140-200 GPa for tetragonal zirconia polycrystals (TZPs).
e. Fully stabilized zirconia (cubic).
f. Partially stabilized zirconia (tetragonal).
(A): [12]; (B): [13]; (C): [14], (D): [15]; (E): [16].

### ii. Matrix

Most usual metallic systems have been explored as matrix candidates in PRMMCs, but aluminium alloys have by far received most attention. We briefly present here other systems that have been considered and then summarize in more details the specific case of aluminium alloys.

Titanium alloys have a high strength/weight ratio as well as good stability at high temperatures, making these some of the most important aerospace materials. A natural extension to further improve some of their properties such as the specific stiffness and the wear resistance has been to use them in MMCs. This approach however suffers from drawbacks associated with difficulties of fabrication: the high melting point of Ti and general issues in dealing with molten titanium almost excludes this system to be produced via liquid-state routes [17]. Its high affinity for oxygen, nitrogen and hydrogen requires also extreme care when solid-state methods (*i.e.* powder metallurgy for MMCs) are used.

Magnesium alloys are another class of light-metals that have been considered for fabrication of MMCs, especially by liquid state methods [18]. They have nevertheless received much less attention than aluminium alloys, and magnesium-based MMCs are still produced only at the laboratory scale. Compared to aluminium-reinforced materials, they show poorer retention of properties at high temperatures, very weak corrosion resistance [19] and a lower workability since magnesium is an hexagonal close-packed metal. Furthermore, molten magnesium is very reactive and necessitates a great degree of care during casting. In addition, it chemically reacts with oxides, which is an issue with many reinforcements in processing the composite.

A last system that is worth mentioning is Cu-based composites. The motivation behind the use of Cu alloys in PRMMCs is their high thermal and electrical conductivity, while the main role of the reinforcement in this system is to reduce as much as possible the coefficient of thermal expansion (and thus to minimize thermal stresses which are a limitation in many electronic devices), making these MMCs attractive for electronic packaging and thermal management [8]. Liquid-state processing in this context is the most attractive method because higher volume fraction of reinforcement can be achieved (thereby leading to lower thermal expansion) together with lower levels of impurity and porosity, which is very important as their presence is known to be detrimental to electrical conductivity of metallic materials [20, 21] and their composites [22]. An additional advantage compared to aluminium alloys is the non-reactivity of copper with most oxides as well as with carbon, so that Cu/carbon can be produced, yielding lighter and more thermally conductive materials. On the other hand, copper-based MMCs are not considered to be attractive for structural applications because of their high density. The higher melting-point of Cu may also necessitate higher performance equipment for their fabrication.

Aluminium and its alloys is by far the dominant matrix system for metal matrix composites. It is in general a low cost material, which presents a low melting point, facilitating fabrication. With its low density (2.7 g/cm$^3$) and the fact that it can be worked into any form by plastic deformation, and cast by all foundry processes, its dominant position for use in MMCs is readily explained. Interestingly, a closer look at the literature indicates that there has not been a large effort to develop alloys specifically designed for use as composite matrices; rather MMCs have largely made use of commercial alloys that were not originally designed for this purpose [23], even though there exist important exceptions *e.g.*, [24]. As a consequence virtually all classes of aluminium alloys have been studied in MMCs; namely cast and wrought alloys with most of the main alloying element systems.

The principal aluminium alloys that are used in MMCs are presented in Table 2-2. The alloy classification according to the Aluminium Association and the content of main alloying elements are indicated, as well as the common heat treatment condition. Many systems have received attention, including pure Al, Al-Cu, Al-Cu-Mg, Al-Mn, Al-Mg-Si, or Al-Zn-Mg-Cu alloys. A closer look at some review articles [25-29] indicates that pure Al and binary alloy systems are much less employed compared to more complex systems, which does not facilitate the interpretation of experimental results. In the cases where alloys with simpler microstructures are employed, it is with the purpose of creating model materials for which data are generally easier to interpret. One also notices a trend for using alloys that have as low a content as possible in minor alloying elements, such as Mn and Cr, because they form intermetallic compounds during processing that are detrimental for the mechanical properties, whereas the purpose of their addition in unreinforced alloys (grain-size control) is not as critical in MMCs. Throughout the rest of the work, the matrix alloys will be designated according to Table 2-2.

**Table 2-2** Composition and designation of Al-alloys commonly used in MMCs. The alloy designation is given according to the Aluminium Association or as indicated in the references. Composition data from [30, 31].

| Alloy designation | Composition, wt% | | | | | | | | | Main aging precipitates |
|---|---|---|---|---|---|---|---|---|---|---|
| | Si | Fe | Cu | Mn | Mg | Cr | Zn | Al | Others | |
| **Pure Al** | | | | | | | | | | |
| 1100 | 1 Si+Fe | | 0.05-0.20 | 0,05 | | | | 99.00 min | 0.1 Zr | |
| 1199 | | | | | | | | 99.99 min | | |
| **Al-Cu alloys** | | | | | | | | | | GP, Al$_2$Cu (θ', θ'') |
| 295,0 | | | 4,5 | | | | | | | |
| Al-4%Cu | | | 4 | | | | | | | |
| 201,0 | 0,05 | 0,10 | 4.0-5.0 | 0.20-0.40 | 0.15-0.35 | | | | 0.15-0.35 Ti; 0.4-1.0 Ag | |
| **Al-Si alloys** | | | | | | | | | | coarse Si, Mg$_2$Si (ß',ß'') |
| Al-10%Si-Mg | 10,5 | | | | 0.3-0.5 | | | | | |
| Al-15%Si-Mg $^*$ | 15,5 | | | | 0.3-0.5 | | | | | |
| Al-20%Si-Mg $^*$ | 20 | | | | 0.3-0.5 | | | | | |
| **Al-Mg-Si alloys** | | | | | | | | | | Mg$_2$Si (ß',ß'') |
| 6061 | 0.4-0.8 | 0,7 | 0.15-0.40 | 0,15 | 0.8-1.2 | 0.04-0.35 | 0,25 | | 0.15 Ti | |
| 356/A356 | 6.5-7.5 | 0.6/0.2 | 0.25/0.20 | 0.35/0.10 | 0.20-0.45 | | 0.35/0.10 | | 0.25 Ti | |
| 357/A357 | 6.5-7.5 | 0.15/0.20 | 0.05/0.20 | 0.10/0.20 | 0.40-0.7 | | 0.05/0.1 | | 0.1/0.2 Ti | |
| **Al-Mn alloys** | | | | | | | | | | |
| 3003 | 0,6 | 0,7 | 0.05-0.2 | 1.0-1.5 | | | 0,10 | | 0.20 Zr + Ti | |
| **Al-Cu-Mg alloys** | | | | | | | | | | GPB, Al$_2$CuMg (S') |
| 2014 | 0.5-0.12 | 0,7 | 3.9-5.0 | 0.4-1.2 | 0.4-0.8 | 0,10 | 0,25 | | 0.15 Ti; 0.20 Zr | |
| 2024 | 0,5 | 0,5 | 3.8-4.9 | 0.3-0.9 | 1.2-1.8 | 0,10 | 0,25 | | 0.15 Ti; 0.20 Zr | |
| 2080 | | | 3,8 | | 1,8 | | | | 0.20 Zr | |
| 2618 | 0.10-0.25 | 0.9-1.3 | 1.9-2.7 | | 1.3-1.8 | | 0,1 | | 0.04-0.1 Ti; 0.9-1.2 Ni | |
| Alcoa MB85 $^+$ ( ≈ 2124) | | | 3,5 | 0,20 | 1,5 | | | | 0.40 Zr | |
| **Al-Zn-Mg-Cu alloys** | | | | | | | | | | GP, MgZn$_2$ (η, η') |
| Alcoa MB78 $^+$ (≈ 7050) | 0,12 | 0,15 | 2.0-2.6 | 0,1 | 1.9-2.6 | 0,04 | 5.7-6.7 | | 0.08-0.15 Zr | |
| 7075 | 0,40 | 0,5 | 1.2-2.0 | 0,3 | 2.1-2.9 | 0.18-0.28 | 5.1-6.1 | | 0.25 Zr + Ti | |
| 7178 | 0,40 | 0,5 | 1.6-2.4 | 0,3 | 2.4-3.1 | 0.18-0.35 | 6.3-7.3 | | 0.20 Ti | |
| 7475 | 0,10 | 0,12 | 1.2-1.9 | 0,06 | 1.9-2.6 | 0.18-0.25 | 5.2-6.2 | | 0.06 Ti | |
| 7090 ° | 0,12 | 0,15 | 0.6-1.3 | | 2.0-3.0 | | 7.3-8.7 | | 1.0-1.9 Co; 0.2-0.5 O | |
| 7091° | 0,12 | 0,15 | 1.1-1.8 | | 2.0-3.0 | | 5.8-7.1 | | 0.2-0.6 Co; 0.2-0.5 O | |
| 7093 ° | similar to 7075 | | | | | | | | | |
| **Al-Li alloys** | | | | | | | | | | Al$_3$Li(δ') |
| 8090 | | | 1,3 | | 0.7-0.9 | | | | 2.2-2.4 Li; 0.1 Zr | |

* : Si content larger than eutectic composition using rapid solidification atomization process.

+ : closest composition according to Metals Handbook.

° : Alloys prepared by powder metallurgy techniques.

Four-digit numerical designations are for wrought alloys; three-digit are for cast alloys.

## 2.2. PARTICLE REINFORCED MMCS: PROCESSING

There are basically two classes of processing methods that are employed to produce particle reinforced MMCs: (i) solid-state processing and (ii) liquid-state processing of the metallic phase. A short presentation of the main methods is given below, with special emphasis on the second class, since the method used in this work (gas-pressure infiltration) falls in this category.

### *2.2.1 Solid state processing*

Powder metallurgy (PM) is probably the most frequently used method of PRMMCs fabrication. The principal steps of PM processing include: (i) blending of the matrix and the reinforcement powder; (ii) cold isostatic compaction (CIP) to obtain a green compact; (iii) degassing; (iv) consolidation at high temperature by a method such as hot isostatic process (HIP); (v) primary deformation processing using standard metal-working methods such as rolling, extrusion or forging; and (vi) final secondary processing.

Step (i) has largely taken advantage of rapid solidification technology in that the matrix is generally used as a pre-alloyed powder produced by atomization, rather than starting from elemental blends. Blending can be carried out dry or in liquid suspensions. A density on the order of 50% is generally achieved after CIPing (step ii). Step (iii) is necessary in order to remove remanant liquid from the wet blending operation and/or adsorbed water from the particles and the matrix powder surface. Hot-consolidation, step (iv), is generally carried out at a rather high temperature (close to the solidus temperature), but limitations exist depending on the thermal stability of the system matrix/reinforcement and the need, in certain situations, to minimize chemical reaction between the reinforcement and the matrix. The consolidated billet generally attains around 98% of theoretical density after hot consolidation. Step (v) is carried out to modify the composite microstructure, for instance by generating new grain boundaries, as well as to improve the mechanical properties, in particular because the thin oxide film around the metal powder particles is mechanically broken up during this stage, leading to strongly bonded interfaces. The final secondary processing plays a similar role in that it promotes the break-up of particle agglomerates, the reduction or elimination of porosity, and the improvement of particle-bonding, all of these mechanisms leading to better mechanical performance of the final billet material.

The limitations associated with this method are the following. First, it is a relatively complex and expensive manufacturing route, with limited final product shapes. Secondly it involves handling highly reactive powders and thus necessitates important safety precautions. There are also drawbacks regarding the material microstructure. One is inhomogeneity in the form of particle clusters (*i.e.* local regions having a much larger volume fraction of particles than average) that are created during powder mixing, in particular with lower volume fractions [32]. Clusters weaken the composite as they act as stress concentrators and localise damage, which promotes earlier failure, see for instance [33-36] and §.2.3.3 for the specific case of fracture toughness. Another typical feature is microstructural anisotropy consecutive to rolling or extrusion, leading to some degree of anisotropy in the composite properties. The PM processing route also leads to the almost inevitable presence of very fine oxide stringers (in the nanometer size range), caused by the fracture of the oxide skin around the metallic powder during extrusion [37-39], and this is another potential source of local weakness. Residual porosity may remain too, especially when manufacturing combines the consolidation and deformation steps in a unique stage [40]. Particle cracking during extrusion has also been reported [41, 42]. Additional information and more complete presentations of the solid-state processing method can be found in references [1, 43, 44].

### 2.2.2 Liquid-state processing

When composites are processed using the molten state of the matrix, different considerations are taken into account. The major concern is certainly matrix-reinforcement reactivity, which has a profound effect on both the ease of processing and the final composite performance. Since metals in the liquid state react generally more rapidly than in the solid-state, a significant amount of brittle interfacial phases is often formed due to reactions between the reinforcement and the matrix, resulting in variations of the interfacial strength and hence of the mechanical properties of the composites [27, 45]. Typical examples are the reactivity of carbides with aluminium above its melting point. For instance, silicon carbide reacts with liquid aluminium [46]:

$$4\mathrm{Al} + 3\mathrm{SiC} \rightarrow \mathrm{Al_4C_3} + 3\mathrm{Si} \qquad (2\text{-}1)$$

leading to an increase of the Si content in the matrix. In such systems, reaction can be avoided by using Al-Si alloys with a high silicon content (above about 7% if temperatures remain below 700°C). Similarly, boron carbide is unstable in molten aluminium above ≈700°C and reacts in a more complex manner (especially because of the very low solubility of boron in aluminium), by forming $Al_3BC$ and $AlB_2$ [47, 48], for example through the following reaction:

$$9\mathrm{Al} + 2\mathrm{B_4C} \rightarrow 2\mathrm{Al_3BC} + 3\mathrm{AlB_2} \qquad (2\text{-}2)$$

On the other hand, $Al_2O_3$ is thermodynamically stable with pure liquid aluminium while it presents significant reactivity in contact with Mg [46]:

$$3\mathrm{Mg} + \mathrm{Al_2O_3} \rightarrow 3\mathrm{MgO} + 2\mathrm{Al} \qquad (2\text{-}3)$$

$$3\mathrm{Mg} + 4\mathrm{Al_2O_3} \rightarrow 3\mathrm{MgAl_2O_4} + 2\mathrm{Al} \qquad (2\text{-}4)$$

which is the reason for the lack of stability of $Al_2O_3$ in many aluminium alloys since these often contain a significant level of magnesium.

These few examples illustrate the problem of reactivity in liquid-state processing of MMCs. Since numerous reinforcement/matrix combinations are possible, interfacial studies related to the matrix-reinforcement reactivity have actually attracted a considerable attention in the MMC research community. For more information on the topic, the reader is referred to references [49, 50].

Generally speaking, the advantages of liquid-state methods compared to solid-state process are the following [46, 51, 52]: (i) cost, as liquid alloys are less expensive than in their powder form, (ii) reduced mechanical degradation of the reinforcement during processing, (iii) higher product fabrication speed, and (iv) the ability to process final shape or near-net shape products which is very interesting considering the machining difficulties associated with MMCs.

As pointed out earlier, liquid-state processes suffer mainly from reactivity between the molten metal and the ceramic reinforcements. Depending on the method used, the volume fraction of reinforcements is furthermore limited to a narrow range, especially when it involves the initial fabrication of a powder preform. Whether this latter point is a disadvantage or not is actually questionable, because it is at the same time the only method for achieving high volume fraction MMCs ( 40% to 75%).

Liquid-state processing can further be divided into four major categories, depending on the method used to mix the powder and the matrix. These are: (i) dispersion, (ii) spraying, (iii) in-situ, and (iv) infiltration processes.These are presented hereafter, with a somewhat greater attention dedicated to infiltration processes since it is used in this work.

### i. Dispersion-Processing

The basic principle of dispersion methods is to incorporate the loose powder of reinforcing particles into the liquid metal matrix. Because dispersing ceramic particles within a metallic melt is generally a non-spontaneous process from the energetic point of view (due to poor wetting of the ceramic particles by the liquid metal), it is often necessary to apply a force on the particles to overcome the surface tension. A common way of doing so is the Vortex method, which involves vigorous stirring of the melt [53]. An alternative widely used for commercial products was developped by Duralcan™ (San Diego, CA, USA) and consists of mixing the liquid metal and the ceramic particles under vacuum, thereby limiting the presence of oxides or gas [54, 55].

Dispersion processes are often considered to be the most simple and economically attractive methods [1] because one simply needs to stir the liquid metal with the solid particles (the method is hence often called “stir-casting”) and then let the mixture solidify. Since all conventional metal processing routes can be used thereafter, the cost of such MMCs is greatly reduced. There are, however, limitations with this processing route. It is restricted to volume fractions of particles in the range of 10-20%. Also, the long contact time between the ceramic and the molten metal is problematic for reacting systems. In addition, a concern inherent to molten metal mixing is the lack of uniformity in the reinforcement distribution. This has several causes: (i) particle agglomeration as a result of mixing [56]; (ii) particle migration after mixing as a result of density differences between the matrix and the reinforcement; and (iii) particle rejection at the solid/liquid interface of the advancing solidification front, which leads to particle segregation in the interdendritic regions, which are last to solidify, a situation that is often observed with hypoeutectic alloys such as alloy 356. In all these cases, very inhomogeneous distribution of particles leads to the presence of clusters in the final component. A way to minimize settling and floating of the particles is to incorporate the particles to a melt which is in the semisolid temperature range. In this case, the melt exhibits a high viscosity that retains particles migration, a method often referred to as “compocasting”; however segregation is still observed because particles are absent from the globular primary phase regions.

### ii. Spray-Forming

The principle of the spray-forming process is to impact a stream of molten metal by highly energetic gas jets, resulting in the disintegration of the molten metal into small and irregular ligaments; this stage of the process is called “spray atomisation”. The ligaments then rapidly transform into spherical droplets, in about $10^{-6}$ s. The droplets are collected onto a cooled substrate to form a dense bulk material; this is the “deposition stage”. An inherent feature of spray-forming compared to conventional casting is the elimination of macrosegregation and the minimization of microsegragation. A second characteristic is the ability to produce alloys containing thermodynamically metastable phases, because the metal droplets solidify very rapidly. One can find many details about spray-forming in reference [57].

The technology of spray-forming was then extended from monolithic alloys to MMCs. Different techniques exist nowadays [58]. The most widely adopted method is to incorporate into the spray a reinforcement injection unit, allowing simultaneous spraying of the reinforcing phase together with the matrix alloy, a technique called “spray co-deposition”. The reinforcing particles being injected with sufficient kinetic energy, they penetrate the individual droplets of the atomized spray, are cooled, solidified, and finally collected on the substrate to form a dense composite. Because the liquid metal and the reinforcement are in contact for a very short time, rapid solidification occurs such that a primary advantage of the process is to limit the amount of reaction in intrinsically reactive systems. The billets produced by spray co-deposition typically contain 2-5% porosity and therefore a secondary-forming process is needed to achieve full density.

### iii. In-situ reaction processes

The principle of *in-situ* processes is to fabricate MMCs in which ceramic particles are not independently added to the matrix, but are produced *in-situ* from the melt by reaction with compounds that are added to the solvent metal, a method initially developped by Martin Marietta Corporation (Baltimore, DE) and called XD™ process. Titanium diboride ($TiB_2$) and titanium carbide (TiC) have received most attention as reinforcements with this method. These are formed by the following reactions [46]:

$$2B + Ti + Al \rightarrow TiB_2 + Al \qquad (2\text{-}5)$$

$$C + Ti + Al \rightarrow TiC + Al \qquad (2\text{-}6)$$

Another approach, developped by Lanxide Corporation (Newark, DE) and called DIMOX™, consists in direct oxydation of the metal by a gaseous oxidant. A typical example is the $Al_2O_3$/Al composite (the ceramic being in this case the matrix) which simply uses air as the oxydant.

There exist many other ceramic/metal systems that have been produced via in-situ methods [59]; one can cite for instance TiC particles obtained by injection of $CH_4$ into a melt of Al-Cu-Ti.

The major attractive feature of *in-situ* processes is the ability to produce particles that have in principle a clean and unoxidized interface and that should therefore provide a high interfacial strength. In addition, nucleation within the melt leads to a generally homogeneous distribution of the reinforcing phase; however, even though process parameters such as reaction temperature can be varied to tailor the microstructure, it has been found so far that particle shape is difficult to control and that the particle size is limited to the 0.25-1.5 µm range [46].

### iv. Infiltration

The general term “infiltration” includes several processing methods. Generally speaking, it involves fabrication of the composite via the filling with a fluid of an initially porous solid called “preform”, and then solidifiation of the infiltrated liquid in this space, leading to the final composite. For the specific case of MMCs, the preform is made of the ceramic reinforcement. Since the matrix metal is relatively easily melted and handled in the liquid state, Al, Cu and Mg based alloys have all been successfully used for manufacturing MMCs through liquid infiltration. The differentiation from one infiltration method to another is based on the technique that is used to cause the molten metal to enter the preform. One can cite, for instance, spontaneous infiltration, mechanical pressure infiltration, gas pressure infiltration or vacuum infiltration. A common characteristic of infiltration process routes as compared to other techniques is a generally more isotropic microstructure. This is due to the use of an initial reinforcement preform in which the particles are tightly packed to form a regular porous body, about 50% dense depending on the particle size, shape and size distribution (short fibers preforms exhibit much lower volume fraction packings). Particles within the preform are hence constrained by their neigbours, such that particle packing inhomogeneity is absent (once the porosity has been replaced by the liquid metal, the final billet can in a sense be thought of as a large and single cluster). The ability to produce complex-shaped parts is another distinct advantage compared to other methods.

### INFILTRATION: FUNDAMENTAL CONCEPTS

Over the past ten years several reviews have been devoted to the process fundamentals, experimental aspects of the technique, and application to MMCs production (or other type of materials) [17, 51, 52, 60-63]. We present here the basic concepts of the process as well as some more experimental details about the most widely used methods: mechanical pressure infiltration –often called “squeeze casting”– and gas-pressure infiltration.

The first fundamental phenomenon that governs infiltration is capillarity: let us denote $\gamma_{sv}$ and $\gamma_{sl}$ the solid reinforcement/atmosphere surface energy and the solid reinforcement/liquid metal energy, respectively. From these definitions, the wettability of the solid by the liquid is given by the work of immersion per surface area, $W_i$:

$$W_i = \gamma_{sl} - \gamma_{sv} \tag{2-7}$$

If $\gamma_{sl} < \gamma_{sv}$, the liquid metal wets spontaneously the solid, whereas in the opposite case, work is required to make the solid/liquid interface. In other words, in the non-wetting case, replacing a unit surface of solid/atmosphere by a unit surface of solid/liquid necessitates an external work contribution, supplied by an applied unidirectionnal or isostatic pressure. This minimum applied pressure $P_0$ required to overcome the capillary pressure difference $\Delta P_\gamma$, is then written in terms of the work of immersion as:

$$P_0 = \Delta P_\gamma = S_i \cdot W_i \tag{2-8}$$

where $S_i$ is the surface area of the liquid/metal interface per unit volume of matrix. Graphically, the wettability is related to the wetting angle $\theta$ (Figure 2-2 ) by the well-known Young Dupré equation:

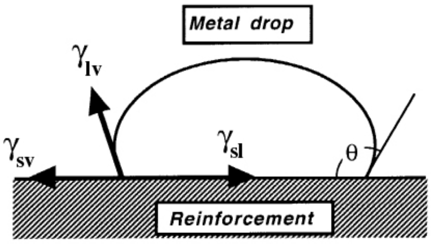

**Figure 2-2.** Definition of the liquid contact angle at the liquid/solid interface and the related Young-Dupré equation.

$$\gamma_{sl} - \gamma_{sv} = -\cos(\theta)\gamma_{lv} \tag{2-9}$$

where $\gamma_{lv}$ is the liquid metal surface tension. Spontaneous infiltration thus occurs for $\theta < 90°$, while when $\theta > 90°$, an external force is needed to overcome the capillary forces and drive the infiltration.

Several experimental techniques exist to measure the term $\gamma_{sl}$ - $\gamma_{sv}$ [64]; these are based either on the capillary pressure drop or on contact angle measurements. In most cases, molten metals do not have low contact angles with ceramics (typically Al/SiC, Al/$Al_2O_3$ or Cu/$Al_2O_3$); however exceptions do exist. In order to promote spontaneous infiltration of these inherently non-wetting systems, several methods are based on the modification of the matrix alloy chemistry or of the reinforcement surface. Alternatively, processing at significantly higher temperatures than the melting point or in an atmosphere that reacts with one of the composite constituents is also used to modify the wettability and to promote spontaneous infiltration [65-68]. As an example, the presence of magnesium and nitrogen is known to permit pressureless infiltration of Al/SiC or Al/$B_4C$ composites. However, there are drawbacks usually associated with the final properties of the composites: since few alloys present good wettability, this limits tailoring of the composite properties via matrix changes. In addition, the presence of interfacial phases that are formed at a higher processing temperature or by reaction with the atmosphere is often detrimental. Porosity in the solidified billet and sometimes slow infiltration times are other issues, which have led to a relatively less frequent use of pressureless infiltration as compared to pressure-driven methods.

Practically, equation (2-8) indicates that, for a given material system (*i.e.* same particle type and volume fraction $V_f$), the threshold pressure $P_0$ to apply to the metal in order to initiate infiltration is inversely proportional to the average size of reinforcement $D$ (since the specific area liquid/particle increases as particle size decreases). This has been well confirmed by analyzing various data on infiltration of several ceramic particulates by pure aluminium [61], where it was empirically shown that the threshold pressure varies linearly as a function of $(V_f / 1\text{-}V_f) \cdot D$ :

$$P_0 = 16 \cdot \frac{V_f}{(1 - V_f) \cdot D} - 0.09 \; [MPa] \qquad D \text{ in } [\mu\text{m}] \tag{2-10}$$

Typically, pressure in excess to 0.5 MPa (5 bar) must thus be employed to initiate infiltration.

The second physical parameter that dictates infiltration is the flow rate of infiltration $v$, defined as the average velocity of the fluid multiplied by the volume fraction of pore space (1-$V_f$):

$$v = \mathrm{d}L / \mathrm{d}t \cdot (1 - V_f) \tag{2-11}$$

where $L$ is the infiltration front position along the direction of flow $x$. In the simplest case of unidirectional flow through a porous medium, this rate is given by the Forscheimer equation [17, 60]. In the majority of infiltration processes, the relevant Reynolds number $R_e$ falls below the critical value $R_{ec} \approx 1$:

$$R_e = \frac{d \cdot \rho_m \cdot v}{\mu \cdot V_f} < R_{ec} \tag{2-12}$$

where $\rho_m$ is the metal density, $\mu$ is its viscosity, and $d$ is a characteristic length of the reinforcement (typically the average particle size) such that inertial losses can be neglected, as well as the body forces (for instance gravity). The Forscheimer equation then reduces to Darcy’s law:

$$v = -\frac{K}{\mu} \cdot \frac{\partial P}{\partial x} \tag{2-13}$$

where $K$ is a constant defining the permeability of the porous solid and $\partial P/\partial x$ is the pressure gradient at the infiltration front. The pressure at the entrance of the preform ($x$=0) is the external applied pressure, $P_e$, and the pressure at the infiltration front ($x$=$L$) is the atmospheric pressure plus the capillary pressure difference, $P_a + \Delta P_\gamma$. With these boundary conditions, and by combining (2-11) with (2-13) and then integrating with respect to position and time, it is found that kinetics of infiltration obey:

$$L^2 = \frac{2}{1 - V_f} \cdot \left(\frac{K}{\mu}\right) \cdot \left(P_e - P_a - \Delta P_\gamma\right) \cdot t \tag{2-14}$$

meaning that, under a constant pressure diffential, the infiltration height has a parabolic dependence with both time and pressure. One also sees that $P_a+\Delta P_\gamma$ and $K/\mu$ are accessible via experimentation when plotting $L^2/t$ versus the applied pressure $P_e$.

Heat and mass transport phenomena are other important issues in infiltration processing. Heat exchange between the metal and the reinforcement occurs because the initial preform temperature often differs from that of the metal. This is more precisely desirable when the preform is initially at a temperature below the matrix liquidus temperature in order to minimize the matrix-reinforcement reactivity. Heat transfer can have important practical implications, in that heat exchange can cause local solidification of the solid within the preform, hence reducing the preform permeability and affecting the rate of infiltration. The analysis of heat transfer within a volume element of infiltrated region includes heat transport by conduction and convection, which will in turn alter both the local temperature and the local fraction of solid (*i.e.* the latent heat of solidification of the matrix must be taken into account). A complete theoretical treatment can be found in [69-71] as well as in review articles by the same authors [17, 60].

Mass transfer occurs in alloy matrix composites,  mainly by solute rejection as the solidification front advances in the composite or due to chemical reaction between matrix and reinforcement. Mass transfer is governed by convection, while diffusion can be neglected. In the absence of chemical reaction, solute transport is then governed by:

$$\frac{\partial \bar{C}}{\partial t} = -\frac{\partial\left[(1-g_s)C_L v\right]}{\partial x} \tag{2-15}$$

where $\bar{C}$ is the local average matrix composition, $C_L$ is the composition of the liquid matrix, $v$ is the flow velocity, and $g_s$ is the solid fraction in the matrix. A practical implication of this effect results in macrosegregation during alloy solidification if concommitant with infiltration, leading to solute enrichment in the last solidified part of the composite [70, 72, 73]. Infiltration conditions must thus be considered with care in order to produce a composite with a microstructure and composition as uniform as possible. Typically, when using reinforcements that are chemically inert in contact with the liquid metal, the preform must be heated to a temperature above the matrix liquidus temperature, such that solidification does not start during infiltration, but only after the latter is completed.

The last step of the process is matrix solidification. While the physical laws governing composite solidification remain the same as in unreinforced alloys (nucleation and growth of the solid phase, governed by heat transport, solute diffusion, convection in the liquid and capillarity effects), the rules derived to control the microstructure of monolithic alloys do not apply directly to cast MMCs because the presence of a reinforcing phase significantly modifies matrix solidification. Theoretical and experimental investigations on the subject have been mainly carried out on continuous fibre-reinforced composites. Systematic work on PRMMCs is far less extended, in particular because they exhibit a more complicated inter-reinforcement geometry, such that quantification is more difficult. Nevertheless, there exist some general characteristics common to both type of composites: nucleation is greatly dependent on the chemistry of reinforcements, more exactly on the contact angle solid matrix phase/reinforcing phase within the liquid [17, 60]. In some situations, the reinforcing phase can act as preferential catalysis sites inducing grain size refinement of the matrix. In the majority of cases involving Al-alloys and usual reinforcements (SiC, $Al_2O_3$), such refinement does however not occurs.

With pure metallic matrices, grain orientation and grain boundary morphology are the only features influenced by the solidification process. In alloy matrix systems, the situation is far more complicated. As mentioned earlier, when the preform is at a low temperature, significant macrosegregation occurs along the final billet. This effect can be minimized, in non-reacting systems, by preheating the preform to a temperature above the liquidus, so that infiltration and solidification are two distinct steps in time. In this situation, and when the reinforcing phase does not act as a heterogeneous nucleation site (namely, growth of the primary alloy phase begins within the matrix), the growing solid tends to avoid the reinforcements because the latter act as a barrier to solute diffusion during solidification. As a result, solute-rich phases (*i.e.* eutectic mainly) which correspond to the last liquid to solidify, are often located around the reinforcements. This is a well-known mechanism in fibre-reinforced composites, as illustrated in Figure 2-3 [72, 73], but has been much less documented in particle reinforced composites. References [74][1] and [75] are the few studies (at least to our knowledge) where coarse eutectic regions were reported around the ceramic particles in as-cast composites prepared by squeeze-casting.

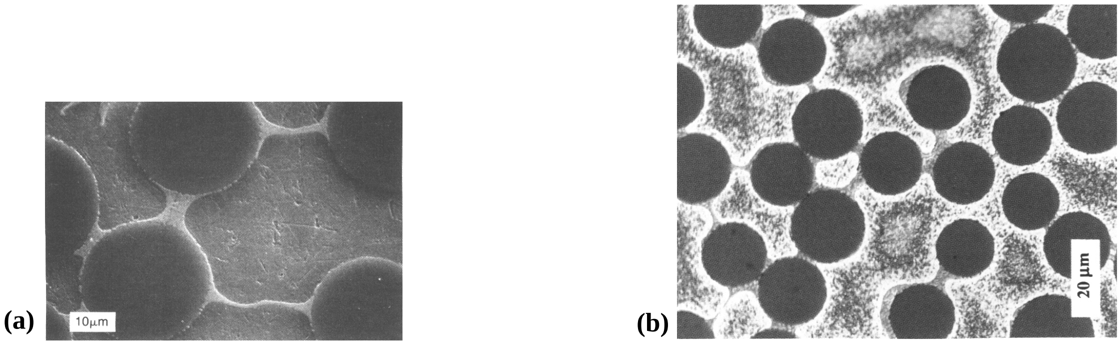

**Figure 2-3.** **(a)**: SEM micrograph of an Al-4.5%Cu reinforced by $Al_2O_3$ fibre and **(b):** optical micrograph of the same material after etching. Both illustrate the presence of second phase surrounding the fibres. From [72].

### Engineering Aspects of Infiltration: Preform Preparation

As for any infiltration process, the initial step prior to infiltration itself is preform preparation, which is of crucial importance since any defect introduced at this stage will remain in the final cast composite. There are various methods to fabricate a preform. The simplest is the natural packing of powder in a container under the single action of gravity. With particles of roughly mono-modal size distribution, the typical preform density is then on the order of 40-60% depending on shape and size of the particles. Various ways of modifying the natural packing can be employed. In order to achieve higher packing density, multimodal particle size distributions have been used [76, 77]. Inversely, means of reducing the volume fraction also exist, for instance by combining short fibers with particles, a method called “hybridation”[78, 79].

Ensuring cohesion of the preform during handling and manipulation necessitates the use of somewhat more sophisticated methods than simple tapping. Among various possibilities, one can cite uniaxial or isostatic cold pressing, sintering, or slurry-casting. Binders are also often added during preform preparation, in the form of polymers that are burned out during processing, or of inorganic compounds (colloidal silica being a typical example) when the binder must resist elevated process temperatures. Other methods for preform preparation allow the creation of a three-dimensionnal connected network of the reinforcing phase, for instance via sintering [80, 81]. Composites infiltrated from this type of preform are then often designated as “interpenetrating network composites”.

---

[1] In this cited reference, the presence of coarse intermetallic precipitates around SiC particles was not attributed to the effect mentioned in the text, but to the nucleation induced by high-density dislocations regions appearing during post-solidification cool-down.

### ENGINEERING ASPECTS OF INFILTRATION: SQUEEZE CASTING

In squeeze-casting or die-casting processes, the principal feature is the use of a piston to mechanically push the melt into the preform. Once the preform is prepared, it is placed into a preheated die, followed by pouring of the liquid metal. The pressure is then applied by lowering the piston at a controlled velocity and is maintained during solidification. The mold, preform and melt temperatures are the parameters to be controlled to optimize the process. When the pressure is directly applied to the entire surface of the molten metal, the technique is called “direct squeeze-casting”. A common alternative is to separate the preform-containing die from the piston; and in this configuration, the pressure is then exerted on a gate that transmits the pressure to the component. Depending on the gate configuration, the process is designated as “indirect squeeze-casting” or as “die-casting”.

The range of applied pressures in piston-driven infiltration typically ranges from 50 to 100 MPa. These are rather high values in materials processing, requiring the use of manufacturing facilities equipped with heavy-walled dies, made of hot-working tool steels. As the dies are held below the liquidus temperature of the matrix to prevent leakage and in order to minimize sticking of the matrix along the walls, solidification is rapidly induced, in general before infiltration is completely achieved, such that it is necessary to maintain or even increase the pressure to terminate the process. High pressure involved in squeeze-casting is associated with two advantages of this technique over gas-pressure infiltration. First, it allows infiltration of lower permeability preforms, made of quite small reinforcements: preforms containing particles as small as 25 nm in diameter have for instance been infiltrated in this way [82]. Secondly, since the process can be controlled in a way that infiltration and solidification take place rapidly, this can be used to reduce the contact time between the liquid metal and the ceramic reinforcement, such that the amount of reaction in thermodynamically unstable systems can be minimized. In addition, lower melt temperatures can be used, which is another factor in favor of decreasing the interfacial reaction products. Regarding cost, significantly high production rates can be achieved which makes squeeze-casting the most used method to fabricate cast composites at the industrial scale; however tooling is expensive.

On the other hand, the fact that lower temperatures and higher pressures are used in squeeze-casting brings some limitations. In particular, there is little flexibility for the choice of mold materials, because the mold is subjected to high tensile stresses. Refractory materials, for instance, cannot be employed given their low toughness, thus limitating the use of higher melting-point matrix alloys. Another drawback, which is associated with the need to apply a high pressure if partial solidification occurs during infiltration, is damage of the preform during processing. Such damage takes the form of cracks initiated by preform deformation due to the applied pressure. As a result, the presence of reinforcement-free zones (or matrix channels without reinforcements) is found in the final composite, with a width that can vary from a micrometer to the millimeter scale [74, 83]. Such defects can somehow be seen as the opposite of clusters; namely they are characterized by a lower local volume fraction of reinforcement than the average value in the composite. The origin of these “veins” is, however, not fully elucidated yet: the preform preparation or another step can also be invoked to explain their presence, as will be described later.

### ENGINEERING ASPECTS OF INFILTRATION: GAS-PRESSURE INFILTRATION

Alternatively, molten aluminium can be forced to enter into the preform porosity by means of pressurized gas. Regarding the experimental principles, it can be divided into four principal steps, schematically depicted in Figure 2-4: (i) preform preparation, (ii) evacuation of the preform and melting of the metal, (iii) pressurization by the mean of an inert gas (generally argon) to promote infiltration, and (iv) solidification of the metallic matrix.

As for squeeze-casting, preform preparation is the first processing step. Methods indicated above for preform preparation remain identical. Typically, the preform is directly prepared in the mold, which is then placed into the pressurized chamber. In this way, a feature characteristic of gas-pressure infiltration is that the mold is subjected to a compressive stress state, allowing the use of a larger choice of materials (in particular refractory ceramic materials like alumina or mullite), and in turn enlarging the range of processing temperature and of potential matrix materials [51].

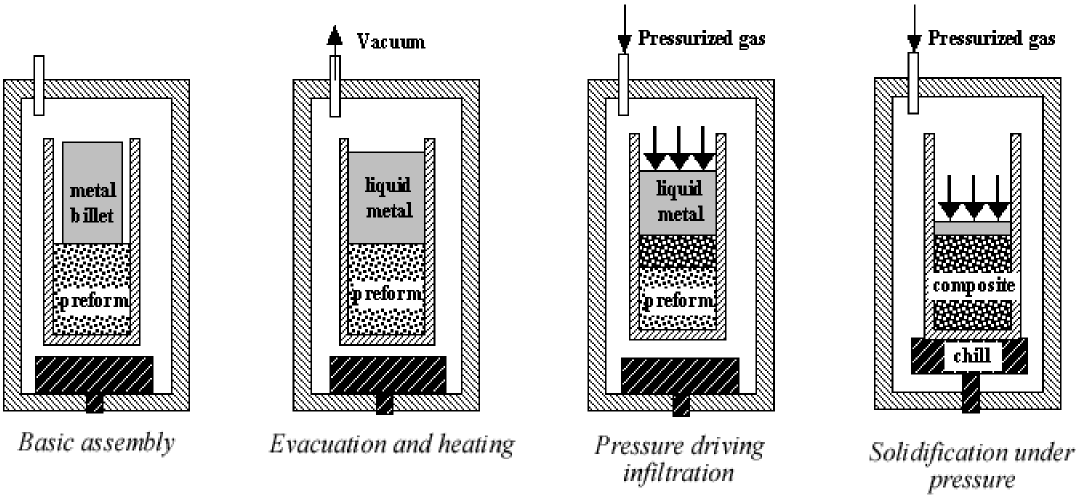

**Figure 2-4.** Schematic description of the gas-pressure infiltration, showing the four main process steps, from [63].

A considerable advantage of this technique lies in the fact that the preform can be easily evacuated prior to heating. Hence, contamination by oxygen, which is well known to have a strong affinity with aluminium by forming fines oxides (with a rate of reaction that increases in the liquid-state), is minimized. Evacuation also permits to reduce the residual porosity by eliminating the gas that is trapped in the preform and that would lead to residual uninfiltrated regions. On the other hand, evacuating a loose powder bed can cause fluidization of the powder and cracking within the preform by shearing [63], leading during subsequent infiltration to the same type of defects as in squeeze-casting, namely particle-free zones or “veins”. There are also indications in the literature to attribute the vein formation to the pressurization step, as explained earlier. In the absence of any quantitative and systematic studies of this effect in the literature, it is still considered at the moment to be an open question. In any case, the problem seems to be minimized by evacuating the preform very slowly and, in addition, by heating (because of degassing) and pressurizing at a very low rate [84].

Since the preform and the mold can be easily heated to a temperature well above the matrix liquidus, the process affords a greater flexibilty in the sense that infiltration and solidification are two distinct steps. In other words, there is no simultaneous solidification during infiltration, as opposite to squeeze-casting where high cooling rates and colder die walls can lead to the initiation of solidification while the preform is not yet fully infiltrated. This fact is advantageous in the view of producing MMCs with a better microstructural homogeneity. In terms of mold design, there is a also a greater versatility because any die shape can be placed into the pressurized gas chamber.

The chief disadvantage compared to piston-driven machines lies in the range of pressures available for infiltration. Higly-pressurized gas can typically provide pressure in the range of 100 bar (≈ 10 MPa), which is enough to promote infiltration of many particulate-reinforced systems (for which pressure in the order of 1 MPa is required). In practice, however, the preform permeability $K$ is strongly dependent on the reinforcement size $D$ and varies roughly as $D^2$, such that the pressure allowed by a gas-driven infiltration machine may not be sufficient for very small particle sizes. In addition, it should be emphasized that, for safety reasons, great caution is required in designing and manipulating these machines. Another drawback compared to squeeze-casting is the longer infiltration time and external cooling after infiltration. This causes a longer exposure time between the preform and the liquid metal, leading to an increasing amount of brittle interfacial phases in reactive systems.

Regarding engineering aspects of gas-pressure infiltration, it is finally to be mentioned that directional solidification is generally induced in order to eliminate solidification shrinkage. This is achieved by contacting the bottom of the mold with a chill situated further down in the pressurized chamber, leading to solidification in the direction opposite to the infiltration path. Feeding solidification shrinkage is also aided by maintaining the pressure during solidification.

### 2.2.3 Summary

As in any materials, the microstructures (and properties) of PRMMCs are directly dependent on the processing route. Depending on the properties one is looking for, what application the composite is planned for, or what initial constituants are used, there are many solutions offered to produce these materials. Processing and constituant cost, as well as availability of the manufacturing equipment, also enter into consideration. In order to illustrate this general survey of processing techniques, typical microstructural features of PRMMCs are summarized in Figure 2-5. This should of course not be seen as an exhaustive review, but rather as an illustration of characteristics that are regularly reported in the literature.

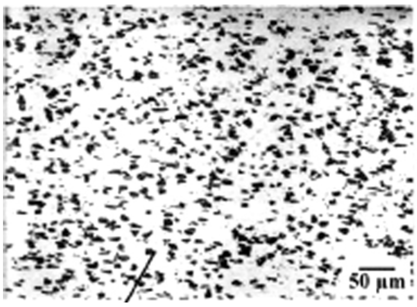

Powder metallurgy (PM) MMC, 15 vol. % particles [85].

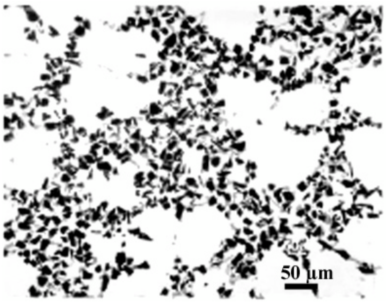

Clustering in a MMC produced by stir-casting [46].

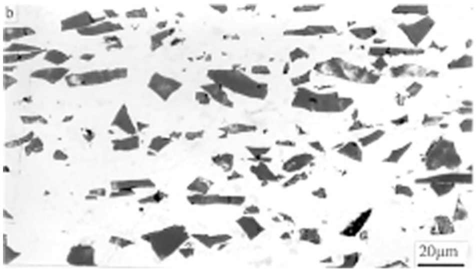

Microstructure anisotropy after extrusion of a PM MMC [86].

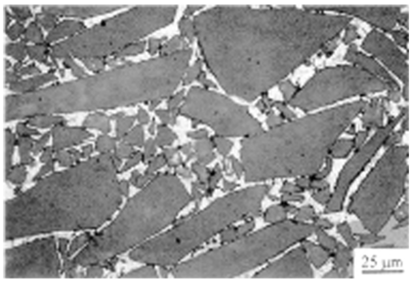

High volume fraction MMC (70 vol. %) prepared by infiltration of particles with a bimodal size distribution [1].

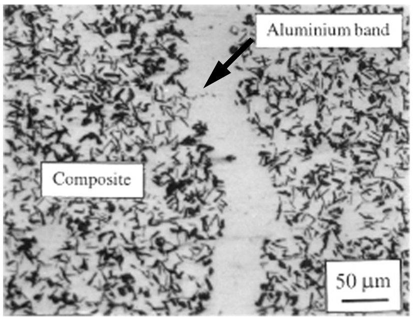

Vein in a MMC produced by squeeze casting [83].

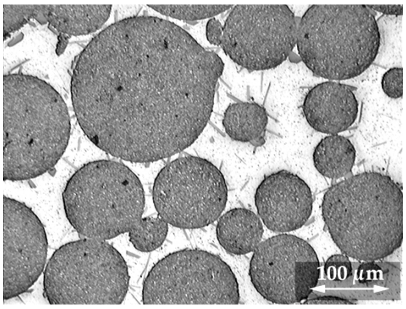

Reaction phases (needles) in a Al-$B_4C$ composite produced by gas-pressure infiltration. Unpublished research in our laboratory.

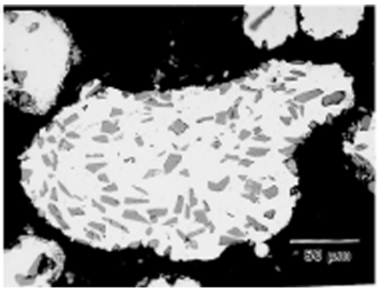

Spray drop of MMC produced by spray-forming [46].

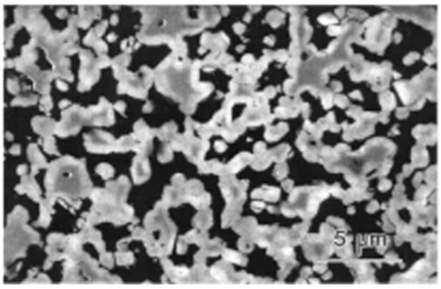

Interpenetrating phase composite ($Al/Al_2O_3$). $Al_2O_3$ in bright [87].

**Figure 2-5.** Some microstructures of PRMMCs produced via various processing techniques, illustrating some typical features and/or defects inherent to the processing route. References are indicated between brackets.

# 2.3. FRACTURE TOUGHNESS OF PRMMCS: REVIEW OF EXPERIMENTAL DATA

For a background of basic theory and concepts of fracture mechanics, readers are referred to Appendix A, where both Linear Elastic Fracture Mechanics (LEFM) and Elastic-Plastic Fracture Mechanics (EPFM) are summarized.

It is well accepted that fracture toughness is a, if not the, major drawback of PRMMCs in term of mechanical performance. Hence many experimental investigations have been conducted in the past 15 years to assess the root causes for these rather poor properties, in order to improve them. Microstructural effects and extrinsic factors[1] that affect the fracture of these materials are nowadays extensively documented and the damage events leading to failure have been identified. These fracture micromechanisms can be classified into the following modes:

(i) particle fracture;
(ii) debonding or cracking along the reinforcement/matrix interface;
(iii) failure in the matrix via microvoid coalescence;
(iv) failure in the matrix by shear.

The fracture modes as classified here are thought in terms of initiation: when cracking of particles initially occurs, it must necessarily be followed by subsequent damage in the matrix to link the cracked particles,:this is however still considered to be mode (i). On the other hand, mode (iii) involves fracture initiation in the matrix. Generally speaking, damage is highly localized in front of the crack tip due to the local stress and strain amplifications, whereas by comparison damage is more uniformely dispersed along the gage length in tensile specimens [88, 89]. While each of the damage processes might operate in a particular composite, one mode is generally dominant for a certain combination of reinforcement/ matrix alloy/heat treatement. What is still lacking is a clear knowledge of the importance of each of these modes, and what are the key microstructural variables that control fracture and in which manner they do so, in particular because the processing defects sometimes overshadow the influence of other parameters.

## *2.3.1 Summary of existing reviews*

This large body of information has been periodically reviewed during the last 10 years [24-28, 90, 91] with different objectives depending on the author. The combination of these publications covers most of the features of PRRMCs fracture. Before going into further detail, the general picture that emerges from these review papers is given as follows:

Mortensen [26] has summarized most experimental data published in the 1980s. He concluded that toughness values were dominated by the microstructural defects. Few correlations were thus apparent and it was concluded that controlling the processing was crucial in order to achieve higher toughness. For instance, when plotting the compiled toughness data as a function of yield stress, no correlation was found and the data were almost randomly scattered on the plot. A simple analysis was proposed to link the total fracture energy with the microfracture events in the process zone.

---

[1] The term “extrinsic factors” refers here to factors influencing toughness that are not related to the microstructure or in other words that are not material parameters. While in general clear, such a distinction can be somewhat arbitrary.

Davidson [90] focused on the mechanisms that control fracture toughness, and how this can be predicted, to point out that fracture is particularly sensitive to how well the particles are distributed within the matrix and how readily they break. An important conclusion was that the main contribution of fracture toughness is by plastic dissipation in front of the crack tip, namely that particle-reinforced metal composites are metallic from the point of view of toughness. It was also suggested that constraint in the matrix caused by the elastic particles should have a major effect on composite fracture.

Hunt [24] emphasized the fact that the reinforcement properties, such as their brittleness and their intrinsic resistance to fracture, should play an important role in controlling fracture and that the potential improvement afforded by tougher particles had not been explored yet.

Lloyd [27] discussed the various micromechanical models existing at that time to predict the composite toughness, to conclude that extensive developments were needed to explain the toughness of PRMMCs regarding the complexity and the interaction of factors influencing fracture toughness.

In his first review article, Lewandowski [91] has covered mainly toughness data published in the first part of the 1990s and exhaustively compiled them as a function of microstructural factors (particle size, particle spacing, volume fraction, matrix alloy and matrix microstructure). It was concluded that there is a general loss in toughness with increasing volume fraction of reinforcement, a comment that is not supported by Mortensen and Davidson in their respective reviews. Both pointed out that a lower volume fraction is not necessarily accompanied by a higher toughness, but that the microstructural homogeneity is more important. A second general feature Lewandowski commented on in PRMMCs is the non-recovery of toughness upon overaging of the composite, which is an opposite trend as compared to traditional characteristics of unreinforced aluminium alloys. It was also argued that more significant enhancements of strength/toughness combinations are achieved via extrinsinc toughening approaches, as presented in §.2.3.6.

Sinclair and Gregson [28] concluded also that although quantitative information about damage and fracture in PRMMCs has increased, the correlation betwee toughness ranges and other mechanical properties such as ductility were not yet elucidated, and that various complicating micromechanical interactions rendered the comparison between experimental data and modeling difficult. According to these authors, a quantitative understanding of failure in PRMMCs should be carried out specifically for individual composite systems.

The most recent review devoted to fracture toughness of PRMMCs was provided by Lewandowski [25], who basically completed the earlier review with data published in the second part of the 1990s. As compared to the previous review, it was noticed that comparatively high toughness could still be achieved with a larger volume fraction of reinforcement, while other conclusions were equivalent to the first overview.

In what follows, we first summarize testing procedures preferentially employed in assessing fracture toughness of PRMMCs, focussing on their inherent experimental difficulties and limitations. Then we present in greater details the microstructural factors that have been found to influence the toughness of PRMMCs. These include: (i) the volume fraction of reinforcement, (ii) their type, shape and size, (iii) the role of the matrix and its heat-treatment. The role of these factors on both quantitative data and micromechanisms of fracture is considered. Extrinsic factors that are susceptible of influencing the experimental data and the recent appoaches attempted to enhance the fracture properties of PRMMCs are finally presented.

### 2.3.2 Testing procedures

While particle reinforced metal matrix composites are significantly more brittle than their alloy counterparts, they generally are metallic materials in terms of their elastic-plastic deformation behaviour. Fracture testing of these materials is therefore based on standard test procedures for unreinforced metals, as was stated earlier [26, 92]. Plane-strain fracture toughness testing according to ASTM-E399 standard [93] has been largely applied to PRMMCs, using in general compact tension (CT) specimens [94-98], or single edge notched bend (SENB) geometries, [99, 100]. In some instances, double-notched bend bar specimens tested in 4-point bending have been employed, taking advantage of the fact that only one notch fails and allowing the examination and identification of the fracture initiation events in the remaining notch [35, 36, 101]. In these references, sufficiently sharp cracks were initiated and propagated in the specimen by fatigue loading, thereby ensuring a high triaxial stress state at the crack tip.

The creation of precracks by fatigue loading is difficult in MMCs; hence this step is sometimes ommited. Instead, notches are machined by use of electro-discharge machining (EDM) or with a diamond saw have been used [102-104]. According to these investigators, the argument for this sample preparation is that below a certain notch radius (in the order of 50-100 µm) the same results are obtained as with fatigue pre-cracked samples. Another issue in meeting the requirements of ASTM-A399 is the difficulty in obtaining a sufficiently straight crack front by fatigue, a feature that is attributed to residual stresses in particulate MMCs [94].

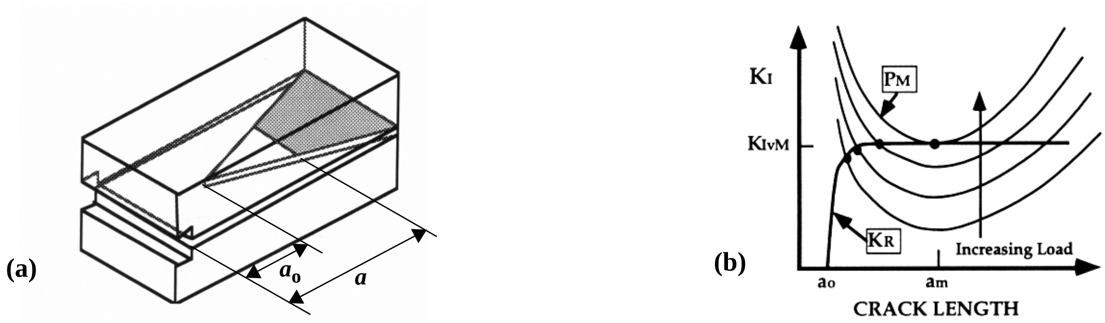

**Figure 2-6.** Chevron-notched testing**. (a)**: specimen geometry, $a_0$ is the initial crack length; **(b)**: crack-driving force for increasing load and material resistance curve. Maximum load is attained at a specific crack length only dependent on the geometry of the specimen for limited *R*-curve behaviour.

A method to overcome pre-cracking and its difficulties altogether is to use chevron-notched specimens according to the normalized method ASTM-E1304 [105]. In short, a chevron-shape notch is machined into the specimen (Figure 2-6a). Because the load is applied over a very small area, the initial stress-intensity factor in the chevron-notched specimen is very high. The crack forms and propagates early, but because of the increasing width of the crack, the driving-force for crack propagation decreases with crack length. A higher load is required to grow the crack further, allowing stable initial crack propagation (Figure 2-6b). The maximum load $P_m$ is attained during the test when the minimum of the crack driving force curve becomes tangent to the material resistance curve. For materials with a flat $R$-Δa curve, $P_m$ is attained at a certain crack length $a_m$ depending on the specimen geometry. The critical stress intensity factor is computed from the maximum load. Another advantage associated with chevron specimens is that plane strain is more readily maintained in the ligament, allowing the use of smaller specimens and reducing the machining operations as compared to CT specimens. The technique is, on the other hand, not suitable for materials with rising *R*-curve behaviour, because the maximum load does not occur at a fixed crack-length: it varies depending on the material resistance, $K_R$. In this situation, the crack length is inferred through an unloading compliance technique which permits to extend the validity of the method. For even tougher materials exhibiting extending plasticity during crack propagation, the method is no longer appropriate; hence the standard places criteria roughly similar to ASTM-E399 [106] which restricts specimen plasticity for a test to be valid. For additional details on chevron-testing, one can refer to [107, 108].

It has been shown in high-strength aluminium alloys (in which chevron specimens have found a a large field of application), that $K_c$ data obtained from ASTM-E1304 were closely equivalent to $K_{Ic}$ data measured with the ASTM-E399 method for toughness levels near 20 MPa·m$^{1/2}$ [109-111] and that significant differences were obtained for toughnesses higher than 35 MPa·m$^{1/2}$ [111, 112]. Chevron-notched testing is hence considered to be highly suitable for PRMMCs [26, 113], given their range of toughness (typically lower than 35) and the simplicity of the method. Fracture toughness testing using this method has for instance been reported in [26, 92, 113-115], while comparison with ASTM-E-399 have been carried out in [101, 116] where good agreement was found.

For more ductile and tougher composites which do not satisfy requirements of LEFM, the determination of *J-R* curves has also been carried out in PRMMCs, based on the ASTM-E813 or more recently ASTM-E1737 procedures [117, 122, 133, 154, 156, 315]. As more ductile materials are by definition easier to precrack by fatigue, all investigators who have measured *J-R* curves used pre-cracked samples, with the exception of one study [117]. Among other methods that have been used when LEFM is invalid, one can cite the essential work of fracture approach [118], which can be useful in gaining data on thin specimens.

## 2.3.3 Effects of particle volume fraction and particle clustering

### i. Volume fraction of reinforcement

Looking at data collected in review papers cited above, the influence of the volume fraction of reinforcements ($V_f$) is rather controversial. It appears that the toughness decreases rapidly at low $V_f$ (0-10%) and that the rate of decrease in fracture resistance slows down as $V_f$ increases further [25, 88] such that there is a relatively little loss in toughness when $V_f$ is raised to 30-40 %. Interestingly, some data for large volume fractions (40 - 60%) suggest that toughness is almost not affected in this range and, that toughness as high as for 10% of reinforcement can be obtained [119-121].

Comparing data from a wide range of sources has the advantage that a general picture of the effect of $V_f$ emerges. On the other hand data are given for quite different matrices, particle type and size, or processing routes which all affect toughness. It hence turns out that a large scatter in the data exists [26]. For instance, for 15% reinforcement, one can find published $K_Q$ values ranging from 8 to more than 30 MPa·m$^{1/2}$ for different matrix/reinforcement combinations. Similary, for higher particle contents (55%), values from 7 MPa·m$^{1/2}$ [77] up to 20 MPa·m$^{1/2}$ have been reported [114] for composites with different matrices. In addition one must exercise caution regarding what parameter is chosen to compare toughness data. In many cases, the fracture energy $G_{Ic}$ or $J_{Ic}$ is used, while the parameter that matters in design is rather $K_{Ic}$ which is correlated to $G_{Ic}$ via the relation: $K_{Ic} = \sqrt{(G_{Ic}E)/(1-\upsilon^2)}$ (or to an equivalent $K_{Jc}$ if $J_{Ic}$ is used: $K_{Jc} = \sqrt{(J_{Ic}E)/(1-\upsilon^2)}$ ). Hence, if there is a decrease in toughness as expressed by the energetic factor $J$ for a larger volume fraction, it is somehow compensated for when it is expressed in term of the stress intensity factor because the modulus $E$ increases with $V_f$. This effect is well visible in the review by Lewandowski [25] and is even more obvious in [114].

A fundamental understanding of the effect of volume fraction requires looking at data for which $V_f$ is the only microstructural variable. There exist few such studies because changing $V_f$ over a large range may necessitate the use of different processing techniques to produce the composites, which are then no longer comparable. Systematic work reported is therefore focused on a limited range of $V_f$. Among these, clear results were obtained from a study [122] conducted on an alloy used as a model for composite: the authors used Al-Si-Mg alloys with a Si content varying from 10 to 20%, produced via a rapid solidification powder atomization process. This avoided the formation of primary Si in hypereutectic compositions (Si > 12.7%) such that they could form brittle Si particles to a level up to 20%[1], which were moreover uniformly dispersed in the matrix. Both the initiation toughness $J_{Ic}$ and the tearing modulus $T_R$ clearly decreased with increasing $V_f$ from 10 to 20% for different heat treatment conditions. A similar trend for $V_f$ varying from 10 to 30% was also reported in extruded 2080/SiC composites [24]. In the high volume fraction range (> 40%), one can cite studies conducted on infiltrated composites where the volume fraction was varied by packing the particulates to different green densities [114], or using a bi-modal particle size distribution [77, 97]. In these works, toughness as expressed in term of $K$ was seen to be independent of $V_f$.

### ii. Clustering

As compared to the effect of volume fraction, there is more agreement concerning the detrimental influence of particle clustering on the toughness of PRMMCs. This is extensively documented [34, 36, 56, 88, 123, 124]. The commonly accepted reason for this effect is related to a local enhancement of the stress state in a cluster due to the constraint imposed by the closely spaced elastic particles [125-127]. This higher degree of triaxiality results in the development of high local stress relative to the applied global strain and in turn to a faster accumulation of such damage. Hence, the particle clusters rapidly concentrate damage and provide a favorable path for linkage of the damage [124, 128], as can be seen in Figure 2-7a. This mechanism reduces the fracture toughness. The comparison of quantitative studies of this effect is nevertheless rather difficult because it is not yet clear how clustering should be quantified among the various means reported [34, 56]. The most useful approach seems to measure the degree of clustering as the distribution of minimum reinforcement spacing in a composite, as seen in Figure 2-7b, where fracture toughness is unambiguously reduced when the degree of particle clustering increases, while $V_f$ remains constant [36]. Whatever is the method of cluster quantification, it is in any case admitted that high levels of clustering are to be avoided if one wishes to improve the fracture resistance of PRMMCs. This also gives an explanation for the lack of influence of $V_f$ in the high volume fraction range: clustering is essentially reduced, if not eliminated, for this class of MMCs.

---

[1] The microstructure of the alloy is hence similar to MMCs with the exception that reinforcements are not ceramic particles but “in-situ processed” Si particles.

In terms of the fracture micromechanisms, it appears that if the particles are prone to crack, there is simply a larger number of broken particles for larger $V_f$. Other microstructural parameters, presented hereafter, have much more influence on the fracture micromechanisms.

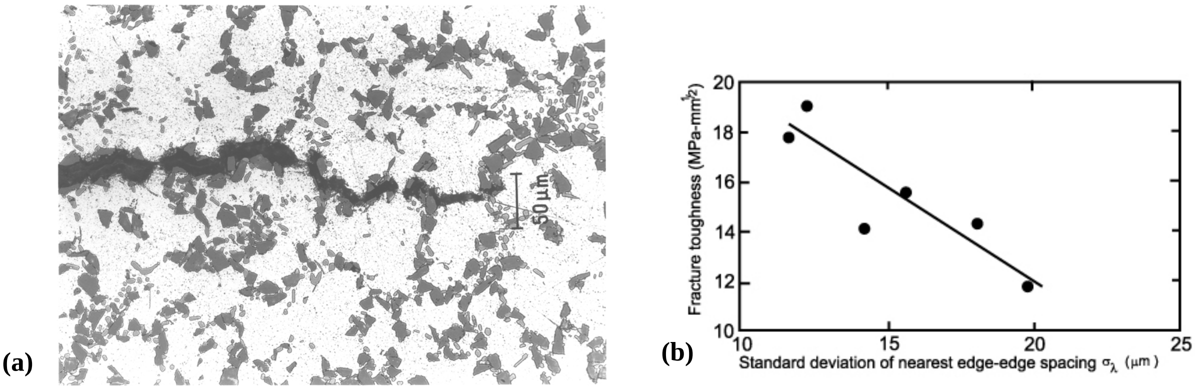

**Figure 2-7.** **(a)**: Crack propagation in an as-cast composite of A356 reinforced with 15 vol.% of SiC particles, illustrating the preferential crack path through clusters. Unpublished research by Roudier and Mortensen; **(b)**: effect of clustering on fracture toughness of similar composite, with constant $V_f$, from [36].

## 2.3.4 Effects of the reinforcement

### i. Particle size

As for the volume fraction, clearer effects appear in published data where either the particle type, the particle size, or the particle shape, is the only variable, other microstructural factors being held constant. Concerning particle size, a tendency that has been regularly observed is an increase of fracture toughness as particle size increases [129, 130] (or equivalently as interparticle spacing increases if the volume fraction remains constant), provided however that the particle size is below a critical value [97, 103, 117, 131]. Looking at data from other authors indicates that such a trend is less evident [24] or non-apparent [99, 132-134] and that toughness is independent on the particle size, although a decrease of toughness for very large particle sizes was observed in one of the studies [133]. In this last work, which employed pure powder-metallurgy Al matrix, it is to be mentioned, on the other hand, that crack growth resistance as expressed in terms of the tearing resistance clearly increased with increasing particle size.

In terms of the fracture micromechanisms, it is well agreed that particle cracking dominates in larger particle size composites, while fracture initiates and propagates predominantly in the matrix for fine particle size composites because small ceramic particles are more resistant to cracking. Such observations have been often reported in the above mentioned references and are even more extensively documented for tensile tests, see for instance [38, 89, 120, 127, 135-137]. These trends are explained in terms of the Weibull theory of brittle cracking: the probability of particle cracking increases with increasing particle diameter because the probability that a defect of critical size exists in the particle increases as well [138-141]. This transition of the operative damage mode has been invoked to explain the toughness decrease in large particle size composites.

### ii. Particle type

The influence of particle type (in terms of the chemical nature of the ceramic) does not emerge clearly from the literature. The data from the review by Mortensen have, for instance, indicated that SiC, $Al_2O_3$ or $B_4C$ particle reinforced composites all fall in a similar range of yield stress/toughness combination, although the toughest composites were the SiC-reinforced ones. In composites with a given matrix and particle size, there are studies reported where alloys reinforced with $Al_2O_3$ particles are tougher than those reinforced with SiC particles [115, 142, 143]. In one work, SiC-reinforced composites were seen to exhibit a higher fracture resistance than $B_4C$-reinforced composites [129]; while results from another investigation and for a different matrix showed that $B_4C$/Al alloy composites were tougher than SiC/Al alloy and $Al_2O_3$/Al alloy composites [130], and that these two last materials were roughly equivalent. It also appears that comparing the effect of particle type only is not really relevant because a same matrix alloy may exhibit different adhesion and/or levels of chemical interactions with various particle types. For instance, alloy 6061 reacts with SiC to form $Al_4C_3$, which weakens the interface more significantly than the $Mg_2Al_2O_4$ phase formed by reaction of the same alloy with $Al_2O_3$ particles.

Rather than their composition, it has been pointed out by a few authors that the quality of the particles themselves should play a more important role [24, 88, 90] and more recently in [144, 145] but this factor has not been studied in a systematic manner. When pre-existing cracks or flaws are found in the particle, crack propagation through the particle is more likely to occur [146]. Numerical methods to simulate the interaction of a crack and a second phase particle in discontinuously reinforced composites have also indicated that a pre-existing flaw on the interface of a particle acts to attract the crack [147]. As in bulk ceramics, for which fracture toughness can vary over a wide range for a certain ceramic type (see Table 2-1), it is hence expected that the fracture resistance of particulates strongly depends on their processing method and the supplier, which should in turn reflect on the apparent particle fracture Weibull modulus. What comes out from the literature is that initial investigations of particles are rarely conducted while methods to characterize the individual particle strength simply do not exist at the moment. The potential improvement by use of stronger particles has thus not been assessed, because it is one of the less controlable parameters in particle-reinforced MMCs.

#### iii. Particle shape

The influence of particle shape on the mechanical properties of PRMMCs has also been studied in the past years, with greater emphasis on the flow stress and ductility while its effect on fracture toughness has been adressed less. Early numerical simulations [148] indicated that the particle shape influences constraint in the matrix (expressed by the maximum hydrostatic stress). In particular, it was found in this study that local constraint is several times larger for angular-shape reinforcements than for spherical particles, and that sharp corners result in a rise of localized plastic strains, leading to local void formation in the matrix. Other FEM simulations conducted since then by various authors confirmed such local shape effects and their influence on the global deformation behaviour [77, 86, 149-152].

Experimental investigations have been conducted mainly on commercially available composites [96, 116, 153], produced by "Duralcan" (San Diego, CA) and "Comalco" (Melbourne, Australia) because these exhibit similar microstructural characteristics but different particle geometry: both consist of a 6061 Al matrix reinforced with 20 % vol. $Al_2O_3$ particles that are angular for the Duralcan composite, while they are microspheres for the Comalco composite. Flow stress was indeed proven to be higher for angular reinforced composite but higher ductility was achieved for the spherical shape reinforced composite. This higher ductility for round particles was also confirmed in a study where two SiC/6061Al composites were made by stir-casting, with blunted particles in one case (produced by high-speed atomization) and commercial angular particles in the other [86].

In order to quantify the constraint on plastic flow imposed by both the elastic ceramic particles and superimposed crack tip stress field, Davidson and Hennes [96] experimentally observed local deformation using a stereoimaging technique allowing resolution at the microstructural scale in the Duralcan and Comalco composites. Their observation revealed that the crack trip strains are influenced by the particle shape: local strain-hardening in the matrix is more pronounced with sharp cornered particles than with spherical particles. They suggested that higher values of toughness should be obtained when local constraint is lower, namely for round particles. Fracture toughness measurements on the same composite [116] did not confirm such expectations because: (i) the particle chemistry was different as well as the particle dispersion within the composite, and (ii) there was a higher level of impurities (Fe, Si and Cr) in the Comalco composite, leading to a higher amount of fine secondary intermetallic phases that embrittle the material.

Again this highlights the issue of comparing materials that features in principle similar microstructure but that are in fact produced via different processing techniques and by different investigators (or companies in this case). The effect of particle shape on local matrix constraint remains nevertheless proven and is well accepted among investigators, but experimental quantification of its influence on fracture toughness has not been achieved yet.

### *2.3.5 Effects of matrix alloy and microstructure*

The matrix properties have been found to play a critical role in the fracture resistance of PRMMCs, the key variables being the matrix composition and the heat treatment. A feature specific to PRMMCs is the lack of recovery of the toughness after an overaging (OA) heat-treatment. This is in contrast with most unreinforced aluminium alloys where it is generally observed that, when evolving from underaged (UA) to peak aged (PA) condition, toughness decreases with an increase in strength up to peak strength, and then recovers upon overaging [25]. These two behaviours are summarized in Figure 2-8 for various composite systems (including 2xxx, 6xxx, 7xxx and 8xxx matrix composites) and for monolithic alloys, in terms of fracture toughness vs. yield strength plots. This lack of recovery has generally been attributed to a change in the micromechanisms of fracture, which evolve from particle fracture in the UA condition to near interfacial failure in the matrix nucleated by coarser precipitates in the OA condition. Such a transition is in addition reflected by a faster accumulation of damage in the overaged composite [154, 155]. Also included on Figure 2-8 are data from recent work [156] on an Al-7093/SiC powder metallurgy composite, for which optimized overaging heat-treatment did provide recovery of the fracture toughness. Such uncommon behaviour was attributed to a precipitate-free zone (PFZ) region in the immediate vicinity of the particles which led to a lower local matrix yield strength (while high interface strength remained), which protected the interface and promoted dimple rupture in this region. The PFZ zone mechanism was corroborated in [157]. One notices that this finding is in contrast with the mechanism explained above (*i.e.* that near-interfacial failure results in lower toughness as compared to particle fracture); this is because in non-PFZ materials, the overaged precipitates lead to accelerated fracture by voiding or, worse, to brittle interfacial decohesion.

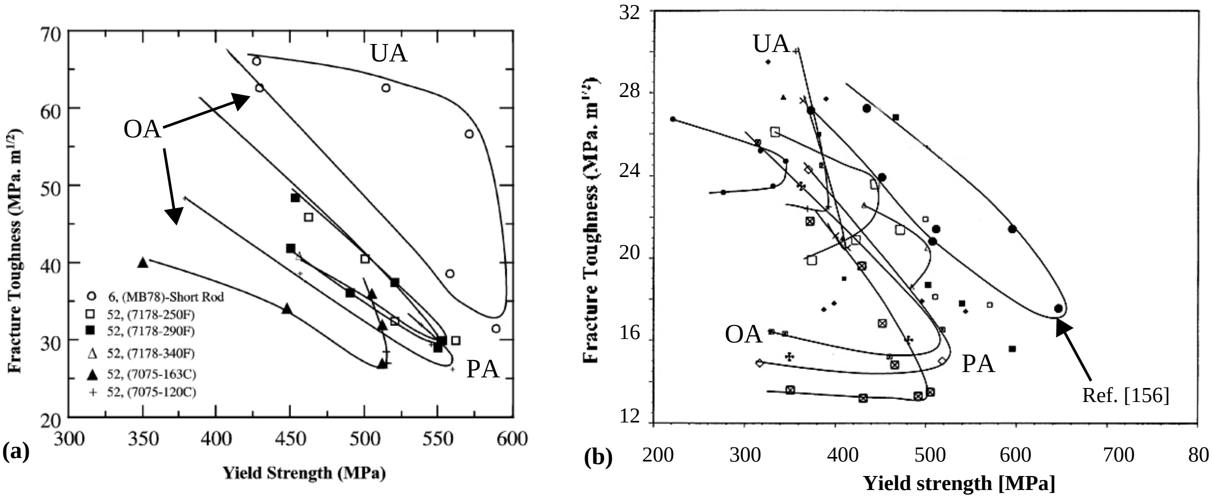

**Figure 2-8.** Fracture toughness vs. yield strength plots illustrating the influence of matrix heat-treatment on toughness of **(a)**: monolithic aluminium alloys; and **(b)**: PRMMCs. From [25].

The effect of matrix composition does not always clearly emerge given the wide range of fracture toughness/yield strength combinations covered by just one type of matrix. Rather, it comes out from recent investigations that superiority of one matrix over another should be due to the ability to provide toughness recovery after over-aging treatment. In a study [158] where a quite high toughness (almost 30 MPa·m$^{1/2}$) was measured for an Al-2014/15 vol.% SiC composite in the PA condition as compared to other matrices tested, it was proposed that the matrix influence on the overall composite toughness is reflected through its influence on the crack-tip plastic zone formed in the composite, because this zone accounts for the major toughness contribution. By extension, this means that an appropriate way to improve composite toughness is by increasing the ductility of the matrix. This is not in contradiction with the PFZ assumption, since the latter also involves reduction in strength and increasing ductility, but in a region localized around the particles.

The dominant contribution of the crack-tip plastic zone to the fracture resistance of PRMMCs is confirmed when looking at published data in terms of the tearing modulus $T_R$, since the shape of *J-R* curves is mainly governed by the plastic zone development. $T_R$ in Al-7050/20% SiC reinforced material [154] is indeed strongly dependent on the matrix aging conditions, and the lowest values of $T_R$ corresponded to the highest yield strength. When further comparing these data with those publised in [133], where the only significant microstructural difference is the pure Al matrix (*i.e.* $V_f$, particle type, and particle size are similar), one notices a tearing modulus about two orders of magnitude larger in the pure Al matrix composite. On the other hand, the initiation toughness is larger for the Al-7050 matrix composite. Hence a clear evidence of the influence of the matrix strength translates into the ability for the composite to exhibit a fracture response with significant tearing resistance[1].

---

[1] The fact that stable crack growth is not observed does not mean that a *J-R* curve behaviour does not exist, since crack propagation stability strongly depends on the compliance of the loading system. It is nevertheless a good indication that the resistance to ductile tearing is quite weak.

### 2.3.6 Extrinsic factors influencing the fracture toughness: specimen geometry and stress state

#### i. Notch geometry

The difficulty in pre-cracking particle-reinforced metals, caused by their inherent brittleness, has led investigators to overcome this issue by either using chevron-notched specimens, or by employing specimens with electrodischarge-machined (EDM) or saw-cut notches instead of fatigue precracks. The loss of constraint on the toughness of PRMMCs resulting from the notch geometry has been adressed in some references. In [102], fracture toughness was seen to decrease linearly with the square root of the radius, until $\rho$ = 60-80 µm below which toughness did not vary significantly. Such observations were confirmed in [104] where toughness values measured on specimens containing a 60 µm notch radius were equivalent to those measured on pre-cracked specimens. In [159], a lower bound toughness was obtained for a 50 µm notch radius; however, work in [160] did not yield the same conclusion: the toughness of specimens with a fatigue pre-crack was about 50% lower than that of specimens with a notch having a 125 µm radius machined by EDM. The latter value corresponded quite well with measures from another reference [154] on specimens with a 30 µm notch radius, the same thickness, and similar material and heat-treatment conditions. Accordingly, it was claimed that PRMMC specimens should be pre-cracked in order to obtain valid toughness measurements. In [100], various pre-cracking conditions were also seen to have some effect on $K_{\mathrm{Ic}}$ measures, and lower-bound values were obtained for samples pre-cracked in tensile fatigue at a smaller applied $K$.

To account for the notch root effect, the measured toughness is sometimes corrected through the following empirical formula:

$$K_{\mathrm{Ic}}(\rho)=\frac{K_{\mathrm{Ic}}(1+\rho/2c)^{3/2}}{1+\rho/c} \tag{2-16}$$

where $K_{\mathrm{Ic}}$ is the initiation toughness of a geometrically sharp crack and $c$ is an adjustable constant related to the microstructure.

#### ii. Specimen size and stress state

PRMMCs fall into the category of elastic-plastic materials, for which the specimen thickness strongly affects constraint during fracture testing. Still, as they typically exhibit a much reduced plastic regime and a higher yield strength compared with their alloy couterparts, one may raise the question as whether the thickness effect is as important in composites. In one of the first systematic studies on this effect (conducted on Al-6061/SiC 25 vol.% and Al-2124/SiC 30 vol.% composites [94]) toughness was larger only for very small thicknesses, while specimens thinner than required by the validity criteria were not significantly tougher than the average values for the thicker “valid” specimens. Tests conducted on a cast A359/SiC 20 vol.% composite [98] revealed no influence of the thickness below the standard validity criteria. Shear lips were not observed even in the thinnest specimens. The low ductility and the local triaxial stress state provided by the SiC particles was the reason invoked for this lack of influence of thickness. Such results for fracture initiation were confirmed in [161] for a 2080/SiC-20 vol.% composite produced via powder-metallurgy, although the thinnest specimens clearly showed an increase in the crack growth toughness.

Based on these results, some authors have suggested that the thickness criteria in LEFM (eq. A-20) could be relaxed for particulate reinforced MMCs. More recent studies [156, 160] have on the other hand indicated that the influence of the specimen thickness is very sensitive to the microstructure, more specifically to the elastic-plastic behaviour of the composite: in the latter reference a well-marked thickness dependence was observed on the crack initiation toughness measured by the *J*-integral test method. This material (Al-7093/SiC15 vol.% ) was also much more ductile (6% strain to failure versus 0.4% in [98]) and exhibited shear failure on the sides of the thinnest samples, revealing a dominance of plane-stress conditions there. This means that a sensivity of toughness on the specimen thickness appears mostly for fairly ductile composites.

As also pointed out in [160], the dependence of toughness on the stress state is revealed in tensile experiments conducted under high hydrostatic pressure (*i.e.* under reduced hydrostatic tension) which show an increase in strain to failure for certain PRMMCs, caused by a slower evolution of damage in the form of void growth [162, 163]. Interestingly, such experiments bring about an explanation for other effects such as clustering since it was found that a superimposed hydrostatic pressure was not effective in improving the ductility of clustered MMCs [56, 123]. Clearly, local tensile triaxiality within clusters was too high to be exceeded by the external applied pressure.

### iii. Toughened MMCs

Many recent studies with a view on improving fracture toughness of PRMMCs have been performed by modifying the architecture of the material at the larger mesoscopic scale [85, 164-167]. Because the manipulations are not directly made at the microstructural scale, such MMCs are often called “extrinsically toughened MMCs”. The principle behind these toughening approaches is to increase crack stability by providing alternative crack propagation paths, leading to a reduction in the effective driving force for crack growth. Most such structures that were fabricated and investigated are laminated PRMMCs, which consist of alternating layers of composites and aluminium alloys (Figure 2-9a). These are obtained via various techniques such as vacuum hot pressing, roll bonding, extrusion or spray deposition (see [25] for a general review). Alternatively, structures in the form of fibers of PRMMCs embedded within a monolithic alloy and produced by extrusion (Figure 2-9b) have been reported [167], as well as structures consisting of aluminium alloy particles incorporated into the composite [166], Figure 2-9c.

Such structures have been proven to feature enhanced toughness, both in initiation and in growth toughness. For instance, in [85, 161, 165] for laminated composites the toughness level approaches that of the monolithic alloys, giving a priori an interesting engineering potential for these materials. The mechanisms leading to toughening are obviously very dependent on the loading orientation with respect to the structure, the two main orientations being denominated as crack arrestor and crack divider (Figure 2-9d). Generally speaking, shielding of the crack tip from the applied sress includes crack deflection, crack bridging by the ductile layers, and crack trapping. Optimization of toughness in PRMMC/Al alloy laminates can be obtained by control of the interfacial strength between composite and unreinforced regions, so as to cause a certain degree of delamination. The choice of the layer thickness results from a compromise between two opposite effects: thicker layers offer a more marked *R*-curve behaviour, while thinner layers can take advantage of the toughening effect brought by the plane stress state in thin composites [85] (an effect that depends, however, on whether the PRMMCs used for the laminate does exhibit a toughness dependence on the stress state).

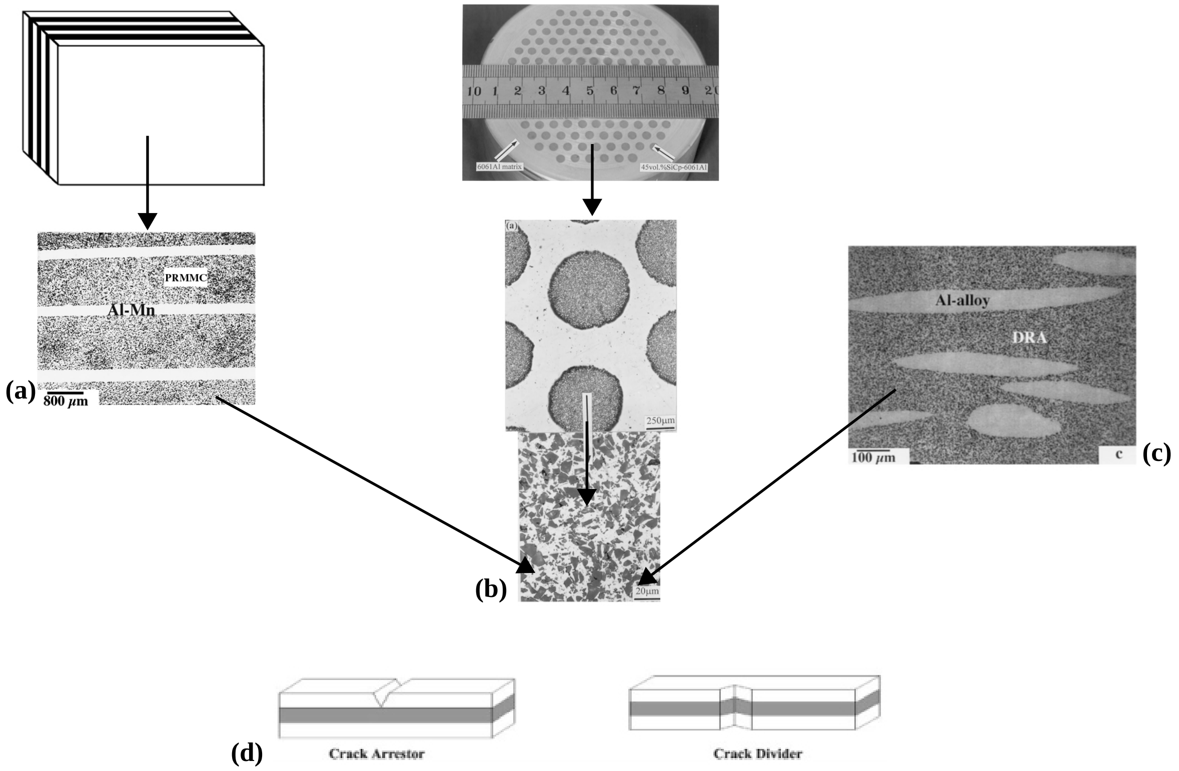

**Figure 2-9.** Structure of toughened MMCs. **(a)**: laminated composites with alternative layers of composite (darker) and alloys [85]; **(b)**: fibre like structure [167]; **(c)**: beam-shape aluminium particles within PRMMCs[166]; **(d)**: crack divider and crack arrestor laminate orientations [91].

When assessing the performance of such extrinsically toughened structures, it should be kept in mind that they contain a lower global volume fraction of reinforcements. Hence for a comparison with the toughness of PRMMCs, the values obtained from *J*-integral testing (which is the most frequently used to characterize laminates) should be converted into an equivalent stress intensity factor that takes into account Young's modulus. The latter is larger for homogeneous PRMMCs due to their higher reinforcement volume fraction, and compensates somehow their lower toughness as expressed by the energetic release rate. Also, it should be noted that this lower $V_f$ applies to all other (especially mean-field) properties and that the resulting material is highly anisotropic, especially if weak interfaces are used. The price paid for extrinsic toughening is, thus, very high.

### 2.3.7 *Typical data*

To conclude this review of experimental data of PRMMCs, typical fracture toughness data are given in Table 2-3, in which volume fraction, Young's modulus, yield strength and UTS are included as well. Rather than presenting an exhaustive list of data from the literature, we concentrate on more widely available commercial composites, as well as on PRMMCs for which fairly high fracture toughness data have been reported.

**Table 2-3** Typical fracture data of some commercial PRMMCs, and PRMMCs for which relatively high toughness values have been reported.

| **Composite type** | **Processing method** | **Temper** | $V_f$ **[%]** | $K_{Ic}$ **[MPa·m$^{1/2}$]** | $E$ **[GPa]** | $\sigma_y$ **[MPa]** | $\sigma_{UTS}$ **[MPa]** | **Ref.** |
|---|---|---|---|---|---|---|---|---|
| Alyn Co., 6092/SiC | Extrusion | T6 | 15 / 25 | 22.6 / 20.4 | 98 / 119 | 427 / 462 | 496 / 538 | [29] |
| “ “ /$B_4C$ | | T6 | 15 / 25 | 22.6 / 20.4 | 98 / 119 | 372 / 386 | 448 / 483 | |
| Duralcan 6061/$Al_2O_3$ | Extrusion | | 10 | 21.5 - 24.1 | | 290 -350 | 350-370 | [29] |
| “ 2618/ “ | “ | | 20 | 19.3 - 20.3 | | 400-420 | 460-470 | |
| Duralcan 359/SiC | Gravity casting | T6 | 10 / 20 | 17.4 /15.9 | 86/ 99 | 303 / 338 | 338 / 359 | [29] |
| Alcoa Inometal X2080/SiC | Powder metallurgy | | 10 | 30 - 32 | | 375 -390 | | [24] |
| | | | 20 | 20 - 27 | | 390 - 415 | | |
| | | | 30 | 15 - 20 | | 415 - 490 | | |
| Lanxide Al-10Si-1Mg/SiC | Sand casting | T6 | 20 / 30 | 15.8 / 14.7 | 108 / 125 | 334 / 353 | 353 / 371 | [29] |
| Lanxide MCX-xxx | Pressureless infiltration | | 55 | 9.5 | 225 | | | [29] |
| Ceramics Process Systems A356.2/SiC | Pressure infiltration | | 54 / 63 | 11.4 / 11.7 | 167 / 192 | 427 / 430 | 450 / 550 | [29] |
| Ametek Hivol Al/SiC/68p | Pressure infiltration | | 68 | > 20 | 228 | | 210 | [29] |
| Dural 2014/SiC/15p | Powder metallurgy | | 15 | 23.8 - 29.5 | 107 | 345 | 450-470 | [158] |
| 2014/$Al_2O_3$/15p | Powder metallurgy | UA | 15 | 24.2 | | 331 | | [168] |
| | | PA | | 19.5 | | 469 | | |
| | | OA | | 18.1 | | 372 | | |
| 6061/$Al_2O_3$/15p | | UA | | 24.7 | | 221 | | |
| | | PA | | 22.7 | | 345 | | |
| | | OA | | 21.2 | | 276 | | |
| 7093/SiCp DRA | Powder metallurgy | ST | 15 | 25.4 | 91 | 430 | 577 | [156] |
| | | UA | | 19.0 | 90 | 503 | 629 | |
| | | PA | | 15.7 | 96 | 642 | 694 | |
| | | OA | | 19.6 - 25.3 | 89 - 93 | 369 - 591 | 451 - 642 | |
| 2014/$Al_2O_3$ | Gas-pressure infiltration | T4 | 55 | 22.3 - 26 | | | 300 | [121] |
| | | T6 | | 19.5 - 24 | | | 300 - 360 | |
| | | T7 | | 21.5 - 27 | | | 295 - 371 | |

## *2.3.8 Summary and comments*

Experimental work dedicated to the fracture toughness of PRMMCs of roughly the last 15 years has been reviewed. Since earlier reviews, the increasing amount and quality of data has led to a better understanding, often from systematic work conducted on well controlled systems and model materials, or thanks to studies carried out on the same materials and produced by similar techniques but by different investigators. One can now conclude with clarity on the unambiguously deleterious effect of clustering, and the role of matrix microstructure on the resistance to ductile tearing. Some ambiguities remain, however, for instance regarding the sometimes high toughness reported for high volume fraction PRMMCs. The role of reinforcement nature and shape is also not yet fully assessed, in particular because the initial quality of reinforcing powders is very variable.

The elimination or reduction of microstructural defects through well-controlled processing seems to be crucial in order to obtain attractive properties and deduce clearer trends. As the microstructure homogeneity is improved, the influence of the matrix microstructure should for example be more clearly revealed. The studies dedicated to the role of extrinsic factors on the value of toughnes in PRMMCs provide useful information for the investigators, especially regarding some experimental limitations. It also emerges from recent work that improving the toughness via extrinsic approaches, by manipulating the architecture of the materials rather than by changing the intrinsic microstructural variables, receives an increasing attention due to their promising engineering potential. We now turn to existing analytical micromechanical models that have been developed to predict the fracture toughness of PRMMCs.

# 2.4. MICROMECHANICAL MODELS OF FRACTURE TOUGHNESS IN PRMMCS

## *2.4.1 Rice and Johnson based approaches*

Attempts in describing fracture toughness of PRMMCs have often been based on the early model by Rice and Johnson [169]. This model was originally developed to correlate microstructural features with the fracture toughness of materials which fail by the nucleation, growth and coalescence of voids; for instance steels in which primary inclusions are the void nucleation sites. Rice and Johnson considered a spherical inclusion of radius $R_{\mathrm{i}}$ centered a distance $X_{\mathrm{i}}$ ahead of the crack tip. The inclusion is in this case regarded as a pre-existent void (*i.e.* the bond between the matrix and the inclusion is weak). It was assumed that crack propagation initiates when there is coalescence between the blunted crack tip and the growing void nucleated at the nearest neighboring primary inclusion, Figure 2-10a. The assumed criterion for this event was that it occurs when the distance between the crack tip and the void becomes equal to the vertical radius of the growing void. For a fixed inclusion volume fraction, if $X_{\mathrm{i}}$ is taken to be the average three-dimensional distance between inclusions $\lambda$, this analysis predicts that fracture toughness $K$ is proportionnal to $\lambda^{1/2}$, or that $J$ scales linearly with $\lambda$:

$$J_{\mathrm{Ic}} = \sigma_{\mathrm{f}} \lambda \tag{2-17}$$

where $\sigma_{\mathrm{f}}$ is the flow stress. While certainly pertinent in emphasizing the role of the interparticle spacing, this approach has not been successful in quantifying the role of particle spacing [170]. More specifically, the extent of void growth, which influences significantly the coalescence stage, is not considered in this model [171]. This rather restrictive applicability has led to some modifications of this analysis by different authors who proposed to describe toughness in terms of the micro-roughness of fracture surfaces produced by microvoid coalescence [171, 172]. The characteristic dimple dimensions defined in these models are shown in Figure 2-10b.

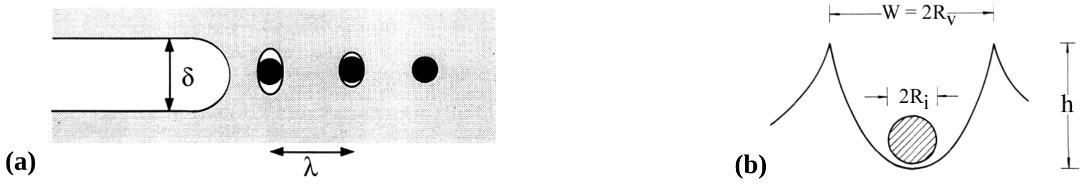

**Figure 2-10. (a)**: Rice and Johnson analysis of ductile fracture with voids nucleated at inclusions; **(b)**: Dimple characteristic dimensions as defined in [170].

These approaches were analyzed in greater details by Bray *et al.* [170] in the light of experimental measures of both toughness and void sizes.

These comments, based on investigations on steels, are nevertheless relevant in our case because the models that have often been used to describe the toughness of PRMMCs are adapted from these approaches, or are closely related to them. A conclusion of this work is that the model of Rice and Johnson, traditionally used to explain the role of particle spacing on the fracture properties in many structural alloys, can in general not be used to rationalize the role of particle spacing for ductile-type fracture. Regarding the models assuming the scaling of toughness with the fracture-surface roughness, it was shown that such approaches were reasonable only for materials of limited ductility, small particle spacing, and a constant blunting behaviour.

COMPARISON WITH EXPERIMENTAL DATA

Some attempts have been made to verify whether the Rice and Johnson model applies to PRMMCs [97, 103, 131]. It appears that $J_{\mathrm{Ic}}/\sigma_{\mathrm{f}}$ scales with the interparticle spacing $\lambda$ for small $\lambda$ only, while the model does not capture at all the toughness for large interparticle spacings. Compilation of many data by Lewandowski [25] also revealed fairly poor agreement. It can thus be concluded that this approach is not relevant for PRMMCs.

## *2.4.2 Hahn-Rosenfield models*

### i. Original model

Following the work of Rice and Johnson, Hahn and Rosenfield developed a model [173] to correlate the fracture toughness in aluminium alloys that fracture by microvoid nucleation, growth and coalescence, at dispersed particles of average size $d$ and volume fraction $V_{\mathrm{f}}$:

$$K_{\mathrm{c}} = \left[2\sigma_{\mathrm{y}} E \left(\frac{\pi}{6}\right)^{1/3} d\right]^{1/2} V_{\mathrm{f}}^{-1/6} \tag{2-18}$$

where $\sigma_{\mathrm{y}}$ is the yield stress of the material. This model predicts an increase in toughness with increasing matrix flow stress. Furthermore for a fixed volume fraction of second phase, toughness increases for larger interparticle distance $\lambda$, the latter parameter being often expressed in PRMMCs [174] by:

$$\lambda = \left[\left(\frac{\pi}{6V_{\mathrm{f}}}\right)^{1/2} - \frac{2}{\pi}\right] \cdot d \tag{2-19}$$

COMPARISON WITH EXPERIMENTAL DATA ON PRMMCS

When applying the Hahn and Rosenfield model to rationalize the toughness of PRMMCs, the correlation with experimental data agrees well in some instances [154, 158, 174], but (sometimes in the same investigation) it does not describe the effect of matrix aging condition [154]. It also tends to overestimate the toughness, as was also observed in [175] and commented by Clyne and Withers [1]. In a study where toughness of a PRMMC was measured at different temperatures [95], the model, on the other hand, was seen to underestimate the measured values, in particular at temperatures between 200 and 300°C where the yield strength is low. The major criticism adressed to the Hahn and Rosenfield model is its prediction of increasing toughness with increasing strength, a feature that is traditionally not observed in PRMMCs (recall Figure 2-8), as also confirmed by the high temperature study [95].

With the exception of this last study, one notices that the model is in good agreement for relatively tough PRMMCs, namely those exhibiting toughness larger than 25 $\mathrm{MPa{\cdot}m^{1/2}}$. In terms of fracture mechanisms, the model assumes nucleation at the reinforcement particles and does not take into account smaller dimples nucleated by finer second-phases, which could explain the deviation for composites tested in different heat-treatment conditions. A second assumption is that the fracture surface is entirely composed of the matrix phase, while fractured or decohered particles are not considered. Since these events typically dissipate less energy than voiding and are widely reported, their occurence provide a reasonable explanation for the overestimation of predicted values with the model [176].

To conclude the discussion of the Hahn and Rosenfield model, there is also a confusion as to whether the composite or the matrix yield stress should be used in this equation, since intense plastic deformation (through microvoiding) is present in the soft matrix phase only. If it is more appropriate to use the matrix yield strength, this complicates the prediction since the latter can be somewhat larger than that of the unreinforced alloy due to the presence of the rigid elastic particles. Indeed, these generate additional dislocations upon cooling [89, 177-179] and, in addition, they constrain plastic flow leading to high local stress triaxiality [86, 96, 149, 180]. Hence there exists a local, *in-situ* flow stress of the matrix, the determination of which is not a trivial task.

### ii. Stress-modified fracture strain model

In this model, which was proposed by Ritchie and Thompson [181], and which is another extension of the Rice and Johnson approach, failure is postulated to occur when a critical strain ($\varepsilon^*$) is accumulated over a characteristic microstructural distance ($l^*$) ahead of the crack tip comparable to the mean spacing between the particle-initiated voids (*i.e.* the interparticle spacing), Figure 2-11:

$$K_{\mathrm{Ic}} \approx \sqrt{E'\sigma_0\varepsilon^* l^*} \qquad \text{or} \qquad J_{\mathrm{Ic}} \approx \sigma_0\varepsilon^* l^* \tag{2-20}$$

where $\sigma_0$ is the yield stress and $\varepsilon^*$ is a local equivalent plastic strain that is specific to the relevant stress state. The model hence implies that $J_{\mathrm{Ic}}$ for ductile fracture is proportional to strength times ductility, which according to the authors permits rationalization of the toughness/strength relation in cases where microstructural changes which increase strength also cause a more rapid reduction in the critical fracture strain. The main problem here is to define the term $\varepsilon^*$ that cannot, for example, be equated to the tensile ductility as conventionally measured. Some authors have claimed that toughness in PRMMCs is consistent with the critical strain model, but without quantification [115, 143].

More recently, Majumdar and Pandey [144] have adapted this approach to PRMMCs and obtained an expression that can be seen as a combination of the Hahn and Rosenfield model and the stress-modified critical strain model:

$$K_{\mathrm{Ic}} = 0.77\left[\frac{\sigma_0 \cdot \beta(\theta, N) \cdot d \cdot E}{d_{\mathrm{n}} \cdot \left(1 - \nu^2\right)}\right]^{1/2} \cdot V_{\mathrm{f}}^{-1/6} \tag{2-21}$$

where $\sigma_0$ is the yield stress as expressed in the Ramberg-Osgood expression, $\nu$ is the Poisson ratio of the composite, $d$ is the mean particle size, $d_{\mathrm{n}}$ is the Shih factor of the HRR field and $\beta$ is a parameter that contains information about the critical strain. $\beta$ is a critical parameter in their analysis and was suggested to depend on the crack propagation angle $\theta$. More specifically, it was acknowledged by Majumdar and Pandey that in their higher strength composites (in the PA heat-treatment condition) crack growth occurs along 45° slip bands in the matrix where the critical strain for rupture is lower than at the zero $\theta$ angle. This in turn influences $\beta$ with the interesting consequence that their model succeeds in predicting a gradual decrease in toughness with increased strength, although it somewhat understimated their measured values.

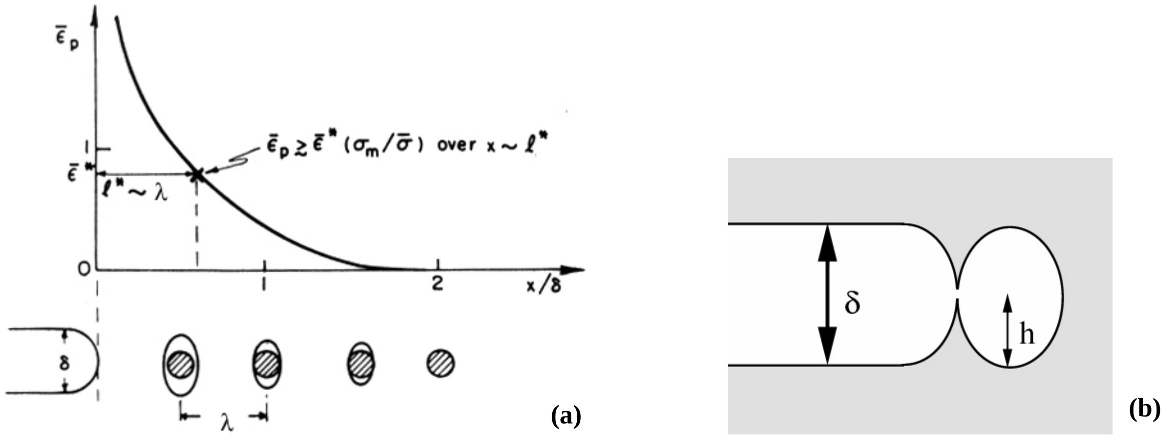
$\bar{\epsilon}_p$
1
$\bar{\epsilon}^*$
$\ell^* \sim \lambda$
$\bar{\epsilon}_p \gtrsim \bar{\epsilon}^* (\sigma_m/\bar{\sigma})$ over $x \sim \ell^*$
0
1
2
x/δ
δ
λ
(a)
δ
h
(b)

**Figure 2-11.** Models of materials fracturing by microvoiding. **(a)**: The stress-modified critical strain model of Ritchie *et al.*[181]); failure is assumed when the effective plastic strain $\varepsilon_p$ attains a critical value $\varepsilon^*$ (dependent on the stress state) over a characteristic microstructural distance *l**; **(b)**: fractographic model by Crowe *et al.* [102]; fracture is assumed to occur when the crack opening displacement coalesce with the leading void, δ = 2*h*.

### 2.4.3 Fractography-based models

The simple model proposed by Crowe *et al.*[102] assumes that the crack grows as the leading void in the process zone coalesces with the crack tip. In this case, the critical crack opening displacement ($\delta$) is simply two times the dimple height *h*, as depicted in Figure 2-11b. The toughness is then:

$$K_{\mathrm{Ic}} = \left( \frac{2hE\sigma_{\mathrm{y}}}{\alpha} \right)^{1/2} \qquad \text{(2-22)}$$

where $\alpha$ is a coefficient that varies with the work hardening characteristic. According to the author, the model has the advantage of somehow taking into account void interaction and thereby of compensating the overestimation inherent to the Hahn and Rosenfield approaches (which ignore such interactions). Quantitative agreement with experimental data was however not convincing. This was also confirmed in other investigations where the dimple size was measured using SEM fractography, which found that the model clearly underestimated the measured toughness [95, 175]. A minor modification has been proposed to express the toughness as a function of the interparticle spacing rather than dimple height [182], assuming a diameter-to-height ratio, *d/h*, of 3, with the implication that toughness depends also on particle spacing.

More generally, this approach implies a direct scaling between toughness and the fracture surface roughness, similarly to what has been proposed in steels. To assess the validity of this idea, Davidson [183] conducted extensive image analysis of surface roughness in various PRMMCs to conclude that fracture toughness does not correlate with either the fractal dimension or the surface roughness. He nevertheless anticipated that the fracture surface roughness parameter would correlate with fracture toughness for materials exhibiting very ductile fracture, and that a method of ensuring an acceptable toughness in particulate-reinforced composites is to manufacture materials that create relatively large microvoids over much of the crack surface during fracture [9]. Further details about fractographic characteristics and their link with toughness are given in Section 2.5

### 2.4.4 Energy based models: work spent in the plastic zone

There are mainly three contributions to the fracture energy $G$ (or $J$ ) in a ductile material: (i) the work done within the plastic zone of the crack per unit area of crack $dW_p/dA$, (ii) the work necessary to create the void layer on the fracture surface (*i.e.* $\gamma_{pl}$ according to the section devoted to the energy dissipation rate, Appendix A: A.2.5.iv), and (iii) the fracture surface energy ($\gamma_s$):

$$G_c = dW_p/\mathrm{dA} + \gamma_{pl} + \gamma_s \tag{2-23}$$

Davidson [175] computed the first term from the stress-strain curve and the distribution of strain ahead of the crack tip, which was measured using a stereo-imaging technique. For the second term, the void formation strain was estimated by measuring the dimple dimensions of fractured specimens, while the surface energy values were obtained using handbook values. It was thus recognized that approximately 90% of the fracture energy is spent in forming the plastic zone. The fracture surface work contribution amounts to the remaining 10%, while the fracture surface energy is negligible (less than 1%). He thus concludes, in a quantitative manner, that the plastic dissipation in the plastic zone accounts for the major part of toughness in PRMMCs. Experimental evidence for this finding was confirmed by the same author for tougher composites [158], and was qualitatively corroborated by Flom and Arsenault [133].

The main issue with this approach is associated with the necessity to evaluate the strain distribution in front of the crack tip, which is a difficult experimental task apparently only performed by Davidson (along free surfaces). This would explain why only few investigators have rationalized their results in terms of this model, while some experimental evidence reported in the literature would in our eyes support this approach. For instance in the study by Park and Lucas [115, 143] the plastic wake surrounding the crack path in two different composites (Al-6061/$Al_2O_3$ and Al-6061/SiC) was examined, to find that the composites with larger plastic wakes are tougher. As also pointed out by Mortensen [26], one should also exercise care when applying elastic-plastic continuum calculations of the stress field in such composites, which exhibit highly heterogeneous deformations on a microscopic level and an extensive damage zone where the deformation is strongly inhomogeneous.

### 2.4.5 Summary and comments

In reviewing the modeling approaches proposed for the fracture toughness in PRMMCs, it appears that the prediction of fracture properties in these materials based on the knowledge of their microstructure and tensile characteristics cannot be performed yet in a fully convincing manner. In approaches limited to one particle spacing, void coalescence and interaction are not taken into account. Particle cracking, which is experimentally recognized as important, never clearly appears in such models because it is either assumed that particles and interfaces are strong (and hence do not crack), or that it plays a role only through the voiding process following particle cracking. Because the complexity of fracture processes is neglected, correlation with experimental data might simply be fortuitous. For instance the trend that is predicted from the Hahn and Rosenfield model does not agree with the experimental evidences in terms of the strength/toughness relation.

Considering the fracture mechanisms with greater care and modifying the models in consequence has yielded more reasonable predictions. Finally, as also mentioned in the preceding sub section, analysis of the observed crack tip deformation fields shows unambiguously that most of the fracture toughness in PRMMCs is brought by the contribution of the plastic zone, which is reduced in composites as compared to the unreinforced alloys because they can sustain lower strain at the crack tip. Fracture micromechanisms and damage are, on the other hand, neglected in this approach: this does not seem reasonable. Also one should take care when using continuum approaches to composite materials that are highly inhomogeneous. In this sense, modeling of fracture toughness based on uniaxial tensile properties is an oversimplification.

# 2.5. LOCAL AND GLOBAL FRACTURE ENERGY

In the context of the discussion that follows, it is useful to recall some basic definitions (see Appendix A). In LEFM, the Orowan modification adds a plastic work term to the Griffith criterion such that the fracture energy is given by (eq. A-17):

$$G_\mathrm{c} = \gamma_\mathrm{s} + w_\mathrm{p} \tag{2-24}$$

where $\gamma_s$ is the surface energy and $w_p$ is the plastic work term. It was then specified (eqs. (2-23) and (A-41)), that a term accounting for the energy to create the fracture surface profile ($\gamma_{pl}$) should be added:

$$G_\mathrm{c} = \gamma_\mathrm{s} + \gamma_\mathrm{pl} + w_\mathrm{p} \qquad \text{or} \qquad G_\mathrm{c} = \gamma_\mathrm{s} + \gamma_\mathrm{pl} + \mathrm{d}W_\mathrm{pl}/\mathrm{d}A \tag{2-25}$$

It is often implicitly considered that $w_p$ and $\gamma_s$ (or $\gamma_s+\gamma_{pl}$) are independent material parameters: $w_p$ being by far the largest among these, this implied that $\gamma_s$ or $\gamma_{pl}$ matter little in determining $G_c$. It has since been recognized that this is not the case; instead $w_p$ is a function of $\gamma_s$ or $\gamma_{pl}$. This was apparently first recognized by Rice [184] and used to explain embrittlement phenomena. Jokl *et al.* [185] later extended this idea for the case of brittle fracture of crystalline solids which are capable of being plastically deformed. Their model indeed showed that the plastic work of fracture ($w_p$) is a function of $\gamma_s$ for the cases of both transgranular cleavage and intergranular brittle fracture. They derived an expression to explain in a quantitative manner embrittlement due to segregation and found that a relatively small absolute decrease in $\gamma_s$ (due to embrittlement) may lead to a large decrease of $w_p$.

Similar links were then derived for materials in which well distinct fracture processes are considered in front of the physical crack tip [26, 186, 187]. In these cases, $w_p$ was shown to be a function of $\gamma_s$ or of $\gamma_{pl}$, depending on the author and on the definition of the fracture energy. More recent finite element computations (FEM) of the cohesive zone model introduced by Needleman [188] and refined by Tvergaard and Hutchinson [189] are actually founded on the same principle, and have found successful application for the description of phenomena such as fracture of interfaces or ductile fracture. We summarize in what follows such local/global links that are recognized to be relevant for our specific case.

## 2.5.1 Approach of Hirth and Froes

Hirth and Froes [186] derived several expressions in order to correlate the fracture toughness of titanium alloys with their strength and microstructure. The starting point of their analysis was to relate the plastic work term to the yield stress and the volume of plastically deformed material, which they considered to be done in a region of width $2R_p$ (Figure 2-12a). For an ideally elastic-perfectly plastic material, the total work of fracture for a unit increment of crack propagation d*a* is:

$$\mathrm{d}W \cong 2\gamma_\mathrm{s}\mathrm{d}a + 2R_\mathrm{p}\sigma_\mathrm{ys}\varepsilon_\mathrm{f}\mathrm{d}a \tag{2-26}$$

where $\varepsilon_f$ is the local strain to fracture and $\sigma_{ys}$ the yield strength. If work-hardening of the Hollomon type is considered ($\sigma = \mathrm{k}\varepsilon^\mathrm{n}$ where *n* is the work hardening exponent and *k* a constant), (2-26) becomes:

$$\mathrm{d}W \cong 2\gamma_\mathrm{s}\mathrm{d}a + 2R_\mathrm{p}\frac{k\varepsilon_\mathrm{f}^{\mathrm{n+1}}}{n+1}\mathrm{d}a \tag{2-27}$$

If crack growth occurs, (2-26) or (2-27) must be equal to the strain energy release rate multiplied by the unit area of crack which is[1]:

$$G\mathrm{d}a \cong \frac{K_\mathrm{Ic}^2}{E'}\mathrm{d}a \tag{2-28}$$

By combining (2-28) with (2-26) or (2-27), the following relations are obtained for the $K_\mathrm{Ic}$:

$$K_\mathrm{Ic} = (2E')^{1/2}\cdot\left(R_\mathrm{p}\sigma_\mathrm{ys}\varepsilon_\mathrm{f} + \gamma_\mathrm{s}\right)^{1/2} \quad \text{for the elastic-perfectly plastic case} \tag{2-29}$$

and

$$K_\mathrm{Ic} = (2E')^{1/2}\cdot\left(\frac{R_\mathrm{p}k\varepsilon_\mathrm{f}^{\mathrm{n+1}}}{n+1} + \gamma_\mathrm{s}\right)^{1/2} \quad \text{for the work-hardening material} \tag{2-30}$$

In SSY conditions, the plastic zone size $R_\mathrm{p}$ is related to the stress-intensity factor by:

$$R_\mathrm{p} \cong C\frac{K_\mathrm{I}^2}{\sigma_\mathrm{ys}^2} \tag{2-31}$$

where $C$ is a factor depending on the stress state and geometry. Using the energy definition of toughness eq.(A-8), and combining (2-31) with (2-29) or (2-30) the final relation of this model can be written as:

$$G_\mathrm{Ic} = K_\mathrm{Ic}^2/E' = \frac{2\gamma_\mathrm{s}}{\left(1 - \frac{2E'C\varepsilon_\mathrm{f}}{\sigma_\mathrm{ys}}\right)} \quad \text{for the elastic-perfectly plastic case} \tag{2-32}$$

and

$$G_\mathrm{Ic} = K_\mathrm{Ic}^2/E' = \frac{2\gamma_\mathrm{s}}{\left(1 - \frac{2E'Ck\varepsilon_\mathrm{f}}{(n+1)\sigma_\mathrm{ys}^2}\right)} \quad \text{for the work-hardening material} \tag{2-33}$$

Hence, the fracture energy scales with the surface energy $\gamma_\mathrm{s}$. In other words, even if the latter is one or more orders of magnitude smaller than the measured toughness, it still governs the toughness of the material. The authors took the surface energy $\gamma_\mathrm{s}$ into account in this approach, but considered this term to be negligible for cases involving hole growth and did not introduce any term related to the formation of a ductile fracture surface. As a consequence one notices that although their analysis provides a link between the local and the global fracture energy, it is restricted to brittle failure; hence the authors concentrated on the link between $K_\mathrm{Ic}$ and the yield strength. One must also note that estimating the work spent in the plastic zone using the strain at fracture $\varepsilon_f$ is not consistent with the definition of the plastic zone, with the implication that the denominator in (2-32) could be negative if $\varepsilon_f$ is too large.

---

[1] In their original derivation, Hirth and Froes found a strain energy release rate a factor two smaller than here because of their approximation of the stress field; in addition they used the definition $K=\sigma a^{1/2}$, while for coherence with the rest of the work, we take $K=\sigma(a\pi)^{1/2}$. Hence, the relations as presented here are not exactly the same as in their work.

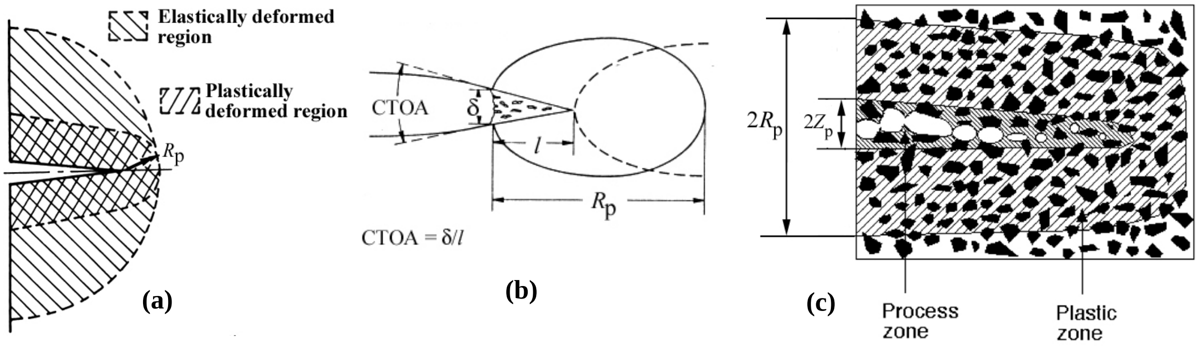

**Figure 2-12.** Schematic description of micromechanical models linking the local and the global fracture energy. **(a)**: Hirth and Froes model [186] where the work done is plastic work plus energy to create new surfaces; **(b)**: Gerberich [187] model, where the process zone, $l$, is imbedded in the plastic zone; **(c)**: Mortensen [26] approach for the case of PRMMCs, where the material is separated between the process zone where fracture micromechanisms occur and the plastic zone treated as a continuum.

### 2.5.2 Approach of Gerberich

Gerberich [187] reviewed the different types of discontinuities that form in front of the crack tip such as microcracking, microvoiding or microbranching; caused by the interactions between the microstructural features and the crack tip stress field. These mechanisms have in common that they produce ligaments in front of the tip, which form the so-called crack-tip “process zone” introduced by McClintock [190]. Gerberich based his analysis by treating the process zone concept using a Dugdale-type model, assuming in particular that the process zone should be embedded in the plastic zone (Figure 2-12b). With this hypothesis, the expression for the steady-state plastic zone is given as:

$$R_p = \frac{l}{4e}\exp\left(\frac{\pi E \delta}{4\sigma_{ys} l\left(1-\nu^2\right)}\right) \qquad (2\text{-}34)$$

where $l$ is the length of the process zone, $\delta$ is crack tip displacement and $e$ = exp(1). Using the plastic zone size given by the Dugdale model eq.(A-14) (corrected for plane strain conditions) and the relation existing between the stress intensity factor and the crack tip opening displacement in SSY $\delta \cong K_I^2/(2\sigma_{ys}E)$, transforms (2-34) into

$$R_p = \frac{l}{4e}\exp\left(\frac{R_p}{l}\right) \qquad (2\text{-}35)$$

Gerberich thus provided a link between the process zone size and the plastic zone size that develops concomitantly during the fracture process. Since the plastic zone size directly governs the fracture energy, this implies that the fracture toughness of a material which fails via the linkage of events within the process zone scales with the size of the latter. This can also be seen as an extension of the Rice and Johnson approach in which the process zone size replaces the mean intervoid distance. At fracture, one obtains the following expression for $K_{Ic}$ by using again the Dugdale plastic zone size model in plane strain and by solving numerically (2-35):

$$K_{Ic} = \sigma_{ys}\left[\left(8(1-\nu^2)/\pi\right)\cdot 3.7l\right]^{1/2} \cong 2.9\sigma_{ys}\cdot l^{1/2} \qquad (2\text{-}36)$$

which is obviously far too simple to explain many mechanisms. It nevertheless provides a qualitative indication, based on realistic physical arguments, of the importance of the process zone size (and thereby of the mechanisms occurring in this zone) for the fracture of a variety of materials, including PRMMCs for which damage in front of the crack tip is a typical definition of the process zone.

### *2.5.3 Approach by Mortensen for the case of PRMMCs*

Mortensen [26] closely followed the approach by Hirth and Froes with the difference, however, that $\gamma_s$ is replaced by the more general term $\gamma_{pz}$ taking into account all the energy consumed in the process zone, or in other words the energy needed to drive locally the micromechanisms of fracture. Outside this zone of highly inhomogeneous deformation, the surrounding material is treated as an elastic-plastic continuum having the properties of the composite, as depicted in Figure 2-12c. In a sense, this approach is somehow a combination of the Hirth and Froes and the Gerberich ones. Following the derivation of (2-26) to (2-33), the expression for his model is almost exactly as (2-32), with the difference that $\gamma_{pz}$ is a more general term taking into account the various micromechanisms of fracture at the local scale, and that *E*' and $\sigma_{ys}$ are the elastic modulus and the yield strength of the composite, respectively. A major modification is to use the average composite strain in the plastic zone $\varepsilon_m$ rather than the strain to fracture $\varepsilon_f$ which is never attained in the plastic zone:

$$G_{Ic} = K_{Ic}^2 / E' = \frac{2\gamma_{pz}}{\left(1 - \frac{2E'C\varepsilon_m}{\sigma_{ys}}\right)} \tag{2-37}$$

This expression can also be readily transformed to take into account work hardening in the composite, similarly to (2-33). This expression highlights the importance of $\gamma_{pz}$, emphasizing the central role of microfracture events that take place in the vicinity of the crack tip. While the global fracture energy of the composite is still mainly spent in the plastic zone (as pointed out by Davidson), it is simply an amplification of the local work of fracture. Also, since $R_p$ scales with *G* (2-31) the plastic zone size should be larger for larger values of $\gamma_{pz}$. Several implications for composite toughness were then discussed. In particular, the role of the matrix yield stress is neither simple nor unique because it influences both $\gamma_{pz}$ and the composite yield stress. The presence of microscopic defects can also be rationalized because these have a strong incidence on $\gamma_{pz}$. In addition, the latter value is also influenced by the particle size, strength, or even the volume fraction as will be explained in the next chapter. In summary, and even though some limitations exist (in particular SSY is assumed), this approach summarizes a simple rationalization of fracture in PRMMCs, and also of other fracture phenomena such as embrittlement.

### *2.5.4 Cohesive zone models (CZM)*

Initially developped by Needleman [188] for the study of decohesion in the presence of plastic deformation, the cohesive zone model (CZM) was further considered in greater detail by Tvergaard and Hutchinson [189, 191-193] to develop a more fundamental understanding of the role of plasticity in the toughness of elastic-plastic solids. This approach is based on the Barenblatt analysis [194] of closure stresses: an adhesive layer is considered which is characterised by its work of separation and its interface strength. In this zone, within which the failure process is assumed to occur, failure micromechanisms are summarized by a traction-separation law, as depicted in Figure 2-13b. The work of separation $\Gamma_0$ is simply the area under the curve. The other important parameter is the peak separation strength $\hat{\sigma}$, which represents the maximum stress locally attained during the separation process. A last parameter which is dependent on the other two is the maximum separation $\delta_c$ once the traction stress has dropped to zero. When fracture is by voiding at interfaces, typical orders of magnitude of these parameters are:

$\Gamma_0 \approx$ 0.1-1kJ/m$^2$, $\hat{\sigma} \approx$ 0.1-1GPa, $\delta_c \approx$ 1-100 µm

Most of the local work of separation is consumed in the growth and coalescence of voids such that the spacing between voids or void-nucleating particles provides a fundamental scaling parameter of the fracture process.

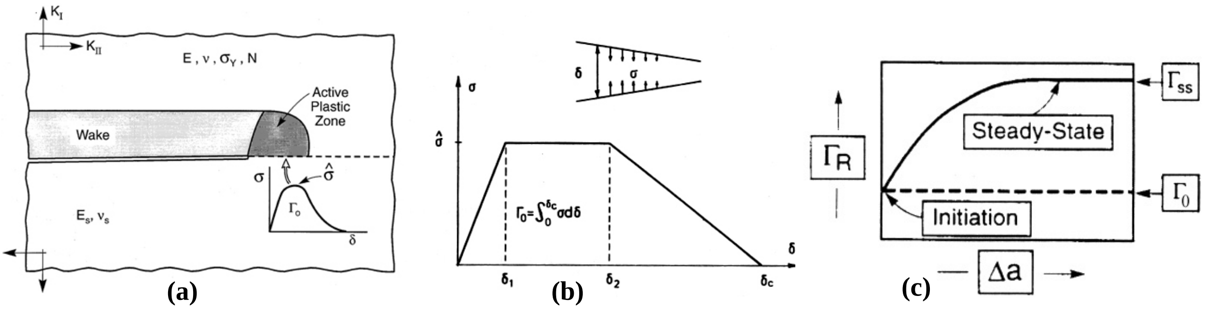

**Figure 2-13.** The cohesive zone model. **(a)**: Schematic description of the model, showing the continuum body in which the plastic zone develops and surrounding the process zone (PZ); **(b)**: traction-separation law characterizing the failure process in the PZ; **(c)**: *R*-curve response of the model, in ideal SSY case. From [195] and [196].

Around the process zone, $J_2$ flow theory of plasticity characterizing isotropic solids with isotropic strain hardening is commonly used. Continuum parameters needed to describe the deformation behaviour are Young's modulus $E$, Poisson's ratio $\nu$, the yield stress in uniaxial tension $\sigma_y$, and the strain hardening exponent $n$. As the process zone develops, the plastic zone simultaneously builds up in the continuum (Figure 2-13a), such that once the latter is completely formed, steady-state crack propagation occurs under small-scale yielding conditions. This gives typical $R$-curves as represented in Figure 2-13c. The total steady-state work of fracture is denoted $\Gamma_{ss}$ and corresponds to the total remote energy release rate. Two length quantities related to the size of the plastic zone are then introduced:

$$R_0 = \frac{E \cdot \Gamma_0}{3\pi\left(1-\nu^2\right)\sigma_y^2} \tag{2-38}$$

and

$$R_{ss} = \frac{E \cdot \Gamma_{ss}}{3\pi\left(1-\nu^2\right)\sigma_y^2} \tag{2-39}$$

$R_0$ can be identified as the size of the plastic zone if the remote energy release rate was $\Gamma_0$ or the active plastic zone if the total work of fracture was close to $\Gamma_0$. $R_{ss}$ is an estimation of the size of the active plastic zone in front of the crack tip advancing at steady-state. For separation involving the ductile void growth mechanism, $R_0$ is typically in the range 0.1 to 1 mm, while $R_{ss}$ can be as large as 100 times $R_0$ if plastic dissipation is pronounced. Invoking dimensional considerations, Tvergaard and Hutchinson found that $\Gamma_{ss}/\Gamma_0$ have a functional interdependence of the form:

$$\frac{\Gamma_{ss}}{\Gamma_0} = F_{CZM}\left(\frac{\hat{\sigma}}{\sigma_y}, n\right) \tag{2-40}$$

Hence, in the steady-state regime (*i.e.* for a fully developed SSY plastic zone advancing with the crack), the toughness scales with the local work of the fracture process, $\Gamma_0$. As mentionned by Rice and Wang [197], this value can actually be seen as $\gamma_{pz}$ introduced earlier. This approach is in other words similar to those proposed by Hirth and by Froes and Mortensen, emphasizing the crucial role of local microfracture events. Among the implications of this model that are relevant here, the authors noticed that the steady-state toughness is highly dependent on the ratio $\hat{\sigma}/\sigma_y$. More specifically, for composite materials made of a soft and a rigid phase, they introduced an overall limit flow stress of the composite given by $\sigma_y = c\sigma_0$, where $c$ is in the range of 1.5 and 2 and $\sigma_o$ is the flow stress of the softer phase, and claimed that plastic dissipation would be important only for ratios $\hat{\sigma}/\sigma_y$ larger than about 3. In other words the peak stress of the bridging fracture process should exceed 4-5 times the flow stress of the soft phase for plastic dissipation to make an important contribution to toughness.

The CZM model has been applied to model fracture at metal/ceramic interfaces [195, 196], a process that presents many similarities with the fracture of PRMMCs. In particular, the fracture micromechanisms at metal/ceramic interfaces can include brittle debonding or ductile void growth in the metal adjacent to the interface [196, 198], while failure may be accompanied by a more or less extended zone of plastic deformation, depending on the interface strength, as depicted in Figure 2-14. For clean and tough interfaces, crack blunting prior to crack extension appears in the metal layer, and the crack propagates by the coalescence of growing voids, as in the ductile fracture of metals. In the presence of segregants at the interface, cracks are much sharper and there is significant local embrittlement while a much smaller plastic zone develops ahead of the crack, as would be anticipated by the simple analysis of Gerberich and Mortensen.

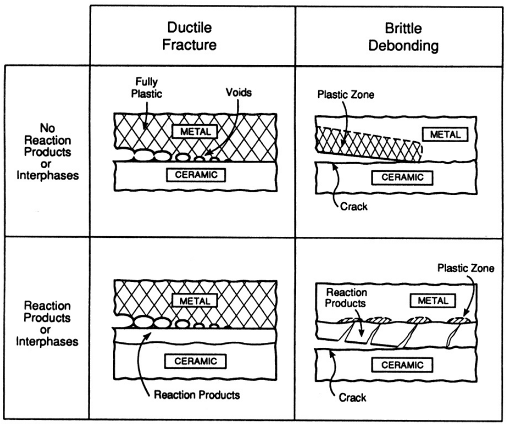

**Figure 2-14.** Micromechanisms of fracture at a metal/ceramic interface, illustrating the similarities with particle reinforced metals: a plastic zone develops in the metallic phase and its extension depends on the interface strength. From [198].

Application of the CZM model to ductile crack growth has also been recently conducted by Siegmund and Brocks [199, 200], who compared it to the more physically-based modified Gurson model. The two models were not in complete agreement, indicating that the determination of the cohesive zone parameters must be performed with care. Indeed the constitutive traction-separation law of the CZM model is in general not based on physical arguments or measurable materials parameters. For instance, the most frequently used law is of the form:

$$\sigma = -\hat{\sigma} e z \frac{\delta}{\delta_{\mathrm{n}}} \exp\left(-z \frac{\delta}{\delta_{\mathrm{n}}}\right) \tag{2-41}$$

where $z=16e/9$, $e = 2.718$, and $\delta_{\mathrm{n}}$ is a characteristic length of the cohesive zone model, while the cohesive energy for this relation is:

$$\Gamma_0 = 9/16 \cdot \left(\hat{\sigma}\delta_{\mathrm{n}}\right) \tag{2-42}$$

Any relation that would describe the traction-separation law could, however, also be used. In addition, Siegmund and Brocks underline that the CZM does not account for the change of triaxiality with crack advance, such that the cohesive zone parameters can only be regarded with caution as material properties.

### 2.5.5 Additional comments and summary

It has been recognized that there are many materials and fracture processes which feature a macroscopic toughness one or more orders of magnitude higher than the Griffith energy or the energy spent in the process zone, and that, still, there is a direct link between these two quantities. Embrittlement segregation, PRMMCs, or fracture of soft/rigid interfaces are systems which are addressed by using such approaches. Simple micromechanical models reviewed above apparently provide a suitable analysis framework for handling simple and even complex fracture phenomena. There also exist other approaches, such as models developed for describing cleavage accompanied by plastic flow, that yield the shielding ratio afforded by the plastic zone as a function of Griffith energy [201-203]. All of these have in common that they predict the macroscopic fracture energy to be an amplification of the local fracture energy. This local fracture energy is the subject of the last section of the literature review.

Numerical calculations of the cohesive zone model (which was specifically based on the recognition that no simple fundamental relations exist between the total work of fracture and the work of the fracture process) have confirmed these findings in many instances and hence afford a complementary tool to quantify this fundamental link. It is therefore not surprising that the concept of dividing the overall fracture process into two distinct domains which are analyzed separately and then linked together are receiving increasing attention in the research community, as mentioned by Hutchinson and Evans [204] and Cotterell [205] in recent overview articles. We note, however, that only one attempt in modeling mechanical behaviour of PRMMCs with the CZM model has been found in the literature [206] (which concentrated on tensile response), although Tvergaard and Hutchinson [189] proposed in their original paper that PRMMCs could be an appropriate candidate for the CZM approach.

# 2.6. LOCAL MODELS OF FRACTURE FOR MATERIALS SIMILAR TO PRMMCS

From the precedent section, it appears important to quantify the local fracture energy. To this end, we summarize in what follows analytical modeling approaches for assessing the local fracture energy that have been developed for materials for which we have identified similarities –in terms of the microstructure and the fracture path– with particle reinforced composites. This review is more specifically conducted with the objective to assess how these concepts could be used and adapted to the case of PRMMCs.

## 2.6.1 *The work spent to form a ductile fracture surface*

### i. The analysis of Stüwe

The early paper of Stüwe [207] attempts to correlate in a simple manner toughness with the relief of a ductile fracture surface. Stüwe considers a cross-section of a slab of material with a given thickness *r* and a cross section $F_0$ (Figure 2-15a) which transforms into an array of dimples of idealized regular geometry after a ductile-type fracture, (Figure 2-15b). His idea is that the volumetric plastic work of deformation for this transformation, $W_{\text{pl, void}}$, is uniquely determined by the local strains at fracture and can be deduced from the dimple geometry and the work hardening law of the material. This plastic work at any height of the profile, and the total work *A* to create the whole profile are expressed as:

$$W_{\text{pl,void}} = \int_0^{\varepsilon} \sigma \mathrm{d}\varepsilon \qquad \text{and} \qquad A = \oint W_{\text{pl,void}} \mathrm{d}V \tag{2-43}$$

where $\varepsilon$ is the local strain and $\sigma$ the true flow stress of the material. He then used an assumption of the elementary theory of plastomechanics (that plane sections remain plane) such that $\varepsilon$ is expressed as:

$$\varepsilon = \ln(F/F_0) = \ln(1/z) \qquad \text{with } z = F/F_0 \tag{2-44}$$

where *F* is the material part of a cross section at height *h* through the fracture surface and $F_0$ is the initial cross section. *z* is a function of *h* (or *x* with $x = h/h_0$) and contains the geometry of the fracture surface.

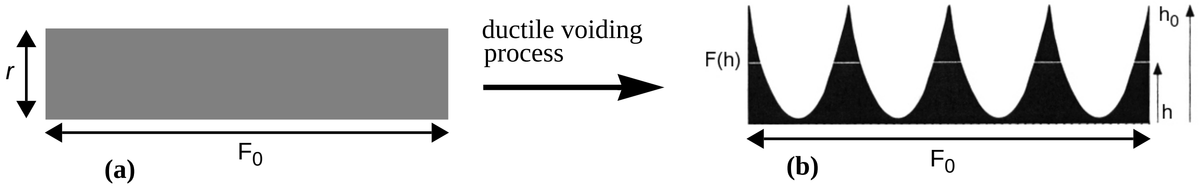

**Figure 2-15.** Schematic principle of Stüwe's model relating toughness with the fracture surface profile. **(a)**: Slab of material before deformation and **(b)**: the profile of the slab after ductile type fracture.

The work per unit area to form the fracture surface is given by $\gamma_{\text{pl}} = A/F_0$ which is, using (2-43) and (2-44):

$$\gamma_{\text{pl}} = \frac{1}{F_0} \int_0^{h_0} \int_0^{\varepsilon} \sigma(\varepsilon) \mathrm{d}\varepsilon \cdot F \,\mathrm{d}h = h_0 \int_0^1 \int_0^{\varepsilon} \sigma(\varepsilon) \mathrm{d}\varepsilon \, z \mathrm{d}z \tag{2-45}$$

By using standard power-law hardening for the stress-strain curve, $\sigma(e) = k\varepsilon^n$ where $n$ is the strain hardening exponent of the material, the relation for $\gamma_{\mathrm{pl}}$ is finally:

$$\gamma_{\mathrm{pl}} = \frac{h_0 k}{n+1}\int_0^1 z(x)\left[\ln\left(\frac{1}{z(x)}\right)\right]^{n+1} \mathrm{d}x \tag{2-46}$$

The equation can be solved numerically, but in the region $0 < n < 1$ which is of interest for the power-law hardening, the integral is quite insensitive to $n$ and close to 0.25 which is the approximation generaly used [208]. It might be also convenient in some cases to simplify the stress-strain relation law, using for $\sigma$ an average flow stress of the form $\bar{\sigma} = m\sigma_{\mathrm{UTS}}$, where $m$ is a coefficient which depends on the strain hardening exponent $n$ of the material and $\sigma_{\mathrm{UTS}}$ its ultimate tensile strength. With this simplification, the relation for $\gamma_{\mathrm{pl}}$ becomes:

$$\gamma_{\mathrm{pl}} \approx \bar{\sigma} \cdot h_0 \cdot S \qquad \text{where} \qquad S = \int_0^1 z(x)\ln\left(\frac{1}{z(x)}\right)\mathrm{d}x \tag{2-47}$$

The value of $S$ and in turn the local fracture energy are thus dependent of the function $z(x)$ which describes the shape of the relief. In the situation where one population of dimples is considered, it was shown by Stüwe that any reasonable curve describing the fracture relief leads to a value $S = 0.25$. Hence for convenience the simplest function $z(x) = x$ is generally used, which enables to simplify further eqs. (2-46) and (2-47). In summary, this analysis provides a useful tool in calculating in a simple manner the local work of fracture, provided that the deformation law of the material as well as quantitative data on the surface profile are known.

To this end, stereophotogrammetic means have been employed by Kolednik and Stüwe to study the topography of ductile surfaces [209]. They determined the crack opening displacement at the moment of crack initiation by searching corresponding points on the fracture halves of broken specimens (*i.e.* points that were physically connected prior to fracture). Stereo-image pairs of these regions were subsequently produced in the SEM, from which profiles were analyzed using a stereo comparator. It was found that the technique provides an accurate method for the determination of the critical CTOD value, with a small scatter of measured values.

The main disadvantage of the technique is the time required for measurement of surface profiles on the stereo-images. Recently, Stüwe's approach has received new attention, triggered by the development of a commercially available software that is able to reconstruct the topography of a fracture surface by taking stereophotograms in the scanning electron microscope [210, 211]. The reconstructed fracture surfaces are called Digitation Elevation Models (DEMs) [212, 213]. From these the energy required to create the fracture surface is numerically calculated using the model initially developed by Stüwe, eq.(2-45). This new technique seems quite promising since only few minutes are necessary to fully reconstruct the surface, with a resolution that is only restricted by the resolution of the SEM. In the two references cited above, the method has for instance been used for high-strength steels to separate the fracture energy spent in the formation of the fracture surface from the plastic energy spent for sub-surface processes.

As the knowledge of one fracture surface is not sufficient to evaluate the fracture energy because the topography of one DEM could alternatively match or mirror the topography of its opposite (for instance in the case of brittle fracture), two opposite DEMs must be generated and superimposed, such that $\gamma_{\mathrm{pl}}$ is finally calculated by the misfit of the two fracture surfaces. The procedure then becomes more evolved and the gain of time which is –besides precision– the main advantage of the technique is somewhat lost. More simply, extracting height profiles along the fracture surface of the DEM (which is possible with the software) and measuring individual dimple profiles is sufficient if one uses (2-46) instead of (2-45) because as shown in the original model, $\gamma_{\mathrm{pl}}$ is quite insensitive to the relation $z(x)$ used to describe the surface profile.

### ii. The contribution of stress triaxiality

In Stüwe's model, only the result of the fracture process is considered and the crack tip stress triaxality during void growth, which is known to strongly affect the fracture of structural materials, is neglected. While most attempts of trying to solve this problem have been carried out using numerical methods, there have been only few attempts with analytical or semi-analytical methods. Poech and Fischmeister [214] have attempted to fill this gap by proposing a model that calculates the stress versus displacement curve of a volume element containing a growing void under different levels of stress triaxiality.

Their approach is to consider a volume element in front of the crack tip containing a pore that grows as the element is stretched by the stress acting ahead of the crack tip, Figure 2-16. They derived the expression $\Sigma_z$(u) where $\Sigma_z$ is the axial stress acting on the cylinder and *u* the displacement of the cylinder. From this expression, the local work of fracture $\gamma_{\mathrm{pl}}$ is obtained by integrating the energy increments dissipated during the tearing process:

$$\gamma_{\mathrm{pl}} = \int_0^{u^*} \Sigma(u)\mathrm{d}u \qquad \text{(2-48)}$$

By assuming the growing pore to be an ellipsoid of revolution, and the average true strain of the deforming material to be a function of the cylinder height, they expressed the volume-averaged true strain as a function of the volume of the growing pore, *f*:

$$\varepsilon = \ln\left(\frac{1}{1-f}\right) \qquad \text{with} \qquad f = \frac{2}{3}\cdot x^3 \qquad \text{(2-49)}$$

where *x* is a dimensionless parameter representing the pore growth (for *x* = 0, no void is present and for x = l, the void is completely formed and the cell is broken).

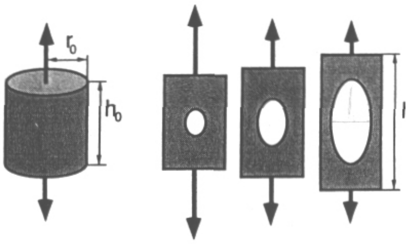

Figure 2-16. The volume element in front of the crack tip, as suggested in the model of Poech and Fischmeister [214]. The cross-sections illustrate the growing cavity at different levels of deformation.

Their model is then based on Gurson's criteria for yielding of porous media:

$$\frac{\Sigma_{\mathrm{eff}}^2}{\sigma_{\mathrm{f}}^2} + 2f\cosh\left(\frac{3\Sigma_{\mathrm{H}}}{2\sigma_{\mathrm{f}}}\right) - (1+f^2) = 0 \qquad \text{(2-50)}$$

where $\Sigma_{\text{eff}}$ is the effective stress applied on the cell, $\sigma_{\text{f}}$ is the uniaxial flow stress of the pore-free medium, and $\Sigma_{\text{h}}$ is the hydrostatic stress acting on the cell. The stress triaxiality cas be expressed as $\eta = \Sigma_{\text{H}}/\Sigma_{\text{eff}}$. As Gurson's model is strictly valid for a rigid-ideally plastic material, strain hardening is taken into account by defining a relative effective flow stress of the cell as $Y = \Sigma_{\text{eff}}/\sigma(\varepsilon)$ where $\sigma(\varepsilon)$ is the hardening law of the material and replaces $\sigma_{\text{f}}$ in (2-50). With these definitions, Gurson's criterion can be rewritten as:

$$Y^2(x) + f \cdot \left[ \exp\left(\frac{3}{2}\eta Y(x)\right) + \exp\left(-\frac{3}{2}\eta Y(x)\right)\right] - \left(1 + f^2\right) = 0 \tag{2-51}$$

This equation must be solved for different stages of pore growth, using numerical procedures to generate the function $Y(x)$. Recalling the definitions of $\Sigma_{\text{eff}}$ and $\Sigma_{\text{h}}$ in terms of principal stress components, one obtains for the axial stress $\Sigma_{\text{z}}$ the following relation:

$$\Sigma_{\text{z}}(x) = \sigma\left(\varepsilon(x)\right) \cdot Y(x) \cdot \left(\eta + \frac{2}{3}\right) \tag{2-52}$$

With this equation, the stress falls to zero at very high strains and not when the void is fully grown as should be the case according to the geometrical assumptions of the model; and this is a direct consequence of the inability of Gurson's potential to account for void coalescence. Thus, Poech and Fischmeister finally corrected their expression by recognizing that the stress is increased in proportion to the cross-section ratio (1/1-$f$) and that at the same time, the stress that can be transmitted by the hollow cell is limited by the smallest cross-section of the solid, *i.e.* (1-$x^2$). With these corrections, the stress drops to zero as the cavity is fully grown and the final equation is:

$$\Sigma_{\text{z}}(x) = \sigma\left(\varepsilon(x)\right) \cdot Y(x) \cdot \left(\eta + \frac{2}{3}\right) \cdot \frac{\left(1 - x^2\right)}{\left(1 - f\right)} \tag{2-53}$$

The axial stress can thus be evaluated for a chosen material constitutive law and for various levels of crack tip triaxiality. Triaxiality was shown by the authors to have a strong influence on $\Sigma_{\text{z}}$ in the early stages of deformation and in turn on the local work of fracture as the latter is simply the area under the curve. One must however be aware that the final stretching $u^*$ is directly defined by the geometry of the cell and is influenced by the stress triaxiality in this model. This might be a crude assumption, as seen later for similar problems. The argument brought by the authors to neglect the exact value of final stretching is that 90% of the plastic work has already been spent when $U/h_0 = 1$ (while final stretching is $U/h_0 = 2$).

### 2.6.2 Toughness of hard refractory alloys (WC-Co composites)

High volume fraction particle reinforced MMCs exhibit very similar features to cermets refractory alloys such as carbide tungsten/cobalt (WC-Co), for which numerous models for the fracture toughness and deformation behaviour have been developed over the past years. As in PRMMCs, the microstructure consists of two phases with strongly different mechanical properties: for example very hard WC grains embeded in relatively soft Co. In WC-Co alloys, the different fracture paths that can be distinguished are [215, 216]:

(i) transgranular fracture through the carbides or along the carbide grain boundaries, which corresponds in MMCs to particle fracture;
(ii) transgranular fracture through the binder phase (corresponding to ductile voiding in the MMCs);
(iii) fracture along binder/carbide boundaries (corresponding in the composites to debonding at the particle/matrix interface).

While all these mechanisms have been observed, it has been shown that cracks propagate preferentially through the matrix, leaving behind bridges of ductile metal that are stretched to the point of rupture [216], and that the plastic work involved in stretching and fracturing this multiligament zone is the main toughening phenomenon [217, 218]. A typical fracture path propagation in these materials is schematically shown in Figure 2-17. The more successful approaches in modeling this toughening effect are summarized hereafter.

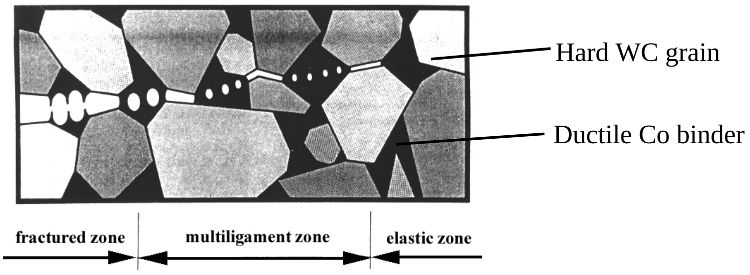

**Figure 2-17.** Schematic microstructure and fracture path in WC-Co two-phase alloys, from [219].

### i. Toughening due to ligament zone formation

The early work of Krstic and Komac on toughening in WC-Co composites [217] was one of the first to emphasize the role of ligament zone formation behind the advancing crack. They proposed a model which assumes that the crack propagates in a brittle fashion through the carbide matrix, while a portion of the load is supported by the ductile cobalt ligaments.

According to the model, the overall fracture toughness of the composites, $K_\mathrm{L}$, is the sum of the fracture toughness of the brittle carbide matrix $K_\mathrm{m}$ plus the contribution of the ligaments:

$$K_L = K_m + 2\sigma_L\sqrt{\frac{2L}{\pi}} \tag{2-54}$$

where $\sigma_\mathrm{L}$ is the stress transmitted through the ligaments and $L$ the length of the crack bridged by the ligaments. The idea of the model is that when the most-extended ligament fractures, the critical crack-opening displacement of this ligament at the moment of fracture $l_\mathrm{c}$, must be equal to the crack opening displacement in the carbide matrix at a distance $L$ from the crack tip, $COD_\mathrm{m}$. Using the relation linking the *COD* with the stress intensity factor and the *in-situ* fracture stress $\sigma_\mathrm{b}$ of an isolated ligament subjected to a remotely applied stress, they derived the following relation:

$$K_\mathrm{L} = K_\mathrm{m} + \frac{\sigma_\mathrm{L} l \sigma_\mathrm{b} E_\mathrm{m}}{\left(1-\nu_\mathrm{m}^2\right)\cdot K_\mathrm{m} E_\mathrm{b}} \tag{2-55}$$

where $\nu_\mathrm{m}$ is the Poisson's ratio of the carbide grains, $E_\mathrm{m}$ their Young's modulus and $l$ the initial (undeformed) length of cobalt forming the ligament. Finally, the portion of the fracture surface ($A_\mathrm{b}$) occupied by the binder is used to calculate the load supported by the ligaments: $\sigma_\mathrm{L} = A_\mathrm{b}\sigma_\mathrm{b}$ where $A_\mathrm{b}$ is correlated with the volume fraction of the binder $V_\mathrm{b}$ or with the interparticle spacing and the mean carbide grain diameter $D$.

Above all, this model was one of the first to introduce the concept of *in-situ* fracture strength of the ligaments and to point out its strong influence on the toughness of this class of materials. This observation is important in the sense that very different strengths of the binder have been observed depending on whether it is in the form of a thin layer or in its bulk form; the former being much stronger due to spatial constraint to which the binder is subjected. It is even argued that strength could approach the value of the theoretical shear stress of cobalt for very thin layers.

A more complete approach was developed by Sigl and Fischmeister in a model that is presented below [219] where it was indeed shown that quite high values of the binder flow stress can be expected. The interesting feature to highlight is that the loss of toughening when reducing the volume fraction of the binder is somewhat compensated for by the increase of its *in-situ* fracture strength, as shown in the paper of Krstic and Komac [217]. When comparing this model with experimental values, the general trend of toughness versus volume fraction of the binder is followed, but absolute values are seen to systematically underestimate the measured toughnesses. The authors attributed this to the uncertainty associated with the selected *in-situ* fracture strength of the ligaments.

### ii. The approach of Sigl and Fischmeister

When all fracture micromechanisms are taken into account, fracture occurs when the strain energy release rate ($G_{\mathrm{Ic}}$) equals to the energy consumed in propagating the crack, *R*. The latter is composed of the energy terms for the different fracture paths:

$$R = \sum_i R_{\mathrm{i}} = \sum_i 2\gamma_{\mathrm{i}} \cdot A_{\mathrm{i}} \tag{2-56}$$

where $\gamma_{\mathrm{i}}$ is the specific energy of path *i* (WC cracking, Co voiding or interfacial or near-interfacial failure) and $A_{\mathrm{i}}$ is the area fraction of path *i* on the fracture surface. The specific energy for carbide cracking, $\gamma_{\mathrm{CC}}$ is simply the critical strain energy of pure carbide, that can be found in the literature. Even if some errors exist in estimating $\gamma_{\mathrm{CC}}$, the error then reflected on the global toughness of the composite remains low as the largest contribution is by far that from the dimple fracture of the binder.

The model developed by Sigl and Fischmeister [219] for the contribution of voiding of the binder phase closely follows the approach by Stüwe; the main difference with the latter is that the dimple structure is described by hexagonal array of dimples. They assumed that the dimple walls have a power-law shape described by the relation $z = cx^{\mathrm{m}}$, with the parameter *m* fitted to stereometric SEM measurements of dimple profiles. With these assumptions, and using a Voce law to describe the strain hardening behaviour, they obtained the following expression for the energy consumed in creating a unit area of dimple topography, $\gamma_{\mathrm{pl}}$:

$$\gamma_{\mathrm{pl}} = \frac{r}{2} \cdot \left[ \sigma_{\mathrm{y}} + \frac{\sigma_{\mathrm{s}} - \sigma_{\mathrm{y}}}{2\varepsilon_{\mathrm{c}} + 1} \right] \tag{2-57}$$

As in the Stüwe model, the energy to create the dimple landscape is simply related to the microstructure of the material (*r*, the average distance between two carbide grains ) and to the stress-strain characteristics of the binder ($\sigma_{\mathrm{y}}$, $\sigma_{\mathrm{s}}$ and $\varepsilon_{\mathrm{c}}$). If one uses a Hollomon power-law hardening of the form $\sigma = k\varepsilon^{\mathrm{n}}$ instead of the Voce-law, the energy $\gamma_{\mathrm{pl}}$ changes into:

$$\gamma_{\mathrm{pl}} = k \cdot h \cdot S_2, \quad \text{where} \quad S_2 = \frac{1}{n+1} \int_0^1 \left(1 - u^{2/m}\right) \cdot \left[ \ln\left( \frac{1}{1 - u^{2/m}} \right) \right]^{n+1} \mathrm{d}u \tag{2-58}$$

an expression which is similar to that obtained in Stüwe's model. Thus, like in the approach of Krstic and Tomac, this model emphasizes the importance of the *in-situ* behavior of the binder. In the case of WC-Co alloys, the analysis of Sigl and Fischmeister showed that a very high degree of strain hardening and in turn a saturation stress was obtained, and that these values yield a much better correlation with experimental data than if one simply uses the flow stress data of bulk WC- saturated Co.

### iii. The *in-situ* flow behaviour of the binder

As seen in the previous paragraph, the *in-situ* behaviour of the binder play a crucial role in improving the toughness of two-phase materials. Sigl and Fischmeister assumed that very high strain hardening occurs inside the ligaments (expected to be much higher than average hardening observed in a tensile test). First the initial yield stress $\sigma_\mathrm{y}$ is analyzed in terms of a Hall-Petch relation for two-phase composites, and values of $\sigma_\mathrm{y}$ between 2.2 and 3.7 GPa are found. Then, the initial hardening is determined from literature and is given by $\phi_\mathrm{o} \approx$ 20GPa. Finally, the saturation stress cannot be extrapolated from conventional tensile tests because of the formation and growth of internal voids. Thus, the saturation stress is theoretically calculated by considering that it will be reached when the density of stacking faults (which are formed during the deformation of Co) has reached a level such that there are no slip planes left on which dislocations can move. This leads to the value $\sigma_\mathrm{s}$-$\sigma_\mathrm{y} \approx$ 9GPa, which seems to be an extremely high value, but still below the theoretical shear strength estimated for Co. With these values, they obtained a much better correlation with experimental data.

Ravichandran [220] approximated the flow properties of the ductile Co by assuming that it behaves as a ductile layer sandwiched between rigid platens. By assuming perfect bonding between the layer and the platens, the binder *in-situ* flow stress due to constraint $\sigma_\mathrm{b}$ is given by:

$$\sigma_\mathrm{b} = \sigma_0\left[1+\frac{2k}{3}\left(\frac{d}{2h}\right)\right] \tag{2-59}$$

where $\sigma_0$ is the bulk flow stress of the binder in the absence of constraint, $d$ and $h$ are respectively the width of the platens and the thickness of the binder, and $k$ is the maximum shear factor taken as 0.77. To express the toughness of the composite, he then followed the approach given in [221, 222], for the ductile-toughening of brittle materials. This yields the critical strain energy release $G_\mathrm{c}$ rate as:

$$G_\mathrm{c} = (1-V_\mathrm{f})G_\mathrm{m} + V_\mathrm{f}\int_0^{u^*}\sigma(u)\mathrm{d}u = G_c = (1-V_\mathrm{f})G_\mathrm{m} + V_\mathrm{f}\sigma_0 h\chi \tag{2-60}$$

where $\sigma(u)$ is the stress/stretch relationship of the binder, $u^*$ is the crack opening displacement upon binder rupture, and $\chi$ is a work of rupture parameter related to the constrained flow behaviour of the ductile phase:

$$\chi = \frac{\int_0^{u^*}\sigma(u)du}{\sigma_0\cdot h} \tag{2-61}$$

In other words, the second part on the right hand side of (2-60) represents the contribution of plastic stretching of the binder to the composite toughness, which takes into account its *in-situ* behaviour. Ravichandran finally expressed the toughness in terms of the critical stress intensity factor.

It is interesting to note that the two approaches presented above are based on different mechanisms, but that both fit generally well with experimental data. Both models emphasize the importance of the *in-situ* flow stress but actually in a quite different manner. In the model developed by Ravichandran, the flow stress of the binder is assumed to increase due to geometrical constraint imposed by the rigid carbide grains. Strain hardening is however not taken into account (whereas it is expected to be high in a ductile phase surrounded by rigid grains) and very crude assumptions are used for the description of the stress-displacement curve of the binder. It is indeed highly unlikely that constraint is maintained during stretching of the ductile binder, as assumed in the model. According to the Poech and Fischmeister analysis (§2.6.1.ii), it is probably because most of the energy is spent in the early stages of stretching that the model matches the data in this case. In contrast, in the model of Sigl and Fischmeister the *in-situ* flow stress of the binder is supposed to increase due to very high strain hardening that occurs during ligament stretching. The mean flow stress as calculated by $\sigma_m = (\sigma_s - \sigma_y)/(2\phi_c + 1)$ (for a Voce law) is thus very high and in turn the toughness increases as expressed by (2-57).

### 2.6.3 Brittle materials toughened by ductile-phase particles

When ductile particles are incorporated into a brittle matrix, it is well recognized that toughening occurs due to plastic stretching and ligament formation by the ductile particles that bridge the two faces of the crack [221-226], as schematically depicted in Figure 2-18. Both the microstructure and crack propagation process are actually very similar to the case of WC-Co alloys, with the difference that in the latter the ductile binder forms a connected network, while in ductile particle reinforced ceramics the brittle matrix is connected. Hence the same general concepts are used to describe toughening mechanisms in these two classes of materials.

#### i. The ligament zone concept

Krstic [223] applied exactly the same concept as in his analysis for WC-Co composites to describe the toughening mechanism of brittle matrices with ductile particles. The only difference is that the critical elongation at failure of the ductile particle, $u_L$, was used while for the model of WC-Co composites, this variable was linked to the *in-situ* binder stress and to the initial ligament length. Hence, he did not establish how the constraint imposed on the ductile phase affects the composite toughness.

To account for this effect, the increase in toughness (in terms of the critical energy release rate $\Delta G_c$) for a crack intercepting ductile particles is expressed as:

$$\Delta G_c = V_f \int_0^{u^*} \sigma(u) \mathrm{d}u \tag{2-62}$$

where $\sigma(u)$ is the stress/stretch relationship of the ductile reinforcement and $u^*$ is the crack opening at the point when the ductile material fails. All modeling efforts have thus the objective to describe the function $\sigma(u)$ when the ductile phase is submitted to constraint. The most successful and convincing approaches are summarized hereafter.

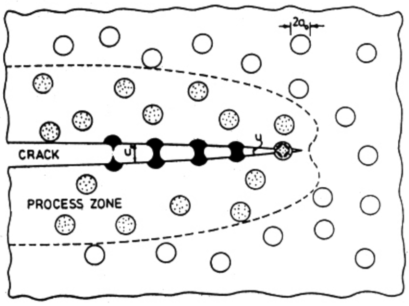

**Figure 2-18.** Crack propagation in a brittle matrix reinforced by ductile particles, in which stretching of the latter increases global toughness of the two-phase materials.

### ii. Bridgman analysis of stretched particles

In order to obtain the stress-displacement curve of ductile ligaments forming from ductile particles, Sigl *et.al.*[221] assimilated the stretch particle to a cylindrical bar and used the Bridgman solution to calculate the mean axial stress acting on this cylinder, $\sigma_z(a,R)$:

$$\sigma_z = \sigma_f\left(1+\frac{2R}{a}\right)\ln\left(1+\frac{a}{2R}\right) \tag{2-63}$$

where $R$ is the radius of curvature, $a$ the neck radius (Figure 2-19a), and $\sigma_f$ the uniaxial flow stress of the constituant material of the ductile particle. This is described by a Hollomon hardening law: $\sigma_f = k\varepsilon^n$, where $\varepsilon$ is the plastic strain of the particle defined according to the Bridgman analysis as $\varepsilon = 2\ln(a_0/a)$. To relate particle stretching with the initial particle size $a_0$ and to subsequently derive the expression $\sigma(u)$, Sigl *et al.* used the principle of volume conservation and assumed that the matter displaced from the void to form the neck geometry ($V_1$ in Figure 2-19a) is "moved" into the plate on an area governed by the original spacing between void centers ($V_2$). After rearrangement, the solution for $\sigma(u)$ is:

$$\sigma(u) = k\cdot 2^n\cdot[-\ln(1-x)]^n\cdot\ln\left(\frac{1}{x}\right)\cdot(1-x) \tag{2-64}$$

where $x = \sqrt{(2u)/(\pi a_0)}$. When rupture occurs by hole nucleation, growth, and coalescence, the same authors claimed that the form of the stress-displacement curve is unchanged, but $a_0$ then becomes the half-spacing between voids. It is also important to keep in mind that in the original model the law used to describe the flow curve is not written $\sigma_f = k\varepsilon^n$, but $\sigma = \sigma_0(\varepsilon/\varepsilon_0)^n$, where $\sigma_0$ and $\varepsilon_0$ are fixed parameters. Eq. (2-64) then becomes:

$$\sigma(u) = \frac{\sigma_0\cdot 2^n\cdot[-\ln(1-x)]^n\cdot\ln\left(\frac{1}{x}\right)\cdot(1-x)}{\varepsilon_0{}^n} \tag{2-65}$$

Thus $k$ is given by $k = \sigma_0\varepsilon_0^{-n}$ in this form.

To predict the toughening due to particle stretching, (2-62) and (2-65) are combined to obtain the relations :

$$\Delta G_c = f\cdot k\cdot\pi\cdot a_0\cdot g(n) \qquad \text{for} \quad \sigma = k\varepsilon^n \tag{2-66}$$

$$\Delta G_c = f\cdot\sigma_0\cdot\varepsilon_0{}^{-n}\cdot\pi\cdot a_0\cdot g(n) \qquad \text{for} \quad \sigma = \sigma_0(\varepsilon/\varepsilon_0)^n \tag{2-67}$$

where $g$(n) is given by:

$$g(n) = 2^n \int_0^1 \ln\left(\frac{1}{x}\right) \cdot (1-x) \cdot x \cdot \left[-\ln(1-x)\right]^n \mathrm{d}x \qquad (2\text{-}68)$$

Eq.(2-68) can be solved numerically. Hence, independently of the law used to describe the flow propeties, the void spacing is a scale parameter that dictates the toughening. According to this approach, reducing the interparticle spacing should thus decrease the local work of fracture as long as it is not compensated for by a gain in yield stress (which is reflected by the values of $k$ and $\sigma_0$ in (2-66) and (2-67), respectively).

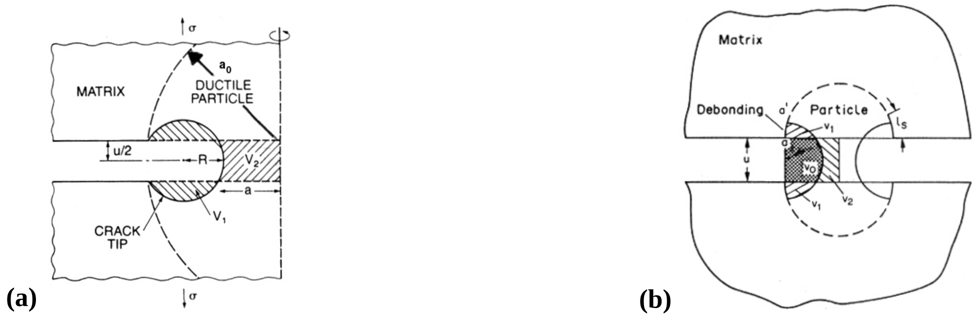

**Figure 2-19.** Bridgman analysis of a ductile particle being stretched in front of the crack tip. **(a)**: Perfect bonding case [221]; in order to maintain volume conservation, the model assumes that the volume added to the neck $V_2$, is equal to the volume removed to create the void $V_1$; **(b)** modification of the model by Bao and Hui [227] to take into account partial debonding.

When Sigl *et al.* compared their model with experiments, it was found that, while giving the correct trends of toughness as a function of volume fraction, the absolute calculated values of $\Delta G_c$ underestimated the measured level of toughness. One explanation for this discrepancy is brought by incorporating the initial residual stress in the ductile particle due to thermal expansion mismatch during cooling. As also explained earlier for the WC-Co alloys, the plastic flow properties of the ductile particles surrounded by the rigid ceramic matrix can also significantly differ from bulk properties. In PRMMCs for instance, it has already been mentionned that the *in-situ* flow properties back-calculated from the measured composite flow curves [135, 179], using the Nan and Clarke approach [228] depend strongly on particle size.

### iii. Influence of debonding

Using the same approach as Sigl *et al.*, Bao and Hui [227] refined the model in order to incorporate the effect of partial decohesion. For this purpose, they considered partial debonding at the particle/matrix interface over the arc length aa' as shown in Figure 2-19b. This involves loss of lateral constraint, and a larger critical ligament length at fracture $u^*$. The relation $\sigma(u)$ is then obtained exactly as above, namely using the Bridgman solution, while the toughening is also expressed according to (2-66) and (2-67). The difference lies in the function $g$(n) which becomes for partial debonding:

$$g(n) = 2 \cdot 2^n \int_0^1 \ln\left(\frac{1}{2} + \frac{1}{2x}\right) \cdot \left(1 - x^2\right) \cdot x \cdot \left(1 - \frac{2x}{\pi}\right) \cdot \left[-\ln(1-x)\right]^n \mathrm{d}x \qquad (2\text{-}69)$$

where $x = R/a_0$ in this case. Basically, this model results in equivalent trends in terms of the variation of $\Delta G_c$ as a function of $n$ and $a_0$; however, the presence of debonding increases slightly the toughness values[1].

### iv. Flow characteristics of highly constraint ductile particles

An original study of the influence of lateral constraint on the stress-stretch curve of ductile ligaments was conducted by Ashby, Blunt and Bannister [226]. The idea was to conduct tensile tests on lead (Pb) wires that were highly constrained by bonding them into a thick-walled glass capillary that was cracked in a plane normal to the axis of the wire (Figure 2-20a). The shape of the stress-displacement curves they measure differ depending on the level of constraint on the wires. By observing the different failure mechanisms of the wires, they correlated the shape of the stress-displacement curves with these mechanisms, which were of three different types:

(i) complete ductile failure of the lead without decohesion or cavitation, leading to a classical necking cone peak on both fracture surfaces

(ii) nucleation of a single cavity that grew until it occupied the whole section;

(iii) partial debonding at the interface over a distance of 0.1 to $1a_0$, (where $a_0$ is the initial wire radius) plus growth of an internal void; however when decohesion was extensive, internal voids were not found.

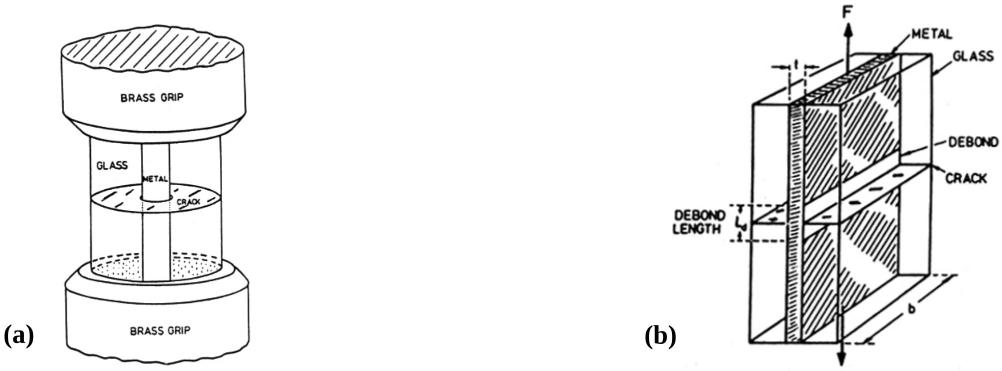

**Figure 2-20.** Sample geometries used to quantify the influence of constraint on the flow behaviour of soft materials. **(a)**: lead wire [226] bonded inside a glass tube; **(b)**: sandwich arrangement [229] where debonding is controlled via pre-coating a selected fraction of the glass with carbon.

When mechanisms (i) and (ii) were observed (*i.e.* perfect adhesion between lead and glass), high normalized stresses $\sigma/\sigma_0$ of about 6 were achieved, where $\sigma$ is the external applied stress and $\sigma_0$ comes from the definition of the true stress-strain curve of the unconstraint wire $\sigma_y = \sigma_0(\varepsilon/\varepsilon_0)^n$; while displacement to failure was low. This reflected the very large constraint imposed on the soft lead. In the case of mechanism (iii), the maximum stress was lower (in other words, constraint was smaller) and greater elongations were obtained. The energy absorption for the final failure (which can be linked to the toughening effect in ductile-particle reinforced brittle materials) was highest for lower levels of constraints, namely for the cases where partial debonding occurred.

Following their experimental observations, the authors derived several analytical solutions for the stress-displacement curves of the constrained wires corresponding to the mechanisms mentioned above. In summary, the principle of their analysis is to write first for each case the overall conservation of volume of the wire. Then, the incremental radial displacement of any point of the wire lying at a radius $r$, $dv(r)$ is written as function of axial incremental extension, $du$. For case (i) this is for instance done by noting that for any radius, $f(u,r) = \pi r^2 u = \text{const.}$ where $u$ is the crack opening, and by differentiating this expression:

---

1. In their paper, Bao and Hui claimed that the toughening was 80% higher in the presence of debonding, but the curve they actually presented seemed incorrect compared to the Sigl *et al.* paper and some verifications that we carried out. Therefore, we quote a less significant increase.

$$\frac{\mathrm{d}f(u,r)}{\mathrm{d}u}+\frac{\mathrm{d}f(u,r)}{\mathrm{d}r}=0 \qquad (2\text{-}70)$$

Finally, the work done by the external stress $\sigma$ in a small increment of crack opening d$u$ is equated to the plastic work done on the cylinder, which is itself separated into that needed to extend the cylinder and that used to shrink the wire. To estimate the strains in the cylinder $\varepsilon$, they assumed it to be on the order of ($u/u_0$-1) where $u_0$ is the initial crack opening such that $\sigma_y$ is replaced by:

$$\sigma_{\mathrm{y}}=\sigma_0\left[\frac{1}{\varepsilon_0}\cdot\left(\frac{u}{u_0}-1\right)\right]^n \qquad (2\text{-}71)$$

while for the case of partial debonding, $u$ is replaced by $u+l_{\mathrm{d}}$ where $l_{\mathrm{d}}$ is the decohesion length, and $u_0$ by $u_0+l_{\mathrm{d}}$. Further details can be found in their paper, where derivations are well documented.

The force-displacement curves they derived from their models are summarized on Figure 2-21. They indicate that the degree of toughening that can be obtained by the stretching of the particles depends on their properties, volume fraction and size, and on the strength of the interface between the inclusions and the rigid matrix. The occurrence of internal voiding does not fundamentally modify the shape of the curve, and has a much less pronounced influence than partial decohesion.

In summary, the experimental study of Ashby *et al.* showed in a very elegant manner the influence of constraint on the stress-stretch curve of a ductile inclusion in a rigid matrix. Their observations, together with their analytical modeling approach, are also relevant in the case of PRMMCs, for the cracked glass capillary can be assimilated in these materials to a cracked particle from which voiding is initiated.

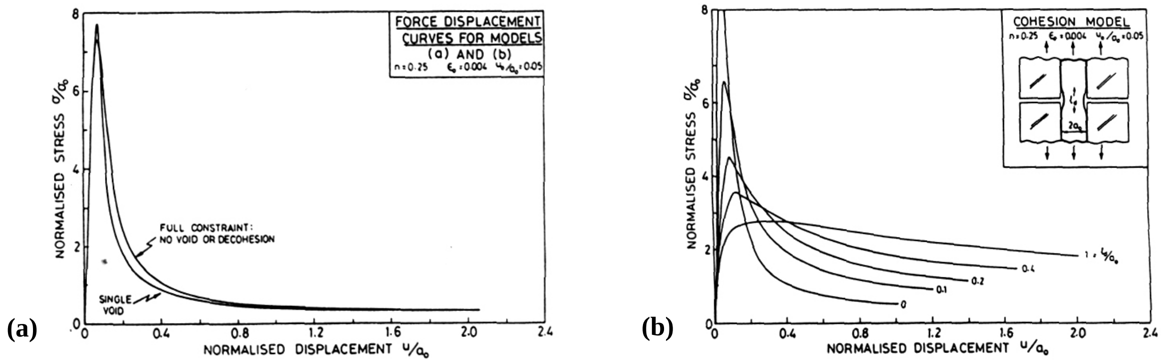

**Figure 2-21.** Normalized stress-stretch curves of to the analysis of Ashby *et al.* **(a)**: fully constrained and internal void mechanism; **(b)** limited decohesion mechanism.

In order to quantify more clearly the influence of the interface strength, Bannister and Ashby conducted a second set of experiments [229], where wires were replaced by thin sheets of lead that were bonded between two glass plates in a sandwich arrangement, Figure 2-20b. To control further debonding during the test, they deposited a thin band of carbon on a selected length of the glass prior to melting the high purity lead. They introduced a precrack into the glass by slightly bending the sample. When no debonding occured, the peak stress ($\sigma_{\max}/\sigma_0$) was high and the normalized failure displacement $u_{\max}/t$ (where $t$ is the thickness of the lead sheet) was low. Conversely, when debonding was present the constraint was lost and they observed a decrease of the normalized peak stress, together with larger maximum stretch as the extent of debonding increased. In terms of work of fracture per unit area (given by the area under the stress-displacement curve), it increased with increasing debonding length. Their typical experimental stress-displacement curves are given in Figure 2-22a, while peak-stress and work to fracture are shown on Figures 29b and c respectively.

These results clearly pointed out the importance of constraint and show that partial debonding following brittle fracture of the rigid phase in a two-phase material should be distinguished from the case where stretching (or voiding) of the ductile phase occurs without initial debonding at the interface. Limited debonding reduces the peak stress necessary to stretch the ligaments, but the overall fracture energy of this mechanism is higher, in agreement with the Bridgman analysis [221] and its modification to account for debonding [230].

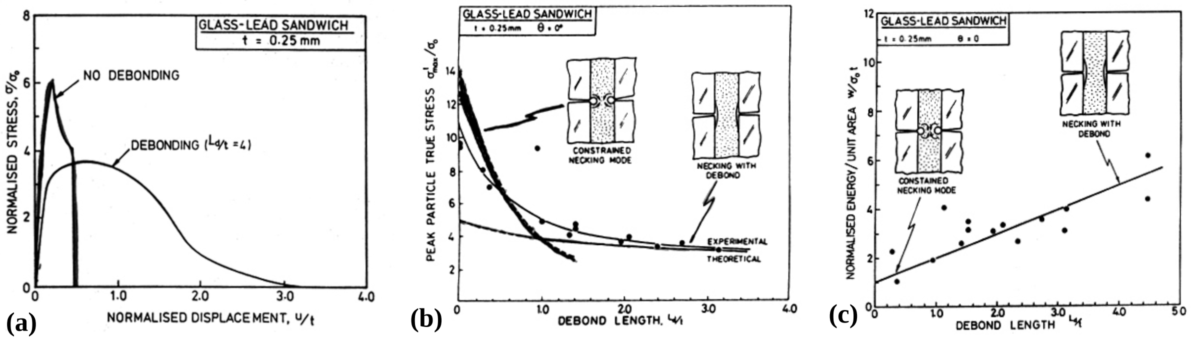

(a) (b) (c)

**Figure 2-22.** **(a)**: Typical normalized stress/normalized displacement curves for the sandwich specimen of Bannister and Ashby; **(b)**: normalized true peak stress vs. debond length (data and model), **(c)**: normalized fracture energy per unit area vs. debond length.

## 2.6.4 Summary and comments

Various approaches that we have found useful in providing quantitative information of the local fracture energy $\gamma_{pz}$ in PRMMCs have been presented. The analysis based on the fracture surface profile describes the ductile voiding process and its quantification is improved via SEM observations coupled with a system for automatic image processing. The similarities between the microstructure of high volume fraction PRMMCs and that of hard refractory alloys (WC-Co) provide relevant concepts, for instance the analysis of the toughening effect brought by the ligaments bridging the crack faces. When this mechanism operates, the *in-situ* behaviour of the ductile phase should not be neglected, as also observed in brittle matrix composites reinforced by ductile particles. Concerning this class of materials, the work by Ashby *et al.* provides important information regarding the constraint effect due to the rigid phase and constraint loss in the presence of partial debonding.

There is, however, a major difference between the two-phase materials presented here and PRMMCs: the global toughness in the former is mainly contained in the term $\gamma_{pz}$ while only a little contribution is due to dissipation in the plastic zone, although experimental evidences in one study [231] indicated the presence of a larger plastic zone than expected and in turn a significant contribution to the overall toughness[1]. Finally, one notices that the local fracture energy $\gamma_{pz}$ (defined as the integral under the local stress-stretch curve) is equivalent to $\Gamma_0$ in the cohesive zone models, with the difference that it is based here on micromechanical analysis, while phenomenological laws are employed in the CZM approaches.

---

[1] In this reference, the authors claimed that the model of Sigl and Fischmeister underestimates the measured toughness by about 80%. This is true when the *in-situ* flow stress is not considered. But this latter was actually estimated by Sigl and Fischmeister in the same paper to take into account the very high local strain hardening, and the calculated toughness was then much closer to experiments.

# CHAPTER 3

# EXPERIMENTAL PROCEDURES

## 3.1. MATERIALS PROCESSING

### *3.1.1 Selection and characteristics of the constituents*

#### i. Matrix

Pure aluminium (purity 99.99 %.), purchased from “VAW Highpural GmbH” (Grevenbroich, Germany), was used in order to produce “model composites” with a ductile matrix free of secondary phases. Stronger matrices used were binary Al-Cu alloys, with nominal Cu content of 2 and 4.5 wt.% respectively, purchased from “Alusuisse SA” (Neuhausen, Switzerland). They were selected because a simple microstructure can be obtained that consists of a single solid-solution phase of Cu into Al (eutectic composition being at 5.65%) by quenching after solution treatment. Chemical analysis was carried out on the as-received alloys at the Swiss Federal Laboratories for Materials Testing and Research (EMPA) using GDOE (Glow Discharge Optical Emission) spectroscopy, in particular to check the iron content. Details of the alloy chemical compositions are given in Table 3-1.

**Table 3-1.** Chemical composition of matrices (wt. %), according to supplier data sheets and additional chemical analysis. If not indicated, standard deviation is on the order of $10^{-4}$.

| Matrix | Si | Fe | Cu | Mn | Mg | Cr | Zn | Ti |
|---|---|---|---|---|---|---|---|---|
| Pure Al, sup. | 0.0020 | 0.0025 | 0.0025 | | 0.0030 | | | |
| control | 0.0040 | < 0.001 | 0.001 | 0.002 | < 0.001 | 0.001 | < 0.001 | < 0.001 |
| Al-Cu 2%, sup | 0.020 | 0.035 | 1.96 ± 0.06 | < 0.003 | < 0.005 | < 0.003 | < 0.003 | < 0.01 |
| control | | 0.014 | | | | | | |
| Al-Cu 4.5%, sup. | 0.022 | 0.041 | 4.58 ± 0.14 | < 0.003 | < 0.005 | < 0.003 | < 0.003 | < 0.01 |
| control | | 0.014 | | | | | | |

#### ii. Reinforcements

The ceramic powders used as reinforcement are classified into three different categories: (i) angular $Al_2O_3$ (alumina), (ii) polygonal $Al_2O_3$, and (iii) angular $B_4C$ (boron carbide). Alumina was selected because it is chemically inert in contact with liquid aluminium such that a two-phase composite free of reaction phase can be obtained; boron carbide was chosen because it exhibits a very high hardness (it is the third hardest material next to diamond and cubic boron nitride) and stiffness, combined with a low density (Table 2-1). It shows, on the other hand, some reactivity with liquid aluminium. This choice allows us to assess the influence of particle chemistry (angular $Al_2O_3$ *vs*. angular $B_4C$) and shape (angular

$Al_2O_3$ *vs*. polygonal $Al_2O_3$). In addition, particle size effect is studied by selecting various average particle sizes for each category of powders.

### ANGULAR ALUMINA

Angular-shape alumina produced by “Treibacher Schleifmittel” (Laufenburg, Germany), type Alodur™ WSK, was employed. These powders are made by the Bayer process and involve melting in an electric arc furnace at a temperature of about 2100°C leading to the formation of the stable $\alpha$-crystalline structure and a typical purity of 99.5 % according to the supplier [232]. Various size distributions are then obtained by crushing, milling and classification after cooling down to room temperature. Five different nominal size distributions were used: F220, F320, F400, F600 and F1000 which according to the Federation of the European Producers of Abrasive (FEPA) correspond to average particle sizes of 58, 29, 17, 9, and 4.5 µm respectively.

### ANGULAR BORON CARBIDE

$B_4C$ particles (Tetrabor™) were purchased from “Elektroschmelzwerk Kempten GmbH” (Munich, Germany). Boron carbide powders are produced by carbothermal reduction of boric acid or $B_2O_3$ in electric arc furnaces, followed by standard size reduction and classification (such as wet sedimentation or air classification). The nominal size distributions used were the same as for angular alumina, namely ranging between F220 and F1000 according to the FEPA denomination.

### POLYGONAL ALUMINA

Low aspect ratio $Al_2O_3$ powders (type “Sumicorundum”) were purchased from “Sumitomo Chemicals Co., LTD” (Tokyo, Japan). These powders are manufactured using additional purification treatments via hydrolysis of aluminium alchoxide [233], which leads to high purity products (>99.99% alumina). They were selected because they exhibit narrow particle size distributions with regular geometrical faces free of angular corners; hence these particles are denominated as “polygonal” according to the definition presented in Figure 2-1b. Three nominal average particle sizes (as measured by the manufacturer) were used: 18, 10, and 5 µm.

Because of the presence of larger-than-average particles in the 18 µm powder (as revealed by optical microscope observations that will be presented later), this powder was sieved in a “Fritsch” sieving machine (Idar-Oberstein, Germany), model “analyzette 3 Pro”. To separate the larger particles from the average size ones, sieves with grit sizes of 125 and 45 µm were employed. About 300 grams of the powder was placed in the 125 µm grit sieve and vibrated at an amplitude of 1.5 mm for 10 mn, after which powder in the 45 µm grit sieve was recovered and used for preform fabrication.

### SIZE DISTRIBUTION AND OBSERVATION OF POWDERS

The particle size distribution of the powders was measured in order to verify the distribution curves given by the suppliers. For this purpose the optical transmission method combined with centrifugal sedimentation was employed, using a “Horiba Capa-700” (Sulzbach, Germany) particle size analyser available in the “Laboratory of Powder Technology” (Institute of Materials, EPFL): between 10 and 100 mg of powder were dispersed into 20 ml of a solution made of 75 wt.% glycerol and 25 wt.% distilled water, the powder concentration being chosen to achieve an optical absorbance of the dispersion ranging between 0.6 and 0.8. An ultrasonic cleaner was used to ensure adequate dispersion in the medium. The solution was held at a temperature of 28-32°C using a hot water double-boiler, before measurement. The needed amount of dispersion was rapidly transferred into the measurement cell which is then inserted into the particle size analyser. The centrifugation speed was set between 300 and 2000 rpm depending on the powder particle size, such that the time of measurement was comprised between 5 and 15 minutes (centrifugation speed is increased for smaller powder sizes due to the longer sedimentation time in these). At least three reproducible measures were carried out for each powder. The experimental conditions used during analysis are summarized in Table 3-2

**Table 3-2.** Experimental conditions for the measures of particle size distribution with the Horiba Capa 700.

| Dispersion medium | Disp. density (28°C) | Powder density | Speed [rpm] |
|---|---|---|---|
| 75 wt.% glycerol<br>25 wt % distilled water | 1.20 [g/cm$^3$] | $Al_2O_3$: 3.98 [g/cm$^3$]<br>$B_4C$: 2.5 [g/cm$^3$] | large particles (>20 µm): 300<br>medium “ (10-20 µm): 500-1000<br>small “ (1-10 µm): 1000-2000 |

Detailed examination of particle shape and surface quality of the purchased powders was carried out by Scanning Electron Microscopy (SEM), on a “Philips XL-30” field emission microscope available at the “Centre Interdépartemental de Microscopie Electronique” (CIME-EPFL). Prior to observing the powder samples, they were prepared in the following manner: a conductive double-side adhesive tape was stuck on a flat SEM specimen holder and a small amount of powder (a few milligrams) was deposited on top of the adhesive. Vacuum was then pumped in order to eliminate loose particles that were not well stuck on the adhesive, and that would contaminate and damage the SEM vacuum pump. For $Al_2O_3$ particles, a thin gold layer was then deposited on the surface of the particles by physical vapor deposition (PVD) in order to reduce electron charging effects during observation. This last step was found unnecessary with $B_4C$ particles.

In order to check the efficiency of sieving, polygonal alumina particles with a nominal particle size of 18 µm were observed by optical light microscopy prior and after sieving. A transparent double-side adhesive tape was stuck on a glass microscopic slide, and a few milligrams of powder were simply dispersed on the adhesive. Observations of particles recovered from the bottom recipient of the sieving machine, the 45, and the 125 µm grit sizes, were carried out on a “Zeiss Axioplan” universal microscope (Oberkochen, Germany), in dark field conditions.

### 3.1.2 Preform preparation

Ceramic preforms were prepared by packing the ceramic particles directly into alumina crucibles, purchased from “Vesuvius McDanel” (Beaver Falls, PA, USA) and “Siderval SA” (Montagny, Switzerland). The crucibles are of 99.8% pure $Al_2O_3$ with a cylindrical shape of the following dimensions: 36-38 mm. inner diameter, 44-46 mm external diameter, and 300 mm length with a semi-spherical bottom Prior to inserting and packing the powders, the inside of the crucibles is coated with a graphite aerosol in order to facilitate casting removal after infiltration. When the coating was not properly made, the infiltrated ingot sticks strongly to the crucibles and removal of the latter tends to be very difficult. Optimal coating (in term of adhesion to the crucible surface) was achieved by initially heating the crucibles to a temperature of 70 to 90°C and applying graphite spray while the crucibles were still hot. In addition, two 4 mm diameter holes were drilled at a distance of 10 mm from the top of the crucibles to hold the crucible inside the infiltration machine.

The amount of powder to be packed is selected to meet a chosen preform height in the crucibles, which is a function of the tapped density of a specific powder. To achieve a maximum and uniform tapped density of the preform, the following procedure was used: a fraction of the initial powder was introduced into the crucible through a plastic funnel and packed by carefully tapping the outside of the crucible with a metallic rod, a process that we call “lateral packing”; this process was performed in alternance with “longitudinal packing” consisting of hitting several times the bottom of the crucibles against a soft wooden support. Each of these methods induces geometrical reorganization of particles within the preform, thereby allowing optimal packing. When the reinforcement was well packed, more powder was added into the crucible and the tapping procedure was repeated. Once all the powder was introduced and packed, the preform height was measured by simply inserting a metallic rod inside the crucible and by marking the outer surface of the crucible. Then, tapping procedures as described above were performed again and the preform height was controlled at various intervals. Tapping was continued until the preform height remained constant, meaning that maximum packing density of the preform was achieved. By controlling the exact amount of powder introduced and knowing the density of the particles and the geometrical dimensions of the crucible, the preform volume fraction could be estimated. As the remaining porosity is subsequently filled by the liquid metal during infiltration and since this process does not cause any further packing, the preform packing density could be used as the final volume fraction of reinforcemens in the composite ($V_f$) with a good approximation. This was verified by more precise measurements of $V_f$ on some composites.

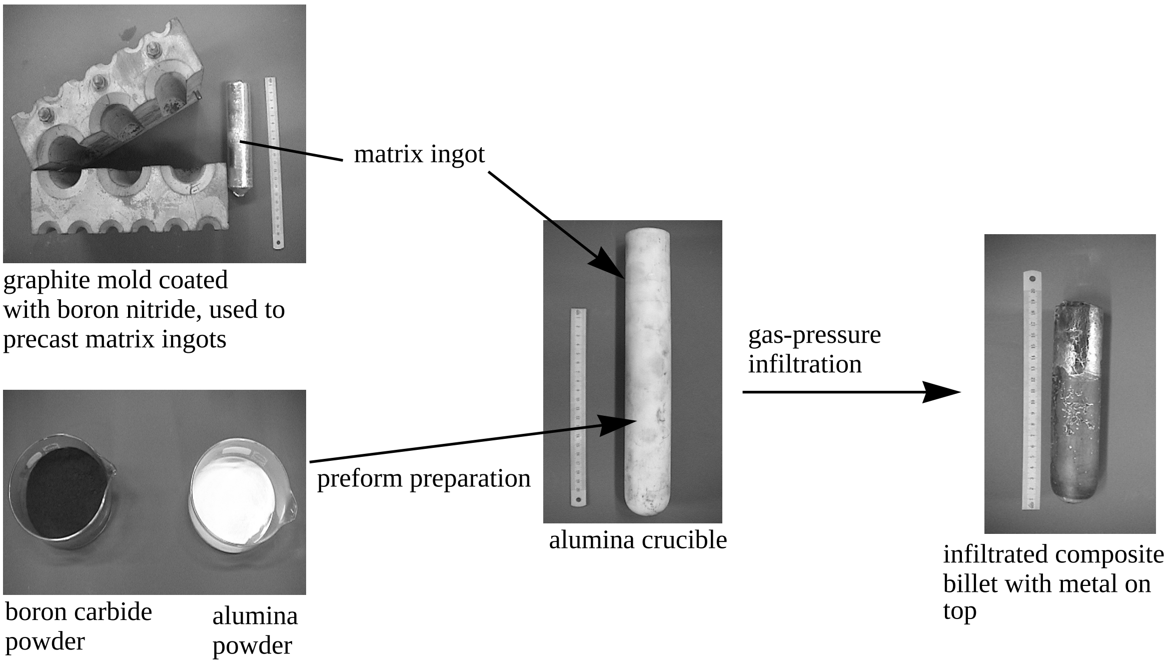
matrix ingot
graphite mold coated with boron nitride, used to precast matrix ingots
gas-pressure infiltration
preform preparation
alumina crucible
infiltrated composite billet with metal on top
boron carbide powder
alumina powder

**Figure 3-1.** Initial constituents used to fabricate the composites and a typical infiltrated composite billet.

The preform tapping density achieved is a function of particle size distribution and of electrostatic forces between individual reinforcements. Hence, it was observed that the time needed to obtain maximum tapping was longer for finer particle powders due to stronger eletrostatic interactions, which in turn necessitated reduced amount of powder additions at each packing step. For the same reason, very careful tapping was necessary with such small powders (< 15 µm) to obtain a uniform distribution of density inside the preform, to avoid localized regions of lower packed density, which create veins in the cast composite (as will be described later).

### 3.1.3 Gas-pressure infiltration

#### i. Apparatus

All the composites were processed using a gas-pressure infiltration machine that was built in the laboratory prior to this work, shown in Figure 3-2. In short, the machine consists of a cylindrical pressure vessel with threaded flanges at both extremities that are sealed via bolted, water-cooled side-plates and O-rings. The vessel is surrounded by a resistance furnace, which heats the tube by convection and radiation, to a temperature high enough to allow melting of the matrix alloy placed in the alumina crucible, inside the vessel. The top plate is connected with a vacuum pump and a high-pressure line through a single flexible pipe. In addition, the plate is also machined to allow introduction of a heat-resistant rod that holds the crucible, and can be manipulated in the longitudinal direction through the top plate. The pressure vessel is designed to support a maximum pressure of 200 bars as 750°C, although for safety reasons, such extremes conditions are not used. The resistance furnace (fabricated by “Rescal SA”, Epone, France) is made of three zones that can be controlled and programmed independently by thermal controllers; its maximum attainable temperature is 1150°C. To protect the O-rings, side-plates, and bolts from heating, cooling coils surround the upper and the lower parts of the pressure vessel. Inside the vessel, a copper chill is fixed to the bottom side-plate with a thread. It is used to induce directional solidification of the composite from the liquid state once infiltration is completed: this is achieved by lowering the positioning rod until the bottom of the crucible enters in contact with the chill, thereby allowing heat extraction from the bottom of the composite and in turn advancing of the solidification front upwards to feed shrinkage.

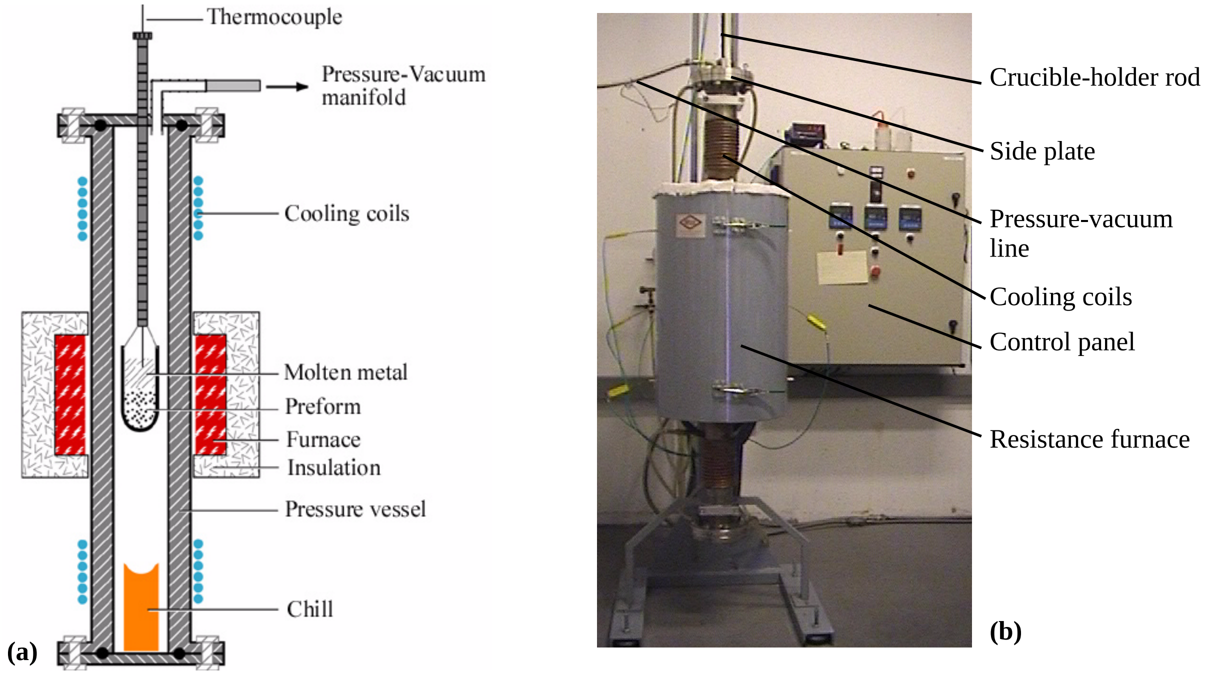

**Figure 3-2.** Gas-pressure infiltration machine used for composite fabrication. **(a)**: schematic cross-sectional view; **(b)**: overall picture of the apparatus. The furnace height is about 0.8 meter.

### ii. Processing technique

Matrix billets were pre-cast in cold stainless steel or graphite molds pre-coated with boron-nitride to a shape that fits the inner crucible dimensions, as shown in Figure 3-1. The precast billets were then carefully introduced into the crucible, over the preform. In some cases, a thin layer of alumina wool was placed between the preform and the matrix billet. Once this preparation was completed, the crucible was suspended to the moving rod with a high temperature resistance Ni-Cr alloy wire such that it was positionned well in the middle part of the furnace. Then the bolts of the top plate were strongly tightened. Before each infiltration experiment, O-rings were carefully coated with vacuum grease. The experimental procedures then followed the description summarized in Figure 2-4.

The first step of processing consists of evacuating the pressure vessel with a vacuum pump. A very low evacuation rate was necessary, because if a high pressure gradient is applied on the powder, the particles move or can even fluidize, which in turn leads to the presence of veins in the composite. Smaller particle size preforms are particularly sensitive to this effect and hence necessitated even greater care. To control the evacuation rate, the pressure was measured at the entrance of the chamber with a Pirani cold cathode gauge, while the valve separating the pump from the vessel was opened very slowly: for large particle size preforms (> 25 µm), the valve opening was controlled such that the measured pressure at the entrance did not exceed $4 \cdot 10^{-1}$ mbar, while for medium and smaller particles the pressure must not exceed $2 \cdot 10^{-1}$ mbar. Once pressure was stabilized, the valve was opened further (while always controlling the pressure) and the process was repeated until the valve was fully opened. The whole procedure took typically 6 to 8 hours. The vessel was then evacuated overnight and the minimum pressure inside the chamber attained its minimum value, of about $2 \cdot 10^{-2}$ mbar.

The second step was heating the vessel until the matrix was molten. As for the evacuation stage, very slow heating rate was necessary to prevent too rapid a gas release from the particles, which would also cause the preform to expand and crack locally, leaving veins in the final composite. To this end, the three zones of the furnace were programmed in the following manner:

(i) heating from room temperature to 125°C in one hour and stabilization for another hour;
(ii) heating to 175°C in 30 min and stabilization for 30 min;
(iii) and (iv) same heating and stabilization times as for (ii), at temperatures of 225°C and 275°C respectively;
(v) heating to 750°C and stabilization for at least one hour.

During all the heating stage, the vessel was simultaneously evacuated to permit degassing of adsorbed gaseous molecules from the particles, such that at the end of heating the final pressure was slightly above $2 \cdot 10^{-2}$ mbar.

The third processing step is pressure infiltration of the preform with liquid metal, using pressurized argon. As in the precedent steps, pressurization was applied at a relative slow rate since an excessive pressure gradient along the preform promotes cracking of the preform. In typical experiments, the pressure was first increased to 5 bar at a rate of ≈ 2bar/min. The pressurization rate was then adjusted to about 10 bar/min until a maximum pressure of 80 bar was reached, such that the whole process lasted about 10 min. For smaller particle size preforms, maximum pressure was sometimes raised to 100-120 bar to ensure full infiltration in these lower permeability preforms. Finally, the maximum pressure was maintained for several minutes for $Al_2O_3$ reinforced composites before lowering the crucible onto the chill.

In the case of $B_4C$ composites it was kept during less than a minute to reduce the contact time between the liquid aluminium and the ceramic particles, hence minimizing the amount of reaction in this system.

The last step of the process is directional solidification of the casting composite. The maximum pressure was released to atmospheric pressure to allow the positioning rod to be moved downward, until the crucible contacted the chill. The pressure was then rapidly increased to 80 bar again, in order to solidify the composite under pressure and hence avoid partial dewetting and formation of solidification pores.

### iii. Composite designation

The composite designation used follows the definition introduced by Kouzeli [89] and takes the form:

“*(X)*Y-ZDi”.

*(X)* designates infiltration run. *Y* designates the matrix alloy and *Z* the initial chemical formula of the reinforcements, according to the following codes:

| | | | |
|---|---|---|---|
| **Y (matrix):** | A for pure aluminium | A2C for Al-Cu2% | A4.5C for Al-Cu4.5% |
| **Z (reinforcement):** | A for $Al_2O_3$ | B for $B_4C$ | |

*D* is a number corresponding to the average particle size. For consistency, since the powders were not purchased from the same manufacturer, the measured average sizes were used instead of the nominal sizes given by the supplier, allowing better comparison since we used the same technique to measure all powder size distributions. The letter *i* is used to distinguish particle shape and is omitted for the $B_4C$ reinforced composite (since only one shape of particles was used). For $Al_2O_3$ reinforcement, the adopted codes are:

| | | |
|---|---|---|
| **i (reinforcement shape):** | a for angular alumina | p for polygonal alumina. |

Hence, *(101)*A-B35 designates infiltration run 101, and is a composite made of an aluminium matrix reinforced with boron carbide particles of average size 35 µm; as another example, *(283)*A4.5C-A15p stands for an Al-Cu 4.5% matrix composite reinforced with 15 µm polygonal alumina particles produced during run 283.

# 3.2. MICROSTRUCTURAL CHARACTERIZATION

## *3.2.1 Metallography*

In a first step, slices a few millimeter thick were cut from as-cast composite billets on a “Mesotom AT73” high speed saw (Struers, Rødovre, Denmark), using silicon carbide cut-off wheels of Type 06 TRE. These slices were then sectioned into smaller pieces (of area in the range of 1 cm$^2$) on a “Acutom-50” high-speed diamond saw (Struers), with saws of diameter 10 to 15 cm and thicknesses of 0.2 to 0.5 mm. Two types of mounting agent were used to fabricate metallographic samples, which both gave similar results in terms of the final quality of polished samples. One was a thermoset plastic, type “Bakelit black S” (Jean Wirtz GmbH, Düsseldorf, Germany), which was mounted using a hot-press (model Hydropress A, Jean Wirtz) set to 170°C for 12 min at 15 Pa. The second is a cold-polymerizing thermoset (Demotec™10, Germany) which was polymerized in a “Technomat” pressure unit (Kulzer GmbH, Wehrheim, Germany) at a pressure of 2 bars to obtain pore-free samples, and in silicon molds. The second method has the advantage that a higher number of samples can be produced in one run. The size of mounted samples was in both cases 2 cm in diameter.

Grinding and polishing of PRMMCs necessitates particular attention when choosing cloths, abrasives, lubricants and polishing conditions because the extreme difference in hardness between the matrix and the reinforcement can lead to various experimental artefacts such as particle removal from the matrix, embedding of abrasive particles within the soft phase, or particle cracking. For pure Al matrix composites, mounted samples were ground with fine (grade 600) silicon carbide paper. Coarser grain paper was not used because it tends to pull out some particles from the matrix during grinding. This effect was not observed in alloyed matrix composites such that grinding could then be started with coarser papers. Polishing was carried out on a Struers “DAP-7 automatic polishing machine” using a three-specimen holder. Abrasive material was polycrystalline diamond produced by Struers and applied in the form of stick (DP-stick P) and spray (DP-spray P); polishing cloths were hard Struers MD*Dur*™ attached with a magnetic fixation to the polishing disk; blue Struers lubricant was used because it provides the maximum cooling. The first step of polishing was carried out with abrasive sizes of 15 µm. The cloth was initially coated with the diamond stick, and well humidified with the lubricant. The pressure was set at the second mark on the machine (corresponding to roughly 400 N) and the lubricant was applied at a rate of about two drops per second, such that the cloth was always wet. Polishing time was set between 20 to 25 min and abrasive was reapplied at various intervals by means of the spray. The same procedure was repeated with abrasive sizes of 9, 3 and 1 µm for 20, 15 and 25-30 min respectively, at the same pressure. The metallographic samples were checked under the microscope after each step (that is repeated if necessary) and carefully cleaned in an ultrasonic bath before being polished with a finer grade abrasive.

## *3.2.2 Volume fraction determination*

As mentioned earlier, an acceptable approximation of the reinforcement volume fraction ($V_f$) is obtained by measuring the preform height within the crucible and weighing the powder introduced in the latter. In addition, $V_f$ of pure aluminium matrix composites was measured earlier by Kouzeli [89], using densitometry and a high precision microbalance, and results obtained in this work could be compared with the approximations based on the preform geometry and weight. The reader is referred to this reference for more details. Systematic determination of $V_f$ using densitometry is unnecessary in alloyed matrix composite, because the preform preparation technique and the powders used (which govern $V_f$) were the same as for pure Al matrix composites. $V_f$ in some of these composites was nevertheless determined by densitometry to verify agreement with the calculations based on the preform characteristics.

### 3.2.3 Interparticle distance

The average interparticle distance was measured mainly in Al-Cu matrix composites. For pure Al matrix composites, the values measured in [89] were used, although some measurements were conducted as well for verification. This was done by measuring the characteristic length $\lambda_m$ defined as the mean edge-to-edge distance between two neighbouring particles along straight lines in isotropic materials:

$$\lambda_m = \frac{1 - V_f}{N_L} \tag{3-1}$$

where $V_f$ is the volume fraction of particles and $N_L$ is the number of particle interceptions per unit length of test line [234]. The advantage of (3-1) is that $\lambda_m$ represents a statistical three-dimensional interparticulate distance which is independent of the particle shape and size. A “Photoshop“ (Adobe systems Inc., San Jose, Ca, USA) numerical layer made of seven random lines was superposed on a minimum of five optical micrographs for each material investigated. The image magnification was chosen such that between 200 and 300 particles were analyzed per micrograph. The number of intercepts $N_p$ was then counted manually and divided by the total length of individual straight lines $L_t$, to obtain $N_L = N_p/L_t$.

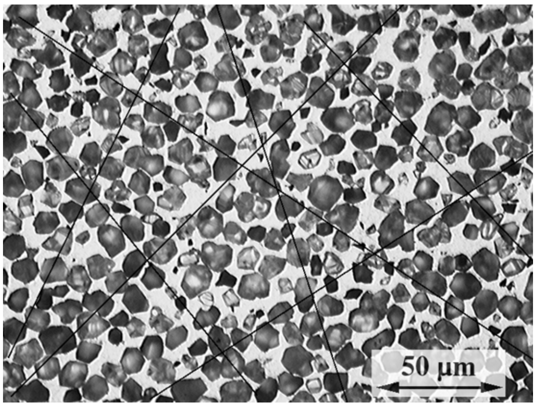

total length of the
straight lines = 1220 µm

**Figure 3-3.** Statistical method for the determination of the average interparticulate distance: random straight lines are superposed on optical micrographs and the number of particle/line interception is counted.

### 3.2.4 Determination of reaction phases and of the boron solubility in the matrix

The system liquid Al/$B_4C$ being chemically unstable, reaction phases are formed during infiltration. These were determined using X-ray analysis. In addition, the solubility of boron in aluminium (known to be very low according to materials handbooks) was controlled by Secondary Ion Mass Spectroscopy (SIMS) to ensure that there was not a solid-solution strengthening effect of the matrix in the Al/$B_4C$ composites; this is presented in Appendix 3.

#### i. Reaction phases: observation and XRD analysis

Reaction phases were determined on the *(60)*A-B60 composite, in which a contact time of 15 mn between liquid aluminium and reinforcements was purposely allowed during processing in order to increase the amount of reaction phases and hence facilitate their characterization. These were initially observed by optical microscopy, such phases being easy to distinguish without etching [235]. Their crystalline structure was determined by X-Ray Diffraction (XRD) analysis using facilities available at the Ceramic Laboratory of EPFL: a disk 20 mm in diameter and 3 mm in thickness was machined from the composite casting by EDM and the measurements were conducted on a diffractometer functionning with a Cu anode, using the $CuK_{\alpha 1}$ radiation (emitting at a wavelength of 0.154056 nm), and the $\theta/2\theta$ method to obtain the diffraction pattern. Chemical composition of the reaction phases was finally obtained by comparing the diffraction patterns with data from the literature.

### 3.2.5 Analysis of secondary phases in Al-Cu matrix composites

The presence of ceramic reinforcements modifies matrix solidification as compared to unreinforced alloys through various mechanisms, as explained in the literature review. In addition, diffusion paths and characteristic diffusion distances during subsequent heat-treatments are altered as well by the reinforcements, depending on the reinforcement size, volume fraction, distribution and type. Hence, the microstructural features –in terms of secondary intermetallic phases of the matrix– of as-cast and heat-treated Al-Cu alloy matrix composites were ascertained using the SEM. In particular, the dissolution or possible presence of residual precipitates after solid-solution heat-treatment was checked.

#### i. Observation by SEM with the BSE detector

Various as-cast Al-Cu alloys matrix composites (with both 2% and 4.5% wt.% Cu) reinforced with angular and polygonal particles (as well as control samples from the unreinforced alloys) were cut into small pieces for subsequent heat-treatment. A sample carrier containing aluminium foils shaped in the form of a basket was introduced into a “Solo resistance furnace” (Porrentruy, Switzerland) and heated to 515°C, corresponding to the region of complete solubility of Cu in Al according to the Al-Cu phase diagram. Two thermocouples (type *K*) were inserted into the sample carrier, through the aluminium foils. Once the temperature had stabilized, the sample carrier was removed, the samples were rapidly placed into the aluminium basket and the sample carrier was then reinserted into the furnace. The samples were kept at this temperature of 515°C for at least 8 hours and up to several days, followed by a water-quench. The as-cast and quenched heat-treated samples were mounted and polished, and the mounting was removed before introduction in the SEM. Aluminium and copper having well distinct atomic masses, observations were performed with a backscattered electron (BSE) detector which yielded a clear chemical contrast between the various phases. The microscope was set at a an acceleration voltage of 15 kV and at working distance of 10 mm.

In addition, a more detailed study of Cu solubility and its evolution in our MMCs as a function of heat-treatment time was carried out in our laboratory by Stücklin [236]. More specifically, he studied the changes in second-phase content and kinetics of Al-Cu2%/$Al_2O_3$ composite systems (*(255)*A2-A35a, *(256)*A2-A60a and *(253)*A2-A15p). More details can be found in the above cited reference.

### ii. Chemical analysis with EDAX

The composition of second-phases observed in the as-cast and heat-treated materials for both the composites and the control specimens were analyzed under the SEM by X-ray energy dispersive analysis (EDAX). The analyzed regions were selected from the images obtained in the BSE mode, by focusing the incident electron beam on the chosen precipitate. The same experimental conditions as for BSE observation were chosen (namely an acceleration voltage of 15 kV and a working distance of 10 mm). The spectra were acquired and visualized with the program "EDXi", implemented on the computer controlling the microscope, and allowing comparison of EDS peaks with the $K_{\alpha/\beta}$ and $L_{\alpha/\beta}$ characteristic X-rays of the elements. The peaks corresponding to an element were accordingly marked, and once the peaks were identified, the program calculated the proportion of the elements in a quantitative manner using the $K$ lines, and corrected the relative intensities with the so-called ZAF factors which take into account the effects of the atomic number $Z$, the absorption $A$, and the fluorescence $F$ of the elements, respectively.

# 3.3. MECHANICAL TESTING

All mechanical testing samples were machined by Electro-Discharge Machining (EDM) in the machine shop of the Institute of Materials at EPFL. While rather expensive, this method appeared to be the only able to cut our high volume fraction PRMMCs with the tolerance needed.

## *3.3.1 Aging curves and heat-treatments*

Ageing characteristics of the alloyed matrix composites were measured on small cut samples from the as-cast billets which were solution treated at 515°C for at least 12 hours, and quenched in cold water. Artificial ageing was carried out at 100°C for various durations (with a maximum of 30 hours) after which the Vickers macrohardness was measured at an applied load of 20 kg, on a “Wolpert Dia Testor 2Rc” hardness tester (Otto Wolpert-Werke GmbH, Ludwigshafen, Germany). An average of five indentations for each condition was taken. The indentation being far larger than the reinforcement, hardness values are averages for the composites.

The mechanical testing samples (fracture, tensile) were heat-treated according to the ageing curves measured on various composites. All specimens were treated to one of the three following conditions: (i) as-cast (AC), (ii) solutionized (ST), and (iii) peak-aged (T6). For the last condition, the heat-treatment time had to be adjusted for the different composites.

## *3.3.2 J-Integral fracture toughness testing*

### i. General description

Despite the high volume fraction of ceramic particles, the pure Al matrix composites were too ductile for Linear Elastic Fracture Mechanics (LEFM) testing with reasonably sized specimens as compared to the size of a casting billet. Hence, their fracture characteristics were tested by Elastic-Plastic Fracture Mechanics (EPFM) testing, using the single specimen technique according to ASTM E-1737, which allowed generation of the entire *J-R* curve. A few Al-Cu matrix composites were also tested with this procedure, in order to compare such measures with a LEFM method which could be applied for these less ductile composites.

The principle of the measure is based on the energy-based definition of $J$ (Appendix A.2.4) and the division of $J$ into elastic and plastic components, according to eq.(A-28). During a test, the load $P$ versus the crack mouth displacement $V$ (measured at the load line with a clip-gage extensometer) is monitored and at a specific load increment ($V_{\mathrm{i}}$, $P_{\mathrm{i}}$), $J_{\mathrm{i}}$ is given by:

$$J_{(\mathrm{i})} = J_{\mathrm{e(i)}} + J_{\mathrm{pl(i)}} = \frac{K_{\mathrm{I(i)}}^{2} \cdot (1 - \nu^{2})}{E} + J_{\mathrm{pl(i)}} \qquad (3\text{-}2)$$

At regular intervals, the specimen is partially unloaded, allowing to compute its elastic compliance and in turn the actual crack length, $a_{\mathrm{i}}$. $J_{\mathrm{e(i)}}$ is obtained directly from the current load and crack length, which allows computation of $K_{\mathrm{I(i)}}$, the LEFM stress intensity factor for the sample at crack length $a_{\mathrm{i}}$. The computation of the plastic component $J_{\mathrm{pl(i)}}$ is based on deformation theory for a growing crack, which is related to the area under the load-*plastic* displacement curve for a *stationary* crack (and not the area under the *actual* load-displacement curve). Since the crack length changes continuously during a *J-R* curve test, the *J* integral is calculated incrementally according to:

$$J_{(i)} = J_{e(i)} + J_{p(i-1)} + \Delta J_{p(i)} \tag{3-3}$$

A concise presentation of the experimental estimation of *J* using the deformation theory for a growing crack, as well as the derivations of related equations can be found in Appendix 7 of [237].

### ii. Specimen geometry and pre-cracking procedures

#### SPECIMEN GEOMETRY

Compact tension (CT) specimens were machined by EDM from slices cut in the direction perpendicular to the composite ingot. If a micro-vein was identified on the initial slices, the CT specimens were cut such that the vein did not intercept the crack path in the first few millimeters of crack propagation. Two types of specimens were used: the first type had a thickness *B* of 13 mm and a specimen width *W* (defined as the distance between the load line to the the back edge of the specimen) of 20 mm, which corresponds to a value of *W*/*B* slightly smaller than ASTM requirements (2 <*W*/*B* <4). The reason for this was to make use of the maximum amount of material available from the composite billet diameter, and to obtain samples with a sufficient thickness. For the second type, grooves were machined into the sides of the specimen, generally before fatigue pre-cracking, such that the net thickness of the specimens was 80% of the gross thickness. Geometrical characteristics of the specimens are shown in Figure 3-4; these meet the other specifications of the standard. In particular, the crack geometry was drawn such that the crack mouth opening displacement (CMOD) was measured on the load line and in a manner that allowed a proper attachment of the clip-gage extensometer within the notch. The relative initial crack length *a*/*W* was 0.40 to permit further crack extension by fatigue loading according to ASTM requirements.

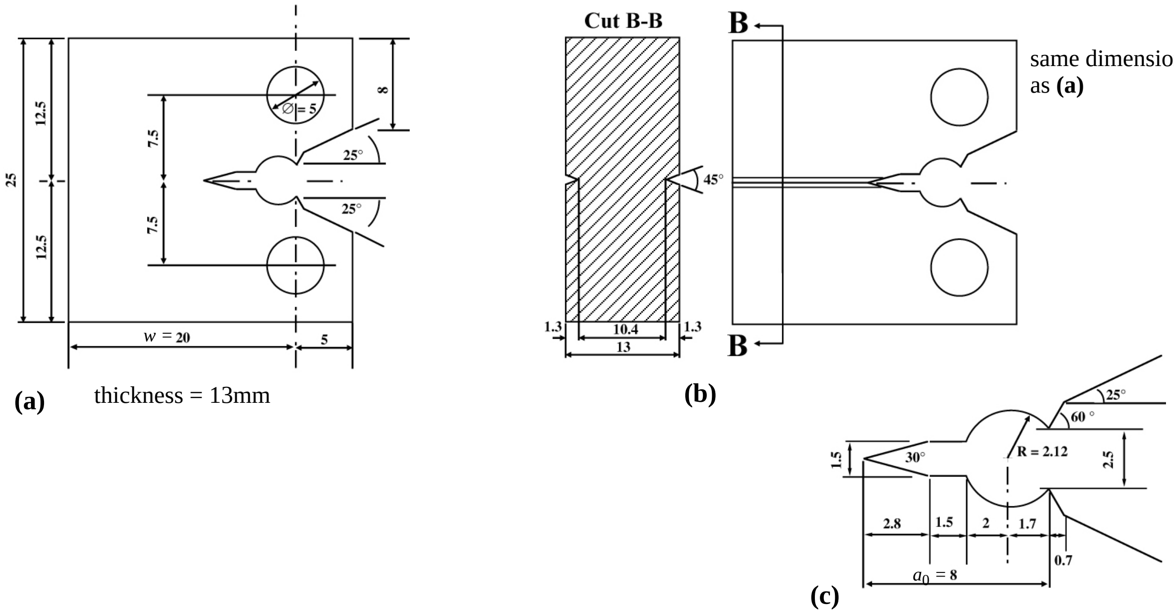

**Figure 3-4.** CT specimen geometry for *J*-integral fracture testing. **(a)**: flat specimen; **(b)**: side-grooved specimen; **(c)**: details of the notch geometry. Dimensions in mm.

### PRE-CRACKING PROCEDURES

The specimens were pre-cracked by fatigue loading on a 25 kN “Instron” (Instron Corp., Canton, MA, USA) universal servohydraulic testing machine (model 8872). Machine control and data acquisition were carried with via a personal computer. As already mentionned, pre-cracking of high volume fraction PRMMCs is not a trivial task, and necessitates a careful procedure to control the crack propagation. The method we adopted is essentially to:

(i) conduct a series of one to few thousands load cycles at a controlled load amplitude (corresponding to a certain initial stress intensity factor amplitude, $\Delta K = K_{max}$-$K_{min}$);

(ii) remove the specimen from the machine and measure the crack propagation on the surface using a non-destructive method;

(iii) reinsert the specimen into the machine and conduct a new series of load cycles at a load adapted to take into account the degree of crack advance from the precedent series of cycles;

(iii) repeat the different steps until the crack length satisfies crack length requirements of ASTM E-1737, namely $0.45W \leq a_0 \leq 0.70W$.

A sinusoidal wave form was employed for fatigue cycling, and the stress intensity factor ratio R $= K_{min}/K_{max}$ was set equal to 0.1 for all materials. The initial maximum stress intensity factor $K_{max}$ has to be adapted for each material and was typically in the range of 5.5-10 MPa·m$^{1/2}$ for pure Al matrix composites. It was found that $B_4C$ reinforced materials required a higher applied $K$ to initiate and propagate the crack (typicall 8-10 MPa·m$^{1/2}$) as compared to $Al_2O_3$ reinforced with the same particle size (5.5-8 MPa·m$^{1/2}$), and that the smaller particle size composites were more resistant to fatigue loading: this translated either into a higher $\Delta K$ needed in order to initiate the crack, or into a higher number of cycles at a given $\Delta K$ to achieve a certain amount of crack propagation. In Al-Cu matrix composites reinforced by polygonal alumina particles, the $K_{max}$ necessary for fatigue pre-cracking was higher, on the order of 13 MPa·m$^{1/2}$, while for angular particle reinforced composites a $K_{max}$ of about 9 MPa·m$^{1/2}$ was applied.

It was verified that the maximum load $P_{max}$ during fatigue pre-cracking did not exceed load $P_m$ defined as:

$$P_m = \frac{0.4\sigma_y Bb^2}{2W + a} \qquad \text{where} \qquad \sigma_y = \frac{\sigma_{ys} + \sigma_{UTS}}{2} \tag{3-4}$$

and that $K_{max}/E$ was less than $1.6 \cdot 10^{-4}$ m$^{1/2}$, as specified in the standard. Furthermore, compliance measurements during fracture testing (presented in the next paragraph) revealed crack closure effects due to fatigue loading. Among the various mechanisms for fatigue closure identified by Suresh and Ritchie [238], the most plausible effect in the present case was plasticity-induced closure related to residual plastic strains in the wake of the crack [238-241]. This was confirmed by the observation that the degree of crack-closure was significantly reduced by lowering the maximum load during fatigue cycling. If possible, pre-cracking was therefore preferentially conducted using a higher number of cycles at a lower $K_{max}$, rather than a lower number of cycles at a higher $K_{max}$.

In order to inspect the crack length and to control crack propagation between two series of fatigue cycling, a fluorescent penetrant dye was used, designated as “Magisglow 17” according to the producer (Cigiemme, Opera, Italy). The sides of the specimens were initially cleaned and degreased with the “Velnet/Solnet” solvent produced by the same manufacturer, after which the aerosol fluorescent was applied and allowed to penetrate the crack for about one minute. The surface of the CT specimen was then cleaned with water and ethanol, such that the penetrant remained inside the crack exclusively. The crack was finally revealed by observation of the specimen sides by optical microscopy, under ultraviolet (UV) light and at relatively low magnification[1], as typically shown in Figure 3-5 for the two types of fracture specimens. In the case of significant crack propagation (typically more than 0.5 mm), further fatigue cycling was conducted at a lower load, which corresponded approximately to the same stress intensity factor as applied in the previous series of cycles. If crack propagation was not detected or was too short, 10’000 to 40’000 thousand cycles (depending on the material) were reapplied at the same fatigue load, and the crack length was checked again under the microscope. Then, if the crack had not propagated yet, fatigue cycling was conducted at a larger $\Delta K$, while in the case of crack propagation $\Delta K$ was set as in the precedent series by reducing the applied load. All these procedures were repeated until a crack propagation $\Delta a$ of at least 1 mm was achieved, corresponding to a relative crack length $a/W$ of 0.45 ($a_0$ before fatigue cracking being equal to 8 mm). Details of the pre-cracking parameters for the various composites, including the level of stress intensity factors and the number of cycles, are given in Appendix B.

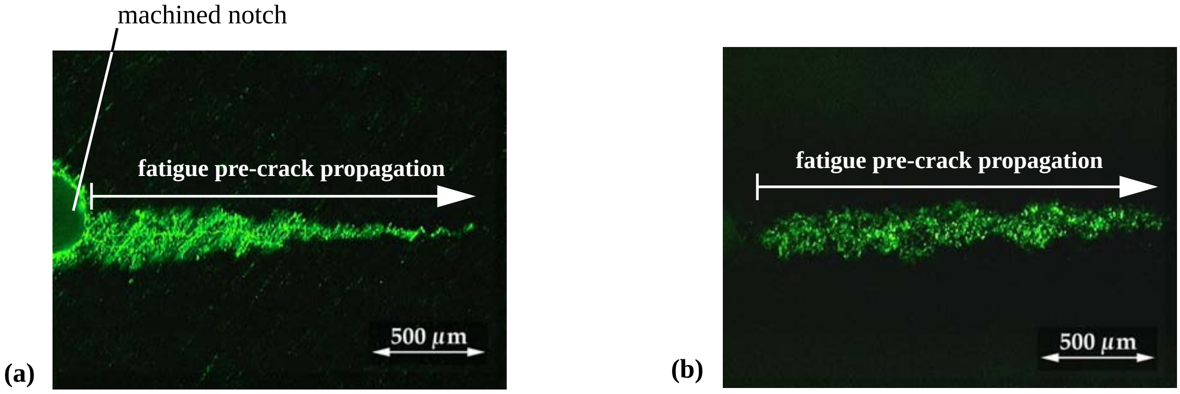

**Figure 3-5.** Detection and control of crack propagation after fatigue cycling. The fluorescent penetrant within the crack is revealed on the surface of the CT specimen under the microscope, using UV light. **(a)**: flat specimen; **(b)**: side-grooved specimen for which the resolution was sometimes lower due to the side-grooves.

In Al-Cu matrix composites, the procedure based on the fluorescent penetrant could not be performed because the fatigue precracks were shorter on the surface compared to the center of the specimen such that the observations on the surface were not representative of the average crack length. Therefore, the crack length after a series of cycles was estimated from the specimen elastic compliance, using the equipment (namely machine and extensometer) and procedures for *J*-integral fracture testing described in the next section.

### iii. Experimental set-up and testing procedure for *J*-*R* curves

#### TESTING PROCEDURE

*J*-integral fracture testing was conducted on a 100 kN screw-driven universal testing machine, manufactured by “Zwick” (Ulm, Germany). Loading clevis were machined in accordance to ASTM E-1737 specifications to provide rolling contact between the loading pins and the clevis holes; this was accomplished by machining the holes with small flats. The machine was manually controlled to allow selection of unloading and reloading points at any time during a test. A clip-on gauge extensometer, purchased from MTS (Minneapolis, USA), model 632.03F-30, was used to measure the load-line crack mouth opening displacement (CMOD). The extensometer had a 2 mm compressed gauge length and a resolution of 0.1 µm. Once the clip-gauge was inserted between the machined knife-edges of the CT specimen, its signal was allowed to stabilize for about 10 mn.

---

[1] For flat specimens, the crack propagation length $\Delta a$ on the surface of the specimen was slightly shorter than in the middle; for side-grooved specimens on the other hand, $\Delta a$ was 1.5 to 2 times longer at the sides (*i.e.* where measured) and this had to be taken into account to estimate the average crack length. To overcome this, side-grooves were machined after fatigue pre-cracking.

The tests were conducted under crosshead control at a velocity of 50 µm/mn (the lowest possible on the machine). Displacement, load, and time were acquired using a LabView™ program (National Instrument, Austin, Texas, USA) that we named “Zwick_acquire_v4.6”. Initial unloading/reloading cycles (at least three) were carried out in the elastic regime to estimate the initial crack length from the specimen compliance according to relations given hereafter.

The first unloading was done at a load slightly lower than the maximum load used during precracking, and subsequent unloading/reloading cycles in the growing load regime were made at regular load increments of 0.1 kN or 0.2 kN[1]. The minimum load during a cycle was set between 15 to 20% of the maximum load at unloading. When is was detected from the load-displacement curve that the load was about to reach its maximum, the cycles were carried out at closer intervals. This allowed us to gain a higher amount of points in a critical region of the *J-R* curves, in particular when the maximum load was rapidly followed by unstable fracture. In the case of stable crack propagation, only a few cycles were accomplished in the decreasing load region because this corresponds to the region of fully-plastic regime, where *J*-dominance is lost. The specimens were eventually fully broken in two for subsequent optical and SEM observations. In some instances, the specimens were not completely broken in order to verify the crack length by optical methods, as explained below.

### DATA ANALYSIS

Fracture data were analyzed after test completion. The data pairs ($V_i$, $P_i$) at the instant of unloading were manually determined from the plots, Figure 3-6. As also seen on the same figure, the unloading and reloading curves did not perfectly coincide, in that when the force at reloading attained its value at the moment of unloading the displacement was significantly larger. Hence, the data selected for computing the elastic compliance by linear regression were those lying on the same straight line during an unloading/reloading cycle. The compliance $C_i$ used for subsequent calculations was the average value obtained from the unloading and the reloading parts. All equations that follow can be found in ASTM E-1737.

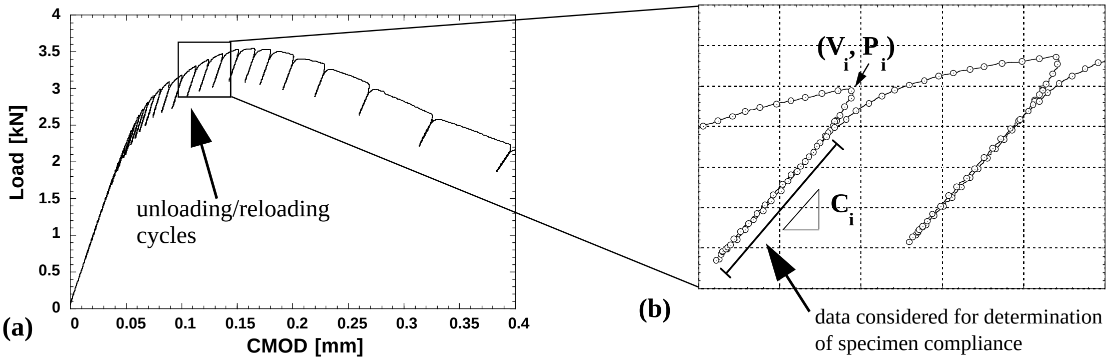

**Figure 3-6.** Method of crack length estimation from the compliance method. **(a)**: typical fracture curve; **(b)**: detail of an unloading/reloading cycle, with the data used for computing the specimen compliance $C_i$, and the increment ($V_i$, $P_i$) used for computing $J_i$.

---

1. In the earlier tests, loading cycles were done every 0.1 kN in order to obtain a sufficiently high number of data to construct the *J-R* curve. It was later found that performing cycles every 0.2 kN was sufficient.

At each increment, the crack length $a_\mathrm{i}$ was updated using:

$$a_\mathrm{i}/W = 1.000196 - 4.06319\cdot U_\mathrm{x} + 11.242\cdot U_\mathrm{x}^2 - 106.043\cdot U_\mathrm{x}^3 + 464.335\cdot U_\mathrm{x}^4 - 650.677\cdot U_\mathrm{x}^5 \qquad (3\text{-}5)$$

where $U_\mathrm{x}$ is given by:

$$U_\mathrm{x} = \left[\left(B_\mathrm{e}E'C_\mathrm{ci}\right)^{1/2} + 1\right]^{-1} \quad \text{where } B_\mathrm{e} \text{ is the net thickness: } B_\mathrm{e} = B - \left(B - B_N\right)^2 / B \qquad (3\text{-}6)$$

$C_\mathrm{ci}$ is the corrected compliance accounting for specimen rotation, $B_\mathrm{n}$ is the thickness between side-grooves, and $E'$ is the corrected Young's modulus for plane-strain conditions equal to $E/(1\text{-}\nu^2)$. The stress intensity factor $K_{(\mathrm{i})}$ used to compute the elastic part of $J$ was calculated by:

$$K_{(\mathrm{i})} = \left[\frac{P_\mathrm{i}}{\left(BB_\mathrm{N}W\right)^{1/2}}\right] f\left(a_\mathrm{i}/W\right) \qquad (3\text{-}7)$$

where $f(a_\mathrm{i}/W)$ is a geometrical factor for the CT specimen. The plastic part of $J$, $J_{\mathrm{pl(i)}}$ was calculated with the expression:

$$J_{\mathrm{pl(i)}} = \left[J_{\mathrm{pl(i\text{-}1)}} + \left(\frac{\eta_{(\mathrm{i}-1)}}{b_{(\mathrm{i}-1)}}\right)\frac{A_{\mathrm{pl(i)}} - A_{\mathrm{pl(i\text{-}1)}}}{B_\mathrm{N}}\right]\left[1 - \gamma_{(\mathrm{i}-1)}\frac{a_{(\mathrm{i})} - a_{(\mathrm{i}-1)}}{b_{(\mathrm{i}-1)}}\right] \quad \text{where} \quad b_{(\mathrm{i}-1)} = W - a_{(\mathrm{i}-1)} \qquad (3\text{-}8)$$

where $\eta_{(\mathrm{i}\text{-}1)} = 2.0 + 0.522\cdot b_{(\mathrm{i}\text{-}1)}/W$, $\gamma_{(\mathrm{i}\text{-}1)} = 1.0 + 0.76\cdot b_{(\mathrm{i}\text{-}1)}/W$, and $A_{\mathrm{pl(i)}}$ is the "plastic area" under the load-displacement curve:

$$A_{\mathrm{pl(i)}} = A_{\mathrm{pl(i\text{-}1)}} + \frac{\left[P_{(\mathrm{i})} + P_{(\mathrm{i}-1)}\right]\cdot\left[V_{\mathrm{pl(i)}} - V_{\mathrm{pl(i}-1)}\right]}{2} \qquad (3\text{-}9)$$

where $V_{\mathrm{pl(i)}}$ is the plastic part of the load-line displacement, $V_{\mathrm{pl(i)}} = V_\mathrm{i} - P_\mathrm{i}C_\mathrm{ci}$. The *J-R* curves were eventually constructed and their validation was verified according to ASTM-E1737.

### iv. A posteriori determination of Δ*a*

FULLY-CRACKED SPECIMENS

Since fluorescent penetrant was applied after the last series of fatigue cycling, it could be used to reveal the initial Δ*a* value prior to monotonic loading on the fracture surface of completely broken specimens.

As well-distinct crack growth mechanisms operate in fatigue and in monotonic fracture, fractography also provided a clear contrast under the light microscope or the binocular microscope. Fractographic observations were hence conducted in some cases to confirm the observations under UV light. The fatigue crack length was measured at regular intervals along the crack front (typically 10 to 20 measures), and the average value was compared to the initial crack length as measured by the compliance measurements.

PARTIALLY-CRACKED SPECIMENS

Crack propagation during monotonic loading as estimated from the elastic compliance was verified as follows: some fracture tests were arrested before final fracture, the sample was completely unloaded, and it was then fatigue loaded until final failure. Observation of the global crack front was undertaken under optical light microscopy and with binocular microscopy techniques, at low-magnification to measure the crack-length. For a closer look at the transition zone between the two crack growth modes, SEM was also used.

Crack marking was in particular made at three levels of fracture testing: the first type of marking was made early after the load-displacement curve indicates the end of the elastic regime, and SEM observations were useful in this regime to reveal the extent of the fracture process zone. The two other types of marking and subsequent observations were conducted slightly before, and soon after the maximum load respectively, because it was detected from the compliance measures that the crack propagation rate suddenly increased in this part of the load-displacement curves.

### 3.3.3 Observation of crack-tip plastic zones by photoelasticity

#### i. General description

Photoelastic coating was employed as a tool to identify and analyze the crack-tip strain fields on the surface of specimens during *J*-integral testing. In summary, photoelasticity is the property by some transparent isotropic solids to become birefringent when subjected to stress. Their index of refraction is then a function of the intensity of stresses applied and of their direction, allowing to visualize these quantities when illuminating with a polarized light. In photoelastic coating, a layer of birefringent material is bonded to the actual structure, and because the photoelastic coating is intimately and uniformely bonded to the surface of the specimen, the strains in the specimen surface are faithfully transmitted to the coating.

With a reflection polariscope, which was used here, the principle of double passage of light is employed, Figure 3-7a: the light source is initially polarized by passing through the polariscope; it then propagates through the photoelastic coating where it is reflected by the adhesive bonding, and the reflected light is finally observed through the analyzer. Under these conditions, the basic relationship relating the strains in the photoelastic coating with its strain-optical coefficient $k$ is:

$$\varepsilon_1 - \varepsilon_2 = \gamma_{\max} = N_{\mathrm{n}}\lambda/2kt = N_{\mathrm{n}} f \qquad \text{where} \qquad f = \lambda/2kt \tag{3-10}$$

where $\varepsilon_1$ and $\varepsilon_2$ are the principal strains in the coating, $N_{\mathrm{n}}$ is the normal-incidence fringe order, $\lambda$ is the wavelength of yellow light (575 nm), $t$ is the thickness of the coating, the factor 2 is introduced to take into account the fact that the light traverses the coating twice, and $f$ is the fringe value of the coating. The fringe value is equivalent to the coating sensitivity and represents the maximum shear strain to produce one fringe.

Hence, the photoelastic effect is caused by alternately constructive and destructive interferences between light rays that have undergone a relative retardation in the stressed photoelastic coating. With white light, the photoelastic fringe pattern appears as a series of successive and contiguous different-colored bands in which each represents a different degree of birefringence corresponding to the underlying strain in the test part. The maximum shear strain in the test part can be obtained by simply recognizing the fringe order in the coating and multiplying by the fringe value of the plastic.

### ii. Apparatus and sample preparation

A “031-Reflection polariscope Model”, purchased from “Measurements Group, Inc.” (Rayleigh, N.C., USA) was employed. It is a dark-field instrument, which means that the coating appears black when no stress is applied on the coated test object. A photograph of the experimental set-up is given in Figure 3-7b. The polariscope equipment consists of the light source, polarizer and analyzer filters, a 35 mm camera (Canon Inc., Tokyo, Japan) and a mounting tripod. As crack-tips are regions of high strain gradient, the fringes are closely spaced, with the highest-order fringes immediately adjacent to the tip, such that accurate measurement of the fringe order required magnification provided by a telemicroscope (Measurements Group, Model 137). The telemicroscope was supplied with a “Model 038” camera adapter which allowed attachement of the camera and acquisition of the magnified images through the telemicroscope. Finally, a 28-105 mm “Nikon” zoom lens, (model AF Zoom-Nikkor, 28-105 mm, F/3.5-4.5DIF, Nikon Co., Tokyo, Japan) was fixed in front of the analyzer filter, and permitted further magnification of the region of interest. Focusing was accomplished while viewing through the camera.

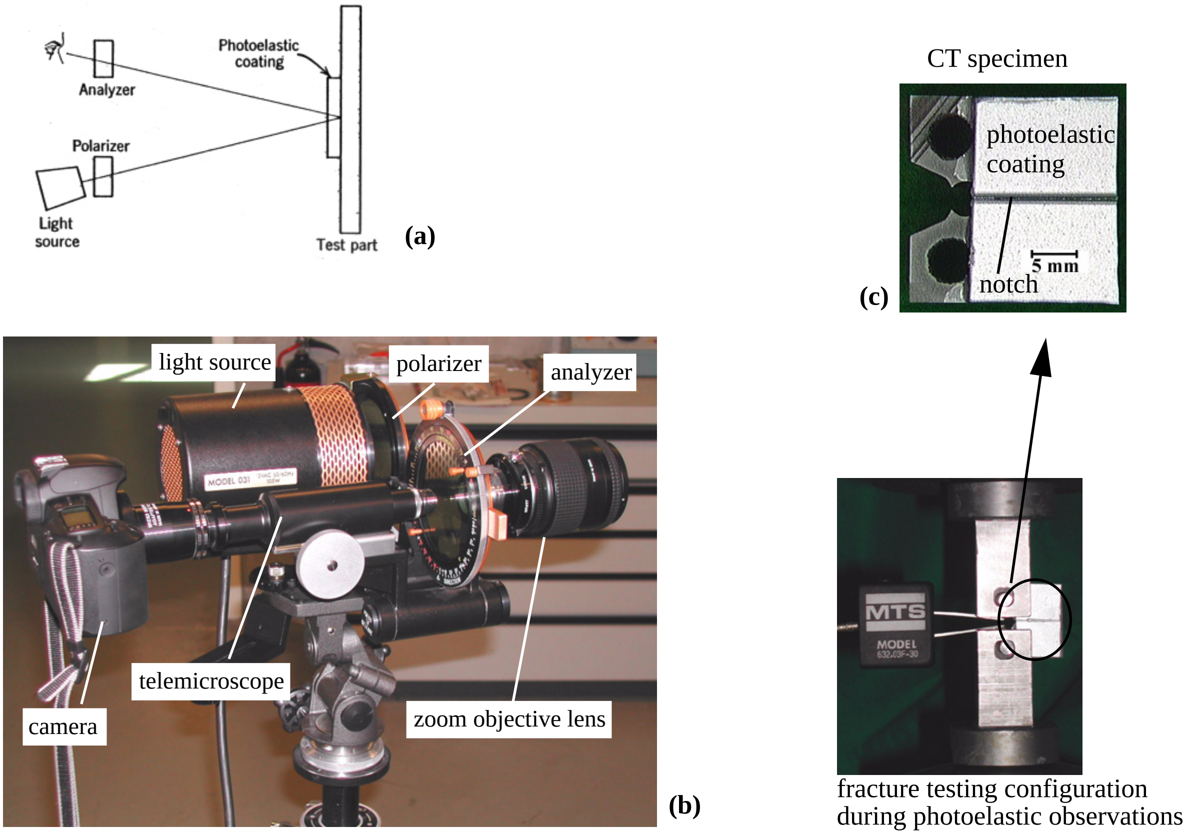
Photoelastic coating
Analyzer
Polarizer
Light source
Test part
(a)
CT specimen
photoelastic coating
5 mm
notch
(c)
light source
polarizer
analyzer
telemicroscope
camera
zoom objective lens
(b)
MTS
MODEL
fracture testing configuration during photoelastic observations

**Figure 3-7.** Photoelasticity observations of the crack-tip strain fields. **(a)**: principle of the measure; **(b)**: experimental set-up; **(c)**: detail of a CT specimen coated with a photoelastic coating.

The photoelastic coatings used, purchased from Measurements Group, were of the types “PS-1P” and “PS-1C”. The characteristics of the coatings are given in Table 3-3. The thicker coating (PS-1P) was the most sensitive and exhibited a higher resolution in strain. The thinner sheet had a lower resolution, but on the other hand, had the advantage of allowing observation of higher strains. The sheets were cut to match the geometry of the region situated in front of the crack tip. The reflective adhesive that was employed to bond the coatings on the fracture specimens was a two-component type consisting of resin “PC-6” and hardener “PCH-6”, mixed in the proper proportions indicated by the supplier. About 0.5 gr. were needed per specimen. Prior to bonding, the surface of the specimen was prepared by degreasing, abrading, conditioning and neutralizing. A thin layer of adhesive was applied on the clean specimen surface, the coating sheet was positionned using moderate finger pressure, excess adhesive was squeezed out, and the adhesive was finally let to harden overnight. For the majority of observations a final operation was applied that consisted of notching the middle of the coating film through its whole thickness, as indicated in Figure 3-7c. This was necessary in order to avoid loading of the photoelastic coating film itself across the open crack, as this resulted in artefacts in the photoelastic pattern. Observations conducted without this final cut were however more precise in revealing the position of the crack-tip and the strains on the crack plane.

**Table 3-3.** Characteristics of the photoelastic coatings.

| Coating type | *k* factor | thickness [mm] | *f* [-] | strain resolution | max. observable strain (4*N*) |
|---|---|---|---|---|---|
| PS - 1P | 0.15 | 0.508 ± 0.005 | $3.79 \cdot 10^{-3}$ | ≈ 0.05 % | ≈ 1.6 % |
| PS - 1C | 0.15 | 1.118 ± 0.005 | $1.72 \cdot 10^{-3}$ | ≈ 0.025 % | ≈ 0.7 % |

#### iii. Observation method

Observations of the photoelastic patterns were conducted in the full-field interpretation mode, *i.e* by identifying the fringe orders with different colors. In this mode, the fringe orders observed are proportional to the difference between the principal strains in the surface of the coating, *i.e.* to twice the maximum shear strain $\gamma_{\max}$ at any point, eq.(3-10).

The images of the photoelastic pattern were taken in parallel with *J*-integral fracture testing, using Kodak™ ASA 200 color negative films. In order to correlate the crack-tip strain fields with the value of the *J*-integral, the photographs were taken at the instant of updating the values of crack length and *J*, namely at the higher point of a loading cycle. Images were acquired along a whole fracture test if possible. For this purpose, the test was temporarily interrupted to allow the observations, which were performed by keeping the ambient light level as low as possible. Exposure times of 20 to 30 seconds were necessary to yield optimized quality of the images. In general, two exposures were taken, at low and high magnification of the zoom lens.

Identification of fringe orders and corresponding shear strains was made using the isochromatic fringe characteristics given by the supplier, and the fringe value of the coating *f*. With incident white light, identification of fringes until order 4 was possible, corresponding to observable values of $\gamma$ given in Table 3-3.

### 3.3.4 Chevron-notched fracture testing

Chevron-notch testing according to ASTM-E1304 was mainly used to measure the fracture toughness of Al-Cu matrix composites. In addition, it was employed in some occasions for pure Al matrix composites, although preliminary experiments indicated that these composites are too ductile to satisfy ASTM requirements related to LEFM testing. The principles of fracture toughness determination using chevron-notch testing are given in Section 2.3.1.

#### i. Specimen Geometry

Chevron-notched bar specimens were of square cross-section, with a thickness *B* of 18 mm and a length $W^1$of 26.1 mm. The specimens were extracted with the plane of the chevron-notch machined perpendicular to the composite ingot axis, such that the chosen dimensions optimize the available amount of material from composite castings. If a micro-vein was identified in the initial square bar, the chevron was machined such that the vein did not intercept the crack path or alternatively such that this interception would occur in the final part of the crack propagation (in the deacrasing part of the load-displacement curve ). All other dimensions were determined by the ratio $W/B = 1.45$, as specified in the standard, including the distance to the chevron tip $a_o$, the notch on centerline, and the slot angle $\phi$. A general view of a short bar specimen is given in Figure 2-6, and the dimensions used here are indicated in Figure 3-8c.

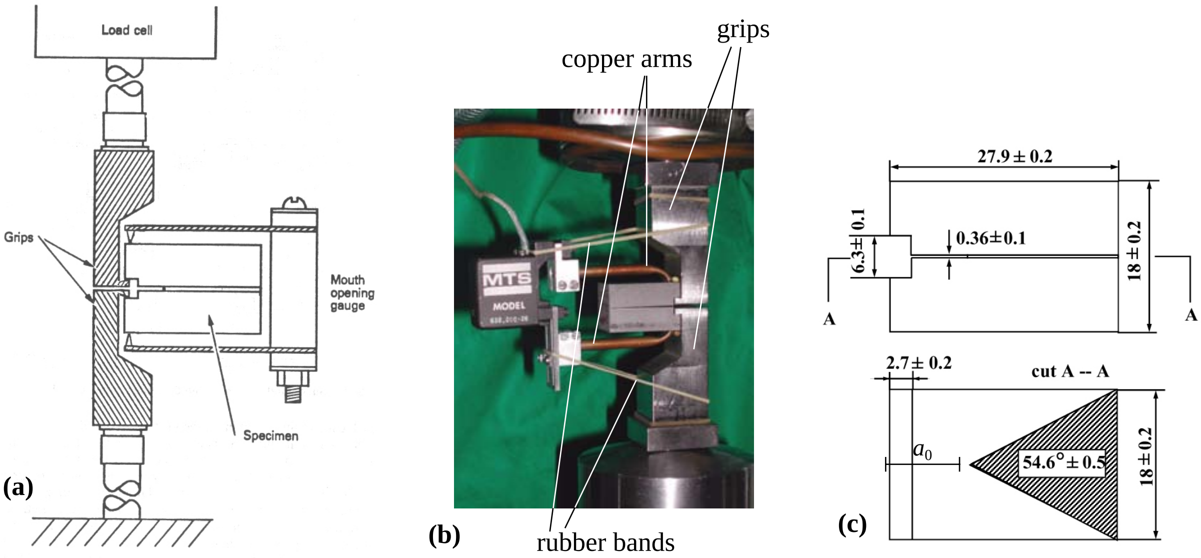

**Figure 3-8.** Chevron-notch fracture testing. **(a)**: Test configuration as recommended in ASTM - E1304; **(b)**: picture of the experimental set-up; **(c)** details of specimen dimensions (in mm).

### ii. Experimental Set-up and Testing Procedure

#### TESTING PROCEDURE

Chevron testing was conducted on the same “Zwick” screw-driven testing machine as for $J$-Integral fracture testing; it was manually controlled and the data were acquired with the same “LabView” software. A picture of the experimental set-up is given in Figure 3-8b. The load grips were designed according to the standard specifications, and machined in a high strength maraging steel. The displacement was measured with a “632.20c-20 MTS“ extensometer, at which were fixed “in-house” produced copper arms which allowed measurement of the CMOD on the outside faces of the specimen. The displacement resolution of the extensometer was in the range of 0.1 µm. Wooden shims were glued on both faces of the chevron bar, on its extremities and along the width, in a manner that permitted the gauge arms to be well positionned against them. In addition, the shims ensured that the displacement was measured at the load line.

The specimens were installed in the testing machine according to the following steps: (i) the grips were brought sufficiently close such that they fit into the grip slot in the specimen face; (ii) the spacing between the grips was carefully increased until an opening load just sufficient to hold the specimen in place was reached; (iii) the alignement of the specimen with respect to the grips was checked as well as the alignement of the grips with respect to each other; and (iv) the extensometer was placed with its

---

1. $W$ is defined as the distance from the back of the specimen to the load line. Hence, the value indicated on Figure 3-8c is not $W$ but the total length of the specimen $W$ + x where $x$ is the distance between the specimen front and the load line as specified in the standard.

gauge arms set against the glued shims. In order to equilibrate the spring forces between the gauge arms and the specimen, rubber bands were attached between the extensometer and the loading grips such that once in place, the extensometer did not move; this was verified by the output signal.

The tests were conducted under displacement control, at a velocity of 250 µm/mn, and involved recording of the load versus mouth opening displacement. Two unloading-reloading cycles were conducted slightly before and after the maximum load, respectively, and were subsequently used as a mean to: (i) determine the location of the crack (based on the elastic compliance), (ii) determine the load used to calculate the plane-strain fracture toughness, and (iii) provide validity checks of the test, as described in the next paragraph. The minimum load during a cycle was approximately 10% of the load at the start of an unloading-reloading cycle. The tests were either completed until final failure for subsequent SEM fractographic analysis, or arrested for observation of the micromechanisms of fracture in the process zone and along the fracture path according to a technique described below (Section 3.4.1).

For all the composites tested and in each heat-treatment condition, one half of each fully broken specimen was kept after fracture in a refrigerator until its Vickers macrohardness was measured using the apparatus and conditions described in Section 3.3.1. These measures served as a control for the efficiency of the heat treatments.

DATA ANALYSIS

The recorded load-displacement curves were analyzed as specified in the standard. The main points of data analysis of a typical curve (Figure 3-9) comprises the following steps:

(i) the two effective unloading lines from the unloading-reloading cycles are drawn (the effective unloading line is defined as having its origin at the high point where the displacement reverses direction, and joining the low points on the reloading line where the load is one half that at the high point);

(ii) the horizontal average load line between the two effective unloading lines is drawn in a manner that the shaded areas in Figure 3-9 are approximately equal, the values $\Delta x$ (the distance between the effective unloading lines along the average load line) and $\Delta x_0$ (the distance between the effective unloading lines along the zero load line) are measured, and the plasticity parameter $p$ of the test is calculated:

$$p = \frac{\Delta x_0}{\Delta x} \tag{3-11}$$

(iii) the initial elastic loading angle $\theta_o$ is measured, from which the critical angle $\theta_c$ is calculated using $\theta_c = \tan^{-1}(r_c \tan \theta_o)$, where $r_c$ is the critical slope ratio (corresponding to the unloading slope ratio at the critical crack length), equal to 0.62 for the specimen configuration used;

(iv) the critical slope ratio line (with slope $\theta_c$) is drawn from the point of intersection of the two effective unloading lines and its intersection with the load-displacement curve is noted; this point is called $P_c$ and represents the load required to advance the crack when it is at the critical crack length;

(v) finally, the maximum load $P_m$ during a test is noted and the ratio $P_m/P_c$ is calculated.

The conditional value, $K_{Qv}$, of the fracture toughness is calculated as follows:

$$K_{Qv} = \frac{Y_m^* P_c}{B\sqrt{W}} \tag{3-12}$$

where $Y^*_\mathrm{m}$ is the minimum stress intensity factor coefficient, equal to 25.11 for the present specimen geometry. This value is validated as the plane-strain (chevron-notch) fracture toughness $K_\mathrm{Iv}$ if the following conditions are met:

$$B \geq 1.25\left(K_\mathrm{Qv}/\sigma_\mathrm{YS}\right)^2 \tag{3-13}$$

$$P_\mathrm{m} \leq 1.1 P_\mathrm{c} \tag{3-14}$$

$$-0.05 \leq p \leq 0.10 \tag{3-15}$$

The first criterion is the minimum specimen dimension as required in ASTM-E1304 to ensure plane-strain conditions. It is less stringent than the criteria given by the plane-strain fracture toughness according to ASTM-E399 [93] because the chevron-notched geometry ensures higher constraint within the specimen. The second criterion limits the degree of plastic tearing and imposes that the load at the critical crack length be close to the maximum load $P_\mathrm{m}$ (in the ideal linear-elastic case of brittle materials exhibiting flat *R*-curves, $P_\mathrm{c}$ would exactly coincide with $P_\mathrm{m}$). The upper value of the last criterion places a limit on plasticity effects: if $p$ is larger than 0.1, it indicates excessive plasticity and violation of LEFM assumptions, while negative values of $p$ are indicative of the presence of residual stresses in the specimen.

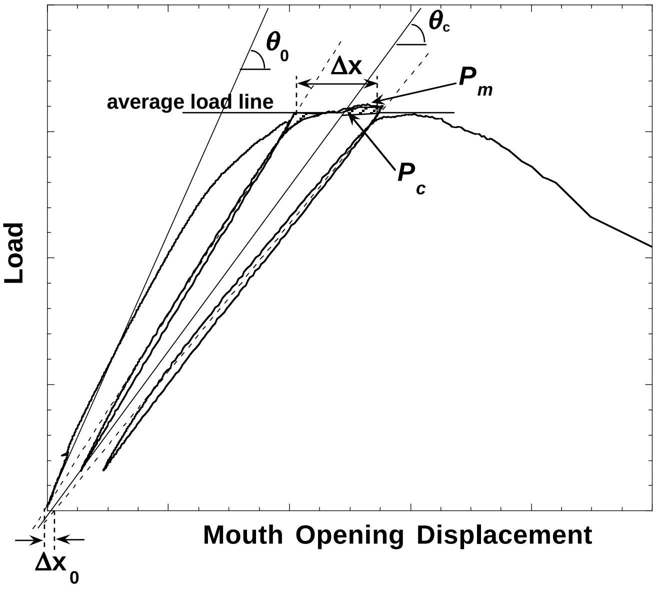

**Figure 3-9.** Schematic load-displacement curve of a chevron-notch test, with unloading/reloading cycles, data reduction constructions, and definition of terms.

### 3.3.5 Tensile testing

Tensile test of the Al-Cu matix composites were run on the “Instron” servo-hydraulic testing machine described earlier. Such experiments were conducted for general assessment of tensile properties of the alloyed matrix composites (Young’s modulus *E*, yield strength $\sigma_{0.2}$, ultimate tensile strength *UTS*). For the general tensile characteristics of pure Al matrix composites, the data from the work of Kouzeli [89] that was conducted in our laboratory are used.

The dogbone specimen geometry was selected according to ASTM standard B557M, Figure 3-10. Specimens were machined in the longitudinal direction from the as-cast composite billets. The surface finish quality obtained in these materials by EDM was sometimes rather poor due to their low conductivity and dual-phase microstructures. Hence, to erase all visible irregularities, the specimen surfaces were ground prior to testing with fine SiC polishing papers down to F-600 grit sizes. Before testing, the width and thickness of the samples were controlled with a caliper-gauge at three different positions along the sample gauge length.

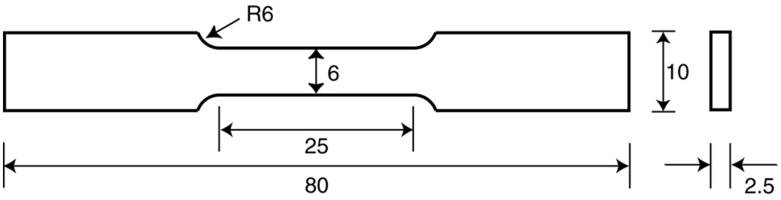

**Figure 3-10.** Tensile specimen geometry, dimensions in mm.

The alignment of the loading system was verified before testing, with an Instron alignement fixture allowing to align the upper and lower hydraulic grips. The alignement fixture consists of an 8 strain-gauges steel specimen, a computer interface, and the “Instron Align-Pro“ software measuring the strain from each gauge and comparing each other. The longitudinal strain was measured over a 10 mm gauge length using a clip-on “MTS” extensometer (model 632.13C-20) featuring a displacement resolution of 0.1 µm. The tests were operated in piston displacement control of the machine, at a speed of 1 µm/sec (corresponding to a nominal strain rate of $10^{-4}$/sec) until final failure. To determine precisely Young’s modulus, a series of unloading-reloading cycles after a low amount of plastic strain was implemented during the standard tensile test, similarly to experiments conducted on pure Al matrix composites [89]. As explained by Prangnell *et al.* [242], the principle behind this technique is to minimize microplasticity phenomena by reducing the dislocation motion by local work-hardening. To this aim, the measurement of the composite stiffness is made subsequent to prestraining and low stress fatigue cycling. 8 cycles were made with each cycle lasting 20 sec, and the magnitude of stress cycling was chosen as a function of UTS measured in preliminary tests conducted without cycling: for angular reinforced composites, the first unload cycle was started at a stress of 100 MPa and the series of cycles was performed between 30% and 70% of this value (*i.e.* between 30 and 100 MPa), while for polygonal reinforced composites, the initial unloading stress was 150 MPa and the next cycles were accordingly performed between 45 and 105 MPa.

The raw data from tensile tests (including the unloading-reloading cycles) were analyzed automatically, using a LabView program written in the laboratory (called “Ecycler”). This routine program facilitated greatly the determination of Young’s modulus as measured during the cycles, by recognizing reversing of the loading direction, and separating and calculating the modulus of each data subset.

# 3.4. OBSERVATION AND QUANTIFICATION OF THE MICROMECHANISMS OF FRACTURE

## *3.4.1 Arrested crack technique*

Besides the advantage that chevron-notch testing does not necessitate pre-cracking and is somewhat less stringent with regard to specimen dimensions than ASTM E-399, an interesting feature is that it allows to achieve stable or semi-stable crack propagation even in materials exhibiting a relatively flat *R*-curve. This was used to arrest some tests prior to complete fracture and subsequently introduce a rapid adhesive bond (type Cyanolit™ produced by the company “3M”) into the crack while the specimen remained under load to preserve the crack opening. While chevron testing was essentially used to measure the toughness of Al-Cu matrix composites, chevron-notch specimens were also machined from pure Al matrix composites, tested and arrested before fracture. Although the fracture data clearly violated LEFM assumptions, the technique nevertheless allowed us to gain clear observations of the crack propagation path.

### i. Sample preparation for optical microscope observations

Once the adhesive was introduced into the crack, it was dried for a few hours. Although a rapid adhesive was used –which hardens in a few minutes in normal air condition–, this longer time was needed because the glue within the crack was not in direct contact with the atmosphere. A simple method to ensure complete hardening of the glue was to keep monitoring the load once the test had been arrested. As the glue dries, the load increases slightly because it shrinks and bridges the crack faces. Once the load had stabilized it was considered that hardening was terminated.

The glued specimens were then cut in the center plane with the high-speed diamond saw in the direction of crack propagation, perpendicular to the crack plane, as depicted in Figure 3-11. The degree of crack propagation was hence revealed and its surrounding region subsequently cut, mounted, and polished according to the metallographic procedure described in 3.2.1. Observations along the crack propagation path and in front of the physical crack-tip (in the process zone) were carried out by optical light microscopy using both bright field and Differential Interferential Contrast (DIC) conditions.

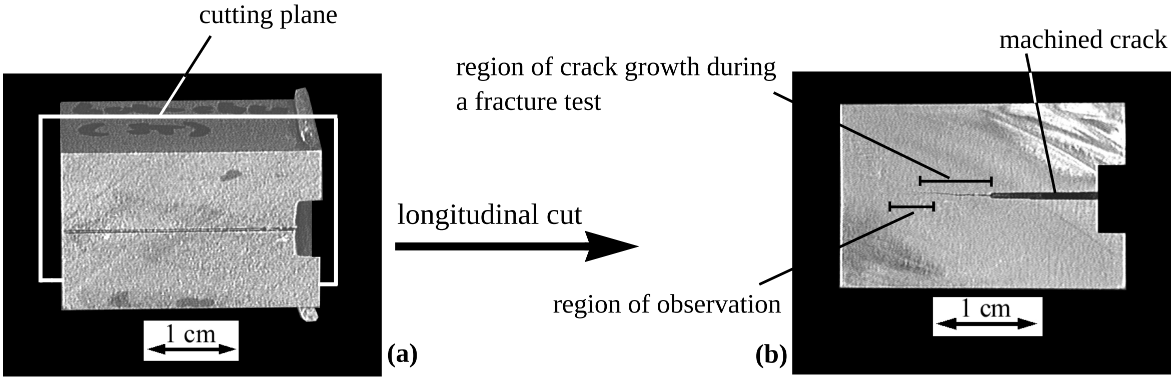

**Figure 3-11.** Sample preparation for observation of fracture mechanisms. The tested, glued chevron sample **(a)** is longitudinally cut through its center plane. The degree of crack extension is revealed on the cut halves **(b)** and the region of interest is further cut and mounted for observation. The observed region includes the end of the physical crack tip and the process zone**.**

### ii. Quantification of fracture phenomena

An advantage of the technique employed to identify the micromechanisms of fracture is that both sides of the crack are visualized, such that there is no ambiguity distinguishing particle fracture and interfacial debonding. For the same reason, it is obvious on the images whether a ductile cavity was nucleated by a broken particle or directly within the matrix. It was hence possible to quantify the dominant mode of fracture within each composite. In order to gain a representative statistical sampling, a sufficiently high number of digital pictures were taken along the crack path at various magnifications. For-instance, typically 15 to 20 pictures were acquired at the 1000x magnification for 10 µm particle reinforced composites. Then, the total number of broken particles $n_j$ was counted manually on every image *j*, as well as the actual crack length. Crack deflection was taken into account by precisely following the crack path and measuring the length $l_i$ of individual segments *i* of the crack, where $l_i$ is expressed in pixels, as shown in Figure 3-12. The fraction of the crack path $f_b$ occupied by broken particles was eventually defined through Eq. (3-16):

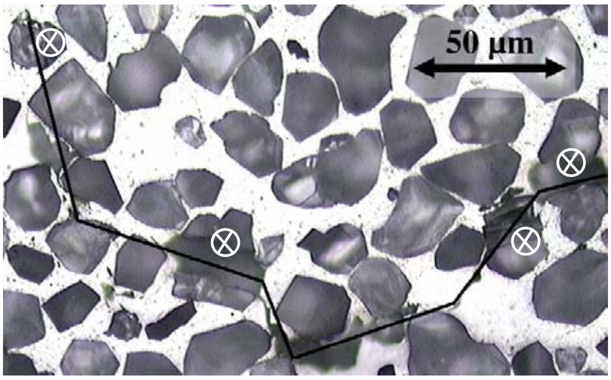

⊗ : broken particle $n_j = 4$

/ : crack segment *i* of length $l_i$

$$f_b = \frac{D \cdot \sum_j n_j}{L_X \sum_i l_i} = \frac{D \cdot N}{L_X \cdot L} \qquad (3\text{-}16)$$

**Figure 3-12.** Example of particle counting and measure of actual crack length along the crack path.

where *D* is the average measured particle size in µm, *N* is the total number of counted broken particles, $L_X$ is the pixel size in µm/pixel at magnification *X* and at the resolution of the numerical images, and *L* is the total crack length analyzed, in pixels.

## 3.4.2 Fractography

Uncoated fracture surfaces were examined by SEM, using the Philips XL-30 electron microscope described earlier and under similar working conditions, namely an acceleration voltage of 5 to 15 kV and a working distance of 10 mm. In addition to conventional observation with the secondary electron (SE) detector, the fracture surfaces were visualized with the backscattered electron (BSE) detector to identify secondary intermetallic phases (in this mode, adjustement of optimized observation conditions had to be made at slow scan rates because no contrast was produced at the video scan rate).

Additional fractography was performed under a “Olympus SZX12” stereomicroscope (Olympus Optical Co., Tokyo, Japan), as this provided a clear contrast between the fatigue crack propagation mode and the ductile fracture mode. It was hence used to visualize at the macroscopic level the pre-crack region and the degree of crack propagation during *J*-integral fracture tests that were arrested prior to complete specimen failure.

### 3.4.3 Three-dimensionnal reconstruction of fracture surface topography

Electron microscopy provides a projection of the three-dimensional surface structure onto a two-dimensional image plane, which in turn results in the loss of the depth information of the viewed specimen. In order to overcome this limitation and to obtain quantitative information regarding the surface profile of the broken composites at the microstructural scale, the “MeX” imaging software (Alicona Imaging GmbH, Grambach, Austria) allowing three-dimensional reconstructions of the fracture surfaces from SEM pictures was employed. In short, this tool creates a so-called anaglyph image from two SEM images of the same object taken under two slightly different angles by eucentric tilting. Then, the surface geometry of the examined specimen is digitally reconstructed by generating a “Digital Elevation Map” (DEM) that forms the basis for subsequent analysis of the surface profile. The resolution of the system is defined by that of the SEM.

#### i. Image acquisition

The final quality of DEMs is greatly dependent on the initial SEM images, and this stage therefore required special attention. The first parameter is to minimize charging at the dimple walls, because this would result in saturation of the gray-scale level and would lead to abberations in the final DEM. The acceleration voltage was hence kept between 1 and 5 kV and the working distance was set at 10 mm. The most important point is then to acquire the images with eucentric tilting: as depicted in Figure 3-13a, this means that a static center point has to be defined that remains unchanged after tilting. The tilt axis of the microscope does not allow to have a static center point; namely the center point in the image migrates during tilting (Figure 3-13b). Hence, the following procedures was applied:

(i) the region of interest for the final DEM was positioned, and the first (left) image captured and exported in high resolution mode in a common file format; the center point of the image –which was chosen to be a significant microstructural detail– was marked;

(ii) the specimen was tilted at an angle $\alpha$ (which was typically between 2 and 6° depending on the magnification, larger angles being used at lower magnification) and the relative angle was noted;

(iii) during tilting, the significant microstructural detail chosen previously almost vanished at the image border. Hence the position of the specimen was adjusted such that the significant detail was again in the center point of the image (eucentric tilting), and the second image (right) was then captured and exported. The working distance was not changed as compared to the first image;

(v) the images were then imported into the software; since the tilt axis was horizontal, the images were rotated 90 degrees clockwise before being imported into MeX.

A typical example of a pair of SEM pictures captured with eucentric tilting is given in Figure 3-13b and c. As explained above, in this case the position of the specimen was readjusted in the y-direction after tilting.

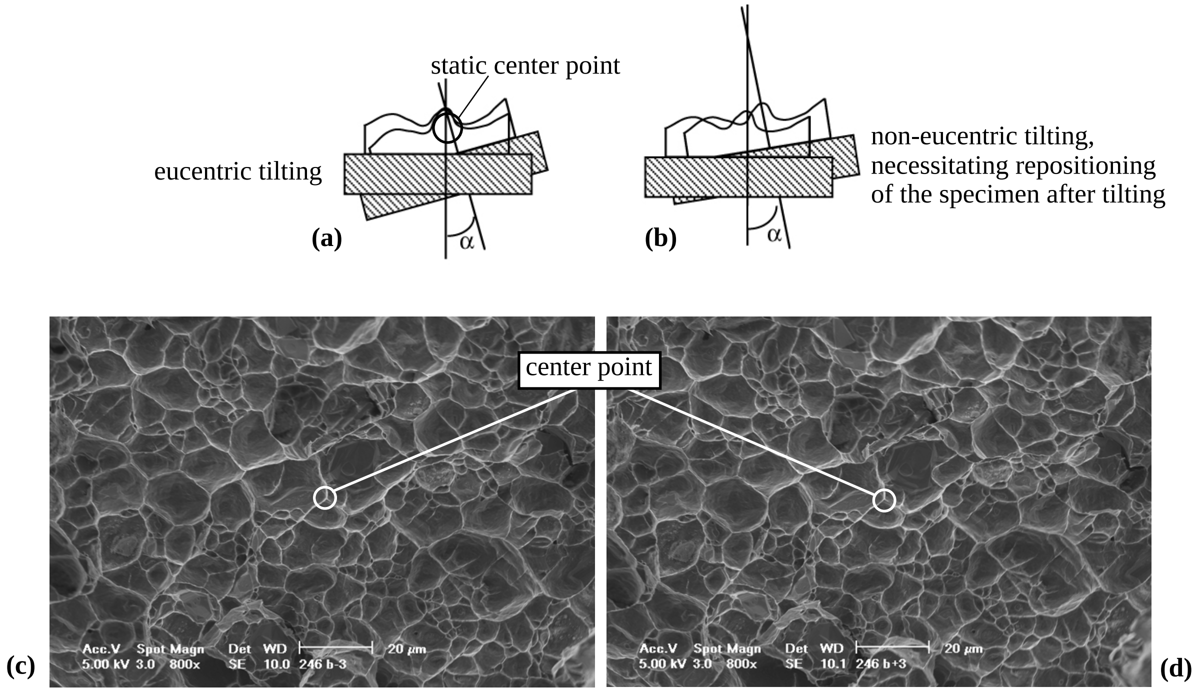
static center point
eucentric tilting
non-eucentric tilting,
necessitating repositioning
of the specimen after tilting
(a)
(b)
α
α
center point
(c)
(d)
Acc.V Spot Magn Det WD 20 μm
5.00 kV 3.0 800x SE 10.0 246 b-3
Acc.V Spot Magn Det WD 20 μm
5.00 kV 3.0 800x SE 10.1 246 b+3

**Figure 3-13.** Stereoscopic reconstructions of a fracture surface under the SEM. **(a)** and **(b)**: principle of eucentric tilting showing the static center point; **(c)** and **(d)**: a typical pair of SEM pictures used for reconstruction**,** captured at a relative angle of 6.2° (horizontal tilt), with the static center point corresponding to a significant microstructural feature.

### ii. Stereographic reconstruction

The reconstruction software overlays and colors the imported images to form an anaglyph image when viewed with the provided red-blue glass. This gives the impression of a real three-dimensional view. The input required for these reconstructions are the working distance, the pixel size (which depends on the magnification and on the image resolution) and the relative tilt angle.

### iii. Digital elevation models (DEMs) of the fracture surfaces

The last step in creating the final DEM simply consists for the user to choose the region of interest to be reconstructed.The software is run on a personal computer and 3 to 15 minutes are necessary to reconstruct a stereopair. More details on image processing and algorithms used to reconstruct the surface topography are exposed in the references [211, 212].

From the reconstructed DEMs, quantitative features of the fracture surface profiles were determined using the various possibilities offered by the software, such as the determination of rougness profiles along a defined line, accurate measurements of local height differences, or mapping of the depth levels. More specifically, in our case, characteristic dimple heights *h* were measured on all pure Al matrix composites. At least 3 DEMs at various magnifications were generated, from which individual dimple heights were determined. A minimum of 20 dimples were measured in total to obtain a statistical representative sampling, from which the average cavity size of the fractured composites was calculated.

# CHAPTER 4

# RESULTS

## 4.1. MICROSTRUCTURAL CHARACTERIZATION

### 4.1.1 *Powder characteristics*

**i. Average particle size**

The powder distributions as measured by centrifugal sedimentation, given in terms of the medium particle size (value at 50% of the cumulative distribution), are presented in Table 4-1 and compared with the supplier designations. One notices some deviations between the nominal and the measured values. In particular, powder sizes that are nominally equivalent according to the supplier specifications (for instance when comparing angular $Al_2O_3$ with angular $B_4C$ of the same designation) may actually differ, and the powders feature relatively wide distributions, especially for smaller particle sizes. We also note

**Table 4-1.** Powder size distribution as given by the suppliers and as measured by centrifugal sedimentation. The average particle size is given in terms of the medium value (value at 50% of the cumulative distribution).

| Particle type | Supplier designation | Nominal particle size [µm] | Measured particle size [µm] | Size used for composite designation |
|---|---|---|---|---|
| Angular $Al_2O_3$ | F220 | 58.0 [a] | 59 ± 10 | 60 |
| | F320 | 29.2 [a] | 33.3 ± 8 | 35 |
| | F400 | 17.3 [a] | 19.5 ± 7 | 20 |
| | F600 | 9.3 [a] | 9.9 ± 5 | 10 |
| | F1000 | 4.5 [a] | 3.7 ± 1.5 | 5 |
| Polygonal $Al_2O_3$ | AA 18 | 20.0 [b] | 25.1 ± 7 | 25 |
| | AA 10 | 10.5 [b] | 15.0 ± 4 | 15 |
| | AA 5 | 5.0 [b] | 5.8 ± 2 | 5 |
| Angular $B_4C$ | F220 | 58.0 [a] | 62 ± 10 | 60 |
| | F320 | 29.2 [a] | 34.4 ± 9 | 35 |
| | F400 | 17.3 [a] | 21.3 ± 7 | 20 |
| | F600 | 9.3 [a] | 8.0 ± 2 | 10 |
| | F1000 | 4.5 [a] | 5.6 ± 1.5 | 5 |

a. According to FEPA (Federation of European Producers of Abrasives), standard 42-1984 R 1993.
b. Manufacturer specifications.

significant deviations for the nominal 10 and 18 µm polygonal $Al_2O_3$ powders, for which we measured average sizes of 15 and 25 µm, respectively. For consistency, the powders –and in turn the composites– are hereafter designated according to the measured values rounded to the closest multiple of 5. For all computations involving the particle size, the measured values will be used in what follows.

### ii. Particle morphology

Typical SEM observations of angular alumina powders are shown in Figure 4-1a. Surface defects are often observed, as shown at larger magnification (Figure 4-1b). Such crack-like defects were detected in all powders, including the finest average size powders of 5 µm; however their frequency of appearance increases with increasing average particle size.

In comparison, boron carbide powders do not exhibit corners as sharp as angular alumina poders, and are characterized by a smaller aspect ratio, Figure 4-1c (these remarks remain qualitative and are not based on a detailed image analysis study). Defects are also observed, but are not of the same type as the sharp cracks found in angular alumina. Rather, they take the form of small pores found in the center of the particles, Figure 4-1d.

Polygonal alumina powders are clearly characterized by a more regular geometry, by rounded corners and by the absence of visible surface defects, Figures 4-1e and f. As mentioned in Chapter 3, a population of larger-than-average particles (about 50 to 100 µm) is observed in the 25 µm powder; this is not present in the two other powders. When observed under the optical microscope (Figure 4-2a, before sieving), these larger particles appear opaque and are hence clearly distinct from the transparent 25 µm particles. A polished section of a composite produced with this powder (Figure 4-2b) indicates that they are actually agglomerates of much smaller particles. As mentioned, these agglomerates were eliminated prior to preform preparation by sieving, Figure 4-2c.

## *4.1.2 Metallography*

Optical micrographs of pure Al matrix composites are presented in Figure 4-3, and typical characteristics (volume fraction, measured interparticulate distance) of all composites are summarized in Table 4-2. The volume fraction is approximated from the tapped density of the preform, and is verified in some cases by densitometry measurements.

Overall, the composite microstructures are characterized by a homogeneous distribution of reinforcements, and a limited presence of microstructural defects in some of them, as exposed below. The volume fraction achieved varies between 0.4 and 0.6 and is determined by the packing characteristics of the reinforcing powders.

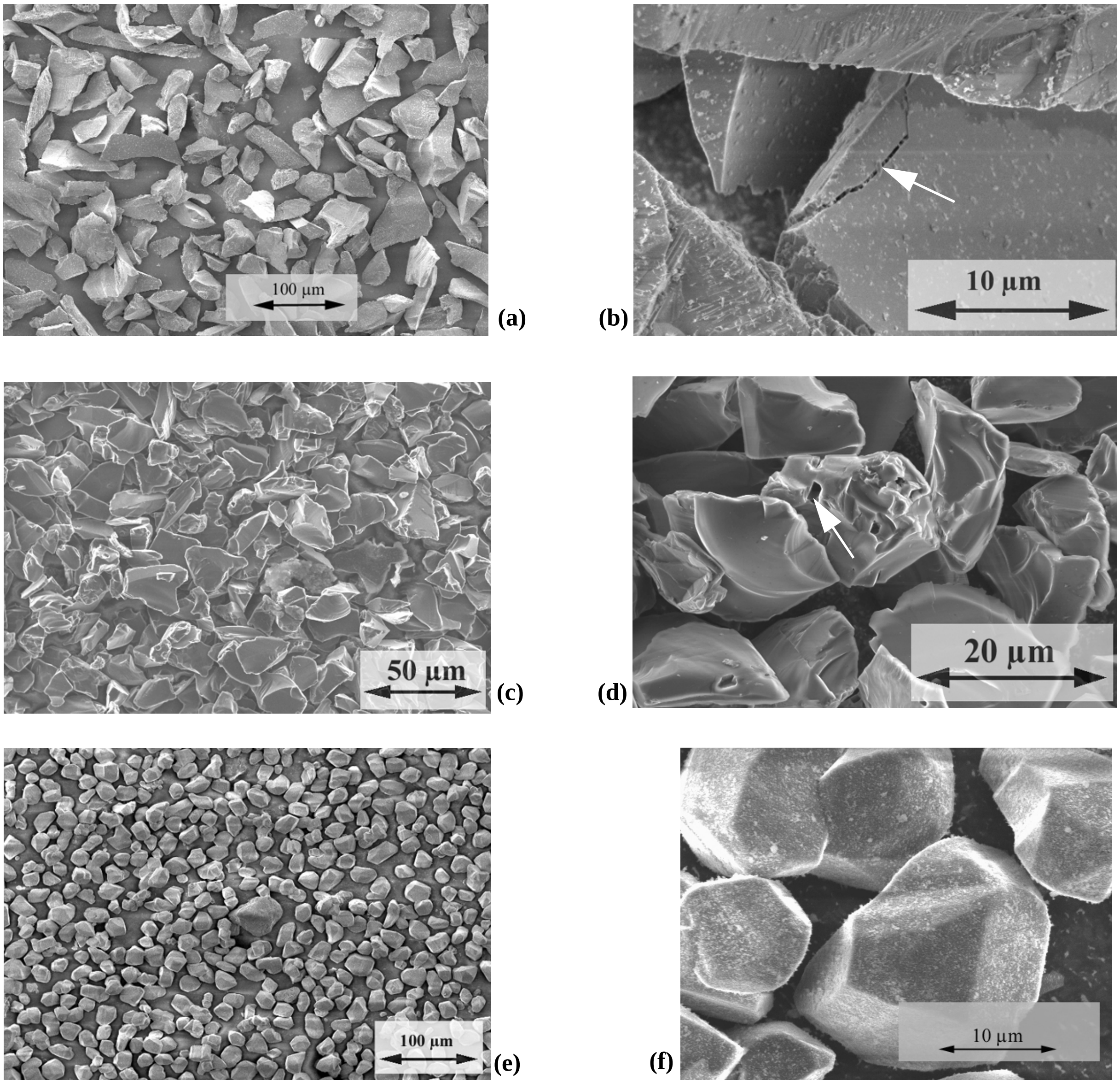

**Figure 4-1.** SEM micrographs of the reinforcing powders. **(a)** and **(b)**: $Al_2O_3$ angular powder (35 µm), general aspect and typical crack-like defect at the surface of a particle; **(c)** and **(d)**: $B_4C$ angular powder (20 µm), general aspect and typical surface defect; **(e)** and **(f)**: $Al_2O_3$ polygonal powder (15µm), no visible surface defects.

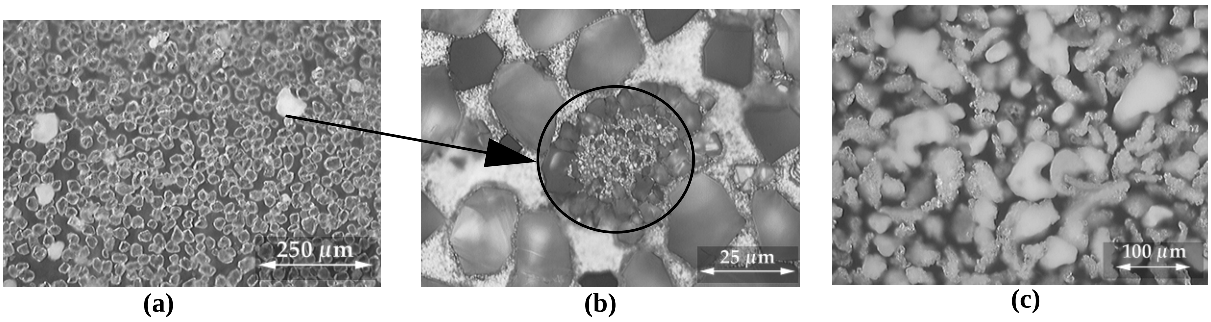

**Figure 4-2.** Optical micrographs of polygonal 25 µm $Al_2O_3$ powder. **(a)**: particles before sieving; **(b)**: polished section of a A-A25p composite prepared with the powder, illustrating the agglomerate structure of the larger particles; **(c)**: agglomerate particles separated from the initial powder by sieving.

### i. Angular alumina composites

In the Al-angular alumina composites (Figure 4-3a-c), the lowest volume fraction (0.4 - 0.43) is obtained for the 5 µm particle size material. This can be attributed to stronger electrostatic interactions between the particles and to their higher aspect ratio, which both prevent optimal packing. In the largest particle size composites (35 µm and 60 µm), the volume fraction is contained between 0.45 and 0.5 depending on the casting and on preform preparation[1]. The composites reinforced with 10 µm particles exhibit the largest volume fraction of angular alumina composites; this is a result of the bimodal size distribution of the powder, as seen in Figure 4-3 b: the smaller (< 10µm) particles are arranged in the spaces available between the larger (> 15 µm) particles, which in turn increases the total volume fraction.

### ii. Angular boron carbide composites and reaction phases

In Al-$B_4C$ composites (Figure 4-3d-g), the volume fraction for a given particle size is generally larger than in their angular $Al_2O_3$ counterparts, with values ranging between 0.55 and 0.6. The exception is the A-B10 material for which the particle size distribution is also narrower compared to the A-A10a material.

Besides this specific case, the lower aspect ratio of the primary $B_4C$ powders (compare Figures 4-3a and d) explains differences of a few percent. Reaction phases are found in these composites and are readily distinguished from the starting $B_4C$ particles thanks to their different optical properties, which facilitate their identification: according to [235] and [47], the $AlB_2$ phase appears yellow under the optical microscope while $Al_3BC$ has a bluish grey tin. In addition, the crystal structure and chemical composition of $Al_3BC$ were recently published in [48] and allow comparison with X-ray analysis.

The relative amount of reaction phase depends on the particle size and increases with decreasing average particle size. It also depends on the contact time between the ceramic preform and the liquid aluminium: in the coarser particle size composites, isolated particles of $AlB_2$ significantly smaller than the average particle size are occasionally observed: these are nucleated by impurities of $TiB_2$ (which was verified by EDAX analysis prior to composite fabrication to be present in the starting powders), Figure 4-3f. In the finer particle size composites (10 and 5 µm particle sizes), $AlB_2$ surrounds and binds $B_4C$ particles together, as illustrated in Figure 4-3e; this phase was estimated by image analysis to attain about 5 vol. %, while it was estimated to be less than 2% in the larger particle size composites (20 to 60 µm). When leaving the liquid aluminium for a longer time in contact with the preform, $Al_3BC$ phase appears at the Al-$B_4C$ interfaces, as seen on Figure 4-3g, for which the metal was maintained in its liquid state for 15 mn after infiltration. The presence of $Al_3BC$ is corroborated by X-ray diffraction analysis on this specimen, for which diffraction angles agree with those in [48]. Additional information regarding the reaction products and their extent as a function of the interaction time (measured by precise densitometry) can be found in the work of Kouzeli [89, 243]. In our case, the interaction time in all Al-$B_4C$ composites was kept short to minimize the amount of reaction products.

### iii. Polygonal alumina composites

The composites of this type (Figures 4-3h to j) exhibit the higest volume fraction of all materials (0.59 - 0.62), as a result of the higher tapped-density achieved with these powders featuring a regular

---

[1] As we gained experience with composite processing, we found that very careful preform preparation was necessary to eliminate microstructural defects. Since the Al-Cu alloy matrix composites were fabricated last and with longer tapping times, this explains their somewhat higher volume fraction.

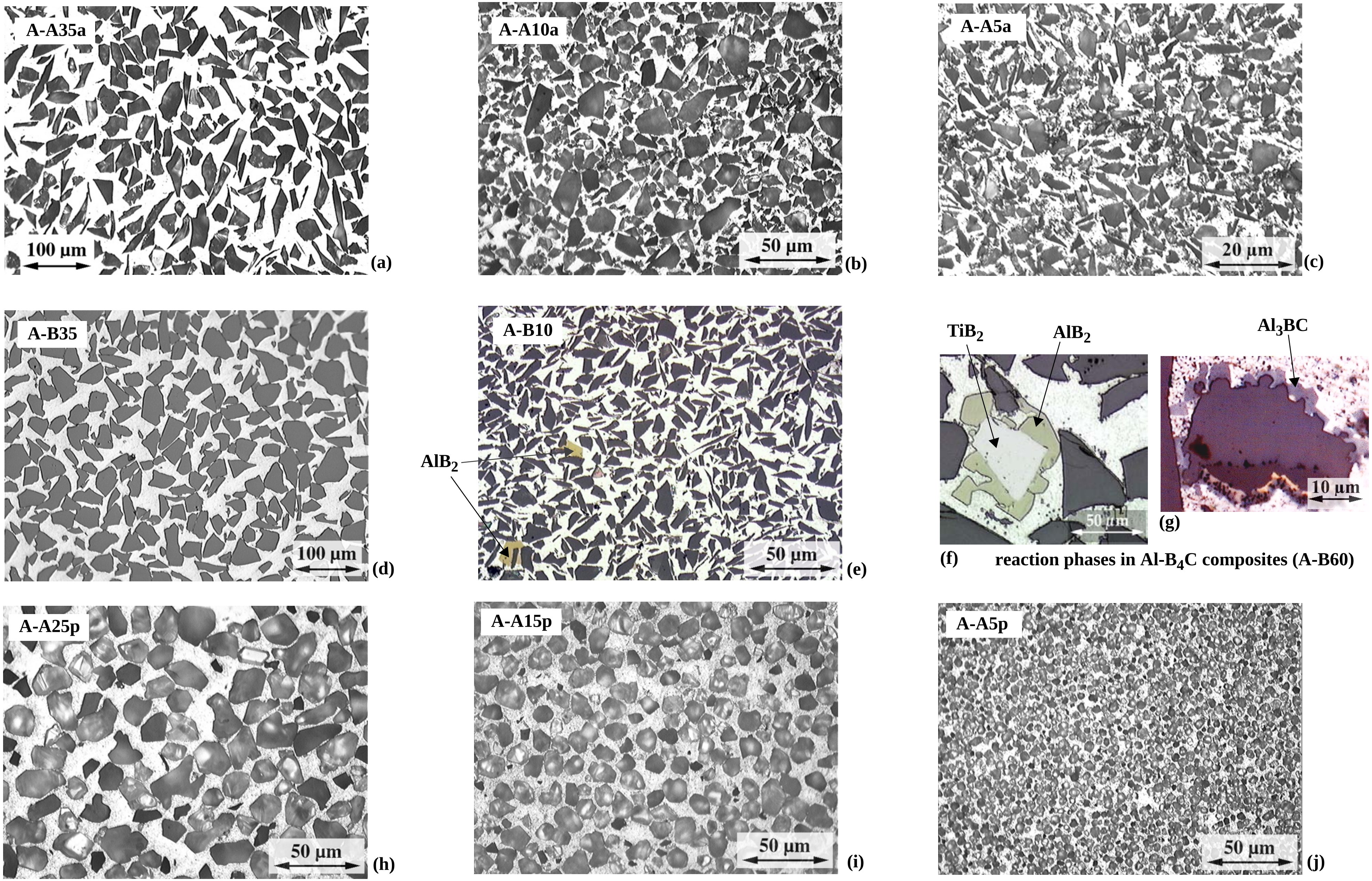
A-A35a
100 µm
(a)
A-A10a
50 µm
(b)
A-A5a
20 µm
(c)
A-B35
100 µm
(d)
A-B10
AlB$_2$
50 µm
(e)
TiB$_2$
AlB$_2$
50 µm
(f)
Al$_3$BC
10 µm
(g)
reaction phases in Al-B$_4$C composites (A-B60)
A-A25p
50 µm
(h)
A-A15p
50 µm
(i)
A-A5p
50 µm
(j)

**Figure 4-3.** Optical micrographs of composite microsotructures. **(a)**, **(b)**, and **(c)**: angular $Al_2O_3$ reinforced composites (various magnifications); **(d)**, **(e)**, **(f)** and **(g)**: angular $B_4C$ reinforced composites (various magnifications), including details of reaction phases; **(h)**, **(i)**, and **(j)**: polygonal $Al_2O_3$ reinforced composites (same magnification to illustrate the characteristic microstructural length scale).

shape and a finer size distribution. Contrary to angular reinforced composites, the volume fraction is almost independent of the average particle size. As explained above, Al-Cu matrix composites are characterized by slightly higher volume fractions. The separation of agglomerate-like particles in the 25 µm powder also probably helped in increasing the tapped density in the composite produced with this powder. The presence of residual porosity (uninfiltrated regions) was observed in some A-A5p composites. Residual porosity remains, however, very low since volume fraction as measured by densitometry does not reveal significant differences with 15 and 25 µm particle composites, as seen for instance for Al-Cu4.5% matrix composites.

**Table 4-2.** Typical composite characteristics. $\lambda_c$ given by for both angular and polygonal particle reinforced composites. * : measured data from [89]**.**

| **Matrix** | **Composite designation** | **$V_f$ [-] (tapped density)** | **$V_f$ [-] (densitometry)** | **Measured interp. distance $\lambda_m$ [µm]** |
|---|---|---|---|---|
| Al 99.99 | *(114)*A-A35a | 0.44 | 0.45 | 17.6 |
| | *(222)*A-A20a | 0.45 | 0.46 | 10.7 |
| | *(224)*A-A10a* | | 0.54 | 3.1 |
| | *(166)*A-A5a | | 0.40 | 2.5 |
| | *(189)*A-A25p* | | 0.59 | 8.9 |
| | *(225)*A-A15p* | | 0.58 | 5.2 |
| | *(230)*A-A5p | | 0.56 | 2.7 |
| | *(70)*A-B60* | | 0.54 | 17.8 |
| | *(171)*A-B35 | | 0.58 | 11.0 |
| | *(195)*A-B20* | | 0.54 | 8.1 |
| | *(229)*A-B10* | | 0.51 | 2.8 |
| | *(235)*A-B5* | | 0.53 | 2.6 |
| Al-2%Cu | *(158)*A2C-A35a | 0.45 | 0.45 | 17.4 |
| | *(322)*A2C-A10a | 0.57 | 0.58 | 4.2 |
| | *(278)*A2C-A5a | 0.43 | 0.41 | 2.3 |
| | *(274)*A2C-A25p | 0.60 | 0.59 | 9.4 |
| | *(253)*A2C-A15p | 0.60 | 0.58 | 5.0 |
| Al-4.5%Cu | *(404)*A4.5C-A60a | 0.49 | 0.52 | 29.3 |
| | *(359)*A4.5C-A35a | 0.50 | 0.50 | 13.1 |
| | *(328)*A4.5C-A25p | 0.62 | 0.60 | 9.1 |
| | *(283)*A4.5C-A15p | 0.61 | 0.61 | 4.9 |
| | *(354)*A4.5C-A5p | 0.58 | 0.60 | 2.4 |

### iv. Regions of lower volume fraction (veins)

The major microstructural defects sometimes observed in the composites are “veins” described in the literature review (Figure 2-5). These consist of two-dimensional bands of matrix in a composite casting. Veins are mainly of two types: large “macroveins”, with a typical width of 1 to 5 mm. They were found in the initial castings but later completely eliminated by applying more careful procedures during composite processing. The second type of vein is less than 1 mm wide down to a size of about 5 to 10 times the particle size, Figure 4-4c. Such “microveins” are essentially found in the composites reinforced by finer reinforcements, namely in the A10a, A5a, B5, A15p and A5p systems, and they sometimes remained even when the processing was carefully executed. Their appearance was however not systematic.

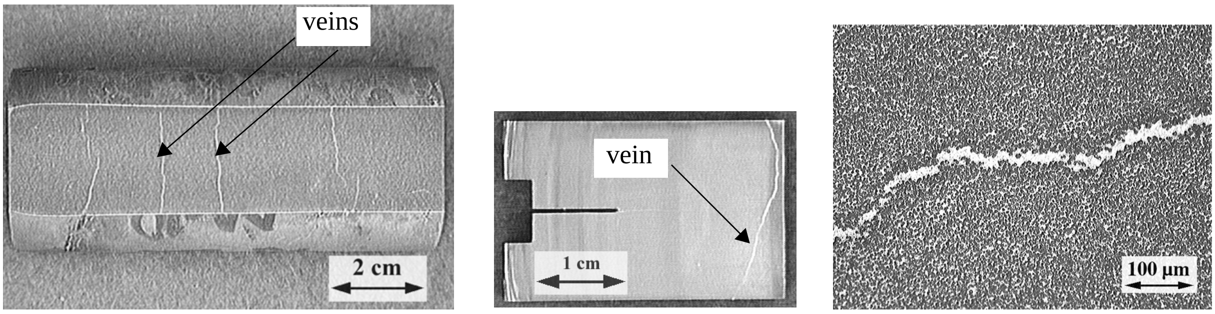

**(a)** **(b)** **(c)**

**Figure 4-4.** Veining in the infiltrated composites. **(a)**: *(295)*A2C-A15p composite with layers of veins along the composite ingot; **(b)**: chevron specimen of the *(275)*A2C-15p composite, machined such that the vein does not interact with the crack path and the crack-tip stress field; **(c)**: a typical microvein at higher magnification in the *(244)*A-A5p composite.

The phenomena responsible for the vein formation are not elucidated yet. However, some experimental evidences do exist. In the preform preparation step, the packing density should be as uniform as possible because inhomogeneity in the preform will remain during infiltration. In the preliminary infiltrations when powders were not carefully packed, veins were for instance systematically present in the smaller particle size composites. The second important step is the preform evacuation: in our infiltration experiments, the slower the evacuation, the fewer veins in the castings. In the preforms made of smaller ceramic particles, the fluid permeability is lower such that a higher pressure gradient is necessary to evacuate the gas molecules at a given flow rate. The force applied on the preform is therefore larger such that the probability of fracturing the preform increases as well, leaving cracks which remain in the form of veins after infiltration. For the same reasons, the presence of veins is minimized by increasing the temperature at a low rate because degasing occurs slowly in this case. Finally, it is qualitatively observed that veining is reduced by increasing the pressure very slowly, because overly high-pressure gradients can promote shearing fracture of the preform. Experimental evidence to attribute vein formation to solidification was not found, and vein formation was not influenced by the matrix type.

If possible, the specimens for mechanical testing were machined from vein-free castings. This was especially crucial in tensile testing, because the elongated dimensions of the tensile specimens had to be machined along the composite axis, leading to the almost inevitable presence of veins in the gauge length. In contrast, microveins did not cause as much problems in fracture toughness testing, because the specimen orientation could be chosen such that interaction between the main crack and a vein was not an issue. An example is illustrated in Figure 4-4: presence of microveins along the casting is cleary observed in Figure 4-4a; in Figure 4-4b, the vein present at the extremity of the chevron-notch specimen does not intercept the crack during the critical part of the fracture experiment. If it was later found from the post-mortem investigations that a vein had intercepted the crack in the critical region during crack propagation, the test was discarded. For the photoelastic observations, only vein-free specimens were employed to avoid any interaction with the crack-tip deformations fields.

### 4.1.3 Al-Cu matrix composites

Typical SEM micrographs of Al-2%Cu alloy as-cast composites with both angular and polygonal particles are given in Figures 4-5a and b. Under backscattered electron (BSE) observation, intermetallic phases appear in clear contrast to $\alpha$-Al and particles. With both angular and polygonal particles, many second phase precipitates are present in the as-cast composites: these are mainly located along the particle/matrix interface. Figures 4-5c and d show SEM micrographs of the same materials after solution treatement at 515°C. While many precipitates have disappeared, complete dissolution has not been achieved. Longer solutionization treatments (up to 200 hours) were explored on two composites (A2C-35a and A2C-15p), and the amount of second phase was quantified by image analysis: no significant

**as-cast composites**

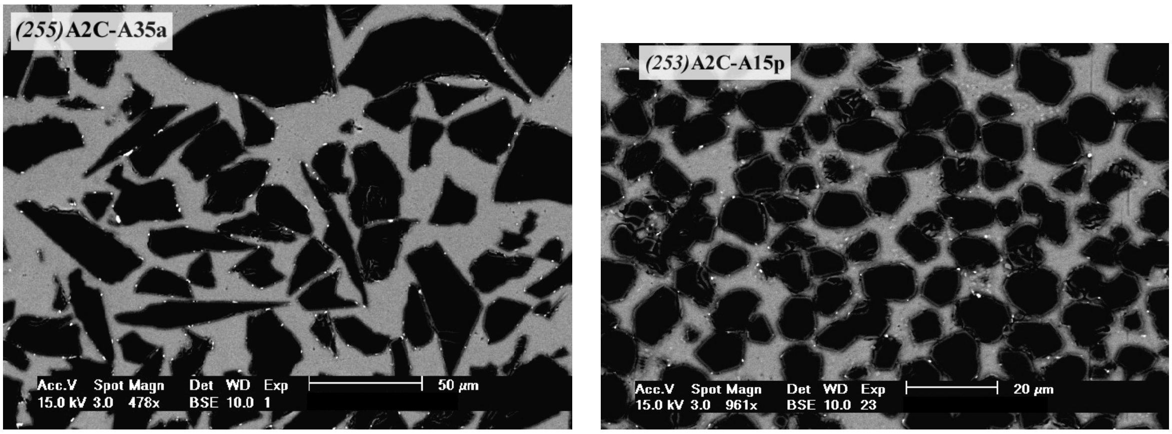
(255)A2C-A35a
Acc.V Spot Magn Det WD Exp 50 μm
15.0 kV 3.0 478x BSE 10.0 1
(253)A2C-A15p
Acc.V Spot Magn Det WD Exp 20 μm
15.0 kV 3.0 961x BSE 10.0 23

(a) (b)

**solution-treated composites**

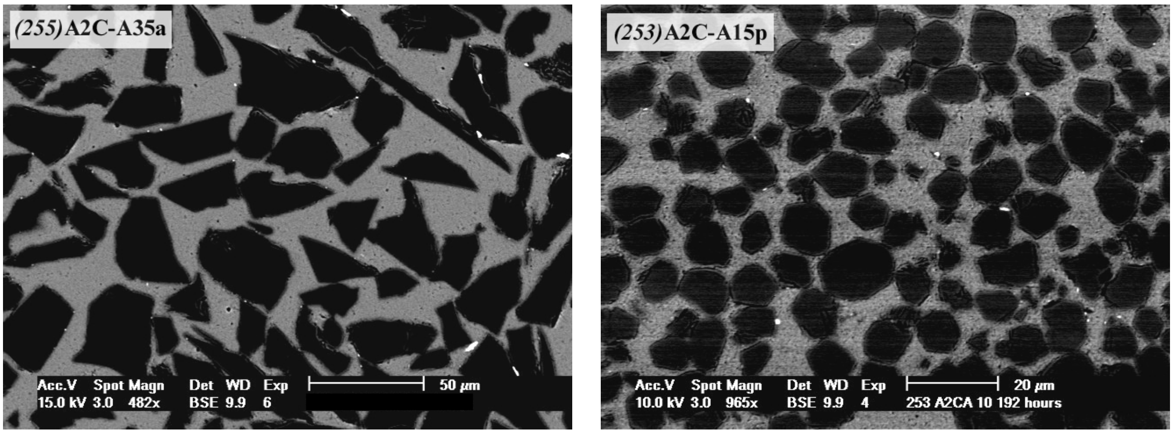
(255)A2C-A35a
Acc.V Spot Magn Det WD Exp 50 μm
15.0 kV 3.0 482x BSE 9.9 6
(253)A2C-A15p
Acc.V Spot Magn Det WD Exp 20 μm
10.0 kV 3.0 965x BSE 9.9 4 253 A2CA 10 192 hours

(c) (d)

**Figure 4-5.** BSE detector micrographs of Al-2%Cu matrix composites with both angular and polygonal alumina particles. **(a)** and **(b)**: as-cast conditions, secondary-phase precipitates (in bright) are located mainly at the particle/matrix interface; **(c)** and **(d)**: after solution treatment (515°C, 192 hours), complete dissolution is not achieved.

change of the second-phase content was observed after solutionisation for more than 8 hours at 515°C [236]. In terms of absolute values, these measurements indicate that the amount of second phase is slightly higher in angular reinforced composites than in polygonal composites: about 0.1 vol.% for the former versus 0.05 vol. % for the latter. In all materials, many of the non-dissolved copper-rich precipitates are located in the narrow region between neighboring particles, often bridging them, Figures 4-5c and d.

**as-cast composites**

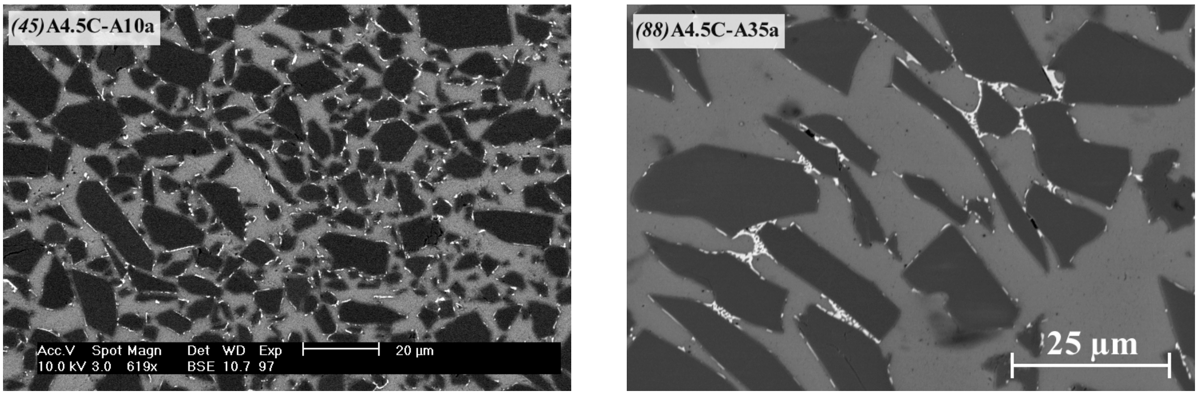
(45)A4.5C-A10a
Acc.V Spot Magn Det WD Exp 20 µm
10.0 kV 3.0 619x BSE 10.7 97
(88)A4.5C-A35a
25 µm

**(a)** **(b)**

**solution-treated composites**

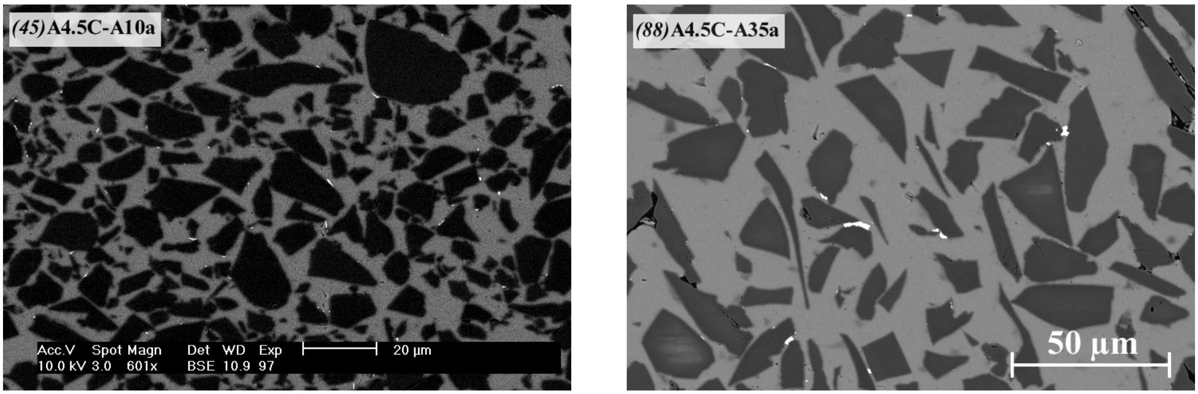
(45)A4.5C-A10a
Acc.V Spot Magn Det WD Exp 20 µm
10.0 kV 3.0 601x BSE 10.9 97
(88)A4.5C-A35a
50 µm

**(c)** **(d)**

**Figure 4-6.** BSE detector micrographs of Al-4.5%Cu matrix composites reinforced with two different sizes of angular alumina particles. **(a)** and **(b)**: as-cast conditions, eutectic structure of the second phase; **(c)** and **(d)**: after solution treatment (515°C, more than 24 hours).

SEM micrographs of as-cast Al-4.5%Cu matrix composites reinforced with two different average sizes of angular alumina particles are shown in Figures 4-6a and b. Similar microstructures are noticed with many intermetallic second phases surrounding the primary alumina particles, and taking the form of a typical eutectic solidification structure for the largest particle size composites (Figure 4-6b). The amount of second-phase in the as-cast conditions is clearly larger than in the Al-2%Cu matrix composites. After solutionization heat treatment, on the other hand (Figures 4-6c and d), no major differences are obtained compared to the Al-2%Cu matrix composites: a residual amount of second-phases, often trapped between two near reinforcement particles, remains, independent of the heat-treatment duration.

EDAX analysis on individual precipitates in the as-cast composites such as given in Figure 4-7 reveals two types of second-phase: the first type contains Al and Cu only, which according to the binary Al-Cu phase diagram corresponds to $\theta$-Al$_2$Cu. The second type of precipitates contains Fe in addition to Al and Cu. After solutionization, all remaining precipitates contain a significant amount of iron, indicating that the $\theta$-phase has dissolved and remanent precipitates after prolongued solutionization are Al-Cu-

Fe intermetallics. Observation and EDAX analysis of coarse intermetallics containing iron was also confirmed in the as-received matrix alloys, and after solution heat-treatment. The presence of Fe as a trace element (Table 3-1) in the matrix is therefore responsible for incomplete dissolution by forming iron-containing precipitates that are stable at the heat treatment temperature.

EDAX only permits semi-quantitative analysis and is not suitable for the determination of the exact intermetallic composition. However, ZAF correction gave a Fe:Cu ratio close to 1:2, which is in good agreement with the ternary compound $Al_7Cu_2Fe$, usually found in cast aluminium copper alloys, and known not to dissolve during solution heat treatment at 515°C [244, 245], as also noticed more recently by Cayron [75] in a 6xxx alloy (with 4% of Cu in the matrix) reinforced by short alumina fibers and produced by squeeze casting. It is hence concluded that dissolution of Cu rich intermetallics in Al-Cu matrix composites is incomplete due to the stable iron-containing precipitates $Al_7Cu_2Fe$ [236].

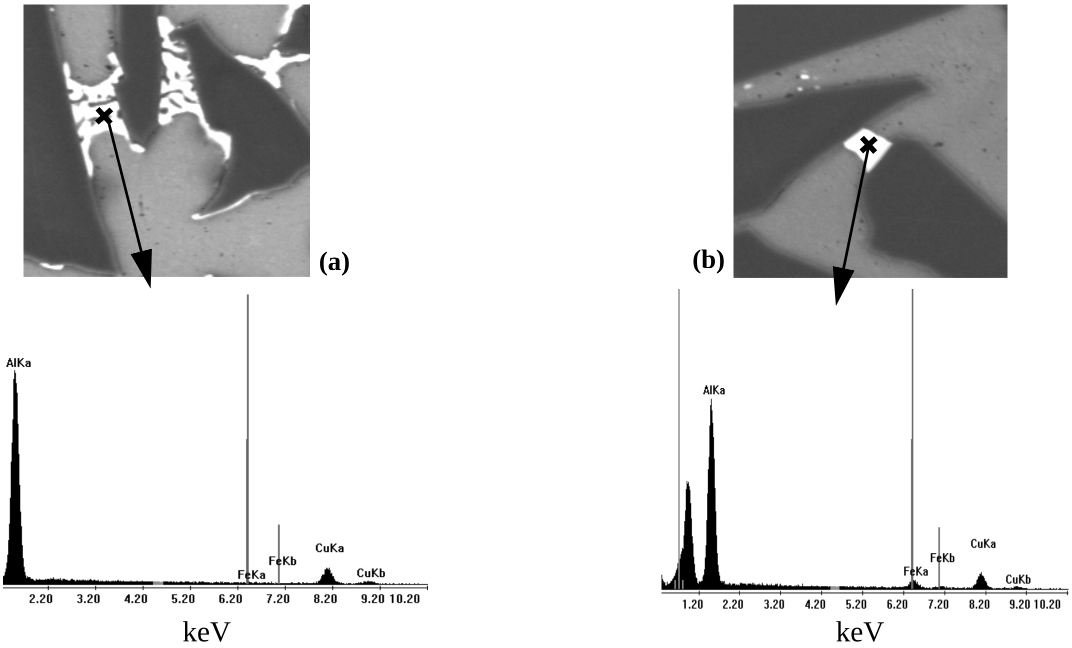

| Element | Wt % | At % | K-Ratio | Z | A | F |
|---|---|---|---|---|---|---|
| Al-K | 56.3 | 75.1 | 0.3 | 1.052 | 0.582 | 1.000 |
| Fe-K | 0.78 | 0.51 | 0.0 | 0.948 | 0.994 | 1.090 |
| Cu-K | 42.9 | 24.4 | 0.4 | 0.913 | 1.000 | 1.000 |

| Element | Wt % | At % | K-Ratio | Z | A | F |
|---|---|---|---|---|---|---|
| Al-K | 50.6 | 69.9 | 0.3 | 1.056 | 0.568 | 1.000 |
| Fe-K | 13.9 | 9.3 | 0.1 | 0.952 | 0.994 | 1.058 |
| Cu-K | 35.5 | 20.8 | 0.3 | 0.917 | 0.993 | 1.000 |

**Figure 4-7.** EDAX spectra of coarse intermetallic phases located around the reinforcements, with related semi-quantitative analysis of their chemical composition with the ZAF method. **(a)**: Al-Cu ($\theta$–$Al_2Cu$) phase; **(b)**: Al-Cu-Fe ($Al_7Cu_2Fe$) phase.

# 4.2. *J*-INTEGRAL FRACTURE TESTING

Systematic determination of fracture properties by EPFM testing was performed for pure Al matrix composites. The typical *J-R* curve characteristics in these composites as well as the influence of the microstructural variables are presented in detail. Verifications of the validity of the method are also given for different materials (including post-mortem observations of the crack propagation length during fatigue pre-cracking and fracture test, control of the important validity criteria, and analysis of *J*-dominance). The key data extracted from *J-R* curves that will be used in the discussion are then summarized. Finally, the micromechanisms of fracture in this class of materials as identified by SEM fracography and by the arrested crack technique are presented. For Al-Cu matrix composites, most fracture investigations were conducted on chevron-notched specimens (Chapter 4.5); the limited number of *J*-integral fracture tests for this class of materials is nevertheless presented as well, for comparison to pure Al matrix composites and with chevron-notch testing.

## *4.2.1 J-R curves: General characteristics*

### i. Typical curves

Generally speaking, significant *R*-curve behaviour is observed in the pure Al matrix composites. This is a priori surprising regarding the amount of brittle phases in these materials (40 to 60%). The *J*-integral resistance curves are characterized by three distinct domains, as depicted in Figure 4-8:

(i) An initial steeper part, attributed in unreinforced metallic alloys to crack blunting. In the present case, however, significant crack extension occurs simultaneously, as will be discussed below. This first portion always ends in the region of qualified data according to ASTM E-1737.

(ii) A second part with a lower slope of the *J*-integral vs. crack length. This region starts close to, or at, the maximum load during a fracture experiment. As compared to the first portion of the curve, it corresponds to manifest macroscopic crack propagation, as detected by the sudden increase in the crack propagation rate. On some occasions, but mainly in the finer particle size composites or for side-grooved specimens, the crack propagates in an unstable manner in this second portion of the curve (generally soon after the peak load).

(iii) When fully-stable crack propagation occures, a plateau value is attained, in a region well beyond the validity domain of *J*-controlled fracture. As presented later, this plateau value strongly depends on the specimen geometry and is no longer a material parameter. In this domain of large crack propagation, the precision of the crack length measurement as given by the elastic compliance is not ensured any more.

### ii. Crack closure effects

A slight crack-closure is noticed at the beginning of the tests: this is detected by a decrease of the specimen compliance as the load increased. This effect is found to be associated with residual stresses from pre-cracking: as seen in Figure 4-9 for a large spectrum of materials, the load at which the minimum compliance is measured during a *J* fracture test corresponds well to the maximum load during fatigue pre-cracking. As was already explained in Chapter 3, a method to minimize the crack closure effect is thus to use a fatigue load as low as possible.

To compute the *J-R* curves, the initial crack length ($\Delta a = 0$) was taken as the value corresponding to the minimum compliance. In addition, because the fracture energy cannot be neglected in this region, the elastic part of $J$ (which initially strongly dominates over $J_{\mathrm{pl}}$ ) was computed with this initial value of crack length, hence explaining the small offset at zero crack extension. Comparing experimental curves of the same material with various degrees of crack closure effect reveals an insignificant difference in the $J$ values of interest that are extracted from the curves.

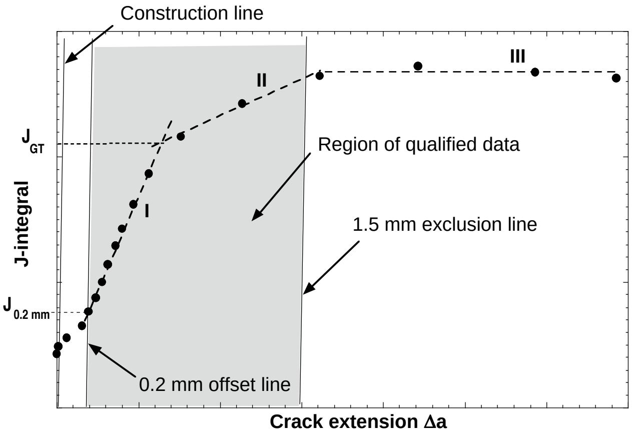

I: initial part (blunting and process zone formation)

II: initiation of the ductile tearing regime

III: ductile tearing regime in large-scale yielding

**Figure 4-8.** Typical *J*-resistance curve of an Al matrix composite, including regions of qualified data according to ASTM E-1737. The curve is divided into three distinct parts. The initiation of macroscopic crack propagation corresponds at the transition from I to II; unstable fracture occurs sometimes in region II.

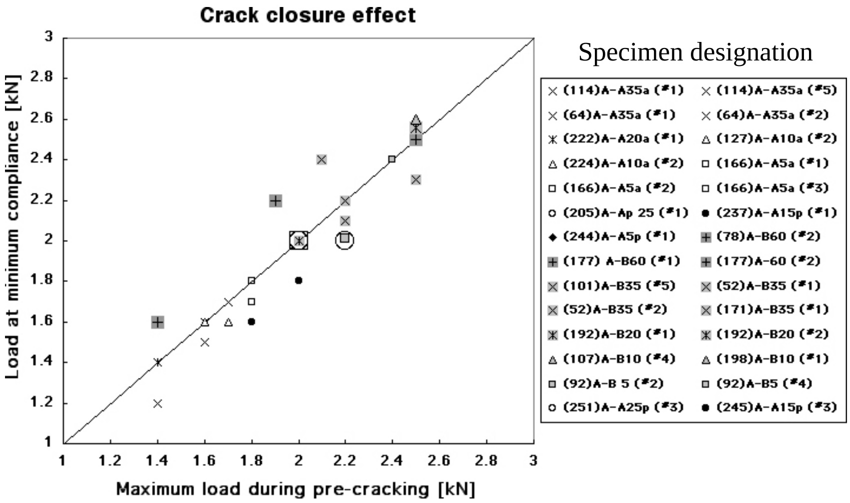

**Figure 4-9.** Crack closure effect prior to crack tip blunting and process-zone formation: during a $J$ fracture test, the compliance decreases in the first cycles and its maximum value is attained at a load corresponding to the maximum fatigue load during pre-cracking.

### iii. Data analysis

From the observations exposed above, it was decided to report the following values:

(i) The interception of the resistance curve with the 0.2 mm offset line as defined in ASTM E-1737, because it is the standard value. It is emphasized that this value has no fundamental meaning here. In addition, it depends on the crack closure effect since, if the latter is more marked, it shifts the *J-R* curves slightly to the right, resulting in a variation of the intersection with the 0.2 mm offset line.

(ii) The second value deduced from the *J*-*R* curves that represents in our eyes a more significant material parameter is the *J* value at the slope change of the curve, namely at the end of the initial steep part of the curve (the end of blunting in metals). Indeed, it clearly corresponds to the initiation of the macroscopic crack propagation regime, or in other words to the initiation of the ductile tearing mode. Additional arguments in favor of this parameter are that: (i) it is still in the region of *J*-controlled crack growth and can hence be considered a material constant, (ii) a corollary of the latter is that it is not affected by the specimen geometry, as confirmed in many of our experiments, and (iii) it does not depend on the crack closure effect either. To obtain this parameter in a systematic manner for all fracture experiments, two linear regression lines were drawn for each part of the curves and the value called "$J_{GT}$" was defined at the intersection line, Figure 4-8.

## 4.2.2 Effect of reinforcement type (chemistry, size, and shape)

### i. Aluminium-angular alumina composites

Typical load-displacement fracture curves and their associated *J*-resistance curves in angular alumina reinforced composites are shown in Figures 4-10a and b, respectively. The largest particle size composites (35 µm) exhibit fully stable crack propagation in all samples, and the most marked *R*-curve behaviour. In comparison, the 10 µm and 5 µm particle size composites are characterized by a less

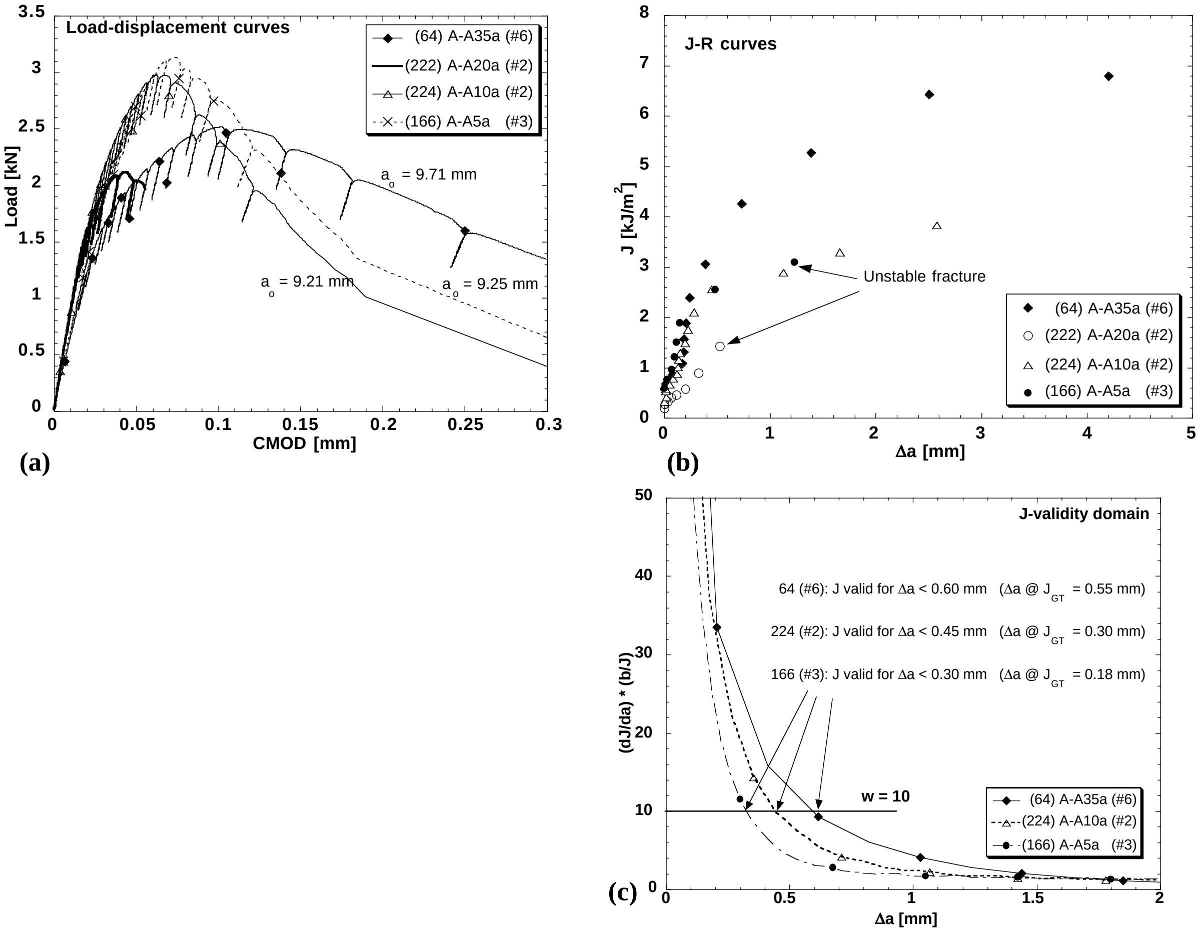

**Figure 4-10.** Crack-propagation behaviour in Al-$Al_2O_3$ angular composites. **(a)**: load-displacement curves with loading cycles; **(b)**: $J_R$ curves computed from (a); **(c)**: *J*-validity domain according to the analysis of Hutchinson and Paris. All curves from non side-grooved specimens.

marked increase of the fracture energy as the crack advances, and in some occasions by unstable fracture, which did not allow to perform unloading/reloading cycles after the peak load. No significant differences in terms of fracture behaviour are noticed between these two composites.

The 20 µm particle size composite is a special case for which the very low fracture energy is due to a micromechanism of fracture seen only in this material. For this reason, it will always be treated separately from the other composites in the rest of the work.

The verification of *J*-validity during crack extension is shown in Figure 4-10c. To determine the validity domain, the $J_R$ curves were first fitted with an appropriate analytical function, from which eq. (A-34) was computed:

$$\omega \equiv \frac{b}{J_\mathrm{R}} \frac{\mathrm{d}J_\mathrm{R}}{\mathrm{d}\Delta a} > 10 \qquad \text{(A-34)}$$

This analysis reveals deviation from *J*-controlled crack growth in all materials slightly after the slope change, meaning that the $J_{GT}$ value at the onset of ductile tearing is still usable as a single parameter to describe the fracture behaviour (as indicated on Figure 4-10c). As soon as faster crack propagation takes place, however, *J* is no longer valid. The loss of *J*-validity is hence induced by rapid early crack extension, or in other words by a relatively large region of elastic unloading as compared to the *J*-dominance zone of the deformation theory solution (see Figure A-7). This is in contrast with what is generally seen in monolithic metal alloys, in which the loss of *J*-validity is rather related to the region of non-proportional loading ahead of the crack tip, whereas the region of elastic unloading is initially smaller than here because the rate of damage accumulation is much lower. In turn, it appears that the ASTM criterion for allowed crack extension ($\Delta a < 0.1 b_0$) is not stringent enough in our composites, because it would validate the *J* data until 0.9 to 1 mm of crack extension (the initial ligament length being typically 9 to 10 mm), whereas the present analysis shows that crack extension larger than 0.5 mm is no longer in the validity domain.

### TESTS INTERRUPTED PRIOR TO FAILURE

As seen from Figure 4-10b, some degree of simultaneous crack propagation accompanies blunting in the initial part of the *J-R* curve. The increase in elastic compliance (which is used to compute $\Delta a$) can be attributed to physical crack extension, but also to damage in front of the crack tip. Indeed in these composites, damage occurs very early in the deformation process [135, 246] (before the 0.2% offset yield stress) and is well captured by the stiffness decrease. Hence, interrupting fracture tests and physically marking the crack front by fatigue loading was employed as a means to verify to what extent crack propagation as detected by the compliance variation could be attributed to damage in the process zone. In Figure 4-11a and b, load-displacement curves and related *J-R* curves of two different specimens of the A-A35a composite are given. The first test was interrupted at a relatively low level of *J* (1 kJ/m$^2$) after limited crack extension (80 µm according to the increase of compliance). No crack growth was detected for this specimen, under either binocular microscope or in more detailed SEM investigations. This indicates that the stiffness reduction can be attributed to the damage process zone which is not clearly revealed on post-mortem investigations.

The second test was interrupted at about the peak load, which corresponded to a more significant crack growth (480 µm according to the compliance decrease) and to the onset of regime II. About 500 µm of of crack advance is in this case revealed under the binocular microscope, Figure 4-11c. The region of crack propagation during fracture is also clearly observed under SEM, because changes in the micromechanisms of fracture are visible (Figure 4-11d), which confirm a significant level of crack growth.

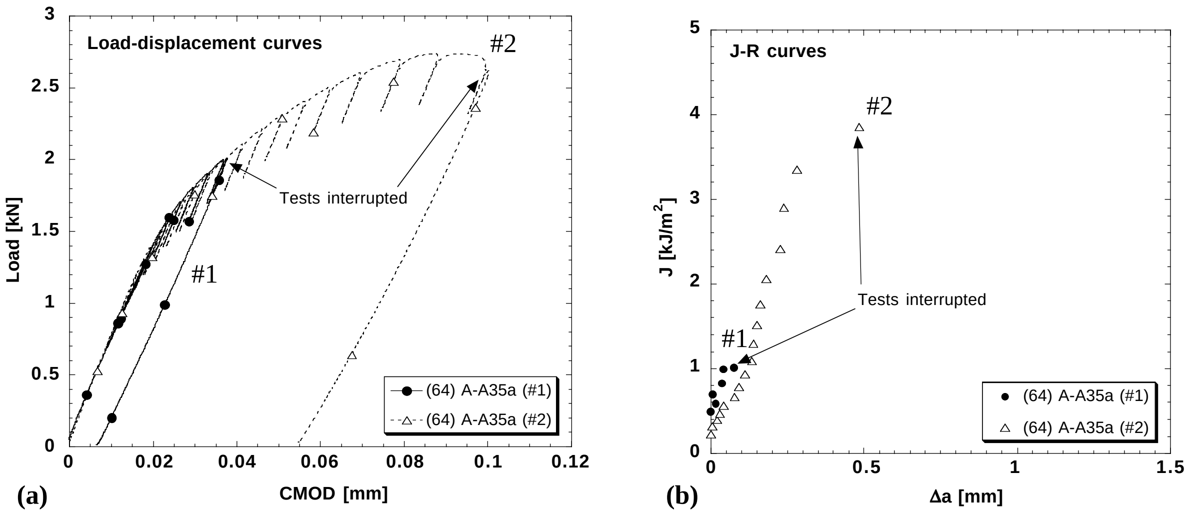

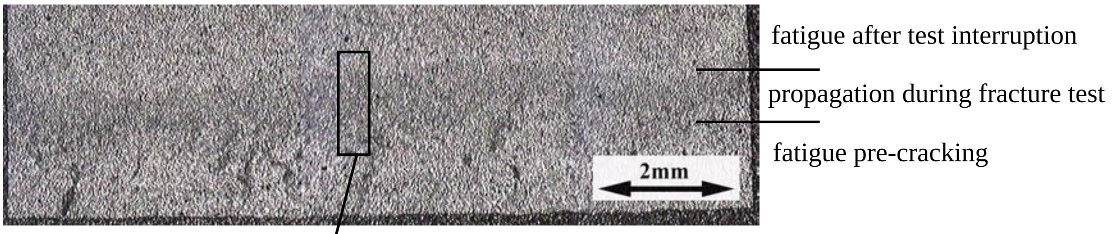
fatigue after test interruption
propagation during fracture test
fatigue pre-cracking
2mm

**(c)** crack front, specimen #2

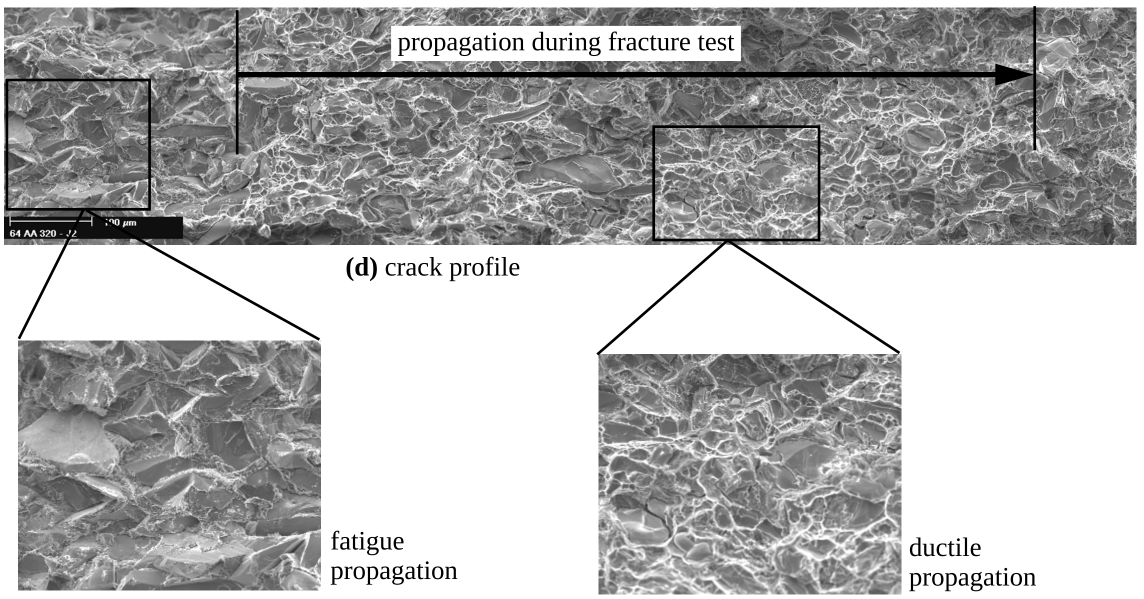
propagation during fracture test
100 µm
fatigue propagation
ductile propagation

**(d)** crack profile

**Figure 4-11.** *(64)*A-A35a specimens interrupted prior to final failure and subsequently marked in fatigue. **(a)**: load-displacement curves; **(b)**: corresponding *J-R* curves; **(c)**: binocular micrograph of the fracture surface after final failure, specimen #2; **(d)**: SEM micrographs along the crack profile, the differences in the failure modes are well distinguished in the high magnification windows. Tests conducted on side-grooved specimens.

A fracture test on a A-A5a composite interrupted slightly before the peak load is shown in Figure 4-12. Compared to the previous cases, the transition between the various crack propagation modes (fatigue-fracture-fatigue) is better contrasted under the binocular microscope thanks to more significant differences in the micromechanisms of failure (as will be discussed in Section 4.2.6). The onset of ductile crack growth is therefore unambiguously marked, and the profile given in Figure 4-12b indicates a crack extension of 300 to 400 µm. The boundary between the arrest of ductile fracture and the second series of fatigue cycles is on the other hand not as distinct, showing a gradual transition zone about 50 - 100 µm wide.

It is hence concluded that the crack propagates on a macroscopic scale even in the initial portion of the *R*-curve regime I), such that the latter cannot be attributed only to damage in front of the crack tip. The process zone is formed very early during fracture and is evaluated (from the first interrupted sample shown in Figure 4-11) to be about one order of magnitude more extended than the average particle size.

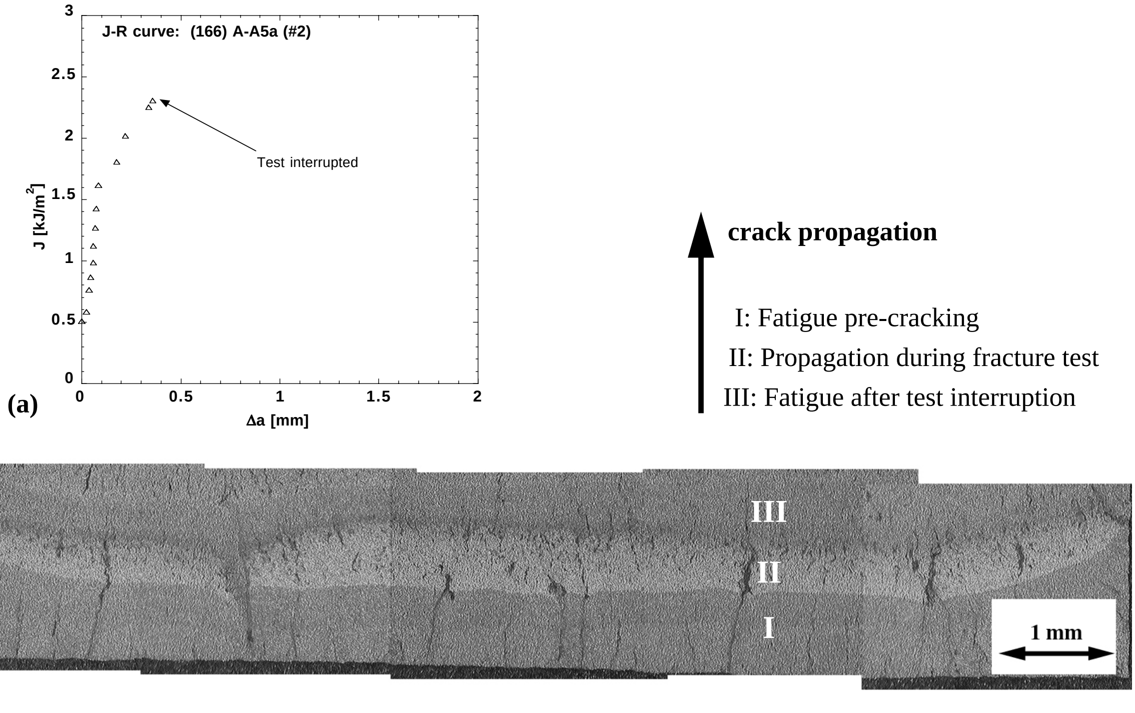

**Figure 4-12.** *(166)*A-A5a specimen interrupted prior to final failure and subsequently marked in fatigue. **(a)**: *J-R* curve; **(b)**: binocular micrograph of the fracture surface after final failure, the boundary between fatigue pre-cracking and the beginning of crack growth during monotonic loading is well marked, while the second boundary with the fatigue region after test interruption is less sharp. Test conducted on side-grooved specimen.

### REPRODUCIBILITY OF EXPERIMENTS

The reproducibility of *J-R* curves is not always ensured in EPFM testing. Hence, at least three valid tests were conducted on the same material to control this issue and determine the average toughness. In our case, good reproducibility between different tests are achieved in the region of validity, as seen for instance on Figure 4-13a for the A-A5a composite. More significant differences are occasionally observed for larger particle size composites. These are mainly due to variations in the crack propagation rate in the initial part of the curve; as depicted in Figure 4-13b. However, one notices that this difference is reflected by the value of *J* at 0.2 mm of crack propagation, while the relative difference in toughness at the slope change of the resistance curve is smaller, supporting the choice of this quantity to compare the fracture characteristics of the composites.

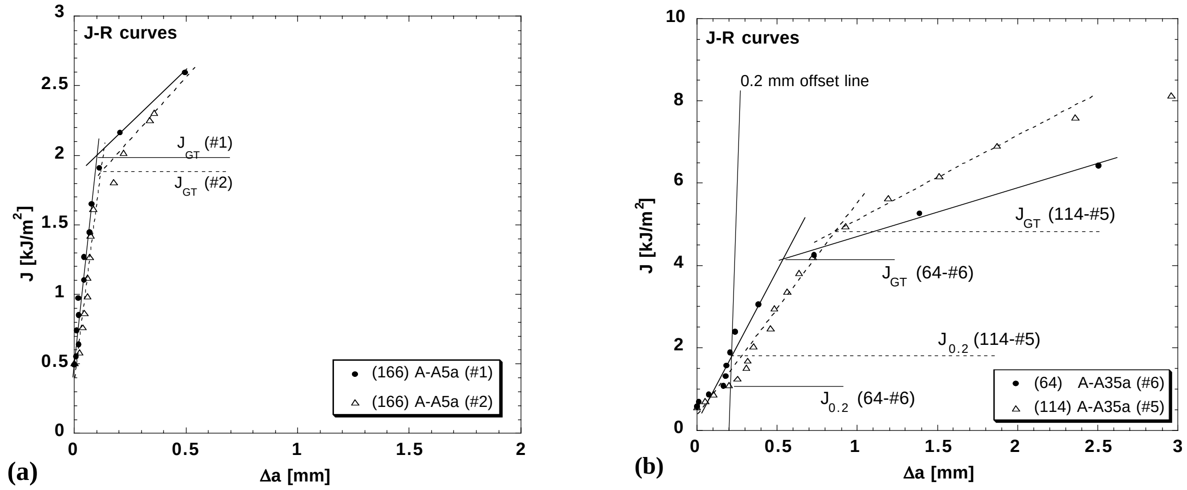

**Figure 4-13.** Verification of reproducibility of *J-R* curves in angular alumina reinforced composites. **(a)**: Al-$Al_2O_3$ 5 µm composite; **(b)**: Al-$Al_2O_3$ 35 µm composite.

### ii. Aluminium-polygonal alumina composites

Representative load-displacement and *J-R* curves of Al-$Al_2O_3$ polygonal composites are shown in Figure 4-14. There is a clear particle size effect in this type of composites, more evident than in angular alumina reinforced composites. The 25 µm particle composite exhibits the highest toughness (be-

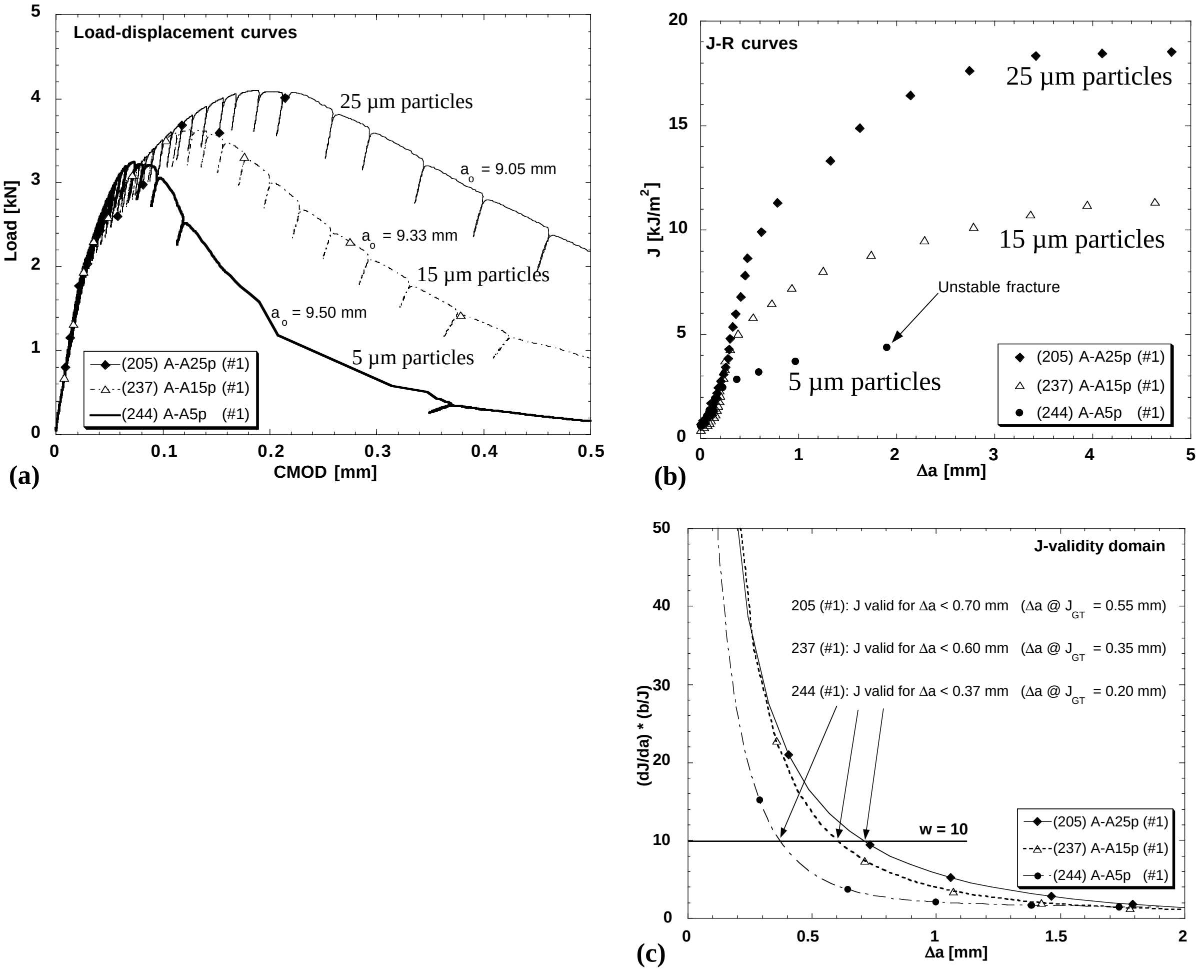

**Figure 4-14.** Crack-propagation behaviour in Al-$Al_2O_3$ polygonal composites. **(a)**: load-displacement curves with loading cycles; **(b)**: *J-R* curves computed from (a); **(c)**: validity domain according to the analysis of Hutchinson and Paris. All curves from non side-grooved specimens.

tween 8 and 9 kJ/m$^2$ for $J_{GT}$, which is also the highest of all tested composites including angular $Al_2O_3$ and $B_4C$ reinforced composites), followed by the 15 µm particle size composites, while the 5 µm particle size composite has a much less marked *R*-curve behaviour. In the latter, no sample exhibited stable crack growth after attaining the peak load. As with angular alumina composites, $J_{GT}$ is located in all composites within the limit of *J*-controlled crack growth, which vanishes also as soon as the ductile tearing regime appears, Figure 4-14c.

### TESTS INTERRUPTED PRIOR TO FAILURE

Two CT tests of the 25 µm particle size composite were stopped before final failure, and the fracture surface subsequently marked by fatigue cycling. The objective, however, was different in the present case in that one of the tests was interrupted slightly before the peak load, while the second test was interrupted just after having reached the peak load, Figure 4-15a. As seen in Figure 4-15b, the first specimen was hence still in the initial, higher slope portion of the *J-R* curve when the test was interrupted, while the second was located in the second portion of the curve. The fracture surfaces of the two specimens after final fatigue loading as observed under binocular microscopy are given in Figures 4-15c and d. Crack propagation is clearly more extensive in the second specimen, indicating that the crack sudden-

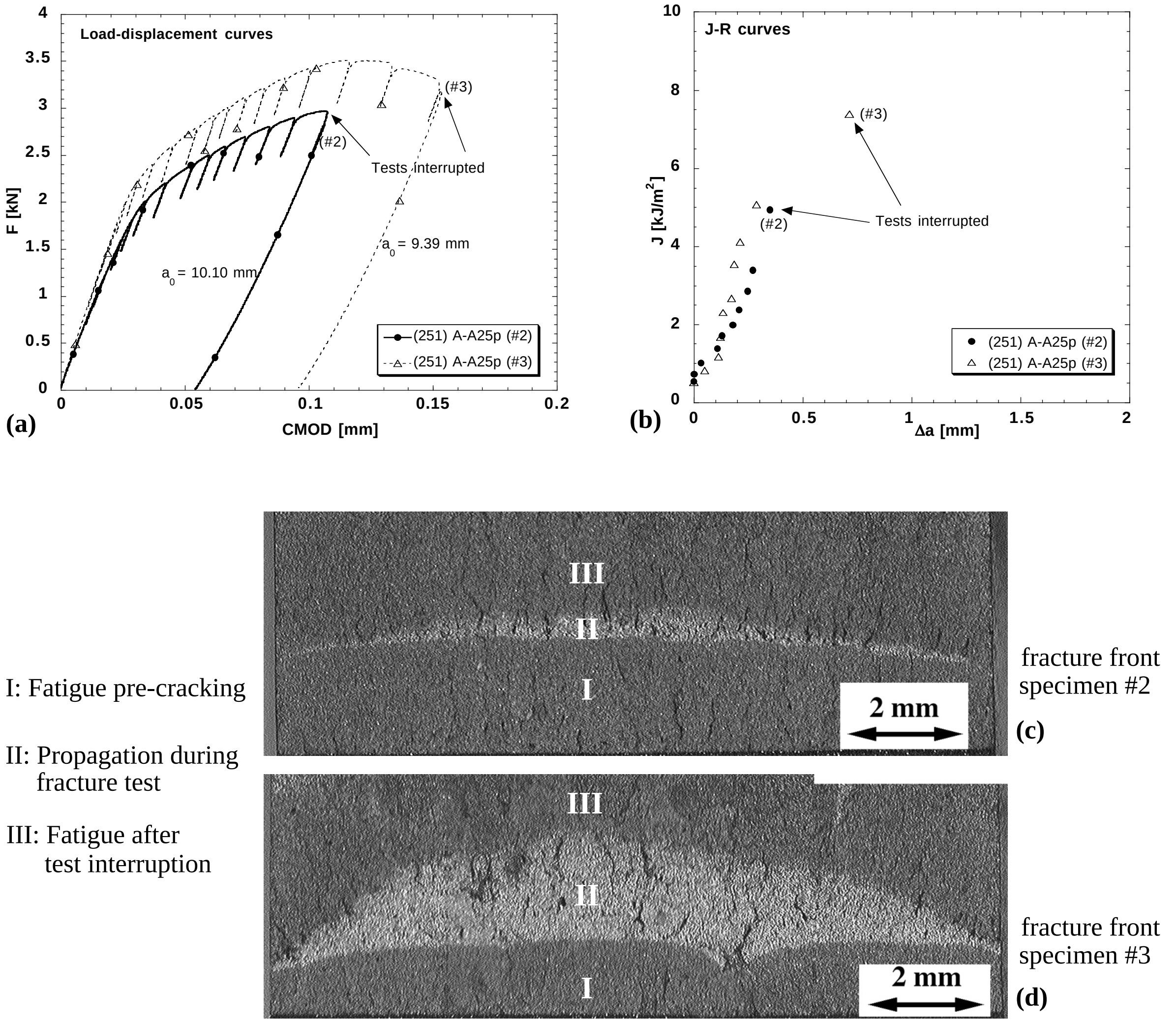

**Figure 4-15.** *(251)*A-A25p composite specimens interrupted prior to final failure and subsequently marked in fatigue. **(a)**: Load-displacement curves, one specimen arrested just before and the other just after the peak load; **(b)**: corresponding $J_R$ curve, **(c)**: binocular micrograph of the fracture surface, specimen #2; **(d)**: binocular micrograph of the fracture surface, specimen #3. Non side-grooved specimens.

ly propagates on a macroscopic scale, such that the $J_{GT}$ value can indeed be considered as a critical fracture energy in these materials.

These experiments confirm on the one hand a significant advance of the physical crack together with its associated process zone in the initial portion of the *J-R* curve, and on the other hand a sudden and much more rapid propagation of the macroscopic crack as the slope changes. The behaviour is thus comparable to that of metals failing by fully ductile crack growth, but with the difference in the composites, that the crack advances significantly before the ductile tearing regime. There is in other words some degree of “damage coalescence” prior to the onset of ductile tearing.

REPRODUCIBILITY OF EXPERIMENTS

The reproducibility of *J-R* curves was also verified in the polygonal alumina reinforced composites. In particular, for the composite reinforced with 5 µm particles, some residual porosity was noticed on the polished surfaces, which led to a large scatter of the fracture strain and ultimate tensile strength under tensile tests [89]. It was hence important to verify whether this would lead to a large standard deviation in fracture testing as well. As seen on Figure 4-16a for three different specimens of the same casting, the values of $J_{GT}$ all fall between 2.7 and 3 kJ/m$^2$, although one notices some variation in the initial slope. Therefore, it is concluded that the residual microstructural defects in this material do not significantly influence the toughness. *J-R* curves measured on specimens coming from two different castings of the composite reinforced with the 15 µm particles are given in Figure 4-16b. We again note excellent reproducibility until the onset of ductile tearing, with $J_{GT}$ ranging between 5.5 and 6 kJ/m$^2$.

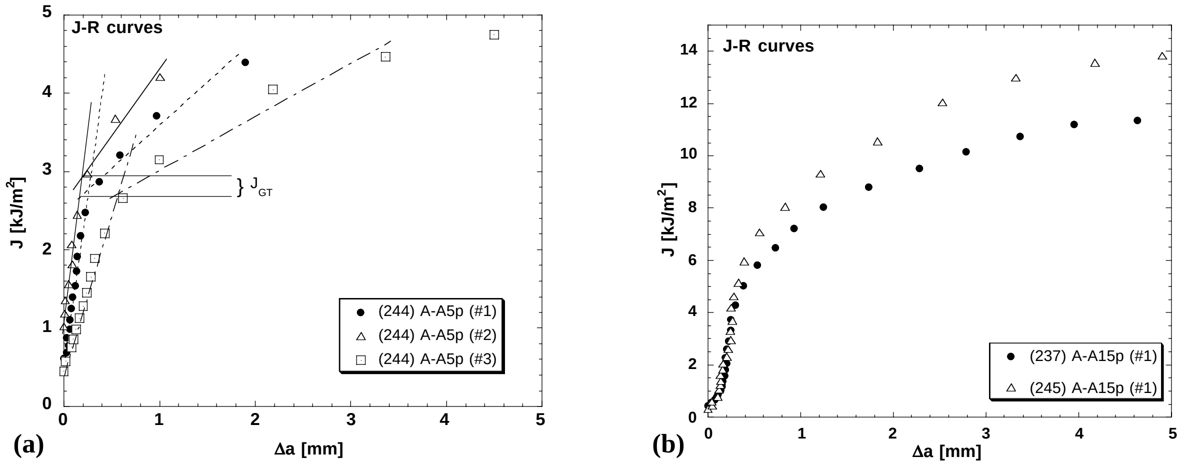

**Figure 4-16.** Verification of the reproducibility of $J_R$ curves in polygonal alumina reinforced composites. **(a)**: Al-Al$_2$O$_3$ 5 µm composite, 3 tests on the same casting; **(b)**: Al-Al$_2$O$_3$ 15 µm composite, 2 tests on different castings.

### iii. Aluminium-boron carbide composites

The fracture characteristics of B$_4$C reinforced composites for the various average sizes of reinforcements are shown in Figure 4-17. For clarity, the load-displacement curves of only three different composites are presented in Figure 4-17a, while typical *J-R* curves are given for all the composites in Figure 4-17b. As in the previous systems, the fracture energy is characterized by an obvious dependence on the particle size. The 60 µm particle size composite exhibits the most significant *J-R* curve behaviour, followed by the 35 and the 20 µm particle size composites which have a similar fracture response. The composite reinforced with 10 µm particles exhibits a significantly lower fracture energy, while the finest particle size composite (5 µm of average particle size) is the least resistant to fracture. The whole *J-R* curve could never be completely measured in this system because unstable crack always occured beyond the maximum load, indicating an almost flat *R*-curve.

The validity regime of *J*-controlled crack growth exhibits the same behaviour as the alumina reinforced composites, in that *J* is no longer valid after the initiation of stable ductile tearing.

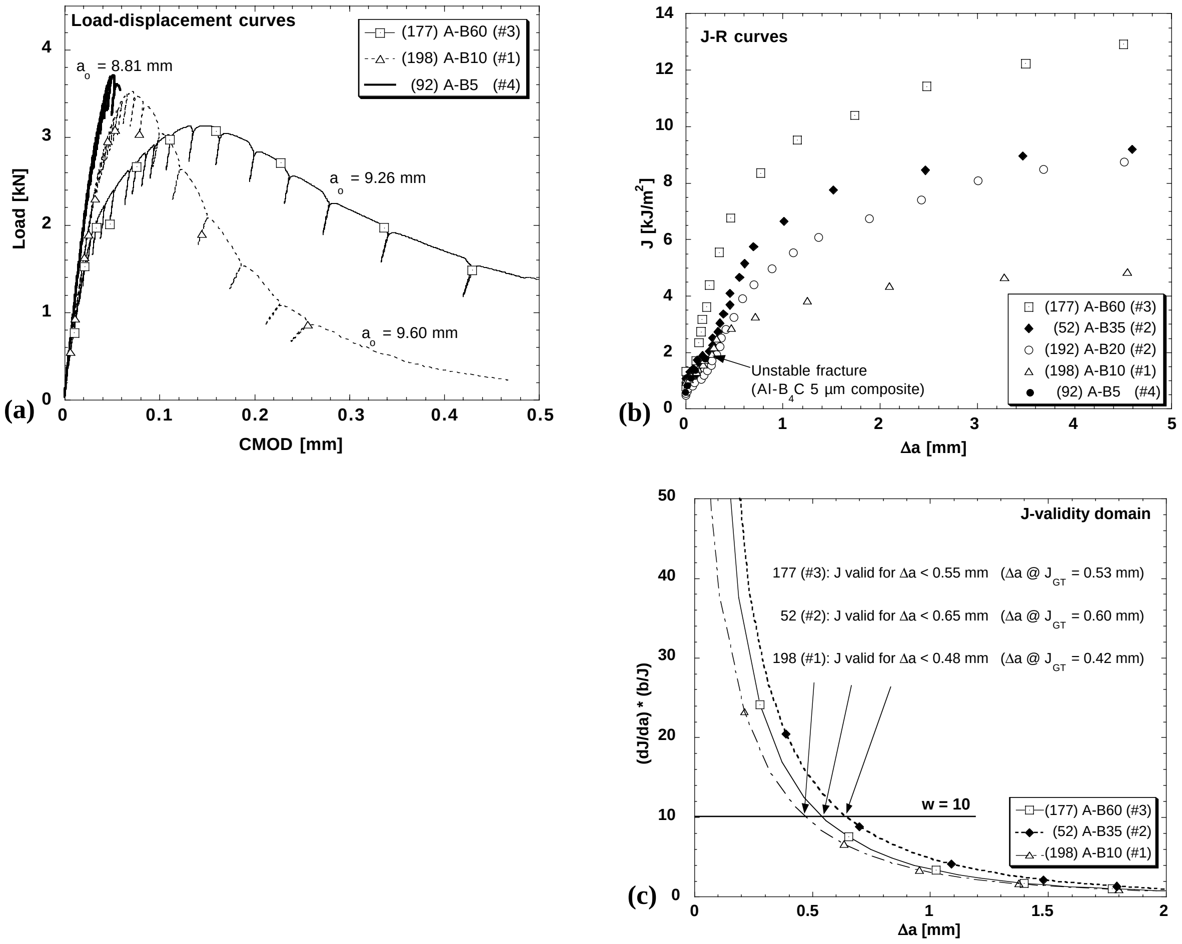

**Figure 4-17.** Crack-propagation behaviour in Al-$B_4C$ composites. **(a)**: load-displacement curves of three particle size composites (60, 10 and 5 µm), with loading cycles; **(b)**: *J-R* curves computed for all composites; **(c)**: validity domain according to the analysis of Hutchinson and Paris. All curves from non side-grooved specimens.

### REPRODUCIBILITY OF EXPERIMENTS

In Figure 4-18a, *J-R* curves of the largest particle size composites (A-B60) for two different specimens of the same casting are shown, while tests conducted on two specimens of different A-B10 composites are shown in Figure 4-18b. Good reproducibility is confirmed, specifically for $J_{GT}$.

The only exception common to all composites is the more stable crack propagation behaviour in the fine particle size composites when the crack intercepted a vein in the initial portion of the curve. All tests that presented this behaviour were discarded.

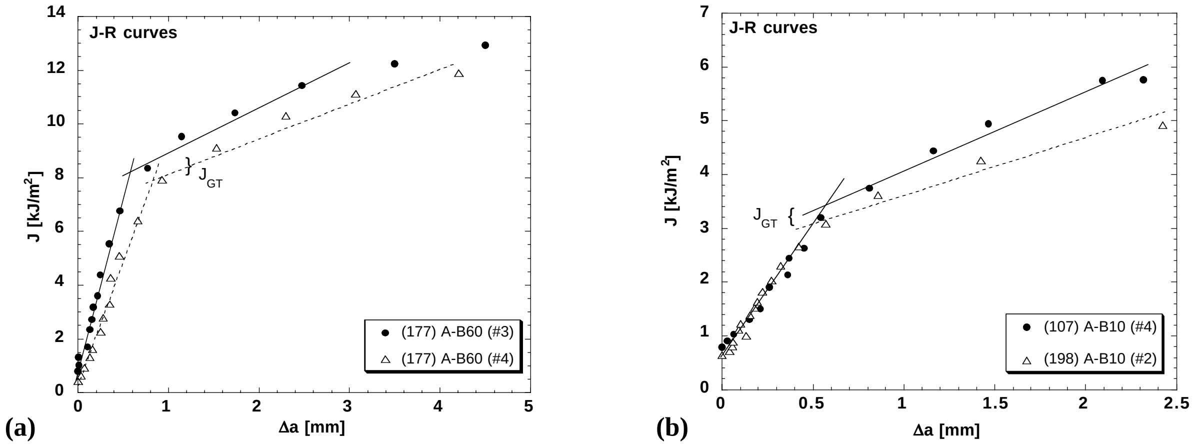

**Figure 4-18.** Verification of the reproducibility of the *J*-*R* curves in boron carbide reinforced composites. **(a)**: Al-$B_4C$ 60 µm composite, 2 tests on the same casting; **(b)**: Al-$B_4C$ 10 µm composite, 2 tests on different castings.

## *4.2.3 Influence of specimen geometry*

### i. *J*-*R* curves

Since many of the pure Al matrix composites exhibit large-scale yielding (see chapter 4.3) and loss of *J*-controlled fracture during crack growth, it can be expected that the *J*-*R* curves would exhibit a dependence on the specimen geometry. Hence, *J*-integral fracture tests on highly constrained side-grooved specimens were also conducted on all composites. A summary of the *J*-*R* curves measured on these specimens and comparison with non side-grooved specimens is given in Figures 4-19a and b for angular $Al_2O_3$ composites, in Figures 4-19c and d for polygonal $Al_2O_3$ composites, and in Figures 4-19e and f for $B_4C$ composites.

In all but two materials, the effect of specimen constraint appears at the onset of ductile tearing, and becomes more evident as the loss of *J* validity increases. It is thus more visible with materials exhibiting extensive *R*-curve behaviour, as seen for instance for the A-B60 (Figure 4-19e), the A-A35p (Figure 4-19c), and the A-A15p (Figure 4-19d ) composites, where the stable regime corresponds to a lower level of *J* that is, in addition, attained at lower $\Delta a$. The fracture energy at the initiation of ductile tearing $J_{GT}$ remains, nevertheless, almost unaffected. In materials with reduced *J*-*R* curve behaviour, namely in smaller particle size composites (roughly 10 µm and less, see Figure 4-19b for the A-A5a and Figure 4-19f for the A-B10 composites), side-grooves led to systematically unstable fracture in the descending part of the load-displacement curve; meaning that the reduction of the tearing modulus $T_R$ (due to larger triaxiality) as compared to the applied tearing modulus $T_A$ did not allow determination of the entire *J*-*R* curve. The occurence of unstable fracture in side-grooved specimens corresponds to the onset of ductile tearing for the non side-grooved specimen (*i.e.* to the end of the initial part of the curve), such that the value of $J_{GT}$ in side-grooved specimens fracturing in a catastrophic manner corresponds to that of smooth specimens.

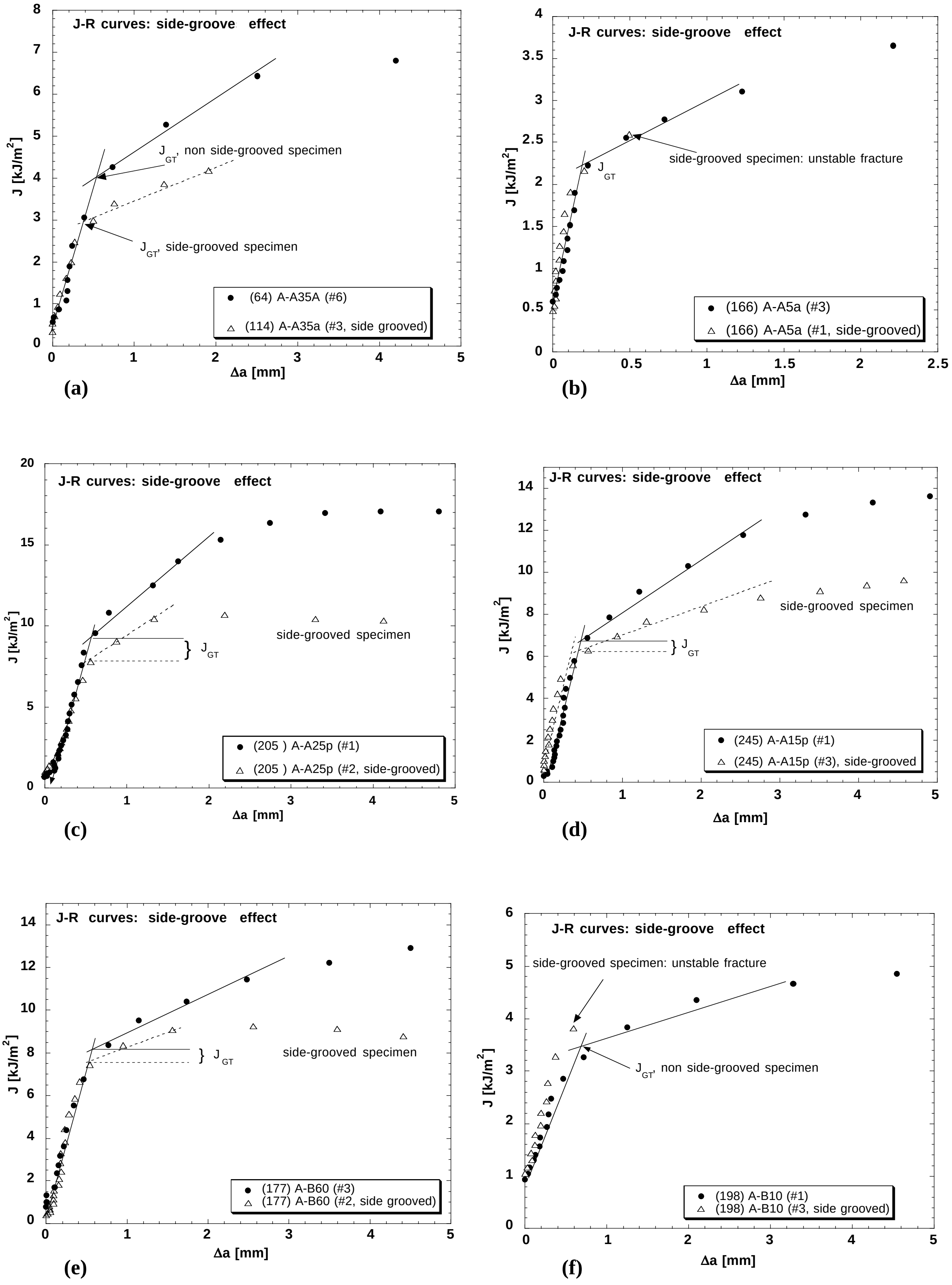

**Figure 4-19.** Effect of side-grooves on the *J-R* curves of pure Al composites. **(a)**: A-A35a composite; **(b)**: A-A5a composite; **(c)**: A-A25p composite; **(d)**: A-A15p composite; **(e)**: A-B60 composite; **(f)**: A-B10 composite. The highly constrained side-grooved specimens reduce the apparent ductile tearing resistance, but the value of *J* at initiation ($J_{GT}$) is not significantly affected, with the exception of (a).

An exception to the general rule that $J_{GT}$ measured on side-grooved specimens matches the value measured on non side-grooved specimens is however noticed for two angular alumina reinforced composites: the 35 µm particle size composite and the 10 µm particle size composite. In these, $J_{GT}$ is lower in the side-grooved specimens, as seen in Figure 4-19a for the A-A35a composite. This effect is attributed to the micromechanism of failure in these materials (section 4.2.6) that is more influenced by the stress triaxiality. In such cases, the toughness $J_{GT}$ measured on side-grooved samples is considered for the discussion, in order to ensure a geometrically independent fracture parameter.

The regime of *J*-controlled crack growth in the A-A25p and the A-B60 composites for the two different specimen geometries is shown in Figure 4-20. The region of *J*-validity is not affected by the specimen geometry, which is not surprising given the fact that the validity region is limited by the degree of crack propagation and not by the occurence of large scale yielding.

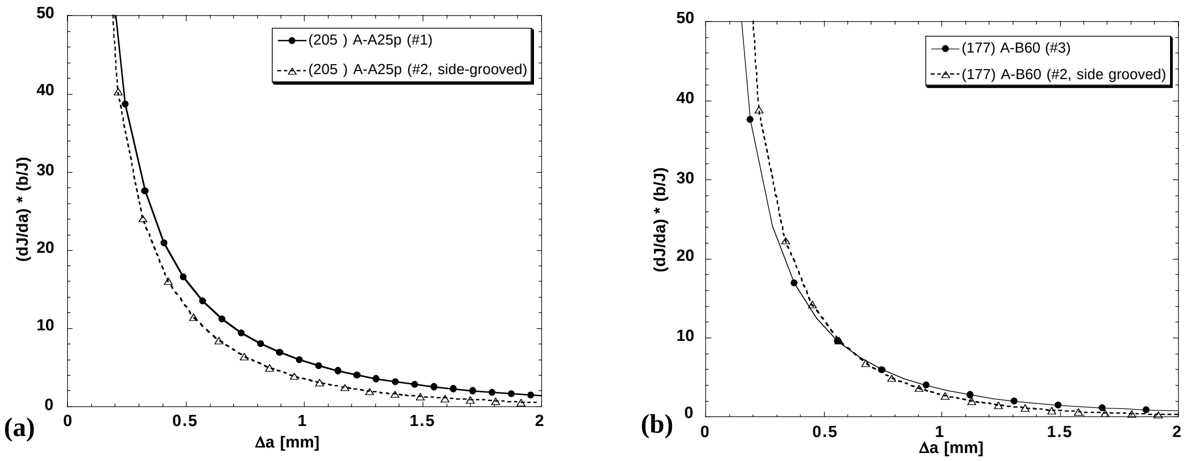

**Figure 4-20.** Comparison of the *J*-validity domain for the two specimen geometries, showing an absence of influence of side grooves. **(a)**: A-A25p composite; **(b)**: A-B60 composite.

### ii. Crack front shape

Qualitative information regarding the degree of stress triaxiality within the specimen is obtained by optical and binocular microscope observations of the pre-crack and of the ductile crack fronts. In flat surface specimens, the pre-crack has a more or less straight front, although the crack length is slightly longer in the center of the specimen, as seen in Figure 4-21a. In side-grooved specimens, the pre-crack after fatigue loading is longer on the surface of the specimen, as seen on Figure 4-21b. In this specific case, the crack front is best revealed under UV light using the fluorescent penetrant that was applied on the specimen surface after pre-cracking, Figure 4-21d.

After some degree of crack propagation during the fracture test, the crack front shape changes in flat specimens, as is also shown in Figures 4-15c and d: in the center of the specimen, the crack clearly propagates at a faster rate, which is regularly observed in ductile crack propagation and is due to higher stress triaxiality in the middle of the specimen. In side-grooved specimens on the other hand, the crack tip curvature remains unchanged during the fracture test, as shown in Figure 4-12b, indicating that the higher degree of stress triaxiality is well maintained along the specimen width. In some experiments, the grooves were machined within the specimen after fatigue pre-cracking, yielding the straighter crack front given in Figure 4-21c. The *J-R* curves measured on specimens side-grooved after pre-cracking were similar within the scatter to those obtained on specimens side-grooved prior to pre-cracking.

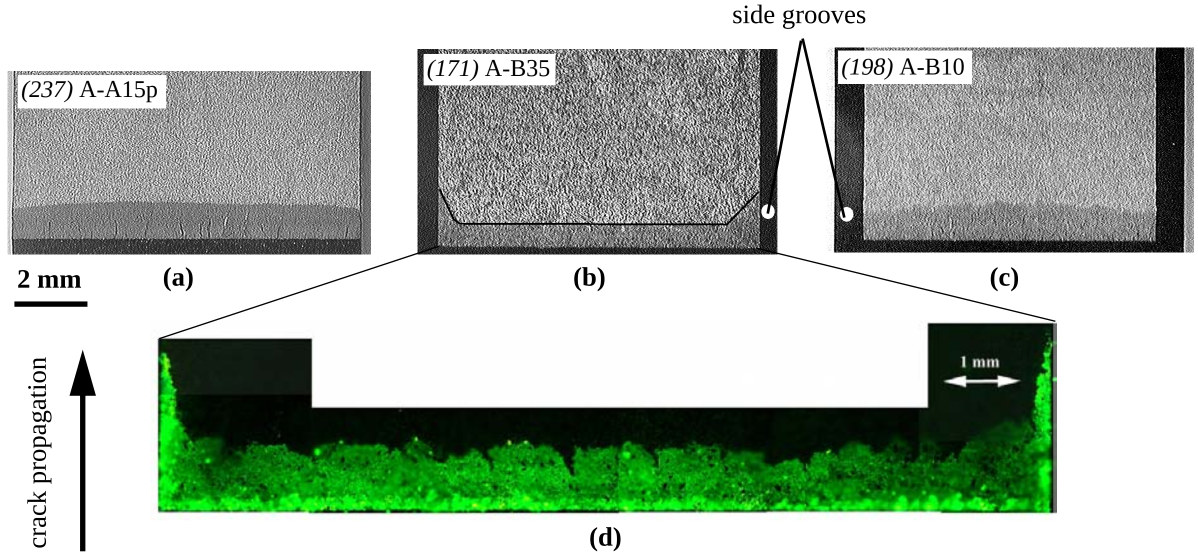

**Figure 4-21.** Binocular fractographic micrographs, illustrating the effect of side-grooves. **(a)**: flat surface specimen; **(b)**: side-grooved specimen, with the pre-crack front marked by a drawn line, **(c)**: specimen side-grooved after pre-cracking; **(d)**: same specimen as (b), the crack front is revealed under optical microscopy and UV light using the fluorescent penetrant introduced after pre-cracking. See also Figures 4-12 and 4-15 for visualization of crack fronts after ductile crack propagation.

## *4.2.4 Al-Cu matrix composites*

As was mentioned in the introduction of Chapter 4.2, a few *J*-resistance fracture tests were conducted on Al-Cu alloy matrix composites (with flat surface CT specimens), but not in a systematic manner due to the difficulty in pre-cracking. Values are not statistically representative (with the exception of material A2C-A15p). A more complete study of the fracture properties of these composites was conducted by chevron-notch testing, Section 4.5.

Tested composites were:

- *(253)*A2C-A15p in the solutionized (ST) condition (3 specimens);
- *(158)*A2C-A35a " " (1 " );
- *(256)*A2C-A60a " " (1 " );
- *(179)*A4.5-A35a as-cast (AC) " (1 " ).

**i. Angular alumina composites**

The load-displacement and *J*(Δa) curves of these composites are given in Figure 4-22. In all composites, unstable fracture occur at the peak load, such that *R*-curve behaviour by ductile tearing is not observed and the behaviour is *K*-dominated. For the Al-Cu2% matrix composites reinforced with the largest 60 µm particles (256), fully brittle behaviour is even noticed, *i.e.* no crack growth is detected before unstable fracture. A slight degree of crack propagation occurs in the 35 µm reinforced composite (158), which exibits a higher toughness. The Al-Cu4% matrix composite reinforced with 35 µm size particles (179) is characterized by a similar behaviour to the A2C-A35 composite, with a small degree of crack advance before catastrophic fracture.

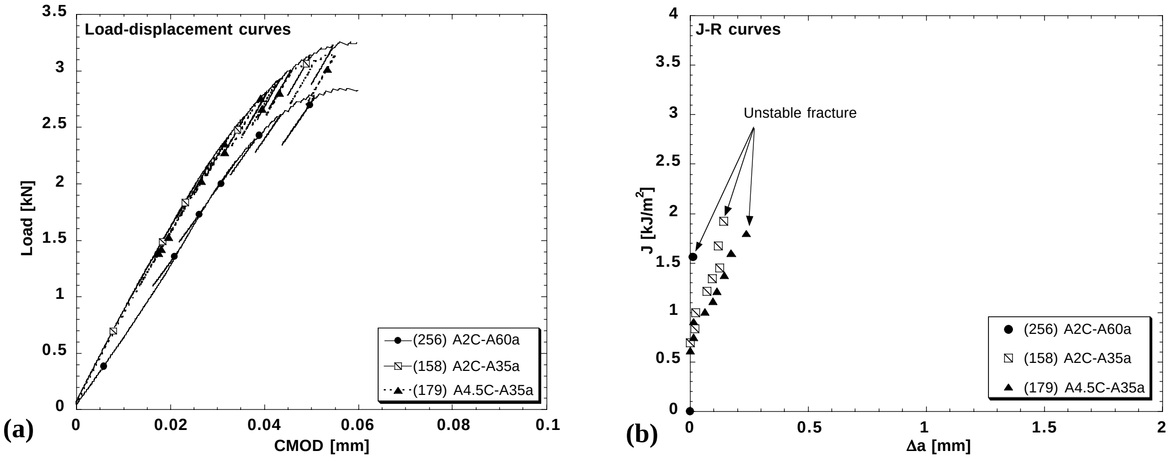

**Figure 4-22.** Crack-propagation behaviour in Al-Cu matrix/angular $Al_2O_3$ composites**.** **(a)**: load-displacement curves of three different materials; **(b)**: corresponding *J-R* curves illustrating the linear elastic behaviour.

### ii. Polygonal alumina composites

Three specimens of the same composite (Al-Cu2% / polygonal $Al_2O_3$ 15µm) were tested for this class of materials, and the fracture curves are given in Figure 4-23. Unstable fracture occurred just beyond the peak load in one specimen. One loading-reloading cycle was possible for the second specimen. The third specimen was arrested at the peak load and marked by fatigue loading. In contrast to angular alumina reinforced composites, the onset of ductile tearing is detected (Figure 4-23b) and the composites exhibit a fracture energy more than twice that of angular $Al_2O_3$-reinforced Al-Cu2% composites. The tests exhibit a good level of reproducibility, but compared to the pure Al matrix composites the *R*-curve behaviour is much reduced.

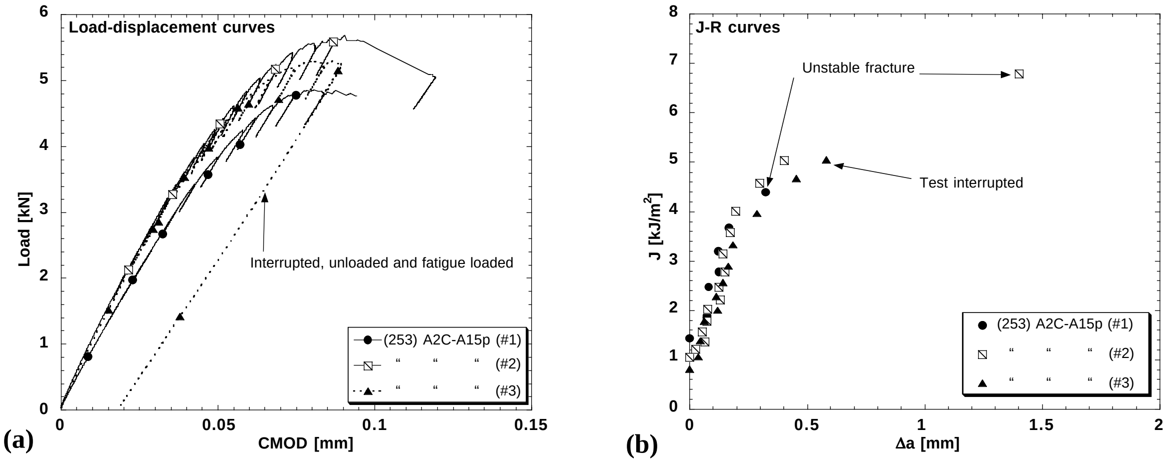

**Figure 4-23.** Crack-propagation behaviour in Al-2%Cu/polygonal 15µm $Al_2O_3$ composites (solution treated)**.** **(a)**: load-displacement curves of 3 different specimens of the same material; **(b)**: corresponding *J-R* curves, with the onset of ductile tearing recorded before unstable fracture.

### iii. Crack front shape

Fracture surface binocular macrographs of two specimens are shown in Figure 4-24. The fatigue pre-crack fronts exhibit an important curvature with almost no crack propagation by fatigue on the outer surface of the specimens (this is the reason why the determination of crack propagation was not possible by the the fluorescent penetrant method). This is a significant difference compared to the case of Al matrix composites, in which the crack front of flat specimens is almost straight after fatigue pre-cracking (see Figure 4-21a). Different crack curvature behaviour in MMCs depending on the matrix type has already been reported by Roebuck and Lord [94]. The curvature effect is an indication of residual stresses, which are seemingly higher in Al-Cu alloy matrix composites. Since the specimens are quenched after solid-solution heat treatment, one can attribute this effect to macroscopic residual quench stresses. The curvature can even be amplified due to microscopic residual stresses which are determined by the thermo-mechanical properties of the matrix.

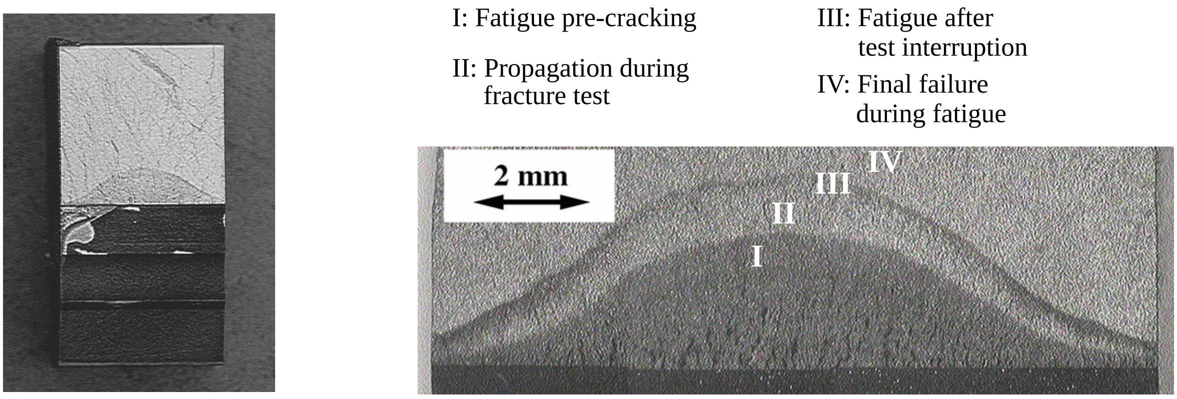
I: Fatigue pre-cracking
II: Propagation during fracture test
III: Fatigue after test interruption
IV: Final failure during fatigue
2 mm
IV
III
II
I

**(a)** *(253)*A2C-A15p (#1) **(b)** *(253)*A2C-A15p (#3)

**Figure 4-24.** Fracture surfaces of A2C-A15p composite (solution treated). **(a)**: low magnification micrograph, showing the pre-crack curvature effect; **(b)**: higher magnification micrograph of a specimen marked in fatigue, the crack growth extent during fracture testing is larger in the center.

After monotonic fracture testing up to the peak load, the crack propagates more rapidly in the specimen center, enhancing again the differences in crack length between the specimen edges and the center, Figure 4-24b. As compared to pure Al matrix composites, this effect is however less marked, as seen by comparing with Figures 4-15c and d. The crack curvature effect prevents full validation of the toughness values measured on CT specimens because the straight crack front criterion of the standard is violated. One notes that this specific criterion is the most frequent source of invalidity reported in fracture testing of PRMMCs [94].

### *4.2.5 Summary of data*

The fracture data have so far been presented for the individual composite types. Comparing the *J-R* curves of the various composite systems for roughly equivalent size of reinforcements provides a clearer insight into the influence of the reinforcement type, Figure 4-25. These curves show unambiguously that polygonal alumina composites yield the highest toughness, followed by boron carbide composites, while angular alumina composites exhibit the lowest toughness. This is especially obvious for large (Figure 4-25a) and medium sizes of reinforcement (Figure 4-25b). For the smallest particle sizes, however, the difference between the different classes of composites is largely reduced (Figure 4-25c).

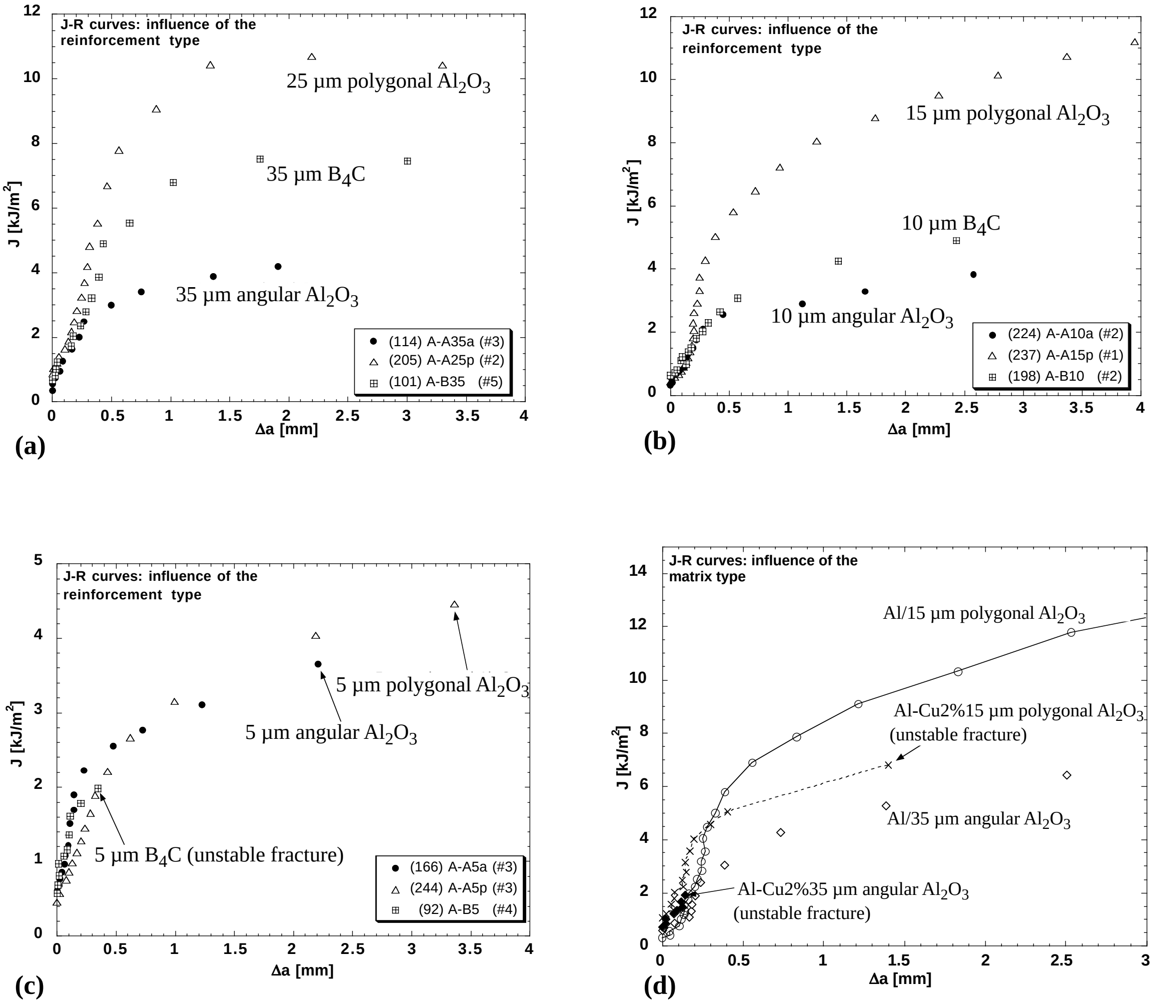

**Figure 4-25.** Comparison of *J-R* curves for equivalent particle size composites but different reinforcement type or matrix. **(a)**: large particle size composites (side-grooved specimens); **(b)**: medium particle size composites (flat specimens); **(c)** fine particle size composites (flat specimens); **(d)**: matrix effect for 35 µm angular $Al_2O_3$ and 15 µm polygonal $Al_2O_3$ composites (flat specimens).

The influence of the matrix is shown in Figure 4-25d. In angular alumina reinforced composites, the resistance to ductile tearing is apparently fully lost with an alloyed matrix and the $J$ value at unstable fracture (which corresponds to $J_{GT}$ in pure Al matrix composites) decreases as well. In polygonal alumina reinforced composites, the fracture energy $J_{GT}$ at initiation of macroscopic crack propagation decreases slightly for Al-Cu matrix composites, and one notices that the crack propagation length at the end of the initial part is lower as well. The matrix influences to a much stronger extent the ductile tearing regime, since unstable fracture occurs in this regime with alloyed matrix. Additional comments concerning the toughness of Al-Cu matrix composites and the meaning of their measured *J-R* curves will presented in more details in Section 4.5 and in the discussion.

The fracture energy data in terms of $J_{0.2}$ and $J_{GT}$ are given for all materials tested in Table 4-3. For all the composites but A-A10a and A-A35a, the values of $J_{GT}$ are the average measures for both specimen geometries (with and without side-grooves). For A-A10a and A-A35a, the average fracture energy measured on the two specimen geometries are indicated. The equivalent toughness values $K_{\text{eq-0.2}}$ and $K_{\text{eq-GT}}$, computed from

$$K_{\text{eq}-0.2} = \sqrt{\frac{J_{0.2}E}{1-\nu^2}} \quad \text{and} \quad K_{\text{eq}-GT} = \sqrt{\frac{J_{\text{GT}}E}{1-\nu^2}} \tag{4-1}$$

are also given for all the composites. The tensile characteristics are from reference [89]. Also included in the table is the specimen size criterion according to the ASTM standard:

$$B_{\text{c}} = 25 \cdot J_{\text{GT}}/\sigma_{\text{y}} < B \quad \text{where} \quad \sigma_{\text{y}} = \left(\sigma_{0.2} + \sigma_{\text{UTS}}\right)/2 \tag{4-2}$$

The specimen thickness being 13 mm and the initial ligament length $b_0$ about 10 to 11 mm, all the $J_{\text{GT}}$ data satisfy ASTM requirements. The tensile data for the few Al-Cu matrix composites tested by *J*-integral testing are from the results given in Section 4.3.

**Table 4-3.** Average fracture energy data, given in terms of both *J* and equivalent stress intensity factors *K*. With the exception of the A-A35a and A-A10a materials, the data are averages from the two different specimen geometries. Tensile characteristics and validity criteria according to (4-2) are also given.

| Composite designation | $J_{0.2}$ [kJ/m$^2$] | $K_{\text{eq-0.2}}$ [MPa·m$^{1/2}$] | $J_{\text{GT}}$ [kJ/m$^2$] | $K_{\text{eq-GT}}$ [MPa·m$^{1/2}$] | E [GPa] | $\sigma_{0.2}$ [MPa] | $\sigma_{\text{UTS}}$ [MPa | $B_{\text{c}}$ [mm] |
|---|---|---|---|---|---|---|---|---|
| A-A35a* | 1.6 ± 0.4 | 15.6 ± 1.8 | 4.4 ± 0.2 | 25.8 ± 0.7 | 141 | 80 | 125 | 1.07 |
| ° | 1.9 ± 0.3 | 18.3 ± 0.8 | 3.1 ± 0.4 | 21.6 ± 0.9 | | | | 0.76 |
| A-A20a | 0.6 ± 0.03 | 9.5 ± 0.3 | 1.2 ± 0.1 | 13.9 ± 0.8 | 148 | 91 | 114 | 0.30 |
| A-A10a* | 1.5 ± 0.2 | 16.2 ± 0.8 | 2.0 ± 0.4 | 18.7 ± 1.9 | 164 | 134 | 194 | 0.30 |
| ° | 1.5 | 16.4 | 1.6 | 17.0 | | | | 0.24 |
| A-A5a | 2.3 ± 0.2 | 17.8 ± 0.7 | 2.2 ± 0.2 | 17.6 ± 0.8 | 133 | 154 | 245 | 0.28 |
| A-A25p | 2.8 ± 0.05 | 23.0 ± 0.2 | 8.5 ± 0.5 | 40.4 ± 1.2 | 175 | 117 | 189 | 1.39 |
| A-A15p | 2.8 ± 0.9 | 25.2 ± 3.2 | 5.4 ± 0.3 | 32.5 ± 0.8 | 175 | 120 | 229 | 0.77 |
| A-A5p | 2.0 ± 0.5 | 19.1 ± 2.6 | 2.6 ± 0.1 | 22.2 ± 0.4 | 176 | 158 | 190 | 0.37 |
| A-B60 | 2.9 ± 0.4 | 22.7 ± 1.7 | 7.1 ± 0.4 | 35.9 ± 1.0 | 169 | 91 | 132 | 1.58 |
| A-B35 | 2.5 ± 0.4 | 22.2 ± 1.6 | 5.4 ± 0.4 | 32.6 ± 1.2 | 185 | 133 | 204 | 0.80 |
| A-B20 | 1.8 ± 0.7 | 17.9 ± 1.7 | 4.0 ± 0.1 | 27.3 ± 0.5 | 170 | 119 | 194 | 0.64 |
| A-B10 | 1.8 ± 0.2 | 17.4 ± 0.9 | 3.2 ± 0.3 | 23.5 ± 1.0 | 161 | 173 | 273 | 0.36 |
| A-B5 | 1.9 ± 0.4 | 18.4 ± 1.8 | 2.1 ± 0.4 | 19.1 ± 1.9 | 167 | 167 | 272 | 0.24 |
| A2C-A60a (ST) | - | - | 1.56 | 16.5 | 144 | 97 | 97 | 0.40 |
| A2C-A35a (ST) | - | - | 1.9 | 17.2 | 142 | 180 | 190 | 0.26 |
| A4.5C-A35a (AC) | - | - | 1.8 | 16.5 | 142 | 204 | 204 | 0.22 |
| A2C-A15p (ST) | 3.9 ± 0.3 | 26.9 ± 1.1 | 4.3 ± 0.2 | 28.4 ± 0.5 | 175 | 235 | 345 | 0.37 |

* non side-grooved specimen
° side-grooved specimen

As explained earlier, the parameter we take to be representative of the composite fracture resistance irrespectively of the specimen geometry is $J_{\text{GT}}$ and its equivalent toughness $K_{\text{eq-GT}}$. The data from Table 4-3 are summarized by plotting these critical fracture parameters as a function of particle size (Figure 4-26) and interparticle distance $\lambda_{\text{c}}$ (Figure 4-27). Again, the better properties achieved in polygonal particle reinforced composites are well illustrated. The effect of particle size is also evident on these plots for the polygonal $Al_2O_3$ and the $B_4C$ reinforced composites, namely that toughness increases as the average particle size increases. For the angular $Al_2O_3$ reinforced composites on the other hand, the largest particles also yield the toughest composites, but the A-A5a composite has a slightly larger fracture energy than the A-A10a composite. This difference almost vanishes when the toughness is expressed in terms of $K_{eq\text{-}GT}$ because it is compensated by the higher Young's modulus of the A-A10a composite. The 20 µm angular $Al_2O_3$ reinforced composite (shown into brackets) exhibits the lowest fracture energy, and is a special case that will be explained later.

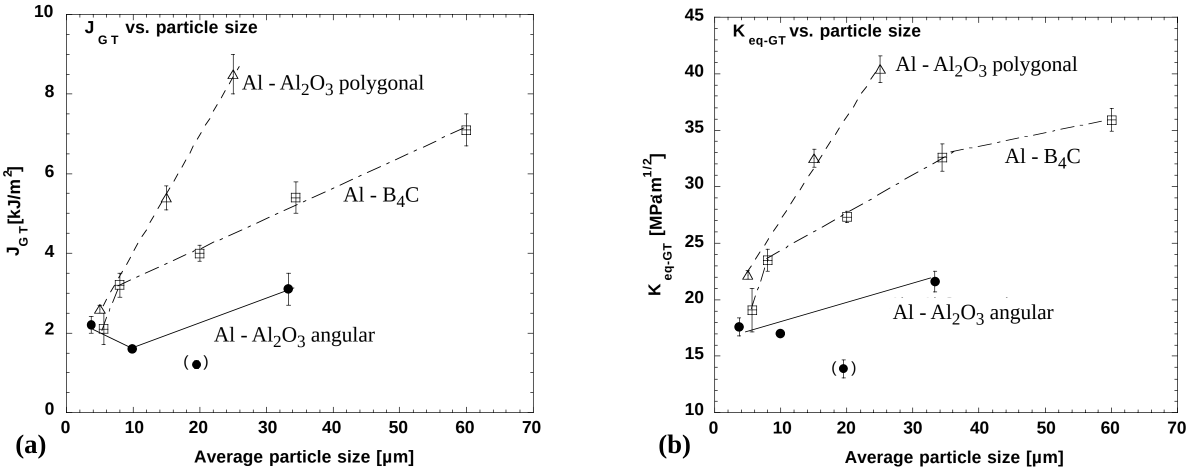

**Figure 4-26.** Composite fracture toughness vs. average reinforcement size, expressed in terms of **(a)**: *J*-fracture energy, $J_{GT}$; and **(b)**: its equivalent stress intensity factor, $K_{eq\text{-}GT}$.

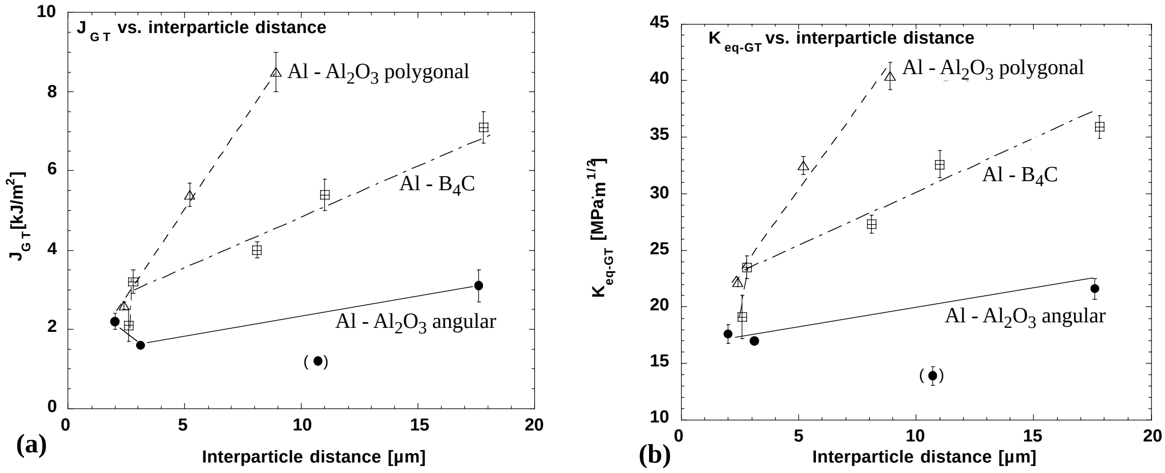

**Figure 4-27.** Composite fracture toughness vs. interparticle distance, expressed in terms of **(a)**: *J*-fracture energy, $J_{GT}$; and **(b)**: its equivalent stress intensity factor, $K_{eq\text{-}GT}$.

### *4.2.6 Pure Al matrix composites: fracture micromechanisms*

The investigations related to the determination of the dominant micromechanism modes of failure in pure aluminium matrix composites are presented in this section; these include optical and electron microscope observations. As for the fracture toughness investigations, the results concerning the micromechanisms of fracture in Al-Cu matrix composites are presented in Section 4.5 devoted to chevron-notch testing.

#### i. Arrested-crack method: crack profiles

ALUMINIUM-ANGULAR ALUMINA COMPOSITES

Metallographic observations near the crack tip (along the crack path or in the crack tip process zone) for Al angular $Al_2O_3$ composites are given in Figure 4-28. In the composites reinforced by 35 or 10 µm particles (Figures 4-28a, b and d), the dominant fracture mode is particle cracking. The whole failure process is hence governed by particle fracture in the process zone (Figure 4-28b), which subsequently nucleates voids in the matrix. The crack eventually propagates by coalescence of these voids between broken particles. In the 10 µm particle size composite, the fraction of broken particles is smaller than in the 35 µm composite. One also notices that the bimodal particle size distribution plays a role in that larger than average particles are more often cracked.

In the 20 µm particle size composite, the crack propagates by decohesion at the particle/matrix interface, as seen in Figure 4-28c. Only intact particles are found on the crack faces. This composite is the only one featuring this failure mode, which seems to result from a lower interfacial strength of the metal/ceramic interface.

Observation of the 5 µm particle size composite by optical microscopy is difficult because the microstructure length scale approaches that of the microscope resolution. Observation under the SEM on gold-coated metallographic samples (Figure 4-28e) reveals much less particle cracking in this composite than in those reinforced with 35 and 10 µm particles (a thin layer of matrix directly adjacent to the crack is indeed seen on the picture). Rather, the crack propagates mainly by void nucleation, growth and coalescence throughout the matrix, as also confirmed by fractographic investigations (see next section).

ALUMINIUM-POLYGONAL ALUMINA COMPOSITES

Optical micrographs of the crack path (near the tip) are given in Figure 4-29 for Al polygonal $Al_2O_3$ composites. Clearly, cracks propagate predominantly by the ductile mechanism of matrix voiding in all such composites, with only few broken particles along the crack path, found with 25 µm particles. Higher magnification observations in the 25 µm (Figure 4-29b) and the 15 µm (Figure 4-29e) particle composites reveal that the ductile dimples are nucleated at the particle poles and that their size is limited by the interparticle distance. A higher magnification SEM micrograph of a 25 µm composite sample that was electropolished prior to observation is given in Figure 4-29c: it shows in a clear manner how the crack passes around the particles.

The details are not as clearly seen in the 5 µm composite because we attain the resolution limit of the microscope, but a thin layer of matrix in the form of small dimples is nevertheless well visible (Figures 4-29e and f).

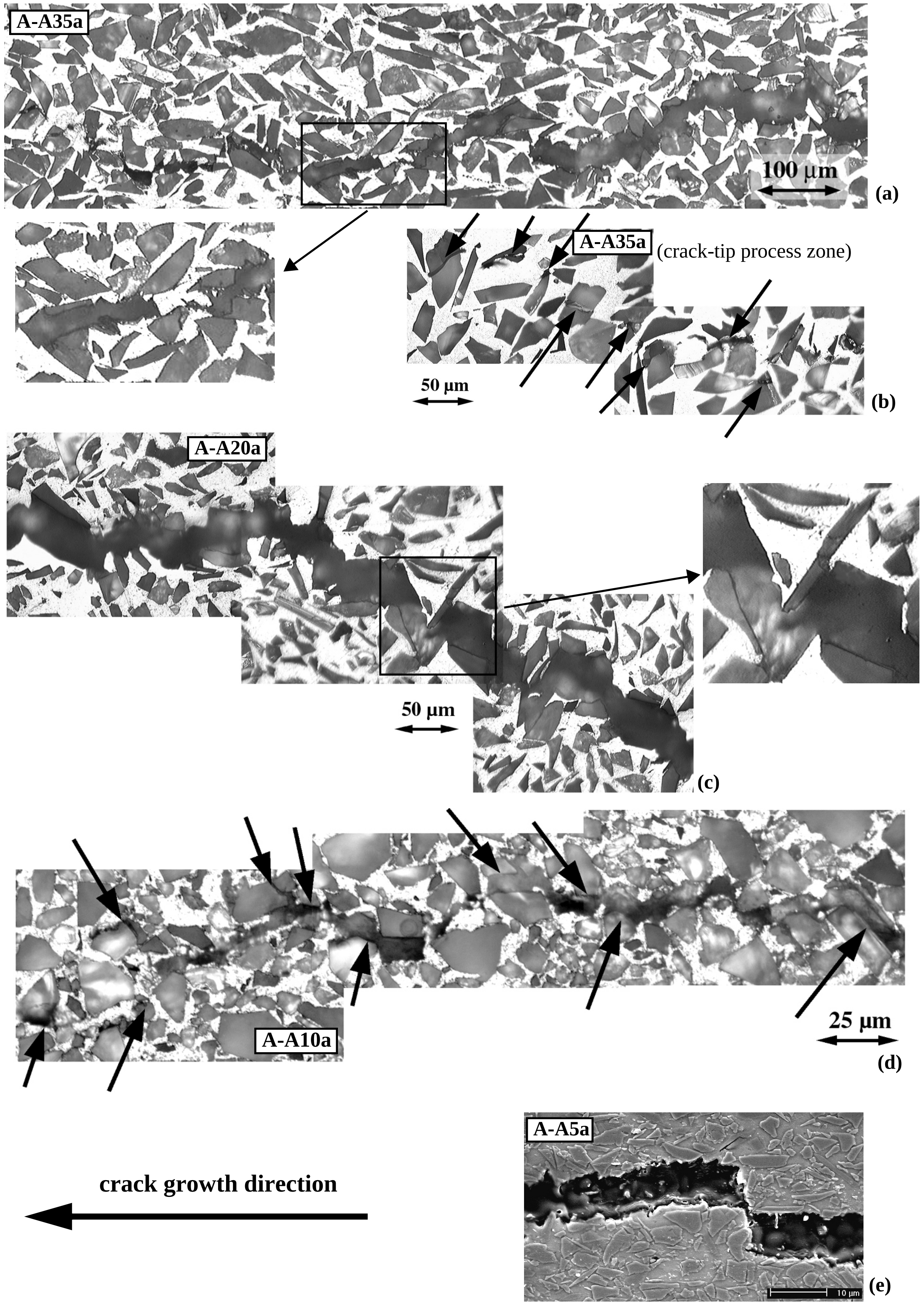
A-A35a
100 µm
(a)
A-A35a
(crack-tip process zone)
50 µm
(b)
A-A20a
50 µm
(c)
A-A10a
25 µm
(d)
A-A5a
crack growth direction
10 µm
(e)

**Figure 4-28.** Angular $Al_2O_3$ reinforced composites: optical micrographs near the crack tip of interrupted fracture tests showing the dominant micromechanisms of fracture. **(a)** and **(b)**: Al-$Al_2O_3$ 35 µm (crack path and process zone), particle cracking; **(c)**: Al-$Al_2O_3$ 20 µm, interfacial decohesion; **(d)**: Al-$Al_2O_3$ 10 µm, particle cracking; **(e)**: SEM micrograph of Al-$Al_2O_3$ 5 µm, failure through the matrix by matrix voiding. In (b) and (d) arrows indicate broken particles. Crack growth direction from right to left.

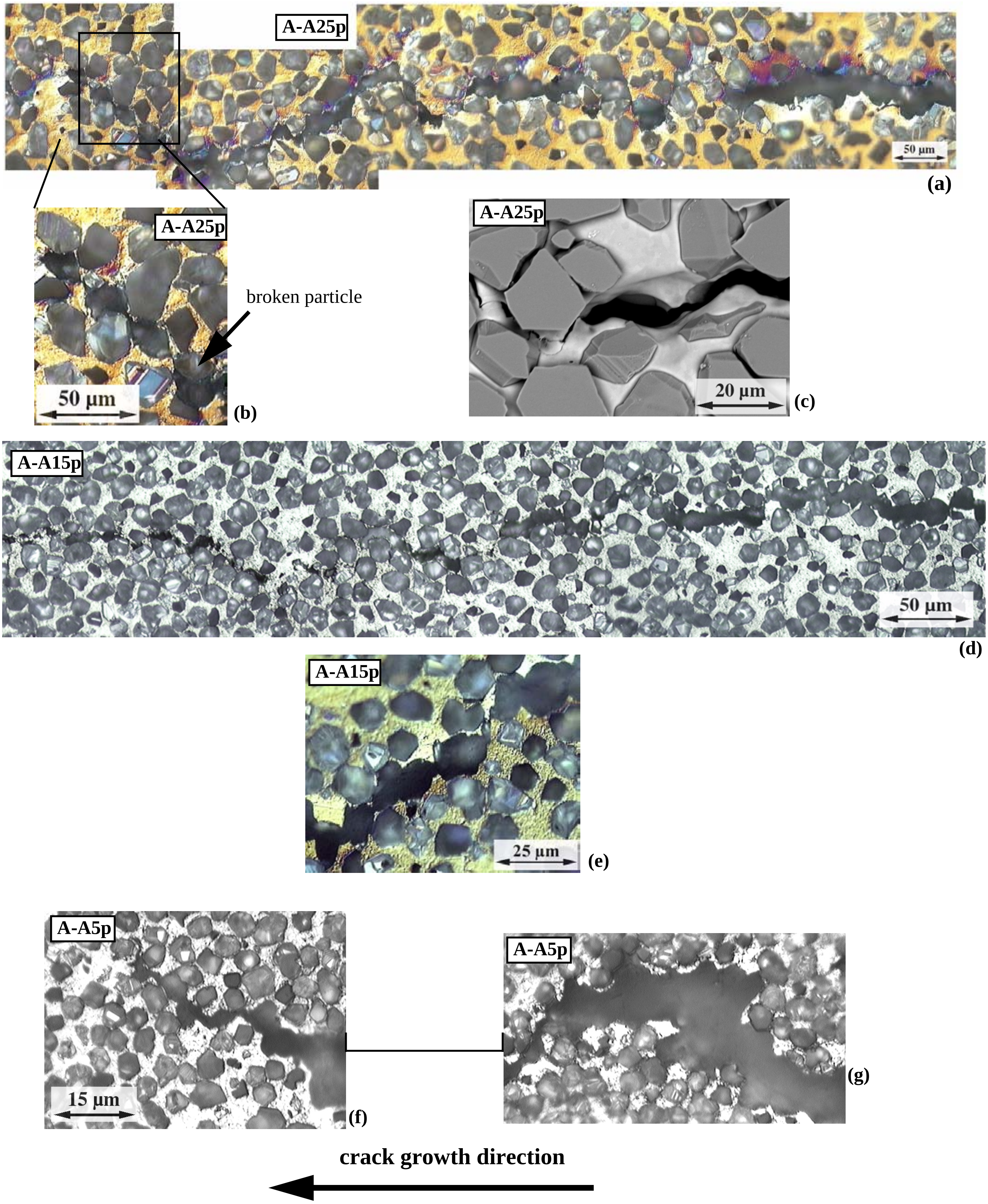
A-A25p
50 µm
(a)
A-A25p
broken particle
50 µm
(b)
A-A25p
20 µm
(c)
A-A15p
50 µm
(d)
A-A15p
25 µm
(e)
A-A5p
15 µm
(f)
A-A5p
(g)
crack growth direction

**Figure 4-29.** Polygonal $Al_2O_3$ reinforced composites: optical micrographs near the crack tip of interrupted fracture tests showing the dominant micromechanisms of fracture. **(a)** and **(b)**: Al-$Al_2O_3$ 25 µm, matrix voiding and few particle cracking; **(c)**: same material, SEM micrograph of an electropolished sample; **(d)** and **(e)**: Al-$Al_2O_3$ 15 µm at different magnification, matrix voiding; **(e)** and **(f)**: Al-$Al_2O_3$ 5 µm (same specimen at various locations along the crack path), matrix voiding. Crack growth direction from right to left. Color contrast in (a), (b) and (e) due to a DIC filter.

### ALUMINIUM-BORON CARBIDE COMPOSITES

Optical and SEM micrographs of the crack profile of $B_4C$ reinforced composites are given in Figure 4-30. The crack propagates predominantly by nucleation, growth, and coalescence of cavities within the matrix, but a significant amount of broken particles are also found along the crack path. We may actually differentiate three types of failure modes:

(i) in the 60 µm particle size composite, there is approximately an equivalent amount of cavities nucleated in the matrix and by particle cracking, as seen on Figure 4-30a-c at three different locations of the crack path (note that cracked particles located distant from the crack plane are broken mainly during polishing);

(ii) in the 35 µm, the 20 µm and the 10 µm composites, particle cracking is significantly reduced compared to the above case, and voids are mainly nucleated in the matrix. A crack profile of the A-B35 composite is shown in Figure 4-30d, a higher magnification view of the crack path in the A-B20 composite is given in Figure 4-30e, and a SEM micrograph ahead of the crack tip showing voids nucleated within the matrix in the A-B10 composite is given in Figure 4-30f;

(iii) in the 5 µm particle size composite, crack propagation occurs also mainly by matrix cavitation, as seen on the SEM micrograph of Figure 4-30g, but we note in addition some cracking of the large reaction phases (Figure 4-30h) that are formed in this material even for short infiltration times.

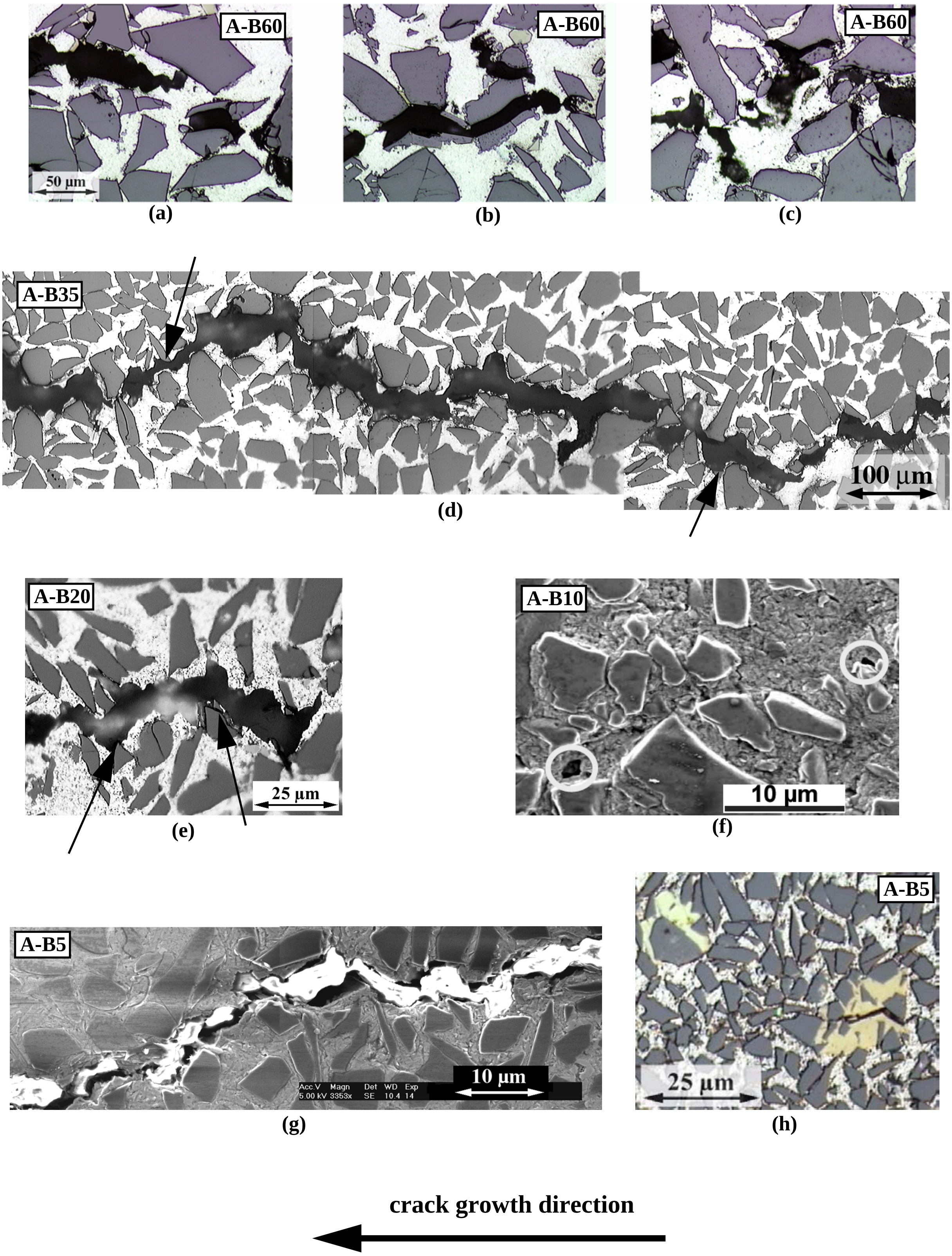
A-B60
50 µm
(a)
A-B60
(b)
A-B60
(c)
A-B35
100 µm
(d)
A-B20
25 µm
(e)
A-B10
10 µm
(f)
A-B5
Acc.V Magn Det WD Exp
5.00 kV 3353x SE 10.4 14
10 µm
(g)
A-B5
25 µm
(h)
crack growth direction

**Figure 4-30.** $B_4C$ reinforced composites: optical micrographs taken near the crack tip of interrupted fracture tests showing the dominant micromechanisms of fracture. **(a)**, **(b)** and **(c)**: Al-$B_4C$ 60 µm, matrix voiding and particle cracking; **(d)**: Al-$B_4C$ 35 µm, matrix voiding and few particle cracking; **(e)**: Al-$B_4C$ 20 µm, detail of the crack path (matrix voiding); **(f)**: Al- $B_4C$ 10 µm, SEM micrograph showing nucleated voids in the process zone; **(g)**: Al-$B_4C$ 5 µm, SEM micrograph illustrating matrix voiding; **(h)**: Al-$B_4C$ 5 µm, cracking of reaction phases. Broken particles indicated by arrows, crack growth direction from right to left, except for (f).

### ii. SEM fractography

ALUMINIUM-ANGULAR ALUMINA COMPOSITES

Fracture surfaces of angular $Al_2O_3$ reinforced composites observed under the SEM are shown in Figure 4-31. Such observations complement those made on crack profiles: in the 35 µm reinforced composites (Figure 4-31a), broken particles are generally found at the bottom of relatively large dimples (of approximately the same size as the particles), confirming the fact that the large voids are nucleated by broken particles. In the 10 µm reinforced composites (Figure 4-31b) cracked particles are also observed and are surrounded by many smaller dimples (much smaller than in the A-A35a composite), indicating that fracture occurs both by particle cracking and by matrix-nucleated voiding. The fracture surface of the 20 µm reinforced composite (Figure 4-31c) is almost exclusively constituted of particles and flat matrix interface facets. The interfacial failure mode is confirmed by the presence of a secondary crack on the picture, where debonding is unambiguously seen. Finally, in the 5 µm particle composite (Figure 4-31d), the fracture surface is made of fine dimples with very few broken particles, such that it can be concluded that fracture is governed by matrix voiding in this composite.

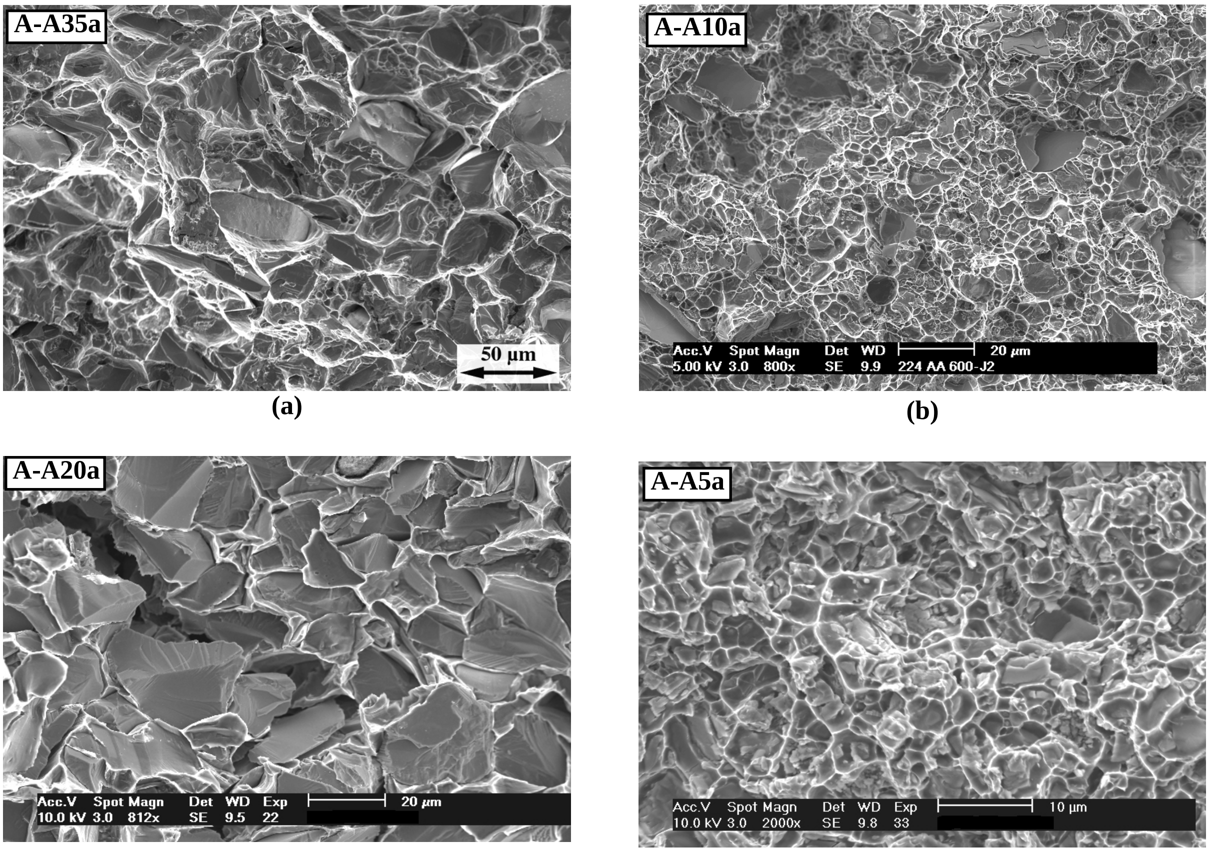
A-A35a
50 µm
A-A10a
Acc.V Spot Magn Det WD 20 µm
5.00 kV 3.0 800x SE 9.9 224 AA 600-J2
A-A20a
Acc.V Spot Magn Det WD Exp 20 µm
10.0 kV 3.0 812x SE 9.5 22
A-A5a
Acc.V Spot Magn Det WD Exp 10 µm
10.0 kV 3.0 2000x SE 9.8 33

(a) (b)

(c) (d)

**Figure 4-31.** SEM fractographs of Al-angular $Al_2O_3$ composites. **(a)**: Al-$Al_2O_3$ 35 µm, cracked particles and large dimples; **(b)**: Al-$Al_2O_3$ 10 µm, cracked particles and small dimples; **(c)**: Al-$Al_2O_3$ 20 µm, interfacial debonding; **(d)**: Al-$Al_2O_3$ 5 µm, small dimples and few cracked particles.

### ALUMINIUM-POLYGONAL ALUMINA COMPOSITES

SEM fractographs of polygonal $Al_2O_3$ reinforced composites presented in Figure 4-32 establish in a clear way the ductile failure mode by micro-cavitation in these materials. In addition, comparison of the composites at the same magnification (A-A25p, Figure 4-32a; A-A15p, Figure 4-32b; and A-A5p, Figure 4-32c) illustrates that the narrowly distributed size of the ductile dimples scales with the characteristic composite microstructural length. In other words, the growth of cavities is controlled by the thickness of the aluminium layer available between neighbouring particles, *i.e.* by the interparticulate distance, such that the final cavity size increases with increasing reinforcement size. The micrograph given in Figure 4-32d ( A-A25p composite) shows the sharp border between the fatigue pre-crack and the initiation sites of the ductile fracture process.

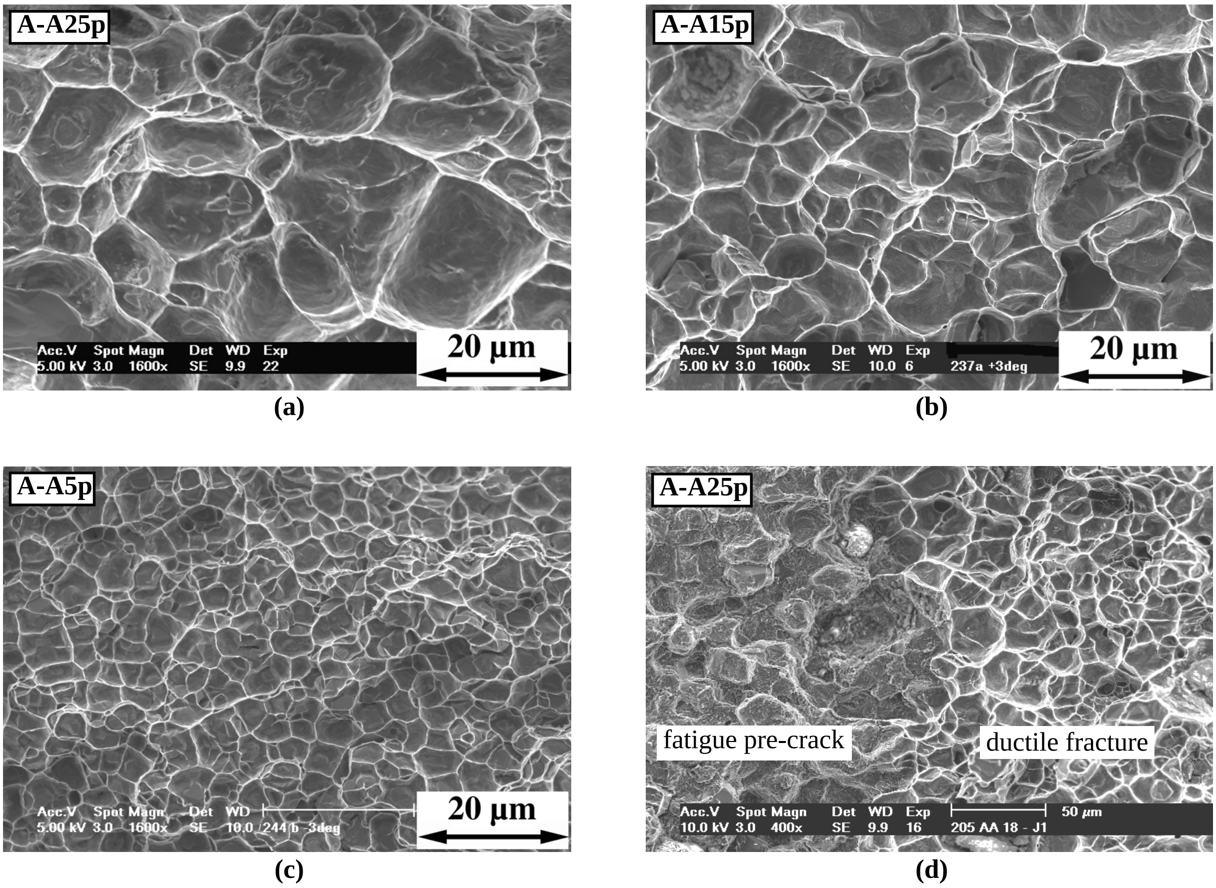
A-A25p
Acc.V Spot Magn Det WD Exp
5.00 kV 3.0 1600x SE 9.9 22
20 µm
A-A15p
Acc.V Spot Magn Det WD Exp
5.00 kV 3.0 1600x SE 10.0 6 237a +3deg
20 µm
A-A5p
Acc.V Spot Magn Det WD
5.00 kV 3.0 1600x SE 10.0 244b 3deg
20 µm
A-A25p
fatigue pre-crack
ductile fracture
Acc.V Spot Magn Det WD Exp
10.0 kV 3.0 400x SE 9.9 16 205 AA 18 - J1
50 µm

**(a)** **(b)** **(c)** **(d)**

**Figure 4-32.** SEM fractographs of Al-polygonal $Al_2O_3$ composites. **(a)**: Al-$Al_2O_3$ 25 µm; **(b)**: Al-$Al_2O_3$ 15 µm; **(c)**: Al-$Al_2O_3$ 5 µm, images acquired at the same magnification illustrating scaling of the cavity size with the average reinforcement size. **(d)**: Al-$Al_2O_3$ 25 µm, boundary between the fatigue pre-crack and the initiation of ductile fracture.

### ALUMINIUM-BORON CARBIDE COMPOSITES

Fractographic observations by SEM of $B_4C$ reinforced composites are presented in Figure 4-33. While fracture occurs mainly by ductile cavitation within the matrix in the large particle size composites (A-B60, Figure 4-33a; A-B35, Figure 4-33b), a significant degree of particle cracking is noticed. This is more extensive than in the polygonal $Al_2O_3$ reinforced composites, but much less than in the angular $Al_2O_3$ composites. When broken particles are found, they are surrounded by walls of large deformed matrix. As in the polygonal $Al_2O_3$ composites, the dimple size scales with the average particle size and with the interparticle distance (compare Figures 4-33a and b, taken at the same magnification). Broken particles are no longer observed in the fine 5 µm particle size reinforced composites (Figure 4-33c), and the dimples are about one order of magnitude smaller than in the largest particle composites. The border of the fatigue pre-crack with the beginning of the ductile failure region in the A-B60 composite is shown in Figure 4-33d. The initiation of the ductile crack propagation is again well detected, and we note an equivalent level of nucleation sites in the matrix and by particle cracking.

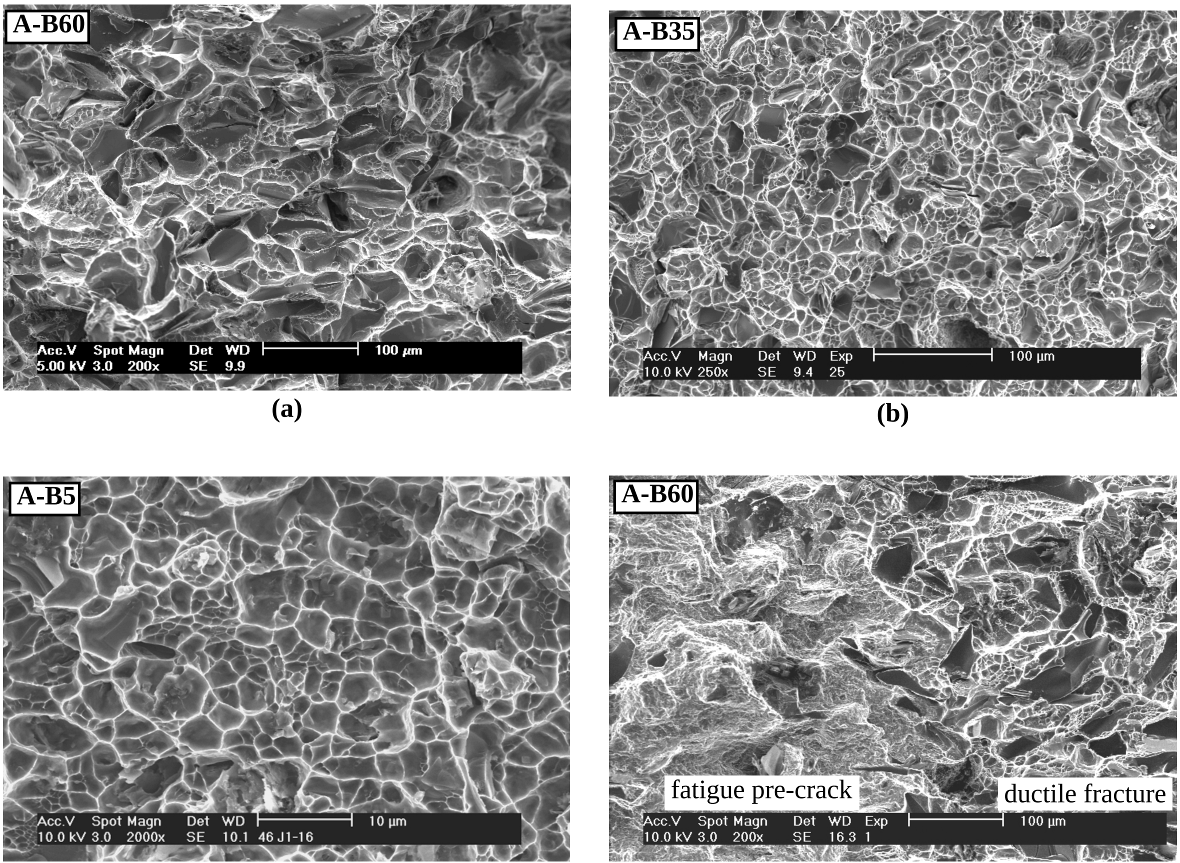
A-B60
Acc.V Spot Magn Det WD 100 µm
5.00 kV 3.0 200x SE 9.9
A-B35
Acc.V Magn Det WD Exp 100 µm
10.0 kV 250x SE 9.4 25
A-B5
Acc.V Spot Magn Det WD 10 µm
10.0 kV 3.0 2000x SE 10.1 46 J1-16
A-B60
fatigue pre-crack
ductile fracture
Acc.V Spot Magn Det WD Exp 100 µm
10.0 kV 3.0 200x SE 16.3 1

**(a)** **(b)** **(c)** **(d)**

**Figure 4-33.** SEM fractographs of Al-$B_4C$ composites. **(a)**: Al-$B_4C$ 60 µm; **(b)**: Al-$B_4C$ 35 µm, images acquired at the same magnification: scaling of the cavity sizes with the average reinforcement size. **(c)**: Al-$B_4C$ 5 µm (larger magnification), small dimples; **(d)**: Al-$B_4C$ 60 µm, boundary between the fatigue pre-crack and the initiation of ductile fracture, note broken particles at nucleation sites.

### iii. 3D Reconstruction of the fracture surfaces

Conventional SEM observation can provide data of the lateral cavity size, but information regarding the cavity depth is not possible. This issue was solved by digitally reconstructing the fracture surface with the MEX software described in Section 3.4.3. This also allowed to measure the micro-roughness of the fracture surfaces.

#### STEREOIMAGES OF THE FRACTURE SURFACES (ANAGLYPHS)

Stereoimages of the fracture surfaces of the various composite systems are given in Figure 4-34. These must be visualized with the red-blue glasses furnished with the report, after turning the page by 90° (a few seconds are needed to get used to the three-dimensional perspective), which then provides a much better impression of the degree of surface roughness and local plastic deformation than the SEM fractographs given above. Also given in Figure 4-34 are the corresponding Digital Elevation Maps (DEM) reconstructed from the stereopairs or the height maps. Three examples are more specifically presented:

In Figures 4-34a and b, the fracture surface of the 35 µm angular alumina reinforced composite at relatively large magnification is shown together with its DEM, visualized from a top-view angle. As the 3-D scene develops, one sees the presence of particles at the bottom of large dimples, which appear much deeper than in the 2-D SEM projection.

In Figures 4-34c and d, a general fracture surface view of the 25 µm polygonal alumina composite is presented. We note that the bottoms of the ductile dimples are actually located in very different planes on the fracture surface, with some behind the sheet plane, while others are situated in front of the plane. The fracture surface hence appears rather “hilly”, as also visualized on the DEM shown with a side-view angle.

A high magnification view of the A-B35 composite is shown in Figure 4-34e. Small dimples are sometimes found at the bottom of the large ones. Instead of the DEM, the altitude map of the reconstructed stereopair is given in Figure 4-34f to illustrate the height difference between the highest and the lowest point of the picture.

### COMPARISON OF THE CAVITY SIZES

All the quantitative information regarding the fracture surface profiles is contained in numerical DEMs such as those given in Figures 4-34b and d. Among the various tools offered by the software, a useful feature is to trace the roughness profile along a user-defined line. Global profiles or individual cavity depths can hence be measured by selecting the region of interest on the images. Some typical fracture surface profiles of composites with well distinct particle sizes are presented in Figure 4-35a. These illustrate that the fracture surface micro-roughness increases with the microstrucural length scale of the composite.

Comparison of individual dimple profiles in the different composite systems is given in Figures 4-35b, c, and d. One sees in all the composite systems that not only the cavity diameter scales with the average interparticle distance, but also the cavity depth, which is directly correlated to the extent of local plastic deformation during the voiding process. In a composite with a given size of reinforcement, one notices that the depth of the dimples nucleated by broken particles (see the A-A35a composite, Figure 4-35b) is generally larger than when the dimples are nucleated within the matrix (compare with the A-B35 composite shown in Figure 4-35d). The following conclusions are drawn from analysis of the dimple geometry:

(i) in the composites failing by the fully ductile voiding mechanism, the dimple size scales with the average interparticle distance (see Figure 4-35c);
(ii) when particle cracking occurs and creates dimples, the size of the latter scales with the size of the particles responsible for dimple nucleation;
(iii) in composites with a given size of reinforcement, the depth of dimples nucleated by broken particles is larger than that of dimples nucleated between particles.

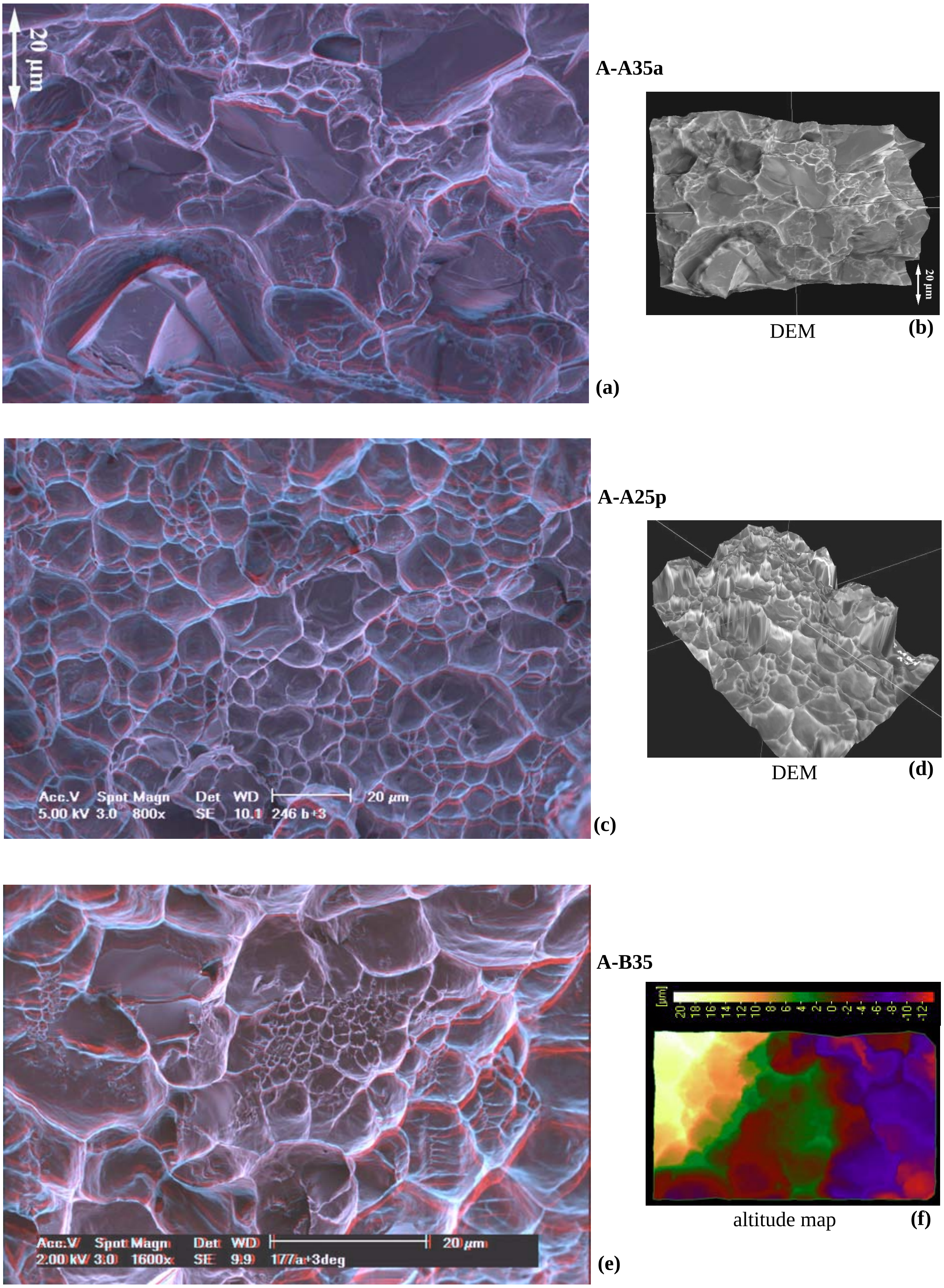
20 µm
A-A35a
20 µm
DEM
(b)
(a)
A-A25p
DEM
(d)
Acc.V Spot Magn Det WD 20 µm
5.00 kV 3.0 800x SE 10.1 246 b+3
(c)
A-B35
[µm] 20 18 16 14 12 10 8 6 4 2 0 -2 -4 -6 -8 -10 -12
altitude map
(f)
Acc.V Spot Magn Det WD 20 µm
2.00 kV 3.0 1600x SE 9.9 177a+3deg
(e)

**Figure 4-34.** Fracture surface SEM stereopairs of various composites. To obtain the 3-D impression, red-blue glasses must be used and the page must be turned by 90° counter-clockwise. **(a)**: A-A35a composite and **(b)**: corresponding Digital Elevation Map (DEM); **(c)**: A-A25p composite (low magnification view of the fracture surface) and **(d)**: corresponding DEM; **(e)**: A-B35 composite (detailed view of the dimples) and **(f)**: altitude map of the fracture surface generated from the DEM.

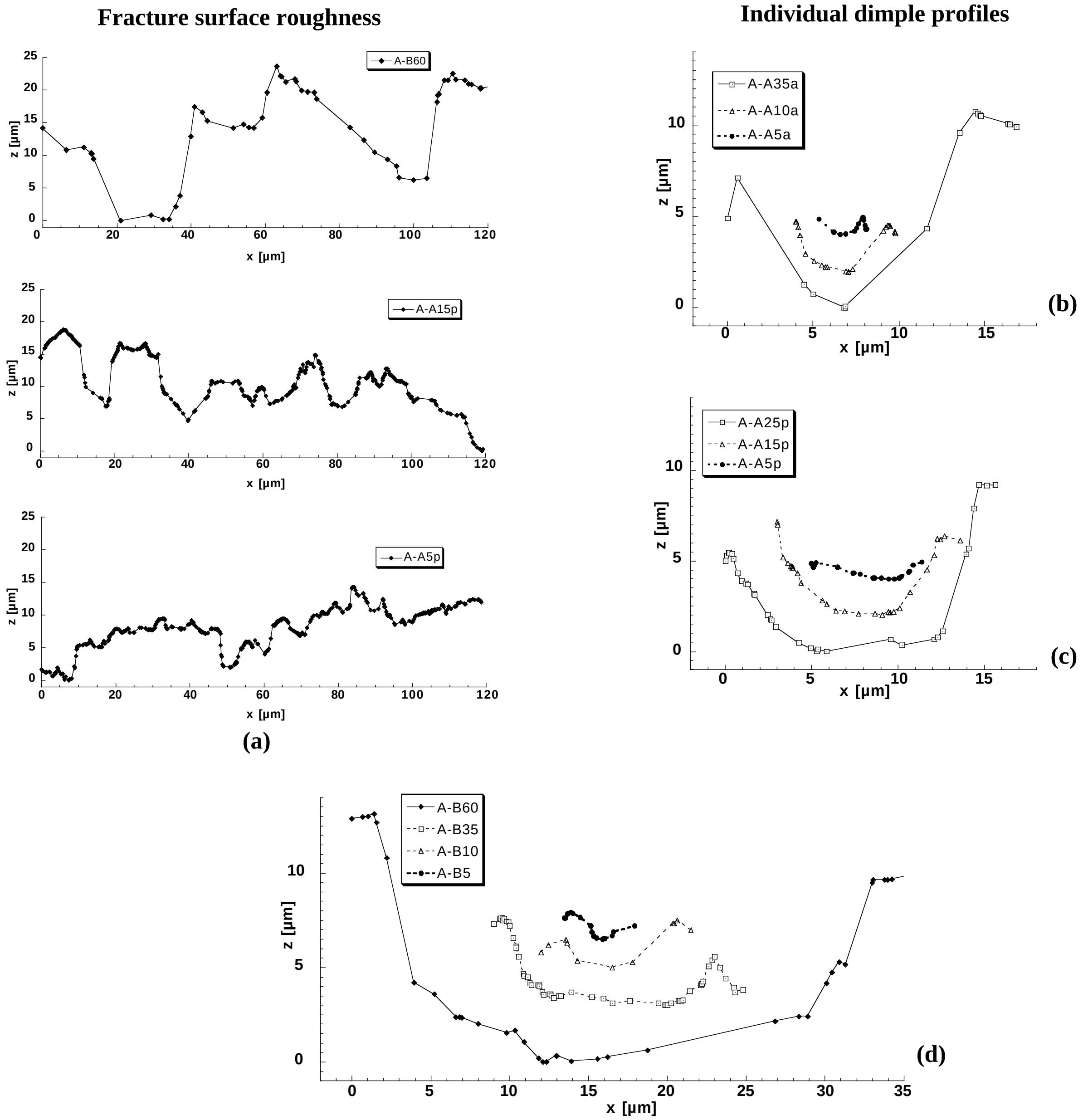

**Figure 4-35.** Fracture surface profiles obtained from the DEMs. **(a)**: Global profiles of three composites having distinct microstructural length scales (60 µm $B_4C$, 15 µm polygonal $Al_2O_3$, and 5 µm polygonal $Al_2O_3$); **(b)**: typical individual dimples in A-Aa composites; **(c)**: typical individual dimples in A-Ap composites; **(d)**: typical individual dimples in A-B composites, plots (b), (c) and (d) at the same scale.

### iv. Summary: quantification of the micromechanisms of fracture

The dominant micromechanisms of failure in the pure aluminium matrix composites have been presented in this chapter. All our observations are summarized in Table 4-4, in which quantitative characteristics of the fracture surfaces are also included. For the composites in which particle cracking was observed, the fraction of the crack path occupied by broken particles was determined according to the method described in §.3.4.1.ii. The uncertainty is controlled by the microscope resolution with regard to the typical microstructural size and by the dispersion of the particle size distribution.

In large and medium particle size composites, unambiguous counting of broken particles is possible and the relative uncertainty is rather linked to the fact that the broken particles are assumed to exhibit the average particle size. In particular in the A-A10a composite, optical micrographs reveal a bimodal particle size distribution, where larger than average particles are more often cracked. For this case, it was observed and taken into account in the statistic that about 70% of broken particles were larger than average (about 20 µm) and that the remaining 30% had the average particle size of 10 µm. The uncertainty for the A-A5a composites is rather linked to the microscope resolution because distinction of broken particles (which were still not large) was not as clear on the optical micrographs. It was hence decided to measure the fraction of broken particles by image analysis on the SEM micrograph of the fracture surfaces.

The average dimple heights also included in Table 4-4 were obtained by measuring individual dimples such as those shown in Figure 4-35 on the digitally reconstructed fracture surfaces. The uncertainty reported for this feature is the average standard deviation of the measures.

**Table 4-4.** Micromechanisms of fracture in pure Al matrix composites, as measured on optical micrograph crack profiles, on SEM fractographs, and on 3-D reconstructed SEM fracture surfaces.

| **Composite system** | **Composite designation** | **Dominant micromechanism of fracture** | **Fraction of the crack path occupied by broken particles [-]** | **Average ductile dimple height [µm]** |
|---|---|---|---|---|
| **Al-$Al_2O_3$ angular** | A-A35a | particle cracking | 0.72 ± 0.06 | 10.0 ± 4.1 |
| | A-A20a | interfacial decohesion | - | - |
| | A-A10a | particle cracking (large particles) & matrix voiding | 0.64 ± 0.07 | 2.6 ± 1.2 |
| | A-A5a | matrix voiding | 0.10 ± 0.05 | 1.6 ± 0.8 |
| **Al-$Al_2O_3$ polygonal** | A-A25p | matrix voiding & few particle cracking | 0.05 ± 0.01 | 8.4 ± 2.4 |
| | A-A15p | matrix voiding | - | 4.3 ± 1.8 |
| | A-A5p | matrix voiding | - | 1.4 ± 0.8 |
| **Al-$B_4C$** | A-B60 | particle cracking & matrix voiding | 0.51 ± 0.05 | 12.1 ± 4.5 |
| | A-B35 | matrix voiding & few particle cracking | 0.12 ± 0.03 | 5.9 ± 2.5 |
| | A-B20 | matrix voiding & few particle cracking | 0.15 ± 0.03 | - |
| | A-B10 | matrix voiding | 0.10 ± 0.02 | 2.2 ± 0.9 |
| | A-B5 | matrix voiding & reaction phase cracking | 0.04 ± 0.01 | 1.6 ± 0.9 |

# 4.3. PHOTOELASTIC PATTERNS OF THE CRACK TIP PLASTIC ZONE

In the precedent section, fracture micromechanisms occuring in the process zone and main features of formation of the fracture surfaces have been presented and quantified. We now turn to the energy dissipative process operating at the more global scale of the sample during fracture testing, namely plastic deformation in the crack-tip plastic zone. This is observed here on the surface of the specimens by using photoelasticity. The isochromatic fringe characteristics expressed through the difference of the in-plane principal strains were determined for both coating thicknesses employed by using the compensator calibration curve of the polariscope; they are given in Table 4-5. The reader is referred to this table for all photoelasticity figures that are presented in the chapter.

**Table 4-5.** Isochromatic fringe characteristics of the photoelastic coatings, obtained from the compensator calibration curve (given in terms of the difference of the principal strains $\varepsilon_1$-$\varepsilon_2$).

| **Color** | **fringe order N** | **0.5 mm coating thickness** $\varepsilon_1$-$\varepsilon_2$ **[%]** | **1 mm coating thickness** $\varepsilon_1$-$\varepsilon_2$ **[%]** |
|---|---|---|---|
| Black | 0.00 | 0.00 | 0.00 |
| Gray | 0.18 | 0.07 | 0.03 |
| White | 0.25 | 0.09 | 0.04 |
| Pale yellow | 0.39 | 0.15 | 0.07 |
| Orange | 0.57 | 0.22 | 0.10 |
| Dull red | 0.71 | 0.27 | 0.12 |
| Purple | 0.86 | 0.33 | 0.15 |
| Deep blue | 1.00 | 0.38 | 0.17 |
| Blue-green | 1.13 | 0.43 | 0.19 |
| Green-yellow | 1.23 | 0.47 | 0.21 |
| Orange | 1.43 | 0.54 | 0.25 |
| Rose-red | 1.66 | 0.63 | 0.29 |
| Rose | 1.84 | 0.70 | 0.32 |
| Purple | 1.96 | 0.74 | 0.34 |
| Green | 2.11 | 0.80 | 0.36 |
| Green-yellow | 2.48 | 0.94 | 0.43 |
| Red | 2.71 | 1.03 | 0.47 |
| Red/green transition | 3.05 | 1.16 | 0.53 |
| Green | 3.21 | 1.22 | 0.55 |
| Pink | 3.66 | 1.39 | 0.63 |
| Pink/green transition | 4.16 | 1.58 | 0.72 |
| Green | 4.38 | 1.66 | 0.75 |

### 4.3.1 Sample with notched coating

The evolution of the strain field in the course of a complete *J*-integral fracture test is presented in Figure 4-36 for an A-A35a composite specimen. The load-displacement plot and its related *J-R* curve are given in Figures 4-36a and b, respectively. The instants of image acquisition are indicated on the curves, and the photoelastic patterns are given in Figures 4-36c to n. On each picture, the load and the value of *J* are indicated as well.

The boundary between the plastic zone and the elastic field is somewhat arbitrary, especially because no clear yield point is measured during tensile testing of these composites [89]. A reasonable assumption is to consider that macroscopic yielding starts when $\varepsilon_1$-$\varepsilon_2$ exceeds 0.2% strain, which according to Table 4-5 means that the plastic zone boundary for the 0.5 mm thick coating corresponds approximately to the orange fringe (between the pale yellow and the red fringes). With this definition, it is clearly noticed that the plastic zone begins to form while the *J-R* curve is still in its initial steeper part.

As loading progresses, one sees that critical events occur between (g) and (j), that is, when the load approaches its peak value and then decreases. This corresponds on the *J-R* curve to the change from the process zone formation and slow crack propagation to macroscopic crack growth. At (i), namely on the last point of the initial portion of the *J-R* curve, it is reasonable to consider elastic-plastic conditions at the crack tip. At (j), large-scale yielding sets in. The crack has then propagated at the macroscopic level, implying that the validity of *J* is lost. The plastic zone then progresses along all the remaining ligament, and eventually links with the plastic hinge of the specimen (k-m). The photoelastic pattern after final failure, shown in Figure 4-36n, illustrates the important level of residual plastic strain in the composite, with strains exceeding 1% in the highly deformed regions (the maximum sustainable strain in the photoelastic coating is exceeded in some regions).

Two conclusions are drawn from Figure 4-36. The first, which was already established in Section 4.2, is that the toughness of these composite containing 40 to 60 % of brittle phase is controlled by plastic dissipation in the plastic zone. The second is a corollary of the first, namely that the plastic zone size at the onset of macroscopic crack growth is a material parameter that can be used to compare the various composites, and in which a large fraction of the fracture energy $J_{GT}$ is dissipated.

### 4.3.2 Sample with unnotched coating

The initial observations for many composites were conducted on unnotched photoelastic coatings, in which loading of the coating itself resulted in some modification of the deformation fields (see §.3.3.3). Since the composites were not all re-evaluated with center-notched coatings, we present in Figure 4-37 the same results as in Figure 4-36 *(i.e.* on the same composite), but with a sample observed through an unnotched photoelastic coating.

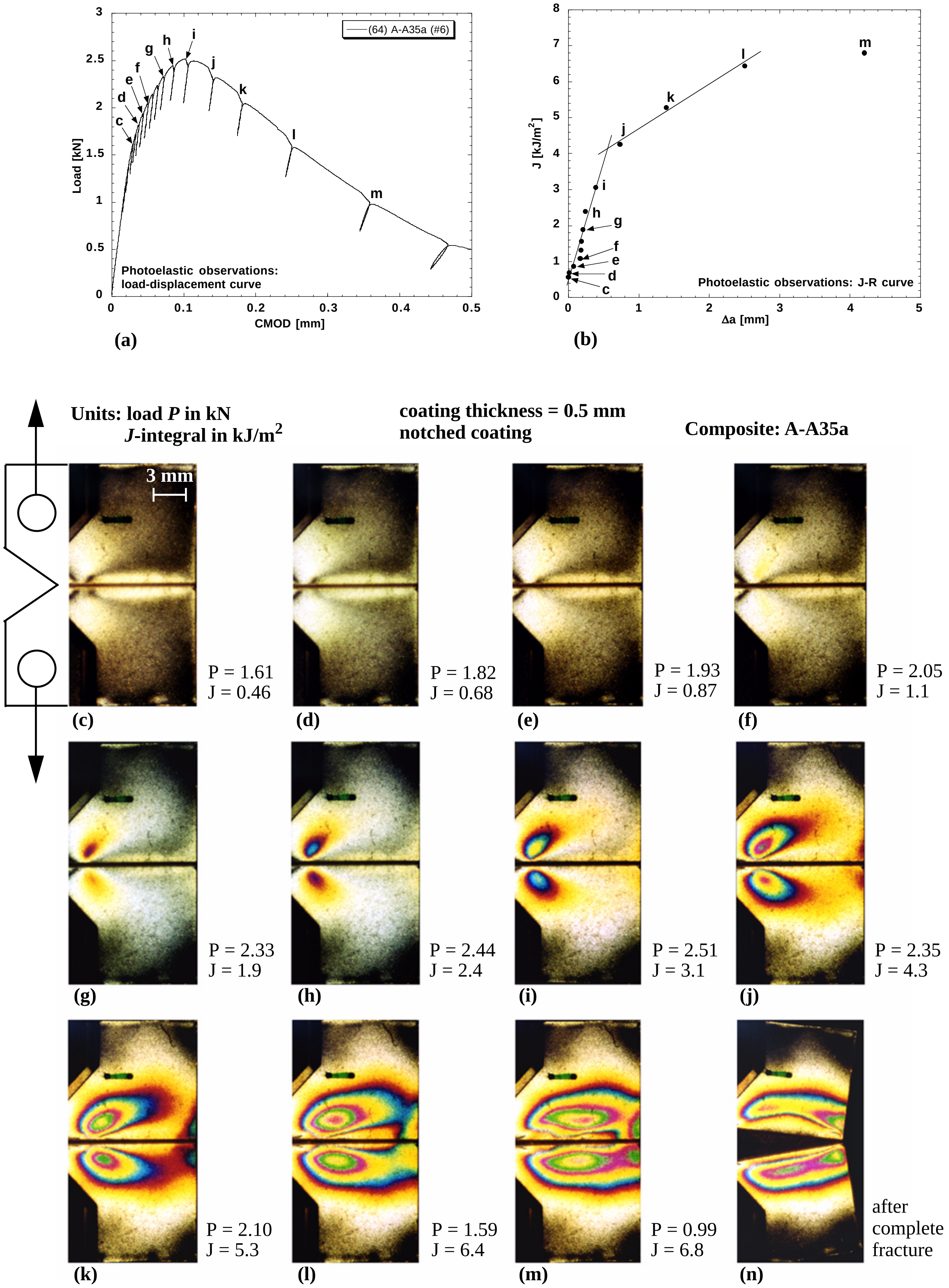

**Figure 4-36.** Photoelastic patterns of the crack-tip strain field ($\varepsilon_1$-$\varepsilon_2$) during a *J*-integral fracture test on the A-A35a composite, notched coating. **(a)**: load-displacement curve; **(b)**: correspondant *J-R* curve; **(c)-(m)**: deformation fields at the instants indicated on (a) and (b); **(n)**: deformation field after complete fracture illustrating residual plastic strains in the CT specimen.

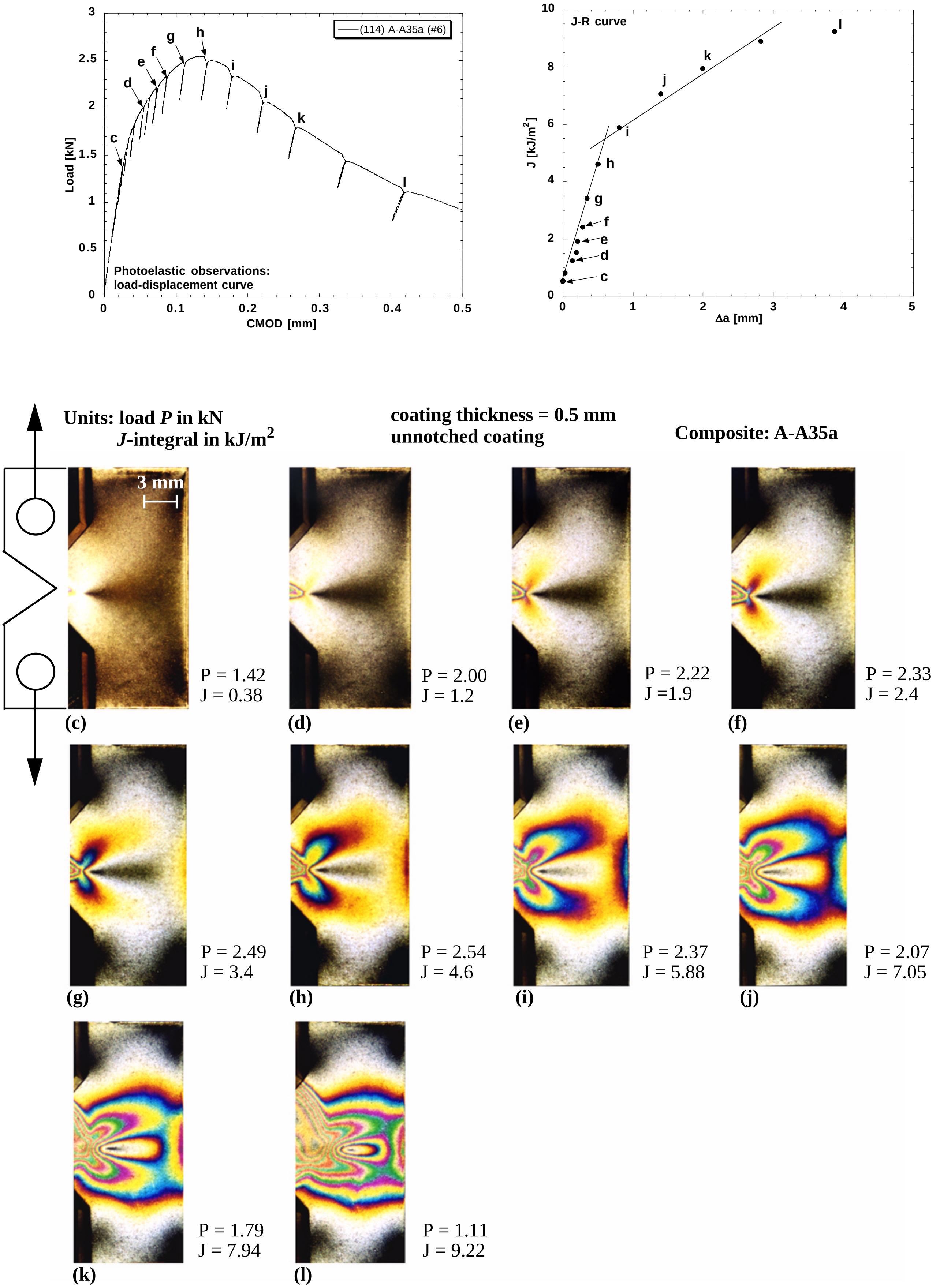

**Figure 4-37.** Photoelastic patterns of the crack-tip strain field ($\varepsilon_1$-$\varepsilon_2$) during a *J*-integral fracture test on the A-A35a composite, unnotched coating. **(a)**: load-displacement curve; **(b)**: correspondant *J-R* curve; **(c)-(l)**: deformation fields at the instants indicated on (a) and (b).

No significant difference with Figure 4-36 is noticed in terms of the formation of a distinct plastic zone, which is detected at a *J* comprised between 1.2 and 2 kJ/m$^2$ (d-e). There is a clear increase of the plastic zone size around $P_{\max}$ (from g to h) while in addition, large-scale yielding is also observed as the load passed its maximum (i). The size and shape of the plastic zone are actually similar to those observed with notched coatings. The major difference is the location of the outer-layer fringes near the crack-tip: while the fringes take the form of a closed contour in the notched coating, they do not enclose the crack tip with an unnotched coating because strain continuity must be ensured with the field created by the loading of the coating; this difference is more marked as the crack propagates (j-l). Another advantage of notched coatings is the possibility to observe post-failure residual strains. On the other hand, the strain field on the crack propagation plane can be visualized with unnotched coatings and the plastic hinge is shown more clearly.

In summary, the observed shape of the plastic zone is not affected by the fact that the photoelastic layer is unnotched, with the exception of the region situated behind the crack tip, where the deformations cannot be measured with the unnotched coatings. This allows us to use both types of coating to compare –at least qualitatively– the degree of plastic deformation at the critical fracture point in the different composites.

### 4.3.3 Deformation fields during fracture testing: comparison of the composites

From the observations in Figures 4-36 and 4-37, and the results presented in Chapter 4.2, it appears that the plastic zone patterns of the composites must be compared at loading levels close to the peak load, which corresponds to a value close to $J_{GT}$ as well. It was indeed seen that *J* is still valid at that point and that it is governed by the plastic zone, while it becomes geometry dependent beyond this point. Such comparisons for the various composite systems are given in Figure 4-38 to Figure 4-41. The instantaneous value of *J* (always close to $J_{GT}$) is also indicated on the images.

#### i. Aluminium-angular alumina composites

Photoelastic patterns of the crack tip are presented in Figure 4-38. For the composite reinforced with the large 35 µm particles, please refer to Figures 4-36i or 4-37g. For the A-A20a and the A-A10a composites (Figures 4-38a and b), observations were carried out with the thicker coating, meaning that the boundary of the plastic zone coincides with the blue-green fringe on these images. Therefore, while the largest plastic zone at the onset of ductile tearing is unambiguously for the A-A35a composite, it appears that a slightly larger plastic zone has developped in the 5 µm particle size composite (Figure 4-38c) (for which a thin film was used) than in the 10 µm composite. It is remembered here that the A-A5a composite also exhibits a higher fracture energy than the A-A10a composite (Table 4-3). In the A-A20a composite (which has the lowest fracture energy and fails by interfacial decohesion), Figure 4-38a, it is clear that a very low amount of plastic deformation is found near the crack tip as compared to the other composites, the maximum strain observed not even attaining 0.1%.

#### ii. Aluminium-polygonal alumina composites

Observations of the crack-tip plastic zone in polygonal $Al_2O_3$ composites are presented in Figure 4-39a for the 15 µm (thin coating) and in Figures 4-39b and c for the 5 µm particle composites. Clearly, the A-A15p composite is characterized by a much larger plastic zone than the A-A5p composite.

Hence, the value of $J_{GT}$ (larger for the A-A15p composite) correlates with the size of the plastic zone. For the A-A5p composite, observations with both the thin (Figure 4-39b) and the thick (Figure 4-39c) coatings are given to illustrate the consistency between the measures: for the two types of coatings (considering the orange fringe for the thin coating and the blue/green fringe for the thicker coating) a plastic zone of approximately 1 to 2 mm is measured at 45° from the crack tip.

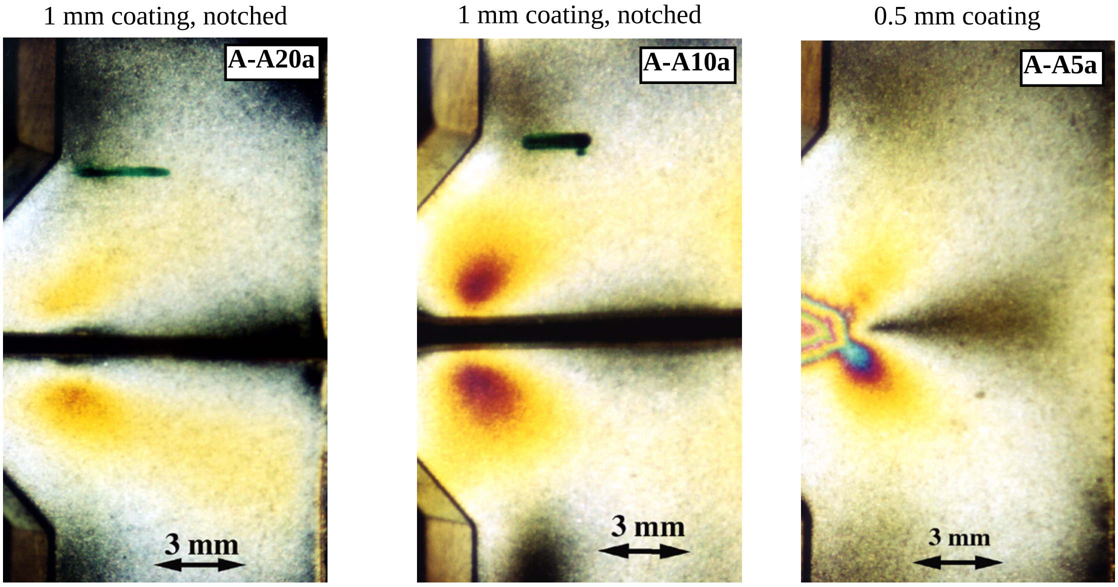
1 mm coating, notched 1 mm coating, notched 0.5 mm coating

(a) J = 1.1 kJ/m$^2$ (b) J = 1.8 kJ/m$^2$ (c) J = 2.6 kJ/m$^2$

**Figure 4-38.** Crack-tip strain fields in Al-Al$_2$O$_3$ angular composites, at loading conditions close to $J_{GT}$. **(a)**: 20 µm particles composite (thick coating); **(b)**: 10 µm particle composites (thick coating); **(c)**: 5 µm particles composite (thin coating). Compare also with Figure 4-36i and Figure 4-37g. All pictures at the same scale.

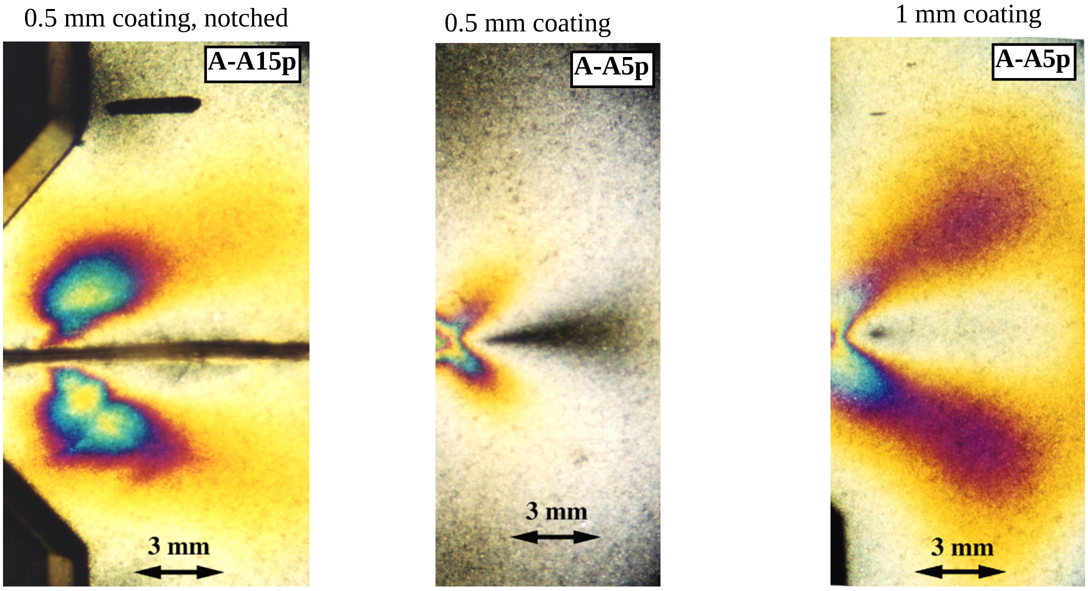
0.5 mm coating, notched 0.5 mm coating 1 mm coating

(a) J = 5.7 kJ/m$^2$ (b) J = 3 kJ/m$^2$ (c) J = 2.5 kJ/m$^2$

**Figure 4-39.** Crack-tip strain fields in Al-Al$_2$O$_3$ polgonal composites, at loading conditions close to $J_{GT}$. **(a)**:15 µm particles composite (thin coating); **(b)**: 5 µm particles composite (thin coating); **(c)**: 5 µm particles composite (thick coating). All pictures at the same scale.

### iii. Aluminium-boron carbide composites

Photoelastic patterns close to the onset of ductile tearing are shown in Figure 4-40. The image of the 5 µm particle size reinforced composite (Figure 4-40d) was obtained with the thick 1 mm photoelastic coating, while all others pictures presented were acquired with the thin coating. All images have the same scale, which allows for comparison between the composites: in the A-B60 composite (Figure 4-40a), the plastic zone has already spread over a large part of the specimen, while it is more and more confined as the average particle size decreases (A-B20 composite: Figure 4-40b, A-B10 composite: Figure 4-40c, and A-B5 composite: Figure 4-40d). Hence, it is concluded that the plastic zone size at the onset of ductile tearing scales with the average reinforcement size, which is a similar trend as measured for the fracture energy in terms of *J*.

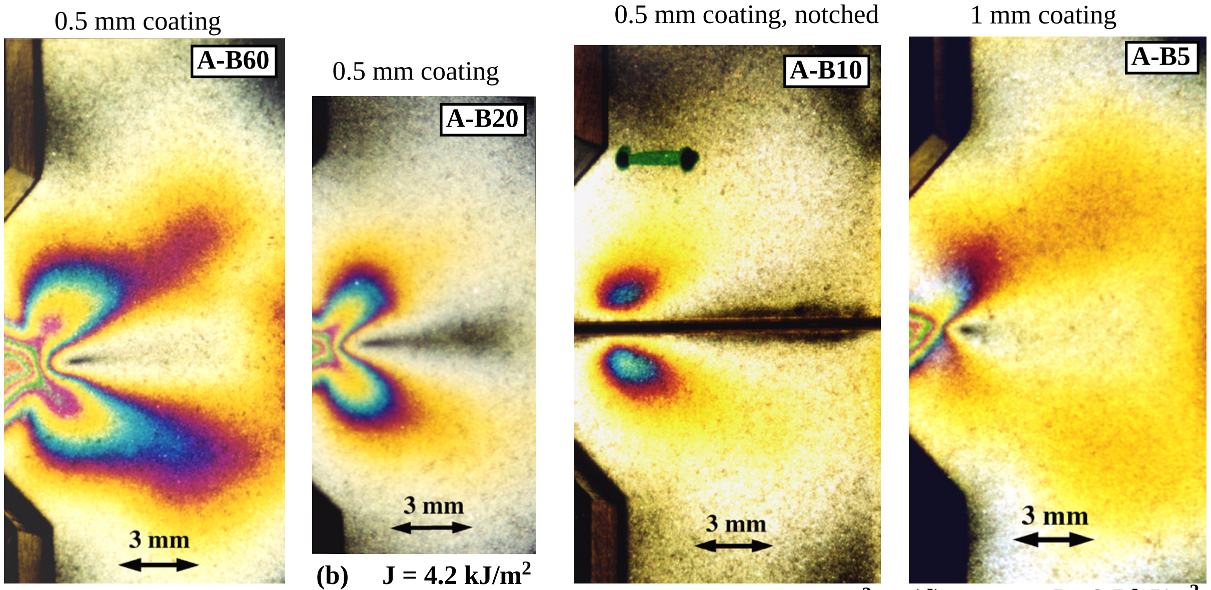

**(a)** $J = 6.5$ kJ/m$^2$ **(b)** $J = 4.2$ kJ/m$^2$ **(c)** $J = 2.9$ kJ/m$^2$ **(d)** $J = 2.5$ kJ/m$^2$

**Figure 4-40.** Crack-tip strain fields in Al-B$_4$C composites, at loading conditions close to $J_{GT}$. **(a)**: 60 µm particles composite (thin coating); **(b)**: 20 µm particles composite (thin coating); **(c)**: 10 µm particles composite (thin coating); **(d)**: 5 µm particles composite (thick coating). All pictures at the same scale.

### iv. Aluminium-copper matrix composites

Photoelastic observations in Al-Cu2% matrix composites during *J*-integral fracture testing were carried out for two materials: the 15 µm alumina polygonal composite, shown in Figure 4-41a, and the 60 µm alumina angular composite, shown in Figure 4-41b. The images presented were acquired using the thicker 1 mm photoelastic coating. In the A2C-A15p (for which the *J-R* curve is presented in Figure 4-24), a distinct plastic zone has developed at the crack tip. It is, however, significantly smaller than in the pure Al matrix composite reinforced with the same particles (Figure 4-39a). This does not, however, directly translate into a large decrease of $J_{GT}$ (5.4 kJ/m$^2$ for the Al matrix composite versus 4.3 kJ/m$^2$ for the Al-Cu2% composite) because the smaller plastic zone in the alloyed matrix composites has a higher average flow stress, which leads to a larger absorbed plastic energy for a given plastic zone size.

In the A2C-A60a composite on the other hand, no distinct plastic zone is observed in front of the crack tip prior to fracture (the picture in Figure 4-41b was acquired just before unstable fracture). Fracture is *K*-dominated and *R*-curve behaviour caused by plastic zone formation does not appear. This is consistent with the flat *J-R* curve measured on this composite (see Figure 4-22: fully unstable fracture at $J = 1.6$ kJ/m$^2$).

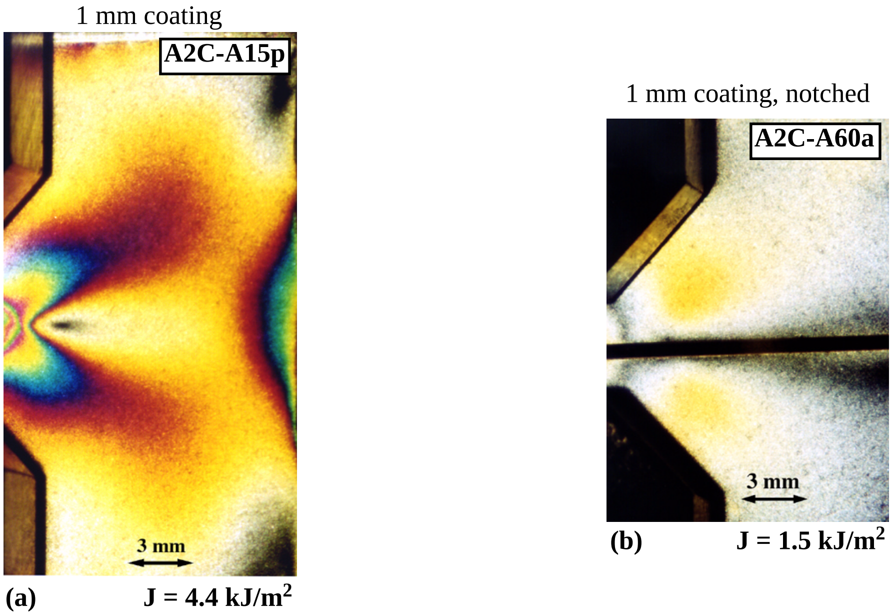

1 mm coating

**(a)** **J = 4.4 kJ/m$^2$**

1 mm coating, notched

**(b)** **J = 1.5 kJ/m$^2$**

**Figure 4-41.** Crack-tip strain fields in Al-Cu2% matrix composites $Al_2O_3$ composites, at loading conditions close to $J_{GT}$ or just before unstable fracture. **(a)**: 15 µm polygonal $Al_2O_3$ particles composite (thick coating); **(b)**: 60 µm angular $Al_2O_3$ particles composite (thick coating). All pictures at the same scale.

### *4.3.4 Residual strains after final fracture*

A visual representation of the amount of plastic deformation absorbed by a specimen during fracture and its contribution to the material toughness can be obtained by looking at residual strains after final failure along the crack wake. Such observations, possible only with notched coating (the unnotched coating being still under remote load after complete fracture of the CT specimen), are presented in Figure 4-42. The composites investigated can be classified into three broad categories.

In the first are the composites with a very large plastic wake. These all present a quite marked *J-R* curve behaviour as well (see Figure 4-25). Among them, one finds pure Al matrix reinforced with large $B_4C$ (60, 35, 20 µm) or angular $Al_2O_3$ (35 µm, Figure 4-42b) particles, as well as pure Al reinforced with 25 and 15 µm polygonal $Al_2O_3$ particles (in the last, shown in Figure 4-42a, only the outer fringes are visible because the high plastic strains close to the crack plane led to partial debonding of the coating). Such debonding is an indication of the high level of plastic deformation and was seen on other composites exhibiting a relatively high *J-R* curve.

In the second class of composites, one finds composites with more limited *R*-curve behaviour, in which a smaller plastic wake is observed. The pure Al matrix composites with smaller particles (10 µm and less) are characterized by this behaviour, for instance the 10 µm $B_4C$ reinforced composite (Figure 4-42c) or the 10 µm $Al_2O_3$ angular composite (Figure 4-42d, note that the photoelastic pattern is observed with the thicker coating on this picture). The Al-2%Cu matrix composites reinforced with medium or large polygonal particles (15 and 25 µm) fall into this category as well.

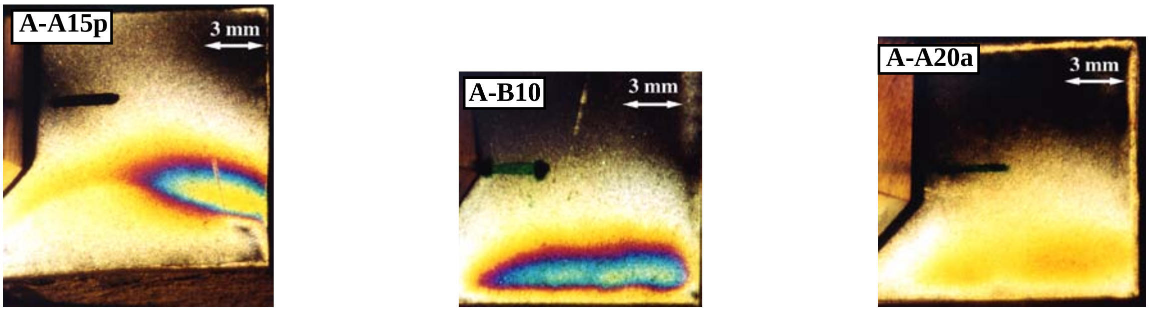

**(a)** 0.5 mm coating **(c)** 0.5 mm coating **(e)** 1 mm coating

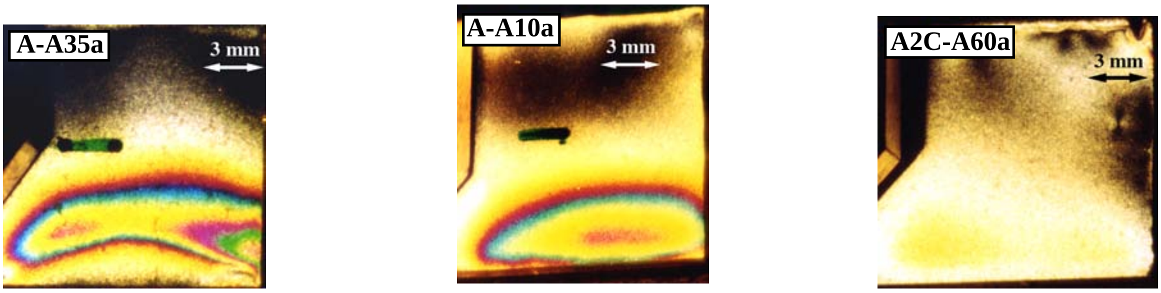

**(b)** 0.5 mm coating **(d)** 1 mm coating **(f)** 1 mm coating

**Figure 4-42.** Residual plastic strains along the crack wake after final failure (one half of the specimens shown). **(a)**: Al-$Al_2O_3$ 15 µm polgonal composite and **(b)**: Al-$Al_2O_3$ 35 µm angular composite, large region of residual deformations. **(c)**: Al-$B_4C$ 10 µm composite and **(d)**: Al-$Al_2O_3$ 10 µm angular composite (thick coating), smaller region of residual strain. **(e)**: Al-$Al_2O_3$ 20 µm angular composite and **(f)**: Al/Cu2%-$Al_2O_3$ 60 µm angular composite, little residual strain in the crack wake.

The third group includes the composites with the lowest fracture energies; here a distinct plastic zone is not formed during crack propagation. Two of these materials are presented here, the Al-20 µm $Al_2O_3$ angular composite (Figure 4-42e) and the Al-Cu2% matrix composite reinforced with the large 60 µm $Al_2O_3$ angular particles (Figure 4-42f). The low level of residual plastic strains present in these materials suggest a far smaller contribution of crack tip plasticity to the fracture energy. This is consistent with data shown in Figure 4-10b for the A-A20a composite and in Figure 4-22b for the A2C-A60a composite.

# 4.4. AGEING AND TENSILE BEHAVIOUR OF Al-CU MATRIX COMPOSITES

## 4.4.1 Ageing characteristics and macrohardness

Age-hardening curves at 100°C of Al-Cu2% and Al-Cu4.5% matrix composites are given in Figures 4-43a and b, respectively. The relative hardness increase is rather low, between 8 and 20% depending on the composites tested. The age hardening response therefore does not yield a well-defined peak: clearly the effect of age-hardening is masked by the particle contribution to the hardness of the composites.

Angular alumina composites display significantly lower hardness values than polygonal alumina particles with equivalent average particle size. For Al-Cu2% matrix composites, the ageing peak is generally attained after 10 to 15 hours, while for Al-Cu4.5% matrix composites, slightly longer times (15 to 20 hours) are necessary.

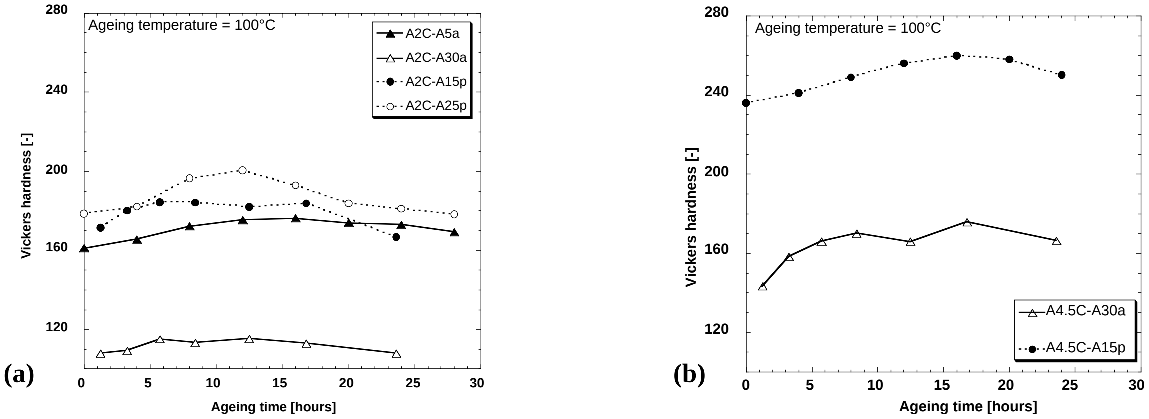

**Figure 4-43.** Age hardening curves of alloyed matrix composites at 100°C, after solution treatment at 515°C. **(a)**: Al-Cu2% matrix composites; **(b)**: Al-Cu4.5% matrix composites.

The hardness data of all Al-Cu matrix composites tested in the as-cast (AC), solutionized (ST) and peak-aged (T6) conditions are presented in Figures 4-44a (Al-Cu2%) and b (Al-Cu4.5%). For a composite with a given reinforcement, the hardness is larger with a higher amount of Cu in the matrix. The absolute increase in hardness after solution heat treatment is also larger for the Al-Cu4.5% matrix composites. No clear trend emerges in terms of the influence of the average particle size. In angular alu-

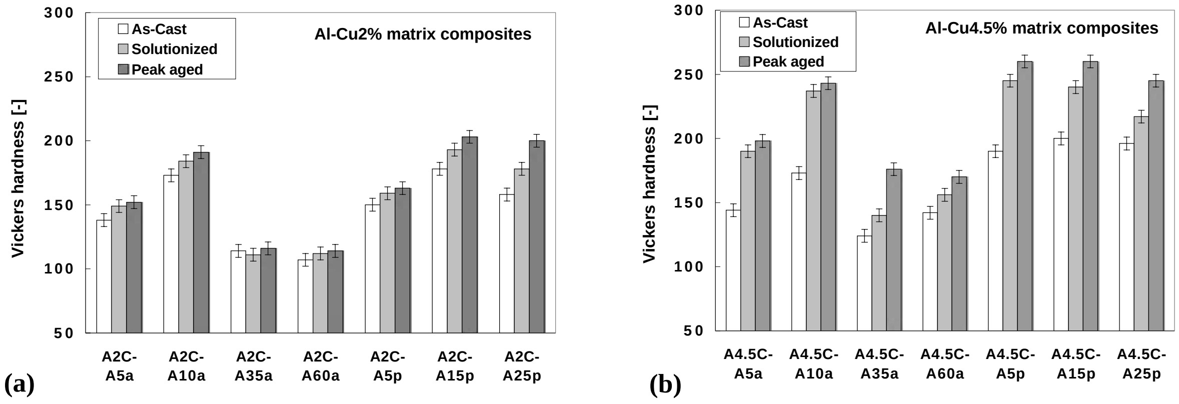

**Figure 4-44.** Vickers hardness of Al-Cu matrix composites in AC, ST and T6 conditions. **(a)**: Al-Cu2% matrix composites; **(b)**: Al-Cu4.5% matrix composites.

mina composites, we note that the 10 µm reinforced composites exhibit the highest hardness, followed by the 5 µm particle size composites, whereas composites reinforced with larger particles (35 and 60 µm) exhibit significantly lower hardness values. In polygonal reinforced composites, it is concluded from Figure 4-44b that the hardness is not influenced by the reinforcement size.

### *4.4.2 Tensile flow curves*

Tensile characteristics of Al-Cu matrix composites were not investigated in detail since such a study is currently being conducted in our group. We thus present a few typical tensile flow curves in order to provide a general picture of the mechanical performance of these materials.

#### i. Angular alumina composites

Typical tensile curves of Al-Cu alloy matrix composites reinforced with 5 and 35 µm angular particles are given in Figure 4-45a and b, respectively. Tensile curves of pure Al matrix composites are also shown on the pictures for comparison. Generally speaking, as the Cu content increases the yield stress and UTS increase, but elongations to failure are greatly reduced such that a transition to an almost fully brittle behaviour is noticed for the Al-Cu4.5% matrix composites.

Solution treatment of the 5 µm reinforced composite is seen to increase the yield strength, UTS and strain to failure ($\varepsilon_f$). This was systematically observed in all tested samples of this material. After ageing, tensile properties are in general enhanced, but there is also more scatter in the data, such that an improvement of average properties is hard to discern. In the 35 µm angular particle composites, solutionization and ageing do not lead to an improvement of tensile properties because scatter in the final elongation is high.

Comparison of the two Al-Cu2% matrix composites (5 µm and 35 µm particles) shows that the yield stress and UTS increase with decreasing particle size, a trend that is similar to pure aluminium reinforced with the same particles [89]. We also note that the reduction of elongation to failure is significantly more marked in the larger particle size composites.

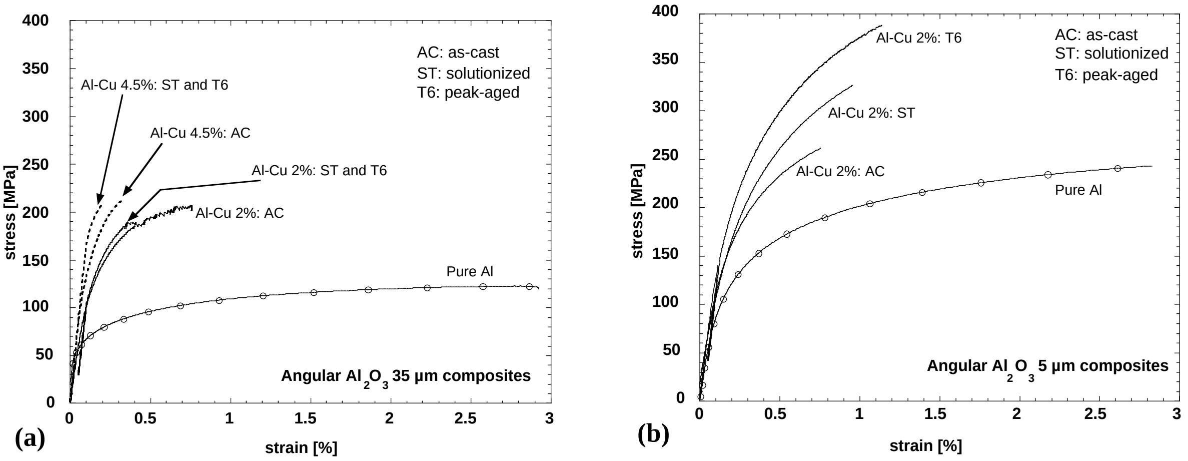

**Figure 4-45.** Tensile flow curves of Al-Cu matrix/angular particle composites, and comparison with pure Al matrix composites. **(a)**: 35 µm particle composites; **(b)**: 5 µm particle composites.

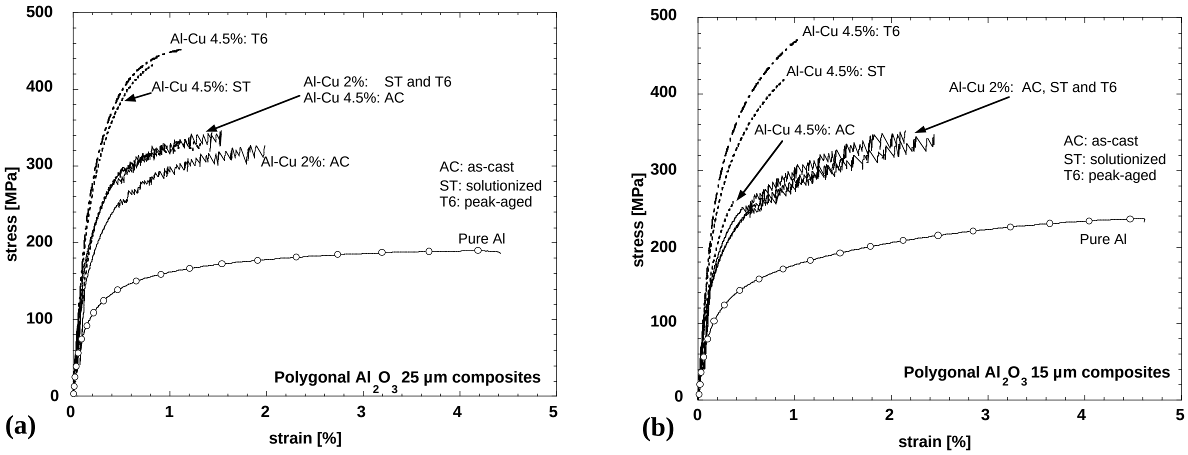

**Figure 4-46.** Tensile flow curves of Al-Cu/polygonal particle composites and comparison with pure Al matrix composites. **(a)**: 25 µm particle composites; **(b)**: 15 µm particle composites. In some cases, note the presence of discontinuous yielding (or load instabilities) in the plastic regime, attributed to a Portevin-Le Chatelier effect (PLC) in the matrix.

### ii. Polygonal alumina composites

Typical tensile flow curves of polygonal reinforced composites are given in Figures 4-46a and b. These composites display significantly higher tensile elongations than angular particles composites. With the Al-Cu2% matrix, the following systematic features are observed, for the two composites characterized in tension (A2C-A15p and A2C-A25p):

(i) a significant amount of plastic deformation is observed for all heat treatment conditions, with a maximum value of 2.5% in one of the 15 µm particle composites in the ST condition;

(ii) in all samples, after the onset of macroscopic yielding, stress instability (or discontinuous yielding) is observed: the present composites show the so-called Portevin-Le Chatelier effect (PLC). While this mechanism has been widely observed and studied in age-hardenable aluminium alloys [247-251] and is known to be caused by the dynamic interaction between mobile dislocations and solute atoms, it has so far to our knowledge not been reported in MMCs, probably because early fracture often occurs in these (before or soon after the onset of yielding).

(iii) in general, composites tested in the ST and T6 conditions show a slight increase of their yield stress and UTS as compared to as-cast composites. The strain to failure is not significantly altered and varies more from sample to sample. When comparing the ST and T6 conditions, experimental scatter is on the order of differences observed; hence no visible effect of ageing is detected for tensile properties of these composites;

(iv) the particle size effect for the two Al-Cu2% polygonal composites tested is not very significant given the small difference in particle size.

As the matrix Cu content is increased to 4.5%, the composite flow stress clearly raises for all heat treatment conditions, Figure 4-46. Maximum UTS values exceed 450 MPa (around 200 MPa in pure Al matrix composites). Comparatively, the increase of yield stress and UTS after heat-treatment is more distinct than with Al-Cu2% matrix. This increase in flow stress is accompanied by a reduction in the elongation to fracture; since fracture instability sets in earlier, it also results that the PLC effect is less systematically observed[1].

### iii. Summary and comments

The tensile data of alloyed matrix composites are summarized in Table 4-6 (together with the fracture toughness values as measured by chevron-notch testing). The important points to remember for the discussion are:

(i) polygonal particle reinforced composites yield better properties that angular composites and exhibit still significant plastic deformation (elongations exceed values found in the literature for this class of composites [29]);

(ii) increasing the amount of copper in the matrix leads to higher yield strength and UTS and reduces fracture strain in all composites, leading to brittle behaviour in some materials;

(iii) the influence of solution heat treatment is more visible for the Al-Cu4.5% matrix composites;

(iv) whereas solutionization leads to an increase in strength and flow stress, ageing does not increase significantly the flow stress and strength of the composites. An explanation of this observation is that it is not strenghtening by solid solution which increases the composite yield stress and UTS, but rather a reduction in internal damage accumulation, itself caused by the reduced amount of coarse brittle intermetallic phases (see Figures 4-5 and 4-6).

---

1. It must be mentionned that the A4.5C-A15p composite presented in Figure 4-46b contained a small vein in the casting which initiated premature fracture in all samples. It is thus expected that slightly larger $\varepsilon_f$ values would be obtained in vein-free materials.

# 4.5. CHEVRON-NOTCH FRACTURE TESTING

The determination of fracture toughness by chevron-notch testing was carried out systematically for all Al-Cu matrix composites. The influence of the various microstructural variables (particle type and size, Cu concentration and heat-treatment) is hence presented in detail in this chapter. The characterization of the micromechanisms of fracture (arrested-crack method and SEM fractography) in Al-Cu alloy matrix composites is presented in this section as well.

## *4.5.1 Angular-alumina composites*

Typical chevron-notched load-displacement fracture curves of angular alumina reinforced composites are presented in Figure 4-47. These allow a comparison of the composite toughness since the load value used to compute the toughness is always very close to the peak load.

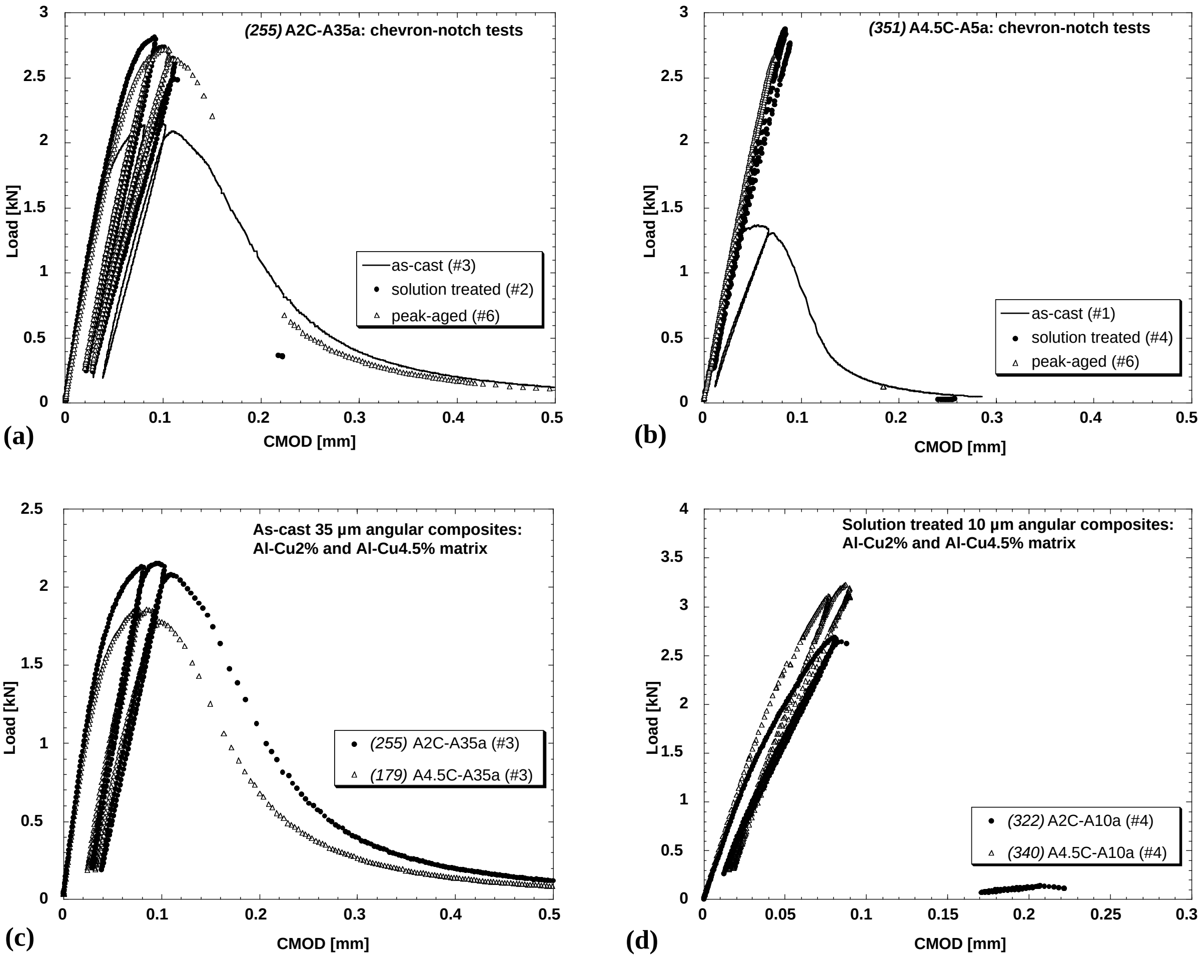

**Figure 4-47.** Chevron-notch fracture testing curves of Al-Cu matrix composites reinforced by angular $Al_2O_3$ particles. **(a)**: Al-Cu2%/35 µm composite; **(b)**: Al-Cu4.5%/5 µm composite; **(c)**: influence of Cu content on the toughness of 35 µm particle composites (as-cast condition); **(d)**: influence of Cu content on the toughness of 10 µm particle composites (solution treated condition).

### i. Validity

The thickness criterion was fulfilled in most composites for which tensile curves are available, or the deviation from the criterion was minimal (around 10% for the A2C-A35a composite in the ST and T6 conditions). For the smaller particle size composite (A2C-A5a) and the Al-Cu4.5% matrix, the criterion was always valid because the yield strength is higher. The second requirement, the plasticity criterion $p$ ($-0.05 < p < 0.1$), is more often violated, depending on the particle size and heat-treatment. For the large particle composites (60 and 35 µm) in the as-cast condition, it is systematically above 0.1, with values ranging from 0.2 to 0.4. This would indicate excessive plasticity; however, since these composites feature an almost fully brittle behaviour, it does not seem realistic that large scale yielding has occured in these (as also confirmed by photoelastic observations on CT specimens, Figures 4-41b and Figure 4-42f. This behaviour is hence attributed to extensive damage in front of the crack-tip, which leads to irreversible crack opening. Therefore, data are valid because criterion violation is not due to plasticity. After heat-treatment, on the other hand, $p$ decreases and most of the tests are valid according to this criterion.

For smaller particle size composites (5 and 10 µm), tests are valid in the as-cast condition, but negative values of $p$ are measured after heat-treatment. This is an indication of the presence of residual stresses. The $p$-values are actually sometimes well below -0.05 such that the data are not valid according to ASTM-E1304. As explained below for polygonal particle reinforced composites, the measured values are nevertheless still representative of the composite plane-strain fracture toughness.

### ii. Trends

One common feature to all materials is the obvious increase in toughness after solutionization, by 30 to 60% for the Al-Cu2% matrix composites. This is shown in Figure 4-47a for the A2C-A35a composite. After subsequent peak-ageing the toughness is not significantly modified, as seen on the same plot.

This effect is even more obvious with 4.5% of Cu in the matrix, as shown in Figure 4-47b for the A4.5C-A5a composite. Indeed, while the toughness in the as-cast conditions decreases as the Cu concentration in the matrix is raised to 4.5% (Figure 4-47c, 35 µm particle composite), this trend is reversed once the composites have been heat-treated: in the ST and T6 conditions and for all the composites, the toughness is slightly larger with 4.5% Cu in the matrix than with 2% Cu, such that the toughness nearly doubles after solutionization, attaining values that exceed 25 $\mathrm{MPa \cdot m^{1/2}}$ for the toughest composites (see Section 4.5.3 for quantitative values). An example is shown in Figure 4-47d for the 10 µm particles composites in the ST condition. Therefore, the general rule established in many alloys (for instance aluminium alloys) that toughness decreases with increasing yield strength is not valid in our composites since $\sigma_{0.2}$ is also larger with Al-Cu4.5% matrix, as seen for the 35 µm particle composite (Figure 4-45). Tensile properties of other Al-Cu4.5% angular reinforced composites were not evaluated but it is strongly expected that the same trend would be observed (this is also well confirmed in the next paragraph for polygonal reinforced composites).

## 4.5.2 Polygonal alumina composites

Typical chevron-notch load-CMOD plots of polygonal alumina particle composites are given in Figure 4-48. Generally speaking, these composites systematically feature a higher toughness than angular alumina composites for a given particle size. This is discussed later when comparing the two types of composites.

### i. Validity

The thickness criterion is fulfilled for all composites such that it is concluded that fracture toughness has been measured in plane-strain conditions. For the plasticity criteria, the composites exhibit the same response as angular particle composites, namely the *p* criterion is not verified ($p > 0.1$) in the as-cast conditions (except for the A4.5C-A5a composite). One could therefore argue that the reported toughness of as-cast specimens are actually underestimated. The correlation that exists between specimen thickness and the *p*-criterion was examined in [106], to conclude that the admissible maximum *p* value should probably be doubled such that most of the present data would then be valid.

For the heat-treated samples having a negative *p*-value, it is found that the present composites display a significant loading/reloading hysteresis loop. Measured values of *p* are, therefore, largeley subject to how the unloading curves are extrapolated with a straight line to the abscissa. One could for instance use the reloading points: all specimens would then exhibit a small positive *p* value. In addition, since the residual stresses are due to quenching, they are of tensile nature in the middle of the specimen (and hence in the chevron-notch). They would therefore tend to decrease the apparent toughness. The measured values are hence considered to be conservative and close to $K_{Ic}$, the plane strain toughness measured on pre-cracked CT specimens.

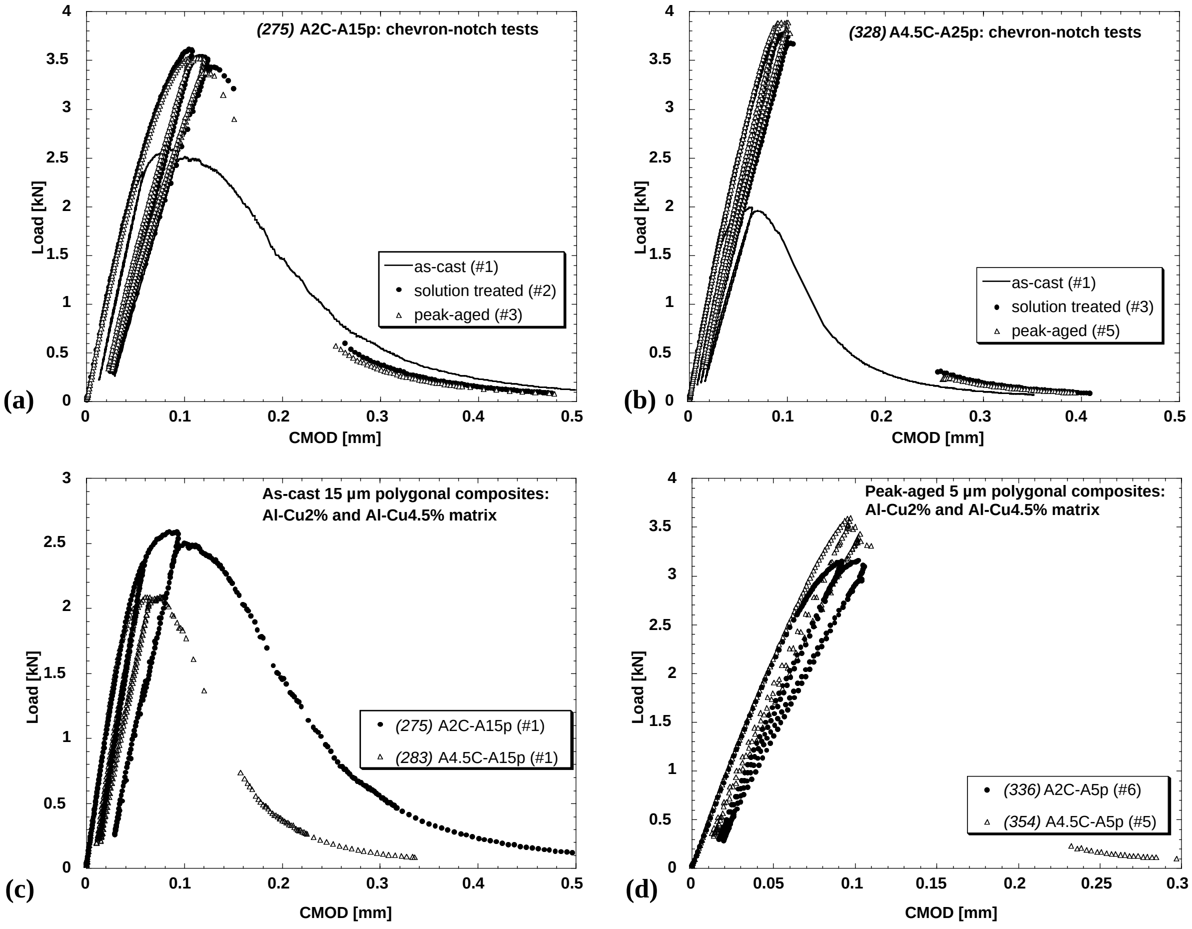

**Figure 4-48.** Chevron-notch fracture testing curves of Al-Cu matrix composites reinforced with polygonal $Al_2O_3$ particles. **(a)**: Al-Cu2%/15 µm composite; **(b)**: Al-Cu4.5%/25 µm composite; **(c)**: influence of Cu content on the toughness of 15 µm particle composites (as-cast condition); **(d)**: influence of Cu content on the toughness of 5 µm particle composites (peak-aged conditio).

**ii. Trends**

We note many similarities with angular $Al_2O_3$ reinforced composites concerning the effect of heat-treatment and copper concentration in the matrix. The toughness is greatly improved after solutionization and remains constant after peak-ageing (see Figure 4-48a for Al-Cu2%/15 µm particle composites). For the Al-Cu4.5% matrix, the increase in toughness after solution treatment is even more impressive, Figure 4-48b (25 µm particle size): the toughness almost doubles after heat-treatment.

The effect of Cu content in the matrix at the various heat-treatment conditions is also confirmed: in the as-cast condition, the composites containing 4.5% Cu are more brittle than those containing 2% Cu (Figure 4-48c, for the 15 µm particles composites). After solutionization treatment, on the other hand, the toughness of Al-Cu4.5% matrix composites increases for the 15 and the 5 µm particle composites (shown in Figure 4-48d in the T6 condition). It remains constant for the larger 25 µm particles composites. Again, this involves the interesting implication that in these materials, increasing the solute content allows to improve yield strength and UTS (Figure 4-46) without affecting the fracture toughness, which is even improved for the smaller particle size composites.

Quantitative values of toughness are also interesting: average toughness as high as 34 $MPa \cdot m^{1/2}$ are measured for the toughest composites, with a peak value of 35.7 $MPa \cdot m^{1/2}$ for two specimens (one A2CA-A15p and one A4.5CA-A25p). This is quite high for materials made of more than 60% ceramic by volume.

### 4.5.3 Data summary

All the fracture toughness data of alloyed matrix composites as measured by chevron-notch testing are summarized in Table 4-6. When measured, the tensile characteristics are also given in the table. Standard deviations are in general indicated for the different mechanical properties presented, except when only one specimen was tested. Global comparison of the Al-Cu matrix composites toughness as a function of the average particle size is finally given in Figure 4-49 for the as-cast (a), solution-treated (b) and peak-aged (c) conditions. The main conclusions that are obtained from these plots are the following:

(i) as-cast composites are less tough than heat-treated composites, and with Al-Cu4.5% matrix; these composites are the most brittle materials investigated;

(ii) in the ST and T6 conditions on the other hand, the toughness is slightly larger when the Cu concentration in the matrix rises from 2% to 4.5%, while the yield and tensile strengths are also enhanced;

(iii) while solutionization leads to an increase of toughness, subsequent peak-ageing does not affect the composite toughness significantly;

(iv) in angular alumina composites, the toughness increases as the average particle size increases from 5 to 10 µm, for which a peak value is obtained; it then decreases when the average particle size increases further, to finally attain its minimum value for the 60 µm particle size composites;

(v) polygonal alumina composites are tougher than angular particle composites, and their toughness is also increased with increasing the average particle size. A slight difference is noticed depending on the Cu content: while the toughness still rises in Al-Cu2% composites as the particle size is increased from 15 to 25 µm, with Al-Cu4.5% matrix, it remains constant;

(vi) finally, the measured values of toughness are very encouraging for this class of materials, with values close to 35 $MPa \cdot m^{1/2}$. Even in the angular particle composites that are not as fracture resistant, values exceeding 25 $MPa \cdot m^{1/2}$ are obtained (A4.5C-A10a, ST condition).

**Table 4-6.** Tensile and chevron-notch fracture toughness of Al-Cu matrix composites in the various heat-treatment conditions. *P* validity criteria also indicated.

| **Al-Cu2% matrix composites** | | | | | | | | **Al-Cu4.5% matrix composites** | | | | | | | |
|---|---|---|---|---|---|---|---|---|---|---|---|---|---|---|---|
| **Composite type** | **Heat treatment** | **$E^a$ [GPa]** | **$\sigma_{0.2}$ [MPa]** | **UTS [MPa]** | **$\varepsilon_f$ [%]** | **$K_{Iv}$ [MPa·m$^{1/2}$]** | **P [-]** | **Composite type** | **Heat treatment** | **$E^a$ [GPa]** | **$\sigma_{0.2}$ [MPa]** | **UTS [MPa]** | **$\varepsilon_f$ [%]** | **$K_{Iv}$ [MPa·m$^{1/2}$]** | **P [-]** |
| A2C-A60a | AC | 144 ± 5 | | 97 | 0.17 | 13.8 | 0.44 | A4.5C-A60a | AC | | | | | 11.4 ± 0.5 | 0.45 |
| | ST | | | 107 | 0.15 | 17.5 ± 0.5 | 0.17 | | ST | | | | | 17.7 ± 1.5 | 0.24 |
| | T6 | | | | | 16.8 ± 1 | 0.25 | | T6 | | | | | 18.7 ± 0.5 | 0.27 |
| A2C-A35a | AC | 142 ± 5 | 190 ± 15 | 190 ± 15 | 0.60 ± 0.20 | 19.1 ± 0.5 | 0.40 | A4.5C-A35a | AC | 148 ± 5 | | 204 $^b$ ± 20 | 0.2 ± 0.1 | 16.9 ± 1 | 0.34 |
| | ST | “ | 190 | 190 | 0.45 | 23.7 ± 1 | 0.05 | | ST | | | 215 $^b$ ± 20 | 0.1 ± 0.05 | 25.6 ± 0.5 | 0.09 |
| | T6 | “ | 170 ± 20 | 170 ± 20 | 0.35 ± 0.15 | 23.3 ± 1 | 0.14 | | T6 | | | 196 $^b$ | 0.14 | 24.3 ± 0.5 | 0.01 |
| A2C-A10a | AC | | | | | 14.5 ± 0.5 | 0.08 | A4.5C-A10a | AC | | | | | 13.4 ± 0.5 | 0.12 |
| | ST | | | | | 24.1 ± 0.5 | -0.15 | | ST | | | | | 27.6 ± 0.5 | -0.35 |
| | T6 | | | | | 23.3 ± 0.5 | -0.23 | | T6 | | | | | 25.4 ± 0.5 | 0.05 |
| A2C-A5a | AC | | 220 | 265 | 0.75 | 13.2 | 0.06 | A4.5C-A5a | AC | | | | | 12.4 ± 0.5 | 0.05 |
| | ST | | 260 ± 20 | 345 ± 15 | 0.85 ± 0.1 | 20.2 ± 0.5 | -0.22 | | STz | | | | | 23.5 ± 0.5 | -0.5 |
| | T6 | | 265 ± 25 | 360 ± 40 | 0.95 ± 0.15 | 19.9 ± 1 | -0.28 | | T6 | | | | | 22.7 ± 0.5 | -0.5 |
| A2CA-A25p | AC | 183 ± 3 | 207 ± 10 | 312 ± 5 | 1.8 ± 0.2 | 23.2 | 0.35 | A4.5CA-A25p | AC | 187 ± 3 | 277 | 331 | 1.3 | 17.3 ± 0.5 | 0.24 |
| | ST | | 255 ± 5 | 335 ± 5 | 1.4 ± 0.1 | 32.9 ± 0.5 | 0.07 | | ST | “ | 350 ± 10 | 429 ± 5 | 0.9 ± 0.1 | 33.3 ± 1 | -0.16 |
| | T6 | | 255 ± 5 | 340 ± 10 | 1.4 ± 0.1 | 32.5 ± 0.5 | 0.12 | | T6 | “ | 370 ± 10 | 443 ± 10 | 1.1 ± 0.1 | 33.3 ± 0.5 | -0.26 |
| A2CA-A15p | AC | 172 ± 3 | 217 ± 8 | 305 ± 15 | 1.4 ± 0.1 | 23.3 ± 0.5 | 0.33 | A4.5CA-A15p | AC | 182 ± 3 | 252 | 258 | 0.4 $^c$ | 18.6 ± 0.5 | 0.14 |
| | ST | | 235 ± 15 | 345 ± 15 | 2.2 ± 0.3 | 31.2 ± 0.5 | 0.05 | | ST | “ | 326 | 421 | 0.9 $^c$ | 33.7 ± 0.5 | -0.26 |
| | T6 | | 230 ± 15 | 345 ± 15 | 2.1 ± 0.2 | 30.9 ± 0.5 | 0.10 | | T6 | “ | 365 | 471 | 1.1 $^c$ | 33.7 ± 0.5 | -0.31 |
| A2CA-A5p | AC | | | | | 18.5 ± 1.5 | 0.27 | A4.5CA-A5p | AC | | | | | 14.7 ± 0.5 | 0.07 |
| | ST | | | | | 24.8 ± 0.5 | -0.13 | | ST | | | | | 29.2 ± 0.5 | -0.12 |
| | T6 | | | | | 26.2 ± 1 | -0.14 | | T6 | | | | | 29.6 ± 0.5 | -0.30 |

a. If not given, refer to pure Al composites (very close values).
b. Broke at about 0.2% strain or less, $\sigma_{0.2}$ equivalent to UTS.
c. Broke in a vein

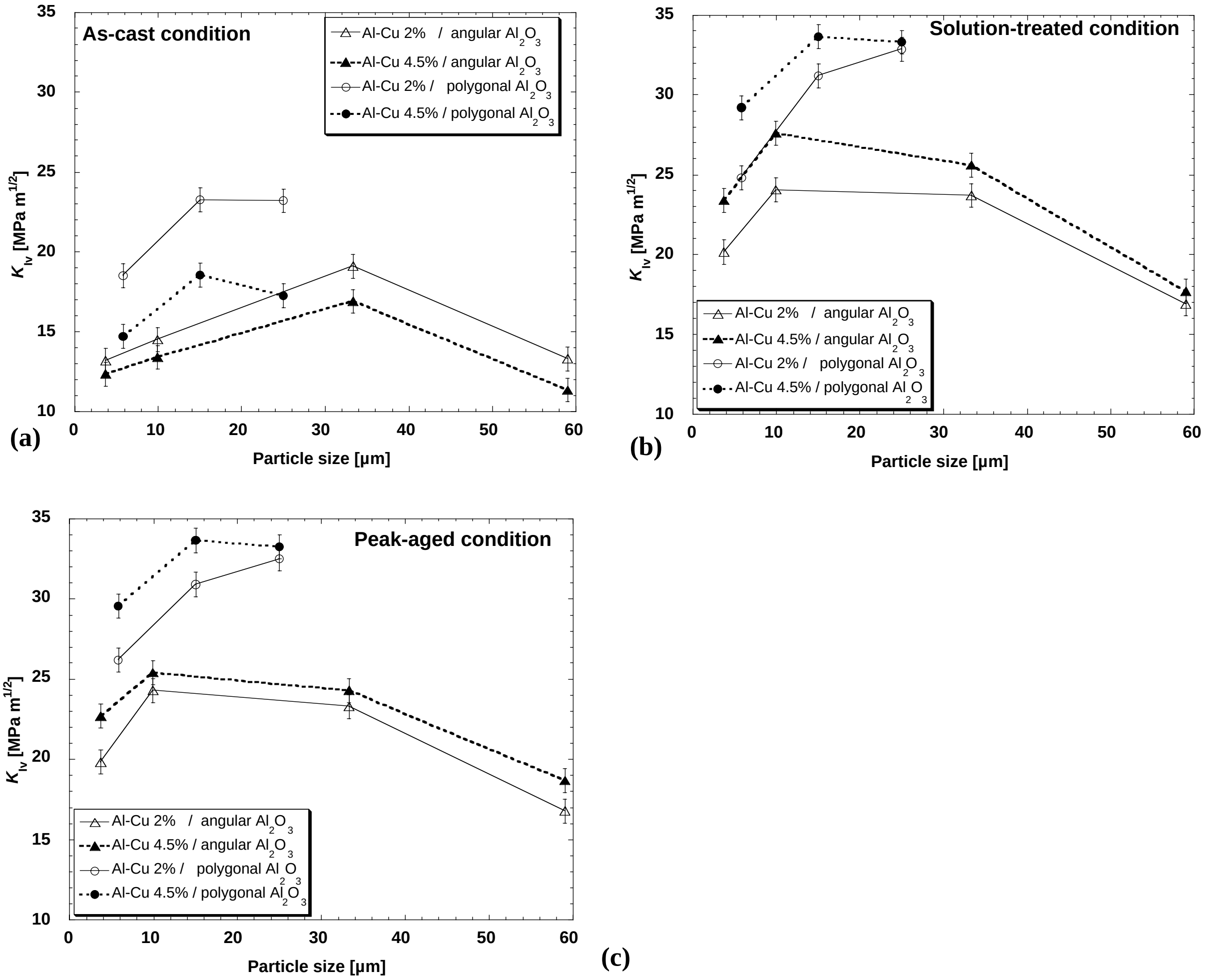

**Figure 4-49.** Plane-strain fracture toughness vs. average particle size in Al-Cu matrix composites, as measured by chevron-notch fracture testing and summarizing the influence of heat treatment and Cu concentration in the matrix. **(a)**: as-cast composites; **(b)**: solution treated composites; **(c)**: peak-aged composites.

## *4.5.4 Al-Cu matrix composites: micromechanisms of fracture*

### i. Arrested-crack method: crack profiles

AL-CU / ANGULAR ALUMINA COMPOSITES

Optical micrographs near the crack tip in Al-Cu/angular $Al_2O_3$ composites are presented in Figure 4-50. For average particle sizes of 10, 35 and 60 µm, particle cracking is clearly dominant regardless the Cu concentration and heat-treatment. Hence, in composites reinforced with large angular particles, all the particles in the wake of the crack are broken (Figures 4-50a and 4-50b). For the 10 µm particle size composites (Figure 4-50c, Al-Cu2% matrix), more broken particles are found along the crack path as compared to the pure Al matrix counterpart.

In the small (5 µm) particle reinforced composites, the crack propagates with a roughly equal level of matrix voiding and particle cracking, Figure 4-50d, implying again that the amount of broken particles along the crack path is larger than in the pure Al matrix composites. It remains, nevertheless, difficult to determine precisely the number of broken particles as compared to larger particle size composites, because one is limited by the microscope resolution.

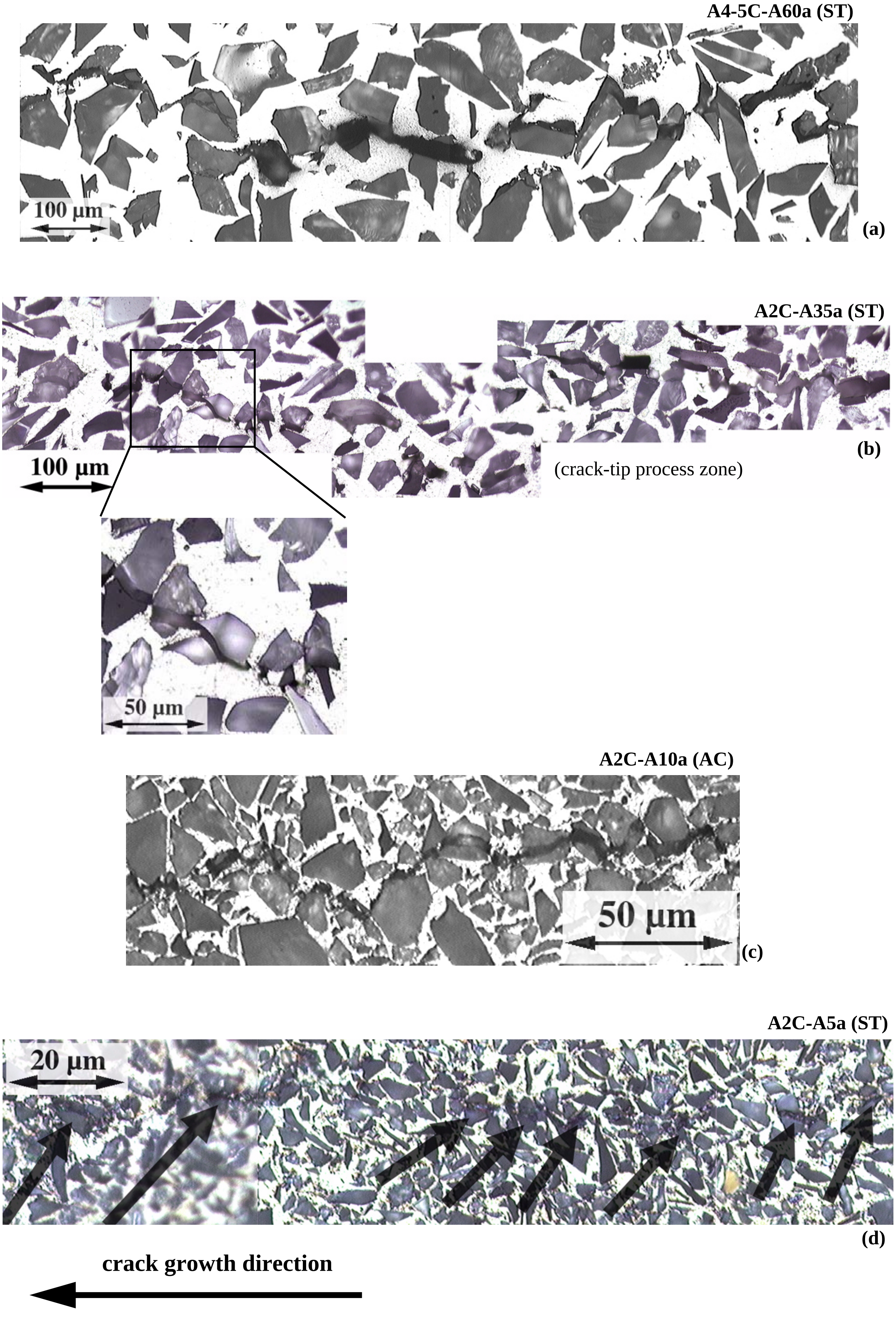
A4-5C-A60a (ST)
100 µm
(a)
A2C-A35a (ST)
100 µm
(b)
(crack-tip process zone)
50 µm
A2C-A10a (AC)
50 µm
(c)
A2C-A5a (ST)
20 µm
(d)
crack growth direction

**Figure 4-50.** Al-Cu/angular $Al_2O_3$ composites: optical micrographs near the crack tip of interrupted fracture tests. **(a)**: A4.5C-A60a (ST condition), particle cracking; **(b)**: A2C-A35a (ST condition), particle cracking; **(c)**: A2C-A10a (AC condition), particle cracking; **(d)**: A2C-A5a (ST condition), particle cracking (indicated by arrows) and matrix voiding. Crack growth direction from right to left.

### Al-Cu / Polygonal Alumina Composites

In contrast to angular particle composites, the dominant mode of failure depends on the Cu content and on the heat-treatment in these materials, at least for the medium and large particle size composites. In the 5 µm composites, matrix voiding remains the main micromechanism of failure whatever the Cu concentration and the heat-treatment (Figures 4-51a and 4-51b).

In the 15 µm particle composite and 2%Cu in the matrix, the fracture micromechanism remains similar as for the pure Al matrix composites, namely matrix voiding is the dominant mode of failure at all heat-treatment conditions, Figure 4-51c. As the matrix Cu content increases to 4.5%, the number of broken particles along the crack path increases, especially for the peak-aged condition, where nearly one-half of the crack path is occupied by broken particles, Figure 4-51d.

A similar behaviour is noticed for the 25 µm particle size composites, but in an amplified manner. For the Al-Cu2% matrix composites (Figure 4-51e), the fraction of broken particles doubles compared to the 15 µm particle size composite, and heat-treatment does not influence much this value. For the Al-Cu4.5% matrix, the fraction of broken particles increases, and becomes clearly dependent on the heat-treatment: in as-cast conditions, matrix voiding is still the dominant failure mode, in the solution-treated composite particle cracking and matrix cavitation operate at equivalent levels, whereas in the peak-aged condition particle cracking becomes dominant (Figure 4-51f).

### Quantification and Summary

Quantification of the micromechanisms of fracture, in terms of broken particles observed by opical microscopy, is given in Table 4-7.

**Table 4-7.** Quantification of the amount of broken particles in Al-Cu matrix composites, for various Cu content in the matrix and heat-treatment conditions.

| Particle type | Fraction of the crack path occupied by broken particles [-] | | | | | |
|---|---|---|---|---|---|---|
| | **Al-Cu2% AC** | **Al-Cu2% ST** | **Al-Cu2% T6** | **Al-Cu4.5% AC** | **Al-Cu4.5% ST** | **Al-Cu4.5% T6** |
| 60 µm angular | - | 0.72 ± 0.05 | - | 0.71 ± 0.05 | - | 0.70 ± 0.05 |
| 35 µm angular | 0.71 ± 0.05 | 0.67 ± 0.05 | 0.69 ± 0.05 | 0.72 ± 0.05 | 0.71 ± 0.05 | 0.74 ± 0.05 |
| 10 µm angular | 0.84 ± 0.10 | 0.78 ± 0.10 | - | - | 0.85 ± 0.10 | 0.82 ± 0.10 |
| 5 µm angular | 0.4 ± 0.10 | 0.4 ± 0.10 | | 0.4 ± 0.10 | | 0.4 ± 0.10 |
| 25 µm polygonal | 0.25 ± 0.05 | 0.24 ± 0.05 | 0.25 ± 0.05 | 0.33 ± 0..05 | 0.48 ± 0.05 | 0.76 ± 0.05 |
| 15 µm polygonal | 0.13 ± 0.05 | 0.20 ± 0.05 | 0.16 ± 0.05 | 0.22 ± 0.05 | 0.28 ± 0.05 | 0.50 ± 0.05 |
| 5 µm polygonal | 0.10 ± 0.05 | 0.17 ± 0.05 | 0.18 ± 0.05 | 0.10 ± 0.05 | 0.12 ± 0.05 | 0.14 ± 0.05 |

In summary, by increasing the average particle size in polygonal $Al_2O_3$ composites, a transition of the dominant fracture mode is detected as the Cu content in the matrix is increased and as the matrix is hardened by heat-treatment.

In angular $Al_2O_3$ composites, on the other hand, particle cracking was already the dominant failure mode in pure Al matrix composites for the large particle sizes. Increasing the matrix flow stress in these does not significantly modify the fraction of broken particles on the crack path, $f_b$, which remains high.

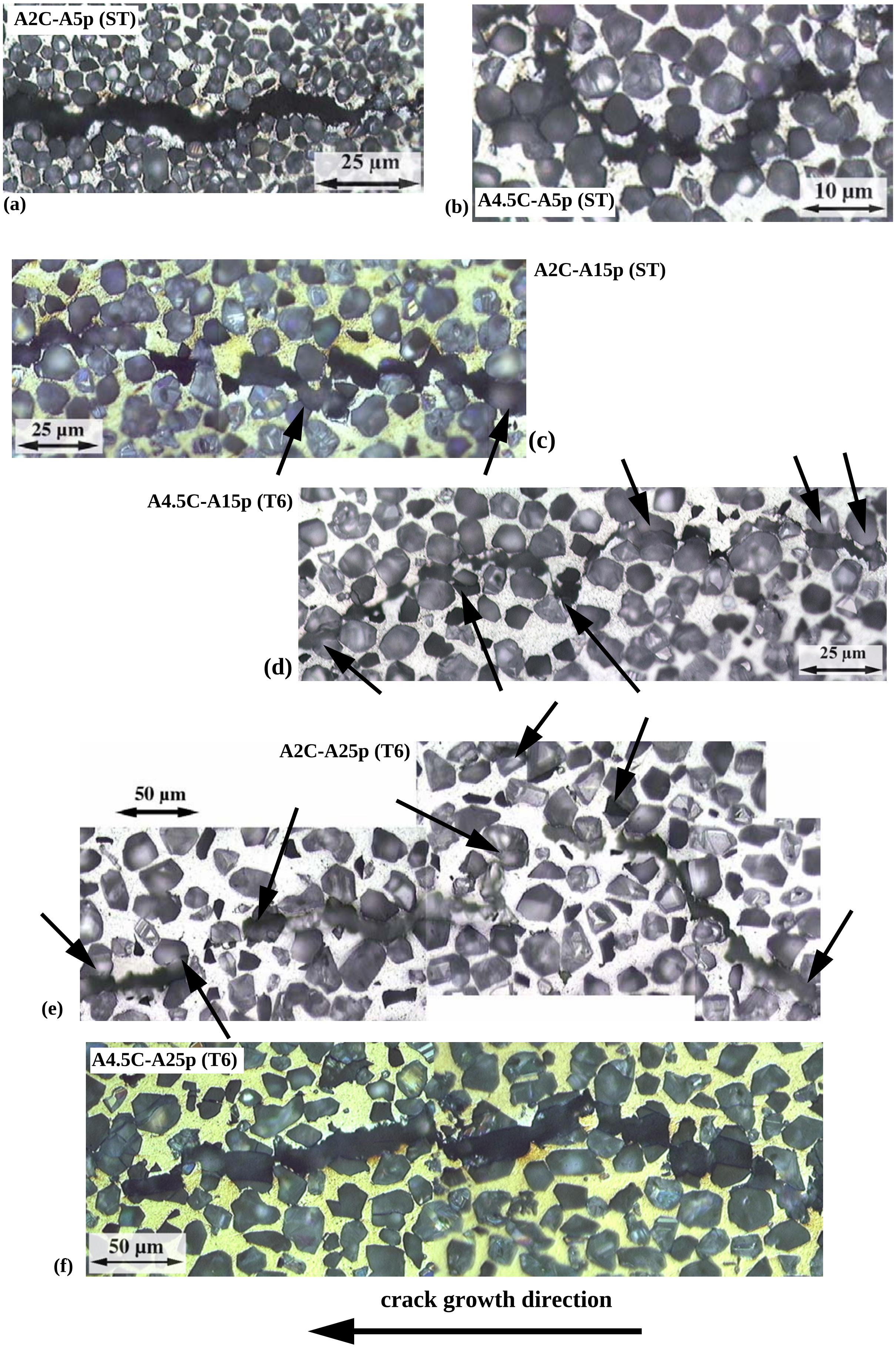
A2C-A5p (ST)
25 µm
(a)
(b)
A4.5C-A5p (ST)
10 µm
A2C-A15p (ST)
25 µm
(c)
A4.5C-A15p (T6)
25 µm
(d)
A2C-A25p (T6)
50 µm
(e)
A4.5C-A25p (T6)
50 µm
(f)
crack growth direction

**Figure 4-51.** Al-Cu/polygonal $Al_2O_3$ composites: optical micrographs near the crack tip of interrupted fracture tests. **(a)**: A2C-A5p (ST condition), matrix voiding; **(b)**: A4.5C-A5p (ST condition), matrix voiding; **(c)**: A2C-A15p (ST condition), matrix voiding and few particle cracking; **(d)**: A4.5C-A15p (T6 condition), particle cracking and matrix voiding; **(e)**: A2C-A25p (T6 condition), particle cracking and matrix voiding; **(f)**: A4.5C-A25p (T6 condition), particle cracking. Crack growth direction from right to left.

For composites reinforced by 10 µm angular particles, $f_b$ is larger for Al-Cu2% matrix (for which most of the crack path is occupied by cracked particles) than for pure Al matrix. It then remains constant as the Cu matrix content is subsequently increased to 4.5%. In addition, a higher fraction of the crack path is occupied by broken particles as compared to larger particle size composites, because the total volume fraction of particles in the composite is also larger. For the 5 µm particle composites, while it is clear that more particles are cracked for alloyed matrix composites, observations remains qualitative. We hence used SEM micrographs to estimate the fraction of broken particles on the fracture surface: this is around 40% for all composites.

### ii. SEM fractography

While in optical microscopy no significant difference is systematically visible between AC, ST and T6 samples regarding the micromechanisms of fracture. SEM investigation of the fracture surfaces with the Back-Scattered Electron (BSE) mode reveal clear differences, Figure 4-52 for Al-Cu2% matrix composites. In the 35 µm angular particle composite (Figure 4-52a), numerous second-phase particles

**as-cast composites**

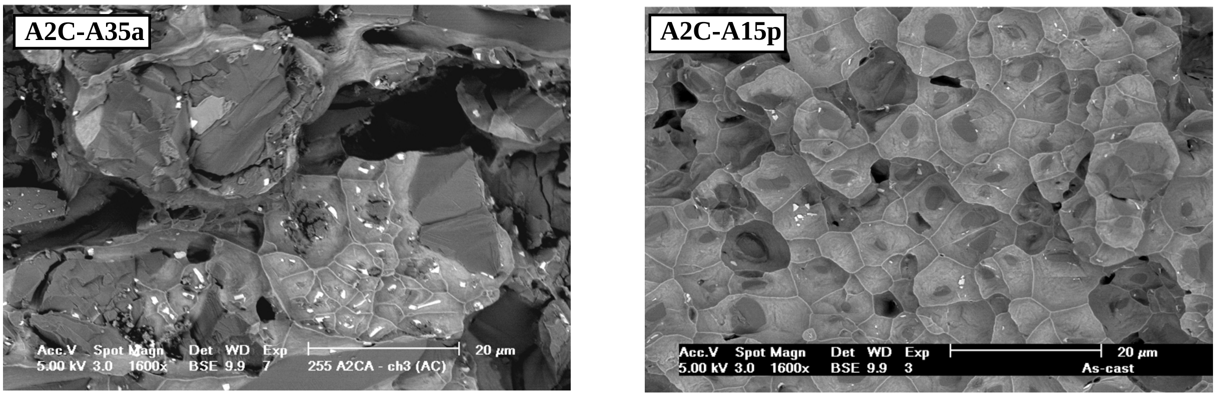
A2C-A35a
Acc.V Spot Magn Det WD Exp 20 µm
5.00 kV 3.0 1600x BSE 9.9 7 255 A2CA - ch3 (AC)
A2C-A15p
Acc.V Spot Magn Det WD Exp 20 µm
5.00 kV 3.0 1600x BSE 9.9 3 As-cast

**(a)** **(b)**

**solution-treated composites**

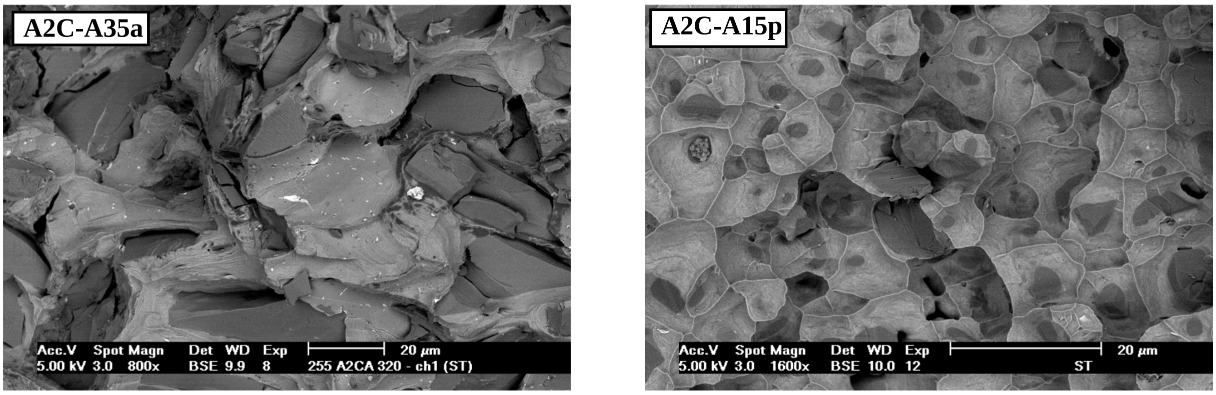
A2C-A35a
Acc.V Spot Magn Det WD Exp 20 µm
5.00 kV 3.0 800x BSE 9.9 8 255 A2CA 320 - ch1 (ST)
A2C-A15p
Acc.V Spot Magn Det WD Exp 20 µm
5.00 kV 3.0 1600x BSE 10.0 12 ST

**(c)** **(d)**

**Figure 4-52.** SEM fractographs of Al-2%Cu matrix composites, observed with BSE detector. **(a)**: 35 µm angular particles composite and **(b)**: 15 µm polygonal particle composite in as-cast conditions, secondary-phase precipitates (in bright) promote additional cavitation. **(c)** and **(d)**: same composites, solution-treated before testing, dimples nucleated by intermetallic phases are greatly reduced.

are located at the bottom of small cavities, indicating that they are responsible for matrix voiding. After solutionization (Figure 4-52c), the number of intermetallics on the fracture surface is clearly reduced. In both cases, a high fraction of the fracture surface is occupied by broken particles, which is in good agreement with optical observations of crack profiles. Similarly, in the 15 µm polygonal particle composite presented in Figure 4-52b, intermetallics are more present in the AC condition. In addition, these seem to nucleate additional cavities, while almost no second-phase is found in the ST condition (Figure 4-52d). As for pure Al matrix composites reinforced by the same particles (Figure 4-32b), particles emerge at the bottom of dimples indicating that cavities are nucleated close to, or at, particle/matrix interfaces.

These findings become more evident for Al-Cu4.5% matrix composites, for which SEM fracture surfaces observed by the BSE mode are presented in Figure 4-53. For the 35 angular particle size composite in as-cast condition (Figure 4-53a), a very large amount of intermetallic is found on the fracture surface. $Al_2Cu$ particles are coarser than in the Al-Cu2% matrix, which agrees with micrographs in Figure 4-5a and Figure 4-6b. After solution treatment (Figure 4-53c), coarse intermetallics are no longer found on the fracture surface, although the presence of smaller residual secondary-phases is noticed. Figure 4-53b shows the fracture surface of the 25 µm polygonal composite in the as-cast condition. We note again the high amount of coarse intermetallic phases that promote cavitation. After heat-treatment (Figure 4-53d), most of the secondary phases have disappeared from the fracture surface. Note also for this material the confirmation of extensive particle cracking, which was not observed for the pure Al matrix reinforced by the same particles (Figure 4-32a and Figure 4-34b), or for the Al-Cu2% matrix composite reinforced by smaller 15 µm particles (Figure 4-52b and d).

#### iii. Dimple size

3-D reconstructions of fracture surfaces in Al-Cu matrix composites was carried out for the 15 µm polygonal particle composites, for both Al-Cu2% and Al-Cu4.5% matrices in ST conditions. The dimple size as measured on the DEM are:

2.4 ± 0.5 µm for the Al-Cu2% matrix composite;
2.6 ± 0.5 µm for the Al-Cu 4.5% matrix composite.

The average dimple depth hence decreases as compared to the pure Al matrix composite reinforced with the same particles (Table 4-4), but no differences is noticed between Al-Cu2% and Al-Cu4.5% matrices. In addition the relative standard deviation is larger than in pure Al matrix composites, because the dimple geometry is less regular.

**as-cast composites**

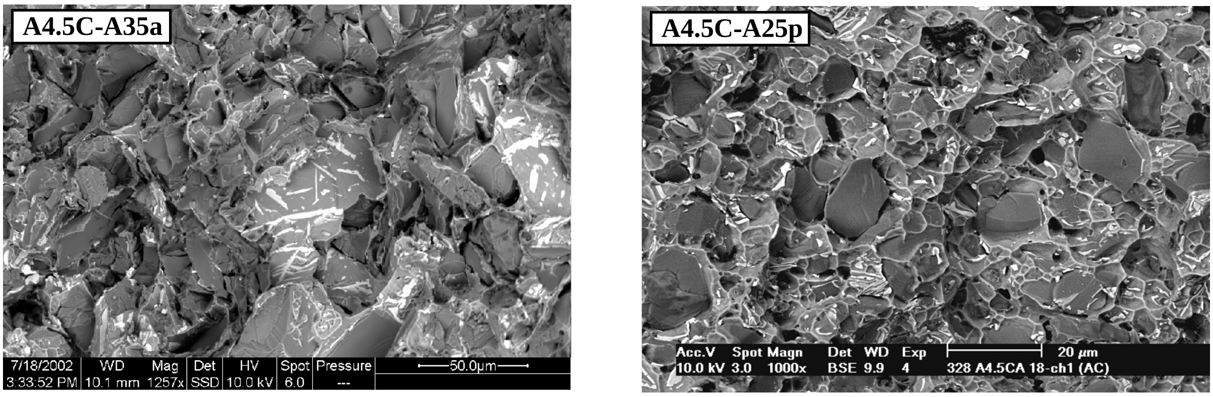
A4.5C-A35a
7/18/2002 3:33:52 PM WD 10.1 mm Mag 1257x Det SSD HV 10.0 kV Spot 6.0 Pressure ---
50.0µm
A4.5C-A25p
Acc.V 10.0 kV Spot 3.0 Magn 1000x Det BSE WD 9.9 Exp 4
20 µm
328 A4.5CA 18-ch1 (AC)

**(a)** **(b)**

**solution-treated composites**

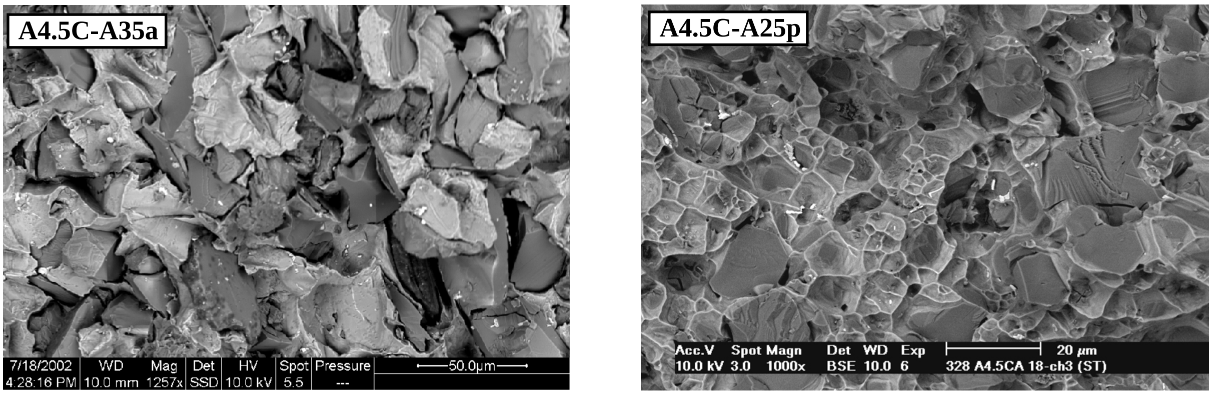
A4.5C-A35a
7/18/2002 4:28:16 PM WD 10.0 mm Mag 1257x Det SSD HV 10.0 kV Spot 5.5 Pressure ---
50.0µm
A4.5C-A25p
Acc.V 10.0 kV Spot 3.0 Magn 1000x Det BSE WD 10.0 Exp 6
20 µm
328 A4.5CA 18-ch3 (ST)

**(c)** **(d)**

**Figure 4-53.** SEM fractographs of Al-4.5%Cu matrix composites, observed with BSE detector. **(a)**: 35 µm angular particle composite and **(b)**: 25 µm polygonal particle composites in as-cast conditions, coarse secondary-phase precipitates (in bright) promote additional cavitation or local brittle fracture. **(c)**: and **(d)**: same composites, solution treated before testing. Note also the extensive presence of broken particles in the polygonal particle composite (b,d), not seen in the pure Al matrix composites.

# CHAPTER 5

# DISCUSSION

The discussion of the work is organized in the following manner. First, the global, measured toughness is correlated with the plastic zone shape in front of the crack tip. For this, the observed crack-tip deformation fields are compared with the analytical Hutchinson, Rice and Rosengren (HRR) solution and with 3-D finite element calculations, using the measured flow behaviour of the composites. In the second part, the micromechanisms of fracture that have been identified are analyzed using micromechanical models presented in Section 2.6, adapted to our materials. The local fracture energy is hence evaluated with these analytical models, and correlated with the global fracture energy, according to the approaches presented in Section 2.5. This link is discussed in more details in part 3 of the discussion, on the basis of Cohesive Zone Model (CZM) approach used in ductile fracture or for the fracture along metal/ceramic interfaces. In the last part of the discussion, the microstructural factors governing the toughness of metal matrix composites are presented, with emphasis on the key mechanisms that can be used to produce composites with optimized toughness.

## 5.1. THE GLOBAL FRACTURE ENERGY

### *5.1.1 The crack tip plastic zone*

It has been shown that despite the high ceramic content in the present PRMMCs, they are metallic materials from the point of view of toughness, in that a large contribution to fracture toughness is by plastic dissipation in front of the crack tip. This confirms early comments by Davidson [9, 158, 175] for composites with a far lower volume fraction of reinforcements (15% to 20%); whereas it is not intuitive to conceive such a large plastic zone for materials featuring up to 62 % of brittle phase, even when ductile pure aluminium is used as a matrix.

Strain fields presented in Chapter 4.3 provide quantitative data that can be compared with the elastic-plastic properties of the composites. Until approximately $J_{GT}$, the fracture of the composite test specimens can be considered as $J$-dominated, whereas after the onset of stable tearing the large region of crack-growth invalidates $J$. At $J_{GT}$, while the plastic zone can be large for the tougher materials relatively to the specimen size, the large-strain region on the other hand remains confined.

In what follows, we test whether the HRR solution describes with reasonable accuracy the strain-field on the specimen surface. We then compare these with more precise FE calculations that simulate the 3-dimensionnal CT specimens.

### i. Computing methods

The uniaxial stress-strain flow properties of the composites are fitted with the Ramberg-Osgood (R-O) equation (upon which the HRR analysis is based):

$$\frac{\varepsilon}{\varepsilon_0} = \frac{\sigma}{\sigma_0} + \alpha\left(\frac{\sigma}{\sigma_0}\right)^n \qquad (5\text{-}1)$$

where $\alpha = 3/7$, $n$ is the strain hardening coefficient, and $\varepsilon_0$ and $\sigma_0$ are the yield strain and stress, respectively. Because damage accumulation occurs from the onset of plastic deformation in the composites during uniaxial strain, we use the "effective" tensile curves corrected for damage. Hence, damage is not taken into account in computing the crack-tip plastic strains. Effective curves were generated for pure Al matrix composites by Kouzeli [89, 252] on the basis of the change in the elastic modulus. We use the same method for the Al-Cu2% matrix composite for which photoelastic observations were carried out. The reason for this choice is that the difference between the experimental, "damaged" tensile curve and the effective curve corrected for damage was in all cases insignificant (especially at low plastic strains). The R-O relation fits the effective tensile data of the composites very well, and the fitting parameters of the three composites for which photoelastic observations are compared with analytical and FEM computations are given in Table 5-1[1].

ANALYTICAL STRAIN FIELDS

To allow a meaningful comparison with the observed strain fields on the specimen surface, computations of the analytical HRR solutions were carried out in plane-stress. The HRR fields were programmed on the Mathcad™ software (Mathsoft Inc., USA), according to the following procedure:

(i) the surface region perpendicular to the crack propagation plane is discretized in sub-elements having a surface of 0.25x0.25 mm$^2$. For each pair of points, the components of the surface deformation fields in polar coordinates (eq. A-25), are computed according to the form given in [253] (in which the numerical factors of HRR are exhaustively listed);

(ii) the principal values of the surface strain tensor ($\varepsilon_1$, $\varepsilon_2$) at each point are computed, from which the largest shear strain component defined as ($\varepsilon_1$-$\varepsilon_2$) is extracted (which corresponds to the values observed by photoelasticity);

(iii) the crack-tip strain field ($\varepsilon_1$- $\varepsilon_2$) is finally drawn at values of $J$ corresponding to the instant of photoelastic observations (values of $J$ close to $J_{GT}$).

FINITE ELEMENT MODELED STRAIN FIELDS

The finite element simulations were carried out on the commercial Finite Element package ABAQUS, version 5.8 [254][2]. User routines were employed for the material law and for the computation of the largest in-plane shear component $\varepsilon_1$- $\varepsilon_2$. Due to symmetry, a quarter of the three-dimensionnal CT specimens was modeled, with 32800 brick elements with linear interpolation and reduced integration.

---

[1] The parameters of the HRR solution ($\tilde{\sigma}\,(r,\theta)$, etc) are available in tabulated form for integer values of the strain hardening parameter $n$. Such integer values were imposed for fitting the parameters of the R-O equation that were used for the HRR solution. No such limitation restricted the choice of parameters used in FEA, such that $\varepsilon_0$ was then defined as $\sigma_0/E$ where $E$ is the actual Young's modulus (R-O law is hence in the form: $\varepsilon = \sigma/E + \alpha(\sigma_0/E)(\sigma/\sigma_0)^n$ ). Both description yield very similar fits for the "non-damaged" tensile curves.

[2] All FE simulations were carried out in the laboratory by Dr. A. Rossoll.

20 layers of elements were employed in the thickness direction. A deacreasing layer thickness was used from the centre plane towards the surface of the specimen, in order to resolve the increasingly steeper gradients. Furthermore, a decreasing size of elements was used in the crack tip region. The crack tip was modeled as straight (*i.e.* without crack tunnelling) and initially blunted, with radius of 1.5 µm. The overall view of the 3-D meshes as well as close-up view of the crack tip region mesh are shown in Figure 5-1. A similar mesh was used for the plane stress model of the CT specimen, with 1577 quandrangular linear elements with reduced integration.

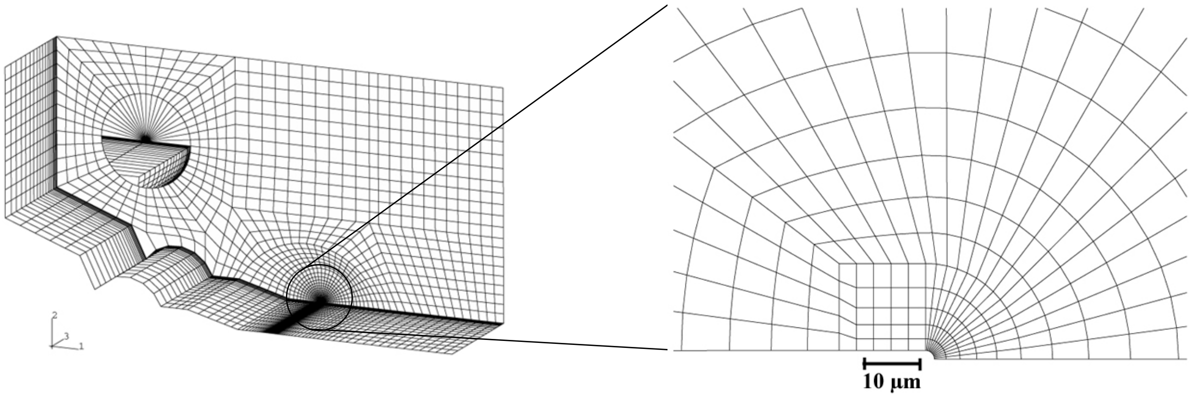

**Figure 5-1.** Mesh of the 3 dimensionnal CT specimen. Overall view and details of the crack-tip region.

The computations were carried out in a large strain framework, using $J_2$ flow theory. The $J$-integral was computed along contours, and averaged over the thickness (3D specimen). A large number of contours is necessary in order to achieve consistent values of the $J$-integral. The reason for this seemingly inconsistent behaviour (the $J$-integral is theoretically contour independent) is that extensive plastic deformation occurs in the specimen (there is no yield point), and plasticity induces a deviation of the local load path from radial loading. However, the latter is implicitly required, by approximating plasticity with non-linear elasticity (which is the framework of the derivation of the $J$-integral). See also the comprehensive discussion by Brocks and Scheider [255]. The $J$ values computed at the 48th contour were used, which is sufficiently far from the crack tip to minimize the influence of plastic deformation.

The crack length $a_0$ was imposed to match the initial crack length of the particular samples used for $J$-$R$ curve measurements and photoelastic observations. Crack advance not being modeled in the computations, it was verified whether this would influence the crack-tip strain fields. Thus a second set of computations was carried out, for a crack length $a_1$ matching the crack length at the instant of photoelastic observations (namely close to the peak load and $J_{\mathrm{GT}}$).

### ii. Computation results and comparisons

The experimental $F$-CMOD plots and $J$-CMOD plots are compared with FE computations for the three composites in Figure 5-2. Since damage and crack motion are not taken into account, the computed $F$-CMOD curves lie above the experimental curves (Figure 5-2a) after the elastic domain.

For the crack length $a_1$ (corresponding in the experiment to the instant of photoelastic observations), the computed load decreases but still remains somewhat too high at the corresponding experimental crack length. We attribute this mainly to viscoplastic effects, which are not accounted for in the FE formulation. Such behaviour is indeed clearly visible on the experimental curve before each unloading cycles. Since the test was temporarily interrupted to allow the acquisition of photoelastic patterns, relaxation occured during this time, in particular for softer pure Al matrix composites. Relaxation is less pronounced in Al-Cu matrix composite (Figure 5-2e), and indeed the computed $F$-CMOD curve for the crack length $a/W$ = 0.48 predicts a load closer to experiment. There also remains some uncertainty regarding the “real” crack advance as measured from the specimen compliance (hysteresis during unloading/reloading cycles becomes more marked as the crack propagates, such that the actual crack length depends on the definition used to measure the elastic compliance).

**Table 5-1.** Input data for the computation of strain fields with HRR solutions and FE simulations.

| **Composite** | **Ramberg-Osgood fit**[a] | | | | | **CMOD [mm]** | | **Load [kN]** | | **$J$ [kJ/m$^2$]** | |
|---|---|---|---|---|---|---|---|---|---|---|---|
| | $n$ | $\sigma_0$ **[MPa]** | $\varepsilon_0$ **[-]** | $E$ **[GPa]** | $a_0/w$[b]<br>$a_1/w$[c] | **exper.** | **calc.** | **exper.** | **calc.** | **exper.** | **calc.** |
| *(64)*A-A35a (#6} | 5 | 65 | 0.00085 | - | 0.45 | - | 0.0977 | - | 2.95 | - | 3.1 |
| | 4.8 | 53 | - | 142 | 0.47 | 0.1027 | 0.1000 | 2.51 | 2.76 | 3.1 | 3.1 |
| (244)A-A15p (#2) | 4 | 64 | 0.00029 | - | 0.46 | - | 0.1227 | - | 4.26 | - | 5.7 |
| | 4.1 | 71 | - | 175 | 0.49 | 0.1344 | 0.1289 | 3.45 | 3.84 | 5.7 | 5.7 |
| (253)A2C-A15p (#2, ST) | 6 | 203 | 0.00148 | - | 0.46 | - | 0.0807 | - | 5.37 | - | 4.4 |
| | 5.3 | 177 | - | 175 | 0.48 | 0.0848 | 0.0840 | 4.80 | 5.05 | 4.4 | 4.4 |

a. First row: fit for HRR computations, second row: fit for FE computations, see the previous footnote.
b. Initial crack length, calculated from the minimum compliance measured during testing.
c. Crack length at the instant of photoelastic observations (close to peal load and $J_{GT}$).

It is of interest here to compare the contour plots of the strain fields at an equivalent value of $J$. As seen on Figures 5-2b and d for the pure Al matrix composites, the $J$-CMOD curves correlates well with experiments; in particular for the Al-Cu matrix composite (Figure 5-2f), both the experimental value of $J$ and the simulated are exactly superimposed for $a/W$ = 0.48.

The strain fields computed with the initial crack length $a_0$ are almost identical with those computed for a crack length $a_1$. Therefore, for simplicity, we present the crack tip fields as calculated for one crack length only, namely the “advanced” crack length, $a_1$. A summary of key parameters (crack length, CMOD, $F$ and $J$) is given in Table 5-1.

The crack-tip strain fields computed by the HRR solution and the 3D FE simulations for the pure Al matrix composites are presented in Figures 5-3 ($Al_2O_3$ 35 µm angular) and 5-4 ($Al_2O_3$ 15 µm polygonal), and compared with the fields observed by photoelasticity. For the pure Al matrix composites, the plane stress HRR fields describe reasonably well the experiments for the largest strain values shown in the plots. In particular, in the planes situated at approximately 30 to 60° from the crack plane, the isostrain values are close to the experimentally measured ones. Correlation remains, nevertheless, incomplete: clearly, the experimental plastic zone contour (the lower strain fringes) is “attracted” towards the back of the specimen, such that the plastic zones exhibit an elongated shape in the horizontal direction.This is not captured by the HRR field because the latter assumes a semi-infinite specimen geometry. Such a plastic zone shape is also well visible on the experimental field of the A-B60 composite (Figure 4-40a).

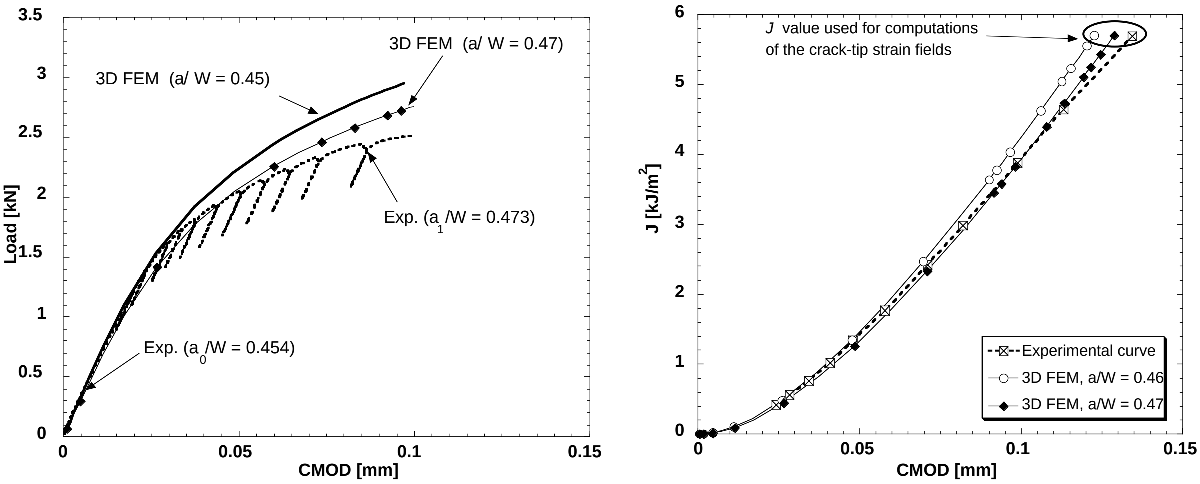

**(a)** Load-CMOD: A-A35a composite **(b)** *J*-CMOD: A-A35a composite

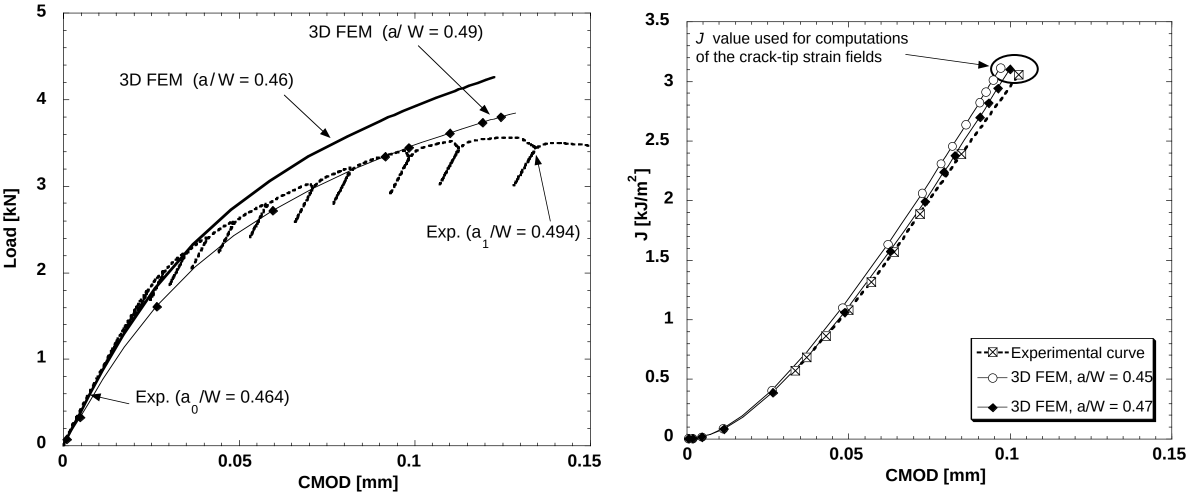

**(c)** Load-CMOD: A-A15p composite **(d)** *J*-CMOD: A-A15p composite

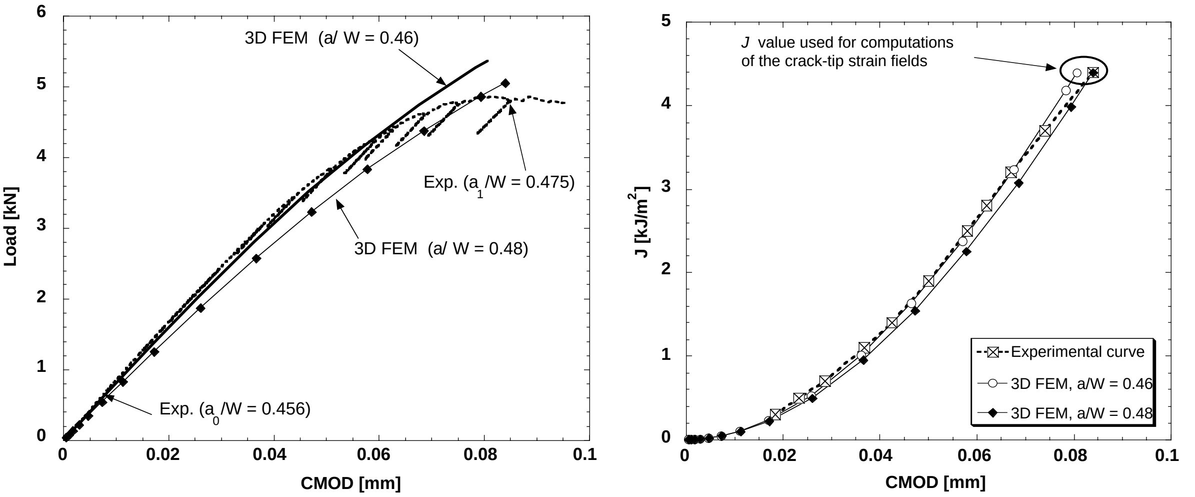

**(e)** Load-CMOD: A2CA-A15p composite **(f)** *J*-CMOD: A2CA-A15p composite

**Figure 5-2.** Load-CMOD and *J*-CMOD curves, comparison between experiments and FEM for three different composites. **(a)** and **(b)**: A-A35a composite*;* **(c)** and **(d)**: A-A15p composite; **(e)** and **(f)**: A2CA-A15p composite (ST condition). Crack-tip strain fields of the CT specimens are subsequently computed at *J* values matching those at the instant of photoelastic observations. Such values are indicated on the plots.

FEM results on the surface of the 3D CT specimens at same levels of *J*, on the other hand, describe well this effect: in Figures 5-3c and 5-4c, the elongated plastic zone size is well predicted for both materials. The plastic zone on the back of the specimen is also observed with the 3D computations, thereby confirming experiments (Figure 5-4). Comparison of the quantitative values of $\varepsilon_1$-$\varepsilon_2$ (refer to the color index indicated on the figures) is also excellent for both the crack-tip field and the plastic hinge.

The plastic zone on the back of the specimen is, on the other hand, overestimated by plane stress FE analysis. This, in turn, influences the crack-tip plastic zone size, which becomes obviously too small compared to experiments. The HRR field actually captures better the real field in the present composites as compared to the plane-stress FE field. This points out the importance of three-dimensional effects in determining the plastic zone size at the specimen surface.

The second feature that is better captured by the 3-D FE simulations is the shape of the contour lines along the crack plane. From the experimental observations, one sees that the isostrain contour lines meet close to the crack tip, which is a feature typical of plane-strain conditions. On the surface of the computed 3D specimen, the same feature is observed. This is not described by the plane stress HRR field, in particular for the low strain fringes. 2D plane stress finite element simulations (Figure 5-3d and Figure 5-4d) yield characteristics similar to the HRR field. In other words, the experimental crack tip strain field on the free surface is roughly intermediate between plane strain and plane stress conditions.

This was also reported by Chan [256] who determined experimentally stationary crack-tip strain fields in Al-Fe-X alloys, and by Dong *et al.* [257]on the basis of FEM in plane strain and plane stress conditions for nodular cast iron. We therefore conclude that along the specimen surface, the deformation fields are significantly influenced by three-dimensional stress effects. While stress normal to the surface is zero, stress and strains gradients are present, and exert a significant influence on in-plane strains, because the surface does not remain plane, in contrast to the plane stress assumptions.

Comparison between experimental and computed fields for (stronger) Al-Cu matrix composites is presented in Figure 5-5[1]. With the exception of the feature explained in the footnote, the description of experimental crack-tip fields by the 3D FEM analysis is again very good. As above, the HRR solution provides a better description of the crack-tip field than the plane-stress 2D FEM simulation but again this has no fundamental meaning. The higher yield strength of the composite has the expected effect that strain contours have an orientation closer to 90°. This is well noticed by comparing the larger strain contours shown in Figure 5-5d with those of pure Al matrix composites. The appearance of the plastic hinge is obviously delayed, which is also the reason why the HRR solution provides a reasonable approximation. Still, purely plane stress conditions do not exist on the surface, which is again in this case between plane stress and plane strain.

---

[1] A word of caution is necessary here: because the bonding strength between the photoelastic coating and the specimen was not as strong as with pure Al matrix composites, debonding of the coating occured when machining the middle of the coating in the crack plane. Hence, photoelastic investigations on unnotched coatings is used for comparison, which somehow perturbs the photoelastic response in the planes perpendicular to the crack tip and behind. Farther from the tip on the other hand, observations remain reliable. Moreover, confidence in the computations is recognized from the good correlation between experiments and 3D FEM for pure Al matrix composites.

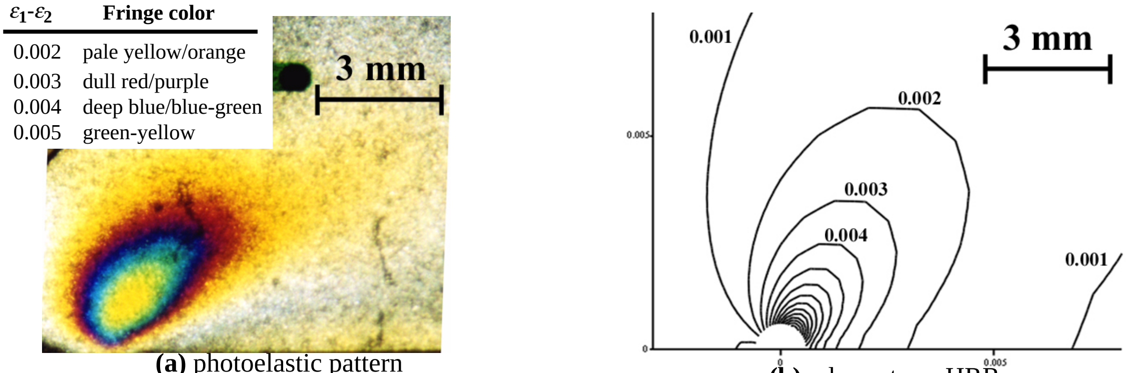

**(a)** photoelastic pattern

**(b)** plane stress HRR

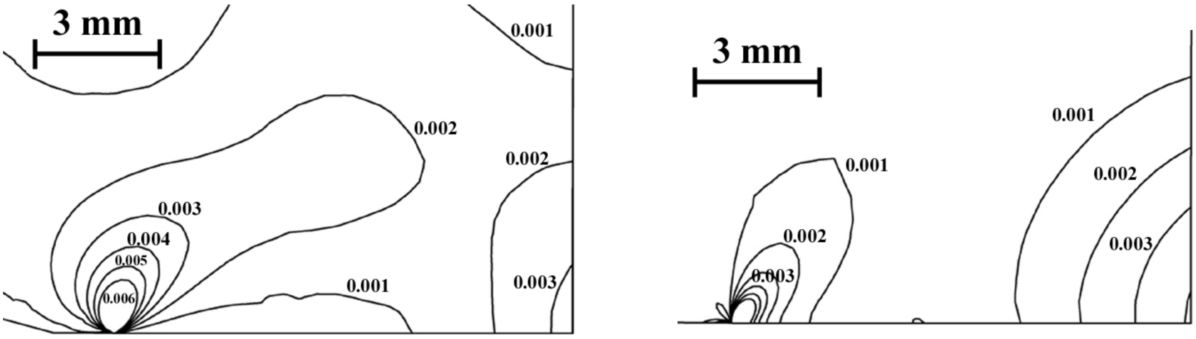

**(c)** FEM, surface of the 3D specimen

**(d)** FEM, 2D specimen, plane stress

**Figure 5-3.** Crack-tip strain fields on the surface of the A-A35a composite at $J = 3.1 \mathrm{kJ/m^2}$, visualized in terms of $\varepsilon_1$-$\varepsilon_2$. **(a)**: observed field; **(b)**: HRR field in plane-stress; **(c)**: FE field (3D specimen surface); **(d)**: FE field (2D specimen, in plane stress).

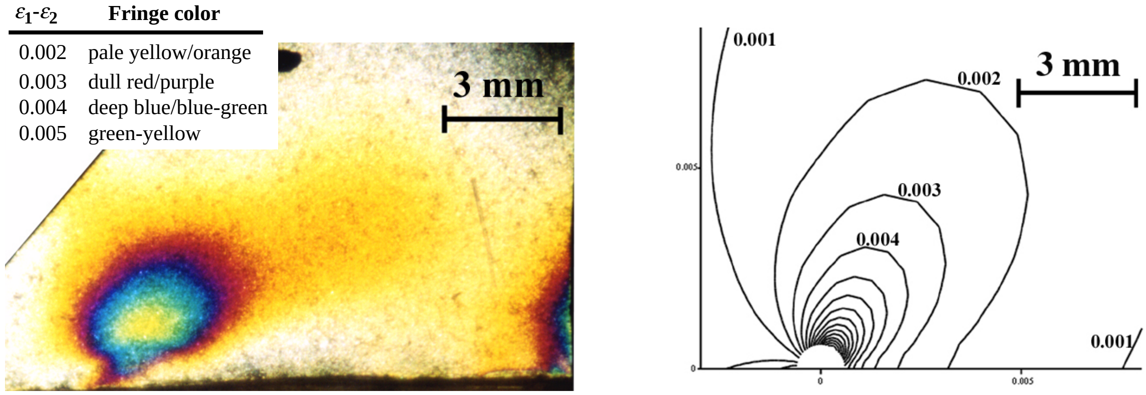

**(a)** photoelastic pattern

**(b)** plane stress HRR

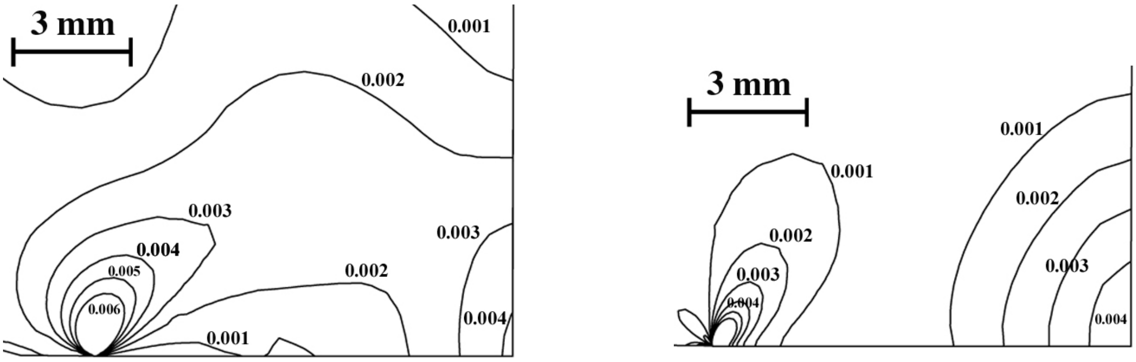

**(c)** FEM, surface of the 3D specimen

**(d)** FEM, 2D specimen, plane stress

**Figure 5-4.** Crack-tip strain fields on the surface of the A-15p composite at $J = 5.7 \mathrm{~kJ/m^2}$, visualized in terms of $\varepsilon_1$-$\varepsilon_2$. **(a)**: observed field; **(b)**: HRR field in plane-stress; **(c)**: FE field (3D specimen surface); **(d)**: FE field (2D specimen, in plane stress).

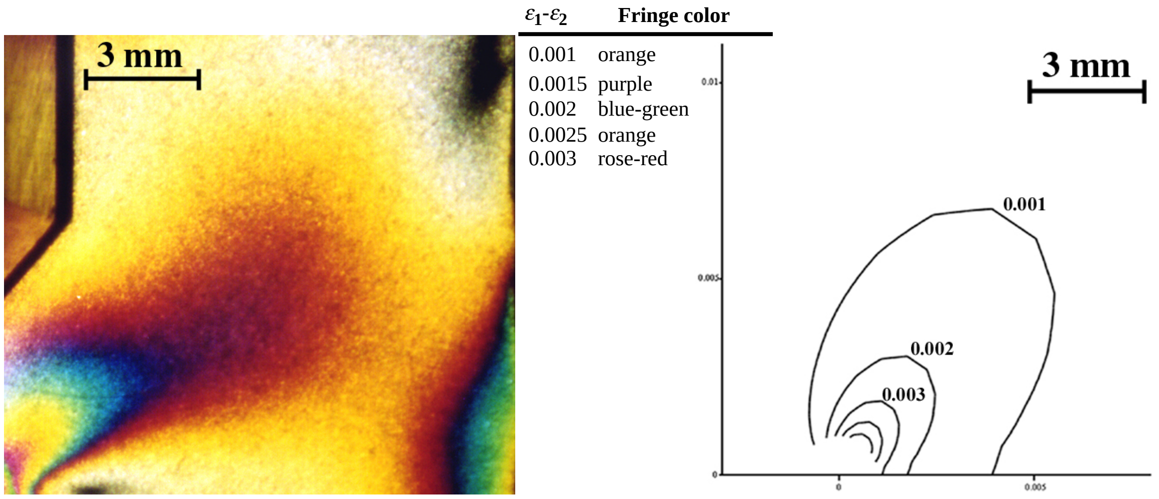

| $\varepsilon_1$-$\varepsilon_2$ | **Fringe color** |
|---|---|
| 0.001 | orange |
| 0.0015 | purple |
| 0.002 | blue-green |
| 0.0025 | orange |
| 0.003 | rose-red |

**(a)** photoelastic pattern

**(b)** plane stress HRR

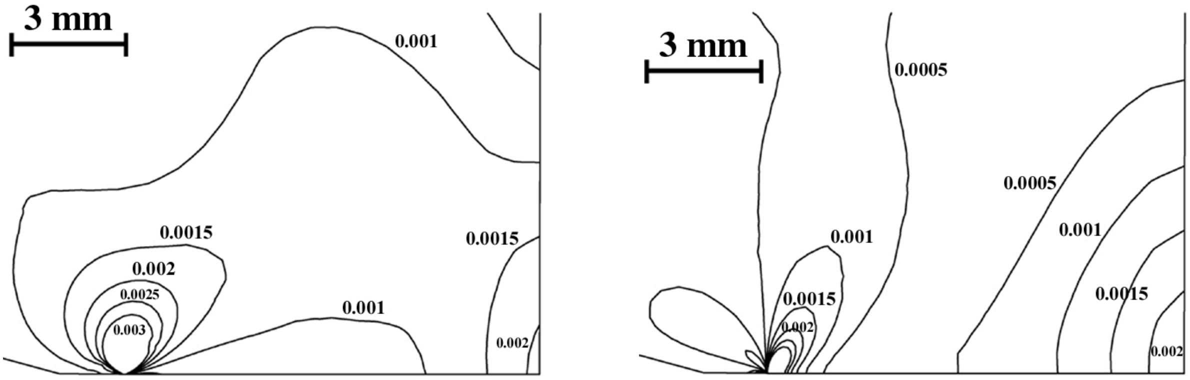

**(c)** FEM, surface of the 3D specimen

**(d)** FEM, 2D specimen, plane stress

**Figure 5-5.** Crack-tip strain fields on the surface of the A2CA-15p composite at $J$ = 4.4 kJ/m$^2$, visualized in terms of $\varepsilon_1$-$\varepsilon_2$. **(a)**: observed field on unnotched coating; **(b)**: computed field (HRR solution in plane-stress); **(c)**: FE field (3D specimen surface); **(d)**: FE field (2D specimen, in plane stress).

### iii. Discussion

Do these composites get tougher as they get more ductile ? Some times this is indeed observed. For instance, Al-Cu matrix composites reinforced with polygonal particles are tougher than angular alumina reinforced composites (Figure 4-49), and at the same time they are fairly ductile in tension, while the second class is much more brittle (Table 4-6).

But they are counter-examples to this inference: knowledge of elastic-plastic properties of the composites is not sufficient to rationalize the composite toughness. Three examples illustrate this remark well:

- Comparing typical tensile curves of pure aluminium reinforced with 10 µm and 35 µm angular particles [89, 179] shows that both materials exhibit fracture strains between 2 and 2.5%, while the former has a higher flow stress. This implies on the one hand a larger plastic zone for the 35 µm composite, but on the other hand a higher density of dissipated plastic work per unit volume in the 10 µm composite (since the flow stress is larger), such that estimating which composite is tougher is difficult. Looking at $J_R$ curves (Figure 4-10) and the toughness $J_{GT}$ (Figure 4-26) of these two composites shows clearly that the 35 µm particle size composite has a higher fracture energy.

- An other illustrative example is found in the Al-$B_4C$ system when comparing the 60 and the 5 µm reinforced composites. Both have maximum elongations of about 2.5%, while the finer 5 µm particle size composite features a flow stress and UTS more than twice those of the coarse 60 µm particle size composite [89]. The 60 µm particle size composite, on the other hand, has a fracture energy approximately four times that of the 5 µm composite (Figure 4-17 and Figure 4-26).
- The last example is taken from Al-Cu matrix composites reinforced by the 25 µm polygonal alumina particles: in tension, the Al-Cu2% matrix composite in the solution-treated condition has a behaviour almost identical to the as-cast Al-Cu4.5% matrix composite (Figure 4-46). One could therefore expect a similar toughness. Chevron-notch toughness data of these two materials (Table 4-6 and Figure 4-49) show that the former has a plane-strain toughness of 33 $\mathrm{MPa{\cdot}m^{1/2}}$, while for the latter this value is only 17 $\mathrm{MPa{\cdot}m^{1/2}}$.

In summary, once the critical fracture parameter is known from experiment, the present experiments and computations lead to two conclusions:

- The main contribution to composite toughness is plastic dissipation in front of the crack tip: the crack-tip plastic zone is finite and increases for tougher composites.
- The plastic zone size and shape are well described by the strain fields modeled from the elastic-plastic properties of the composites, provided that a full three-dimensional analysis of the real specimen is carried out.

### 5.1.2 Comparison of chevron and *J*-integral fracture testing in Al-Cu matrix composites

For Al-Cu matrix composites, systematic fracture toughness data were measured on chevron-notched specimens. Therefore, it is necessary to ensure that chevron-notch fracture testing and *J*-integral fracture testing on CT specimens provide consistent measures of fracture toughness.

As was presented in the literature review (§. 2.3.2), the crack-driving force vs. crack length in the chevron-notched geometry features a parabolic shape producing stable crack propagation even in brittle materials. For materials with a flat *R*-curve, the critical stress intensity factor $K_{\mathrm{Iv}}$ is then inferred from the maximum load during fracture testing, when the minimum of the crack driving force is tangent to the (flat) *R*-curve, which corresponds to the plane-strain critical stress intensity factor at initiation, $K_{\mathrm{Ic}}$, if size requiremeents are met.

For materials with a rising *R*-curve, the situation is different. Let us consider the schematic “real” (*i.e.* geometry independent) composite *R*-curves, Figure 5-6. The initial part of the curve corresponds to process zone formation and a short inital degree of crack growth. This portion of the curve is captured during *J*-integral testing, until the critical event given by $J_{\mathrm{GT}}$ (given in terms of its equivalent stress intensity factor, $K_{\mathrm{JGT}}$). At that point, it was inferred earlier that ductile tearing takes place in our composites. Resistance to ductile tearing is reduced as the matrix is strengthened such that ductile instability in *J*-integral testing occurs slightly after $J_{\mathrm{GT}}$ in polygonal particle reinforced composites (Figure 4-23b) or at the end of the initial portion in angular particle reinforced composites (Figure 4-22b). *J*-analysis becomes in any event invalid after the onset of tearing because the unloading region becomes too high compared to the specimen size.

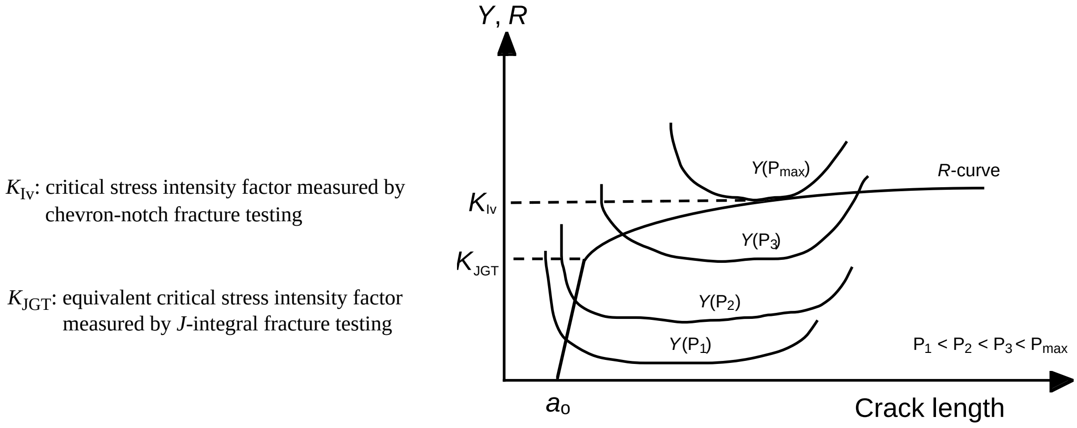
$K_{Iv}$: critical stress intensity factor measured by chevron-notch fracture testing
$K_{JGT}$: equivalent critical stress intensity factor measured by $J$-integral fracture testing
Y, R
$K_{Iv}$
$K_{JGT}$
Y(Pmax)
R-curve
Y(P3)
Y(P2)
Y(P1)
P1 < P2 < P3 < Pmax
$a_0$
Crack length

**Figure 5-6.** Schematic *R*-curves and crack driving force curves of chevron-notched specimens, for composites with Al-Cu matrices.

In chevron-notch fracture testing, on the other hand, Figure 5-6 indicates that the crack grows stably until the load reaches $P_{max}$, at which point crack growth becomes unstable. The chevron-notch stress intensity factor $K_{Iv}$ is then deduced from this maximum load[1], and thus corresponds to the $K$ value after some degree of *R*-curve behaviour. Using the compliance calibration curves of chevron-notched specimens proposed in [260], the crack advance $\Delta a$ at that point is 5.4 mm for the specimen geometry used in the present study. This is more than one order of magnitude larger than $\Delta a$ at $K_{JGT}$ during *J*-integral testing on CT specimens. Consequently, given the *R*-curve behaviour in our composites, the critical $K_{Iv}$ value measured in chevron-notch fracture testing should be larger than $K_{JGT}$.

Data for Al-Cu matrix composites for which both tests were conducted are given in Table 5-2. These confirm this expectation: $K_{Iv}$ is larger than $K_{JGT}$ in all cases. Also the difference between the two values is less pronounced for composites with a lower toughness *(i.e.* as-cast conditions, as well as 60 μm angular particle composite). Similar results have been reported for high-strength Al alloys in [110].

**Table 5-2.** Comparison of *J*-integral ($K_{JGT}$) and chevron-notched ($K_{Iv}$) fracture toughness data for Al-Cu matrix composites.

| **Composite** | A2CA-A15p (ST) | A2CA-A60a (ST) | A2CA-A35a (ST) | A4.5CA-A35a (as-cast) |
|---|---|---|---|---|
| **$K_{JGT}$ [MPa·m$^{1/2}$]** | 28.4 | 16.5 | 17.2 | 16.5 |
| **$K_{Iv}$ [MPa·m$^{1/2}$]** | 31.2 | 17.5 | 23.7 | 16.9 |

This link is valid provided that validity criteria of chevron-notch testing are fulfilled; *i.e.* that the crack propagates under plane-strain and SSY conditions. Plane-strain conditions (which are less stringent in terms of specimen dimensions in chevron-notch testing compared to ASTM E-399) were obeyed in Al-Cu matrix composites. The second criterion of chevron-notch testing, the plasticity criterion *p*, limits the extent of specimen plasticity during fracture testing. This condition was also obeyed for most composites in the ST and T6 conditions.

---

[1] More exactly, in the presence of *R*-curve behaviour, the instability point does not coincid exactly with the minimum value of the crack-driving force curve [258, 259]. The compliance-based method mentioned in ASTM E1304 must hence be used to calculate the stress intensity factor. In doing so, it was seen that differences with the maximum load method was insignificant.

It is interesting to note that large *p* values are, in chevron-notched specimens, an indication of relatively tough materials. In the present composites, however, this criterion is systematically violated for the less tough, as-cast composites, while in the heat-treated composites, negative *p*-values are measured. Negative *p*-values are therefore attributed to quenching stresses.

For Al-Cu matrix composites reinforced by 15 and 25 µm polygonal particles the toughnes measured on chevron-notched specimens is slightly larger than the initiation toughness that would be obtained on CT specimens. This overestimation remains weak because the *R*-curve is not very pronounced after the onset of ductile tearing. For all other composites, (angular particle reinforced and 5 µm polygonal particle reinforced), an even flatter *R*-curve is expected because unstable fracture always occurs at the maximum load before ductile tearing started, such that toughness values as measured by the chevron-notch test are closer to $J_{\mathrm{GT}}$.

In assessing the role of the matrix, one must hence keep in mind that toughness values used for Al-Cu matrices and pure Al matrix composites are not fully equivalent in nature. The critical fracture parameter corresponds to the initiation of ductile tearing for pure Al matrix composites (*J*-integral fracture testing), while for Al-Cu matrix composites it is taken after some degree of *R*-curve behaviour (chevron-notch fracture testing). If values after a larger degree of crack propagation were used for pure Al matrix composites, it is recognized that higher fracture toughnesses may well be obtained.

# 5.2. THE LOCAL FRACTURE ENERGY

## 5.2.1 Experimental evidence

Observations of the crack-tip region by metallography and of the fracture surfaces by SEM enable a clear identification of micromechanisms of fracture operating in these materials. In summary, in pure Al matrix composites particle fracture is the dominant failure process with large and medium angular $Al_2O_3$ particles. With polygonal $Al_2O_3$ composite or small angular $Al_2O_3$ particles, crack propagation occurs mainly through the matrix, by ductile voiding. In $B_4C$ reinforced composites, both processes occur for large particle size composites, while matrix voiding dominates as the average particle size decreases.

For a given particle size, polygonal $Al_2O_3$ particle composites are tougher than $B_4C$ particle composites, while angular $Al_2O_3$ composites are the least tough materials. Also the fracture energy decreases as the average particle size decreases. The ductile dimple size scales with the interparticle distance in all composite systems.

In Al-Cu matrix composites, particle fracture was clearly dominant in most of the angular $Al_2O_3$ reinforced composites, while in polygonal $Al_2O_3$ composites a transition in the mode of fracture is noticed, from matrix voiding to particle fracture, as the Cu content in the matrix increases. This effect is especially marked in larger particle size composites. In both systems, second-phase precipitates in as-cast materials have been found to promote additional voiding. In terms of toughness, polygonal $Al_2O_3$ reinforced composites are tougher than angular $Al_2O_3$ composites, and surprisingly the composites with a higher concentration of Cu in the matrix are tougher (in heat-treated conditions). As-cast composites are systematically less tough than after heat-treatment. Hence, the matrix influences both the failure modes and the toughness.

These observations indicate that a link exists between the local fracture events and the fracture energy of the composites, even though most of the fracture energy is consumed in the plastic zone around the crack tip. In order to quantify this link, the local fracture energy in the various composites is estimated using micromechanical models and experimental observations.

## 5.2.2 Matrix flow stress

### i. Pure Al Matrix

For all calculations involving micromechanical models, the constitutive behaviour of the ductile material undergoing intense plastic deformation must be known: in our case one must estimate the flow stress of the aluminium matrix. As was already mentioned in the literature review, the *in-situ* matrix flow stress in the presence of rigid reinforcements differs from that of the monolithic material. This influence in flow stress influences the local fracture energy. In particular, in our composites there is a scale dependence of the matrix flow stress [179]: the *in-situ* matrix yield strength is larger for smaller particle size composites, an effect that has been rationalized on the basis of geometrically necessary dislocations [179, 261, 262]. Indeed, upon cooling from the processing temperature, differences between the thermal expansion coefficent of the matrix and of the reinforcement result in the generation of geometrically necessary dislocations. Finer composite microstructures lead to a greater strain gradient, which in turn results in a greater density of emitted dislocations, and hence to a more important hardening according to the Taylor relation. In addition, boron carbide reinforced composites feature larger matrix flow stresses for a given average particle size, because the difference of its thermal expansion coefficient with that of pure Al is larger than that of alumina.

For the present pure Al matrix composites, the matrix flow stress was back-calculated from the effective sress-strain curves [179], using the mean-field model developed by Nan and Clarke [228]. Typical in-situ matrix flow curves thus derived were subsequently fitted by the Hollomon power hardening law:

$$\sigma_{\mathrm{m,Al}}(\varepsilon) = k \cdot \varepsilon_{\mathrm{m,Al}}^{n} \tag{5-2}$$

where $\sigma_{\mathrm{m,Al}}$ and $\varepsilon_{\mathrm{m,Al}}$ are the matrix flow stress and the matrix strain respectively, $n$ is the work-hardening exponent and $k$ is the strength coefficient. The fitting paramters ($n$ and $k$) are listed for all composites in Table 5-3. Subsequent calculations involving matrix flow curves are carried out with these parameters.

**Table 5-3.** Parameters of the constitutive relationship for the *in-situ* matrix flow curve, pure Al matrix.

| **Composite** | A-A35a | A-A10a | A-A5a | A-A25p | A-A15p | A-A5p | A-B60 | A-B35 | A-B20 | A-B10 | A-B5 |
|---|---|---|---|---|---|---|---|---|---|---|---|
| **n [-]** | 0.21 | 0.22 | 0.23 | 0.21 | 0.27 | 0.22 | 0.20 | 0.20 | 0.21 | 0.22 | 0.23 |
| **k [MPa]** | 223 | 328 | 417 | 267 | 377 | 352 | 212 | 275 | 336 | 407 | 441 |

### ii. Al-Cu matrices

Obtaining the *in-situ* matrix flow curve, $\sigma_{\mathrm{m,Al\text{-}Cu}}$, of Al-Cu matrix composites is more difficult than with pure Al matrix composites because the strains at fracture are lower, remaining often in the elastic regime for angular alumina composites (Figure 4-45). Hence, extrapolating the matrix flow curve from the composite flow curve using the effective medium approach is not possible in a systematic manner for all composites. In the absence of a complete set of data for all Al-Cu matrix composites, we have to make assumptions to arrive at the *in-situ* Al-Cu matrix flow curves.

The main hypothesis we have made is to assume that the amount and accumulation of additional geometrically necessary dislocations in the Al-Cu alloy matrices is the same as in a pure Al matrix. The difference in yield strength between pure Al and Al-Cu alloys is then mainly due to solid-solution strengthening in the ST conditions; or solid-solution strengthening plus precipitation hardening in T6 conditions. Using the Taylor relation, this assumption is equivalent to writing the *in-situ* flow stress of the deforming plastic phases as:

$$\sigma_{\mathrm{m,Al}} = \alpha G b \sqrt{\rho_{\mathrm{s,Al}} + \rho_{\mathrm{g}}} \quad : \ \textit{in-situ} \text{ matrix flow stress of pure Al} \tag{5-3}$$

$$\sigma_{\mathrm{m,Al\text{-}Cu}} = \sigma_0 + \alpha G b \sqrt{\rho_{\mathrm{s,Al\text{-}Cu}} + \rho_{\mathrm{g}}} \quad : \ \textit{in-situ} \text{ matrix flow stress of Al-Cu alloys} \tag{5-4}$$

where $G$ is the shear modulus of the matrix (= 25 GPa for both Al and Al-Cu alloys), $\rho_{\mathrm{s,i}}$ is the density of stored dislocations in the unreinforced matrix (which depends on macroscopic strain $\rho_{\mathrm{s}} = \rho_{\mathrm{s}}(\varepsilon)$), $\rho_{\mathrm{g}}$ is the density of particle-induced geometrically necessary dislocations (which depends on the macroscopic strain and on the interparticle distance, $\rho_{\mathrm{g}} = \rho_{\mathrm{g}}(\varepsilon,\lambda)$ [179]), $b$ is the Burger's vector of Al (= $2.86 \cdot 10^{-10}$ m), $\alpha$ is a constant equal to 1.25 in aluminium [263], and $\sigma_0$ is the strengthening contribution in Al-Cu alloys due to solid-solution and/or precipitation hardening.

In pure Al matrix composites, flow stress contribution coming from $(\rho_{\mathrm{s,Al}}+\rho_{\mathrm{g}})^{1/2}$ is directly contained within the back-calculated matrix flow curves, Table 5-3. However, the component from $\rho_{\mathrm{s,Al}}$

must be extracted and replaced in Al-Cu alloys by $\rho_{\mathrm{s,Al\text{-}Cu}}$. In [179], it was found that for large strains, $\rho_{\mathrm{s}}$ exhibits a power-law dependence on strain with exponent of 0.4 ($\rho_{\mathrm{s}} \approx \rho_{\mathrm{so}}+A\varepsilon^{0.4}$) such that the contribution due to $\rho_{\mathrm{g}}$ only, $\alpha Gb(\rho_{\mathrm{g}})^{1/2}$, can be calculated as function of strain for each composite using constitutive laws listed in Table 5-3:

$$(\alpha Gb)^2 \rho_g \approx \sigma^2_{\mathrm{m,Al}} - (\alpha Gb)^2\left(\rho_{so} + A\varepsilon^{0.4}\right) \approx \left(k\varepsilon^n_{\mathrm{m,Al}}\right)^2 - (\alpha Gb)^2\left(\rho_{so} + A\varepsilon^{0.4}\right) \tag{5-5}$$

To estimate the *in-situ* matrix flow curves of Al-Cu alloys, tensile curves of unreinforced Al-Cu alloys in ST and T6 conditions, $\sigma_{\mathrm{Al\text{-}Cu}}(\varepsilon)$, were measured. These are assumed to be described by:

$$\sigma_{\mathrm{Al\text{-}Cu}} = \sigma_0 + \alpha Gb\sqrt{\rho_{\mathrm{s,Al\text{-}Cu}}} \tag{5-6}$$

$\sigma_0$ is then directly obtained from the experiments. Eq. (5-6) can now be recast into:

$$\left(\sigma_{\mathrm{Al\text{-}Cu}} - \sigma_0\right)^2 = (\alpha Gb)^2 \cdot \rho_{\mathrm{s,Al-Cu}} \tag{5-7}$$

By adding $\sigma_0$ to the root-square of (5-5) plus (5-7), one finally obtains the *in-situ* matrix flow stress with Al-Cu alloys,$\sigma_{\mathrm{m,Al\text{-}Cu}}$, in the same form as described by eq. (5-4):

$$\sigma_0 + \sqrt{\left(\sigma_{\mathrm{Al\text{-}Cu}} - \sigma_0\right)^2 + \left(k\varepsilon^n_{\mathrm{m,Al}}\right)^2 - (\alpha Gb)^2\left(\rho_{so} + A\varepsilon^{0.4}\right)} = \sigma_0 + \alpha Gb \cdot \sqrt{\rho_{\mathrm{s,Al-Cu}} + \rho_{\mathrm{g}}} = \sigma_{\mathrm{m,Al-Cu}} \tag{5-8}$$

*In-situ* Al-Cu matrix flow curves were computed according to this method for all composites (in ST and T6 conditions). In the last step, these were fitted according to Ludwik'law:

$$\sigma_{\mathrm{m,Al\text{-}Cu}} = \sigma_0 + k \cdot \varepsilon^n_{\mathrm{m,Al\text{-}Cu}} \tag{5-9}$$

which describes reasonably well the large plastic strains involved in microcavitation mechanisms. This enables us to obtain analytical expressions that can be used in subsequent calculations. Parameters of eq.(5-9) for various Al-Cu2% and Al-Cu4.5% composites in both ST and T6 conditions are given in Table 5-4.

The case of as-cast composites is somehow different: the phase that is intensively plastically strained during voiding is the $\alpha$ solid-solution, whereas $\theta$ precipitates are essentially undeformable. It is therefore assumed that the deforming phase is described by the constitutive law of the solution-treated *in-situ* matrix having the same nominal Cu concentration (this remains, of course, a crude approximation, the average concentration of Cu in solution being higher in ST composites).

**Table 5-4.** Parameters of the constitutive relationship for *in-situ* matrix flow curve, Al-Cu matrices. $\sigma_0$ and $k$ in MPa; n adimensionnal.

| **Matrix** | Al-Cu2% (ST) | Al-Cu2% (T6) | Al-Cu4.5% (ST) | Al-Cu4.5% (T6) |
|---|---|---|---|---|
| **Reinforcement** | $\sigma_0$ = 40 | $\sigma_0$ = 55 | $\sigma_0$ = 150 | $\sigma_0$ = 175 |
| 5 µm polygonal | $k$ = 410; $n$ = 0.30 | $k$ = 412; $n$ = 0.30 | $k$ = 574; $n$ = 0.42 | $k$ = 596; $n$ = 0.41 |
| 15 µm “ | 455; 0.37 | 457; 0.37 | 646; 0.49 | 662; 0.48 |
| 25 µm “ | 350; 0.35 | 353; 0.36 | 592; 0.54 | 605; 0.51 |
| 5 µm angular | 467; 0.29 | 468; 0.29 | 602; 0.38 | 624; 0.38 |
| 10 µm “ | 393; 0.32 | 395; 0.32 | 574; 0.46 | 595; 0.44 |
| 35 µm “ | 341; 0.44 | 347; 0.45 | 682; 0.68 | 665; 0.62 |

### 5.2.3 Local fracture energy: approach based on the final fracture process

#### i. Pure Al matrix: Estimation of the local fracture energy

The approach proposed by Stüwe to calculate the energy necessary to create a landscape of ductile dimples on a fracture surface was presented in § 2.6.1. It is used here to estimate the local fracture energy, $2\gamma_{\text{pz}}$.

To this end, let us consider the two typical fracture micromechanisms that were identified in the composites, namely (i) particle fracture which subsequently nucleates voids in the matrix, and (ii) matrix-nucleated voids in the regions of high stress concentrations (Figures 4-28 to 4-30). These two cases are schematically depicted in Figures 5-7a and b, respectively.

(i) In the case of a crack propagating through the matrix (Figure 5-7a), one obtains a fracture surface made of ductile dimples similar to that presented in Figure 2-15. Hence, the local work per unit area to form the fracture surface can be estimated using (2-46):

$$\gamma_{\text{pl}} = \frac{h_0 k}{n+1} \int_0^1 z(x) \left[ \ln\left( \frac{1}{z(x)} \right) \right]^{n+1} \mathrm{d}x \qquad \text{(2-46)}$$

since both the deformation law ($k$, $n$) and the average dimple height $h_0$ (from the 3-D reconstructed fracture surfaces, the DEMs) are known or estimated. For the function $z(x)$, it was shown by Stüwe [207] that any reasonable curve describing the fracture relief leads to almost the same result. Hence for convenience, the simplest function $z(x) = x$ is used, which enables to simplify (2-46).

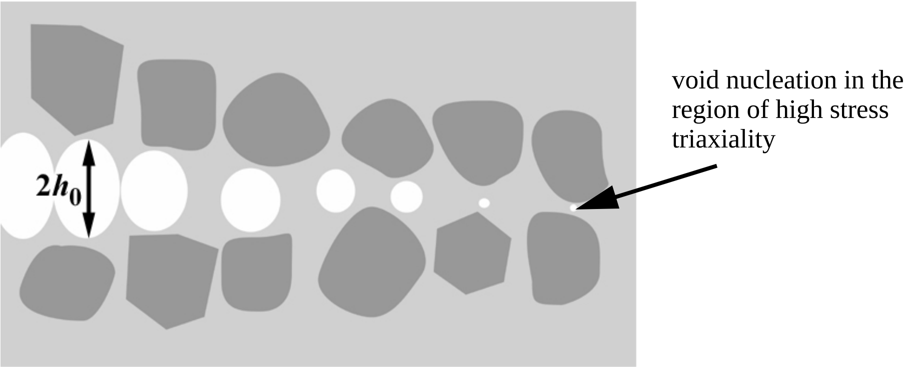
2$h_0$
void nucleation in the region of high stress triaxiality

**(a)** voids nucleated in the matrix

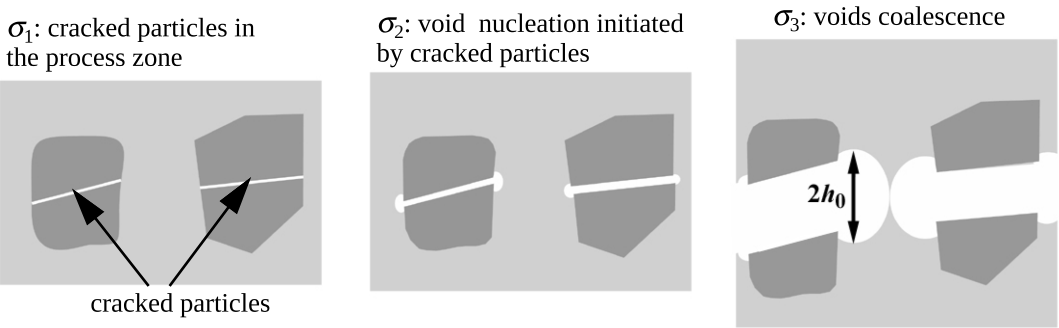
$\sigma_1$: cracked particles in the process zone
$\sigma_2$: void nucleation initiated by cracked particles
$\sigma_3$: voids coalescence
2$h_0$
cracked particles

**(b)** voids nucleated by particle cracking

**Figure 5-7.** Schematic description of crack initiation and propagation in the composites. **(a)**: voids nucleated in the matrix; **(b)**: voids nucleated by particle cracking, crack propagation by coalescence of such voids.

(ii) When particle fracture occurs (at remote stress $\sigma_1$) and nucleates voids (at remote stress $\sigma_2$), the crack then propagates by coalescence of these voids (at remote stress $\sigma_3$), leading to a fracture profile such as that presented in Figure 5-7b. Since only the final result of the fracture process is considered, one actually recognizes that the fracture energy of these broken-particle-nucleated dimples can be described by the same model as in case (i), provided that $h_0$ is known. The major difference with matrix-nucleated dimples then lies in the fact that only a fraction of the fracture surface is occupied by dimples, the remainder being covered by cracked particles. The fracture energy of this particle cracking process, $2\gamma_b$, is simply given by the energy release rate of the ceramic particles, $G_{Ic\text{-}b}$:

$$2\gamma_b = G_{Ic-b} = \left(K_{Ic-b}\right)^2 \cdot \frac{E}{1-\nu^2} \qquad (5\text{-}10)$$

where $K_{Ic\text{-}b}$ is the critical stress intensity factor of the ceramic, $E$ its elastic modulus, and $\nu$ its Poisson's ratio. The $K_{Ic\text{-}b}$ values found in the literature for $Al_2O_3$ and $B_4C$ are tabulated in Table 2-2. For $Al_2O_3$, we use $K_{Ic\text{-}b}$ of 4 MPa·m$^{1/2}$, which is in the range of typical values often reported for high purity alumina [14]; whereas for $B_4C$, fracture toughness of 3.7 is used [16]. As discussed later, this is a rather crude postulate: particles are obviously not equivalent from the fracture energy point of view and their intrinsic toughness can depend on their type and size; however, this has a more profound influence on the nucleation stress for matrix cavitation following particle fracture than on the fracture energy of particle cracking itself.

Adding the contribution of ductile dimple creation and that required to crack the brittle ceramic particles, the total energy to create the local fracture process finally writes:

$$2\gamma_{pz} = 2 \cdot \left[ f_b \cdot \gamma_b + \left(1 - f_b\right) \cdot \left(\gamma_{pl}\right) \right] \qquad (5\text{-}11)$$

where $f_b$ is the fraction of the fracture path occupied by broken particles, $\gamma_{pl}$ is given by solving eq.(2-46) numerically, and the factor 2 is introduced to account for the two fracture surface halves. Therefore, in the present approach, if the composites are produced using reinforcements featuring a lower fracture strength, this translates into a portion of the crack path occupied by a higher amount of broken particles, which is a process consuming less energy than ductile voiding. Using results from quantitative metallography to calculate $f_b$ and $\gamma_{pl}$ (Table 4-4), the computed local fracture energy of pure Al matrix composites are summarized in Table 5-5.

**Table 5-5.** Estimation of the local fracture energy $\gamma_{pz}$ in pure Al matrix composites according to Stüwe's model. Brittle particle fracture is taken into account as well, using quantitative metallography data.

| **Composite** | A-A35a | A-A10a | A-A5a | A-A25p | A-A15p | A-A5p | A-B60 | A-B35 | A-B20 | A-B10 | A-B5 |
|---|---|---|---|---|---|---|---|---|---|---|---|
| $2\gamma_{pz}$ **[kJ/m$^2$]** | 0.276 | 0.146 | 0.218 | 0.845 | 0.607 | 0.193 | 0.627 | 0.569 | - | 0.319 | 0.249 |

Comparing these data with the global fracture energy as defined by $J_{GT}$ (Table 4-3) shows unambiguously that the latter is about one order of magnitude larger than the former. This is not surprising: as shown in the preceding section of this discussion, most of the fracture energy is consumed by plastic dissipation in the crack-tip plastic zone.

As reviewed in Chapter 2.5, a direct link should exist between the local fracture energy spent in the process zone and the global fracture energy; more specifically for PRMMCs one can write:

$$G_{\mathrm{Ic}} = K_{\mathrm{Ic}}^2 / E' \approx \frac{2\gamma_{\mathrm{pz}}}{\left(1 - \dfrac{2E'C\varepsilon_{\mathrm{m}}}{\sigma_{\mathrm{ys}}}\right)} \tag{2-37}$$

for SSY conditions. In our case, at the onset of ductile tearing, fracture is still $J$-dominated; hence $J_{\mathrm{GT}}$ is a critical parameter that is independent of the specimen geometry. One can therefore replace the composite energy release rate $G_{\mathrm{Ic}}$ in SSY with $J_{\mathrm{GT}}$ and examine whether $J_{\mathrm{GT}}$ scales with $2\gamma_{\mathrm{pz}}$.

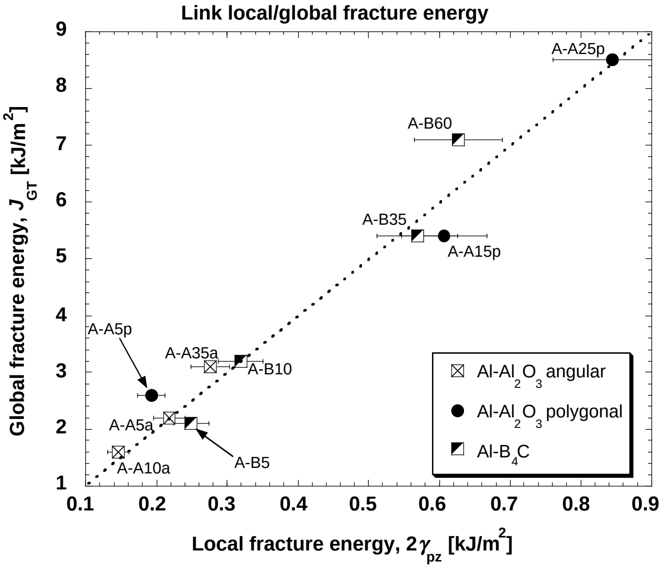

**Figure 5-8.** Correlation between the local work of fracture as determined from Stüwe's model and quantitative metallography, and the global fracture energy as measured at the initiation of ductile tearing.

A plot of $J_{\mathrm{GT}}$ vs. $2\gamma_{\mathrm{pz}}$ for pure aluminium matrix composites is presented in Figure 5-8. The prediction given by (2-37) is confirmed over a wide range of variation in $J$: although a small portion of the fracture energy is spent at the local scale, it still governs composite toughness: the larger the local fracture energy the larger the global fracture for all composite systems. The global fracture energy is in other words an amplification of the local work of fracture, and according to Figure 5-8, the amplification factor with the present model is about 10 for most composites.

This result agrees with that reported in [175] for an Al-Mg4% alloy reinforced by 15 vol.% of SiC particles: the work done within the plastic zone at the instant of fracture was calculated from measurements of the crack-tip strain field and the composite tensile curve, while the local work done in void formation was estimated with a somewhat similar approach as here. The author found that the latter was a factor about 10 less than the work expended within the plastic zone. Interestingly, such a factor in the range of 10 is also recently noticed by Wegner and Gibson [264] for materials with similar microstructure, consisting of hard stainless steel infiltrated by ductile bronze (90%Cu-10%Sn); in which the local work of fracture was estimated by similar means as here, whereas the work dissipated in the plastic zone was calculated from the stress-strain history of a volume element in the wake of the plastic zone.

### ii. The role of dimple size and extent of particle cracking

As explained later, the values of the local fracture energy actually depend on the micromechanical model used to describe the local fracture process; if another model than Stüwe's is used to quantify the fracture process, in particular to account for constraint effects or particle fracture, then $2\gamma_{pz}$ is modified, but its order of magnitude remains similar. Also, for the fine particle size composites, determination of the fraction of broken particles on the fracture surface is not as precise, while $2\gamma_{pz}$ is quite sensitive to this value. The essence of the finding summarized in Figure 5-8 remains in any case unchanged: the measured fracture toughness (defined here as $J_{GT}$) scales with the local fracture energy. This allows to draw a few further conclusions:

- In pure Al/polygonal $Al_2O_3$ particle composites, the final dimple size scales with the reinforcement size, causing $2\gamma_{pz}$ to increase with the particle size. The increase of the matrix flow stress with decreasing particle size is not sufficient to overcome the smaller dimple size. This in turn results in a higher fracture energy. In other words, there exists a direct correlation between the fracture toughness and the fracture surface roughness. In [183], where it was attemped to correlate these two parameters for 2014 and 2024 Al alloys reinforced by about 20% of SiC particles, it was concluded that such link a did not exist in PRMMCs; however, the author anticipated that it would be more likely that fracture surface roughness would correlate with fracture toughness for PRMMCs exhibiting very ductile fracture. This is exactly what is seen in the present situation, although the argument brought for this expectancy is different in our case[1].

- The toughness of pure Al/angular $Al_2O_3$ composites is lower than with polygonal particles. This is due to particle cracking, which reduces $2\gamma_{pz}$ (eq.5-11). Particle cracking is more extensively seen for the larger 35 µm particle size composite. The toughness of this composite is however larger than smaller particle size composites because the increase of particle cracking is compensated for by the higher plastic energy necessary to form the large dimples. This compensation is, however, not sufficient in the 10 µm particle size composite as compared to the 5 µm particle size composite, for which particle cracking is much reduced: the latter is slightly tougher;

- In Al-$B_4C$ composites, the particle size effect on the toughness is similarly explained: the largest particle size composite (60 µm) features the largest average dimple size, which compensates the lower matrix flow stress and particle cracking. As the particle size, and hence the interparticle distance, decreases smaller cavities are formed, thus reducing the local fracture energy and in turn the global toughness.

- A general comparison of all present pure Al matrix composites is also possible in simple terms. At a given particle size, polygonal alumina particle composites are tougher because the particles are strong enough (further details are given later) that they are not craked during crack propagation. Boron carbide reinforced composites are not as tough because some particle cracking occurs during the fracture process. Angular alumina composites are the least fracture resistant because extensive particle cracking occurs in these.

---

[1] In the cited reference, the author postulated that this would be the case because most of the fracture energy would then be spent to create the fracture surface; we show here that even for very ductile micromechanisms of fracture, most of the fracture energy is spent in the plastic zone.

- According to data from the literature, Al-$Al_2O_3$ interfaces feature ductile fracture by microvoid coalescence [198, 265, 266] (*i.e.* typically what we observe in polygonal $Al_2O_3$ reinforced composites), and the measured toughness of such interfaces is comprised between 0.2 and 0.6 kJ/$m^2$ [196, 266]. This is in the range of the local fracture energy calculated from the present micromechanical analysis. In the presence of contaminants and segregants, brittle decohesion often occur in ceramic/metal interfaces, thereby lowering the interface toughness to values in the order of $1 \cdot 10^{-3}$ to $20 \cdot 10^{-3}$ kJ/$m^2$ [195, 196, 303], namely corresponding to the order of magnitude of interfacial energies [267]. We recall here that in the angular alumina 20 µm particle size composite, interfacial decohesion is the dominant mechanism (Figure 4-28c), while this material exhibits the smallest fracture resistance of all pure Al matrix composites. Such behaviour is therefore attributed to the presence of unknown contaminants at the surface of this powder batch, which reduce the interfacial strength. Extrapolating the global vs. local curve for this composite would indicate that the local fracture energy is about 0.1 kJ/$m^2$: this is still at least one order of magnitude above values typical of interfacial energies. Part of these 0.1 kJ/$m^2$ must therefore be attributed to dimple formation between two decohered interfaces. This is again a clear illustration of the importance of the local micromechanisms of fracture: a decrease of $2\gamma_{pz}$ that seems negligible compared to the global fracture energy has a dramatic effect on the global toughness, an effect that was well explained by Rice and Wang [197] in the context of interfacial embrittlement, and that is also receiving increasing attention in the field of fracture along metal/ceramic interfaces [268-270].

### iii. Comparison with prior work

Justification of the correlation between the local and global energies is substantiated by examining fracture data from the literature. In the work by Lucas and Park [115, 143], who measured toughness of two composites (6061 alloy reinforced either by 20% of SiC or $Al_2O_3$ particles), it was mentioned that a larger plastic wake was observed for the tougher composite (6061/$Al_2O_3$). Particle cracking was the dominant mechanism in this material. For the 6061/SiC composite on the other hand, extensive debonding was found due to the presence of $Al_4C_3$ interfacial reaction product. It is therefore not surprising that they observed a smaller plastic wake for the 6061/SiC composite (debonding being a less energy consuming process) and in turn a lower toughness.

More recently, Pandey *et al.* [156] studied the influence of various heat-treatments on the mechanical properties of a 7093/SiC/15% composite prepared by powder metallurgy. In contrast to most previous findings, their composite did achieve a significant recovery of toughness for optimized overaging (OA) heat-treatment. In addition, TEM observations illustrated a precipitate-free zone (PFZ) in the immediate vicinity of the particle-matrix interface; this resulted in a weaker local matrix region in which matrix dimple rupture occurred, and replaced particle fracture that was dominant in under-aged (UA) and peak-aged (PA) condition (which were less tough). This uncommon behaviour was explained in detail in [144], where the authors acknowledged that the energy to create and grow such voids was relatively large. These results are actually in accordance with the local/global link: since near-interfacial matrix voiding replaces particle fracture, it is likely that the local fracture energy of their OA specimens is larger than for their UA and PA composite, in turn resulting in a higher global fracture toughness at initiation.

It is also interesting to compare present calculations with fracture studies on hard refractory WC-Co alloys, and metal toughened ceramics. As mentioned in Chapter 2.6, WC-Co feature a microstructure resembling that of high volume fraction PRMMCs: they are made of a ductile Co binder surrounding hard and brittle WC grains, Figure 2-17. There is no amplification due to a plastic zone contributing to the toughness in WC-Co composites, because they exhibit in tension a high yield strength, and an almost fully brittle behaviour [13, 271]. The micromechanisms of fracture in these materials consist in dimple fracture through the ductile matrix and in transgranular fracture through the carbide grains [215, 217]. These mechanisms are similar to those observed in the present composites. Estimating the local plastic energy $2\gamma_{pz}$ in creating such fracture surfaces describes reasonably well the measured fracture toughness under the important condition, however, that a higher *in-situ* binder stress be taken into account [219, 220], see §.2.7.2. The major contribution to toughness in such composites is, thus, mainly the local fracture energy $2\gamma_{pz}$. This is also the reason why brittle matrix composites reinforced by ductile particles feature much lower toughnesses than our composites, in the range of 4-8 $\text{MPa}\cdot\text{m}^{1/2}$ [221, 222, 272-274]: the interconnected phase being brittle in these, the global tensile response exhibits limited ductility. Amplification of the local work of fracture by crack-tip plasticity cannot then occur and toughness are far lower than in present materials.

### iv. Al-Cu matrix: The role of second-phases and matrix flow stress

In Al-Cu matrix composites, the main conclusions from the fracture toughness results (Figure 4-49) are that: (i) toughness of as-cast composites is much lower than heat-treated composites, and (ii) in the absence of intermetallics, *i.e.*, in ST and T6 composites, increasing the matrix flow stress leads to a slight increase of the toughness over what is found with pure Al. We examine whether data for alloyed matrix composites can be rationalized, as for pure Al compositions, using the observed micromechanisms of fracture and the local/global correlation.

#### AS-CAST COMPOSITES

In as-cast composites, the fracture surface is characterized by many small dimples that were clearly nucleated by intermetallic phases, Figure 4-52a and Figure 4-53b. This is also apparent in higher magnification SEM images (in the BSE mode) of polygonal 25 µm composites in as-cast conditions for both Al-Cu2% and Al-Cu4.5% matrices, Figure 5-9. These observed fracture micromechanisms are schematically illustrated in Figure 5-10a for the case where ceramic particles remain intact during crack propagation, and in Figure 5-10b for the case involving particle cracking.

Given the small dimensions of the dimples in these composites, in the range of 1 µm, 3D reconstruction of stereopairs was not performed, largely because the quality of numerical information acquired on the high-magnification SEM pictures was too low. SEM micrographs suggest, however, that the fracture surface is actually made of distinct populations of dimples: larger dimples nucleated by particle cracking or between particles; and smaller ones, nucleated by intermetallics. This is only seen in as-cast composites since most second-phases are dissolved after heat-treatment.

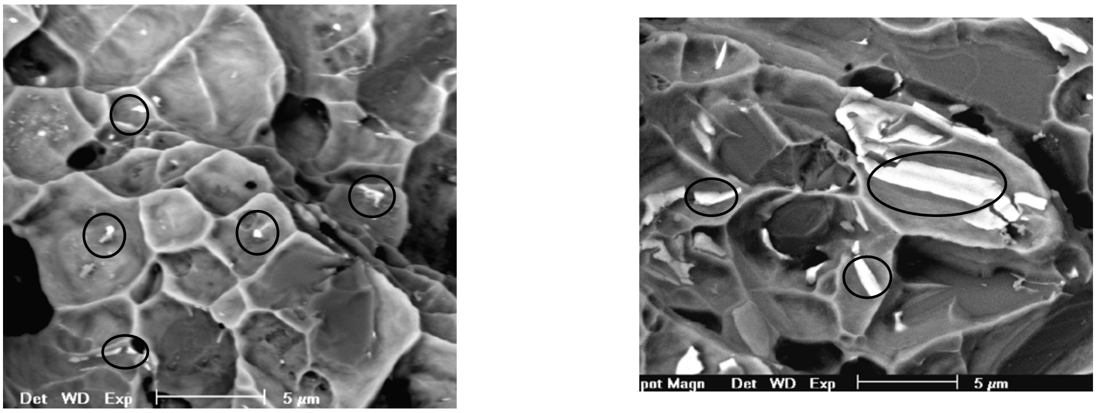

Al-Cu2% matrix Al-Cu4.5% matrix

**Figure 5-9.** High-magnification SEM fractographs (BSE) of as-cast Al-Cu/25 µm polyg. composites, showing cavities nucleated at second-phase intermetallics.

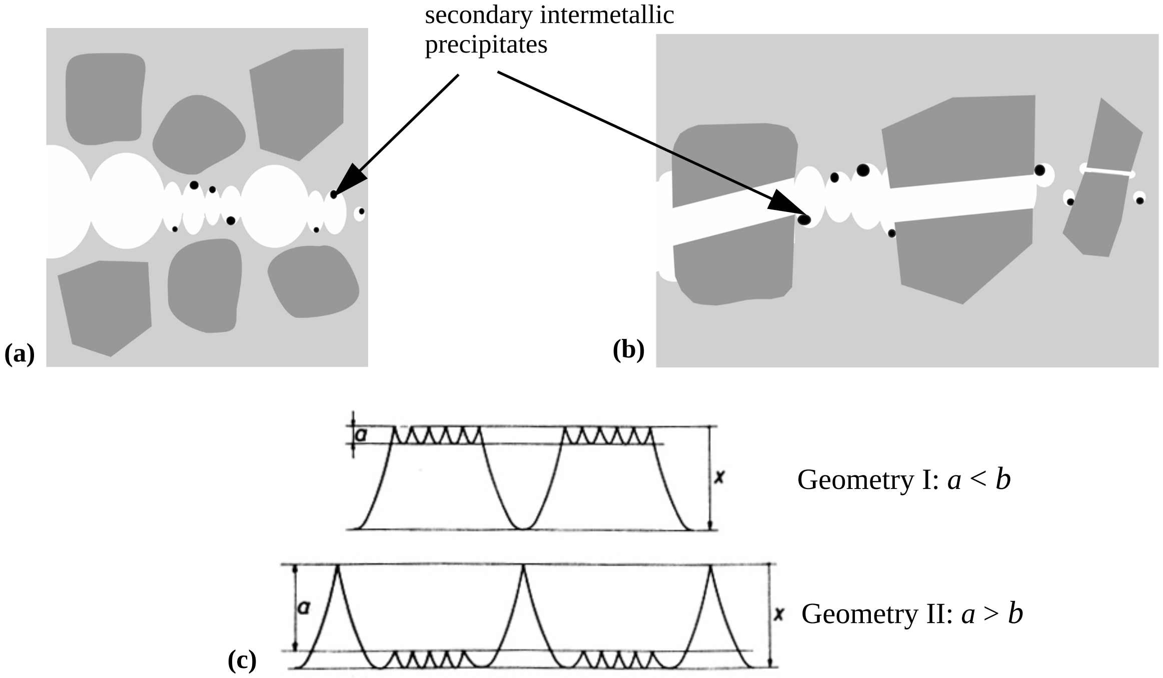

**Figure 5-10.** Schematic description of crack propagation path in the presence of secondary intermetallic phases (as-cast composites), which promote additional cavitation. **(a)**: without particle fracture; **(b)**: with particle fracture in addition to precipitate-nucleated dimples; **(c)**: fracture surface profile in the presence of two populations of voids, from [208].

This implies that the fracture profile can no longer be treated as an ideal regular array of dimples. Rather, we face an irregular fracture profile schematically depicted in Figure 5-10c. For this type of special geometry, Stüwe [208] described the fracture profile $z(x)$ appearing in (2-46) as:

$$\begin{aligned} z(x) &= (b/a)\cdot x \qquad \text{for} \qquad 0 \le x \le a, \\ z(x) &= \left[(1-b)/(1-a)\right]\cdot x + \left[(b-a)/(1-a)\right] \qquad \text{for} \qquad a \le x \le 1. \end{aligned} \tag{5-12}$$

where $a$ is defined in Figure 5-10c, and $b$ is a constant less than unity. If $a < b$ (Geometry I), the surface is made up in part of large dimples and in part of small ones, whereas if $a > b$ (Geometry II) small dimples are present at the bottom of large dimples. The two configurations give different local fracture energies for given (and differing) values of $a$ and $b$; however, both share the fact that they yield lower local fracture energies than a single distribution of the larger dimples alone. In the extreme where all dimples are nucleated by intermetallics, the fracture surface is predicted by eq. (2-46), with of course a far smaller dimple size $h_0$, such that $2\gamma_{\mathrm{pl}}$ is far lower. It is, thus, expected that as-cast composites are less tough than pure Al composites, the underlying reason being a far higher rate of dimple nucleation induced by the intermetallic particles.

The difference between 2 and 4.5 % Cu matrices is also qualitatively evident from microfractographic observation. There is clearly a larger number of second-phase particles in Al-Cu4.5% matrix composites after solidification: compare Figures 4-5a and b with Figure 4-6a and b. A larger number of second phases means that: (i) if the fracture surface is as presented in Figure 5-10c the difference between *a* and *b* in (5-12) becomes larger, and (ii) if the fracture surface is uniquely made of second-phases nucleated dimples, the average dimple height $h_0$ diminishes. Both cases have in common that they reduce $2\gamma_{\mathrm{pz}}$. In short, as-cast Al-Cu4.5% matrix composites are therefore less tough than Al-Cu2% composites because they contain a higher number of intermetallic particles.

### Heat-Treated Composites: Limitation in the Local/Global Correlation

After solution treatment, the intermetallics are essentially removed from the matrix: dimples are, therefore nucleated, as in pure Al matrix composites, predominantly under the influence of the ceramic particles, according to the two mechanisms depicted in Figure 5-7.

To focus the present discussion, we consider two distinct composites: those reinforced with angular 35 µm particles (35a), and those reinforced with polygonal 25 µm particles (25p). With both reinforcements, broken particles were clearly visible along the crack path: measured cracked particle fractions along the crack path, $f_{\mathrm{b}}$, are reported in Table 4-7: as seen, $f_{\mathrm{b}}$ varies significantly from one composite to the other.

To estimate the local fracture energy, $\gamma_{\mathrm{pl}}$ (eq.2-46), we need to know the dimple height $h_0$. Equation (5-9) must also be modified to account for the $\sigma_0$ contribution to the in-situ matrix flow curves:

$$\gamma_{\mathrm{pl}} = \frac{1}{2}\sigma_0 h_0 \cdot S(z) + \frac{h_0 k}{n+1} T(z,n) \qquad (5\text{-}13)$$

$$\text{where } S(z) = \int_0^1 z(x)\left[\ln\left(\frac{1}{z(x)}\right)\right] \mathrm{d}x \quad \text{and} \quad T(z,n) = \int_0^1 z(x)\left[\ln\left(\frac{1}{z(x)}\right)\right]^{n+1} \mathrm{d}x$$

The matrix flow stress is known with far less precision than for pure Al composites: $\gamma_{\mathrm{pl}}$ can therefore only be estimated. For this reason, it was not deemed worthwhile to measure dimple geometrical characteristics with as much precision as for pure Al composites (also, microfractographic characteristics were far more complex with alloyed matrix composites). Dimple heights are, therefore, also estimated; this was done as follows.

Detailed quantitative fractographic measurements were conducted on solution-treated Al-Cu matrix composites reinforced with 15 µm polygonal particle composites (Section 4.5.4.ii). Measurements carried out on reconstructed fracture surfaces for those composites revealed no significant difference between Al-Cu2% and Al-Cu4.5% matrix composites; however, the dimple height was about half that of their pure Al matrix counterpart. This difference can be attributed to: (i) the presence of a few residual precipitates in the matrix (see Figures 4-5c and d, and Figures 4-6c and d), and (ii) differences in the plastic flow path upon dimple formation, for example caused by differences in slip concentration or by cavitation instability for harder matrices [275]. Based on these observations, the dimple height for both Al-Cu matrices was assumed to be half its value in corresponding pure Al matrix composites. As no systematic difference was found between ST and T6 composite fracture surfaces, this same dimple height was assumed for both heat treatment conditions. For the 35a composites, this translates into a dimple height approximately equal to 5 µm, whereas this quantity is 4 µm for the 25p composites.

For smaller particle size composites, SEM images indicates very similar fracture surface characteristics between pure Al and Al-Cu matrices composites (*i.e.* voiding instabilities did not appear because of the already small cavity size). We hence use the same dimple height of 1.4 µm that was measured for the pure Al matrix composite, for both Al-Cu2% and Al-Cu4.5% matrices and in both heat-treatment conditions.

Plots of measured $G_{Iv}$ against $2\gamma_{pz}$ calculated with these assumptions are shown in Figure 5-11. Here, $G_{Iv}$ is the chevron-notch energy release rate, converted from the chevron-notch fracture toughness $K_{Iv}$. Error bars are included for the local fracture energy $2\gamma_{pz}$: these reflect mainly the estimated uncertainty in calculations caused by assumptions regarding dimple height.

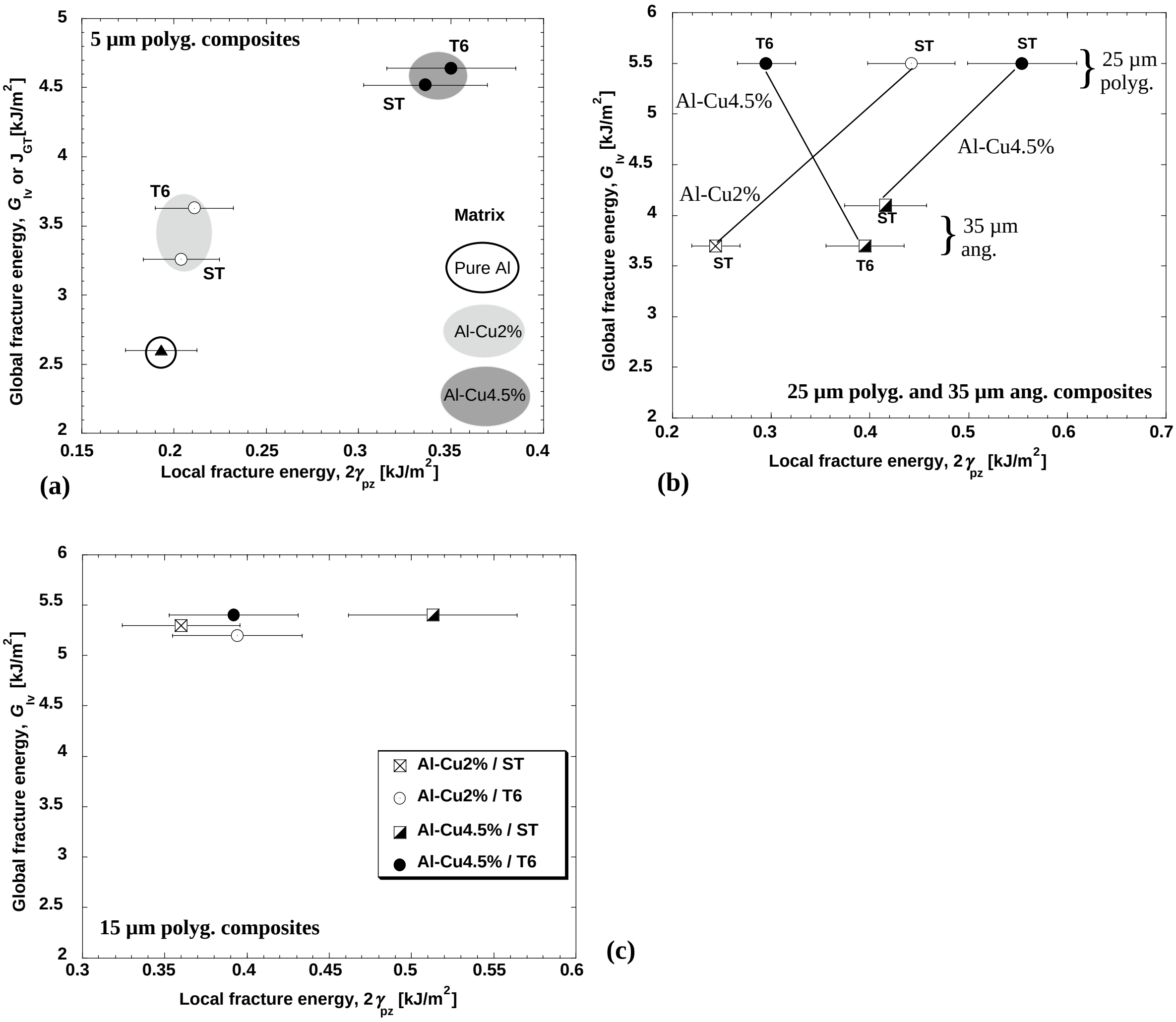

**Figure 5-11.** Global against local ($2\gamma_{pz}$) fracture energy in Al-Cu matrix composites for **(a)**: 5 µm polygonal particle composites; **(b)**: 25 µm polygonal and 35 µm angular particle composites; **(c)**: 15 µm polygonal particle composites. ST: solution-treated, T6: peak-aged.

In 5 µm polygonal composites (Figure 5-11a), as the matrix flow stress is increased by alloying and/or heat treatment, the fraction of broken particles was found to remain constant, around 15%. Both the dimple size $h_0$ and $f_b$ are, therefore, roughly constant across the different composites. The local fracture energy, $2\gamma_{pz}$, is therefore simply roughly proportional to the matrix flow stress. As seen in Figure 5-11(a), the local and global fracture toughness both increase in these composites, roughly in agreement with the global correlation found for pure Al composites. It is interesting to note that this increase is found despite the fact that an increase in matrix flow stress, is expected to decrease the “amplification factor” between $2\gamma_{pz}$ and the global composite toughness (see eq.2-37).

Turning to 25 µm polygonal and 35 µm angular composites, Figure 5-11b, this correlation between the estimated value of $2\gamma_{pz}$ and the global composite toughness breaks down.

Let us focus first on the data for the solution-treated composite. For an Al-Cu2% matrix, the measured $G_{Iv}$ is larger for the 25p composite than for the 35a composite. This agrees with the larger estimated value of $2\gamma_{pz}$. As the Cu content is raised to 4.5%, the 25p composite is still tougher (in, again, the ST condition), and also has a higher local fracture energy. The local energies increase somewhat upon alloying the matrix from 2 to 4.5 % Cu; yet the global fracture toughness is essentially unaffected. The variations in $2\gamma_{pz}$ are, however, not very large.

If we now turn to the peak-aged matrix (T6), the link between $G_{Iv}$ and $2\gamma_{pz}$ clearly vanishes: $2\gamma_{pz}$ is now smaller for the 25p composite; yet its fracture toughness is far higher than for the 35a composite. We face here a situation where particle cracking occurs at an equivalent level ($f_p$ is near 75% for both composites, Table 4-7), the in-situ matrix flow stress does not differ much, and most matrix intermetallics have been eliminated; however, the polygonal particle reinforced composite is still significantly tougher.

Possible explanations for this discrepancy may be sought by detailed fractographic examination. Crack propagation path for the A4.5C-A25p composite is shown in Figure 5-12. Crack branching sometimes occurs in this composite: this was not observed in angular alumina reinforced composites. Such behaviour can be caused by particle cracking occuring on different planes in front of the crack tip. Linking up of such damage with the main crack then yields a longer actual crack path. In turn, this increases the local fracture energy because the total surface in which dissipation mechanism occur is larger. In the present case, it would be necessary that the actual crack path double so as to increase $2\gamma_{pz}$. Crack branching, however, was not so extensive as to compensate for a significant reduction of the local fracture energy. Crack deflection (“zig-zag” pattern) could also be invoked. Indeed, the present calculations consider the work of fracture per unit of *projected* crack area. With crack deflection, the actual crack surface is larger. However, we did not detect significant differences of crack deflection behaviour between this composite and those with same particles but different matrix or heat-treatment. Hence, these explanations do not suffice to explain the toughness data.

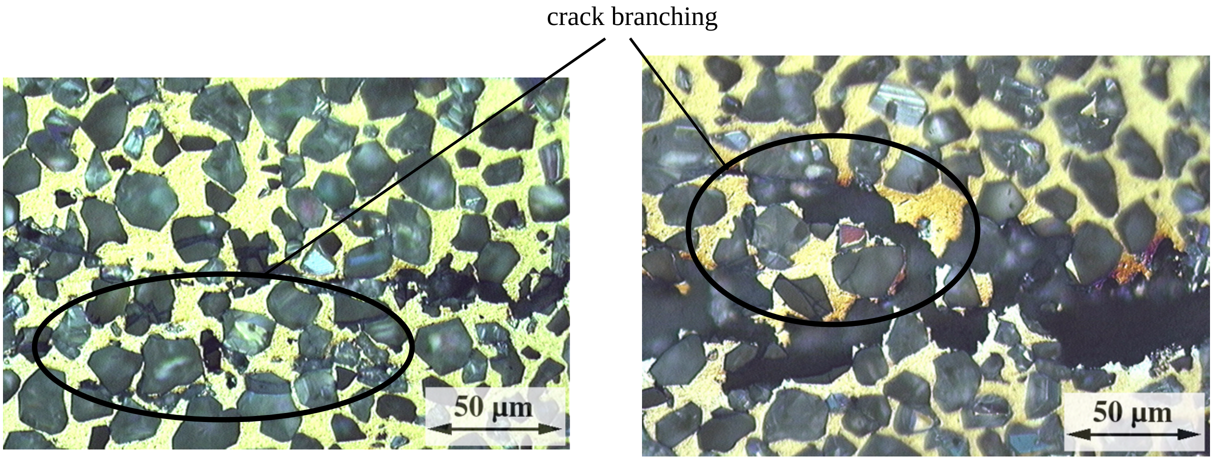

**Figure 5-12.** Crack branching at various locations along the crack path in the A4.5C-A25p composite (T6).

Comparing the 25p and 35a T6 composites, thus, provides a case where the same local energy yields widely different global toughness values: the amplification factor is thus different from one composite to the other. This agrees qualitatively with photoelastic observations: the crack-tip plastic zone is unambiguously larger for Al-Cu/$Al_2O_3$ polygonal composites than for Al-Cu/$Al_2O_3$ angular composite, Figure 4-41 (note, however, that the angular composite is 60a).

The breakdown of the local/global correlation evident with the T6 25p Al-4.5%Cu composite can be viewed in another light, by comparing the 25p Al-4.5%Cu composites in the ST and T6 conditions: the local fracture energy, $2\gamma_{pz}$, is far lower for the T6 25p composite than for the same composite in the ST condition; yet, its global fracture toughness is roughly the same. The main reason why the local work of fracture is lowered in the T6 condition, is the significant increase in the fraction of the crack path occupied by broken particles $f_b$ (from 48% in the ST condition to around 75% after ageing, Table 4-7). Equation (5-11) is indeed far more sensitive to the fraction of broken particles on the crack path ($f_b$) than to the *in-situ* matrix flow stress. To illustrate this, plots of $2\gamma_{pz}$ against $f_b$ at various levels of matrix flow stress are presented in Figure 5-13. One of the factors of Ludwik's law ($\sigma_0$, $n$, and $k$) is varied on each of the plots, while the two others are kept constant, values being chosen so as to vary around the estimated *in-situ* matrix flow stress of the 25p composites. For all calculations, the dimple height $h_0$ is imposed, being equal to 4 µm. The three curves show that variations in $f_b$ exert a far higher influence on $2\gamma_p$ than variations in parameters governing the matrix flow stress: at 75% of broken particles (which corresponds to the situation observed with the A4.5C-A25p composite in T6 condition), the curves do not predict significant differences in $2\gamma_p$. For two similar composites, thus, an increase in the fraction of broken particles does not translate, within the assumptions of the present calculations, in a decreased composite toughness.

Turning now to the 15p composites, the same observations and conclusions can be made upon comparing the Al-4.5% matrix composites in the ST and the T6 conditions, Figure 5-11c.

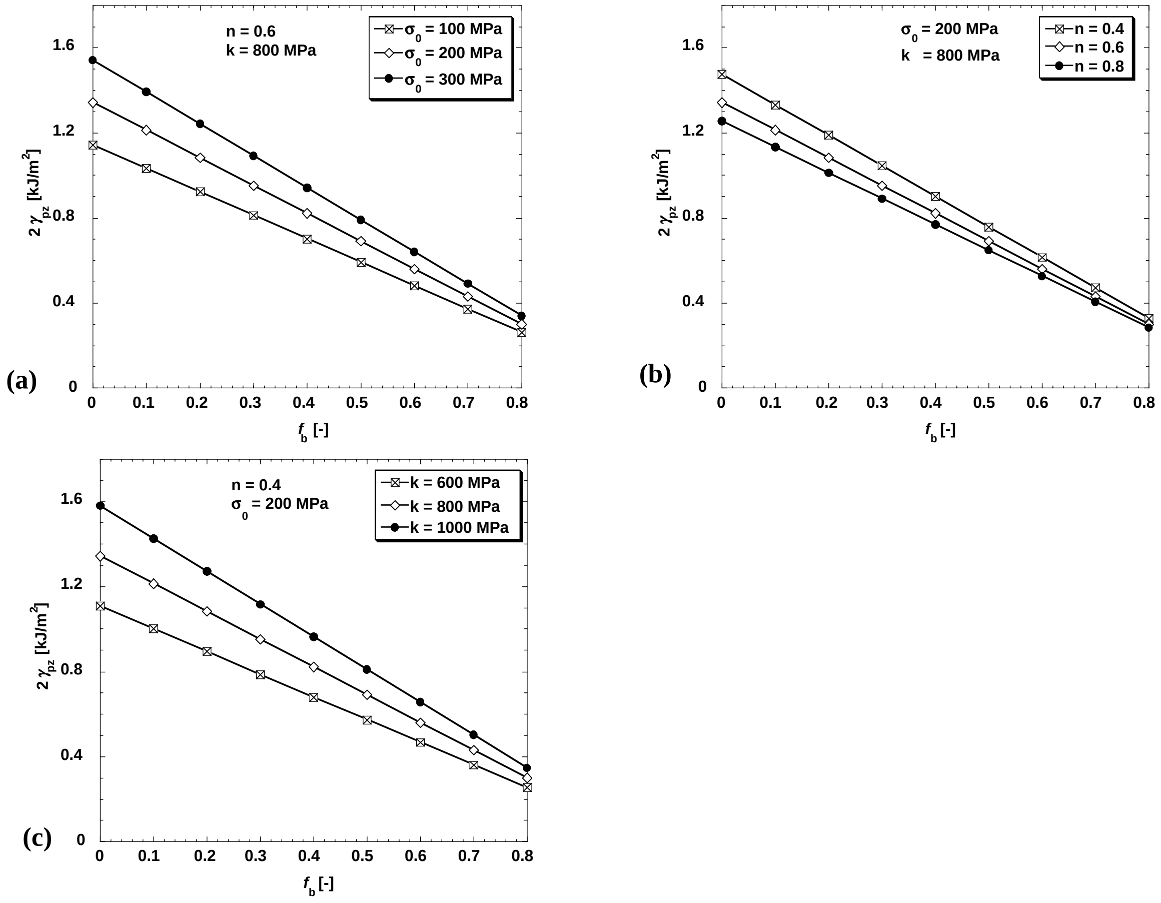

**Figure 5-13.** Influence of the degree of particle cracking on the local fracture energy, as predicted by eqs. (5-11) and (5-13). **(a)**: *n* and *k* constant, $\sigma_0$ varied; **(b)**: $\sigma_0$ and *k* constant, *n* varied; **(c)**: $\sigma_0$ and *n* constant, *k* varied.

### v. Summary

Summarizing, whereas with the pure aluminium matrix composites we found a clear and directly proportional correlation between the local and the global fracture energies, within the assumptions made here in estimating the local fracture energy $2\gamma_{pz}$, this correlation breaks down with the alloyed matrix composites.

There is no fundamental reason why there should be a direct proportionality between the local and global fracture energies between materials with widely different flow stress; see for example eq. (2-37) and Ref. [189]. Yet, one may also question whether the simple calculation method used so far to estimate $2\gamma_{pz}$, namely Stüwe's analyses of dimple formation energy, is not at the root of the discrepancies observed with alloyed matrix composites. We therefore turn to more recent models reviewed above: these introduce the influence of matrix constraint as a parameter in the calculated local fracture energy $2\gamma_{pz}$.

### 5.2.4 Local energy: Influence of constraint between particles

When applied to our composites, particle fracture in Stüwe's approach is taken into account only through post-fracture determination of the dimple height and of fraction of broken particles on the fracture surface. In addition, local triaxiality due to the presence of rigid reinforcements does not appear.

**i. Stress triaxility in constrained microstructures**

In high volume fraction particle reinforced MMCs, high constraint is present between closely spaced hard particles. Voids nucleated in the matrix between ceramic particles are therefore likely to grow under a high level of local stress triaxiality.

The simplest way to account for this effect in PRMMCs is to invoke the slip line field (Prandtl) solution for a perfectly plastic layer between rigid plates [127, 276]. This predicts an average stress $\sigma_H$ in the soft layer of [277]:

$$\frac{\sigma_H}{\sigma_0} = \frac{3}{4} + \frac{b}{2h} \tag{5-14}$$

where $b$ is the width of the rigid plates, and $h$ the height of the soft layer. Taking $b$ as the average particle diameter and $2h$ as the interparticle distance $\lambda$, the ratio of the flow strength over the uniaxial (unconstrained) yield strength of the matrix is nearly 3. In the composite the constraint is three-axial, and there exist many regions where the interparticle distance is significantly smaller than average (these being the regions where cavity nucleation occurs preferentially). Constraint is hence likely to be higher than predicted by eq.(5-14) with this choice of parameter.

Relevant information regarding the level of hydrostatic tension $\Sigma_H$ in the matrix during straining is also obtained from FEM analysis of the composite deformation behaviour. For the hydrostatic tension normalized by the uniaxial yield strength, $\Sigma_H/\sigma_0$, values ranging from 2 to 6 have been reported in the immediate vicinity of particles [148, 206, 278], higher values being obtained close to sharp corners [86, 148, 153]. Most such studies have been conducted for relatively low volume fractions of reinforcement (< 20%); hence it is expected that $\Sigma_H/\sigma_0$ is even higher for 50 to 62% of particles, due to interaction of stress fields of closely spaced particles. Recent computations on high volume PRMMCs in our laboratory indeed do indicate that local stress triaxiality is much larger in the interparticle regions situated between particles perpendicular to the stress direction than between particle sides parallel to the stress [279]. This corresponds quite well to experimental findings of void nucleation sites in these composites [135, 252].

Experimentally, the investigations conducted by Ashby *et al.* [226, 229] on constrained metal wires (see § 2.6.3.iv), show that normalized stresses $\sigma/\sigma_0$ in the wire can attain values as high as 6 due to the high constraint imposed by the stiff material.

Other sources of information are obtained from studies on dual-phase steels consisting of hard martensite particles embedded in a soft ferrite matrix. For such structures with 30% of hard particles, idealized calculation in plane-strain have indicated a ratio $\Sigma_H/\Sigma_{eff}$ comprised between 2 and 3 [280], where $\Sigma_{eff}$ is the effective (Von Mises) stress. A difference with our composites resides in the fact that the difference in Young's modulus is far lower in dual-phase steels; this should lower the ratio $\Sigma_H/\Sigma_{eff}$. Finite element modeling of crack fracture process in WC-Co alloys coupled with experiments has also shown that voids nucleate in the Co ductile phase in regions of high stress triaxiality [216, 218].

### ii. Modeling of void growth under high stress triaxiality

For voids nucleated in the matrix (Figure 5-7), there hence exists a high level of stress triaxiality during the early stages of void growth, even if its value is not exactly known. The model of Poech and Fischmeister, presented in Section 2.6.1.ii, considers void growth under the influence of crack-tip stress triaxiality, defined as $\eta = \Sigma_H/\Sigma_{eff}$. Gurson's yield criterion for a porous ductile medium is used, to obtain relations (2-51) and (2-53) for the uniaxial traction-separation law:

$$Y^2(x) + f \cdot \left[\exp\left(\frac{3}{2}\eta Y(x)\right) + \exp\left(-\frac{3}{2}\eta Y(x)\right)\right] - \left(1 + f^2\right) = 0 \qquad (2\text{-}51)$$

$$\Sigma_z(x) = \sigma(\varepsilon(x)) \cdot Y(x) \cdot \left(\eta + \frac{2}{3}\right) \cdot \frac{(1 - x^2)}{(1 - f)} \qquad (2\text{-}53)$$

In this approach, the stress triaxiality is a free parameter, which is mentioned to attain values as high as 6 at the crack tip in the presence of plastic processes for strain hardening materials.

An alternative method to account for geometrical constraint brought by the stiff particles is to use Bridgman's solution for stretched ductile particles [221], (see §.2.7.3.ii):

$$\sigma(u) = k \cdot 2^n \cdot \left[-\ln(1 - x)\right]^n \cdot \ln\left(\frac{1}{x}\right) \cdot (1 - x) \qquad x = \sqrt{(2u/\pi a_0)} \qquad (2\text{-}65)$$

where $u$ is the stretch opening. This approach is valid for a ductile particle of radius $a_0$ in a brittle matrix. In the case of a ductile matrix, it must be modified by assimilating the region of intense plastic deformation between growing voids to the ductile particle in the original model. $a_0$ then becomes the half-space between voids center, *i.e.* it can be approximated as the interparticle distance $\lambda$ in our composites, Figure 5-14.

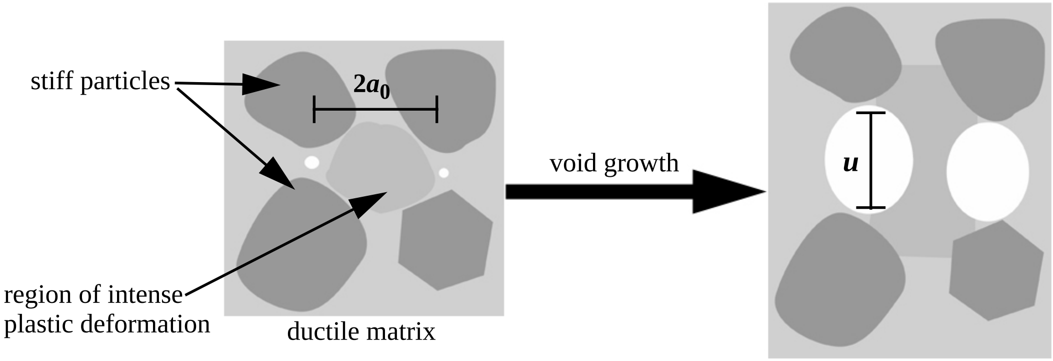

**Figure 5-14.** Plastic stretching in the process zone, between voids nucleated in the matrix. The flow stress in the region of intense plastic deformation is assumed to obey to Bridgman's solution for a cylindrical notched bar.

Calculations of the traction-separation curve for the A-A15p composite according to these two approaches are shown in Figure 5-15a. For the model based on Gurson's yielding criterion, eq.(2-51) was numerically solved at various incremements of void growth and the initial height $h$ was taken as the average interparticle distance. As the level of stress triaxiality increases, the peak stress of the traction separation law is clearly increased, attaining about twice the peak stress if the stress state is uniaxial ($\eta$ = 0.33). With Bridgman's solution, the peak stress attains a value even higher than predicted by the Poech and Fischmeister model with a large stress triaxiality ($\eta$ = 5). Since the stress then decreases more rapidly and since the final plastic stretch $u^*$ is lower (this is imposed by the model), the work of the fracture process is on the other hand smaller. In the presence of large stress triaxiality imposed by geometrical constraint, high local axial stresses are hence attained during the voiding process, even with a pure Al matrix.

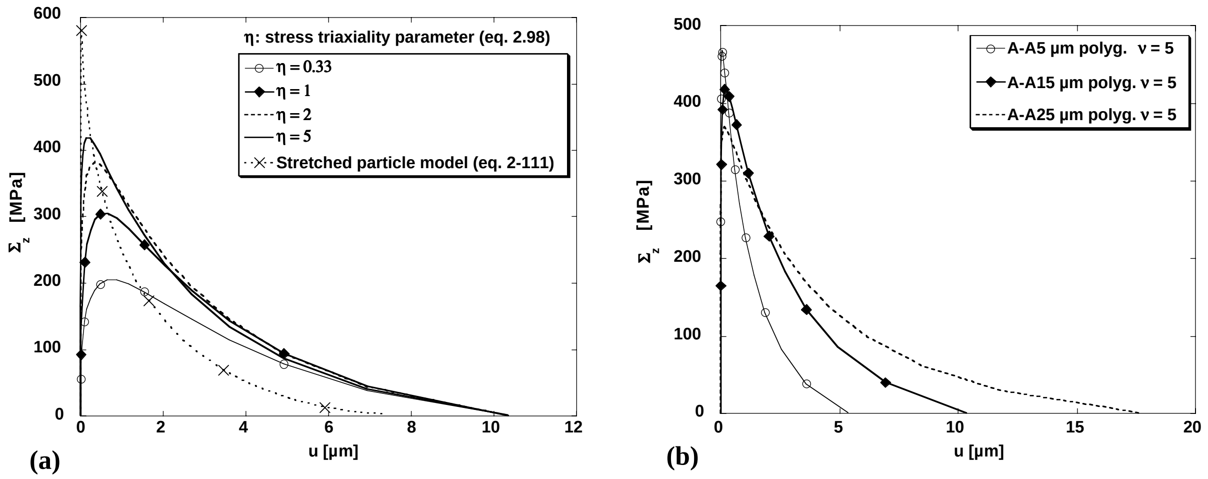

**Figure 5-15.** Local traction-separation curves $\sigma$(u), predicted by the models of Poech and Fischmeister, and Sigl *et.al* (stretched particle). **(a)**: A-A15 composite, influence of the local contraint; **(b):** shape of $\sigma$(u) at a given stress triaxiality for polygonal alumina reinforced composites.

In Figure 5-15b, the traction-separation curves are plotted for pure Al matrix composites reinforced by the three different sizes of polygonal particles, for a fixed value of $\eta$[1]. Since the *in-situ* matrix flow stress of fine particle size composites is higher, the peak stress increases slightly too; however, the void growth is restricted by the smaller interparticle distance. In other words, the local work of fracture still scales roughly with the interparticle distance, whatever the level of triaxiality (provided the crack propagates mainly through the matrix).

This is illustrated in Figure 5-16 for pure Al matrix composites reinforced by polygonal $Al_2O_3$ where the global vs. local fracture energies are plotted for various local triaxiality parameters; and also according to the Bridgman's analysis. The local energy is simply the area under the $\sigma(u)$ curves:

$$\gamma_{\mathrm{pl}} = \int_{0}^{u_{\mathrm{max}}} \sigma(u)\mathrm{d}u \qquad (5\text{-}15)$$

(in the case of plastic stretching, one can alternatively use expressions (2-66) to (2-68)). Particle cracking is also taken into account and is assumed for the moment that it does not influence the traction-separation laws (this is reasonable since for the composites considered in Figure 5-15, little particle cracking occurs).

The results are also compared with the model of Stüwe, and indicate that whatever the local law used to describe the voiding process, the local/global link is confirmed, which is expected since the interparticle distance is the scaling factor governing local fracture events. However, a certain degree of uncertainty remains because differences exist depending on the model used to describe the local micromechanisms events, which in turn affect the estimation of $2\gamma_{pz}$.

---

[1] It is the arrangement of particle that dictates geometrical constraints and, in turn, local stress triaxiality. Hence, the latter remains constant when varying particle size because the ratio particle size/interparticle distance remains constant as well.

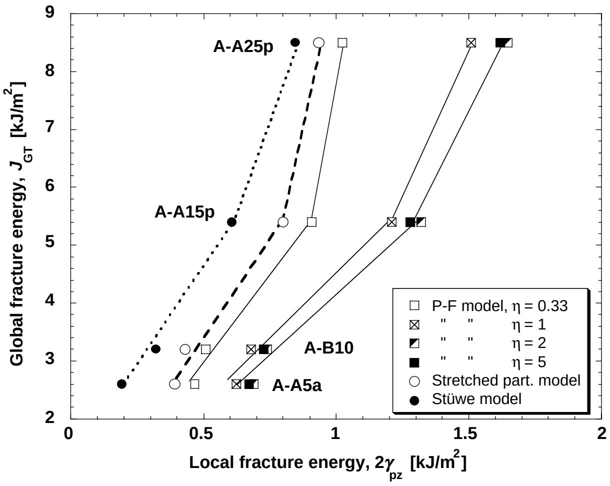

**Table 5-6.** Comparison local/global values: polygonal $Al_2O_3$ (15 and 25 µm) and $B_4C$ (35 µm) reinforced composites (all values in kJ/m$^2$).

| | $\eta = 0.33$ | $\eta = 1$ | $\eta = 5$ | stretched particles | $J_{GT}$ |
|---|---|---|---|---|---|
| **A-A25p** | 1.18 | 1.59 | 1.73 | 1.70 | 8.5 |
| **A-A15p** | 0.91 | 1.21 | 1.32 | 1.29 | 5.5 |
| **A-B35** | 1.3 | 1.78 | 1.95 | 1.91 | 5.4 |

**Figure 5-16.** Correlation local/global fracture energies, for various descriptions of the micromechanisms of fracture in four composites. In cases where of the ductile dimple height as imposed by the model is significantly different than the measured value, the global energy does not scale with the local one (see Table 5-6).

### iii. Limitations of micromechanical analysis

We have probably reached here the limits of simple micromechanical analysis. While all models certainly give correct orders of magnitude of $2\gamma_{pz}$, refined quantification is more difficult because it is not straightforward to decide which model describes best the local fracture events, and in turn what is the amplification factor brought by plastic shielding. Numerical simulations are hence necessary to improve our quantitative understanding of PRMMCs fracture [281].

Table 5-6 also indicates that precise quantification of the fracture surface micro-roughness is important and cannot be neglected. For the A-B35 composite, calculated values of $2\gamma_{pz}$ yield larger values than for the 25 µm polygonal composite, whereas its macroscopic toughness is lower. This is because the interparticle distance $\lambda$ is larger in the A-B35 composite, such that the “voiding” models predict larger dimple heights. This is not confirmed by measurements, *i.e.* the imposed $u^*$ does not always match with the dimple depth measurements. Hence, differences in fractographic features that seem insignificant might actually play a decisive role. A reduction of the average dimple height by a factor 2 (from, say, 10 to 5 µm) will significantly reduce the local fracture energy.

### iv. Void growth: comparison with unreinforced alloys

Upon assumption that Gurson’s model yields a reasonable description of the voiding process, loss of local constraint ($\eta = 0.33$) results in a significant reduction of the local work of fracture. Conversely, this means that increasing the volume fraction, $V_f$, of stiff particles in PRMMCs leads to higher $2\gamma_{pz}$ since this allows to increase the stress triaxiality. On the other hand, increasing $V_f$ also means a reduced allowed degree of cavity extension, while the global composite yield strength increases with $V_f$, which will result in a lower amplification of the local energy by plastic dissipation. Hence an optimal $V_f$ may exist. In any case, this may bring a reasonable explanation for the relative lack of influence of $V_f$ on the toughness of the present PRMMCs, and the high toughness values reported in this study and elsewhere (see §.2.3.3): increasing the volume fraction of ceramic reinforcement in PRMMCs does not necessarily cause a loss in fracture toughness.

Such a prediction might sound surprising, given the well-known behaviour in ductile fracture that higher constraint limits large-scale plasticity, and enhances local damage and its rate of accumulation, resulting in lower apparent fracture energy (a review of this is given by Brocks [282]). At the local scale in ductile monolithic alloys, the expression developped by McClintock [283] and Rice and Tracey [284] predict that the growth rate of a single cavity features an exponential dependence on the stress triaxiality. As also demonstrated by more recent studies, cavitation instability sets in earlier for higher level of stress triaxiality [285, 286], leading to reduced fracture toughness. In high volume fraction PRMMCs on the other hand, simple analysis of void growth, as well as dimple depth measurements on fractured specimens, indicate that it is the geometrical arrangement at the microstructual scale (*i.e.* the interparticle spacing $\lambda$) which governs coalescence of growing cavities. In a sense, one can conceive the effect of interparticle spacing as similar to that of stress triaxiality in unreinforced ductile alloys: if $\eta$ increases in the latter, voids coalesce earlier; in PRMMCs voids coalesce earlier when $\lambda$ decreases (Figure 5-15).

### 5.2.5 Local energy: particle cracking

When particle fracture occurs during crack propagation, this makes the composites less tough, as discussed for pure Al matrix composites. This is, however, not sufficient to rationalize composite toughness: in the case of polygonal reinforced composites, as stronger (alloyed) matrices are used, the fraction of cracked surface occupied by broken particles increases (as seen with 25 µm particles, and at a less extent 15 µm particles). This transition is, however, not accompanied by a drop in toughness (Table 4-6 and Figure 4-49). It is thus useful at this point to discuss the intrinsic particle characteristics, and address the question: what causes a particle to fracture ?

**i. Weibull statistics appplied to particles**

Experimental investigations and related analysis on the cracking of inclusions within steels [138], and of ceramic particles in composites [139, 140, 287] have shown that the probability of fracturing a brittle particle embedded within a ductile matrix can be taken to follow weakest link statistics (Weibull statistics): for a given ceramic type, large particles are more likely to crack because the probability of finding a critical flaw increases too. Furthermore, in the case of metal matrix composites, Lewis and Withers [140] have shown that the influence of particle aspect ratio and applied strain should be included in the Weibull model. The probability of fracture $P_c$, of a particle of volume $V$, and aspect ratio $\alpha$, subjected to stress $\sigma_p$ is then given by:

$$P_c = 1 - \exp\left[ -\frac{V}{V_0} \cdot \left( \frac{\sigma_p(\alpha, \varepsilon, V)}{\sigma_0} \right)^m \right] \qquad (5\text{-}16)$$

where $\sigma_p$ is a function of the particle aspect ratio $\alpha$, the particle volume $V$ and the applied strain $\varepsilon$, $\sigma_0$ and $V_0$ are representative stress and volume respectively that are introduced for dimensional purposes, and $m$ is the Weibull modulus. Particle fracture according to Weibull statistics was succesfully incorporated into numerical computations to describe the stress-strain response of PRMMCs [141, 288-290].

Qualitatively, weakest-link statistics is supported by our observations. For pure Al matrix composites reinforced by angular $Al_2O_3$ and $B_4C$, particle cracking increases as the average particle size increases (Table 4-4). For polygonal $Al_2O_3$ composites, one must refer to observations on Al-Cu matrix composites: for Al-4.5%Cu (Table 4-7), the fraction of broken particles on the crack path is unambiguously seen to augment as the average particle size increases.

The difference between polygonal and angular particles can also be viewed in the framework of Weibull statistics. According to numerical simulations on unit cells, the probability of particle fracture increases for higher particle aspect ratio $\alpha$, because higher stress is built up at corners, especially for elongated particles [86, 206, 291, 292]. Hence, since angular particles are more elongated and exhibit sharps corners, the stress distribution in these is more inhomogeneous than in their polygonal counterparts, and their probability of fracture is larger, as observed.

The second factor, which plays a more crucial role, is the intrinsic quality of particles. Clearly, SEM micrographs presented in Figure 4-1 indicate the presence of elongated surface defects (namely cracks) in the initial angular $Al_2O_3$ powder, whereas defects in $B_4C$ particles take the form of micropores at the surface of the particles. In polygonal $Al_2O_3$, defects are not detected under the SEM. Other illustrative pictures of the same powders can be found in Refs. [89, 252]. In terms of Weibull statistics, the quality of particles is contained in the Weibull modulus, $m$. High $m$ is an indication of a homogeneous distribution of defects, which causes the particles to fracture in a narrow range of stress around the characteristic reinforcements strength, $\sigma_0$. Conversely, a low value of $m$ means that particle fracture can occur at values well below $\sigma_0$.

With a stronger matrix, higher load is transferred to the particles, in turn increasing the probability of fracture [137, 206, 287]. Thus polygonal particles which did not crack with the weak pure Al matrix are more prone to crack as the matrix strength increases. According to Weibull statistics, this effect is more pronounced for larger particles: indeed most of the fine 5 µm particles remain intact even with the strongest matrix used in the present work (Al-4.5% Cu in the peak-aged condition, Table 4-7).

### ii. Estimations of the intrinsic particle strength

If pre-existing flaws are indeed initiation sites, one can estimate typical critical stresses required to crack a particle, $\sigma_{fp}$. For all angular $Al_2O_3$ powders, the particles are modeled as Single Edge Notched Samples loaded in tension, having a crack of length $a$ (the pre-existing flaw), similar to assumptions used in [174]. The critical fracture stress for such a configuration is [293]:

$$\begin{aligned} \sigma_{\mathrm{fp}} &= \frac{K_{\mathrm{Ic}}}{\sqrt{\pi a}\cdot Y(a/D)}, \text{ where} \\ Y(a/D) &= \frac{\sqrt{2\tan(\pi a/2D)}}{\cos(\pi a/2D)}\left[0.752 + 2.02(a/D) + 0.37\big((1-\sin(\pi a/2D))\big)^3\right] \end{aligned} \qquad (5\text{-}17)$$

where $K_{Ic}$ is the fracture toughness of $Al_2O_3$, taken as 4 $MPa{\cdot}m^{1/2}$. We further assume a normal distribution of flaw sizes, centered around a mean value taken as 20% of the average particle size $D$, with a standard deviation equal to 5% of the particle size[1].

For polygonal $Al_2O_3$ powders, surface defects were almost not visible under the SEM. The average flaw size is thus much smaller, but other types of internal defects cannot be excluded. Since surface cracks are the most deleterious flaws, we still use the solution for the Single Edge Notched Specimen, but we assume an average flaw size equal to 2% the average particle size (*i.e.* 0.5 µm for the 25 µm particle powder, which remains an overestimation according to SEM investigations). For $B_4C$ powders, the characteristic geometry of flaws differs from that of angular $Al_2O_3$, as these take rather the form of pores emerging at the particle surface (Figure 4-1d). To a first approximation, semi-elliptical surface cracks are assumed, with an aspect ratio *a/c* of 2 (where *c* is the length of the ellipse longitudinal axis). According to the stress intensity factor solution for this type of cracks ([237], pp.59), the critical fracture stress is:

---

[1] This estimation is based on SEM micrographs of the initial powders; however more systematic observations of individual particles would be necessary to obtain a statistically representative sampling.

$$\sigma_{\mathrm{fp}} = \frac{K_{\mathrm{Ic}}}{\lambda_{\mathrm{s}}} \cdot \sqrt{\frac{Q}{\pi a}}, \quad \text{where} \qquad Q = 1 + 1.464(a\ c)^{1.65} \quad \text{and} \quad \lambda_{\mathrm{s}} = 1.13 - 0.09(a/c) \tag{5-18}$$

For the mean flaw size, we take a value equal to 10% of the average particle size (again estimated based on SEM observations).

Critical stress distributions for the different type of powders and for various average particle size are shown in Figure 5-17. It is important to mention that such plots should not be confused with Weibull distributions; they represent the strength of particles having a constant size and an imposed flaw distribution.

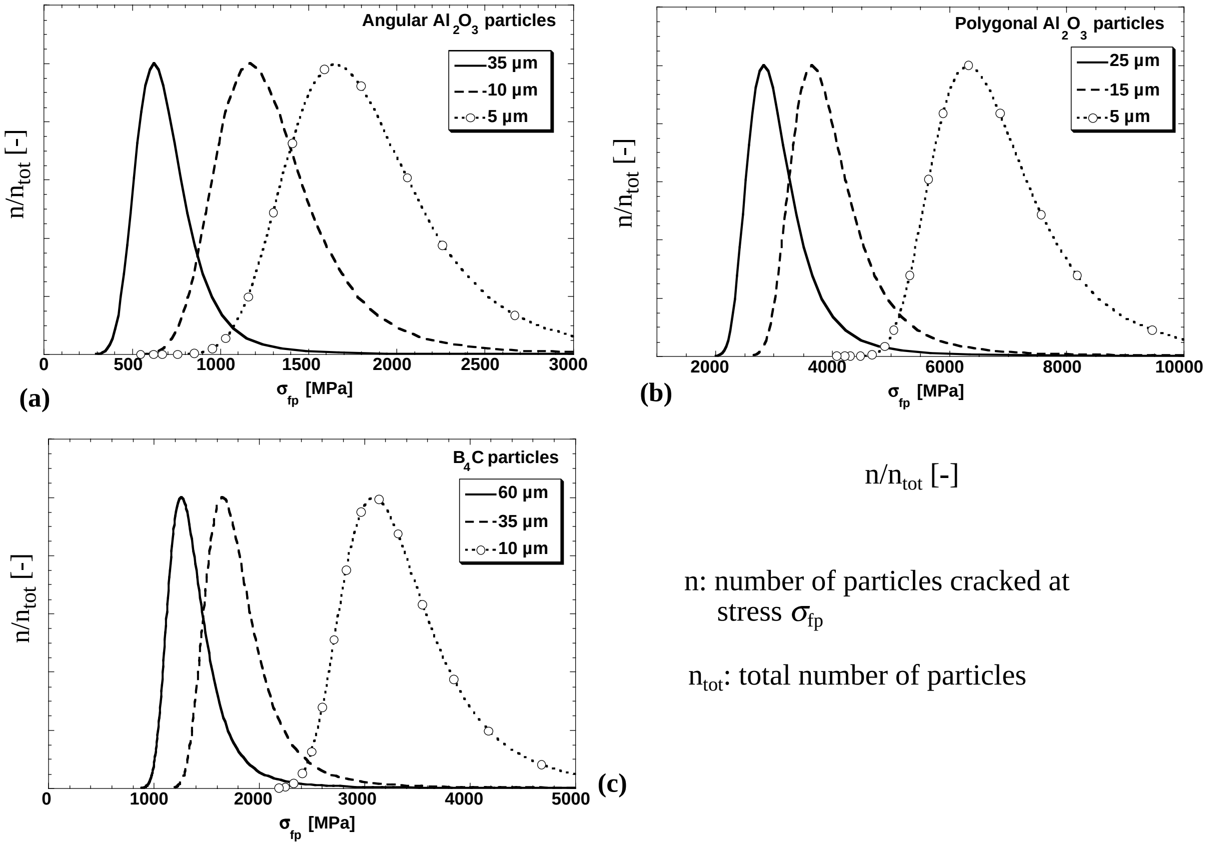

n/n$_{tot}$ [-]

n: number of particles cracked at stress $\sigma_{fp}$

n$_{tot}$: total number of particles

**Figure 5-17.** Distribution of particle fracture stresses for the various types of ceramic powders. The curves are computed by assuming uniform particle sizes and imposed distributions of flaw sizes, based on SEM observations.

### iii. Implications for high volume fraction PRMMCs

The plots in Figure 5-17 are based on crude estimations. In particular, the particle size distribution is not taken into account (whereas it plays an important role, for instance in the $Al_2O_3$ 10 µm angular powder); nor did we consider multiple interaction of particles containing more than one flaw. Nonetheless, the assumed typical flaw size was large, such that $\sigma_{\mathrm{fp}}$ is probably underestimated.

The average fracture stress for the angular 35 µm particles (which are the least resistant presented) is on the order of 600 - 700 MPa. Refering to load partitioning, the average stress carried by the particles $\sigma_{\mathrm{p}}$ is:

$$\sigma_{\mathrm{p}} = \frac{\sigma_{\mathrm{a}} - \left(1 - V_f\right)\sigma_{\mathrm{m}}}{V_{\mathrm{f}}} \tag{5-19}$$

where $\sigma_{\mathrm{a}}$ is the average composite stress and and $\sigma_{\mathrm{m}}$ is the average *in-situ* matrix stress. At the instant of fracture, the composite stress field in the process zone is not known because continuum hypthothes break down. Nevertheless, it is reasonable to consider that the maximum composite stress in the process zone is in the range of the UTS. According to (5-19), the average particle stress for the A-A320 composite is then in the range of 200 MPa.

This is clearly not sufficient to induce particle cracking, even for the weakest among them. In addition particle cracking already begins at the onset of plastic yielding, namely at even lower average composite stresses. A microstructural feature inherent to the processing route in our high volume fraction PRMMCs is that particles are in direct contact with neighbouring particles. As explained by Kouzeli *et.al.* [135, 252], this implies that during plastic straining, the reinforcements move slightly relative to one another and induce load transfer at mutual contact points. The sharps corners of the angular particles hence induce indentation in the neighbouring particles and very high stress concentrations that probably exceed values in the range of 1 GPa, which can activate existing cracks near the contacts. As the average reinforcement size decreases, the intrinsic particle strength increases (Figure 5-17a), such that the stress concentrations at contact points are not large enough to induce particle cracking. In the case of $B_4C$ particles, the different geometry of flaws imposed and their smaller mean size involves less cracking for a given particle size (Figure 5-17b). This is what is experimentally observed.

If we now turn to the polygonal reinforcements, we find very high fracture stresses with our assumptions: average values are around 2.8 GPa for the 25 µm particles, and even attain 6 GPa for the 5 µm particles (Figure 5-17c).

Are intrinsic particle strengths in the range of 6-8 GPa realistic? One of the strongest known forms of alumina is the fibre Nextel 610™, developed and commercialized by 3M Corp. (MN, USA). Nextel 610 is made of high purity and fine grained $\alpha$-$Al_2O_3$ [294]: with a fibre diameter of 10-12 µm, tensile strengths in the range of 3-3.5 GPa have been reported [295, 296]. Given the smaller volume of particles, a higher strength is not unrealistic according to the weakest link theory. It is also not excluded that polygonal particles are actually closer to whiskers than to particles in terms of mechanical performance. For SiC whiskers, which are the most widely used, strengths in the range of 5-10 GPa were already reported in the 1960’s for 5 µm diameter whiskers [297], while nowadays whiskers with tensile strengths ranging from 3 to 20 GPa are commercially available [298]. Therefore, such high values of intrinsic strengths for the very fine polygonal particles are plausible, given their very small population of defects.

With pure Al matrix composites, our observations hence suggest that such stresses are not attained at the contact points. Moreover, one should mention that the stress concentration due to interparticle contact scales with the contact tip radius [299]; stress amplification is therefore less pronounced with polygonal particles than with angular particles because these feature sharper angles. Now invoking again load partitioning for the Al-Cu matrix composites at UTS, the average particle stress is in the range of 450 to 500 MPa for the Al-Cu2% matrix composite, and rises to values around 550-600 MPa for Al-Cu4.5% matrices. Again, such values are far to small to cause fracture of polygonal particles. Since particle cracking is indeed seen as the matrix strength increases, it is evident that a larger matrix flow stress leads to an enhanced stress concentration effect due particle-to-particle indentation. For the fine 5 µm powder, the results indicate that an even stronger matrix than Al-Cu4.5%/T6 could perhaps be used since particle cracking remains rarely observed.

In summary, it is the combined effect of particle microstructure, shape, pre-existent surface (or volume) defect population that cause the particles to fracture. Higher quality particles (*i.e.* featuring a smaller population of defects) strongly delay the occurence of particle fracture. On the other hand, larger aspect ratio particles feature more inhomogeneous stress distributions, and lead to higher stress concentrations at contact points. One should also mention another deleterious effect associated with pre-existing cracks: a pre-existing surface flaw acts to attract the crack in the reinforcement, as studied by numerical methods [147], hence increasing its probability of fracture.

# 5.3. TOUGHENING MECHANISMS: INTERPLAY OF LOCAL AND GLOBAL PROCESSES

## *5.3.1 Preliminary remarks*

Main findings from this work can be summarized as follows:

- The present composites are surprisingly tough given their high ceramic contents: $K_{Iv}$ values exceeding 30 MPa·m$^{1/2}$ have been achieved.
- Their high toughness is associated with extensive plastic deformation around the crack tip, *i.e.*, the local fracture energy is amplified by global plasticity around the crack tip.
- There are two basic microscopic fracture processes (local fracture processes): (i) matrix voiding between particle surfaces oriented for mode I opening, and (ii) matrix ligament stretching between broken particles.
- The propensity for particles to crack near the crack tip varies strongly. In some composites, nearly all particles along the crack path are cracked: as shown in Table 4-7, the particles then represent about 70 to 80 % of the crack surface. In other composites, there are no broken particles along the crack path; intermediate situations also exist.
- The toughness is a function of the propensity for particle cracking, of the local matrix flow stress, and of the particle size (*i.e.*, the microstructural length scale of local fracture processes).
- In pure aluminium matrix composites, the local fracture energy computed using Stüwe's analysis applied to fractographs of the composites implies a direct linear correlation between the local fracture energy and the toughness of the composites: the latter is about ten times the former.
- In alloyed matrix composites, within the approximations of less detailed fractographic analysis, this correlation seems to break down. Specifically, while the toughness is lower with (fracture-prone) angular particles, it is independent of the extent of particle fracture in polygonal particle reinforced composites.
- Some factors cause a significant lowering of the toughness: weak matrix/particle interfaces, and brittle intermetallics in the matrix.

## *5.3.2 Local/global fracture energy relationship*

Recent finite-element simulations of the fracture process in elastic-plastic power-law hardening materials have been conducted by several authors to simulate fracture by microvoid coalescence, and fracture along metal/ceramic interfaces [189, 195, 196, 300, 301]. Specifically, in the Cohesive Zone Modeling (CZM) framework this body of work has shown that:

(i) the initiation of crack growth occurs when $G$ equals the local fracture energy $2\gamma_{pz}$ (as expected given the fact that, until then, loading is proportional);

(ii) thereafter, the toughness $G$ increases as the crack advances, to reach a steady-state value $\Gamma_{ss}$ (identified as the remote energy release rate $G$ needed to advance the crack in small scale yielding under steady-state conditions).

As explained above, $\Gamma_{ss}$ in Al-Cu matrix composites can reasonably be identified with the chevron-notched fracture toughness, $G_{Iv}$ (expressed in terms of the energy release rate), since this value is measured after significant crack advance (of about 5 mm). In pure matrix composites, the toughness $J_{GT}$ was derived from the $J$-$\Delta a$ curves at the inflexion point where the tearing modulus decreases abruptly. As explained above, these values are somewhat lower than $\Gamma_{ss}$; however, as was found by comparison with chevron-notch data, Table 5-2, the difference is not very high (20 % at most, *i.e.*, not far above experimental uncertainty). For this reason, and also for the simple reason that the inflexion in the $J$-$\Delta a$ curve denotes the onset of a relatively flat region in the curve for constrained specimens (Figure 4-19), we take the measured values of $J_{GT}$ as being relatively close (*i.e.*, conservative) estimates of $\Gamma_{ss}$ in the pure Al matrix composties.

Several parameters influence the relation between $\Gamma_{ss}$ and $2\gamma_{pz}$, or in other words the "amplification factor" between local and global fracture energies in the steady state crack advance regime; however, only two have been found to be important in Mode I ductile fracture [189, 195]: (i) the ratio of the peak stress reached by the tearing material in the fracture process zone near the crack tip, $\hat{\sigma}$, to the plastic flow stress of the material, $\sigma_y$, and (ii) the strain rate exponent $n$ of the fracturing material (eq. 5-20):

$$\Gamma_{ss} = 2\gamma_{pz} \cdot F\left(\frac{\hat{\sigma}}{\sigma_y}, n\right) \tag{5-20}$$

The "amplification factor" $F$ as calculated by Tvergaard and Hutchinson is plotted in Figure 5-18.

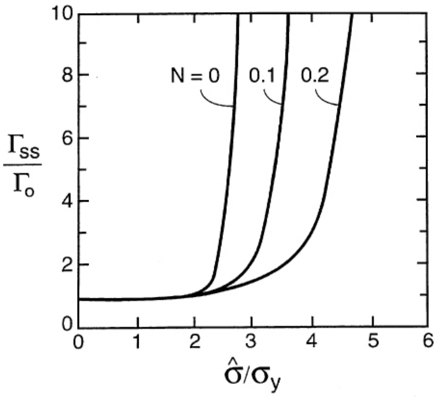

**Figure 5-18.** Ratio of the steady-state toughness, $\Gamma_{ss}$, to the local work of fracture, $\Gamma_0$, (identified here as $2\gamma_{pz}$) vs. the ratio of peak stress to yield stress, as predicted by the cohesive zone model [189].

Comparing this graph with the present data, one finds that:

(i) the "amplification factor" $F$ between the steady-state global toughness and the estimated local (initiation) toughness $2\gamma_{pz}$ increases rapidly above unity as $\hat{\sigma}/\sigma_y$ exceeds a value near three for materials having $n = 0.2$;

(ii) an amplification factor near 10, as obtained in the present work if local energies are computed using Stüwe's model, is not unreasonable if $\hat{\sigma}/\sigma_y$ is sufficiently high, exceeding a value near five with $n$ of 0.2.

In this regard, it is interesting to compare the present data with the remark made by Tvergaard and Hutchinson at the end of that article [189]. The authors pointed out that their results imply that "plastic dissipation (other than that which is associated with the bridging/fracture process) will often be of minor consequence when the overall flow stress of the solid is as much as twice the flow stress of the softest phase". The implication is that materials such as the present composites are unlikely to display toughnesses significantly above the local fracture energy that is consumed in the process zone or, in other words, that $F$ is unlikely to exceed unity.

The rationale for their remark was that the yield stress $\sigma_y$ in (5-20) is the yield stress of the composite, while the peak stress in the local fracture process zone, $\hat{\sigma}$, is linked with deformation of the matrix. It being unlikely (according to the authors) that $\hat{\sigma}$ would exceed the matrix flow stress by more than a factor around 4, given that the composite flow stress is around twice the matrix flow stress (see Figure 5 in [179]). Hence $\hat{\sigma}/\sigma_y$ should not exceed 2.5, such that $F$ remains close to unity (Figure 5-18).

The fact that high toughnesses have been reached in the present composites implies that $\hat{\sigma}$ actually can exceed the matrix flow stress by more than a factor around 5. The reason must be that high levels of triaxiality are reached in matrix ligaments along the crack path, this triaxiality level being on the order of 6 to 8, raising $\hat{\sigma}/\sigma_y$ significantly above 2.5. As shown in what precedes, micromechanical models for ligament tearing in composites such as ours show that this can, indeed, be the case.

This has two implications:

(i) the "trick" behind the high toughness of the present composites is that high triaxiality is reached in ductile matrix ligaments during microvoiding; in turn this implies that the matrix/particle interface must be strong;

(ii) the amplification factor $F$ in our composites is in fact significantly lower than 10, as this value was obtained by computing local fracture energies using Stüwe's model, which implicitely assumes no triaxiality ($\eta = 0.33$). $\hat{\sigma}/\sigma_y$ can, thus, be lower than 5 for Tvergaard and Hutchinson's calculations to remain consistent with our findings concerning the present composites.

### 5.3.3 Influence of particle fracture

What is the influence of particle fracture ? We know that particle fracture is statistical, and that it influences the toughness of the present composites. Particle fracture will influence the global flow behavior of the composite, however, this influence is not very strong at low plastic strains of the bulk plastic region surrounding crack tips (see for example Figure 10 of [252]). Hence, the principal influence of particle cracking is on the local fracture process. How, then, does particle cracking affect the peak stress $\hat{\sigma}$ and local energy $2\gamma_{pz}$ of the local fracture process ?

We know that particle fracture is statistical in nature, and that the matrix flow stress influences the fraction of broken particles along the crack path. We propose a simple analysis of the interplay between the three basic parameters governing the local fracture process, namely the propensity for particle cracking, the local matrix flow stress, and the particle size. To this end, we take a simple rule of mixtures approach to describe the average cohesive law $\bar{\sigma}_{cz}$ of the local fracture process, based on the following assumptions:

1. There are two types of local fracture processes: (i) matrix voiding between uncracked particles, and (ii) matrix stretching between fully cracked particles (see Figure 5-7);
2. Each of these two mechanisms is characterized by a local stress-stretch law $\sigma_c(u/D)$, where the crack opening *u* is normalised over the particle size *D* (this normalization accounts for the influence of particle size). These two basic laws summarize the influence of the matrix on the local fracture stress and energy. Both are influenced by triaxiality on the matrix, and are plotted in terms of the average effective stress per unit composite fracture surface area for the mechanism in question. The curve for mechanism (*i*) is denominated as $\sigma_c = \sigma_{mv}(u/D)$; the curve for mechanism (*ii*) is $\sigma_c = \sigma_{sp}(u/D)$. A priori, it is expected that the $\sigma_{sp}(u/D)$ curve lies below the $\sigma_{mv}(u/D)$ curve, because particle cracking is expected to imply loss of triaxiality and because the cracked particles carry no load, causing a reduction in average effective stress over the crack surface through the composite. These curves are schematically depicted in Figure 5-19a; we emphasize that these are written in terms of the average stress on the composite across the crack path; Figure 5-19a;
3. The same *u* is assumed for both mechanisms locally along the crack path when the two coexist;
4. We assume that a single correlation exists between the average composite stress $\sigma_a$ where particles are intact and the average particle stress in that region, $\sigma_p$, regardless of matrix voiding: $\sigma_a = f(\sigma_p)$;
5. Particles break according to a statistical law: $f_p = g(\sigma_p) = g(\mathrm{f}^{-1}(\sigma_a)) = h(\sigma_a)$. $f_p$ is therefore the fraction of broken particles at particle stress $\sigma_p$, which is equivalent to a fraction $f_p$ of broken particles at the average composite stress $\sigma_a$.

Consider now a crack traversing the composite with local crack opening *u* in the region under consideration. Where particles have not cracked along the crack path, the local average composite stress across the crack is $\sigma_a = \sigma_{mv}(u/D)$ (curve $\sigma_{mv}$ in Figure 5-19a). In these regions, the average stress in surviving particles along the crack path is $\sigma_p = h(\sigma_a) = h(\sigma_{mv})$. If we assume that the crack follows a straight path through the composite, the particles it encounters are an average sampling of particles making the composite. Hence, the fraction of broken particles along the crack path is $f_p = h(\sigma_{mv})$ since unbroken particles have survived this stress (we note that this fraction would be somewhat higher if we assumed that several particles perpendicularly to the crack plane were liable to break). For a given $f_p$, $\sigma_p$ is higher for stronger particles, therefore $\sigma_a$ is also higher (assumptions 4 and 5), leading to the schematic description in Figure 5-19b. Where particles have cracked, the average stress across the crack path is $\sigma_{sp}$ (Figure 5-19a).

With these assumptions, the local average cohesive stress $\bar{\sigma}_{cz}(u/D)$ is given as the weighed average of the average composite stresses where particles are intact and where particles are broken:

$$\bar{\sigma}_{cz}(u/D) = f_p(\sigma_{mv}) \cdot \sigma_{sp}(u/D) + \left[1 - f_p(\sigma_{mv})\right] \cdot \sigma_{mv}(u/D) \qquad (5\text{-}21)$$

At a given point of the statistical curve $f_{p,i}(\sigma_{mv})$, the corresponding cohesive zone stress is then obtained as graphically depicted in Figure 5-19c. The local cohesive law is, thus, a function of two variables: the matrix flow stress and voiding mode, which determine the two basic curves in Figure 5-19a, and the particle strength distribution, which determines the curve in Figure 5-19b.

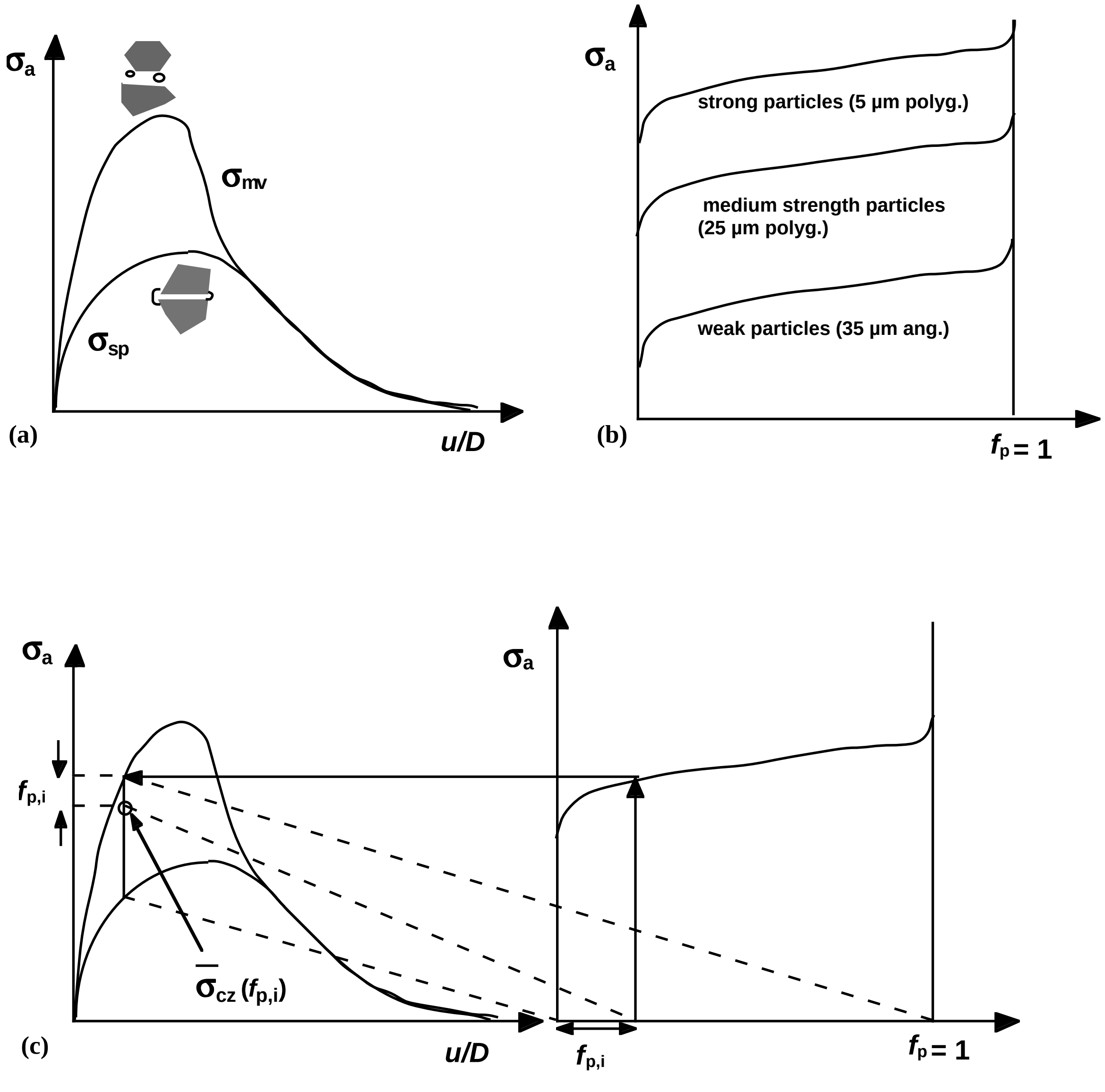
σa
σmv
σsp
(a)
u/D
σa
strong particles (5 µm polyg.)
medium strength particles
(25 µm polyg.)
weak particles (35 µm ang.)
(b)
fp = 1
σa
fp,i
σa
σcz (fp,i)
(c)
u/D
fp,i
fp = 1

**Figure 5-19.** Initial assumptions for the “rule of mixture” approach of the cohesive law, and graphical definition of $\bar{\sigma}_{cz}$ at a given fraction of broken particles, $f_{p,i}$.

We now consider four distinct composites, Figure 5-20:

- **Case 1**: weak particles (ang. 35 µm) / low $\sigma_m$ (pure Al).
In the very initial part of loading, particles are intact, $\bar{\sigma}_{cz}$ hence follows the curve for matrix voiding, $\sigma_{mv}$. The particles then start to crack at low stresses, such that the curve deviates towards the law for matrix stretching between particles, $\sigma_{sp}$. As loading progresses further, all particles on the crack path are broken[1], such that the average cohesive law is fully dominated by $\sigma_{sp.}$ The final result is that most particles along the crack path are cracked after propagation (which is seen experimentally): the local fracture energy and particle stress are low;

- **Case 2**: medium strength particles ( polyg. 25 µm ) / low $\sigma_m$ (pure Al).
In this situation, the average cohesive law $\bar{\sigma}_{cz}$ fully follows $\sigma_{mv}$ because the stress necessary to break the particles is never attained. All voids are hence nucleated in the matrix in the regions of high stress triaxiality, and essentially no particles are found on the fracture surface;

- **Case 3**: medium strength particles $\sigma_{fp}$ (polyg. 25 µm ) / medium $\sigma_m$ (Al-Cu2%, ST).
Compared to the previous case, the matrix stress is higher, such that both $\sigma_{mv}$ and $\sigma_{sp}$ increase. This leads to a situation where the cohesive law is initially dominated by $\sigma_{mv}$; however, a slight deviation occurs in attaining the peak load because some particles crack. Experimentally, about 30% of the crack path was seen to be occupied by broken particles in this composite.

- **Case 4**: medium strength particles (polyg. 25 µm ) / high $\sigma_m$ (Al-Cu4.5%, T6).
The matrix flow stress is further increased compared to the previous case. Hence both $\sigma_{mv}$ and $\sigma_{sp}$ curves attain higher values. While in the initial part, $\bar{\sigma}_{cz}$ it is still dominated by $\sigma_{mv}$, the stress is now large enough to crack numerous particles, causing the average curve to transit towards $\sigma_{sp}$. As a result, most particles along the crack path are broken, as confirmed by experiments. There is here an important distinction with case 1: particle cracking has occurred at relatively large stresses, which cannot be compared with stress levels for cracking weak angular particles in a soft matrix. Thus the peak stress of the cohesive law is much higher.

Hence the peak stress, $\hat{\sigma}$ of the average cohesive law is significantly reduced if particle cracking occurs early, thereby lowering the equivalent $2\gamma_{pz}$. If particle cracking occurs at high stresses, on the other hand, the peak stress of the cohesive law can remain large.

As long as the intrinsic particle strength is not attained, one can expect to increase $\hat{\sigma}$ by using a matrix with a higher flow stress. This corresponds to the 5 µm polygonal composites: in this case, even with Al-Cu4.5% T6, most particles remain intact. Hence, assuming no particle cracking, eq. (5-21) simply becomes given by voiding models such as those leading to eqs. (2-53) or (2-65). Such curves are plotted in Figure 5-21 using the Poech and Fischmeister model. The peak stress then increases as the matrix flow stress increases (assuming the same local triaxiality for each matrix), and attains quite high absolute values. At constant ratio of peak stress to composite yield stress, the composite toughness increases proportionally. An analogous conclusion is reached when all particles are fractured very early in the fracture process (35 µm angular alumina particle composites): in this situation, the peak stress can still be increased by using a higher matrix flow stress since the $\sigma_{sp}$ contribution is also larger in this situation.

---

[1] It is important not to confuse the fraction of broken particles along the crack path $f_p$, with the fraction of crack path surface area occupied by broken particles, $f_b$. If $f_p = 1$, then $f_b$ is about 0.75 in the present composites.

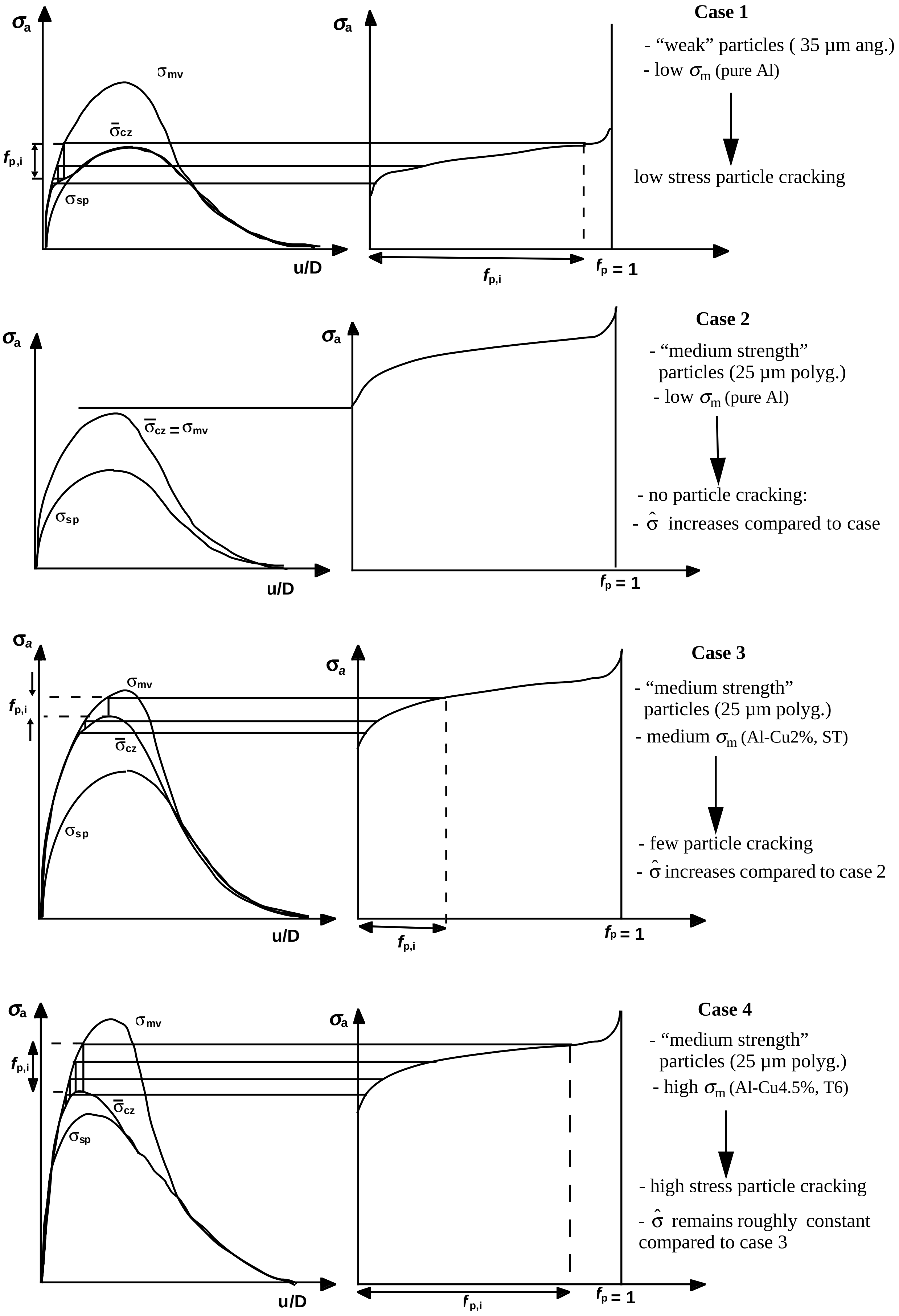
Case 1
- "weak" particles ( 35 µm ang.)
- low $\sigma_m$ (pure Al)
low stress particle cracking
$\sigma_a$
$\sigma_{mv}$
$\bar{\sigma}_{cz}$
$f_{p,i}$
$\sigma_{sp}$
u/D
$f_{p,i}$
$f_p = 1$
Case 2
- "medium strength" particles (25 µm polyg.)
- low $\sigma_m$ (pure Al)
- no particle cracking:
- $\hat{\sigma}$ increases compared to case
$\bar{\sigma}_{cz} = \sigma_{mv}$
$\sigma_{sp}$
u/D
$f_p = 1$
Case 3
- "medium strength" particles (25 µm polyg.)
- medium $\sigma_m$ (Al-Cu2%, ST)
- few particle cracking
- $\hat{\sigma}$ increases compared to case 2
$\sigma_{mv}$
$\bar{\sigma}_{cz}$
$\sigma_{sp}$
u/D
$f_{p,i}$
$f_p = 1$
Case 4
- "medium strength" particles (25 µm polyg.)
- high $\sigma_m$ (Al-Cu4.5%, T6)
- high stress particle cracking
- $\hat{\sigma}$ remains roughly constant compared to case 3
$\sigma_{mv}$
$\bar{\sigma}_{cz}$
$\sigma_{sp}$
u/D
$f_{p,i}$
$f_p = 1$

**Figure 5-20.** Schematic expected cohesive laws for different particle strengths and matrix flow stresses. As long as particle cracking does not arise, the peak stress can be increased by using higher matrix flow stresses.

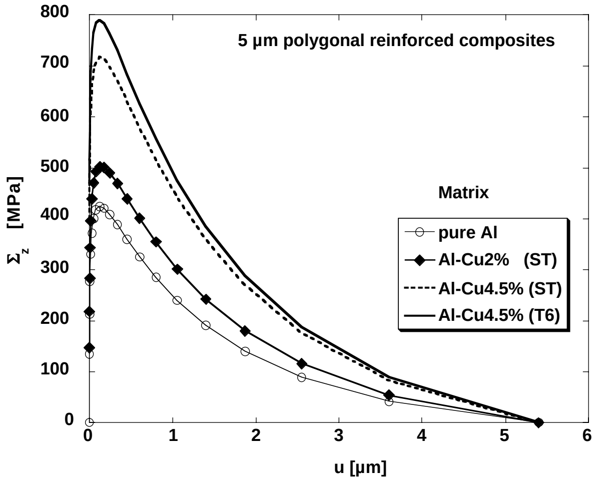

**Figure 5-21.** Local traction-separation curves according eq.(5-20), with $\sigma_{mv}$ described by eqs. (2-51) and (2-53) (stress triaxiality $\eta$ = 2), in polygonal 5 µm reinforced composites, illustrating the influence of the matrix flow stress on the peak stress of the cohesive law.

### 5.3.4 Implications

An effect that comes out from this simple analytical framework is the importance of the shape of the distribution of intrinsic particle strengths: a large Weibull modulus *m* results in a relatively flat particle strength distribution curve, leading in turn to a $\bar{\sigma}_{cz}$ curve that remains close to the $\sigma_{mv}$ curve until it reaches a value relatively close to its maximum. A particle strength distribution with a tail extending to low strengths (corresponding to low *m*), will on the other hand cause the $\bar{\sigma}_{cz}$ curve to deviate early on towards $\sigma_{sp}$. Hence, the peak stress $\hat{\sigma}$ that is reached can depend not only on the matrix flow stress or the final fraction broken particles on the fracture surface, but also on the particle strength distribution, *i.e.*, on when the particles broke. This could explain why the Al-Cu4.5%T6 composites reinforced with 25p particles display a toughness $G_{Iv}$ nearly twice that of composites of the same matrix reinforced with 35a particles (Figure 5-11) even though the final fraction of broken particles along the crack path is the same for both.

A second implication is more intriguing. Indeed, if we turn to the pure Al matrix composites, it is clear that the “amplification factor” *F* assumes a constant value for all present composites. This seems to imply that $\hat{\sigma}/\sigma_y$ is the same for all, and in turn that the peak stress for the $\sigma_{mv}(u/D)$ and $\sigma_{sp}(u/D)$ curves (Figure 5-19) is about the same.

Indeed, if the peak stress of the $\sigma_{mv}(u/D)$ curve were significantly above that of the $\sigma_{sp}(u/D)$ curve, $\hat{\sigma}/\sigma_y$ and hence the amplification factor *F* would be higher in the absence of broken particles (*e.g.*, all 5 µm or polygonal alumina composites, Table 4-4) than in composites that feature broken particles along the crack path (*e.g.*, the 35A particle composite, Table 4-4). The local fracture energy computed with the same level of assumed matrix ligament triaxiality could not, then, lead to a linear correlation with the global fracture energy, as is found in the present work (Figures 5-8 and 5-16). What the data seem to imply, regardless of matrix ligament triaxiality, is that *F*, and hence $\hat{\sigma}/\sigma_y$, is the same for all pure Al matrix composites.

The implication thus seems to be that the triaxiality level in ligaments between fractured particles is be about the same as the triaxiality in ligaments between voids nucleated in the matrix, and that the loss of stress-bearing surface caused by a broken particle is about the same as that caused by matrix voids when the peak stress is reached. This is not completely inconceivable: with a strong matrix/particle interfacial bond, no or little decohesion is expected along the interface. It could then be argued that the two tearing mechanisms are, for example, described by the two cases in Figures 11 (ligament tearing between cracked particles) and 13 (matrix voiding) in Ashby, Blunt, and Bannister [226], which yield the same cohesive law (Figure 14 of that Reference, reproduced here in Figure 2-21). Although some debonding was found along the crack path, Figure 5-22, this was not frequent, as can be seen from the crack path profiles Figures 4-28 to 4-30. Still, we find this (tentative) implication of the data surprising; significantly more work would be needed to elucidate this point.

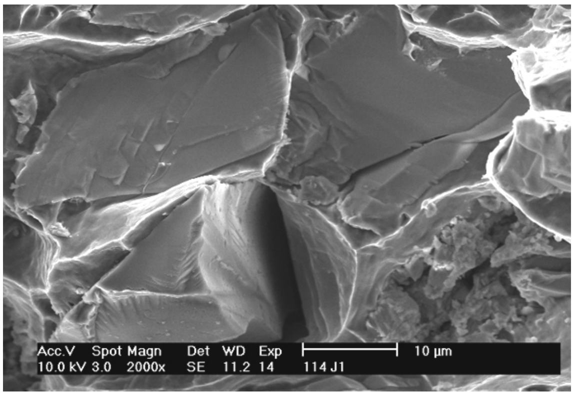
Acc.V Spot Magn Det WD Exp
10 µm
10.0 kV 3.0 2000x SE 11.2 14 114 J1

**Figure 5-22.** High-magnification SEM fractograph showing particle decohesion subsequent to particle cracking in a A-A35a composite.

# 5.4. HOW TO PRODUCE TOUGH PRMMCS ?

How one should proceed to fabricate composites with improved fracture properties ? This is commented based on the above section of the discussion.

## 5.4.1 The role of the reinforcement

The present data provide clear experimental evidence of the importance of intrinsic particle strength, an influence sometimes mentioned in the literature of PRMMCs [24, 90, 127, 144, 145, 174], but rarely studied in detail or exploited in engineering practice. The initial quality of particles is a fundamental (if not the most important) parameter to be controlled in order to fabricate PRMMCs, with improved fracture toughness. A major reason why PRMMCs have so far exhibited rather poor fracture toughness is directly linked to the use of powders that are produced by attrition, and that hence exhibit many and large surface flaws. The local fracture energy in a composite made with such particles is low, such that the fracture toughness of the composite is reduced.

In order to improve the fracture resistance of PRMMCs further, methods for processing ceramic powders with a small and controlled population of defects, and at relatively low price, must therefore be developed. A look at tensile strengths of various ceramic whiskers [298, 302] (for which the density of defects is very low) indicates that maximum strengths attainable are equivalent for $Al_2O_3$, $B_4C$, or SiC whiskers, and in the range of 20 GPa. This implies that the superiority of a reinforcement over another is not dictated by its intrinsic chemical nature, but rather by the two following factors: (i) the ability to produce it with a minimized flaw density, and (ii) its chemical compatibility with the matrix. This is probably the reason why a certain reinforcement type has not been reported to yield better composite fracture properties in the literature. We might actually see one exception to this: given the extremely high strength of diamond, it is expected that diamond particle reinforced composites could exhibit very attractive mechanical properties.

If “ideal”, defect-free reinforcement were to be available, larger particles are preferable in terms of fracture resistance. In reality, there will always remain flaws, the probability of finding them increasing as their average size increases; in addition finer particles are preferable in terms of composite yield strength and UTS. A compromise must be found between these extremes, and our data suggest that average particle sizes in the range of 15-30 µm yield optimized composite properties (Figure 4-49).

Regarding the volume fraction of reinforcement, the common wisdom that low $V_f$ (less than about 25%) is preferable in order to achieve higher fracture resistance is challenged by the present results. It is, rather, more important to produce defect-free composites, devoid of clusters, oxide inclusions or initial reinforcement damage. If this is achieved and if sufficently strong reinforcement are used, attractive high $V_f$ PRMMCs can be obtained, thanks to: (i) a better microstructure homogeneity; (ii) build-up of of large local stress triaxiality in the process zone (to increase the peak-stress and the local fracture energy), and (iii) a high Young’s modulus, which leads to larger toughness as expressed in terms of the stress intensity factor.

### 5.4.2 The role of the matrix

Given the high volume fraction of brittle phase in the present composites (40 to more than 60 vol.%), quite remarkable values of equivalent fracture toughness, $K_{\mathrm{Jeq}}$, have been measured here. These generally exceed 25 $\text{MPa}\cdot\text{m}^{1/2}$ and attain values as high as 40 $\text{MPa}\cdot\text{m}^{1/2}$ for the toughest composites. This remained largely possible thanks to the use of a pure Al matrix. With such a low yield strength matrix, large plastic dissipation occurs in the crack-tip plastic zone; however, the “cost” to pay for this is a low yield strength and UTS. Practically, this largely limits the potential of these composites in structural applications.

Using stronger matrices (with yet simple microstructures) has allowed to improve yield strength and UTS, without affecting the toughness (even increasing the latter significantly for the 5 µm $Al_2O_3$ composites). Plots summarizing this tendency for both angular and polygonal reinforced composites, with alloyed matrices in T6 conditions, are presented in Figure 5-23. A natural step would therefore be to investigate to what limit this trend of increasing both load-bearing capabilities and fracture toughness could be extended.

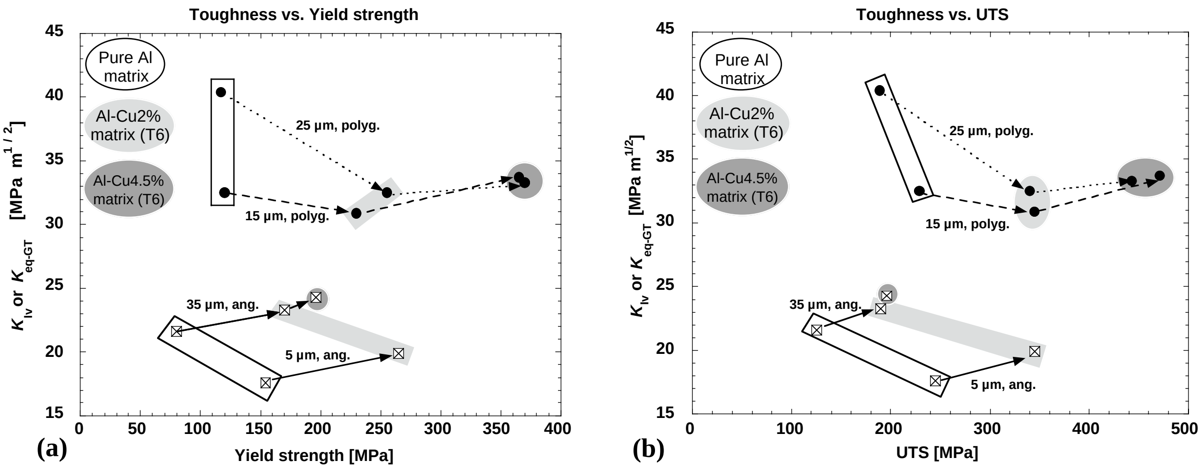

**Figure 5-23.** Effect of Cu alloying to the aluminium matrix on mechanical response of the composites. **(a)**: toughness vs. yield strength; **(b)**: toughness vs. UTS. At maintained levels of fracture toughness yield strength and UTS are significantly increased.

As discussed in the previous section of the discussion the high toughness values obtained in these composites is a combined result of : (i) a high local fracture energy involving high stresses and high ligament deformations, and (ii) the global ductility creating the plastic zone that amplifies the local energy. Tailoring composite property is largely dictated by how the matrix affects these interrelated mechanisms. Provided that reinforcement is strong enough, higher matrix flow stress will lead to an increase in the peak-stress of the cohesive law and/or of the local energy.

Assuming for simplicity that the particles behave as rigid inclusions, the strain hardening exponent $n$ of the composite is the same as that of the matrix, and the composite flow stress increases proportionally with the matrix flow stress [150]. Increasing the matrix flow stress, all else being constant, is then entirely beneficial *provided the local fracture mechanism is not altered*. Thus, as long as the particle strength distribution curve is not reached by the corresponding $\sigma_{\mathrm{mv}}(u)$ curve of the matrix, the stronger the matrix, the tougher the composite: since both $\hat{\sigma}$ and $\sigma_{\mathrm{y}}$ scale with the matrix flow stress, $F$ remains constant. With the local fracture energy increasing with the matrix flow stress, then, the composite toughness should increase proportionally. This is an idealized picture; however, it does show that a strong matrix can actually be beneficial, as found here for the 5 µm particles, Figures 4-49 and 5-23.

Regarding the strain exponent *n*, we note that, according to the Tvergaard-Hutchinson analysis, decreasing *n* will increase, all else being constant, the amplification factor *F*, Figure 5-18. We note, however, that a decreasing *n* is also expected to decrease significantly the local fracture energy, since this should hasten rupture of ductile tearing ligaments (for instance in the case of Bridgman solution of stretched particles, [221] and eqs. (2-66) to (2.68)).

A compromise must obviously be found, but we believe that optimized strength/toughness relation has not been achieved yet in systems such as polygonal 15 and 5 µm particle size reinforced composites.

The strategy for matrix selection is, however, strongly limited by additional microstructural factors, and somewhat ressembles that for unreinforced Al alloys. For instance, the presence of coarse intermetallics, known to be detrimental in unreinforced alloys [31], is also deleterious in the present as-cast PRMMCs, as summarized in Figure 5-24 for polygonal reinforced Al-Cu composites.

Matrix strengthening by age-hardening might not be an adequate method, given the commonly observed phenomenon that fracture toughness of PRMMCs decreases with ageing. As explained in §.2.4.5, this leads to a lack of toughness recovery upon overaging in many SiC reinforced composites, because of a change in the micromechanisms of fracture as ageing proceeds (going towards interfacial debonding due to precipitate coarsening, [35, 155]). In fact as the microstructural complexity of the matrix increases, probability of finding reaction phases, coarse precipitates or submicron dispersoids accelerating cavitation augments in consequence. One should therefore focus on matrices and heat-treatments specifically developed for MMCs such as reported by Pandey *et al*. [156] (see also §.2.4.5).

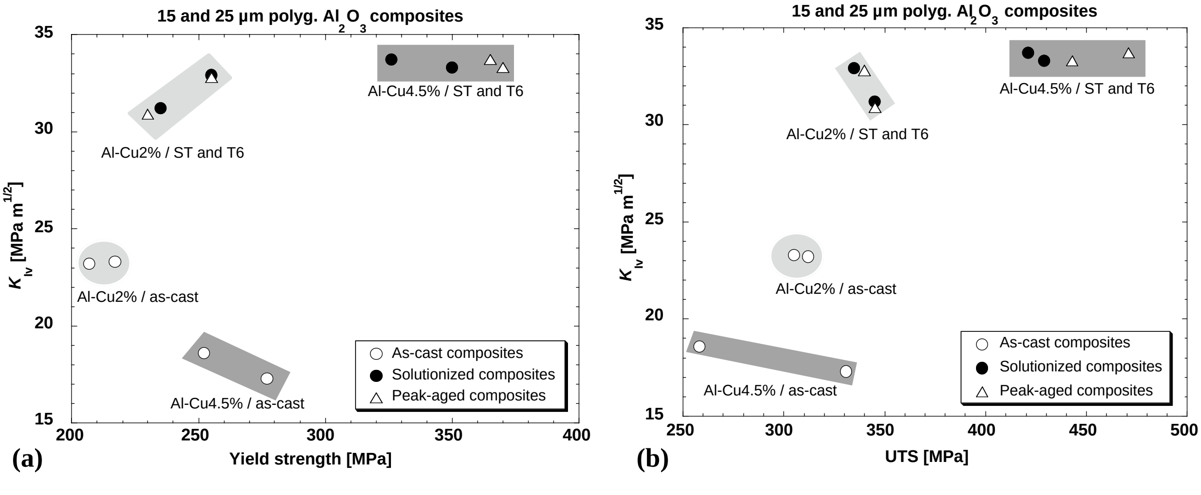

**Figure 5-24.** The role of microstructural factors in the present composites. **(a)**: toughness vs. yield strength relation, **(b)**: toughness vs. UTS relation. As-cast composites feature inferior property due to the presence of coarse Al-Cu based intermetallics at interfaces.

In high volume fraction PRMMCs, there may actually be no need to use high-strength Al alloys, since strengthening is already brought in large part by load sharing of the reinforcement. Note also from our hardness and tensile data that ageing is not as efficient with such a high volume fraction of reinforcements, because the particle somehow hinder hardening effects (while it would probably decrease toughness if coarse precipitates were to interact with the reinforcement, as seen in many cases with SiC).

Instead, moderate strengthening by solid-solution hardening might be sufficient, as in the present work with Al-Cu alloys. The chemical compatibility of solute elements is, in particular, a crucial parameter. For instance, Mg additions shoud be excluded in $Al_2O_3$ reinforced composites given the formation of reaction phases in such systems which embritttle the composites (§ 2.2.2). This excludes alloys of the 6xxx and the 7xxx series. Options are thus largely restricted by such factors, althoug other candidates having a high solubility in aluminium do exist, such as Zn or Ag.

### 5.4.3 The role of the interfacial strength

A high interfacial strength is clearly important to optimize the fracture resistance of PRMMCs. This is readily explained in terms of the local/global correlation. If the interface is too weak, this leads to a low peak-stress $\hat{\sigma}$, which in turn implies crack advance without permitting a fully developed plastic zone to form [189]. In other words, plastic shielding does not appear in this situation and macroscopic fracture toughness is low.

A clear experimental proof of this is offered in the present work by the case of A-A20a composite. This composite fails by interfacial decohesion, with a very small plastic zone, and it clearly features the lowest fracture toughness of all present pure Al matrix composites. In many metal/ceramic interfaces, the presence of impurities at the surface of the powders is known to embrittle interfaces [49, 196, 303-305]. The much lower fracture resistance of A-A20a composite is hence attributed to such contamination, since other $Al_2O_3$ reinforced composites do not fail by interfacial decohesion. More generally, this emphasizes the role of initial powder quality, not only in terms of defect population, but also regarding the presence of impurities at the powder surface.

That impurities are detrimental to the strength of metal/ceramic interfaces is, however, not universal. There exist various cases where their presence is beneficial, by leading to the formation of a thin interfacial phase that improves the interface strength [303, 306, 307], or by modifying the interfacial energy [308].

For MMCs, this implies that the presence of an interfacial reaction product might not always be detrimental to the mechanical performance. Depending on its bonding characteristics with both the metal and the ceramic, a reaction phase should be eliminated in some cases, or promoted in some others. Even one type of phase can play significant different roles depending on its shape, distribution, and size. A typical example is $Al_4C_3$, often reported in SiC reinforced composites to lower mechanical performance of the composites [46, 115, 143]. In some other studies, it is suggested that this deleterious influence can be reversed if the distribution [309] or layer thickness [310] of the reaction phases are better controlled. An other illustrative example of such tailoring of mechanical property by controlling the extent of reaction phases in Al-$B_4C$ composites is presented in [243].

Obviously, the role of impurities and reaction phases in affecting the interfacial strength is strongly system-dependent. Optimization of this fundamental parameter necessitates thermodynamic analysis and interface strength characterization of the metal/ceramic system in question.

### 5.4.4 The role of processing

Processing has a key role in influencing fracture property since many defects introduced at this stage will remain in the final composite. In this respect, the widely employed powder metallurgy methods exhibit many disadvantages towards achieving high fracture toughness. First, initial blending of the powders can lead to particle-to-particle interactions, and in turn to the creation of surface flaws. Introduction of such defects can also be caused by secondary processing, such as extrusion [42]. Second, the presence of fine oxide inclusions is almost inevitable. These are typically deleterious to toughness, since they represent preferential void nucleations sites. Finally particle clusters is also often observed, which is a defect that is widely documented to decrease the toughness (see §.2.3.2).

Melt infiltration processes by dispersion is also often used. As mentionned in §.2.2.2.i, there exist many issues concerning uniformity in the reinforcement distribution. Although liquid dispersion is economically more viable than others processes, such inhomogeneities are not acceptable for high structural properties. More specifically for toughness, local variations of $2\gamma_{pz}$ are likely to yield low fracture energies.

In the present work, gas-pressure infiltration has been successful in fabricating composites with attractive properties. This is largely due to the absence of oxide inclusions (infiltration is done under vacuum), impurities, or particle clusters: in fact a composite ingot is made of one unique and large cluster. As also shown, that fact that composites feature a high volume fraction of reinforcement with this technique is not an issue, provided an adequate choice is made for the matrix and the reinforcement. Towards application of this technique at a larger scale than the laboratory would, however, necessitate improvements. Veining is not fully controlled yet with small particle size composites. While it does not affect much toughness, its influence on tensile strength properties is more problematic. Such macrostructural heterogeneity will have to be understood and eliminated in the future. From an engineering standpoint, it also remains a rather high-cost process. Preform preparation is long and is, so far, performed manually. Crucibles are also in most cases broken after each infiltration. Given the cost and availability of these, this is economically not attractive.

An alternative to gas-pressure infiltration is squeeze-casting. Here again, because squeeze-casting is not done under vaccum, one faces the issue of introducing oxide compounds during processing, which embrittle the composite (as was seen in preliminary experiments of this work). Note, however, that modifying existing machines to pull the vacuum before infiltration does not seem complicated. Another issue, which is common to gas-pressure infiltration, is the presence of veins caused by preform deformation. If one is able to fully elucidate their formation and in turn eliminate them, squeeze-casting is anticipated to be an attractive method towards making tough composites.

### 5.4.5 Comparison of present composites with data from the literature

To conclude, it is of interest to compare the toughness vvalues achieved in this work with prior data from the literature on composites with similar microstructures. In [114], Al-10% Mg was reinforced with up to 52% $Al_2O_3$ particles, and $K_q$ measured using chevron-notch specimens was almost 20 MPa·m$^{1/2}$. Pestes *et al.* [97] produced Al-4%Mg/ $Al_2O_3$ particle composites with an average particle size varying from 3 to 165 µm and volume fractions in the range 45-54%: a maximum $K_{IQ}$ value of 17.5 MPa·m$^{1/2}$ was found. For 520 aluminium alloy reinforced with 65% alumina particles prepared by pressure infiltration, Zhu *et al.* [311] measured a toughness of 8.3 MPa·m$^{1/2}$ on four-point bend specimens. For commercial MMCs displaying the same range of volume fraction of ceramic (*i.e.* about 40 to 65%), Hunt [4] reports values ranging from 9 to slightly higer than 20 MPa·m$^{1/2}$. Seleznev *et al.* [121] achieved toughness slightly exceeding 20 MPa·m$^{1/2}$ for composites having microstructures very similar to those in the present work (Al-Cu4.5%-Mg-Si matrix / 55% of $Al_2O_3$ particles), also prepared by infiltration. Values of higher than 30 $MPa{\cdot}m^{1/2}$ obtained on the present 60 % vol. reinforcement composites, with a tensile strength near 500 MPa, are thus viewed as quite encouraging.

We further note that in terms of toughness, the “best” composites found in the literature (Table 2-3) have been produced with volume fraction of reinforcements lower than 25%. Young’s modulus is significantly improved here, attaining 170 - 180 GPa. From an engineering standpoint, this affords attractive alternatives, since a large specific stiffness has been achieved without affecting fracture properties. The limitations traditionnaly attributed to high $V_f$ composites, such as recently mentionned in an overview related to application opportunities of MMCs [6], could hence be overcome.

At a more general level, compared to commercial aluminium alloys, the present composites exhibit a yield strength/fracture toughness relation in the range of Al-Cu-Mg alloys [31], while in the same time Young’s modulus is more than double. Among other important engineering properties, their thermal expansion is about half that of Al alloys and they have a far better wear resistance.

# CHAPTER 6

# CONCLUSIONS AND PERSPECTIVES

## 6.1. CONCLUSIONS

- Metal matrix composites with a high volume fraction of reinforcement have been produced by gas-pressure infiltration of ceramic particle preforms. These composites are viewed as model ductile/brittle two phase materials in the sense that: (i) the reinforcement is homogeneously distributed in the matrix; (ii) the shape and size of particles are independently controlled; (iii) they are produced free of microstructural defects; and (iv) the matrix microstructure can be kept simple.
- Despite the presence of more than 50 vol.% of ceramic brittle phase, these composites are characterized by a *R*-curve fracture behaviour indicating the formation of a well-defined crack-tip plastic zone. The plastic zone is revealed by photoelastic observations and is found to be accurately described by 3-D finite element computations. Three fundamental parameters are governing this plastic dissipation mechanism: (i) the intrinsic reinforcement characteristic, (ii) the average reinforcement size, and (iii) the matrix flow stress. With a low yield stress pure Al matrix, the plastic zone size increases with increasing average particle size, and higher plastic work is dissipated with stronger particles. For a given reinforcement, the plastic zone size is generally greatly reduced as the matrix flow stress increases.
- On the local scale, a process zone initially develops at the crack-tip upon loading. Linking of damage events in this process zone leads to a small degree of crack propagation in the initial part of the *J-R* curve, until ductile tearing occurs. In *J*-integral fracture testing, a fracture criterion is proposed to account for this critical event, and corresponds to a transition from process zone formation (and small crack advance) to ductile tearing. This criterion is independent of the specimen geometry and of the history of loading, and allows a distinct comparison of the various composites. Once significant ductile tearing is established, *J*-analysis is no longer valid.
- In pure Al matrix composites, the micromechanisms of crack propagation depend on the ceramic type, shape, and size. The most fundamental microstructural variable governing the local fracture events is the intrinsic reinforcement strength, $\sigma_{\mathrm{fp}}$. For large values of $\sigma_{\mathrm{fp}}$, the crack propagates by a ductile cavitation mechanism in the matrix, while as $\sigma_{\mathrm{fp}}$ decreases, voids tend to be nucleated by particle cracking. For a given micromechanism of fracture, the dimple size scales with the interparticle distance.
- Identification and quantification of the micromechanisms was performed using detailed investigations of the crack propagation paths, simple micromechanical models, and estimations of the *in-situ* matrix flow stress. This allowed to estimate the local work of fracture $2\gamma_{\mathrm{pz}}$, and to correlate it

with the global fracture energy. Although the main contribution to the global fracture energy is from plastic dissipation in the plastic zone, fracture toughness is still governed by the (smaller) value of $2\gamma_{pz}$ spent in the process zone: a small decrease of the latter strongly affects the macroscopic toughness.

- In all pure aluminium matrix composites, the local work of fracture $2\gamma_{pz}$ computed using Stüwe's analysis on the basis of quantitative fractographic analysis of the composites implies a direct linear correlation between the local fracture energy and the toughness of the composites: the latter is about ten times the former when computed using Stüwe's analysis.

- Al-Cu matrix composites are characterized by a less marked *R*-curve behaviour. Composites with angular $Al_2O_3$ particles exhibit a very small plastic zone at the onset of unstable fracture, whereas a distinct plastic zone is still seen in polygonal $Al_2O_3$ composites. Fracture properties in these composites were determined by LEFM, using chevron-notch fracture testing. In angular $Al_2O_3$ composites particle cracking is the dominant micromechanism of fracture. A transition in the dominant mode of fracture occurs in polygonal $Al_2O_3$ composites as the matrix flow stress increases, from matrix voiding to particle cracking. This transition towards brittle local fracture is not accompanied by a loss in toughness. If matrix voiding remains the main mechanism, as in the 5 µm particle size composites, fracture toughness increases significantly as the matrix flow stres increases.

- Controlling the matrix microstructure is crucial in alloyed matrix composites. Upon solidification from the processing temperature solute enrichment occurs at the metal/ceramic interface, which leads to the formation of coarse secondary intermetallic phases. These are strongly detrimental to the fracture properties since they accelerate the rate of void nucleation in the composites. They must hence be eliminated by solution heat-treatment.

- The fracture data on Al-Cu matrix composites illustrate the fact that the macroscopic fracture toughness does not simply scale linearly with the local fracture energy. It is suggested that a second fundamental parameter has a decisive role in governing toughness, namely the peak-stress that is obtained in the process zone. This parameter depends on: (i) the particle strength distribution, (ii) the matrix flow stress, and (iii) the local stress triaxiality. A simplified framework for analysis of the local microfracture mechanisms in these composites is proposed. Combined with results of Tvergaard and Hutchinson concerning the link between local and global fracture in ductile materials, this analysis leads to a few simple conclusions concerning the key role played by triaxiality in tearing matrix ligaments and the role of the particle strength distribution. The importance of local stress triaxiality is directly inherent to the microstructure: the large volume fraction of hard and stiff particles severely constrain plastic flow in the matrix, which induces high local stresses during fracture.

- The engineering viability of high volume fraction PRMMCs has been demonstrated. While such composites are traditionally limited by their poor fracture properties, it has been possible to produce them with a plane strain fracture toughness approaching 35 $MPa\cdot m^{1/2}$, coupled with Young's modulus of 180 GPa and UTS of almost 500 MPa. Such high values of toughness for materials containing 60 vol.% of brittle ceramic phases have, to our knowledge, never been attained before. The achievement of such attractive properties was largely a consequence of exploiting the fundamental link existing between the local work of fracture and the high local peak-stress in the process zone, with the macroscopic fracture toughness.

# 6.2. FUTURE WORK

Three main areas of work are anticipated to yield a better understanding of structural properties and the overall superior mechanical performance of particle reinforced metals. These include: (i) improvement at the processing stage, (ii) mechanical characterization at both the macro and the micro-level, and (iii) modeling efforts.

## *6.2.1 Processing*

Although most composites were produced free of microstructural defects, systematic elimination of veins in the smaller particle size composites was not achieved. This significantly limits the tensile properties of the composites. Improved control in the homogeneity of preform density is likely to improve this issue. Preform fabrication techniques allowing better mechanical stability of the preform should be developed. Among them, cold-isostatic pressing (CIP), slip-casting or direct coagulation casting [312] are all methods that have been recently attempted in our laboratory, with encouraging preliminary results. Moreover, such methods also permit to somehow increase the range of volume fraction for composites over simple tapping. Another possibility would be to produce composites in which the interparticle contiguity is increased in a controlled fashion, using sintering of the preform.

Sub-micron particle size composites are also worth investigating, especially given the present data on fine particle size composites for which fracture toughness is improved by increasing the matrix flow stress. Such composites necessitate higher pressure to overcome the lower preform permeability. An infiltration machine operating at higher temperature and pressure is now available in our laboratory. Such composites can hence be soon investigated.

## *6.2.2 Micro and Macro-mechanical characterization*

There are many prospects at the level of mechanical characterization to further improve our fundamental understanding of fracture of PRMMCs.

At the micro-level, developing procedures to characterise the intrinsic particle strength seems crucial, in that the present work has unambiguously shed light on the importance of this parameter. This could be started based on comminution experiments. The *in-situ* matrix flow stress also appears to be a fundamental parameter. Current neutron diffraction experiments in our group has already given some insight, but much uncertainty remains. Nano-indentation experiments in the immediate vicinity of the reinforcement are viewed as possible methods to improve this knowledge [313, 314].

We know from the present work that smaller particle size composites are less tough. Yet, the decrease in toughness is not important enough to rationalize tensile instabilities in small particle size composites (the critical defect size is greater than a millimetre; such defects are not present in our composites). The same remark is relevant for stronger alloyed matrix composites, *i.e.* what causes damage localization in such composites, and in turn prematurely breaking is unclear. There is clearly a need to link the present work with damage accumulation and tensile data from previous work [89]. Test specimens in which internal defects are purposely introduced in order to impose damage localization could be used. In particular, this should allow to observe damage accumulation before general failure of the specimen. Precise strain measurements on various locations along the gauge length could then be performed by laser speckle interferometry.

In the view of exploring the engineering viability of these composites for electronic packaging and thermal managment, physical properties such as thermal and electrical conductivity, as well as thermal expansion coefficient should also be assessed.

### 6.2.3 Modeling

Micromechanical models should be developed based on the present data on Al-Cu matrix composites. In particular, the peak-stress of the cohesive law in the presence and absence of particle cracking needs to be predicted with accuracy, since it is anticipated to strongly govern fracture toughness of PRMMCs. Then a simple model linking the peak-stress with the surrounding continuum stress field, for instance similar to what has been attempted to model cleavage fracture in the presence of plastic flow [202, 203], or in the local approach to fracture [190], could be developed to further quantify the amplification factor linking the local fracture events with the macroscopic toughness or fracture stress. Also, treating the process zone with bridging stress concepts is viewed as an alternative calculation method to estimate the amplification factor.

Numerical studies with cohesive zone models have been started. They are, however, still incomplete and more work is necessary to verify whether the link local/global could be better predicted with such approach. Alternatively, numerical modeling based on Gurson potential could be attractive given the ability in such models to impose an initial layer of materials in which failure will predominantly occur. Seen from a different perspective, the present composites can in some instances be viewed as model materials to validate FE modeling assumptions. Typical examples are the pure Al matrix composites made of particles with distinct intrinsic strengths, as this allows to somehow control the degree of initial void volume fraction.

# BIBLIOGRAPHY

1. Clyne, T.W. and P.J. Withers, *An Introduction to Metal Matrix Composites*. Cambridge Solid State Science Series, ed. E.A. Davis and L.M. Ward. 1993, Cambridge, U.K., Cambridge University Press. 509.
2. Harrigan, W.C., *Metal Matrix Composite Applications*, in *Mechanical Properties of Metallic Composites*, S. Ochiai, Editor. 1994, Marcel dekker, Inc, New York.
3. Maruyama, B., *Progress & Promise in Aluminum Composites.* Advanced Materials & Processes, 1999 (6), p. 47-50.
4. Hunt, W.H., *Metal Matrix Composites*, in *Comprehensive Composite Materials, Volume 6*. Vol. 6, 2000, Pergamon, Oxford UK. p. 57-66.
5. Degischer, H.P., P. Prader, and C.S. Marchi, *Assessment of Metal Matrix Composites for Innovations - Intermediate Report of a European Thematic Network.* Composites: Part A, Applied Science and Manufacturing, 2001, **32**, p. 1161-1166.
6. Miracle, D., *Metallic Composites in Space: A Statut Report.* Journal of Metals, 2001 (April 2001), p. 12-25.
7. Bader, M.G., *The Composites Market*, in *Comprehensive Composite Materials, Volume 6:*. Vol. 6, 2000, Pergamon, Oxford UK. p. 1-13.
8. Chung, D.D.L. and C. Zweben, *Composites for Electronic Packaging and Thermal Management*, in *Comprehensive Composite Materials, Volume 6:*. Vol. 6, 2000, Pergamon, Oxford UK. p. 701-725.
9. Davidson, D.L., *Fracture Tougness of Metal Matrix Composites*, in *Metal Matrix Composites: Mechanisms and Properties*, R.K. Everett and R.J. Arsenault, Editors. 1991, Academic Press, Boston, MA. p. 217-234.
10. Ishizaki, K., *Porous Materials: Process Technology and Applications*. Kluwer Academic Publishers, London.
11. Clyne, T.W., *An Introductory Overview of MMC Systems, Types, and Developments*, in *Comprehensive Composite Materials, Volume 3: Metal Matrix Composites*, T.W. Clyne, Editor. Vol. 3, 2000, Pergamon, Oxford UK. p. 1-26.
12. Cawley, J.D., *Binar Oxide Ceramics: Al203, ZrO2, Structure and Properties of*, in *Encyclopedia of Materials: Science and Technology*, K.H. Buschow, *et al.*, Editors. 2001, Elsevier. p. 524-533.
13. Tressler, R.E., *Structural and Thermostructural Ceramics*, in *Encyclopedia of Materials: Science and Technology*, K.H. Buschow, *et al.*, Editors. 2001, Elsevier. p. 8913-8921.
14. Sglavo, V.M., E. Trentini, and M. Boniecki, *Fracture Toughness of High-Purity Alumina at Room and Elevated Temperature.* Journal of Materials Science Letters, 1999, **18**, p. 1127-1130.
15. Srinavassan, M. and W. Rafaneillo, *chap.2*, in *Carbide, Nitride and Boride Materials Synthesis and Processing*, A. Weimler, Editor. 1997.
16. DeWith, G., *High Temperature Fracture of Boron Carbide : Experiments and Simple Theoritical Models.* Journal of Materials Science, 1984, **19**, p. 457-466.
17. Mortensen, A., *Melt Infiltration of Metal Matrix Composites*, in *Comprehensive Composite Materials, Volume 3: Metal Matrix Composites*, T.W. Clyne, Editor. Vol. 3, 2000, Pergamon, Oxford UK. p. 521-554.
18. Hu, H., *Squeeze Casting of Magnesium Alloys and their Composites.* Journal of Materials Science, 1998, **33**, p. 1579-1589.
19. Rohtagi, P.K., *Aqueous Corrosion of Metal Matrix Composites*, in *Comprehensive Composite Materials, Volume 3: Metal Matrix Composites*, T.W. Clyne, Editor. Vol. 3, 2000, Pergamon, Oxford UK. p. 481-500.
20. Miyake, J., G. Gosh, and M.E. Fine, *Design of High-Strength, High-Conductivity Alloys.* Materials Research Society Bulletin, 1996, **21** (6), p. 13-18.
21. Kittel, C., *Introduction to Solid-State Physics*. 7th ed. 1996, John Wiley & Sons.
22. Yih, P. and D.D.L. Chung, *Titanium Diboride Copper-Matrix Composites.* Journal of Materials Science, 1997, **32**, p. 1703-1709.
23. Prangnell, P.B., *Precipitation Behaviors in MMCs*, in *Comprehensive Composite Materials, Volume 3: Metal Matrix Composites*, T.W. Clyne, Editor. Vol. 3, 2000, Pergamon, Oxford UK. p. 61-90.
24. Hunt, W.H., T.M. Osman, and J.J. Lewandowski, *Micro- and Macrostructural Factors in DRA Fracture Resistance.* JOM, 1993, **45** (1), p. 30-35.

25. Lewandowski, J.J., *Fracture and Fatigue of Particulate MMCs*, in *Comprehensive Composite Materials, Volume 3: Metal Matrix Composites*, T.W. Clyne, Editor. 2000, Pergamon, Oxford UK. p. 151-187.
26. Mortensen, A. *A Review of the Fracture Toughness of Particle Reinforced Aluminium Alloys*. in *Fabrication of Particulates Reinforced Metal Composites*. Proc. Conf., 1990: Montréal, Québec, Canada, ASM International.
27. Lloyd, D.J., *Particle Reinforced Aluminium and Magnesium Matrix Composites.* International Materials Reviews, 1994, **39** (1), p. 1-23.
28. Sinclair, I. and P.J. Gregson, *Structural Performance of Discontinuous Metal Matrix Composites.* Materials Science and Technology, 1997, **13**, p. 709-725.
29. Hunt, W.H., *Particulate Reinforced MMCs*, in *Comprehensive Composite Materials, Volume 3: Metal Matrix Composites*, T.W. Clyne, Editor. Vol. 3, 2000, Pergamon, Oxford UK. p. 701-715.
30. Boyer, H.E. and T.L. Gall, eds. *Metals Hanbook, Desk edition*. 1985, ASM, American Society for Metals: Metals Park, Ohio.
31. Polmear, I.J., *Light Alloys - Metallurgy of Light Alloys*. 3rd ed. 1995, Arnold.
32. Boyd, J.D. and D.J. Lloyd, *Clustering in Particuulate MMCs*, in *Comprehensive Composite Materials, Volume 3: Metal Matrix Composites*, T.W. Clyune, Editor. 2000, Pergamon, Oxford UK. p. 139-149.
33. Wilkinson, D.S., E. Maire, and R. Fougeres, *A Model for Damage in a Clustered Particulate Composite.* Materials Science and Engineering, 1999, **A262**, p. 264-270.
34. Murphy, A.M., S.J. Howard, and T.W. Clyne, *The Effect of Particle Clustering on the Deformation and Failure of Al-Si Reinforced with SiC Particles: A Quantitative Study.* Key Engineering Materials, 1997, **127-131**, p. 919-928.
35. Lewandowski, J.J., C. Liu, and W.H. Hunt, *Effects of Matrix Microstructure and Particle Distribution on Fracture of an Aluminum Metal Matrix Composite.* Materials Science and Engineering, 1989, **A107**, p. 241-255.
36. Tao, S. and J.D. Boyd. *Mechanisms of Damage Accumulation and Fracture in Particulate Reinforced Metal-Matrix Composites*. in *Mechanisms and Mechanics of Composie Fracture*. Proc. Conf., 1993: Pittsuburgh, PA, ASM international, Materials Park, Ohio.
37. Whitehouse, A.F. and T.W. Clyne, *Effect of Test Conditions on Cavitation and Failure during Tensile Loading of Discontinuous Metal Matrix Composites.* Materials Science and Technology, 1994, **10** (6), p. 468-474.
38. Whitehouse, A.F. and T.W. Clyne, *Cavity Formation During Tensile Straining of Particulate and Short Fiber Metal Matrix Composites.* Acta Metallurgica et Materialia, 1993, **41** (6), p. 1701-1711.
39. Whitehouse, A.F. and T.W. Clyne, *Critical Stress Criteria for Interfacial Cavitation in MMCs.* Acta Metallurgica et Materialia, 1995, **43** (5), p. 2107-2114.
40. Babout, L., *et al.*, *Characterization by X-Ray Computed Tomography of Decohesion, Porosity Growth and Coalescence in Model Metal Matrix Composites.* Acta Materialia, 2001, **49**, p. 2055-2063.
41. McKimpson, M.G. and T.E. Scott, Materials Science and Engineering, 1989, **A107**, p. 93.
42. Tham, L.M., M. Gupta, and L. Cheng, *Effect of Reinforcement Volume Fraction on the Evolution of Reinforcement Size During the Extrusion of Al-SiC Composites.* Materials Science and Engineering, 2002, **A326**, p. 355-363.
43. Gosh, A.K., *Solid-State Processing*, in *Fundamentals of Metal Matrix Composites*, S. Sureh, A. Mortensen, and A. Needleman, Editors. 1993, Butterworth-Heinmann. p. 23-41.
44. Gheorge, I. and H.J. Rack, *Powder Processing of Metal Matrix Composites*, in *Comprehensive Composite Materials, Volume 3: Metal Matrix Composites*, T.W. Clyne, Editor. Vol. 3, 2000, Pergamon, Oxford UK. p. 679-700.
45. Kim, J.K. and Y.W. Mai, *Effect of Interface Strength on MMC Properties*, in *Comprehensive Composite Materials, Volume 3: Metal Matrix Composites*, T.W. Clyne, Editor. Vol. 3, 2000, Pergamon, Oxford UK. p. 117-138.
46. Lloyd, D.J. and I. Jin, *Melt Processed Aluminum Matrix Particle Reinforced Composites*, in *Comprehensive Composite Materials, Volume 3: Metal Matrix Composites*, T.W. Clyne, Editor. Vol. 3, 2000, Pergamon, Oxford UK. p. 555-577.
47. Viala, J.C., *et al.*, *Chemical Reactivity of Aluminium with Boron Carbide.* Journal of Materials Science, 1997, **1997** (32), p. 4559-4573.
48. Meyer, F.D. and H. Hillbrecht, *Synthesis and Crystal Structure of $Al_3BC$, the First Boridecarbide of Aluminium.* Journal of alloys and compounds, 1997, **252**, p. 98-102.

49. Eustathopoulos, N. and A. Mortensen, *Capillary Phenomena, Interfacial Bonding and Reactivity*, in *Fundamentals of Metal Matrix Composites*, S. Suresh, A. Mortensen, and A. Needleman, Editors. 1993, Butterworth-Heinemann, Boston. p. 42-58.
50. Lloyd, D.J. *Controlled Interphases in Composites Materials*. in *ICCM-III*. Proc. Conf., 1990: London, Elsevier Applied Science.
51. Mortensen, A., V.J. Michaud, and M.C. Flemings, *Pressure-Infiltration Processing of Reinforced Aluminum.* JOM, 1993, **45** (1), p. 36-43.
52. Michaud, V.J., *Liquid-State Processing*, in *Fundamentals of Metal Matrix Composites*, S. Sureh, A. Mortensen, and A. Needleman, Editors. 1993, Butterworth-Heinmann. p. 3-22.
53. Rohatgi, P.K., R. Asthana, and S. Das, *Solidification, Structures, and Properties of Cast Metal-Ceramic Particle Composites.* International Metals Reviews, 1986, **31** (3), p. 115-139.
54. Skibo, M.D. and D.M. Schuster, *U.S. Patent No. 4 786 467*. 1988: U.S.A.
55. Skibo, M.D. and D.M. Schuster, *U.S. Patent No. 4 759 995*. 1988: U.S.A.
56. Lloyd, D.J., *Clustering in Particulate MMCs*, in *Comprehensive Composite Materials, Volume 3: Metal Matrix Composites*, T.W. Clyne, Editor. Vol. 3, 2000, Pergamon, Oxford UK. p. 139-149.
57. Lavernia, E.J. and Y. Wu, *Spray Atomization and Deposition*. 1996, Chichester, UK, Wiley.
58. Lavernia, E.J., *Spray Forming of MMCs*, in *Comprehensive Composite Materials, Volume 3: Metal Matrix Composites*, T.W. Clyne, Editor. Vol. 3, 2000, Pergamon, Oxford UK. p. 617-653.
59. Lewis, D., *In-Situ Reinforcement Metal Matrix Composites*, in *Metal Matrix Composites: Mechanisms and Properties*, R.K. Everett and R.J. Arsenault, Editors. 1991, Academic Press, Boston, MA. p. 121-150.
60. Mortensen, A. and I. Jin, *Solidification Processing of Metal Matrix Composites.* International Materials Reviews, 1992, **37** (3), p. 101-128.
61. Garcia-Cordovilla, C., E. Louis, and J. Narciso, *Pressure Infiltration of Packed Ceramic Particulates by Liquid Metals.* Acta Materialia, 1999, **47** (18), p. 4461-4479.
62. Klier, E.M., *et al.*, *Fabrication of Cast Particle-Reinforced Metals via Pessure Infiltration.* Journal of Materials Science, 1991, **26**, p. 2519-2526.
63. SanMarchi, C., *et al. Gas-Pressure Metal Infiltration*. in *ICETS 2000-Session 3: Advanced Materials conference*. Proc. Conf., 2000: Beijing, China, New World Press.
64. Eustathopoulos, N., M.G. Nicholas, and B. Drevet, *Wettability at High Temperatures*. Pergamon Materials, ed. R.W. Cahn. 1999, Oxford, Elsevier Science Ltd. 420.
65. Aghajanian, M.K., *et al.*, *The Fabrication of Metal Matrix Composites by a Pressureless Infiltration Technique.* Journal of Materials Science, 1991, **26**, p. 447-454.
66. Nagendra, N., B.S. Rao, and V. Jayaram, *Microstructures and Properties of $Al_2O_3$/Al-AlN Composites by Pressureless Infiltration of Al-alloys.* Materials Science and Engineering, 1999, **A269**, p. 26-37.
67. Zulfia, A. and R.J. Hand, *Role of Mg and Mg+Si as External Dopants in Production of Pure Al-SiC Metal Matrix Composites by Pressureless Infiltration.* Materials Science and Technology, 2000, **16**, p. 867-872.
68. Lee, K.B., *et al.*, *Reaction Products of Al-Mg/$B_4C$ Composite Fabricated by Pressureless Infiltration Technique.* Materials Science and Engineering, 2001, **A302**, p. 227-234.
69. Mortensen, A., *et al.*, *Infiltration of Fibrous Preforms by a Pure Metal: Part I. Theory.* Metallurgical Transactions, 1989, **20A**, p. 2535-2547.
70. Mortensen, A. and V.J. Michaud, *Infiltration of Fiber Preforms by a Binary Alloy: Part I. Theory.* Metallurgical Transactions, 1990, **21A**, p. 2059-2072.
71. Michaud, V.J. and A. Mortensen, *Infiltration of Fiber Preforms by a Binary Alloy: Part II. Further theory and Experiments.* Metallurgical Transactions, 1992, **23A** (August), p. 2263-2280.
72. Mortensen, A., *et al.*, *Alloy Microstructures in Cast Metal Matrix Composites.* Journal of Metals, 1986, **38** (3), p. 30-35.
73. Mortensen, A. and M.C. Flemings, *Solidification of Binary Hypoeutectic Alloy Matrix Composite Castings.* Metallurgical and Materials Transactions, 1996, **27A** (3), p. 595-609.
74. Long, S., *et al.*, *Microstructure and Mechanical Properties od a High Volume Fraction SiC particle reinforced AlCu4MgAg Squeeze Casting.* Materials Science and Engineering A, 1999, **A 269**, p. 175-185.
75. Cayron, C., *TEM Study of Interfacial Reactions and Precipitation Mechanisms in $Al_2O_3$ Short Fiber or High-Volume Fraction SiC Particle Reinforced Al-4Cu-1Mg-0.5Ag Squeeze-Cast Composites, Thèse N° 2246*, PhD Thesis, 2000, EPFL, Lausanne.
76. Premkumar, M.K., W.H. Hunt, and R.R. Sawtell, *Aluminum Composite Materials for Multichip Modules.* JOM, 1992, **44** (7), p. 24-28.

77. Chen, C.-Y. and C.-G. Chao, *Effect of Particle-Size Distribution on the Properties of High Volume-Fraction $SiC_p$.-Al-Based Composites.* Metallurgical and Materials Transactions, 2000, **31A**, p. 2351-2359.
78. Friend, C.M., I. Horsfall, and C.L. Burrows, *The Effect of Particulate: Fibre Ratio on the Properties of Short-Fibre/Particulate Hybrid MMC Produced by Preform Infiltration.* Journal of Materials Science, 1991, **26**, p. 225-231.
79. deBondt, S., L. Froyen, and A. Deruyttere, *Squeeze Casting of Hybrid Al-SiC Fibre-Particle Composite.* Materials Science and Engineering, 1991, **A135**, p. 29-32.
80. Prielipp, H., *et al.*, *Strength and Fracture Toughness of Aluminum/Alumina Composites with Interpenetrating Networks.* Materials Science and Engineering, 1995, **A197**, p. 19-30.
81. Rödel, J., *et al.*, *Ni3Al/Al2O3 Composites with Interpenetrating Networks.* Scripta Metallurgica et. Materialia, 1995, **33** (5), p. 843-848.
82. Geng, L., *et al.*, *Fabrication of Nanocrystalline $ZrO_2$ Particle Reinforced Aluminum Alloy Composite by Squeeze Casting Route.* Scripta Materialia, 1998, **38** (4), p. 551-557.
83. Cardinal, S., M. R'Mili, and P. Merle, *Improvement of High pressure Infiltration Behaviour of Alumina Platelets Preforms: Manufacture and Characterization of Hybrid Preforms.* Composites Part A, 1998, **29A**, p. 1433-1441.
84. SanMarchi, C., *et al.*, *Unpublished research.*
85. Pandey, A.B., B.S. Majumdar, and D.B. Miracle, *Laminated Particulate-Reinforced Aluminum Composites with Improved Toughness.* Acta Materialia, 2001, **49**, p. 405-417.
86. Qin, S., *et al.*, *The Effect of Particle Shape on Ductility of SiCp reinforced 6061 Al Matrix Composites.* Materials Science and Engineering, 1999, **A272**, p. 363-370.
87. Zimmermann, A., *et al.*, *Failure of Metal-Ceramic Composites with Spherical Inclusions.* Acta Materialia, 2001, **49**, p. 3177-3187.
88. Hunt, W.H. *Common Themes in the Fracture Processes of High Volume Fraction Particle Hardened Materials*. in *Intrinsic and Extrinsic Fracture Mechanisms in Inorganic Composite Systems*. Proc. Conf., 1995: Las Vegas, Nevada, The Minerals, Metals & Materials Society, 1995.
89. Kouzeli, M., *Tensile Behaviour of Aluminium Reinforced with Ceramic Particles, Thèse N° 2348*, PhD Thesis, 2001, EPFL, Lausanne.
90. Davidson, D.L., *Fatigue and Fracture Toughness of Aluminium Alloys Reinforced with SiC and Alumina Particles.* Composites, 1993, **24** (3), p. 248-255.
91. Lewandowski, J.J. and P.M. Singh. *Toughness of DRA and Extrinsically Toughened DRA/Aluminium Alloy Laminates*. in *Intrinsic and Extrinsic Fracture Mechanisms in Inorganic Composite Systems*. Proc. Conf., 1995, The Minerals, Metals & Materials Society, 1995.
92. Roebuck, B., T.A.E. Gorley, and L.N. McCartney, *Mechanical Property Test Procedures for Metal Matrix Composites.* Materials Science and Technology, 1989, **5** (February 1989), p. 105-117.
93. ASTM, *E399-90: Standard Test Method for Plane-Strain Fracture Toughness of Metallic Materials*. 1990, Philadelphia, American Society for Testing and Materials. 407-435.
94. Roebuck, B. and J.D. Lord, *Plane Strain Fracture Toughness Test Procedures for Particulate Metal Matrix Composites.* Materials Science and Technoloy, 1990, **6**, p. 1199-1209.
95. Somerday, B.P., *et al. Elevated Temperature Fracture Toughness of a SiC Particulate Reinforced 2009 Aluminum Composite*. in *Advanced Metal Matrix Composites for Elevated Temperatures*. Proc. Conf., 1991: Cincinnati, Ohio, USA.
96. Davidson, D.L. and G. Heness. *The Effect of Particle Shape and Volume Fraction on Matrix Deformation and Fracture in Aluminum Composites*. in *Mechanisms and Mechanics of Composite Fracture*. Proc. Conf., 1993: Pittsburgh, PA, ASM International, Materials PArk, Ohio 44073-0002.
97. Pestes, R.H., S.V. Kamat, and J.P. Hirth, *Fracture Toughness of Al-4%Mg/$Al_2O_3$ p Composites.* Materials Science and Engineering, 1994, **A189**, p. 9-14.
98. Klimowicz, T.F. *The Effect of Thickness on the Mode I Fracture Toughness of Sand-Cast Aluminum Composites*. in *Mechanisms and Mechanics of Composite Fracture*. Proc. Conf., 1993: Pittsburgh, PA, ASM International, Materials Park, Ohio 44073-0002.
99. Rabiei, A., *et al.*, *Fracture Behavior in 6061 Al Alloy Matrix Composites with Different Reinforcements.* Materials Transactions, 1996, **37** (5), p. 1148-1155.
100. Lawson, L.R., *et al. Fracture Toughness and its Variability in an Al-SiCw Composite*. in *Mechanisms and Mechanics of Composite Fracture*. Proc. Conf., 1993: Pittsburgh, PA, ASM International, Materials Park, Ohio 44073-0002.

101. Lewandowski, J.J., C. Liu, and W.H.J. Hunt, . *Microstructural Effects on the Fracture Micromechanisms in 7XXX Al P/M-SiC Particulate Metal Matrix Composites*. in *Processing and Properties of Powder Metallurgy Composites*. Proc. Conf., 1988: Denver, CO, TMS.

102. Crowe, C.R., R.A. Gray, and D.F. Hasson. *Microstructure Controlled Fracture Toughness of SiC/Al Metal Matrix Composites*. in *Fifth International Conference on Composite Materials ICCM*. Proc. Conf., 1985: San Diego, CA, The Metallurgical Society, TMS, Warrendale, PA.

103. Kamat, S.V., J.P. Hirth, and R. Mehrabian, *Mechanical Properties of Particulate-Reinforced Aluminum-Matrix Composites.* Acta Metallurgica, 1989, **9**, p. 2395-2402.

104. Manoharan, M. and J.J. Lewandowski, *Effect of Microstructure and Notch Root Radius on Fracture Toughness of an Aluminum Metal Matrix Composite.* International Journal of Fracture, 1989, **40**, p. 31-34.

105. ASTM, *E1304-89: Standard Test Method for Plane-Strain (Chevron-Notch) Fracture Toughness of Metallic Materials*. 1989, Philadelphia, American Society for Testing and Materials. 863-873.

106. Grant, T.J., L. Weber, and A. Mortensen, *Plasticity in Chevron-Notch Fracture Toughness Testing.* Engineering Fracture Mechanics, 2000, **67**, p. 263-276.

107. Brown, R. and F.I. Baratta, eds. *ASTM - STP 1172: Chevron-Notch Fracture Test Experience, Metals and Non-Metals*. 1992, ASTM: Philadelphia, PA, USA.

108. Underwood, J.H., S.W. Freiman, and F.I. Baratta, eds. *ASTM - STP 855: Chevron-Notched Specimens, Testing and Stress Analysis*. 1983, ASTM: Philadelphia, Pa, USA.

109. Brown, K.R. *The Use of the Chevron-Notched Short-Bar Specimen for Plane-Strain Toughness Determination in aluminium Alloys*. in *ASTM-STP 855: Chevron-Notched Specimens, Testing and Stress Analysis*. Proc. Conf., 1983: Philadelphia, ASTM.

110. Purtscher, P.T., J.D. McColskey, and E.S. Drexler. *Aluminum-Lithium Alloys: Evaluation of Fracture Toughness by Two test Standards, ASTM Method E-813 and E-1304*. in *ASTM-STP 1172: Chevron-Notch Fracture Test Experience. Metals and Non-Metals*. Proc. Conf., 1992: Indianapolis, ASTM, Philadephia, PA.

111. Bray, J.W. *Use of the Chevron-Notched Short Bar Test to Guarentee Fracture for Lot Realease in Aluminum Alloys*. in *ASTM-STP 1172: Chevron-Notch Fracture Test Experience. Metals and Non-Metals*. Proc. Conf., 1992: Philadelphia, ASTM.

112. Eschweiler, J., G. Marci, and D.G. Munz. *Fracture toughness of an Aluminum Alloy from Short-Bar and Compact Specimens*. in *ASTM-STP 855: Chevron-Notched Specimens, Testing and Stress Analysis*. Proc. Conf., 1983: Philadelphia, ASTM.

113. Boothby, R.M. and C.A. Hippsley, *Impact and Chevron Notch Fracture Toughness Testing of Particulate Metal Matrix composites.* Materials Science and Technology, 1994, **10**, p. 565-571.

114. Aghajanian, M.K., *et al.*, *The Effect of Particulate Loading on the Mechanical Behavior of $Al_2O_3$/Al Metal Matrix Composites.* Journal of Materials Science, 1993, **28**, p. 6683-6690.

115. Lucas, J.P. and J.K. Park. *Assessment of Microfracture Mechanisms in $Al_2O_3$/6061 Al and SiC/6061 Al Discontinuous reinforced Composites*. in *11th International Conference on Composite Materials*. Proc. Conf., 1997: Gold Cost, Queensland, Australia, Australian Composite Structures Society.

116. Hadianfard, M.J., *et al.*, *Fracture Toughness Measurements and Failure Mechanisms of Metal Matrix Composites.* Fatigue and Fracture of Engineering Materials and Structures, 1994, **17** (3), p. 253-263.

117. Sun, L., S. Li, and Z. Zhu. *Dependance of Fracture Behaviors on SiCp Size of Al Matrix Composites*. in *Tenth International Conference on Composites Materials*. Proc. Conf., 1995: Whistler, British Columbia, Canada, Woodhead Publishing Ltd.

118. Marchal, Y., F. Delannay, and L. Froyen, *The Essential Work of Fracture as Means for Characterizing the Influence of Particle Size and Volume Fraction on the Fracture Toughness of Plates of Al/SiC Composites.* Scripta Materiala, 1996, **35** (2), p. 193-198.

119. Roudier, P.A.C., *Mechanical Properties of Cast Pure and Alloyed Aluminum Reinforced with a High Volume Fraction of Carbide Particles,* MS Thesis, 1989, Massaschusset Institute of Technology, Cambridge, MA.

120. Hu, M.S., *Some Effects of Particle Size on the Flow Behaviour of Al-SiCp Composites.* Scripta Metallurgica et Materialia, 1991, **25**, p. 695-700.

121. Seleznev, M.L., *et al.*, *Paper no. 980 700: Effect of Composition, Particle Size and Heat Treatment on the Mechanical Properties of Al-4.5WT.% Cu Based Alumina Particulate Reinforced Composites.* SAE Technical Paper Series, 1998.

122. Manoharan, M., J.J. Lewandowski, and W.H. Hunt, *Fracture Characteristics of an Al-Si-Mg Model Composite System.* Materials Science and Engineering, 1993, **A172**, p. 63-69.

123. Lloyd, D.J. and P.L. Morris, *The Fracture Behaviour of Particulate Metal Matrix Composites*, in *Science and Engineering of Light Metals*. 1991, Japan Institute of Light Metals, Tokyo. p. 465-469.
124. Leggoe, J.W., X.Z. Hu, and M.B. Bush, *Crack Tip Damage and Crack Growth Resistance in Particulate Reinforced Metal Matrix Composites.* Engineering Fracture Mechanics, 1996, **53** (6), p. 873-895.
125. Lloyd, D.J. and P.L. Morris, *The Fracture Behaviour of Particulate Metal Matrix Composite.* 1992, p. 465-470.
126. Wang, Z., T.K. Chen, and D.J. Loyd, *Stress Distribution in Particulate-Reinforced Metal-Matrix Composites Subjected to External Load.* Metallurgical Transaction A, 1993, **24A** (January 1993), p. 197-207.
127. Lloyd, D.J., *Aspects of Fracture in Particulate Reinforced Metal Matrix Composites.* Acta Metallurgica et. Materialia, 1991, **39** (1), p. 59-71.
128. Manoharan, M. and J.J. Lewandowski, *In-Situ Scanning Electron Microscope Studies of Crack Growth in an Aluminum Metal Matrix Composite.* Scripta Metallurgica et Materialia, 1990, **24**, p. 2357-2362.
129. Stephens, J.J., J.P. Lucas, and F.M. Hosking, *Cast Al-7Si Composites: Effect of Particle Type and Size on Mechanical Properties.* Scripta Metallurgica, 1988, **22**, p. 1307-1312.
130. Zhao, D. and F.R. Tuler, *Effect of Particle Size on Fracture Toughness in Metal Matrix Composites.* Engineering Fracture Mechanics, 1994, **47** (2), p. 303-308.
131. Kamat, S.V. and J.P. Hirth, *Fracture of Alumina Particulate Reinforced Alloy Matrix Composites.* Bulletin of Material Science, 1991, **14** (5, October 1991), p. 1197-1203.
132. Doel, T.J.A., M.H. Loretto, and P. Bowen, *Mechanical Properties of Aluminium-Based Particulate Metal-Matrix Composites.* Composites: Part A, Applied Science and Manufacturing, 1993, **24** (3), p. 270-275.
133. Flom, Y. and R.J. Arsenault, *Effect of Particle Size on Fracture Toughness of Sic/Al Composite Material.* Acta Metallurgica, 1989, **37** (9), p. 2413-2423.
134. Downes, T.J. and J.E. King. *The Effect of SiC Particle Size on the Fracture Toughness of a Metal Matrix Composite*. in *12th Riso International Symphosium on Metallurgy and Materials Science: Metal Matrix Composite-Processing, Microstructure and Properties*. Proc. Conf., 1991: Roskilde, Denmark, Riso National Laboratory, Roskilde, Denmark.
135. Kouzeli, M., *et al. Quantification of Damage During Tensile Straining of Particle Reinforced Aluminium*. in *Advances in Mechanical Behaviour, Plasticity and Damage*. Proc. Conf., 2000: Tours, Elsevier.
136. Mawsouf, N.M., *A Micromechanical Mechanism of Fracture Initiation in Discontinuously Reinforced Metal-Matrix Composite.* Materials Characterization, 2000, **44**, p. 321-327.
137. Llorca, J., *et al.*, *Particulate Fracture During Deformation of a Spray Formed Metal-Matrix Composite.* Metallurgical Transactions, 1993, **24A** (July 1993), p. 1575-1588.
138. Wallin, K., T.Saario, and K. Törrönen, *Fracture of Brittle Particle in a Ductile Matrix.* International Journal of Fracture, 1987, **32**, p. 201-209.
139. Brechet, Y., *et al.*, *Damage Initiation in Metal Matrix Composites.* Acta Metallurgica et. Materialia, 1991, **39** (8), p. 1781-1786.
140. Lewis, C.A. and P.J. Withers, *Weibull Modelling of Particle Cracking in Metal Matrix Composites.* Acta Metallurgica et Materiala, 1995, **43** (10), p. 3685-3699.
141. Mussert, K.M., *et al.*, *Modelling Fracture in an* $Al_2O_3$ *Particle Reinforced AA 6061 Alloy using Weibull Statistics.* Journal of Materials Science, 1999, **34**, p. 4094-4104.
142. Xia, X. and H.J. McQueen. *Crack Propagation and Microstructure in Hot Torsion and Cold Bending Particulate Aluminum Matrix Composites*. in *Eleventh International Conference on Composite Materials*. Proc. Conf., 1995: Gold Coast, Queensland, Australia, Woodhead Publishing Limited, Cambridge UK.
143. Park, J.K. and J.P. Lucas. *Effect of Aging on Fracture Mechanisms in Al Matrix Particulate Reinforced Metal Matrix Composites*. in *Processing, Properties and Applications of Cast Metal Matrix Composites*. Proc. Conf., 1996: Cincinnati, OH, The Minerals, Metals & Materials Society.
144. Majumdar, B.S. and A.B. Pandey, *Deformation and Fracture of Particle-Reinforced Aluminium Alloy Composites: PartII. Modeling.* Metallurgical and Materials Transactions A, 2000, **31A**, p. 937-950.
145. Hu, H.M., *et al.*, *Microstructural Investigation on* $B_4C$*/Al-7093 Composite.* Materials Science and Engineering, 2001, **A297**, p. 94-104.
146. Wu, S.B. and R.J. Arsenault, *The Fracture Mode in SiC-Al Composites.* Materials Science and Engineering, 1991, **A138**, p. 227-235.
147. Bush, M.B., *The Interaction Between a Crack and a Particle Cluster.* International Journal of Fracture, 1997, **88**, p. 215-232.
148. Christman, T., A. Needleman, and S. Suresh, *An Experimental and Numerical Study of Deformation in Metal-Ceramic Composites.* Acta Metallurgica, 1989, **37** (11), p. 3029-3050.

149. Llorca, J., A. Needleman, and S. Suresh, *An Analysis of the Effects of Matrix Void Growth on Deformation and Ductility in Metal-Ceramic Composites.* Acta Metallurgica et Materialia, 1991, **39** (10), p. 2317-2335.

150. Bao, G., J.W. Hutchinson, and R.M. McMeeking, *Particle Reinforcement of Ductile Matrices Against Plastic Flow and Creep.* Acta Metallurgica et Materialia, 1991, **39** (8), p. 1871-1882.

151. Watt, D.F., X.Q. Xu, and D.J. Lloyd, *Effects of Particle Morphology and Spacing on the Strain Fields in a Plastically Deforming Matrix.* Acta Materialia, 1996, **44** (2), p. 789-799.

152. Llorca, J. and C. Gonzalez, *Microstructural Factors Controlling the Strength and Ductility of Particle Reinforced Metal Matrix Composites.* Journal of the Mechanics and Physics of Solids, 1998, **46**, p. 1-28.

153. Song, S.G., *et al.*, *Reinforcement Shape Effect on the Fracture Behavior and Ductility of Particulate-Reinforced 6061-Al Matrix Composites.* Metallurgical and Materials Transactions, 1996, **27A** (11), p. 3739-3746.

154. Manoharan, M. and J.J. Lewandowski, *Crack Initiation and Growth Toughness of an Aluminum Metal-Matrix Composite.* Acta Metallurgica et Materialia, 1990, **38** (3), p. 489-496.

155. Singh, P.M. and J.J. Lewandowski, *Effects of Heat Treatment and Reinforcement Size on Reinforcement Fracture during Tension Testing of a SiCp Discontinuously Reinforced Aluminum Alloy.* Metallurgical Transactions, 1993, **24A** (11), p. 2531-2543.

156. Pandey, A.B., B.S. Majumdar, and D.B. Miracle, *Deformation and Fracture of Particle-Reinforced Aluminium Alloy Composites: PartI. Experiments.* Metallurgical and Materials Transactions A, 2000, **31A**, p. 921-936.

157. Nagarajan, R. and I. Dutta, *A Novel Approach for Optimizing the Fracture Toughness of Precipitation-Hardenable Al-SiCp Composites.* Metallurgical and Materials Transactions, 2001, **32A**, p. 433-436.

158. Davidson, D.L., *Tensile Deformation and Fracture Toughness of 2014 + 15 Vol Pct SiC Particulate Composites.* Metallurgical Transactions, 1991, **22A** (1), p. 113-123.

159. Lee, S., D. Kwon, and D. Suh, *Microstructure and Fracture of SiC-Particulate-Reinforced Cast A356 Aluminum Alloy Composites.* Metallurgical and Materials Transactions, 1996, **27A**, p. 3893-3901.

160. Pandey, A.B., B.S. Majumdar, and D.B. Miracle, *Effects of Thickness and Precracking on the Fracture Toughness of Particle-Reinforced Al-Alloy Composites.* Metallurgical and Materials Transactions A, 1998, **29A** (April 1998), p. 1237-1243.

161. Osman, T.M. and J.J. Lewandowski, *Influence of Thickness in the Fractured Resistance of Conventionnal and Laminated DRA Materials.* Scripta Metallurgica et Materialia, 1994, **31** (No.2), p. 191-195.

162. Liu, D.S. and J.J. Lewandowski, *The Effects of Superimposed Hydrostatic pressure on Deformation and Fracture: Part II. Particulate-Reinforced 6061 Composites.* Metallurgical Transactions, 1993, **24A**, p. 609-615.

163. Lewandowski, J.J. and P. Lowhaphandu, *Effects of Hydrostatic Pressure on Mechanial Behaviour and Deformation Processing of Materials.* International Materials Reviews, 1998, **43** (4), p. 145-188.

164. Osman, T.M. and J.J. Lewandowski, Metallurgical and Materials Transactions, 1996, **27A**, p. 3937-3947.

165. Xu, Q., *et al.*, *Mechanical Properties and Fracture Behavior of Layered 6061/SiC$_p$ Composites Produced by Spray Atomization and Co-Deposition.* Acta Metallurgica et Materialia, 1999, **47** (1), p. 43-53.

166. Pandey, A.B., B.S. Majumdar, and D.B. Miracle, *Effect of Aluminium Particles on the Fracture Toughness of a 7093/SiC/15p Composite.* Materials Science and Engineering, 1999, **A259** (296-307).

167. Qin, S. and G. Zhang, *Preparation of High Fracture Performance SiCp-6061Al/6061 Al Composite.* Materials Science and Engineering, 2000, **A279**, p. 231-236.

168. Klimowicz, T.F. and K.S. Vecchio. *The Influence of Aging Condition on the Fracture Toughness of Alumina-Reinforced Aluminum Composites*. in *Fundamental Relationships between Microstructure and Mechanical Properties of Metal Matrix Composites*. Proc. Conf., 1990: Indianapolis, IN, TMS.

169. Rice, J.R. and M.A. Johnson, *The Role of Large Crack Tip Geometry Changes in Plane Strain Fracture*, in *Inelastic Behavior of Solids*, M.F. Kanninen, *et al.*, Editors. 1969, Mc Graw-Hill Book Co., New York. p. 641-672.

170. Bray, J.W., *et al.*, *Fracture Toughness and the Extents of Primary Void Growth.* Metallurgical Transations, 1992, **23A**, p. 485-496.

171. Garrison, W.M., *A Microstructural Interpretation of the Fracture strain and Characteristic Fracture Distance.* Scripta Metallurgica, 1984, **18**, p. 583-586.

172. Thompson, A.W. and M.F. Ashby, *Fracture Surface Micro-Roughness.* Scripta Metallurgica, 1984, **18**, p. 127-130.

173. Hahn, G.T. and A.R. Rosenfield, *Metallurgical Factors Affecting Fracture Toughness of Al Alloys.* Metallurgical Transactions, 1975, **6A**, p. 653-670.

174. Manoharan, M. and S.V. Kamat, *On the Fracture Toughness of Particulate Reinforced Metal-Martix Composite.* Scripta Metallurgica et Materialia, 1991, **25**, p. 2121-2125.
175. Davidson, D.L., *Fracture Characteristics of Al-4 Pct Mg Mechanically Alloyed with SiC.* Metallurgical Transactions, 1987, **18A** (12), p. 2115-2128.
176. Lawson, L.R., *Fracture Toughness and Dimples Formation in a Whisker-Reinforced 6061 Aluminum Matrix composite.* Scripta Metallurgica et Materialia, 1991, **25**, p. 1533-1536.
177. Arsenault, R.J., *The Strengthening of Aluminum Alloy 6061 by Fiber and Platelet Silicon Carbide.* Materials Science and Engineering, 1984, **64**, p. 171-181.
178. Dai, L.H., Z. Ling, and Y.L. Bai, *A Strain Gradient-Strengthening Law for Particle Reinforced Metal Matrix Composites.* Scripta Materialia, 1999, **41** (3), p. 245-251.
179. Kouzeli, M. and A. Mortensen, *Size Dependent Strengthening in Particle Reinforced Aluminium.* Acta Materialia, 2002, **50**, p. 39-51.
180. Chen, C.R., *et al.*, *Finite Element Analysis about Effects of Particle Morphology on Mechanical Response of Composites.* Materials Science and Engineering, 2000, **A278**, p. 96-105.
181. Ritchie, R.O. and A.W. Thompson, *On Macroscopic and Microscopic Analyses for Crack Initiation and Crack Growth Toughness in Ductile Alloys.* Metallurgical Transactions, 1985, **16A** (February 1985), p. 233-248.
182. Jones, R.H., C.A. Lavender, and M.T. Smith, *Yield Strength-Frcture Toughness Relationships in Metal Matrix Composites.* Scripta Metallurgica, 1987, **21**, p. 1565-1570.
183. Davidson, D.L., *Fracture Surface Roughness as a Gauge of Fracture Tougness: Aluminium-Particulate SiC Composites.* Journal of Materials Science, 1989, **24**, p. 681-687.
184. Rice, J.R. in *Third Int. Conf. on Fracture*. Proc. Conf., 1965: Sendai, Japanese Soc. for Strength and Fracture of Metals.
185. Jokl, M.L., V. Vitek, and C.J. McMahon, *A Microscopic Theory of Brittle Fracture in Deformable Solids: A Relation Between Ideal Work to Fracture and Plastic Work.* Acta Metallurgica, 1980, **28**, p. 1479-1488.
186. Hirth, J.P. and F.H. Froes, *Interrelations Between Fracture Tougness and Other Mechanical Properties in Titanium.* Metallurgical Transactions, 1977, **8A**, p. 1165-1176.
187. Gerberich, W.W., *Fracture: Interactions of Microstructure, Mechanisms and Mechanics*, J.M. Wells and J.D. Landes, Editors. 1984, TMS, Warrendale, PA. p. 49-74.
188. Needleman, A., *A Continuum Model for Void Nucelation by Inclusion Debonding.* Journal of Applied Mechanics, 1987, **54**, p. 525-531.
189. Tvergaard, V. and J.W. Hutchinson, *The Relation between Crack Growth Resistance and Fracture Parameters in Elastic-Plastics Solids.* Journal of the Mechanics and Physics of Solids, 1992, **40** (6), p. 1377-1397.
190. Pineau, A., *Global and Local Approaches of Fracture*, in *Topics in Fracture and Fatigue*, A.S. Argon, Editor. 1992, Springer-Verlag, New-York. p. 197-234.
191. Tvergaard, V. and J.W. Hutchinson, *Effect of Strain-Dependant Cohesive Zone Model on Predictions of Crack Growth Resistance.* International Journal of Solids and Structures, 1996, **33**, p. 3297-3308.
192. Tvergaard, V. *Relations between Crack Growth Resistance and Fracture Process Parameters under Large Scale Yielding*. in *IUTAM Symphosium on Nonlinear Analysis of Fracture*. Proc. Conf., 1997, Kluwer Academic Publishers.
193. Hutchinson, J.W. *Closing in on the Crack Tip*. in *IUTAM Symphosium on Nonlinear Analysis of Fracture*. Proc. Conf., 1997, Kluwer Academic Publishers.
194. Barenblatt, G.I., *The Mathematical Theory of Equilibrium Cracks in Brittle Fracture*, in *Advances in Applied Mechanics*. Vol. VIII, 1962, Academic Press. p. 55-129.
195. Wei, Y. and J.W. Hutchinson, *Models of Interface Separation Accompanied by Plastic Dissipation at Multiple Scales.* International Journal of Fracture, 1999, **95**, p. 1-17.
196. Evans, A.G., J.W. Hutchinson, and Y. Wei, *Interface Adhesion: Effects of Plasticity and Segregation.* Acta Materiala, 1999, **47** (15), p. 4093-4113.
197. Rice, J.R. and J.S. Wang, *Embrittlement of Interfaces by Solute Segregation.* Materials Science and Engineering, 1989, **A107**, p. 23-40.
198. Evans, A.G. and B.J. Dalgleish, *The Fracture Resistance of Metal-Ceramic Interfaces.* Materials Science and Engineering, 1993, **A162**, p. 1-13.
199. Siegmund, T. and W. Brocks, *Prediction of the Work of Separation and Implications to Modeling.* International Journal of Fracture, 1999, **99**, p. 97-116.

200. Siegmund, T. and W. Brocks, *The Role of Cohesive Strength and Separation Energy for Modeling of a Ductile Fracture*, in *Fatigue and Fracture Mechanics: 30th Volume, ASTM STP 1360*, P.C. Paris and K.L. Jerina, Editors. 2000, American Society for Testing and Materials, West Conshohocken, Pa, USA. p. 139-151.
201. Suo, Z., C.F. Shih, and A.G. Varias, *A Theory for Cleavage Cracking in the Presence of Plastic Flow.* Acta Metallurgica et Materialia, 1993, **41** (5), p. 1551-1557.
202. Lipkin, D.M. and G.E. Beltz, *A Simple Elastic Cell Model of Cleavage Fracture in the Presence of Dislocation Plasticity.* Acta Materialia, 1996, **4**, p. 1287-1291.
203. Lipkin, D.M., D.R. Clarke, and G.E. Beltz, *A Strain-Gradient Model of Cleavage Fracture in Plastically Deforming Materials.* Acta Materialia, 1996, **44** (10), p. 4051-4058.
204. Hutchinson, J.W. and A.G. Evans, *Mechanics of Materials: Top-Down Approaches to Fracture.* Acta Materialia, 2000, **48**, p. 125-135.
205. Cotterell, B., *The Past, Present and Future of Fracture Mechanics.* Engineering Fracture Mechanics, 2002, **69**, p. 533-553.
206. Finot, M., *et al.*, *Micromechanical Modeling of Reinforcement Fracture in Particle-Reinforced Metal Matrix Composites.* Metallurgical Transactions, 1994, **25A** (11), p. 2403-2420.
207. Stüwe, H.P., *The Work Necessary to Form a Ductile Fracture Surface.* Engineering Fracture Mechanics, 1980, **13**, p. 231-236.
208. Stüwe, H.P. *The Plastic Work Spent in Ductile Fracture*. in *Three-Dimensional Constitutive Relations and Ductile Fracture*. Proc. Conf., 1981: Dourdan, N-H Publishing Company.
209. Kolednik, O. and H.P. Stüwe, *The Stereophotogrammetric Determination of the Critical Crack Tip Opening Displacement.* Engineering Fracture Mechanics, 1985, **21** (1), p. 145-155.
210. Alicona and GdbR, *Mex, 3D-Analysis of Stereoscopic SEM-Images*. 1999: Berchtesgaden, Germany.
211. Stampfl, J., *et al.*, *Determination of the Fracture Toughness by Automatic Image Processing.* International Journal of Fracture, 1996, **78**, p. 35-44.
212. Stampfl, J., *et al.*, *Reconstruction of Surface Topographies by Scanning Electron Microscopy for Application in Fracture Research.* Applied Physics A - Materials Science & Processing, 1996, **63**, p. 341-346.
213. Stampfl, J. and O. Kolednik, *The Separation of the Fracture Energy in Metallic Materials.* International Journal of Fracture, 2000, **101**, p. 321-345.
214. Poech, M.H. and H.F. Fischmeister, *The Contributon of Void Growth to the Crack Resistance of Ductile Materials.* Engineering Fracture Mechanics, 1992, **43** (4), p. 581-588.
215. Sigl, L.S. and H.E. Exner, *Experimental Study of the Mechanics of Fracture in WC-Co Alloys.* Metallurgical Transactions, 1987, **18A**, p. 1299-1308.
216. Spiegler, R. and H.F. Fischmeister, *Prediction of Crack Paths in WC-Co Alloys.* Acta Metallurgica et Materialia, 1992, **7**, p. 1653-1661.
217. Krstic, V.D. and M. Komac, *Toughening in WC-Co composites.* Philosophical Magazine, 1985, **51** (2), p. 191-203.
218. Fischmeister, H.F., *et al.*, *Modelling Fracture Processes in Metals and Composite Materials.* Zeitschrift für Metallkunde, 1989, **80** (12), p. 839-846.
219. Sigl, L.S. and H.F. Fischmeister, *On the Fracture Toughness of Cemented Carbides.* Acta Metallurgica, 1988, **36** (4), p. 887-897.
220. Ravichandran, K.S., *Fracture Toughness of Two Phase WC-Co Cermets.* Acta Metallurgica et Materialia, 1994, **42** (1), p. 143-150.
221. Sigl, L.S., *et al.*, *On the Toughness of Brittle Materials Reinforced with a Ductile Phase.* Acta Metallurgica, 1988, **36** (4), p. 945-953.
222. Flinn, B.D., M. Rühler, and A.G. Evans, *Toughening in Composites of* $Al_2O_3$ *reinforced with Al.* Acta Metallurgica et. Materiala, 1989, **37** (11), p. 3001-3006.
223. Krstic, V.D., *On the Fracture of Brittle-Matrix/Ductile-Particle Composites.* Philosophical Magazine, 1983, **48** (5), p. 695-708.
224. Budiansky, B., J.C. Amazigo, and A.G. Evans, *Small-Scale Crack Bridging and the Fracture Toughness of Particulate-Reinforced Ceramics.* Journal of the Mechanics and Physics of Solids, 1988, **36** (2), p. 167-187.
225. Evans, A.G. *High Toughness Ceramics and Ceramics Composites*. in *10th Riso International Symphosium on Metallurgy and Materials Science*. Proc. Conf., 1989: Roskilde, Denmark, Riso National Laboratory.
226. Ashby, M.F., F.J. Blunt, and M. Bannister, *Flow Characteristics of Highly Constrained Metal Wires.* Acta Metallurgica, 1989, **37** (7), p. 1847-1857.

227. Bao, G. and C.-Y. Hui, *Effects of Interface Debonding on the Toughness of Ductile-Particle Reinforced Ceramics.* International Journal of Solids and Structure, 1990, **26** (5/6), p. 631-642.
228. Nan, C.W. and D.R. Clarke, *The Influence of Particle Size and Particle Fracture on the Elastic/Plastic Deformation of Metal Matrix Composites.* Acta Metallurgica et Materialia, 1996, **44** (9), p. 3801-3811.
229. Bannister, M. and M.F. Ashby, *The Deformation and Fracture of Constrained Metal Sheets.* Acta Metallurgica et Materialia, 1991, **39** (11), p. 2575-2582.
230. Bao, G. and F. Zok, *On the Strength of Ductile Particle Reinforced Brittle Matrix Composites.* Acta Metallurgica et Materialia, 1993, **41** (12), p. 3515-3525.
231. Marshall, D.B., *et al.*, *Toughening Mechanisms in Cemented Carbides.* Journal of the American Ceramic Society, 1990, **73** (10), p. 2938-2943.
232. TreibacherSchleifmittelAG, *Product Information*. 1998.
233. SumitomoChemicalCo., L., *Alumina products information*. 1997.
234. Underwood, E.E., *Quantitative Metallography*, in *Metals Handbook*, A.H. Committee, Editor. Vol. 9, 1985, ASM, Metals Park, OH. p. 123-134.
235. Pyzik, A.J. and D.R. Beaman, *Al-B-C Phase Development and Effects on Mechanical Properties of* $B_4C$*/Al-Derived Composites.* Journal of the American Ceramic Society, 1995, **78**, p. 305-312.
236. Stücklin, S., *Solutionization of Metal-Matrix Composites*, Diploma Thesis, 2001, EPFL, Lausanne.
237. Anderson, T.L., *Fracture Mechanics, 2nd Edition*. second ed. 1995, CRC Press.
238. Suresh, S. and R.O. Ritchie, *Propagation of Short Fatigue Cracks.* International Metallurgical Reviews, 1984, **29**, p. 445-476.
239. Elber, W., *Fatigue Crack Closure Under Cyclic Tension.* Engineering Fracture Mechanics, 1970, **2**, p. 37-45.
240. McClung, R.C., *Crack Closure and Plastic Zone Sizes in Fatigue.* Fatigue and Fracture of Engineering Materials and Structures, 1991, **14** (4), p. 455-468.
241. McClung, R.C., *The Influence of Applied Stress, Crack Length, and Stress Intensity Factor on Crack Closure.* Metallurgical Transactions, 1991, **22A**, p. 1559-1571.
242. Prangnell, P.B., *et al.*, *The Deformation of Discontinuously Reinforced MMCs-II. The Elastic Response.* Acta Metallurgica et Materialia, 1994, **42** (10), p. 3437-3442.
243. Kouzeli, M., C.S. Marchi, and A. Mortensen, *Effect of Reaction on the Tensile Behavior of Infiltrated Boron Carbide Aluminium Composites.* Materials Science and Engineering, 2002, **A337**, p. 264-273.
244. *Al-Cu-Fe*, in *Ternary Alloys*, G. Petzow and G. Effenberg, Editors. Vol. 4, 1991, VCH Verlagsgesellschaft, Weinheim, Germany. p. 475-489.
245. Couture, A., *Iron in Aluminum Casting Alloys - A Literature Survey.* AFS International Cast Metals Journal, 1981, **6** (4), p. 9-17.
246. Kouzeli, M., *et al.*, *Quantification of Microdamage Phenomena During Tensile Straining of High Volume Fraction Particle Reinforced Aluminium.* Acta Materialia, 2001, **49**, p. 497-505.
247. Onodera, R., *et al.*, *Effect of Heat Treatments on the Portevin-Le Chatelier Effects in Aluminium-Silver Alloys.* Acta Metallurgica, 1983, **31** (10), p. 1589-1593.
248. Lebydokin, M., *et al.*, *Statistical Behaviour and Strain Localization Patterns in the Portevin-Le Chatelier Effect.* Acta Materialia, 1996, **44** (11), p. 4531-4541.
249. Pink, E., P. Bruckbauer, and H. Weinhandl, *Stress-Drop Rates in Serrated Flow of Aluminium Alloys.* Scripta Materialia, 1998, **38** (6), p. 945-951.
250. Cheng, X.-M. and J.G. Morris, *The Anisotropy of the Portevin-Le Chatelier Effect in Aluminium Alloys.* Scripta Materialia, 2000, **43**, p. 651-658.
251. Thevenet, D., M. Mliha-Touati, and A. Zeghloul, *The Effect of Precipitation on the Portevin-Le Chatelier Effect in an Al-Zn-Mg-Cu Alloy.* Materials Science and Engineering, 1999, **A266**, p. 175-182.
252. Kouzeli, M., *et al.*, *Influence of Damage on the Tensile Behaviour of Pure Aluminium Reinforced with > 40 Vol. Pct. Alumina Particles.* Acta Materialia, 2001, **49**, p. 3699-3709.
253. Brocks, W., D. Klingbeil, and J. Olschewski, *Lösung der HRR-Feld_Gleichungen der Elastisch-Plastischen Bruchmechanik: Forschungbericht 175*. 1990, Bundenanstalt für Materialforschung und Prüfung (BAM), Berlin: Berlin. p. 112.
254. *ABAQUS User's Manual*. 5.8 ed. 1998, Karlson and Sorensen, Inc.
255. Brocks, W. and I. Scheider, *Numerical Aspects of the Path-Dependence of the J-Integral in Incremental Plasticity: How to Calculate Reliable J-Values in FE Analyses*. 2001, Institut für Werkstofforschung, GKSS-Forschungszentrum Geestacht (technical Note GKSS/WMS/01/08). p. 32.

256. Chan, K.S., *Crack-Tip Behaviors of Stationary and Growing Cracks in Al-Fe-X Alloys: Part I. Near-Tip Strain Field.* Metallurgical Transactions, 1990, **21A**, p. 69-80.
257. Dong, M.J., C. Prioul, and D. François, *Damage Effect on the Fracture Toughness of Nodular Cast Iron: Part II. Damage Zone Characterization Ahead of a Crack Tip.* Metallurgical and Materials Transactions, 1997, **28A**, p. 2245-2262.
258. Newman, J.C. *A Review of Chevron-Notched Fracture Specimens*. in *Chevron-Notched Specimens: Testing and Stress Analysis*. Proc. Conf., 1984: Louisville, KY, ASTM, Philadelphia, PA.
259. Shannon, J.L. and D.G. Munz. *Specimen Size and Geometry Effects on Fracture Toughness of Aluminum Oxide Measured with Short-Rod and Short-Bar Chevron-Notched Specimens*. in *Chevron-Notched Specimens: Testing and Stress Analysis*. Proc. Conf., 1983: Louisville, KY, ASTM, Philadelphia, PA.
260. Orange, T.W., *et al. Analysis of some Compliance Calibration Data for Chevron-Notch Bar and Rod Specimens*. in *ASTM-STP 1172: Chevron-Notch Fracture Test Experience. Metals and Non-Metals*. Proc. Conf., 1992: Indianapolis, ASTM, Philadephia, PA.
261. Fleck, N.A., *et al., Strain Gradient Plasticity: Theory and Experiment.* Acta Metallurgica et Materialia, 1994, **42**, p. 475-487.
262. Nix, W.D. and H. Gao, *Indentation Size Effects in Crystalline Materials: A Law for Strain Gradient Plasticity.* Journal of the Mechanics and Physics of Solids, 1998 (46), p. 411-425.
263. Barlow, C.Y. and N. Hansen, *Deformation Structures and Flow Stress in Aluminium Containing Short Whiskers.* Acta Metallurgica et Materialia, 1991, **39** (8), p. 1971-1979.
264. Wegner, L.D. and L.J. Gibson, *The Fracture Toughness Behaviour of Interpenetrating Phase Composites.* International Journal of Mechanical Sciences, 2001, **43**, p. 1771-1791.
265. Evans, A.G. and B.J. Dalgleish, *The Fracture Resistance of Metal-Ceramic Interfaces.* Acta metallurgica et Materialia, 1992, **S40**, p. s295-s306.
266. McNaney, J.M., R.M. Cannon, and R.O. Ritchie, *Fracture and Fatigue-Crack Growth along Aluminum-Alumina Interfaces.* Acta Materiala, 1996, **44** (12), p. 4713-4728.
267. Saiz, E., R.M. Cannon, and A.P. Tomsia, *Energetics and Atomic Transport at Liquid Metal/$Al_2O_3$ Interfaces.* Acta Materialia, 1999, **47**, p. 4209-4220.
268. Zhang, W., J.R. Smith, and A.G. Evans, *The Connection Between ab initio Calculations and Interface Adhesion Measurements on Metal/Oxide Systems: Ni/$Al_2O_3$ and Cu/$Al_2O_3$.* Acta Materialia, 2002, **50**, p. 3803-3816.
269. Korn, D., *et al., Fracture Properties of Interfacially Doped Nb-$Al_2O_3$ Bicrystals: I, Fracture Characteristics.* Acta Materialia, 2002, **50**, p. 3881-3901.
270. Cannon, R.M., *et al., Fracture Properties of Interfacially Doped Nb-$Al_2O_3$ Bicrystals: II, Relation of Interfacial Bonding, Chemistry and Local Plasticity.* Acta Materialia, 2002, **50**, p. 3903-3925.
271. Doi, H., *Elastic and Plastic Properties of of WC-Co Composites Alloys*, J. Baruck, Editor. 1974, Freund Publishing House Ltd., Haïfa, Israel.
272. Bhattacharya, A.K. and J.J. Petrovic, *Ductile Phase Toughening and R-curve Behaviour in a $B_4$C-Al Cermet.* Journal of Materials Science, 1992, **27**, p. 2205-2210.
273. Sbaizero, A., G. Pezzotti, and T. Nishida, *Fracture Energy and R-Curve Behavior of $Al_2O_3$/Mo Composites.* Acta Materialia, 1998, **46** (2), p. 681-687.
274. Pezzotti, G. and O. Sbaizero, *Residual and Bridging Microstress Fields in Al2O3/Al Interpenetrating Network Composite Evaluated by Fluorescence Spectroscopy.* Materials Science and Engineering, 2001, **A303**, p. 267-272.
275. Huang, Y., J.W. Hutchinson, and V. Tvergaard, *Cavitation Instabilities in Elastic-Plastic Solids.* Journal of the Mechanics and Physics of Solids, 1991, **59**, p. 223-241.
276. Yang, J., *et al., Effects of Damage on the Flow Strength and Ductility of a Ductile Al Alloy Reinforced with SiC Particulates.* Acta Metallurgica et. Materiala, 1990, **38** (12), p. 2613-2619.
277. Hill, R., *The Mathematical Theory of Plasticity, p.230.* Oxford Classic Series. 1998, Oxford University Press.
278. Llorca, J., S. Suresh, and A. Needleman, *An Experimental and Numerical Study of Cyclic Deformation in Metal-Ceramic Composites.* Metallurgical Transactions, 1992, **23A** (3), p. 919-934.
279. Rossoll, A., *To be published.*
280. Zhongua, L. and G. Haicheng, *Hydrostatic Stresses and their Effect on the Macroflow and Microfracture Mechanism of Two-Phase Alloys.* Metallurgical Transactions, 1991, **22A**, p. 2695-2702.
281. Llorca, J., *Void Formation in Metal Matrix Composites*, in *Comprehensive Composite Materials, Volume 3: Metal Matrix Composites*, T.W. Clyne, Editor. Vol. 3.04, 2000, Pergamon, Oxford UK. p. 91-115.

282. Brocks, W. and W. Schmitt, *The Second Parameter in J-R Curves: constraint or Triaxiality*, in *Constraints Effects in Fracture, Theory and Applications: Second Volume (AST STP 1244)*, M. Kirk and A. Bakker, Editors. 1995, ASTM, Philadelphia. p. 209-231.
283. McClintock, F.A., *A Criterion for Ductile Fracture by the Growth of Holes.* Transactions of the ASME - Journal of Applied Mechanics, 1968, **35**, p. 365-371.
284. Rice, J.R. and D.M. Tracey, *On the Ductile Enlargement of Voids in Triaxial Stress Fields.* Journal of the Mechanics and Physics of Solids, 1969, **17** (17), p. 201-217.
285. Tvergaard, V., *Effect of Void Size Differences on Growth and Cavitation Instabilities.* Journal of the Mechanics and Physics of Solids, 1996, **44**, p. 1237-1253.
286. Pardoen, T. and J.W. Hutchinson, *An Extended Model for Void Growth and Coalesence.* Journal of the Mechanics and Physics of Solids, 2000, **48**, p. 2467-2512.
287. Llorca, J., *An Analysis of the Influence of Reinforcement Fracture on the Strength of Discontinuously-Reinforced Metal-Matrix Composites.* Acta Metallurgica et Materialia, 1995, **43** (1), p. 181-192.
288. Brockenbrough, J.R. and F.W. Zok, *On the Role of Particle Cracking in Flow and Fracture of Metal Matrix Composites.* Acta Metallurgica et Materialia, 1995, **43** (1), p. 11-20.
289. Llorca, J. and P. Poza, *Influence of Reinforcement Fracture on the Cyclic Stress-Strain Curve of Metal-Matrix Composites.* Acta Metallurgica et Materialia, 1995, **43** (11), p. 3959-3969.
290. Gonzalez, C. and J. Llorca, *Prediction of the Tensile Stress-Strain Curve and Ductility in Al/SiC Composites.* Scripta Materialia, 1996, **35** (1), p. 91-97.
291. Shi, N., B. Wilner, and R.J. Arsenault, *An FEM Study of the Plastic Deformation Process of Whisker Reinforced SiC/Al Composites.* Acta Metallurgica et Materialia, 1992, **40** (11), p. 2841-2854.
292. Justice, I., *et al.*, *Reinforcement Stresses During Deformation of Sphere- and Particulate-Reinforced Al-Matrix Composites.* Metallurgical Transactions, 1996, **27A** (2), p. 486-490.
293. Tada, H., P.C. Paris, and G.R. Irwin, *The Stress Analysis of Cracks Handbook*. 1985, St. Louis, Paris Production Inc.
294. 3MCompany, *Nextel Ceramic Textiles Technical Notebook (www.mmm.com/ceramics)*. 2001.
295. Wilson, D.M. and L.R. Visser, *High Performance Oxide Fibers for Metal and Ceramic Composites.* Composites, 2001, **32A**, p. 1143-1153.
296. Moser, B., *Deformation and Fracture of Continuous Alumina Fibre Reinforced Aluminium Composites*, PhD Thesis, 2002, EPFL, Lausanne.
297. Gordon, J.E., *The New Science of Strong Materials*. 2nd ed. 1976, Princeton, New Jersey, Princeton University Press. 276.
298. Parvizi-Majidi, A., *Whiskers and Particulates*, in *Comprehensive Composite Materials, Volume 1: Fiber Reinforcements and General Theory of Composites*. Vol. 1-06, 2000, Pergamon, Oxford UK. p. 175-198.
299. Timoshenko, S.P. and J.N. Goodier, *Theory of Elasticity*. 1970, McGraw-Hill, Singapore. p. 409.
300. Xia, L. and C.F. Shih, *Ductile Crack Growth-I. Numerical Study Using Computational Cells With Microstructurally-Based Length Scales.* Journal of the Mechanics and Physics of Solids, 1995, **43**, p. 233-259.
301. Xia, L. and C.F. Shih, *Ductile Crack Growth-II. Void Nucleation and Geometry Effects on Macroscopic Fracture Behavior.* Journal of the Mechanics and Physics of Solids, 1995, **43**, p. 1953-1981.
302. Kelly, A. and N.H. Macmillan, *Strong Solids*. 3 ed. 1986, Oxford, Clarendon Press. 423.
303. Lipkin, D.M., D.R. Clarke, and A.G. Evans, *Effect of Interfacial Carbon on Adhesion and Toughness of Gold-Sapphire Interfaces.* Acta Materiala, 1998, **46**, p. 4835-4850.
304. Elssner, G., D. Korn, and M. Rühle, *The Influence of Interface Impurities on Fracture Energy of UHV Diffusion Bonded Metal-Ceramic Bicrystals.* Scripta Metallurgica et Materialia, 1994, **31** (8), p. 1037-1042.
305. Dalgleish, B.J., *et al.*, *Interface Formation and Strength in Ceramic-Metal Systems.* Scripta Metallurgica et Materialia, 1994, **31** (8), p. 1109-1114.
306. Reimanis, I.E., *et al.*, *Influence of $Cu_2O$ and $CuAlO_2$ Interphases on Crack Propagation at $Cu/\alpha$-$Al_2O_3$ Interfaces.* Journal of the American Ceramic Society, 1997, **80** (2), p. 424-432.
307. Gaudette, F., *et al.*, *The Influence of Chromium Addition on the Toughness of $\gamma$-$Ni/\alpha$-$Al_2O_3$ Interfaces.* Acta Materialia, 1997, **45** (9), p. 3503-3513.
308. Wynblatt, P., *The Effects of Interfacial Segregation on Wetting in Solid Metal-on-Metal and Metal-on-Ceramic Systems.* Acta Materialia, 2000, **48**, p. 4439-4447.
309. Vreeling, J.A., *et al.*, *In-situ Microscopy Investigation of Failure Mechanisms in Al/SiCp Metal Matrix Composite Produced by Laser Embedding.* Scripta Materiala, 2000, **42**, p. 589-595.

310. Tham, L.M., M. Gupta, and L. Cheng, *Effect of Limited Matrix-Reinforcement Interfacial Reaction on Enhancing the Mechanical Properties of Aluminium-Silicon Carbide Composites.* Acta Materialia, 2001, **49**, p. 3243-3253.
311. Zhu, J.H., *et al.*, *Damage Mechanisms in a Cast Ductile Iron and a $Al_2O_3$/Al Composite.* Metallurgical and Materials Transactions A, 1998, **29A** (November 1998), p. 2855-2862.
312. Gauckler, L.J., T. Grauke, and F. Bader, Materials Chemistry and Physics, 1999, **61**, p. 78-102.
313. Liu, C., *et al.*, *Micromechanical Properties of High Fracture Performance SiCp-6061Al/6061 Al Composite.* Materials Science and Engineering, 2002, **A232**, p. 203-209.
314. Qin, S., *et al.*, *Characterization of Thermal Residual Strain in SiCp/6061 Al Composites by Ultramicrohardness.* Journal of Materials Science Letters, 1999, **18**, p. 1099-1100.
315. Ahn, H.K. and T. Kobayashi, *Fracture Toughness in Particulate Reinforced Aluminum Alloy Composite*. Scripta Materialia, 1997, **37** (12), p. 1973-1978.

# APPENDICES

## APPENDIX A. FRACTURE MECHANICS: BASIC THEORY AND CONCEPTS

The goal here is not to expose full details and all theoretical foundations of fracture mechanics, as this is well beyond the scope of this work. For a complete treatment of the subject, readers are referred to reference textbooks, e.g. [1-3]. Nevertheless, an introduction to the general concepts is given, as they are the basis of most of the experimental work and discussion of this research.

### *A.1 Linear-elastic fracture mechanics (LEFM)*

#### *A.1.1 Energy approach*

It has long been a subject of interest, starting apparently with experiments of Leonardo da Vinci [4], to understand the root cause of fracture, and in particular the discrepancy between the theoretical cohesive strength of material and the actual strength of brittle materials (the latter being typically three or four orders of magnitude below the former). When a very sharp crack is present in an infinitely wide plate that is externally loaded, Inglis [5] first showed that the load is locally amplified by the flaw and depends on the curvature radius of the crack tip, $\rho$. By approximating $\rho$ to be on the order of the atomic radius, he found that the remote stress at failure can be approximated by $\sigma_f = \sqrt{E\gamma_s/4a}$ where $E$ is Young's modulus, $\gamma_s$ is the surface energy and $2a$ is the crack length. It was in the 1920s that Griffith [6] proposed his famous energy approach to provide an explanation for the fracture initiated by a crack, and thereby formed the foundation of modern fracture theory[1]. Using a global energy balance that is based on the first law of thermodynamics, he showed that fracture occurs spontaneously if the energy stored in the structure per unit area of crack advance d$A$ exceeds the energy needed to create two new surfaces (the surface energy of the material); and he derived the following expression for the fracture stress of a semi-infinite two-dimensional plate containing a single side crack perpendicular to the applied stress:

$$\sigma_f = \sqrt{\frac{2E\gamma_s}{\pi a}} \tag{A-1}$$

which shows in very simple terms that the fracture load is dependent on a length scale, the crack length $a$. For a sharp crack in an ideally brittle solid, these two approaches are roughly consistent and the major difference is that the Griffith model is insensitive to the crack tip curvature radius.

---

[1] Interestingly, some recent historical research [7] has actually proved that the first analytical investigation in fracture mechanics were conducted prior to Griffith's work by a forgotten pioneer called Wieghardt [7, 8].

Such approaches were however not convenient for solving engineering problems and a major breakthrough was brought a few decades later by Irwin, who introduced the concept of the “energy release rate”, $G$. $G$ is a measure of the energy available for the extension of a unit area of the crack and is defined as the rate of change in elastic potential energy with crack area. The usual way to represent the concept of the energy release rate is to consider the presence of a crack of length $a$ in an elastic body (a plate for convenience) that is loaded to a charge $P$ (Figure A-1a) and to express the potential energy of the system, $\Pi$, given by:

$$\Pi = U - F \tag{A-2}$$

where $U$ is the strain energy stored in the body and $F$ the work done by external forces. If fracture occurs at this load, the crack extends over a small increment d$a$ to $a$ + d$a$. $G$ is then associated with the change of potential energy during this process and is given by (see Figure A-1b):

$$G = -\frac{1}{B}\frac{d\Pi}{da} = -\frac{1}{B}\frac{dU}{da} \tag{A-3}$$

where $B$ is the plate thickness. Hence, during crack extension, there is a deliverable energy equal to the change in strain energy d$U$/d$a$ (d$U$ is graphically defined by the shaded area in Figure A-1b). If, on the other hand, the displacement $V$ is fixed, one can show that $G$ is almost identical to (A-3), with the difference that the sign of $d$U is inverted. In both cases, fracture occurs if $G$ reaches its critical value $G_c$, which is equal to the fracture energy, $2\gamma_s$:

$$G = G_c = 2\gamma_s \quad \text{at fracture} \tag{A-4}$$

The left hand side of (A-4) is called the strain energy release rate, the right hand side the fracture energy or fracture resistance.

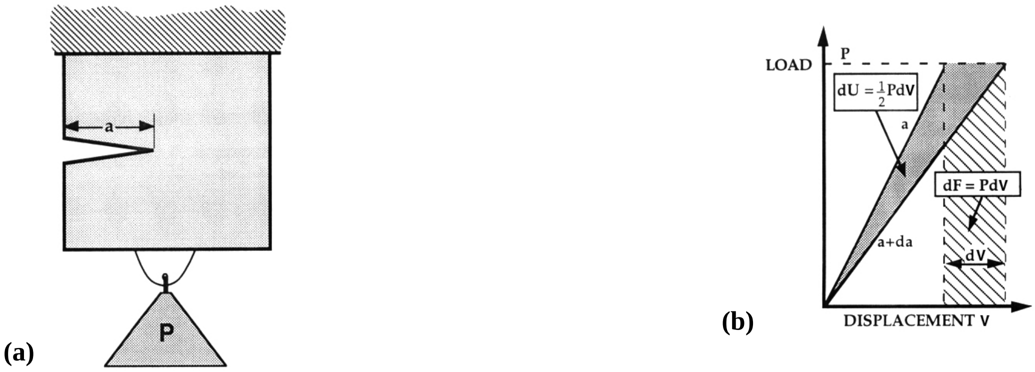

**Figure A-1.** Graphical definition of the strain energy release rate, for a structure in load control. **(a)**: crack plate subjected to a fixed load, $P$; **(b)**: load-displacement response of the plate for a crack of length $a$ and $a$+d$a$. $d$U is the strain energy release rate. From [3].

### A.1.2 Stress approach

In parallel, Irwin (as well as other authors, [9-11]) derived closed-form expressions for the stresses in a cracked body subjected to external forces (Figure A-2a), assuming linear elastic material behaviour. Their fundamental finding was that near the crack tip, there exists a stress singularity that can be fully described by the so-called ″stress intensity factor″, $K$. $K$ depends linearly on the applied external load $\sigma$, on the length of the crack $a$, and on the geometry of the crack and of the component. It is expressed by:

$$K = \sigma \cdot \sqrt{\pi a} \cdot Y(a/W) \tag{A-5}$$

where$Y$ is a dimensionless constant of the relative crack length $a/W$ ($W$ being the distance from the load line to the back-side of the specimen) and depends on the geometry and mode of loading[1]. The $Y$ functions can be found in several handbooks [12, 13]. The most important result of this analysis is that for any loading mode and cracked body geometry, $K$ defines the crack tip stress intensity by relating the local component of the stress tensor to the applied stress and crack size through Sneddon’s equations:

$$\sigma_{\mathrm{ij}} = \frac{K}{\sqrt{2\pi r}} \cdot f_{\mathrm{ij}}(\theta) \tag{A-6}$$

where $(r,\theta)$ are polar coordinates as defined in Figure A-2a, and $f_{\mathrm{ij}}(\theta)$ are angular functions that vary for the different loading modes. These are tabulated in any textbook of fracture mechanics. The major implication of (A-6) is the universal nature of asymptotic stress and displacement fields around the crack tip in a linear elastic solid. This dependence in $r^{-1/2}$ is schematically illustrated in Figure A-2b for the $\sigma_{\mathrm{yy}}$ stress field component.

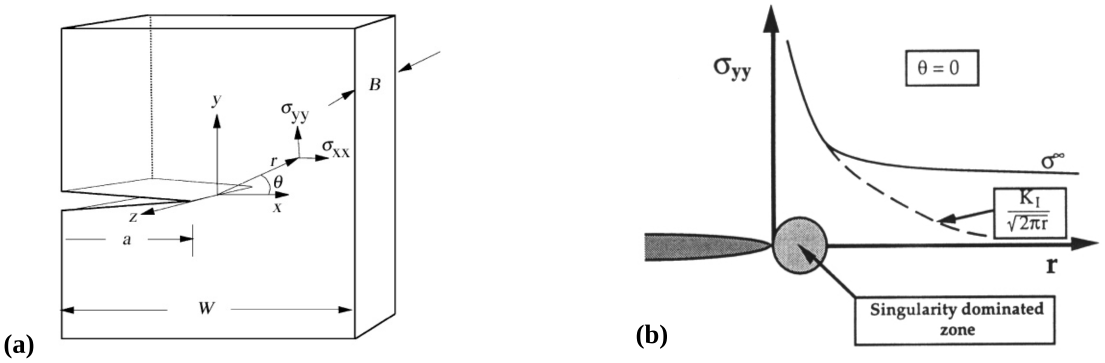

**Figure A-2.** **(a)**: Edge crack in a plate subjected to a remote tensile stress; **(b)**: $\sigma_{\mathrm{yy}}$ component of the stress field in front of the crack tip as given by (A-6) (for $\theta = 0$).

For simplification, most of the classical solutions in fracture mechanics reduce to two dimensions. This is done by assuming that one of the principal components of the stress or strain tensor equals zero. If $\sigma_{\mathrm{zz}} = 0$ as at a free surface, the state of stress is said to be of “plane stress”. In the center of a thick plate, on the other hand, contraction in the $z$-direction is prevented by the surrounding material. This constraint signifies that $\varepsilon_{\mathrm{zz}}$ is zero: the state is of “plane strain”. An important consequence of the plane strain state is that it causes a triaxial state of stress near the crack tip. This is readily explained by writing Hooke’s law for $\varepsilon_{\mathrm{zz}}$:

$$\varepsilon_{\mathrm{z}} = \frac{1}{E}\left[\sigma_{\mathrm{zz}} - \nu\left(\sigma_{\mathrm{xx}} + \sigma_{\mathrm{yy}}\right)\right] = 0 \qquad \text{and then:} \qquad \sigma_{\mathrm{zz}} = \nu\left(\sigma_{\mathrm{xx}} + \sigma_{\mathrm{yy}}\right) \approx 0.3\left(\sigma_{\mathrm{xx}} + \sigma_{\mathrm{yy}}\right) \tag{A-7}$$

In the interior of the plate, a high tensile stress hence develops in the thickness direction. This is however a simplification and fully plane stress or plane strain conditions in general do not exist ahead of the crack: in a real specimen, the stress state evolves from plane stress at the surface to a plane strain deep inside and there is a region in-between (near the plate surface) where the stress state is intermediate. Two-dimensional assumptions are however valid in some limiting cases or at least provide good approximations.

---

[1] The three modes of loading that can be applied to a crack are: mode I, opening; mode II, in-plane shear, and mode III, out-of-plane shear. The loading mode I is by far the most important and is the one considered in this work; hence the index I will be omitted.

To summarize, the stress intensity factor $K$ describes a crack in terms of stresses, strain and displacements near the crack tip; while the energy release rate $G$ quantifies the change in potential energy that accompanies an increment of crack extension. For linear elastic materials, the two parameters are uniquely related. For a wide plate in plane stress, one can show that:

$$G = \frac{\pi\sigma^2 a}{E} \tag{A-8}$$

By combining (A-5) with (A-8), the relation between $K$ and $G$ writes: (where the correction factor $Y$ is omitted for clarity):

$$G = \frac{K_I^2}{E'} \quad \text{where } E' = E \text{ for plane stress, and } E' = \frac{E}{1-\nu^2} \quad \text{for plane strain} \tag{A-9}$$

As for $G$, there exists also a critical value of stress intensity factor, $K_c$, at which crack extension occurs. Because of the unique relation between $G$ and $K$, $K_c$ is related to $G_c$, and at fracture:

$$K_c = \sqrt{G_c E'} = \sqrt{2\gamma_s E'} \tag{A-10}$$

Both quantities are a measure of the toughness of the material, which is a material constant independent of specimen and size geometry when certain conditions are met. In particular, at low degree of triaxiality, namely for small specimen thickness $B$, the toughness is geometry-dependent and increases as $B$ decreases. When $B$ increases on the other hand, the toughness decreases until it attains a plateau. In this case, plane strain dominates within the specimen, resulting in a high degree of triaxality, and the toughness becomes a constant material parameter, the so-called plane strain fracture toughness, $K_{Ic}$ (or similarly, $G_{Ic}$).

### A.1.3 Crack tip plasticity

Linear elastic stress analysis predicts infinite stress at the crack tip. This situation is physically unrealistic. In a metal, stresses are relaxed at the crack tip and a plastic zone of radius $r_p$ develops directly ahead of the crack tip. The elastic stress analysis then becomes inaccurate within the plastic zone; however, simple corrections can be used when moderate yielding occurs at the tip and estimations of the crack tip size can be made. For extensive yielding, a fully elastic-plastic analysis has to be carried out.

In the Irwin approach, Figure A-3a, it is assumed that the normal stress $\sigma_{yy}$ cannot exceed the uniaxial yield strength of the material, $\sigma_{ys}$ and by neglecting strain hardening, the stress distribution for $r \le r_p$ is constant. Calculation of stress redistributions within the plastic zone and a simple force balance give for the plastic zone size in plane stress:

$$r_p = \frac{1}{\pi}\left(\frac{K_I}{\sigma_{ys}}\right)^2 \quad \text{in plane stress} \tag{A-11}$$

To account for the higher effective stress intensity factor in the elastic region (as seen in Figure A-3a), an effective crack length, $a_{\mathrm{eff}}$ slightly longer than the actual crack size is defined and one finds making several approximations that the tip of the effective crack is at the center of the plastic zone, such that:

$$a_{\mathrm{eff}} = a + r_{\mathrm{p}} \tag{A-12}$$

In plane strain, yielding is reduced by the triaxial stress state, and by using the Von Mises criterion for plastic yielding and a few additional assumptions, the plastic zone size is approximately smaller by a factor three:

$$r_{\mathrm{p}} = \frac{1}{3\pi}\left(\frac{K_{\mathrm{I}}}{\sigma_{\mathrm{ys}}}\right)^2 \quad \text{in plane strain} \tag{A-13}$$

A circular plastic zone is assumed in this model. The actual shape of plastic zones (*i.e.* $r_{\mathrm{y}}(\theta)$) in fully plane stress and plane strain conditions are significantly different, and can be estimated using the Von Mises criterion and Sneddon's equations (A-6).

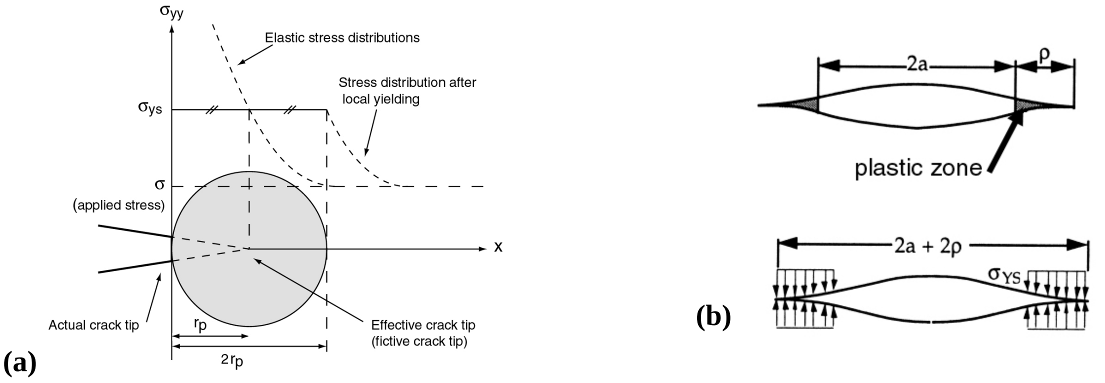
σyy
Elastic stress distributions
Stress distribution after local yielding
σys
σ
(applied stress)
x
Actual crack tip
rp
2rp
Effective crack tip (fictive crack tip)
(a)
2a
ρ
plastic zone
2a + 2ρ
σYS
(b)

**Figure A-3.** Crack tip plasticity models used for correction to LEFM. **(a)**: Irwin correction, plastic zone of size $r_{\mathrm{p}}$ in front of the crack, and fictive crack of length $a_{\mathrm{eff}}$ = a + $r_{\mathrm{p}}$ (from D. Favez, for class notes of A. Mortensen, EPFL); **(b)**: strip yield model, the plastic zone at the crack tip is modeled by a constant distribution of compressive closure stresses equal to the yield stress ([3]).

In the strip yield model, originally developped by Dugdale and Barenblatt [14, 15], an effective crack $a_{\mathrm{eff}}$ is assumed, with a length $2a+2\rho$ where $\rho$ is the length of the plastic zone that develops at the crack tip (Figure A-3b). A nonhardening material in plane stress is considered and the model assumes that a distribution of a closure stress equal to $\sigma_{\mathrm{ys}}$ exists in the strip yielding zone, Figure A-3b. To estimate $\rho$, one expresses the stress intensity due to the closure stress, $K_{\mathrm{closure}}$, so as to obtain, at equilibrium, the stress intensity factor from the remote tensile stress. The expression for the plastic zone size is then:

$$\rho = \frac{\pi}{8}\left(\frac{K_{\mathrm{I}}}{\sigma_{\mathrm{ys}}}\right)^2 \tag{A-14}$$

which is close to the Irwin model in plane stress. To estimate the effective stress intensity $K_{\mathrm{eff}}$, $a_{\mathrm{eff}}$ is set equal to $a + \rho$ and with this correction, one has:

$$K_{\mathrm{eff}} = \sigma \sqrt{\frac{\pi a}{\cos\left(\pi\sigma / 2\sigma_{\mathrm{ys}}\right)}} \tag{A-15}$$

This expressions however tends to overestimate $K_{\mathrm{eff}}$ and a more refined version of the strip yield model yields:

$$K_{\mathrm{eff}} = \sigma_{\mathrm{ys}} \cdot \sqrt{\pi a} \cdot \left[ \sqrt{\frac{8}{\pi^2} \ln\left( \frac{1}{\cos\left(\pi\sigma / 2\sigma_{\mathrm{ys}}\right)} \right)} \right] \tag{A-16}$$

Crack tip plasticity is important on the toughness of materials in that it involves additional energy dissipation during crack propagation. For materials that are capable of plastic flow, the fracture energy –considered so far to be equal to the surface energy $\gamma_s$– is then:

$$\gamma_{\mathrm{f}} = \gamma_{\mathrm{s}} + w_{\mathrm{p}} \tag{A-17}$$

where $w_p$ is the plastic work per unit area of surface created and is typically larger than $\gamma_s$ by one to few orders of magnitude. The toughness as given by (A-1) or (A-4) is then corrected to account for $w_p$, showing that the major part of the fracture energy is actually provided by plastic flow. In many cases, $\gamma_s$ is even neglected; however it still plays an important role because it can be shown in some instances that $w_p$ actually depends on $\gamma_s$ as discussed in more detail in Section 2.5.

### *A.1.4 Rising crack growth resistance ("R-curve behaviour")*

In highly brittle materials, $K_{\mathrm{Ic}}$ or $G_{\mathrm{Ic}}$ are roughly constant during crack extension. In many materials however, during crack propagation the energy necessary to extend the crack varies from its initial value, $G_c = 2\gamma_f$, to a certain value $G_R$, generally denoted as $R$, the material resistance to crack extension. A plot of $R$ versus crack extension, $\Delta a$, is called the resistance curve and such rising behaviour is denominated "*R*-curve behaviour". With this definition, ideally brittle materials exhibit a flat *R*-curve, Figure A-4a and the critical value of the energy release rate $G_c = R$ is unambiguously defined. In rising *R*-curve materials, as illustrated in Figure A-4b, the driving force $G$ at a fixed stress $\sigma_1$ slightly above that for which $G = G_c = 2\gamma_f$ leads to a small increment of crack propagation but further growth is stopped because the driving force $G$ increases at a slower rate than $R$. For crack propagation to continue, the driving force must be raised by increasing the stress to $\sigma_2$. The process is repeated and stable propagation remains until a stress corresponding to a crack driving force $G_R$ is attained. At that critical point one can see on the diagram that the crack driving force rate is higher than the *R*-curve slope and unstable crack propagation occurs. The conditions for stable crack growth translates into:

$$G = R \quad \text{and} \quad \frac{dG}{da} \le \frac{dR}{da} \tag{A-18}$$

while unstable crack growth occurs when

$$\frac{dG}{da} > \frac{dR}{da} \tag{A-19}$$

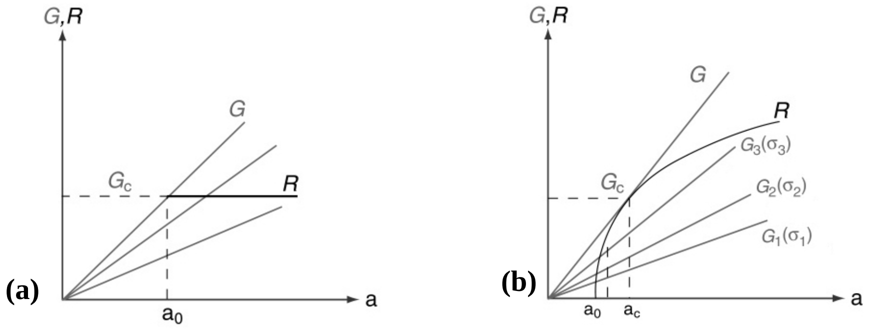

**Figure A-4.** Schematic view of resistance curves, plotted in term of *G* (one can also use *K* for representation of resistance curves). **(a)**: Flat *R*-curve; **(b)**: rising *R*-curve. Drawings by E. Jud, for class notes of A. Mortensen, EPFL.

The stability of crack propagation is highly dependent on the loading conditions. In load control, instability occurs earlier such that *R*-curve determination is limited to its initial part. In displacement control, one could in theory achieve fully stable crack propagation and hence measure the whole *R*-curve if the loading structure exhibited infinite stiffness (or, equivalently, zero compliance). In reality however, loading machines do have a finite compliance and pure displacement control does not exist such that the point of fracture instability lies somewhere between the extremes of pure load and pure displacement control.

There are many effects responsible for *R*-curve behaviour. Physically, these involve the occurence of an energy-consuming process in front of the crack. In ceramic materials for instance, microcracking, crack branching or crack bridging are common mechanisms responsible for *R*-curve behaviour. In ductile metallic materials, the main dissipating process is the development of the plastic zone in front of the crack tip, which increases in size as the crack grows, thereby necessating a driving force increase to maintain crack propagation. In this class of materials, LEFM is generally no longer valid and resistance curves must be treated in the context of elastic-plastic fracture mechanics (EPFM), as discussed in the next section.

Ideally, the *R*-curve should represent a material property and not depend on the size and shape of the cracked body. In reality investigations show that the geometry of the component, and thus the stress distribution in the component, affect the shape of the crack growth resistance curve. The situation is even more complex in elastic-plastic fracture meachanics, for which constraint effects during ductile crack propagation influence the *R*-curve.

### *A.1.5 Limitations of LEFM*

LEFM is limited to the treatment of a cracked body in the elastic regime. Plasticity corrections as described in previous section are in some occasions sufficient to account for the effects of nonlinearity, still allowing the use of the stress intensity factor to describe the level of stress in the vicinity of the crack tip. These corrections, however, rely on the satisfaction of a condition known as “small-scale yielding” (SSY) requiring that the zone of non-elastic deformation be contained well within the cracked component, or in other words that the plastic zone size remains small compared to the characteristic dimensions of the specimen: *a* the crack length, *W-a* the uncracked ligament, and *B* the thickness. A common agreement among standard organization to ensure SSY together with plane-strain conditions along most of the crack edge except near the faces is that the specimen thickness be at least 25 times larger than the plane strain plastic zone size; that translates into:

$$a, (W-a), B \geq 2.5\left(\frac{K_I}{\sigma_{ys}}\right)^2 \qquad \text{(A-20)}$$

If condition (A-20) is respected, the measured value of $K_c$ is a material property, $K_c$, that does not depend on the size or geometry of the cracked body. When nonlinear behaviour becomes significant, LEFM and plasticity corrections break down and one must adopt a crack tip parameter that takes elastic-plastic behaviour of materials into account. This is presented in the next section.

## *A.2 Elastic-plastic fracture mechanics (EPFM)*

### *A.2.1 The J-contour integral*

The concept of the *J*-contour integral, introduced by Rice [16] in the fracture community in the 1960s[1], has povided the basis for extending the validity limits of LEFM and has led to the emergence of Elastic-Plastic Fracture Mechanics (EPFM) which is the tool nowadays used to characterize fracture of nonlinear materials. The basic foundation lying behind the *J*-integral is to consider that the stress-strain behaviour of elastic-plastic materials in monotonic loading is identical to that of nonlinear elastic materials, as long as no unloading occurs. With this assumption the deformation theory of plasticity is closely equivalent to nonlinear elasticity. Considering an arbitrary contour around the tip of a crack (Figure A-5a), Rice defined the line path *J*-integral in cartesian coordinates as:

$$J = \oint_{\Gamma}\left(w\mathrm{d}y - T_{\mathrm{i}}\frac{\partial u_{\mathrm{i}}}{\partial x}\mathrm{d}s\right) \qquad \text{(A-21)}$$

where $\Gamma$ is a closed contour around the tip of a stressed solid, $T_{\mathrm{i}}$ are traction vectors perpendicular to $\Gamma$, $u_{\mathrm{i}}$ are displacement vectors, d$s$ is a length increment along the contour $\Gamma$, and $w$ is the strain energy density given by:

$$w = \int_0^{\varepsilon_{\mathrm{ij}}} \sigma_{\mathrm{ij}} d\varepsilon_{\mathrm{ij}} \qquad \text{(A-22)}$$

By invoking the divergence theorem to convert (A-21) into an area integral, Rice then showed that $J = 0$ for any closed contour. The total contour, $\Gamma$ can be further divided into four segements (Figure A-5b) and the total $J$ value is the sum of $J_{\mathrm{i}}$ along each segment: $J = J_{\Gamma 1} + J_{\Gamma 2} + J_{\Gamma 3} + J_{\Gamma 4} = 0$, ( Figure A-5b), where segments $\Gamma_1$ and $\Gamma_2$ are around the crack tip in opposite directions, and segments $\Gamma_3$ and $\Gamma_4$ join $\Gamma_1$ and $\Gamma_2$ along the crack face. For the latter, $T_{\mathrm{i}}$ and d$y = 0$, thus $J_1 = - J_2$, meaning that any path around the crack tip yields the same value of $J$ which is hence path-independent.

---

[1] Path-independent integrals had actually been developed earlier than Rice’s work for similar physical concepts [17, 18].

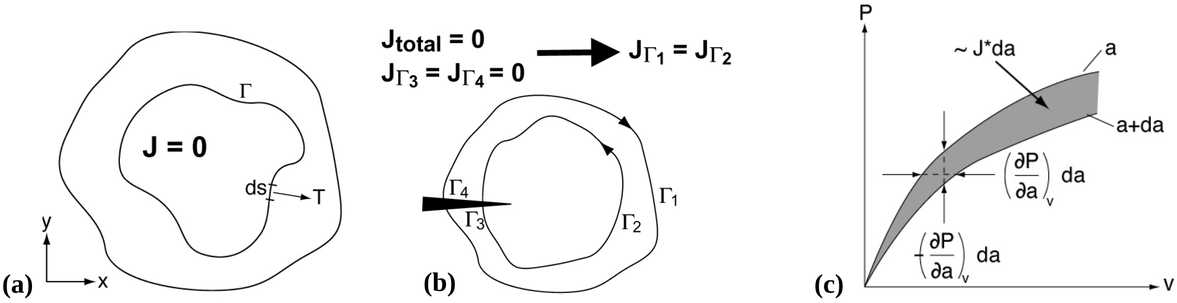

**Figure A-5.** Definition and properties of the *J*-integral. **(a)**: definition of *J* along a closed contour; **(b)**: path-independancy of *J* for any contour around the crack; **(c)**: energy-based definition from load-displacement curves, used for computation of *J*. Drawings by D. Favez, for class notes of A. Mortensen, EPFL.

The second fundamental property of *J* in nonlinear elastic materials is that it is equivalent to the energy release rate *G* in linear materials, namely it represents the energy release rate for nonlinear elastic materials, Figure A-5c. As for *G*, it can be expressed in terms of the rate of change in strain energy stored in the body (d*U)* with increasing crack area and is equivalent –except for the sign– in both load control and displacement control:

$$J = \left(\frac{1}{B}\frac{\mathrm{d}U}{\mathrm{d}a}\right)_P = \int_0^P \left(\frac{\partial V}{\partial a}\right)_P \mathrm{d}P \quad \text{in load control}$$

$$J = \left(-\frac{1}{B}\frac{\mathrm{d}U}{\mathrm{d}a}\right)_V = \int_0^V \left(\frac{\partial P}{\partial a}\right)_V \mathrm{d}V \quad \text{in displacement control} \qquad \text{(A-23)}$$

The above energy-based definition is useful in that it provides the basis for the evaluation of *J* from the experimental load-deflection record for a cracked specimen. Also, one should mention that *J* is a generalization of *G* and for the special case of a linear elastic material, $J = G$. In small-scale yielding, *J* is hence also uniquely related to *K* through the relation $J = G = K^2/E'$. Applying *J* to elastic-plastic materials in the same way as *G* for linear elastic materials (*i.e.* to think of the criterion for initiation of crack growth as an extension of Griffith’s energy-balance criteria) is, nevertheless, incorrect: crack advance in elastic-plastic materials involves elastic unloading and nonproportional loading in the vicinity of the crack tip, and neither is adequately modeled by deformation theory. In a growing crack, *J* is related to the difference in energy absorbed by specimens of different crack lengths. It can, however, still be used as a unique measure of near-tip fracture events under certain restrictions, a situation called “*J*-dominance“ that is summarized later.

### *A.2.2 J as a stress intensity parameter: the HRR field*

Similar to the LEFM case where crack tip fields are uniquely described by the factor *K*, an equivalent description exists in nonlinear materials where *J* characterizes crack tip conditions in this case. This was independently shown by Hutchinson [19] and Rice and Rosengren [20] who each assumed in their analysis that the uniaxial stress-strain behaviour of elastic-plastic materials follows the Ramberg-Osgood power-law relation:

$$\frac{\varepsilon}{\varepsilon_0} = \frac{\sigma}{\sigma_0} + \alpha\left(\frac{\sigma}{\sigma_0}\right)^n \qquad \text{(A-24)}$$

where $\sigma_0$ is a reference stress value usually taken equal to the yield strength, $\varepsilon_0 = \sigma_0/E$, $\alpha$ is a dimensionless constant traditionnally taken as 3/7, and $n$ is the strain hardening exponent. The relationships between $J$ and the crack-tip stress, strain, and displacement fields, are the so-called HRR fields and take the following form:

$$\begin{aligned} \sigma_{\mathrm{ij}} &= \sigma_0 \cdot \left( \frac{J}{\alpha \sigma_0 \varepsilon_0 I_{\mathrm{n}} r} \right)^{\frac{1}{n+1}} \cdot \tilde{\sigma}_{\mathrm{ij}}(\theta, n) \\ \varepsilon_{\mathrm{ij}} &= \alpha \sigma_0 \cdot \left( \frac{J}{\alpha \sigma_0 \varepsilon_0 I_{\mathrm{n}} r} \right)^{\frac{n}{n+1}} \cdot \tilde{\varepsilon}_{\mathrm{ij}}(\theta, n) \\ u_{\mathrm{i}} &= \frac{J}{I_{\mathrm{n}} \sigma_0} \cdot \left( \frac{\alpha \sigma_0 \varepsilon_0 I_{\mathrm{n}} r}{J} \right)^{\frac{1}{n+1}} \cdot \tilde{u}_{\mathrm{i}}(\theta, n) \end{aligned} \qquad \text{(A-25)}$$

where $\tilde{\sigma}_{\mathrm{ij}}(\theta, n)$, $\tilde{\varepsilon}_{\mathrm{ij}}(\theta, n)$, and $\tilde{u}_{\mathrm{ij}}(\theta, n)$ are dimensionless functions of $n$ and $\theta$ that are obtained numerically, and $I_{\mathrm{n}}$ is a integration constant that depends on $n$. This is an important result in that it establishes $J$ as a stress amplitude parameter within the plastic zone, where LEFM is invalid; thus $J$ completely describes the conditions within and also outside the plastic zone. Compared to a linear elastic field where stresses vary as $1/\sqrt{r}$, in a power law material there is a $r^{(-1/n+1)}$ stress singularity, a $r^{(-n/n+1)}$ strain singularity, and a $r^{(1/n+1)}$ displacement singularity. Also, the HRR solution indicates that the stresses in the plastic zone are higher in plane strain that in plane stress (while the linear elastic solution field predicts identical stresses) which provides a theoretical explanation for observed fracture toughness dependence with the thickness.

### *A.2.3 CTOD and equivalence with J*

A different approach (that was actually developped prior to the *J*-integral concept) to define toughness was proposed by Wells [21] and is called the Crack Tip Opening Displacement (CTOD). This concept is based on the observation that prior to crack propagation, an initially sharp crack is blunted by plastic deformation. This in turn leads to relative movement of crack faces prior to fracture and the amount of blunting increases in proportion to the toughness of the material. It was later found that the critical value of CTOD, $\delta$, at which fracture occurs is uniquely related to $J$ [22] and that the fracture toughness of a material can be equivalently quantified by a critical value of $J$ or CTOD.

The analytical proof of the *J-CTOD* relationship in EPFM was made by evaluating the displacement at the crack tip with the HRR solution and by invoking a definition of CTOD based on the intersection of a 90° vertex with the crack flanks. $\delta$ is by definition simply twice the $y$-direction component of the displacement field at that point and the final relation between $\delta$ and $J$ is:

$$\delta = \frac{d_{\mathrm{n}} \cdot J}{\sigma_0} \qquad \text{(A-26)}$$

where $d_{\mathrm{n}}$ is a dimensionless parameter which exhibits a dependence on the strain hardening exponent, $n$ and on the combination of factors of the Ramberg-Osgood equation, $\alpha(\sigma_0/E)$. The $d_{\mathrm{n}}$ values are obtained numerically and are tabulated in various references. In SSY, $\delta$ is calculated using the strip yield model and both approaches agree for a nonhardening material ($n = \infty$).

To measure the CTOD, the displacement $V$ is measured at the crack mouth and the CTOD is calculated by assuming that the specimen halves rotate about a hinge point defined by the cracked specimen geometry. The displacement is further separated into elastic and plastic components: $\delta = \delta_{el} + \delta_{pl}$ where the elastic component $\delta_{\mathrm{el}}$ is a function of the elastic stress intensity factor and of the yield strength while the plastic component $\delta_{\mathrm{pl}}$ is inferred from the plastic displacement of the crack mouth and from a plastic rotational factor, $r_{\mathrm{p}}$.

### A.2.4 $J_{\mathrm{Ic}}$ and the crack growth resistance curves (J-R curve)

In many ductile, tough materials, catastrophic failure at a particular value of $J$ does not exist. There is rather an $R$-curve behaviour due to the developpement of a plastic zone in front of the crack tip and $J$ can be used in a way that generalizes the concept of resistance curve analysis in small-scale yielding: for a crack to advance, the applied $J$ associated with the current crack length and carried load must be equal to the resistance to fracture of the material, $J_{\mathrm{R}}$:

$$J = J_{\mathrm{R}}(\Delta a) \tag{A-27}$$

Such curves generated in elastic-plastic materials are called *J-R* curves and give a description of the fracture behaviour of ductile materials. The computation of *J-R* as a function of crack advance $\Delta a$ is based on the energy definition of $J$ and is obtained from experimental knowledge of the specimen load-displacement curve. Generally, the latter is split into an elastic and a plastic part, with corresponding strain energies, $U_{\mathrm{e}}$ and $U_{\mathrm{p}}$, and the value of $J$ is likewise split into an elastic and plastic part, $J_{\mathrm{e}}$ and $J_{\mathrm{p}}$, such that the total $J$ writes:

$$J = J_{\mathrm{e}} + J_{\mathrm{p}} = \frac{K_{\mathrm{I}}^2}{E'} + \frac{\eta_{\mathrm{p}} U_{\mathrm{p}}}{Bb} \tag{A-28}$$

where $K_{\mathrm{I}}$ is the elastic stress intensity factor, $b$ is the current ligament length (= $W$ - a), $U_{\mathrm{p}}$ is the plastic strain energy (*i.e.* the plastic area under the load-displacement curve), and $\eta_{\mathrm{p}}$ is the so-called $\eta$ plastic factor which depends only on geometry and on the material, for which solutions are available for a wide range of test specimens. Since the load-displacement curve in the deformation theory and (A-28) depend on crack size, calculation of $J$ is performed incrementally and also requires the determination of crack length at various intervals during a fracture test. Commonly, crack growth is monitored from the variation in specimen compliance, or using the potential drop method, which involves application of a current to the specimen and measurement of its potential as the crack grows. Additional details on laboratory measurement of $J$ are presented in Chapter 3, devoted to experimental procedures.

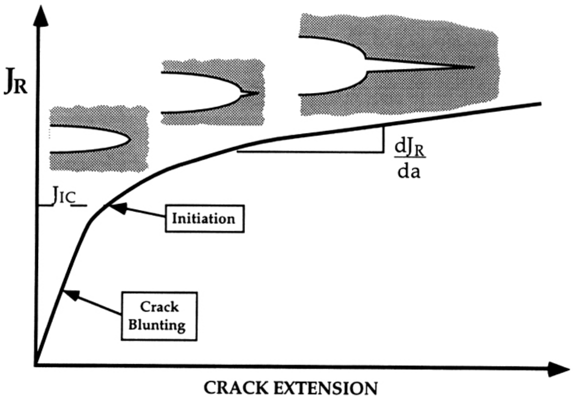

**Figure A-6.** Schematic $J$ resistance curve for a ductile material, from [3]. $J_{\mathrm{Ic}}$ is the value at initiation which is defined in the standard as the intersection of the *J-R* curve with a 0.2 mm offset line.

The *J-R* curve contains essential information about the fracture behaviour of ductile materials. The first parameter is $J_{\mathrm{Ic}}$[1] which corresponds to the critical value of *J* at which the initiation of crack growth occurs (see on Figure A-6). The determination of $J_{\mathrm{Ic}}$ is somewhat arbitrary (and has led to many controversies in the fracture community) in that it involves a definition of what constitutes the onset of crack growth on the *J-R* curve. The choice of the intersection of the *J-R* curve and a 0.2 mm offset line (corresponding to crack blunting) has now been adopted by most standard organisations and was mainly based on many investigations conducted on steels; but it is to be emphasized that it is not based on fundamental physical arguments and there is no reason that this criterion has a meaning in terms of initiation of crack growth for different classes of materials. Since *J* is equivalent to *G* under small-scale yielding conditions, $J_{\mathrm{Ic}}$ is thus a measure of fracture toughness in SSY and is related to $K_{\mathrm{Ic}}$ by:

$$J_{\mathrm{Ic}} = \frac{K_{\mathrm{Ic}}}{E'} \quad \text{under small scale yielding (SSY)} \qquad \text{(A-29)}$$

and has an important practical importance because size specification is much less stringent with $J_{\mathrm{Ic}}$ testing than with $K_{\mathrm{Ic}}$ testing, as presented in the next section.

The second parameter obtained from *J-R* curves is the tearing modulus, introduced by Paris. It is derived from the slope of the *J-R* curve and represents the dimensionless resistance to ductile tearing:

$$T_{\mathrm{R}} = \frac{E}{\sigma_0^2}\frac{\mathrm{d}J_{\mathrm{R}}}{\mathrm{d}a} \qquad \text{(A-30)}$$

Stability of crack propagation is then expressed in terms of the tearing modulus. The condition for stable crack growth is that $T_{\mathrm{app}} \leq T_{\mathrm{R}}$ where $T_{\mathrm{app}}$ is the applied tearing modulus; unstable crack propagation arises if $T_{\mathrm{app}} > T_{\mathrm{R}}$. As in LEFM, displacement control is more stable than load control, but the former is never fully achieved in experimental testing.

### *A.2.5 Limitations of EPFM and recent developments*

Ideally, *J* and more generally *J-R* curves should represent a material property that uniquely characterize crack tip conditions. In reality, there are limitations that one should always have in mind when applying *J*-integral based EPFM to situations when there is excessive plasticity or significant crack growth.

#### i. *J*-controlled fracture

In a stationary crack, *J* can be regarded as a measure of the intensity of the crack-tip singularity fields under the condition that the large strain region in which the microscopic failure process occurs (the fracture process zone) is well contained within the small strain region dominated by the singularity fields, Figure A-7a. Thus, as in LEFM where *K* uniquely characterizes the crack tip condition despite the fact that the elastic singularity vanishes in the plastic zone, *J* also uniquely describes the crack tip conditions even though the singularity is invalid in the large strain region. When the size of the large (finite) strain region becomes significant relative to a characteristic dimension of the structure *L*, (typically, the uncracked ligament length), single-parameter fracture mechanics is invalid and *J* values exhibit a size and geometry dependence; this is the large scale yielding case (LSY). This is the reason why deeply cracked geometries loaded in bending are preferentially used in laboratory testing because such specimens maintain a high degree of triaxiality even in the presence of significant plasticity, therefore retarding the appearance of LSY. FEM computations have been used to define validity criteria in EPFM. For bending-type specimens one finds that plane strain conditions dominate if the following size requirements are met:

---

[1] *J-R* curves were initially developped only as a means of better determining $J_{\mathrm{Ic}}$ by using the curve to extrapolate back to $\Delta a = 0$; it was later considered as a material-based property.

$$B, b_0 \geq 25 \frac{J_\mathrm{Q}}{\sigma_\mathrm{y}} \tag{A-31}$$

where $B$ is the specimen thickness, $b_0$ is the initial ligament length, $\sigma_\mathrm{y}$ is the flow stress taken as the average of the yield and tensile strength, and $J_\mathrm{Q}$ is the temporary value of $J$ at initiation. If (A-31) together with some other secondary criteria are satisfied, then $J_\mathrm{Q} = J_\mathrm{Ic}$. As compared to minimum specimen dimensions in LEFM given by (A-20), these conditions are much less restrictive in EPFM, by about one to two orders of magnitude.

### ii. *J*-controlled crack growth

For a growing crack, Figure A-7b, there is an additional issue because the material behind the crack tip has unloaded elastically and this region violates the assumptions of deformation plasticity. In addition, the zone directly ahead of the crack tip is strongly non-proportionally loaded and therefore violates the single-parameter description. Hutchinson and Paris [23] have proposed that *J-R* still provides a unique description of the crack tip if the region within which deformation theory breaks down is well within the zone of dominance. If we denote the crack extension region by $\Delta a$, the region size in which nonproportional plastic loading occurs by $l$, and the region controlled by the HRR solution by $R$, valid application of $J$ requires that:

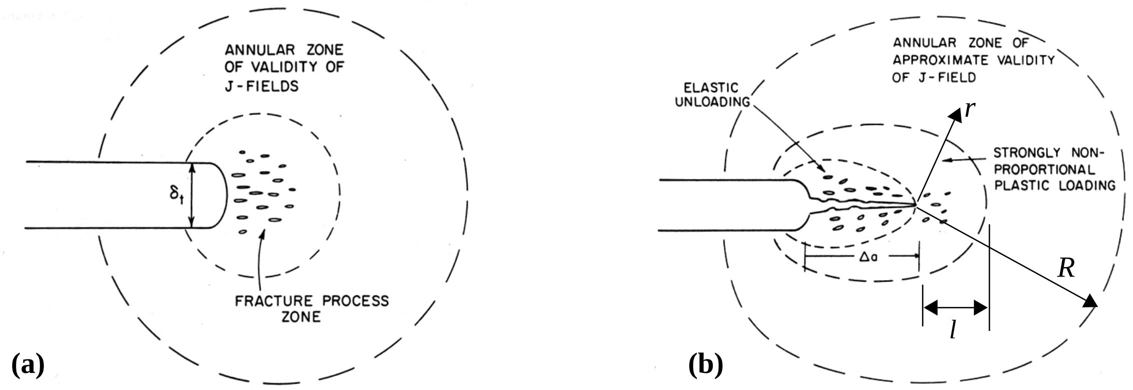
ANNULAR ZONE OF VALIDITY OF J-FIELDS
$\delta_t$
FRACTURE PROCESS ZONE
(a)
ANNULAR ZONE OF APPROXIMATE VALIDITY OF J-FIELD
ELASTIC UNLOADING
r
STRONGLY NON-PROPORTIONAL PLASTIC LOADING
Δa
R
l
(b)

**Figure A-7.** Schematic of near-tip behaviour of *J*-dominance conditions for **(a)**: a stationary crack; and **(b)**: a growing crack. *J* dominates in the annular zone $l << r < R$. From [24].

$$\Delta a << R \quad \text{and} \quad l < R \tag{A-32}$$

A material-based length quantity is further introduced:

$$\frac{1}{D} = \frac{\mathrm{d}J_\mathrm{R}}{\mathrm{d}a} \frac{1}{J_\mathrm{R}} \tag{A-33}$$

and it can be readily shown that condition (A-32) becomes: $D << r < R$ , namely that there exists an annular zone of radius $r$ in which plastic loading is predominantly proportional. Adding the fact that $R$ is a fraction of the uncracked ligament under fully yielded conditions, the final condition for the *J*-analysis to remain valid after crack growth by $\Delta a$ is that:

$$\omega \equiv \frac{b}{J_\mathrm{R}} \frac{\mathrm{d}J_\mathrm{R}}{\mathrm{d}\Delta a} > 10 \tag{A-34}$$

where $\omega$ is a nondimensional parameter which depends on specimen configuration. Its minimum value of 10 to 15 is typical for bend and compact tension specimens. In the range where condition (A-34) is fulfilled, *J-R* curves appear to be geometry-independent and are therefore considered to be a material property. In the standard [25], this condition translates into an allowed crack extension relative to specimen size of:

$$\Delta a_\mathrm{max} \le 0.10 b_0 \tag{A-35}$$

while the maximum value of $J$ allowed, $J_\mathrm{max}$, is:

$$B, b_0 \ge 20 \frac{J_\mathrm{max}}{\sigma_\mathrm{y}} \tag{A-36}$$

Outside this range, *J*-dominance is lost; the stress fields are no longer described by $J$ and the HRR field, and the *J-R* curve becomes dependent on the specimen geometry, more exactly on constraint, which can somehow be seen as the ability of the specimen to maintain *J*-dominance for large amounts of plastic yielding.

### iii. Two-Parameter Approaches

Extending fracture mechanics theory beyond the limits of the single-parameter description has led to two-parameter approaches, which can be used to approximate crack tip fields for the full range of constraint. In the *J-Q* theory [26, 27], the elastic-plastic crack tip field is described by the following representation:

$$\sigma_{ij} = \sigma_{ref} + Q\sigma_0\delta_{ij} \tag{A-37}$$

$\sigma_\mathrm{ref}$ is a high-constraint reference field that may be taken as the HRR field or is more generally determined from a numerical analysis. $Q$, which must be determined numerically, is a constraint parameter which quantifies the deviation from the reference field. It is a hydrostatic stress related to the stress triaxiality at the crack tip. Therefore fracture is characterized by the two parameters $J$ and $Q$, and is no longer viewed as governed by a single scalar value: the critical $J$ value depends on $Q$ and hence $J_\mathrm{c}$(Q) curves describe failure for a given material:

$$J_\mathrm{c} = J_\mathrm{c}(Q) \tag{A-38}$$

Another two-parameter approach [28] is based on the elastic $T$ stress: in the elastic material, the solution of the crack tip stress fields is not only the $1/\sqrt{r}$ singularity, equation (A-6), but is actually described by a power series where the leading term is proportionnal to $1/\sqrt{r}$. The second term is constant with $r$ and can have a profound influence on the plastic zone and the stresses deep inside the plastic zone. The elastic solution then becomes, (in mode I loading):

$$\sigma_\mathrm{ij} = \frac{K_\mathrm{I}}{\sqrt{2\pi r}} f_\mathrm{ij}(\theta) + T\delta_\mathrm{1i}\delta_\mathrm{1j} \tag{A-39}$$

*T* is simply a characterizing parameter that ranks the constraint of different geometries. The advantage of the *T* stress approach is that it is an elastic parameter that can be obtained relatively easily and scales linearly with load. As for the *J*-*Q* theory, fracture can then be described in terms of *J* and *T*. However, the fact that it is an elastic parameter brings limitations in that it has no physical meaning under fully plastic conditions.

### iv. Energy-Dissipation Rate

Ductile tearing has been (and still is) a controversial topic in the fracture mechanics community, because its dependence on constraint limits its use as a material parameter. This has raised the question of whether the rising *J*-*R* curve is a reasonable measure of toughness in the fully-plastic regime during stable crack growth or whether some other measure should be adopted. A energetics based approach that has first been proposed by Turner [29] and which has gained growing attention in the past years is the "energy dissipation rate", because some authors recognized that it provides a better physical understanding of ductile tearing resistance [30-34]. The energy dissipation rate approach is based on an energy balance during stable crack growth. When loading a two-dimensional cracked component of thickness *B*, an increment of work d*U* is transmitted to the cracked body. If no growth occurs, d*U* is given by:

$$\mathrm{d}U = \mathrm{d}w_{\mathrm{el}} + \mathrm{d}w_{\mathrm{pl}} \qquad \text{(A-40)}$$

where $\mathrm{d}w_{\mathrm{el}}$ is the internal elastic energy which is recoverable if the body is unloaded and $\mathrm{d}w_{\mathrm{pl}}$ is the irrecoverable component of energy spent in creating the plastic zone. When crack growth occurs by an increment d*a*, d*U* becomes:

$$\mathrm{d}U = \mathrm{d}w_{\mathrm{el}} + \mathrm{d}w_{\mathrm{pl}} + \mathrm{d}\Gamma \qquad \text{(A-41)}$$

where $\mathrm{d}\Gamma$ denotes the increment of work associated with creation of a fracture surface and is given by: $\mathrm{d}\Gamma = 2B\gamma_{\mathrm{pl}}\mathrm{d}a$ [1]. In the ductile fracture case, involving ductile tearing by void growth, it is a plastic energy, different from $\mathrm{d}w_{\mathrm{pl}}$, which is the plastic work spent remote from the fracture surface. Dividing (A-41) by the increment of crack area, *B*d*a*, and rearranging leads to:

$$\frac{1}{B}\frac{\mathrm{d}(U - w_{\mathrm{el}})}{\mathrm{d}a} = \frac{1}{B}\frac{\mathrm{d}(w_{\mathrm{pl}} + \Gamma)}{\mathrm{d}a} = 2\gamma_{\mathrm{pl}} + \frac{1}{B}\frac{\mathrm{d}(A \cdot w_{\mathrm{A}})}{\mathrm{d}a} \qquad \text{(A-42)}$$

where *A* is the size of the plastic zone and $W_{\mathrm{a}}$ is the energy dissipated in the plastic zone per unit area. The right-hand side of this equation is called the energy dissipation rate, *D*. It is the total resistance of the body against crack growth due to both fracture and plasticity. It is called so because it contains all non-recoverable mechanical energy. The left-hand side is the crack driving force, *C*. It is the energy per unit area available to drive the crack and all plastic deformation associated with it. For stable crack growth to occur, the condition thus writes:

$$C = D \qquad \text{(A-43)}$$

The main physical argument behind this approach is the use of rate equations, viewed as more consistent with the incremental theory of plasticity: indeed in the conventional experimental determination of *J-R* curves, the expression of *J* after crack growth as given by (A-28) can be rewritten in the following form:

---

[1] $\Gamma$ actually contains a component related to the specific surface energy $\Gamma_{\mathrm{s}} = 2B\gamma_{\mathrm{s}}\mathrm{d}a$ , and a component related to plastic energy for the voiding process $\Gamma_{\mathrm{pl}} = 2B\gamma_{\mathrm{pl}}\mathrm{d}a$ . Because the latter is one or more orders of magnitude larger, the former can be neglected. Further details about $\gamma_{\mathrm{pl}}$ are given in Section 2.6.

$$J_R = J_i + \left(\frac{\mathrm{d}J}{\mathrm{d}a}\right) \cdot \delta a = J_i + \sum f\left\{\left[\frac{1}{B}\frac{\mathrm{d}\left(\eta_p U_p\right)}{\mathrm{d}a}\right] \cdot \delta a\right\} \tag{A-44}$$

such that as pointed out by Turner and Kolednik, the d/d*a* rate meaning is destroyed, leading to the fact that *J-R* gives a normalized cumulative work as the measure of crack growth resistance. Thus after initiation and the range of *J*-dominance, (for which they are a correct description), *J-R* curves increase with crack extension even for a constant *R* since work continues to be naturally absorbed in the specimen, hence giving an explanation for the specimen geometry dependence of *J-R* curves [30, 35]. On the other hand, the work rate as described by *D* decreases in the fully plastic case and is simply the increment of work per unit area of growth. Clear examples and physical explanations of these effects have been given in [36].

Much of the analysis of ductile tearing is, however, nowadays examined in terms of *J-R* curves. The energy dissipation rate can in principle still be used because there exists a relation between the two quantities, derived in [37]:

$$D = \frac{W-a}{\eta_p} \cdot \frac{\mathrm{d}J_p}{\mathrm{d}a} + J_p \frac{\gamma}{\eta} \tag{A-45}$$

where $J_p$ is the plastic component of *J* in (A-28), $\eta_p$ is a plastic factor depending on the specimen geometry and $\gamma$ is also a function of specimen geometry. As mentioned in [30], dissipation rate will probably not replace *J* as a tearing quantity, but it can rather be seen as a complementary tool which is moreover easily re-evaluated from existing *J-R* test records, using (A-45).

# APPENDIX B. PRE-CRACKING CONDITIONS

**Table B-1.** Typical fatigue cycling conditions for pre-cracking of CT specimens.

| Composite | Specimen type | $P_{max}$ [kN] | $P_{min}$ [kN] | $K_{max,init}$ [$MPa \cdot m^{1/2}$] | $K_{min,init}$ [$MPa \cdot m^{1/2}$] | Number of cycles | Δa surface [mm] |
|---|---|---|---|---|---|---|---|
| **$Al/Al_2O_3$ angular composites** | | | | | | | |
| A-A35a | flat 13 mm | 1.6 | 0.16 | 6.3 | 0.63 | 20’000 | 0.23 / 0.26 |
| | | 1.6 | 0.16 | | | 20’000 | 0.72 / 0.79 |
| | | 1.6 | 0.16 | | | 10’000 | 1.30 / 1.10 |
| | side-grooved 10.4 mm | 1.6 | 0.16 | 7.1 | 0.71 | 15’000 | 1.17 / 1.53 |
| | | 1.4 | 0.16 | | | 10’000 | 1.5 / 1.8 |
| | | 1.4 | 0.14 | | | 10’000 | 1.5 / 2.1 |
| A-A20a | flat | 1.4 | 0.14 | 5.7 | 0.57 | 20’000 | 0.3 / - |
| | | | | | | 20’000 | 1.8 / 2 |
| A-A10a | flat | 1.7 | 0.17 | 6.7 | 0.67 | 20’000 | - / - |
| | | 1.7 | 0.17 | | | 20’000 | 0.2 / 0.4 |
| | | 1.7 | 0.17 | | | 20’000 | 0.3 / 0.6 |
| | | 1.7 | 0.17 | | | 20’000 | 0.4 / 1 |
| | side-grooved | 1.6 | 0.16 | 7.3 | 0.73 | 20’000 | - / - |
| | | 1.4 | 0.14 | | | 20’000 | 0.8 / 0.7 |
| | | 1.4 | 0.14 | | | 40’000 | 1.26 / 1.39 |
| A-A5a | flat | 1.8 | 0.18 | 7.1 | 0.71 | 30’000 | - / - |
| | | 2.0 | 0.20 | | | 20’000 | 0.41 / 0.23 |
| | | 2.0 | 0.20 | | | 20’000 | 0.74 / 1.01 |
| | side-grooved | 1.8 | 0.18 | 8.0 | 0.80 | 20’000 | 0.89 / 0.56 |
| | | 1.6 | 0.16 | | | 20’000 | 1.13 / 1.04 |
| | | 1.4 | 0.14 | | | 10’000 | 1.43 / 1.18 |
| **$Al/Al_2O_3$ polygonal composites** | | | | | | | |
| A-A25p | flat | 2.2 | 0.22 | 8.7 | 0.87 | 20’000 | 0.81 / 0.66 |
| | | 2.0 | 0.20 | | | 20’000 | 2.12 / 2.46 |
| | side-grooved | side-grooved after pre-cracking | | | | | |
| A-A15p | flat | 2.0 | 0.20 | 8.0 | 0.80 | 40’000 | 0.66 / 0.41 |
| | | 1.8 | 0.18 | | | 30’000 | 1.14 / 1.43 |
| | side-grooved | 1.8 | 0.18 | 8.0 | 0.80 | 40’000 | 1.42 / 1.53 |
| | | 1.8 | 0.18 | | | 40’000 | 4.04 / 4.24 |
| A-A5’ | flat | 2.0 | 0.20 | 8.0 | 0.80 | 40’000 | 0.37 / 0.20 |
| | | 2.0 | 0.20 | | | 20’000 | 0.84 / 0.94 |
| | | 2.0 | 0.20 | | | 10’000 | |
| **$Al/B_4C$ composites** | | | | | | | |
| A-B60 | flat | 1.8 | 0.18 | 7.1 | 0.71 | 40’000 | 0.34 / 0.52 |
| | | 1.8 | 0.18 | | | 30’000 | 0.78 / 0.85 |
| | | 1.8 | 0.18 | | | 10’000 | |
| | side-grooved | 1.4 | 0.14 | 5.7 | 0.57 | 40’000 | 0.49 / 0.50 |
| | | 1.4 | 0.14 | | | 20’000 | 1.40 / 1.36 |
| | | 1.4 | 0.14 | | | 20’000 | 1.66 / 1.53 |
| A-B35 | flat | 2.5 | 0.25 | 9.9 | 0.99 | 20’000 | 0.5 / 0.62 |
| | | 2.3 | 0.23 | | | 10’000 | 0.72 / 0.92 |
| | | 2.3 | 0.23 | | | 5000 | 1.2 / 1.04 |
| | side-grooved | 2.2 | 0.22 | 9.7 | 0.97 | 20’000 | 1.92 / 2.4 |
| A-B20 | flat | 2.0 | 0.20 | 8.0 | 0.8 | 40’000 | - / - |
| | | 2.2 | 0.22 | | | 30’000 | 0.71 / 0.79 |
| | | 2.2 | 0.22 | | | 15’000 | 2.23 / 2.55 |
| | side-grooved | 2.0 | 0.20 | 8.9 | 0.89 | 40’000 | 0.44 / 0.26 |
| | | 2.0 | 0.20 | | | 20’000 | 0.60 / 0.35 |
| | | 2.0 | 0.20 | | | 20’000 | 0.99 / 0.55 |
| | | 1.8 | 0.18 | | | 30’000 | |

**Table B-1.** Typical fatigue cycling conditions for pre-cracking of CT specimens.

| **Composite** | **Specimen type** | **$P_{max}$ [kN]** | **$P_{min}$ [kN]** | **$K_{max,init}$ [$MPa \cdot m^{1/2}$]** | **$K_{min,init}$ [$MPa \cdot m^{1/2}$]** | **Number of cycles** | **Δa surface [mm]** |
|---|---|---|---|---|---|---|---|
| A-B10 | flat | 2.5 | 0.25 | 9.9 | 0.99 | 20'000 | - / - |
| | | 2.5 | 0.25 | | | 20'000 | 0.66 / 0.48 |
| | | 2.3 | 0.23 | | | 20'000 | 0.92 / 1.08 |
| | side-grooved | 2.2 | 0.22 | 9.7 | 0.97 | 20'000 | 1.4 / - |
| | | 2.2 | 0.22 | | | 10'000 | 1.6 / 1.7 |
| A-B5 | flat | 2.4 | 0.24 | 9.5 | 0.95 | 50'000 | - / - |
| | | 2.4 | 0.24 | | | 40'000 | 0.44 / 0.73 |
| | side-grooved | 2.2 | 0.22 | 9.7 | 0.97 | 20'000 | - / - |
| | | 2.2 | 0.22 | | | 20'000 | 1.4 / 0.7 |
| | | 2.0 | 0.20 | | | 10'000 | 1.7 / 1.5 |
| **Al-Cu/$Al_2O_3$ angular composites** | | | | | | | **Compliance method** |
| A2C-A60a | flat | 1.8 | 0.18 | 7.1 | 0.71 | 10'000 | |
| | | 1.6 | 0.16 | | | 10'000 | |
| A2C-A35a | flat | 2.0 | 0.2 | 8.0 | 0.8 | 40'000 | |
| | | 2.0 | 0.2 | | | 40'000 | |
| A4-5C-A35a | flat | 2.2 | 0.22 | 8.7 | 0.87 | 40'000 | |
| **Al-Cu/$Al_2O_3$ polygonal composites** | | | | | | | |
| A2C-A15p | flat | 3.2 | 0.32 | 12.7 | 0.127 | 20'000 | |
| | | 3.2 | 0.32 | | | 20'000 | |
| | | 3.2 | 0.32 | | | 10'000 | |
| | | 3.2 | 0.32 | | | 10'000 | |

# APPENDIX C. SOLUBILITY OF BORON IN ALUMINIUM

## C.1 Experimental procedure

The presence of boron in Al/$B_4C$ composites was measured using a SIMS equipped with a time-of-flight (TOF) analyzer of the Laboratory for Chemical Metallurgy (LMCH) at EPFL. Secondary ion mass spectroscopy features a very high mass resolution allowing to detect all the elements including their isotopes with a better qualitative sensibility than electron spectroscopy methods. It can, in addition, analyze all kind of materials including ceramic insulators and does not necessitate a complicating sample preparation. Given its high sensitivity for isotope $B_{11}{}^{+}$, it was therefore considered to be a suitable method to identify the presence of boron in the various phases. The *(60)*A-B60 metallographic sample (same casting as for XRD analysis) was prepared according to the procedures described in (3.2.1) after which its mounting was removed to allow a proper insertion within the SIMS vacuum chamber. The SIMS was operated in the imaging mode, consisting of constructing maps of elements by scanning the zone of interest with finely focused ions beams, using the secondary ions emitted from the sample surface. If operated in the high mass resolution mode, lateral scanning is in the range of 1 µm. In lower mass resolution conditions, however (which was not an issue in our case, the atomic mass of Al and B being quite different), lateral resolution can be improved down to the submicrometer range. The secondary ions boron ($11^+$) and aluminium ($27^+$) were in particular used to construct element maps. Low magnification maps were initially captured, from which regions of interest were observed at a higher magnification. Mass spectra were then acquired to obtain a detailed chemical analysis by focusing the incident ion beam on the zone of interest from the high-magnification maps. Three different zones were more specifically selected: two zones that were unambiguously identified on the images as the matrix and the reinforcement respectively, and an intermediate region corresponding to the interfacial area.

## C.2 Results

The element maps of aluminium and boron obtained for the *(60)*A-B60 composite by secondary ion mass spectroscopy (SIMS) in the imaging mode are shown in Figure C-1. As previously mentioned such pictures were acquired by constructing the elements maps from the secondary ions emitted from the sample surface. The maps constructed with the ion $27^+$ (using more exactly the range of mass 26.8044 - 27.0178 uma) represent the aluminium, while those with the ion $11^+$ (with the range 10.8933-11.1067) illustrate the presence of boron.

The low magnification image with the ion $27^+$ (Figure C-1a) shows unambiguously the aluminium matrix surrounding a region of much less Al concentration. Mapping with the ion 11+ (Figure C-1b) in the same zone reveals the presence of boron in the region of low Al concentration, while boron is not detected in the matrix region (the darker the color, the lower the concentration). Higher magnification maps are given in c and d, and are represented in a “logarithmic” colorimetric scale to obtain a clearer constrast: as the color turns from dark to yellow, the concentration of the mapping element decreases; however the “zero” concentration of the element is represented in black such that a sharp concentration gradient is more explicitely visualized. Comparing the maps of aluminium (Figure C-1c) and boron (Figure C-1d) in the same zone demonstrate clearly the absence of boron in the aluminium matrix.

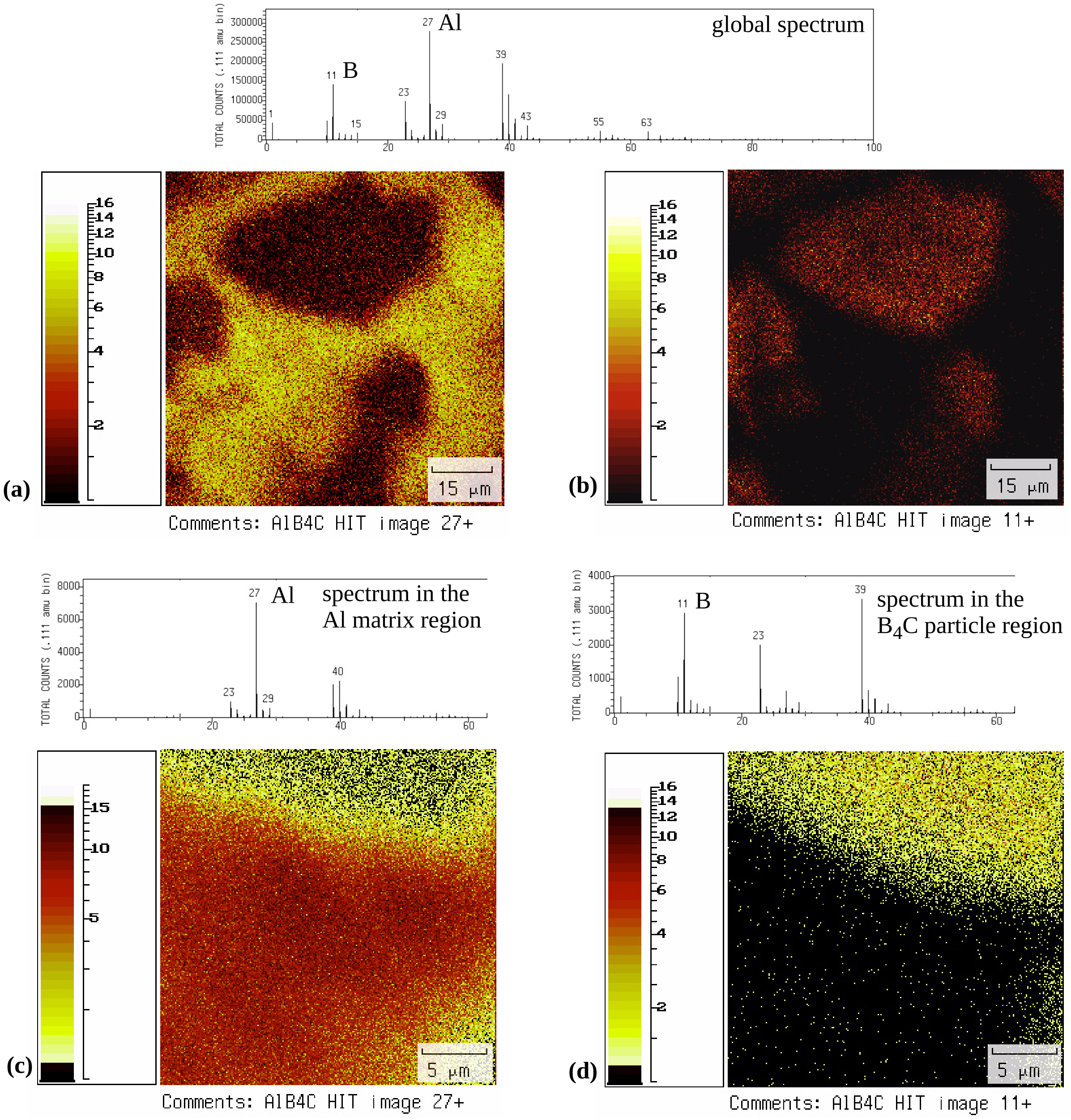

**Figure C-1.** SIMS in the imaging mode of the *(60)*A-B60 composite and related mass spectra. **(a)**: map of the $27^+$uma ions (Al); **(b)**: map of the same region with the $11^+$ uma ions (boron); **(c)**: higher magnification map of the $27^+$ ions, representation in a log scale (zero concentration in dark); **(d)**: same region, map with the $11^+$ ions.

Mass spectra also given in Figure C-1 corroborate the images. In the global spectrum of the region mapped, aluminium and boron are both found; when focussing in the reinforcement region the boron peak appears, while in the matrix region the boron peak is not detected. Given the extremely high mass sensitivity of SIMS, it is confirmed that boron does not dissolve in aluminium and in turn that there should be no matrix by solid solution hardening in Al-$B_4C$ composites.

# BIBLIOGRAPHY OF APPENDICES

1. Kanninen, M.F. and C.H. Popelar, *Advanced Fracture Mechanics*, ed. O.E. Science. 1985, New York, Oxford University Press.
2. Broek, D., *The Practical Use of Fracture Mechanics*. 2nd ed. 1989, Dordrecht, The Netherlands, Kluwer Academic Publishers. 522.
3. Anderson, T.L., *Fracture Mechanics, 2nd Edition*. second ed. 1995, CRC Press.
4. Vinci, L.d., *Codice Atlantico, folio 82 recto-B*. date unknown.
5. Inglis, C.E., *Stresses in a Plate Due to the Presence of Cracks and Sharp Corners.* Transations of the Institute of Naval Architects, 1913, **55**, p. 163-198.
6. Griffith, A.A., *The Phenomena of Rupture and Flow in Solids.* Philosophical Transactions of the Royal Society of London, 1920, **221**, p. 163-198.
7. Rossmanith, H.P., *Fracture Mechanics and Materials Testing: Forgotten Pioneers of the Early 20th Century.* Fatigue and Fracture of Engineering Materials and Structures, 1998, **22**, p. 781-797.
8. Wieghardt, K., *Über das Spalten und Zerreissen Elastischer Körper.* K. Mathematik Physics, 1907, **55**, p. 60-103.
9. Westegaard, H.M., *Bearing Pressures and Crack.* Journal of Applied Mechanics, 1939, **6**, p. 49.53.
10. Sneddon, I.N., *The Distribution of Stress in the Neighbourhood of a Crack in an Elastic Solid.* Proceedings of the Royal Society of London, 1946, **A-187**, p. 229-260.
11. Williams, M.L., *On the Stress Distribution at the Base of a Stationary Crack.* Journal of Applied Mechanics, 1957, **24**, p. 109-114.
12. Tada, H., P.C. Paris, and G.R. Irwin, *The Stress Analysis of Cracks Handbook*. 1985, St. Louis, Paris Production Inc.
13. Fett, T. and D. Munz, *Stress Intensity Factors and Weight Functions*. 1997, Computational Mechanics Publications.
14. Dugdale, D.S., *Yielding of Steel Sheets Containing Slits.* Journal of the Mechanics and Physics of Solids, 1960, **8**, p. 100-104.
15. Barenblatt, G.I., *The Mathematical Theory of Equilibrium Cracks in Brittle Fracture*, in *Advances in Applied Mechanics*. Vol. VIII, 1962, Academic Press. p. 55-129.
16. Rice, J.R., *A Path Independant Integral and the Approximate Analysis of Strain Concentration by Notches and Crack.* Journal of Applied Mechanics, 1969 (June 1968), p. 379-386.
17. Erdogan, F., *Fracture Mechanics.* International Journal of Solids and Structures, 2000, **37**, p. 171-183.
18. Cotterell, B., *The Past, Present and Future of Fracture Mechanics.* Engineering Fracture Mechanics, 2002, **69**, p. 533-553.
19. Hutchinson, J.W., *Single Behaviour at the End of a Tensile Crack in a Hardening Material.* Journal of the Mechanics and Physics of Solids, 1968, **16**, p. 13-31.
20. Rice, J.R. and G.F. Rosengren, *Plane Strain Deformation Near a Crack Tip in a Power Law Hardening Materials.* Journal of the Mechanics and Physics of Solids, 1968, **16**, p. 1-12.
21. Wells, A.A. *Unstable Crack Propagation in Metals: Cleavage and Fast Fracture*. in *Crack Propagation Symphosium*. Proc. Conf., 1961: Cranfield, UK.
22. Shih, C.F., *Relation Between the J-Integral and the Crack Opening Displacement for Stationary and Extending Cracks.* Journal of the Mechanics and Physics of Solids, 1981, **29**, p. 305-326.
23. Hutchinson, J.W. and P.C. Paris, *Stability Analysis of J-Controlled Crack Growth*, in *Elastic-Plastic Fracture, ASTM STP 668*, J.D. Landes, J.A. Begley, and G.A. Clarke, Editors. 1977, ASTM, Atlanta.
24. Hutchinson, J.W., *Fundamentals of the Phenomenological Theory of Nonlinear Fracture Mechanics.* Journal of Applied Mechanics, 1983, **50**, p. 1042-1041.

25. ASTM, *E1737-96: Standard Test Method for J-Integral Characterization of Fracture Toughness*. ASTM Annual Book of Standards. 1996, Philadelphia, American Society for Testing and Materials. 957-980.
26. O'Dowd, N.P. and C.F. Shih, *Family of Crack-Tip Fields Characterized by a Triaxiality Parameter. I: Structure of Fields.* Journal of the Mechanics and Physics of Solids, 1991, **39**, p. 492-502.
27. O'Dowd, N.P. and C.F. Shih, *Family of Crack-Tip Fields Characterized by a Triaxiality Parameter. II: Fracture Applications.* Journal of the Mechanics and Physics of Solids, 1991, **40**, p. 939-963.
28. Hancock, J.W., W.G. Reuter, and D.M. Parks, *Constraint and Toughness Parameterized by T*, in *ASTM STP 1171: Constraints Effects in Fracture*. 1993, American Society for Testing and Materials, Philadelphia. p. 492-502.
29. Turner, C.E. *A Re-Assessment of Ductile Tearing Resistance, Part I: The Geometry dependence of J-R Curves Testing in Fully Plastic Regime. Part II: Energy Dissipation Rate and Associated R-Curves on Normalized Axes*. in *Fracture Behaviour and Design of Materials and Structures, 8th European Conference on Fracture*. Proc. Conf., 1990: Torin, EMAS, Warley; UK.
30. Memhard, D., W. Brocks, and S. Fricke, *Characterization of Ductile Tearing Resistance by Energy Dissipation Rate.* Fatigue and Fracture of Engineering Materials and Structure, 1993, **16** (10), p. 1109-1124.
31. Turner, C.E. and O. Kolednik, *A Micro and Macro Approach to the Energy Dissipation Rate Model of Stable Ductile Crack Growth.* Fatigue and Fracture of Engineering Materials and Structure, 1994, **17** (9), p. 1089-1107.
32. Kolednik, O. and C.E. Turner, *Application of Energy Dissipation Rate Arguments to Ductile Instability.* Fatigue and Fracture of Engineering Materials and Structures, 1994, **17** (10), p. 1129-1145.
33. Sumpter, J.D.G., *An alternative view of R-curve testing.* Engineering Fracture Mechanics, 1999, **64**, p. 161-176.
34. Siegmund, T. and W. Brocks, *The Role of Cohesive Strength and Separation Energy for Modeling of a Ductile Fracture*, in *Fatigue and Fracture Mechanics: 30th Volume, ASTM STP 1360*, P.C. Paris and K.L. Jerina, Editors. 2000, American Society for Testing and Materials, West Conshohocken, Pa, USA. p. 139-151.
35. Brocks, W. and W. Schmitt, *The Second Parameter in J-R Curves: Constraint or Triaxiality*, in *Constraints Effects in Fracture, Theory and Applications: Second Volume (AST STP 1244)*, M. Kirk and A. Bakker, Editors. 1995, ASTM, Philadelphia. p. 209-231.
36. Kolednik, O., *On the Phsical Meaning of the J-Δa Curves.* Engineering Fracture Mechanics, 1991, **38** (6), p. 403-412.
37. Memhard, D. and W. Klemm. *Zusammenhang zwischen Risslaufenergie und J-Risswiderstandskurven*. in *24th Meeting of DWM Working Party on Fracture Events*. Proc. Conf., 1992: Berlin, Germany, Association for Materials Research and Testing.

# Curriculum Vitae

## Ali Miserez

Avenue Dapples 42
1006 Lausanne
Domicile : 021/616 19 03
Bureau : 021/693 29 50
E-mail : ali.miserez@epfl.ch

## Informations personnelles

| | |
|---|---|
| **Date et lieu de naissance** | *le 8 août 1975 à Neuchâtel* |
| **Nationalité** | *Suisse* |
| **Etat civil** | *Célibataire* |

## Formation

| | |
|---|---|
| **Baccalauréat type C**<br>*1991 - 1993* | *Gymnase cantonal de La Chaux-de-Fonds* |
| **Diplôme d'Ingénieur en Science des Matériaux**<br>*1993-1998* | *Ecole Polytechnique Fédérale de Lausanne (EPFL)*<br>*Northwestern University - Department of Materials Science and Engineering - Evanston - USA (travail de diplôme)* |
| **Thèse de Doctorat**<br>*1998 - 2002* | *EPFL - Institut des Matériaux - Laboratoire de Métallurgie Mécanique*<br>Travail de thèse sous la direction du Prof. A. Mortensen<br>Assistant, séances d'exercices et de travaux pratiques |
| **Cours Postgrade en Management de la Technologie**<br>*mars - juin 2002* | *EPFL - Ecole doctorale*<br>"Technology, Innovation and Leadership" (Prof. B Georges, IMD/EPFL) consacré aux stratégies et au management de l'innovation et de la technologie dans des entreprises de haute technologie |

## Expérience professionnelle

| | |
|---|---|
| **Travaux de laboratoire à temps partiel**<br>*1992 - 1997* | *Ingénieurs Chimistes Conseils S.A (ICC SA), La Chaux-de-Fonds*<br>Divers travaux de laboratoire et d'analyse chimique, contrôle de qualité des eaux et expertise de corrosion de métaux |
| **Stage industriel**<br>*février - juin 1997* | *Collaboration entre Galvasol S.A (Le Locle) et le Laboratoire de Métallurgie Chimique de l'EPFL*<br>Projet de semestre en vue d'une application industrielle d'une cellule électrochimique utilisée pour l'optimisation de conditions d'électrodéposition |